Modifying the Antimicrobial Properties of Copper Surfaces by Ultrashort Pulsed Direct Laser Interference Patterning (USP-DLIP)

Dissertation
zur Erlangung des Grades
des Doktors der Ingenieurwissenschaften
der Naturwissenschaftlich-Technischen Fakultät
der Universität des Saarlandes

von

Daniel Wyn Frank Müller

Saarbrücken

2024

Tag des Kolloquiums:	07.07.2025
Dekan:	Prof. Dr.-Ing. Dirk Bähre
Berichterstatter:	Prof. Dr.-Ing. Frank Mücklich
	Prof. Dr.-Ing. Dirk Bähre
	Priv.-Doz. Dr. Ruth Hemmersbach
Vorsitz:	Prof. Dr. Guido Kickelbick
Akad. Mitarbeiter:	Dr.-Ing. Michael Schwarz

„Ein Gelehrter in seinem Laboratorium ist nicht nur ein Techniker; er steht auch vor den Naturgesetzen wie ein Kind vor der Märchenwelt.“

- *Marie Curie*

Table of Contents

Acknowledgements

When I think back to the time when I first arrived in Saarland almost exactly ten years ago, I could never have imagined the rapid development my life would take up to the submission of this thesis. Regardless of my studies, my academic work, but also my private life, these have been the most fruitful and exciting years I have ever experienced. A doctoral thesis is never the work of just one person, but requires a fertile ground of constant support, creative exchange and scientific collaboration in order to mature from the seedling of the first idea to full bloom. I have been very fortunate to have been accompanied on this journey by many people who have supported, encouraged and spurred me on and who have therefore played a significant part in this work. I would like to take this opportunity to thank these dear contemporaries, many of whom I have been able to make friends with:

First and foremost, I express my gratitude to my supervisor, Prof. Dr.-Ing. Frank Mücklich, for enabling me to undertake my doctoral studies at his institution, while allowing me the autonomy to select my own topic. His approach of combining support and trust in the individual abilities of his doctoral students enabled me to grow not only professionally, but also as a person. I am indebted to him for providing me with the invaluable opportunity to spearhead a modest research group already during my doctoral studies and to gain valuable experience in industrial projects, due to his comprehensive support in the development of professional key skills.

I would also like to thank Prof. Dr. Karin Jacobs for assuming the role of my scientific guide and Prof. Dr.-Ing. Dirk Bähre for kindly undertaking the position of the second reviewer of my thesis.

The Chair of Functional Materials has become a second home to me during the time of my doctoral thesis thanks to its warm, friendly and collegial atmosphere. You won't find a working environment like this a second time and I would like to thank all the members of FuWe for the wonderful years we spent together. My special thanks go to my pioneers, drivers, supervisors and mentors Prof. Carsten Gachot, Dr. Philipp Grützmacher, Dr. Leander Reinert, Dr. Christoph Pauly and Dr. Sebastian Suarez, as well as my companions and fellow doctoral students Timothee MacLucas, Tobias Fox, Sarah Lößlein, Aisha Ahmed, Rouven Zimmer, Christian Schäfer, Silas Schütz, Maria Martins, Dr. Pranav Nayak, and Dr. Sebastian Slawik, who have always been at my side with fun, help and advice.

In this context, I would like to express my special gratitude to Prof. Ralf Möller, with whom I had the privilege to share the great enthusiasm of developing and working on the space projects BIOFILMS and Touching Surfaces and friendship. I will always remember our creative exchange and your deeply felt joy in science. My thanks also go to his teams, which particularly addresses Katharina Siems, Stella Timofeev and Carolin Krämer for our great collaboration.

Similarly, I would like to thank the entire team of the former research group of Prof. Silvia Simison at INTEMA in Mar de Plata, Argentina, as well as the research groups led by Prof. Ralf Kautenburger in the Department of Chemistry, Prof .Karin Jacobs in the Department of Physics and Prof. Rolf Müller at the Helmholtz Institute for Pharmaceutical Research for their kind cooperation and the opportunity to benefit from their expertise.

Finally, I want to thank my family - my parents, wife and children – for always supporting me and providing my life with a stable fundament to build upon. My deepest gratitude goes to my beloved wife Milla, whose support, encouragement and love have carried me through every up and down of these turbulent years and provided me with both strength and humbleness at the same time. Thanks to her, these years were not limited to the sole pursuit of academic success, but included the foundation of a wonderful family, as well. It goes without saying that her contribution to this work and my life shines the brightest amongst all.

Zusammenfassung

Bakterien bilden einen fundamentalen Dipol in unserem Alltag. Zum einen unterstützen sie uns in lebenswichtigen Körperprozessen wie der Verdauung, oder bei der Erzeugung von Chemikalien und Medikamenten. Zum anderen kann eine von bakterieller Besiedelung ausgehende Biofilmbildung auf technischen Oberflächen durch Materialerosion oder die Ausbreitung von Infektionskrankheiten ebenso mit hohen gesellschaftlichen und gesundheitlichen Risiken verbunden sein. Die bereits in den Hochkulturen der Antike bekannte antiseptische Wirkung von Kupfer kann hier gezielt zur Dekontamination genutzt werden. Im Rahmen dieser Arbeit wird untersucht, wie Kupferoberflächen durch eine gezielte Funktionalisierung mit ultrakurz gepulster Laserinterferenz hinsichtlich ihrer aktiv antimikrobiellen Eigenschaften weiter optimiert werden können. Dies erfolgt auf topographischer Ebene durch die Erzeugung modifizierter Oberflächenkontaktbedingungen anhand periodischer Strukturen im Größenordnungsbereich einzelner Bakterienzellen. Parallel induzierte prozessbedingte Modifikationen der Oberflächenchemie und dem Gefüge werden zusätzlich bezüglich ihres Einflusses auf die Ausprägung der antimikrobiellen Oberflächeneffizienz betrachtet. Die hierbei erarbeiteten Erkenntnisse erlauben ein vertieftes Verständnis, wie die Bakterien/Oberflächeninteraktion durch komplementäre Oberflächeneigenschaften beeinflusst und zielführend in antimikrobielle Oberflächenkonzepte für Dekontaminationsstrategien integriert werden kann.

Abstract

Bacteria form a fundamental dipole in our everyday lives. On the one hand, they support us in vital body processes such as digestion or can be used in the production of chemicals and medicines. On the other hand, biofilm formation on technical surfaces caused by bacterial colonization can also be associated with high social and health risks due to material erosion or the spread of infectious diseases. The antiseptic effect of copper, already known in the advanced civilizations of antiquity, can be applied in countering decontamination measures. This work investigates how the active antimicrobial properties of copper surfaces can be further optimized by targeted functionalization via ultrashort pulsed laser interference. This is done on a topographical level by generating modified surface contact conditions by applying periodic structures in the size range of individual bacterial cells. Parallelly induced process-related modifications of the surface chemistry and the microstructure are furthermore monitored with regard to their influence on the integrated mechanisms involved in the expression of antimicrobial copper surface efficacy. The insights gained in this work allow for a deeper understanding on how the bacteria/surface interaction can be influenced complementary by functional surface properties and purposefully integrated into antimicrobial surface concepts for decontamination strategies.

Abbreviations and Symbols

α	1/m	Thermal diffusivity / optical absorptivity
AFM	-	Atomic force microscopy
AMR	-	Antimicrobial resistance
$BVMED$	-	Bundesverband Medizintechnik e.V.
c	km/s	Speed of light
$C_{e/l}$	J/m^{3}K^2	Electron / lattice heat capacity (TTM)
$c-di-GMP$	-	intracellular messenger molecule related to biofilm formation
$cAMP$	-	intracellular messenger molecule related to permanent bacterial cell attachment
CFU	1/ml	Colony forming units
CPA	-	Chirped pulse amplification
δ	-	Phase difference
d_{Focus}	mm	Focus diameter
d_L	mm	Seed beam diameter
df	-	Degree of single entity freedom (ERI)
DNA	-	Deoxyribonucleic acid
$DLIP$	-	Direct Laser Interference Patterning
DLR	-	German Aerospace Center
$(X)DLVO$	-	(extended) Derjaguin, Landau, Verwey and Overbeek Theory
DOE	-	Diffractive optical element
E_i	-	E-field
$EBSD$	-	Electron back-scatter diffraction
$ECAP$	-	Equal-channel angular pressing
EDS	-	Energy dispersive X-ray spectroscopy
ERI	-	Engineered roughness index
θ	degree	Single beam incidence angle
f	mm	Focal length
F	J/cm^2	Laser fluence
f_D	%	Valley ratio of surface compartment (ERI)
fs	s	Femtosecond (10^{-15}s)
F_{AB}	N	Forces related to acid-base (hydrophobic/-philic) interactions

F_{abl}	J/cm²	Material specific ablation threshold
F_D	J/cm²	Threshold fluence for specific surface modification
F_E	N	Forces related to electrostatic interaction
F_{LW}	N	Lifshitz-van der Waals forces
F_0	J/cm²	Single pulse ablation threshold
F_N	J/cm²	Ablation threshold after N pulses
F_N	J/cm²	Ablation threshold after N pulses
F_{Total}^{XDLVO}	N	Repulsive or attractive net force according to XDLVO theory
FEM	-	Finite element model (simulation)
FIB	-	Focused ion beam
G	W/m³K	Electron-phonon coupling coefficient (TTM)
GVD	fs²/cm	Group velocity dispersion
$I_{0,i,res}$	W	Laser intensity seed / partial beam / interference modulated
$ICP - MS$	-	Inductively coupled plasma mass spectroscopy
ISS	-	International Space Station
$k_{e/l}$	W/mK	Thermal conductivity electron / lattice system (TTM)
k_i	-	Wave number
l_T	mm	Thermal diffusion length
$LIPSS$	-	Laser induced periodic surface structures
LPS	-	Liposaccharide
$LSFL/HSFL$	-	Low spatial frequency LIPSS / High spatial frequency LIPSS
$(C)LSM$	-	(confocal) Laser scanning microscopy
LTA	-	Lipo-teichoic acid
μG	m/s²	Microgravity
M^2		Beam propagation ratio
MD	-	Molecular dynamics (simulation)
$MRSA$	-	Methicillin-resistant *Staphylococcus aureus*
NIR	-	Near Infrared wavelength spectrum
NP	-	Nano particle(s)
ns	s	Nanosecond (10^{-9}s)
P	µm	Periodicity
PBS	-	Phosphate Buffered Saline
PIA	-	Polysaccharide intercellular adhesion
ps	s	Picosecond (10^{-12}s)

QS	-	Quorum Sensing
r	-	Wenzel´s surface roughness factor
RNA	-	Ribonucleic acid
ROS	-	Reactive oxygen species
$rpoS$	-	Gene related to flagella and curli expression
S	-	Incubation coefficient
SEM	-	Scanning electron microscopy
SP	-	Short pulsed (>10 ps)
SPP	-	Surface plasmon polaritons
STM	-	Scanning tunneling microscopy
$STEM$	-	Scanning transmission electron microscopy
STS	-	Scanning tunneling spectroscopy
$T_{e/l}$	K	Electron / lattice temperature (TTM)
$T4P$	-	Type IV Pili related to surface adhesion and mechano-sensing
TEM	-	Transmission electron microscopy
τ_p	s	Pulse duration
τ_{eq}	s	Electron-phonon relaxation time
TTM	-	Two-temperature model
λ	nm	Laser wavelength
UFG	-	Ultra-fine grained
$USEPA$	-	United States Environmental and Food Protection Agency
USP	-	Ultrashort Pulsed (<10 ps)
$USP-DLIP$	-	Ultrashort Pulsed Direct Laser Interference Patterning
UV	-	Ultraviolet spectrum
VIS	-	Visible spectrum
ω_i	1/s	Circular frequency
w_d	mm	Beam width
WCA	degree	Water contact angle
XPS	-	X-ray photoelectron spectroscopy
x_D	mm	Spot diameter related to specific surface modification via F_D
φ_i	-	(Initial) phase constant
$yggE$	-	Gene related to flagella and curli expression

I | Motivation

Despite major advances in medicine and technology in recent decades, societal challenges remain that have concerned mankind since ancient times. One example is the influence of microorganisms on our daily life, although the knowledge about this is comparatively novel [1]. Without microorganisms such as bacteria, humans would not be able to survive, due to their support in digestion and energy production by breaking down nutrients, as well as the formation of microenvironments that protect us from negative external influences [2]. In turn, microorganisms can also cause great harm by the development of opportunistic pathogenic properties within the wrong environment. This is exemplified by the bacterial species *Escherichia coli* and *Staphylococcus aureus*: Their sub-strains are either part of the natural human microbiome [3], or life-threatening pathogens responsible for a significant proportion of the infectious diseases worldwide [4], solely depending on minor differences in genetic expression.

If microorganisms succeed in colonizing technical or natural surfaces, they tend to form biofilms in order to improve resilience against external impacts and facilitate further spreading. The process of biofilm formation requires a high metabolic activity, which potentially erodes the colonized surface and causes failure of technical structures. In 2019, the economic loss associated with biofilm formation was estimated at more than 4,000 billion USD, of which the majority of over 65% is due to corrosion caused by biofouling [5]. Medical or health care related issues account for about 20% of the costs incurred, while the actual socioeconomic impact, e.g., due to loss of skilled labor, is likely to be even more severe. In addition, biofilm-induced deterioration of technical systems may result in an indirect hazard to humans, which is particularly evident in manned space exploration, where biofilm associated threats for the crew´s health necessitated the replacement of defective equipment on both the Mir and the International Space Station (ISS) [6,7]. According to current knowledge, the vast majority of the microbiome identified on the ISS originates from the microbial flora of human skin and was consequently introduced by the crew into the originally sterile habitat [8]. Health related issues of biofilm formation on technical surfaces in the medical sector include contamination of medical equipment potentially causing implant-related infections (IRI) [9,10] and, above all, the spread of infectious diseases via transfer on contaminated contact surfaces [11]. In conjunction with the prevailing trend of increasing antibiotic resistance in a multitude of pathogenic bacterial strains, this route of infection poses a particular high risk in clinical environments and remote habitats, where patients or inhabitants exhibiting weakened immune capacities may be particularly affected [12,13]. In this context, the BVMED[1] has most recently highlighted the need to counteract with the development of alternative or complementing decontamination measures since the development of novel antibiotics cannot keep pace with current pathogenic adaptation dynamics, whereas Germany is facing an annual death toll of 45,700 cases related to AMR[2]. The prevention of a surface-associated spreading of pathogenic microorganisms - or subsequent treatment/decontamination - is difficult in case of an existing infestation, since bacteria and fungi bound in biofilms are generally less susceptible to external environmental influences, including antimicrobial agents or disinfectants [14]. In this context, biofilm formation or initial colonization as such needs to be prevented to enable a reliable decontamination of technical surfaces, which can be achieved by functional surfaces that exhibit

---

[1] Policy statement of the Bundesverband Medizintechnologie e.V. (BVMED) in September 2023: „Infektionen vermeiden – bewusst handeln: Antimikrobielle Resistenzen (AMR)“

[2] Press release of the Robert Koch-Instituts on 18.10.2022: „Antibiotikaresistenzen, eine schleichende Pandemie: Einweihung des WHO-Kooperationszentrums für Antibiotikaresistenz am RKI“

antimicrobial properties involving contact/growth inhibition or active killing of microorganisms [15–17]. In the best case, these concepts do not require antibiotic agents.

Natural surfaces have developed different strategies to resist infestation by potentially harmful microorganisms over millions of years of evolution. The surfaces of many plants, for example, exhibit topographical structuring in combination with an organic coating that produces water-repellent and thus self-cleaning properties. The lotus effect, named after *Nelumbo nucifera* [18] aims to prevent initial microbial infestation via liquid or solid vehicles, which can also be found on the leaves of European nasturtium, cabbage or tulips. In contrast to this purely passive decontamination strategy, the viability of bacteria is actively reduced on the wings of various *cicada* and *dragonfly* species, which exhibit topographically functionalized surfaces, as well [19]. The needle-shaped asperities found here are one order of magnitude smaller than the bacterial cell size which, in combination with their lateral spacing and high aspect ratio, induces mechanical membrane stress and can rupture the cell wall of adherent bacteria. Following this biomimetic blueprint, similar topographies have been successfully generated on technical surfaces [17]. However, the mechanically induced killing mechanism requires additional attractive forces between bacteria and the surface related to functional surface properties, similar to the lotus effect, and is not necessarily broad-band efficient [20,21].

An inversion of the bactericidal topography effect is observed on engineered surfaces with topographic feature sizes in the scale of single bacterial cells, in turn. A stochastic roughness value in the size range of 1 - 5 µm was described to show increased bacterial retention [22,23], which decreases for roughness values slightly below the bacterial size scale [23]. Here, a direct correlation between retention and the bacterial ability to maximize the contact area to the substrate through attachment within the surface crevices is discussed [22,23]. In the case of roughness values below bacterial size, adhesion predominantly occurs on protruding surface asperities, which greatly reduces contact area and substrate interaction [24–26]. These effects have been observed regardless of whether the topography is formed by random roughness or a deterministic pattern [24–27].

In addition to predominantly topography related decontamination strategies, actively antimicrobial elements and molecule groups in the shape of coatings or as inherent substrate moieties can be used as stand-alone or to complement existing topographic surface concepts. Bacterial cell wall integrity was shown to be similarly affected by antimicrobial peptides [28], reduction of external membrane polarity [29], as well as redox reactions on chemically activated substrate surfaces with decomposing effects on organic molecules [30,31], for example. In the context of decontamination measures, high antimicrobial activity against bacteria has been repeatedly demonstrated for copper (Cu) and silver (Ag) [16,32,33]. In the case of Cu, this extends equally to fungi [34] and viruses [35], which includes the SARS-CoV-2 pathogen of the 2020-2023 Covid-19 pandemic. Records of Cu utilization for the purification of drinking water or wound treatment date back to early advanced civilizations and have been rediscovered repeatedly [36,37]. Thus, in the 18th century, the physician Victor Burq observed an increased resilience of Parisian Cu workers against cholera, which he consequently attributed to the effect of the metal [16]. In fact, Cu is an essential component of the human metabolism and is even used by the body's immune system to fight infections [38–40]. This highlights the metal´s suitability as a biocide in human environment [41] in contrast to Ag, which exhibits toxicity in comparably low accumulated doses [42]. In the same course, the bactericidal effect of the less noble Cu is less dependent on ambient conditions and electrochemical activation [43], which allows a wide scope of application, e.g., in the food industry [44], water treatment [45], functional textiles [46], infection prevention [47], clinical hygiene [48] and implant technologies [49].

When Cu is applied for surface decontamination, certain aspects related to its antimicrobial efficiency must be considered:

- The antimicrobial effect of Cu is directly related to the quantitative release of Cu ions, which should not be compromised in order to maintain high antimicrobial efficacy. A reduction of the Cu content within a given substrate by alloying or oxidation may decrease Cu ion release and thus the antimicrobial efficiency of Cu surfaces [50,51]. In this context, a list of 300 antimicrobial Cu alloys was published in 2008 by the United States Environmental Protection Agency (USEPA), which achieve a microbial deactivation of 99.9% within 2 h, for which their Cu content must not be less than 60% [16]. In the same course, thermal oxidation of the Cu surface was shown to affect its antimicrobial properties by reduced Cu ion release, where the CuO phase exhibits a higher impact compared to Cu_2O [51]. However, the addition of nobler elements can also catalyze the electrochemical dissolution of Cu ions [52].
- A pronounced antimicrobial effect of Cu surfaces is coupled to the direct contact between bacteria and the Cu substrate, which in turn imposes a negative effect on bacterial killing if it is inhibited [53]. This might be related to the suppression of surface passivation when the bacteria reside in proximity to the ion-emitting substrate, which enhances Cu ion release [54], however without claiming to describe the mechanism of action in its entirety [55].
- Although Cu materials have a long history of successful application in microbial decontamination, their universal effectiveness cannot be taken for granted. A reduction in antimicrobial efficacy can occur by triggered bacterial adaptation during sub-lethal exposure over extended periods of time, where Cu resistance might involve both genome regulation and metabolic adaptation [36,56,57]. In the same course, external conditions such as variations in humidity or temperature have been shown to modulate the antimicrobial efficiency of Cu surfaces [32,58].

To enable an efficient application of Cu in antimicrobial measures, it is mandatory to support the mode of action behind the material inherent bactericidal capacities or to supplement it with additional surface functionalization, which can further increase the overall antimicrobial effect. Currently investigated concepts that aim to enhance the antimicrobial properties of Cu include its application in the shape of nanoparticles (NP), coatings, as well as a topographic modification of the substrate surface. In the case of NP, the small particle size targets an increased cell membrane penetration [59,60], whereas recent investigation suggests that the antimicrobial effect of Cu NP actually correlates with quantitative Cu ion release [61]. A significant increase of initial bacterial deactivation was recently achieved by employing a porous Cu substrate design with high surface/volume ratio that effectively increases initial Cu ion release, which is unfortunately forfeited with the onset of chemical surface passivation [62]. The combination of topographic functionalization with the active antimicrobial properties of Cu has recently been achieved in different ways, whereby the surface functionality is mainly based on the mechanically induced bactericidal properties following the surface design of *cicada* and *dragonfly* wings [63–67]. Depending on the implementation of Cu within surface processing, the different concepts rather benefit from the active bactericidal effect of released Cu ions [63,64], or lose it almost completely due to excessive oxide formation, whereby the mechanically driven increase in antimicrobial effectiveness on these surfaces is only short-lived [68,69].

A resilient approach to improve the antimicrobial properties of Cu surfaces with prolonged efficacy must incorporate the material's inherent mechanism of action and its support by bacterial surface interaction. Against this background, this work aims to investigate on how the antimicrobial efficacy of Cu surfaces can be amplified by topographical surface modification in the scale of single bacterial cells. It has previously been shown that bacteria adhere differently on inert surfaces that exhibit periodic surface patterns close to single bacterial cell size [70–73]. Here, laser-based methods such as Direct Laser Interference Patterning (DLIP) stand out, which enable the generation of deterministic topographical surface patterns in the relevant scale between sub- and single-digit µm [74]. However, the extent to which such altered contact conditions affect the antimicrobial efficiency of Cu surfaces has not been demonstrated to this point. Despite promising approaches [75–77], Cu poses an elevated challenge to laser-based surface functionalization that aims to realize both small pattern sizes in the low µm and sub-µm regime as well as the preservation of the material-inherent antimicrobial capacities, due to its high thermal conductivity [78,79] and the process-related formation of CuO [51,77,80]. Recent studies on the physicochemical mechanisms involved in bacterial adhesion furthermore demonstrate that quantitative bacterial surface contact does not solely depend on topography, but rather involves multiple surface properties with a deviating impact on different bacterial species [81–83].

Against this background, optimizing the antimicrobial effect of Cu surfaces through laser-based topographic surface patterning requires a deeper understanding and targeted implementation of the parallelly induced substrate modification. The following section presents a thorough review of the current state of research in the relevant areas that could potentially benefit the targeted application focused on in this thesis.

II | State of the Art

1 | Bacterial Surface Interaction

The ability to adhere and remain in contact either to a technical or natural surface is of high importance for the majority of the bacterial species currently known to mankind. Surfaces can provide both nutrition and anchorage to approaching bacteria, which are both vital to enable reproduction and to develop colonies that further support bacterial viability in a demanding environment [84]. On this behalf, bacteria have a variety of pathways and means to attach to and colonize various surfaces at their disposal. Strategies aimed at reducing bacterial surface burden must consider these mechanisms of bacterial surface attachment and interaction to allow for effective decontamination. Moreover, quantitative antimicrobial efficacy of Cu surfaces is directly linked to the extent of contact between bacteria and the substrate surface based on current understanding [53]. It is therefore obligatory to understand how bacteria interact with surfaces dependent on both bacterial preferences and surface properties to enable a targeted functionalization that focuses to enhance antimicrobial properties of Cu, since it might potentially support or rather weaken the intended effect [20,53]. On this regard, the current state of knowledge on the mechanisms of bacterial surface adhesion and interaction will be briefly summarized in this chapter.

The process of bacterial approach to surfaces up to solid adhesion is divided into three successive phases, as illustrated in **Figure 1** [81,85]: The initial approach in Phase I is impacted by physicochemical interaction processes, such as Brownian molecular motion, Van der Waals and gravitational forces, as well as electrostatic surface charges and flow forces, but might also involve self-motility dependent on the bacterial strain [81]. These driving forces initiate the actual attachment in Phase II where the vicinity between bacterium and substrate enables molecular interaction between the bacterial membrane and surface. In this phase, a rigid substrate contact via surface bonding is pronounced. Phase III comprises the processes that occur after successful attachment, which includes long-term interactions such as proliferation, biofilm formation as well as potential deactivation or killing on active antibacterial surfaces, as targeted in this work [55,85,86].

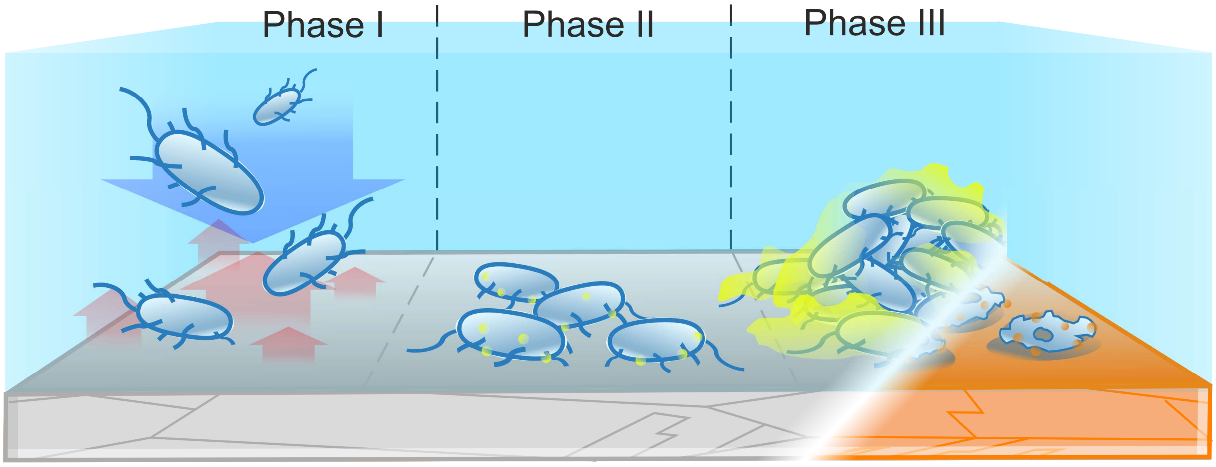

Figure 1: Schematic illustration of the three successive phases of bacterial surface adhesion, where blue/red arrows in Phase I indicate the bacteria/surface related net forces involving rather attractive or repulsive interaction, while the long-term interactions in Phase III after successful solid adhesion might display either biofilm formation (e.g., on stainless steel) or active bacteria deactivation (e.g., on Cu surfaces) dependent on the surface properties. Modified according to [81].

Within a stabilized liquid environment, both bacterial as well as substrate properties govern the actual approach in Phase I as well as the pronunciation of adhesion and long-term interactions in Phase II and

III. Here, the molecular setup of the bacterial membrane as well as the surface chemistry, topography and resulting secondary functional properties like surface wettability of technical surfaces have been shown to impact bacterial/surface interaction [22,81,85,87,88]. Whether and how a solid bacterial adhesion is constituted dependents largely on the mutual suitability of bacteria and surface physiology and chemistry, which will be addressed in individual consideration in the following sections.

1.1 | Bacteriology related to surface interaction

From the bacterial side, forces that directly influence surface approach and consecutive adhesion are directly related to the physicochemical setup of the bacterial surface. The cell membrane itself exhibits a predominantly negative surface polarity that is related to the ionic nature of the biochemical preservation of the membrane integrity. The membrane further contains a multitude of surface molecules and appendages subdivided in classes of, e.g., fimbriae, adhesins, pili, curli and flagella, as schematically illustrated in **Figure 2a**, which are related to sensing, environmental interaction and motility exhibiting differing mechanical properties as well as individual preferential bonding behavior. The surface mesh of functional molecules might expand up to micrometers from the bacterial surface effectively building an orb that enables surface sensing and early-state revertive surface adhesion.

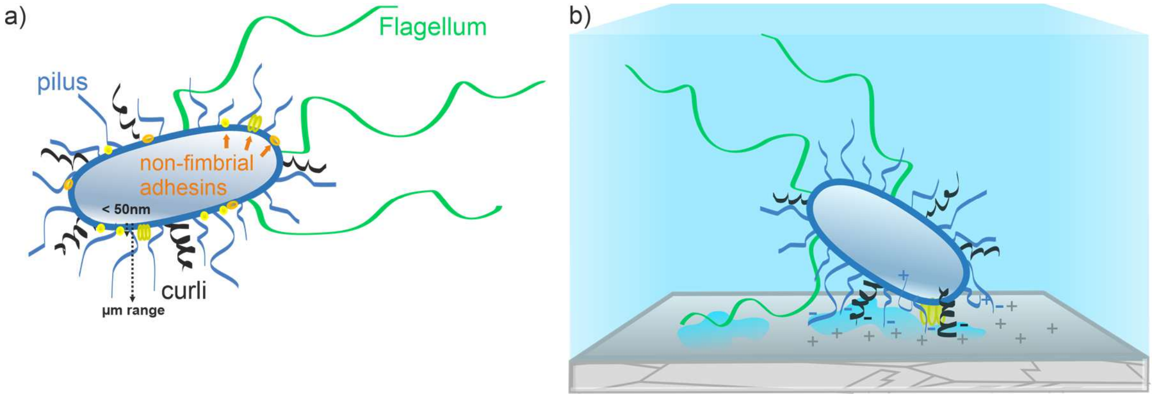

Figure 2: Schematic illustration of: a) The bacterial cell membrane exhibiting various types of appendage classes and adhesins highly involved in surface approach and adhesion which are heterogeneously distributed over the cell body. b) Initial bacteria surface interaction mostly involving extending membrane appendages exploring and adhering to the substrate surface. Surface properties like polar charge, wettability and potentially present conditioning films might induce spatial heterogeneity of rather adhesive or repulsive interaction. Modified according to [81,82].

Surface approach (Phase I)

In a liquid environment multiple factors like, e.g., fluid flow, pH and ionic strength are ruling over the ability of a single bacterial cell to reach and adhere to the surface [89]. External passive forces in bacterial surface approach are fluid drag, Brownian motion and the sedimentation via gravitational forces which are especially important for bacteria without self-motile capabilities [90]. In the vicinity to the surface, shear forces by fluid drag might complicate the ultimate bacterial approach until the flow velocities are decreased by friction within the hydrodynamic boundary layer between fluid and surface. In proximity to the substrate surface, the planktonic bacterial cells become subjected to physicochemical forces, such as van der Waals (always attractive), electrostatic as well as acid–base hydrophobic interaction (both either attractive or repulsive) with decreasing range of action [82]. Whether these forces sum up to rather attractive or repulsive interaction might vary depending on the environment, bacterium and surface chemistries [91]. In case of a weak surface-attachment, adhering cells might as well reverse into planktonic state at this stage within a dynamic liquid environment [81].

Aside of external driving forces, bacteria are able to agitate their surface approach via self-motility. Here, especially flagella but also pili act as bacterial motility provider during approach [92], where flagellar motility has been stated as the most efficient bacterial driving force towards the surface [81]. Directional bacterial motility is driven by the receipt of environmental cues like gradients of chemical signals including nutrition or saline content as well as variations in fluid drag and viscosity, which were shown to trigger bacterial response by modulated flagella rotation rates in *E. coli* and *Pseudomonas aeruginosa* in order to adapt the swimming direction and velocity [93]. In contact to the substrate surface, the flagella of *E. coli* have been shown to act as additional adhesin and can furthermore explore rough surface topographies to improve the bacterial anchorage [94]. Flagella deficient mutants of *E. coli* [94] and several other bacteria strains have in turn been shown to exhibit impaired initial surface attachment. In vicinity to the substrate surface further appendage classes like pili and curli are also involved in nonspecific initial adhesion [92]. A schematic illustration of these early state bonding mechanisms related to membrane appendages is shown in **Figure 2b**.

Permanent attachment (Phase II)

As soon as the substrate contact has been initiated bacteria modify their surface interaction towards an increase of bonding strength to enable permanent attachment. This is governed by chemical and physical rearrangements of both bacteria and the surface potentially including surface conditioning as well as a reorientation of the bacterium for maximum surface contact [90]. Surface sensing was shown to trigger the maturation of the bacterium from planktonic into a sessile phenotype whereas key functions of metabolic behavior related to the strengthening of surface adhesion and colony formation are initiated [82]. How bacteria recognize and respond to surface contact remains mostly unclear, although several mechanisms of surface sensing have been investigated and discussed, so far, that will be summarized in the following.

Advancing planktonic bacterial cell might perceive the vicinity of a substrate surface either by

- changes of environmental physicochemical properties involving osmolarity, ionic strength, pH and the availability of nutrients [81],
- the adhesion of appendages via chemical or mechanical sensing, where, e.g., the flagellum was shown to react on motile containment [95], as well as
- the attachment of the membrane surface itself, perceived by envelope stress.

Multiple different sensing systems have yet been found for *E. coli* that are connected to downstream target gene activation linked to biofilm formation, with an abundancy of redundant systems that might be needed to enable contact to very different surface types [82]. Between these, the sensing of environmental physicochemistry is considered rather unspecific whether liquid bulk or surface changes are perceived. In turn, Mechanical surface sensing involving appendage adhesion as well as external mechanical membrane stress was shown to trigger flagella/curli/pili unfolding and adhesin production [95]. Deficient mutants of *E. coli* lacking type I pili or curli each exhibited decreased surface adhesion properties similar to flagella deficient mutants, which highlights the importance of these macromolecules for initial adhesion [94,96]. Here, pili and curli have been shown to exist in a wide range of varieties (including P-pili and type IV pili) that might be differently expressed even within single strains of *E. coli* [92]. Due to the mostly hydrophobic nature of the individual appendage classes, preferential adhesion can be considered to be highly impacted by surface wettability [81,94].

Surface contact of the actual bacterial cell envelope has been closely linked to electrostatic forces that might either act rather repulsive or attractive depending on the respective surface charge of the cell membrane and substrate surface, where the contact induced membrane stress can be both vital or lethal for biofilm formation [82]. Amplified adhesion forces, e.g., on positively charged surfaces might induce critical membrane stress levels up to rupture, while lower gradients of membrane stress are considered to be involved in contact sensing after identification of biofilm related downstream responses [82,95,97]. Due to the mostly heterogeneous properties of microbial environments on technical surfaces, bacterial interaction related to surface sensing might differ, locally [91].

The role of external mechanical forces that are induced alongside surface interaction have lately been discussed as an important factor in environmental perception and response of several bacterial strains [98]. These forces are sensed via the outer membrane (gram-negative bacteria) or peptidoglycan (gram-positive bacteria) transmitting the mechanical stress to more central core structures like the cytoplasmic membrane, while flagella, pili or curli have been shown to react by elastic deformation or mechano-switching on surface contact. Thus, the membrane appendages provide mechanic feedback by folding and unfolding in contact to substrate surfaces exhibiting spring-like elastic properties (e.g., LapA in *P. fluorescens*) [99]. The strain specific setup of the membrane surface strongly affects the mechanical properties of these proteins, where pili from gram-positive bacteria are found to be stiffer than those of gram-negative bacteria; The membrane protein SasG in *S. aureus* promoting cell-cell adhesion in biofilm formation requires unfolding forces which are 2-10 times higher than those of most other appendages to improve coherence of cell-clusters and biofilms [100]. Under amplified external loads membrane proteins of both *E. coli* and *S. aureus* were found to increase their binding strength to remain adhesion. In several strains, the adhesion-related type IV pili (T4P) was shown to be upregulated after surface contact and promotes surface motility in sessile state by twitching in *P. aeruginosa*, both being triggered by mechanical contact signals and agitated by external drag forces [101].

Surface interaction (Phase III)

Aside from the physical perception of the surface within the initial approach and attachment in Phase I and II, mechanotransduction of external forces into cellular response has further been shown to be directly related to long-term surface interaction in Phase III involving, e.g., the initiating of biofilm formation. Mechanical input, e.g., via T4P pili and flagella from surface contact promotes phenotypic changes in *P. aeruginosa* that induce a cascade of upregulated expression of messenger molecules following an increase of intracellular cAMP [102] within minutes as well as the amplification of c-di-GMP production over an extended time-scale [103,104]. While cAMP is linked to the transcription of several genes promoting permanent attachment involving secretion systems, adhesin production (involving T4P), Quorum sensing as well as downregulation of flagellar genes, c-di-GMP was found crucial for biofilm formation after successful contact initiation in an abundance of bacterial species (including, e.g., *E. coli, P. aeruginosa, P. fluorescens, P. putida, Vibrio cholerae, Yersinia pestis, Salmonella enterica, Bacillus subtilis*, and *Clostridium difficile* [103]). Increased levels of c-di-GMP promote the generation of adhesin as well as extracellular polymeric substrate (EPS) building the structural matrix of a matured biofilm architecture while they further induce motility recession. Bacteria cells deficient of the mechano-sensing T4P have been shown to remain planktonic levels of c-di-GMP and react non-responsive to substrate contact or drag [104] indicating a close connecting between the quality of surface contact and metabolic activity towards biofilm formation, which was also shown to respond to surface properties like stiffness [98]. Aside of response pathways related to appendage adhesion, membrane associated machines in *E. coli* have also been shown to sense and react to mechanical stimuli, e.g., by increased membrane permeability to facilitate nutrient uptake, which probably involves mechanosensitive ion channels in the inner membrane activated by compressive deformations of the cell wall [105].

Up to this point, bacteria/surface interaction throughout the different phases of surface adhesion was shown to be highly affected by surface mediated physicochemical stimuli towards the adhering bacterium, which can be beneficially designed by surface functionalization. The nature of the different surface specific influences on bacterial adhesion as well as potential strategies to modify bacteria/surface interaction by surface design will be addressed in the consecutive **Chapter 1.2**. For the interested reader, the current state of knowledge and recent theorems on long-term bacterial surface interaction in Phase III are further elaborated here, followed by a closer look at the individual characteristics of the two bacterial strains *E. coli* K12 (BW25113) and *S. aureus* SA113 investigated in this work.

Within matured biofilms, the dynamics of biofilm architecture as well as colony expansion have been similarly discussed to be related to the perception of internal and external forces, which govern adaptive responses of individual bacterial cells seeking improvement of their environmental conditions [98,103]. The fabric of biofilms is connected by intercellular adhesins and the extracellular matrix (EPS) consisting of bond-providing polysaccharides and cellular debris like proteins and deoxyribonucleic acid (DNA) that exhibits both viscous and elastic properties allowing the transmission of external stimuli into the bulk biofilm [98]. The structure and architecture of biofilms has previously been shown to be governed by external forces like flow drag, where mechano-sensing of single bacteria within the biofilm is suggested to contribute to its dynamic response, e.g., via triggering of EPS production to enforce its structure. Similar responses might as well be initiated by internal mechanical stress that is induced by biofilm osmosis or bacterial growth deforming the elastic EPS matrix [98]. The position of individual cells within the biofilm determines how they perceive external stimuli and is hence suggested to induce heterogeneity in geno- and phenotype, e.g., related to deviating composition of membrane appendages and adhesins. In Zöllner et al. [106] higher single cell surface adhesion capability was linked to both a higher biofilm growth, while lesser adhering cells are driven to the expanding growth front. Single cell motility was furthermore shown to be an important component within biofilm formation, where bacterial migration on the substrate surface or within the biofilm contributes to the shaping of biofilm architecture in response to environmental influences (like layer-by-layer addition of motile sub-colonies/clusters to grow mushroom biofilms from small initially adhering sub-colonies) [103]. Aside of mechanical stimuli, the availability and source of nutrition has also been shown to shape biofilms, where either mushroom or flat shapes are related to nutrient supply via the bulk liquid or substrate surface, whereas in microgravity (µG) a column-and-canopy shape has furthermore been observed for *P. aeruginosa* [107] (the origin of this biofilm morphology is however highly debated, recently, arguing that it might similarly result from improper handling of the samples during terrestrial retransfer). Quorum sensing (QS) involved in inter-bacterial communication has been shown to be required in the formation of complex biofilm architecture, where deficit-mutants of *P. aeruginosa* remained flat biofilm morphologies, while the wildtype was able to exploit the liquid nutrition source more efficiently by the formation of a mushroom shaped biofilm architecture [108]. QS requires increased amounts of extracellular DNA and ribonucleic acid (RNA), which is driven by programmed lysis in *P. aeruginosa* biofilms rather supporting the overall colony´s instead of single cell well-being [109]. Aside of this, the mechanisms governing biofilm growth and adaptation appear to remain majorly focused on benefitting single cell viability and are therefore mainly related to single cell responses, which sum up in biofilm-spanning dynamics. This is further emphasized by the fact that transcriptomics have yet failed to consistently identify a certain number of regulating genes directly related to programmed biofilm morphology formation regardless of environmental conditions [103].

Following these considerations, physical modelling of biofilm dynamics based on single-cell interaction has recently been applied to identify crucial driving forces in early state colony shaping [110]. Intercellular forces involve steric repulsion, bridging attraction (e.g., by adhesins), depletion attraction (extracellular polymers and matrix, leads to aggregation of bacteria independent of bacteria surface properties) and osmotic pressure in the biofilm (as summarized in **Figure 3**). Within a simulated biofilm, the actual architecture is considered to be actively modulated by variations in adhesin and EPS production of the inhabitant bacteria in response to external stimuli that modifies intercellular interaction involving the aforementioned mechanisms [98,103,110].

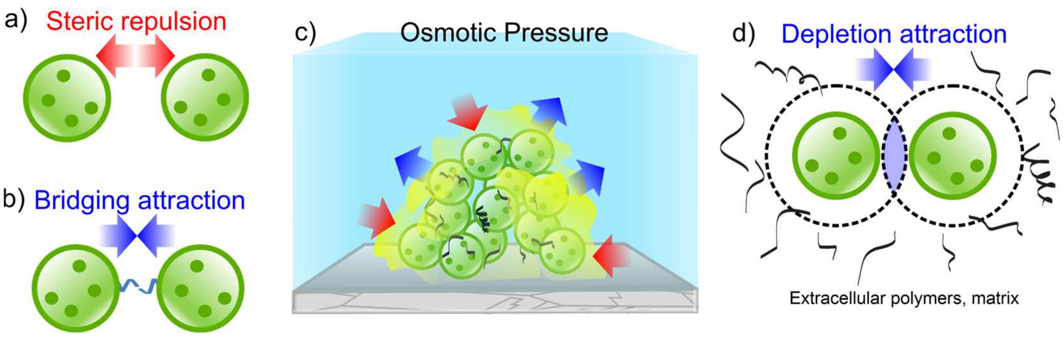

Figure 3: Interbacterial interaction governed by attractive or repulsive forces involved in biofilm dynamics: a) Steric repulsion, b) bridging attraction, c) osmotic pressure, d) depletion attraction. Modified according to [110]

A change in appendage expression in the case of spherical bacteria leads to variations in interbacterial attraction forces by which biofilm dynamics exhibit an either gas-, fluid- and solid-like bulk behavior, where increasing colony density strives for entropy reduction, as illustrated in **Figure 4a**. These colony dynamics for spherical cocci strains have been evaluated experimentally for *Neisseria gonorrhoeae* and *N. meningiditis* were intercellular bridging attractive forces appeared to be directly related to the T4P surface pili present in many species [111]. Spring-like folding and unfolding of T4P has been found to tune the spacing between connected bacteria further driving colony density in the liquid- and solid-like states. The interaction times via appendage connection between individual bacteria are generally smaller than the reproduction rate, by which the corresponding biofilm shaping impact is higher than shaping via growth [110].

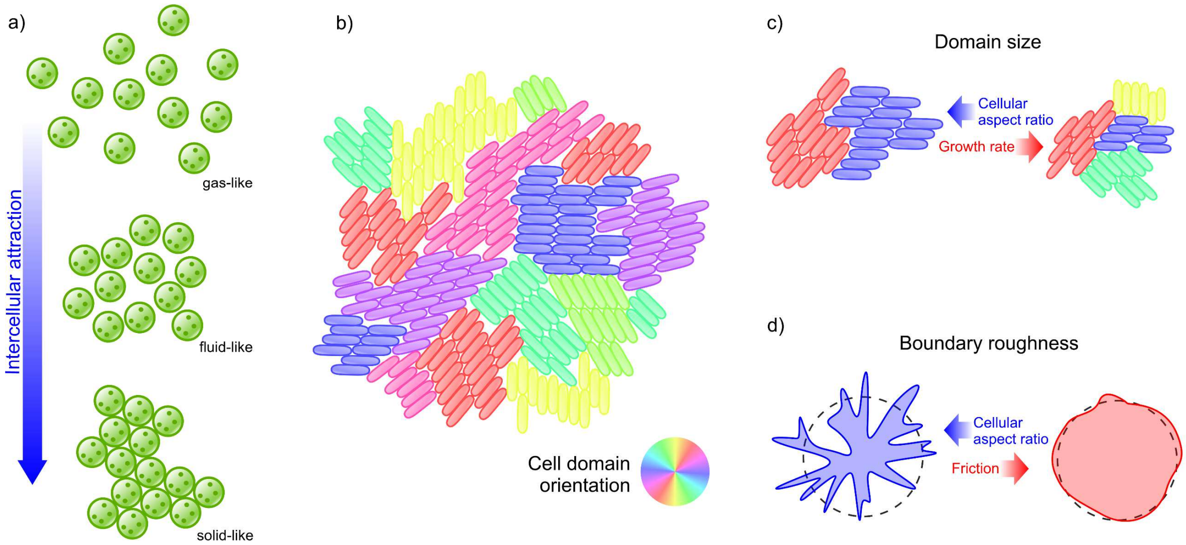

Figure 4: Interbacterial dynamics involved in biofilm shaping: a) Intercellular attraction and bonding, e.g., by T4P generate gas to solid-like agglomeration and cluster states in spherical bacteria. b) Rod-shaped bacteria exhibit crystallographic agglomeration behavior forming individual domains of aligned cell orientation. c) The size of single domains highly depend on strain specific bacterial shape and growth rate. d) The external morphology of the biofilm alters in boundary roughness similarly governed by bacterial shape and intercellular attraction inducing friction. Modified according to [110,112].

For rod-shaped bacteria, intercellular interaction is found to be more complex where single domains of parallelly aligned bacteria exhibit similar kinetic behavior like nucleating crystal domains in solidifying molten metals (see **Figure 4b**). Molecular dynamics (MD) simulations showed that bacterial growth and motile capabilities decrease the mean size of single domains, while steric interaction as well as high cellular aspect ratio increase it (displayed in **Figure 4c**). Within a 2D biofilm, a higher long-range order has therefore been found for rather in-motile strains, which was experimentally verified for *E. coli* [112]. Misorientations between single domains exhibit similar dynamics like grain boundaries and dislocations within polycrystalline materials, where defect sites between differently oriented bacterial cells and domains travel and annihilate during growth-induced expansion. The motility of these defect sites induces inhomogeneous colony growth and hence biofilm shaping, by which high intercellular attraction forces (friction) forms rather round colonies, while low attraction forces lead to heterogeneous expansion (as presented in **Figure 4d**), which can again be tuned by single bacterial expression of related membrane appendages. Also, motile rod-shape bacteria have been shown to spontaneously form oriented clusters that move as one unit [110].

Based on the presented physical models of bacterial surface interaction, a switch from 2D colony to 3D biofilm is considered to be induced by growth related stress on the single cell level, where space for flat surface adhesion is depleted in the colony center and single cells are forced to orient vertically under polar surface adhesion. Surface adhesion is stronger at old adhesion poles, by which daughter cells exhibit weaker surface bond leading to their repositioning in case of stress via steric forces from densely packed neighboring bacteria cells [113]. The critical colony size, where 3D reorientation is induced highly relates to both environment as well as bacterial surface bond and differs by orders of magnitude. Within the as-generated more complex volumetric agglomerates, osmotic pressure by spreading forces has been found to further shape biofilm architecture by bacterial modulation of protein and polysaccharide expression within the EPS matrix [114]. Bacteria are segregated for their individual properties within a mature biofilm, e.g., by strength of adhesion, cell shape and matrix production, which is especially evident in mixed biofilms [110]. Active matrix producers and a rather spherical bacterial shape favors segregation into the outer periphery of the biofilm, while non-producers and rod-shaped bacteria form the internal basis, which was also determined in *E. coli* single-strains models where bacterial cells were segregated dependent on aspect ratio. This sorting behavior provides a growth advantage for the peripherical positioned bacteria due to higher nutrient access and expansion options [110].

With respect to the reported impact of bacteriology on surface interaction that highly depend on individual strain capacities, a more focused review on the physicochemical properties of the *E. coli* and *S. aureus* strains utilized in the experiments is provided in the following sections. This summary aims to connect the previous review on current general knowledge about the mechanisms of bacterial surface adhesion, proliferation and colony/biofilm growth to a potential impact of strain specific bacteriology on bacteria surface interaction within the experiments conducted in this work.

***Escherichia coli* K12 (BW25113)**

E. coli K12 strains are known to exhibit two types of flagellar motility: swimming and swarming. However, the motility of BW25113 is lower than that of most other K12 strains, such as MG1655 [115]. Several pili like pilus type I has been identified in BW25113 [116], while further adhesins like curli are also present in modulated levels, which have been shown to play a role in *E. coli* attachment and biofilm production via stress response and increase bacterial surface hydrophobicity [117]. Mutants lacking the stress responsive genes rpoS and yggE exhibit higher surface flagellum and curli production leading to two-fold increase attachment levels on mostly negatively charged polymer surfaces in comparison to the BW25113 wild-type presenting a lower membrane appendage density under static conditions. However, adhesion strength under flow conditions was only increased of yggE deficient mutant in relation to higher expression of several curli genes, which is also quite high in the wild-type strain, by which the differences in adhesion under static flow conditions appear to be rather impacted by higher mutant motility. Due to this, yggE mutants were also way more successful in surface colonization, since the wild-type was barely able to access the surface under flow conditions [118]. Lipopolysaccharide (LPS) surface polymers where shown to play a major role in reversible (Phase I) and irreversible (Phase II) attachment to surfaces for K12. This especially applies on stainless steel, which was the sole positively charged surface in the study [119]. A quantitative formation of capsular EPS has been shown to effectively provide resistance against photocatalytic deactivation of *E. coli* K12 by TiO_2, when a direct contact is inhibited, but decreases cell viability in direct contact to TiO_2 NP. The latter was linked to promoted adhesion of TiO_2 NP to the cell membrane due to acid-based interactions [120]. NaCl levels have been shown to impair bacterial growth, biofilm formation, motility as well as glucose uptake with an increasing effect between 1% and 3.5% NaCl, whereas oxidative resistance is affected for 1% but gets increasingly promoted in further enhanced NaCl-contents (PBS has 0.8%) [121]. Higher oxygen levels increase bacterial attachment rate by increased growth and EPS production [122]. The availability of phosphate plays an important role on *E. coli* cell attachment under aerobic condition. Amplified phosphate concentrations up to 13.29 g/l have been shown to increase surface attachment (phosphate concentrations in PBS lies below 2 g/l). Here, a similarly high cell growth could be determined for stainless steel and Cu, while a lower dried cell weight was measured on Cu after 24h in LB medium, most likely linked to the material´s antimicrobial effect [123].

***Staphylococcus aureus* SA113**

S. aureus is generally described to be non-motile in liquid environment due to the absence of flagellar membrane appendages by which surface approach is driven predominantly by passive forces. However, they are able to passively move by colony expansion and can hence be termed motile in certain conditions regarding the spreading of biofilm dendrites on solid surfaces [124]. *S. aureus* is a very potent biofilm former and exhibits robust binding proteins for intercellular connections, aside of surface attachment, which react via bond strengthening under stimuli by external forces [98]. These connections are mediated via polysaccharide intercellular adhesions (PIA), which also act as extracellular biofilm matrix. Deficient mutants have been shown lose cell softness and do not adhere in clusters but rather single cells on surfaces, while overall surface adhesion is drastically reduced. Single-cell AFM reveals that PIA also promotes cell-cell adhesion via multivalent electrostatic interaction of polyanionic lipo-teichoic acids (LTA) on the cell surface [125]. Reduced PIA production consequently impairs initial surface attachment which appears to be partly inversed in the presence of iron but not Cu ions [126]. Aside of intercellular adhesion, LTA was also reported to play a role in surface attachment, where reduced formation rates impair adhesion to technical materials [127], while a passivation of the initially negative LTA surface charge may alter strain pathogenicity [128]. An increased negative LTA charge limits the capability of *S. aureus* to bind to glass and polystyrene in contrast, which is likely to be linked to increased electrostatic repulsion [129]. LTA was further shown to be related to cell surface hydrophobicity [127].

In summary, surface interaction deviates significantly between *E. coli* and *S. aureus*, where *E. coli* has been shown to rather adhere in single cell dispersions, while *S. aureus* tends to form cell-clusters in planktonic state and during surface attachment under active involvement of intercellular biofilm matrix proteins. *S. aureus* exhibits increased surface hydrophobicity but can similarly adhere to rather hydrophilic surfaces, whereas *E. coli* has a lower membrane hydrophobicity. Rigid surface adhesion of both strains requires viable cell interaction, where the surface bonding of dead cells have been shown be weakened significantly allowing for facile surface removal by rinsing [130].

1.2 | The impact of technical surface properties

Physicochemistry

The current state of investigation on the influence of bacteriology on bacteria/surface interaction highlights a predominant role of physicochemical driving forces under the involvement of membrane appendages and polarity in surface approach and bond initiation. The further expression of bacterial activity after bond strengthening appears to be impacted by similar external stimuli that are preserved over the same molecular signal channels, by which sessile bacterial interaction is highly dependent on the quality and quantity of the surface anchorage. Whether net forces between bacteria and surface act predominantly attractive or repulsive is considered to be governed by the physicochemical properties of said surfaces. On this behalf, Busscher et al. [131] as well as Cheng et al. [132] discussed a possible implementation of thermodynamic modelling of bacterial surface adhesion involving either Derjaguin, Landau, Verwey and Overbeek (DLVO) or the further extended DLVO (XDLVO) theory. Within the more accurate XDLVO theory, the net force F_{Total}^{XDLVO} resulting from physicochemical interaction between an individual bacterial cell and a surface substrate is governed by Lifshitz-Van der Waals attraction (F_{LW}), electrostatic (F_E) and acid-base (F_{AB}) interaction according to equation (1) [132]:

$$F_{Total}^{XDLVO} = F_{LW} + F_E + F_{AB} \tag{1}$$

Since F_{LW} predominantly act attractive, pronunciation of rather attractive or repulsive interaction depends on F_E related to the respective bacteria/substrate surface charge, as well as F_{AB} which is based on acceptor/donor interactions of individual polar surface compartments connected to macroscopic hydrophobicity/-philicity. In review of a multitude of different approaches both groups concluded that the processes involved in bacteria/surface interaction might follow similar dynamics but are too complex to be fully grasped by modelling attempts, yet. However, certain fundamental aspects of the XDLVO theory have experimentally been shown to be qualitatively applicable:

- Variations of *E. coli, P. aeruginosa* and *S. aureus* adhesion on hydrophilic glass surfaces have been shown to correspond to the F_{AB} related matching of bacterial envelope and substrate wettability, where the least hydrophobic *P. aeruginosa* strain adhered best. Similar observations point towards the befitting of a counteracting impact of similar surface charges inducing an electrostatic repulsion force F_E in the case of *E. coli* adhesion on the negative charged glass surface since they exhibited the highest negative membrane charge among the tested strains [133].
- In similar manner, Wu et al. [134] observed a ten to fifteen-fold decreased attachment rate as well as cluster formation of *P. aeruginosa* and *S. aureus* on nm-rough vs. electropolished steel surfaces combined with further suppressed biofilm formation, where both surface types exhibited hydrophilic surface wetting and a negative surface charge.
- In turn, Chen et al. [29] where able to significantly increased *E. coli* adhesion on glass substrates by applying a positive surface charge via functional coatings.
- Bacterial adhesion on TiO_2 surfaces was furthermore reduced by a combination of surface hydrophilization and topography modification [135].

Apparently, bacterial surface adhesion is influenced by physiochemistry related to both F_E and F_{AB} but cannot be fully averted in case of alleged repulsive net forces, pointing towards adaptive bacterial mechanisms. Corresponding to this, Maikranz et al. [83] were able to show that the binding mechanism of *S. aureus* differs between hydrophobic and hydrophilic Si-surfaces. They found that bonding of *S. aureus* involves many different types of macromolecules with low individual binding force on hydrophobic surfaces, while fewer molecules bind to hydrophilic surfaces however with stronger bond force. Nevertheless, the overall net bonding force on hydrophobic surfaces ranges one order of magnitude higher. The group´s experiments furthermore revealed a significant variance of quantitative adhesion force between different bacteria, which could be traced back to a heterogeneous distribution of surface macromolecules across the bacterial membrane [136]. Adhesion of *S. aureus* was hence found to strongly relate to “adhesion patches” of up to 250 nm diameter, which are distributed heterogeneously over the bacterial membrane. Similar observations have been made for *E. coli* K12 [137].

In an earlier experiment, van der Waals forces F_{LW} involved in *S. carnosus* adhesion were also shown to be impacted by sub-surface properties exhibiting a two-fold increase of the measured bacterial adhesion force in the case of a thin native Si oxide layer compared to a thermally grown SiO_2 layer of 150 nm thickness, independent of surface wetting [138]. Similarly, a higher adhesion and metabolic activity of *P. fluorescence* was monitored on nanograined compared to micrograined TiO_2 substrates in another study [139].

Based on these correlating observations, the F_{Total}^{XDLVO} net force is estimated to be attractive in case of opposing bacteria/substrate surface charge and matching wettability, whereas similar charges and non-compatible wetting properties induce repulsion, which however does not necessarily impede bacterial attachment. In between both F_E and F_{AB}, the acid-base interactions related to surface wetting appear to pose a higher impact due to a further extended effectivity range and higher adhesion forces in case of hydrophobicity-related interaction, especially in liquid environment [131,132]. It has to be emphasized that experimental investigation on individual physicochemical mechanisms involved in bacterial adhesion in an isolated manner is hard to implement due to a mutual dependence to other surface properties like, e.g., the substrate topography, where cavities might geometrically cancel repulsive net forces [132].

Topography

The impact of substrate topography on bacterial/surface interaction has been in the focus of research for more than two decades, considered either in the shape of stochastic roughness or purposefully introduced deterministic surface features [23,132]. Whereas initial approaches to study the role of the topography in bacterial colonization of technical surfaces varied in their interpretation of the underlying processes [132], more recent investigations in the late 2010s were able to attain a rather generalized understanding of its impact on bacterial interaction that is still valid. Whitehead et al. [140] reported an increasing agglomeration/retention of *S. aureus* and *P. aeruginosa* within topographical sinks following an upscaling in diameter from 0.2 to 2 µm that have been produced either stochastically (in the case of sub-µm) or deterministic via physical vapor deposition of hydrophobic TiO_2 layers. In a subsequent work, their consideration of topography involvement in surface retention could identify feature dimensions considerably above the scale of single bacterial cell size as non-effective since bacteria do not sense any topographic impact from them [22]. Topographic feature geometry in combination with the bacterial cell shape might differently affect the retention of various strains, where cocci were trapped in surface scratches, while rod-shaped bacterial might similarly adhere within or span over elongated surface features depending on local adhesion forces. Surface scratches have similarly been shown to induce longitudinal cell orientation. In case of cocci bacteria, feature sizes that match the bacterial cell size were found to induce the highest retention in comparison to larger and smaller dimensions. Rod-shaped bacteria appear to favor higher feature diameters compared to spherical shaped strains [22]. In a similar manner Verran et al. [141] observed variances in preferential cell adhesion on deterministic surfaces gained by the disassembly of DVD and CD discs (the marking grid of these are representing line-like patterns with either 0.59 µm or 1.02 µm valley width): Here, cocci-shaped *S. sciuri* were less retained on the smaller pattern scale, while rod-shaped *Listeria monocytogenes* exhibited preferential adhesion due to an increased surface contact [141]. Hsu et al. [142] investigated bacterial adhesion to either nm- or µm-scaled periodic surface patterns on rather hydrophilic Al_2O_3 and Si substrates taking into account that bacteria may utilize different mechanisms of attachment in response to topography. They were able to show that *E. coli* and *P. aeruginosa* cells reorient themselves within the surface patterns in order to achieve maximum contact to given surface asperities, where also the expression of flagella production altered between the topographies investigated. Similar phenomena of spontaneous bacterial orientation in response to periodic surface topographies were previously reported by other groups, as well, where rod-shaped bacteria expressed a high sensitivity towards surface asperities during initial adhesion and further colony expansion [75,143]. However, within a matured biofilm architecture expanding over the geometrical restrictions of topography, cell orientation was not affected anymore [142]. Another mechanism of bacterial adaptivity towards rather challenging surface geometries was linked to extensive flagella production in *E. coli,* where the appendages explored the topography crevices and amplified anchorage [144]. In this study, surface conditioning by flagellar exploration furthermore induced a wetting transition destabilizing an initial Cassie-Baxter wetting state enabling further surface access of the bacteria within the solution.

For surface features well below the single bacterial cell size, adhesion might be limited to topographic asperities greatly reducing the bacteria/substrate contact area, which is often linked to reduced bacterial adhesion rates [24–27]. This especially comprises topographic scales ranging below 800 to 500 nm, where strain dependent interaction blurs the effective threshold scale [24,142,145,146]. The lower limit on topographically driven adhesion impairment was estimated to range at asperity sizes <100 nm by Siegismund et al. [147] using a DLVO modelling approach to quantify the energy gain by adhesion of *S. epidermidis* on nm-scaled stochastically rough Ti-surfaces. Above this range, energy gain indicates preferential adhesion increase for topographic depths below 70 nm, marking the vertical threshold of bacterial repellant topography scales. This effect is geometrically driven and depends on the fact that bacteria cannot achieve high contact forces, if they are unable to get close enough to the surface. This modelling approach correlates to experimental single cell AFM observations indicating that adhesion relevant membrane macromolecules can adhere up to distances of 50 nm from the bacterial cell envelope, whereas long-range interaction can already be monitored within a distance of 100 nm [88,148]. Nm-scaled roughness between 7 nm and 35 nm led to decreased adhesion forces, where fewer and fewer macromolecules were able to adhere to roughening surfaces. Similarly, Lüdecke et al. [145] reported on altered *E. coli* and *S. aureus* adhesion on nanorough titanium surfaces below an Rq of 6.1 nm, where increasing roughness lead to decreased cell adhesion.

Within a deterministic periodic pattern arrangement, bacteria have been reported to be affected both by pattern scale as well as the geometrical feature arrangement with increasing pattern complexity. Helbig et al. [25] investigated early state attachment of *S. epidermidis* and *E. coli* within 2 min of exposure to periodic dimple, pillar and line-like surface patterns of either 0.5, 1 and 5 µm periodicity on several polymer surfaces. Here, bacterial adhesion was shown to depended on substrate and strain combination most likely related to physicochemical interaction on one hand side but presents pattern specific trends in adhesion on the other hand side. While 0.5 µm pattern sizes invariably boast the lowest and 1 µm pattern sizes the highest adhesion rates within individual pattern geometries, both dimple and pillar patterns remain a lower overall bacterial adhesion compared to the line-like patterns. Similar observations have very recently been made by Pellegrino et al. [149] including a wider range of both bacteria (*S. aureus, P. aeruginosa* and *E. coli*) as well as fungal spores of *Candida albicans* in their study. Instead of DLIP, their surfaces were generated by wrinkling of a PDMS substrates inducing line- and cross-like as well as a wavy "herringbone" surface pattern exhibiting a periodicity of 2 µm periodicity and a depth of 0.2 µm. Bacteria were shown to preferentially adhere within the pattern valleys, where they arrange in highly oriented clusters in line-like patterns, but exhibit lose cluster orientation within both cross-like and wavy pattern geometry. The latter where furthermore shown to impede proliferation in early colonization stages and reduce overall bacterial covering by 50%. On line-like patterns a higher number of bacteria adhered, which however still ranged below the flat reference. *E. coli* were observed to present the most sensitive response to topography in relation to the rod-shape cell envelope, whereas cell clusters of *S. aureus* are also aligned to the pattern valleys. *C. albicans* spores showed a less pronounced retention and alignment effect due to inverse size relation between pattern and microorganism. Aside of the clear segregation of bacterial cells within the pattern valleys, the cell envelopes were shown to be deformed to further increase contact area to the hydrophobic substrate leading to reduced aspect ratios and smaller overall cell expansion. Further proliferation is both depressed and guided within the pattern valleys, where the colonization onset is delayed especially on more complex patterns. Line-like patterns pose a significant impact on cell-orientation and therefore surface interaction, but still a comparably low impact on proliferation and colonization. Similar observations on the impact of both pattern scale and complexity were also made several other studies [26,70].

In conclusion, the topography has a significant impact on bacterial surface interaction where physicochemical interaction forces related to mutual bacteria and substrate properties might be either amplified or cancelled, with respect to certain adaptive bacterial capabilities towards varying physicochemical surface properties [22,142,150]. Topographic feature scales below bacterial size have been shown to act rather impeding while features matching bacterial size increase bacterial adhesion due to the ability of single bacterial cells to enhance surface contact. This is predominantly discussed to be linked to the ability of single bacterial cells to maximize their contact area to the substrate seeking enhanced anchorage [22,142], which especially favors crevices and concave surface morphologies. More shallow topographic feature scales well above bacterial cell size do not impact bacterial adhesion, since they are not perceivable via mechano-sensing [132]. These differences in scale related bacterial surface interaction apply for both stochastic and deterministic surface designs, where however the topographic effect on bacterial adhesion is more pronounced in the latter case. In this context, it additionally has to be considered that dependent on nutrient support, environment and growth/reproductive activity, bacteria might vary in scale even within a single colony, by which the quantitative impact of topography might as well deviate. Although promoting single cell adhesion, pattern dimensions in the single bacteria scale were frequently attributed to a reduction in adhering bacterial cell number [75,140,142], which might originate from limited surface access due to external drag within a fluid environment [73] or critical adhesion induced membrane stress [23,82,149]. Considering the previously presented relation between appendage adhesion and bacterial surface adhesion, a higher ratio of surrounding surface area should increase the amount of contacting adhesins in case of bond-providing physiochemistry between cell and substrate, while repulsive interaction might be increased as well. Surface roughness may therefore be considered to impact the total binding energy between bacteria and substrate similar to the amplification of either hydrophilic or hydrophobic surface properties according to Wenzel [151], where repulsive or retaining physiochemistry might further be amplified by a corresponding topographical impact. A schematic overview of the postulated combined impact of physiochemistry and topography on bacteria/surface interaction based on this literature review is provided in **Figure 5**.

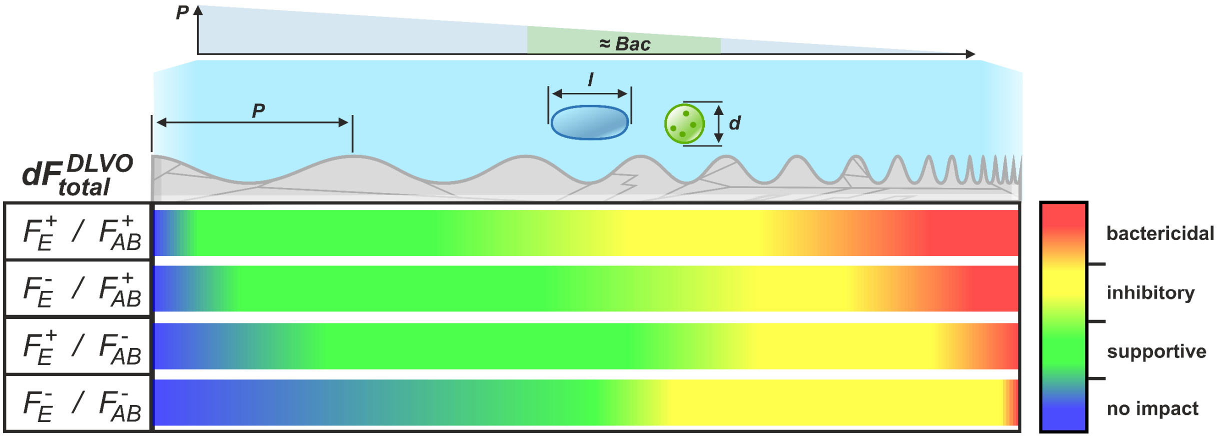

Figure 5: Schematic illustration summarizing the combined impact of topography and physicochemical interaction on bacteria/substrate interaction. Topography is characterized by the deterministic pattern periodicity *P* related to the bacterial cell diameter *d* and length *l* in case of rod-shaped strains. The left side of the topographical spectrum represents pattern sizes above bacterial cell size while the right side transits into bactericidal topographies corresponding to the biomimetic blueprint surfaces of *cicada* and *dragonfly* wings. The spectrum of physicochemical surface interaction is represented by electrostatic $\boldsymbol{F_E}$ and acid-base $\boldsymbol{F_{AB}}$ (hydrophobic/-philic) interactions according to [132] whereby the superscripted $+/-$ indicate adhesive or repulsive interaction.

However, bacterial surface interaction has been reported to be sensitive towards the specific geometry of deterministic surface topographies as well, where complex morphologies irritate bacterial response leading to depressed bacterial activity and proliferation [70,149]. Between the investigated geometries, line-like patterns have been shown to rather promote bacterial adhesion and guided colony growth instead of depleted bacterial activity during sessile surface interaction on contact supporting pattern sizes.

2 | Antimicrobial Surface strategies

2.1 | By topographic impact on bacterial adhesion

In the view of the either impeding or supporting impact of topography on bacterial colonization, an utilization of this very effects has been broadly discussed for implementation in biofouling surface concepts in literature [26,70,72,152]. Here, deterministic surface patterns in the nm- and µm-scale have shown a high potential to decrease biofouling on technical surfaces, exceeding over stochastic or porous surface designs [23]. Within early studies relating to the food industry, grooves and scratches introduced alongside mechanical surface treatment techniques or wear were shown to pose an especially high risk of biofouling, where bacteria have been found to wedge in between the topographic asperities within cavities and groove channels. Here, they remain strongly retained and uneasy to be removed, which further promotes biofilm expansion [153]. In response, Schumacher et al. [154] introduced the biomimetic *Sharklet* surface concept based the topographical blueprint of shark skin, where a reduction of biofouling is linked to targeted surface design. This approach implements an engineered roughness index (ERI) closely related to the conceptional surface description applied in the Wenzel [155] and Cassie-Baxter [156] theories of surface wetting. The ERI calculation (2) involves both the surface roughness factor r of Wenzel and a fractional surface compartment f_D related to topographical valleys that correlates to the heterogeneous wetting description applied in Cassie-Baxter. Both are further complemented by the geometrical degree of single entity freedom df defined by pattern geometry.

$$ERI = \frac{r \times df}{f_D} \tag{2}$$

An increasing ERI linked to mostly higher pattern aspect ratio could be correlated to decreased microbial adhesion, where antibiofouling however targeted marine organisms as algae and barnacles. In smaller pattern sizes close single bacterial cell size, Sharklet topographies were shown to decrease methicillin resistant *S. aureus* (MRSA) cluster size and *E. coli* attachment on implant surfaces to 47% due to topographical constrains, but do not possess sufficient antibacterial properties to consequently fight IRI [23]. In fact, surface topographies in the scale of several µm down to 800 nm have been shown to rather increase bacterial adhesion in static environments, whereas a reduction in adhesion on these surfaces requires additional mechanic involvement of either flow drag [23,73] or modified substrate stiffness [157]. The utilization of lotus-like wetting effects where furthermore discussed to prevent initial bacterial attachment by repulsion of vehiculated liquid droplets [158], which however was shown to be potentially destabilized over time due to bacterial surface conditioning [144].

Further reduction of surface pattern scale below single bacterial cell sizes limits the accessible surface area for bacterial attachment hence reducing overall adhesion force that can be generated between bacteria and substrate, which might furthermore affect biofilm formation [23,150]. The application of both stochastic as well as deterministic nanoscale topographies is being investigated, particularly on the surfaces of implant materials, where bacterial proliferation was shown to be reduced by up to 55% depending on the bacterial strain investigated [21,24,159]. Mechanical membrane stress induced from the punctual surface contact is discussed to also inhibit bacterial metabolism and thus impede surface colonization dynamics [145,160]. In *S. aureus* and especially in *E. coli*, changes in morphology, as well as lower expression of gene groups relevant for the transition from the planktonic to the sessile state were observed in contact with sub-µm pattern sizes [145]. Aside of the individual ratio between topography and the bacterial cell size, the efficiency of adhesion prevention by this strategy has been shown to be primarily governed by strain specific physiology and agglomeration behavior. Gram-positive *S. aureus* exhibit a lower sensitivity to reduced surface feature scales compared to gram-negative *E. coli* and *P. aeruginosa* due to the higher rigidity of the cell wall and the option of forming agglomerates as an alternative to surface adhesion. [145,160,161]. A similar strain specific efficiency of sub-µm scaled surface patterns, mostly related to laser induced periodic surface structures (LIPSS) has furthermore been reported in several other studies [71,72,146,162].

2.2 | By active bactericidal surface properties

Aside of the inhibition of bacterial colonization, nm-scaled surface topographies might effect an active killing of adherent bacteria as soon as their aspect ratio surpasses 0.7 to 0.9 [20,21,163]. Technically applied topographies for bactericidal surface properties follow the biomimetic blueprint of the nanoscale columnar structures found the wings of several insects, e.g., *cicada* and *dragonflies* [20,21]. Due to the high aspect ratio and small feature spacing, bacteria are forced to settle on the sharp asperities, which induces mechanical stress and eventually rupture of the bacterial membrane [17]. Again, due to strain specific differences in cell wall thickness and rigidity, this effect applies differently for gram-positive and gram-negative bacteria, resulting in selective efficacy preferentially affecting gram-negative strains [20,21,163]. By significantly increasing the aspect ratio to 2.0 and higher, the active antibacterial effect was shown to be extendable to gram-positive bacteria, as well [164,165]. Differences in strain specific efficiency has furthermore been linked to physicochemical differences of the cell membrane setup, since the mechanical mode of action requires active forces pushing the bacteria against the nm-scaled asperities [17,166]. The applied force to induce membrane rupture might as well involve external components like fluid dynamic drag [66]. Membrane piercing bactericidal surfaces have been realized applying different methodology and substrates, e.g., involving deep etching to achieve black silicon [19], epitaxial oxide growth on titanium [165] as well as short pulsed laser treatment of Cu [65,68], which however are subject to the same functional restrictions of the natural blueprint in terms of strain specific efficiency. Ghosh et al. [167] furthermore reported on well applied bacterial killing of *Bacillus subtilis* on black silicon, which was however not extendable to the bacteria´s spores.

An interesting approach of mutual topographic and physicochemical surface functionalization was presented by Chen et al. [29] applying line-like patterning in the scale of single bacterial cells on borosilicate glass followed by polyelectrolyte coating, which induces positive surface charge. The hence effected neutralization of negative bacterial membrane charges in combination with mechanical stress introduced by the mutual interaction of high physicochemical attraction forces and the challenging substrate surface induced a bactericidal effect against *S. aureus* and *E. coli*. Here, the gram-negative strain was again shown to be more sensitive due to the weaker outer membrane.

Aside of topographically induced deterioration of the bacterial membrane integrity, active bactericidal surface properties have furthermore been achieved by the application of functional coatings. In several studies, the group of Grohmann [30] reported on the antibacterial properties of AgXX®, which represents a catalytic two-layer coating, where electro-chemical interaction within galvanic Ag-Ru microcells generates reactive oxygen species (ROS) that crack down organic chemistry in close proximity to the surface. Similar redox reactions are also induced on TiO_2 surfaces under photocatalytic involvement of UV radiation, whereby the material´s photo-sterilization effect is exploited in manifold applications [31]. Another class of bactericidal coatings are based on antimicrobial peptides (AMP) that are formed as first defense line against microbial infection in human, animal, plants and invertebrates' immune systems [28]. Similar to all aforementioned bactericidal strategies, they specifically target bacteria membrane, where they bind via positive pole charge (amphiphilicity) to the anionic outer membranes of bacteria. The hence induced neutralization of the bacterial membrane surface charge corrupts the membrane´s lipid organization leading to the formation of transmembrane pores up to a full membrane breakdown.

2.3 | Antimicrobial Activity of Cu

Very potent active antimicrobial capacities are provided by the elementary metals Ag and Cu, which can be applied in bulk or as a functional coating on technical surfaces [32,33]. Historical documentation of the utilization of Cu to sterilize wounds or water dates back to various ancient cultures like the Egyptians and Aztecs [36,37]. Cu based materials were also well-applied in daily live goods for an extended period in modern time until the discovery and uprising of antibiotics [16]. However, especially effected by a progressive reduction in treatment efficiency as a result of the increasing development of bacterial resistance, Cu alloys are more and more reconsidered for decontamination of technical surfaces, especially in critical environments like hospitals or enclosed habitats [168–171].

The antimicrobial effect of Cu has been discussed to be directly related to the thiophilic and physicochemical interactions of Cu^{2+} and Cu^{+} ions with different molecular sub-entities that are vital for microbial organisms [43]. Hence, a quantitative release of Cu ions has be considered as the key feature of Cu based antimicrobial surface concepts [51]. Cu ion emission is directly related to electrochemical surface processes, which might include an either active [172] or passive catalytic involvement of microbiologic processes [54]. Here, the similarly activated bactericidal effect of the more noble Ag requires a higher electrochemical activation potential, whereas the antimicrobial application of Cu is less dependent on ambient conditions [43]. In the same course, Cu builds an important trace element in human metabolism and immune response [39,40], while Ag is considered toxic in low accumulated doses [42]. In this light, the application of Cu for active antimicrobial contact surfaces offers a promising decontaminative potential combined with a high suitability for the application in human environment [41]. The underlying mechanisms of the antimicrobial effect of Cu involving potential strategies of amplification are further discussed in the following sections in more detail.

2.3.1 | Antimicrobial mechanisms of Cu

The overall antimicrobial activity of Cu surfaces was highly investigated in the past two decades, where a certain number of active mechanisms could be identified. Independently, a toxic effect of Cu exposure was described for each bacteria [16], viruses [35] and fungi [34] proving a broadband decontamination efficiency. In which extend the different modes of action individually contribute to antimicrobial Cu activity is controversy discussed and often depends on the targeted microorganism and environmental factors. The following summary especially focusses active antibacterial properties proven, so far [43], which are partly extendable to viruses and fungi as well:

- Independent of their dissolved concentration, Cu ions have been shown to preferentially accumulate on the surface of the cell membrane (schematically illustrated in **Figure 6a**), where they interfere with metabolic processes by the reduction of mass transfer and cellular respiration [173]. This has an inhibitory effect on both bacterial growth and the formation of biofilms [174].
- Under increased Cu concentrations, the aforementioned membrane agglomeration of Cu might as well induce a destruction of the cell envelope, associated with leakage of cellular fluid and rapid cell death, as shown in **Figure 6b**. Membrane disintegration can involve the reduction of the Zeta potential on the bacterial cell surface due to ionic depletion, as well as the generation of hydroxyl radicals from hydrogen peroxide in a Fenton-type reaction, where Cu ions act as electron donors and catalysts [43]. These hydroxyl radicals are reactive oxygen species (ROS) causing oxidative cell wall damage, e.g., targeting lipids in the cell membrane [175]. Due to its grave physiological impact on bacterial cells and a reported cross-species efficacy, this mode of action is currently considered as the most potent [86,176–178].

- When Cu ions gain access to the cell interior, they have been shown to interact with single molecules of DNA by substitutional attachment, which changes the local bond length and thus the molecular structure (see **Figure 6c**). This effects a distortion and destruction of the DNA´s double helix structure resulting in metabolic dysfunction of the bacterium inducing both inhibited cell division and potentially cell death [16,43,86,177]. In a few studies, DNA destruction is discussed as the major cause of cell death [173], whereas quantitative access of Cu to the cytoplasm might require a certain state of membrane disintegration depending on the bacterial strain [177]. On this behalf, Wang et al. [179] presumed an increased Cu ion trans-membrane mobility by membrane charge neutralization via Cu aggregation on the cell envelope that leads to an "avalanche collapsing".
- Due to the high affinity to thiols, intracellular amounts of Cu ions are furthermore discussed to form redox reactions with iron-sulfur compounds of essential proteins exchanging the Fe sites within the molecular structure (example in **Figure 6d**) [16,36,180,181]. Similar to DNA, the hence induced modification in bond length and electron arrangement distorts the protein´s structure and disrupts its metabolic functionality. A quantitative removal of these proteins from the bacterium's respiration and fermentation cycle potentially eliminates vital subprocesses, whereas again sufficiently high intracellular Cu levels might require increased membrane permeability due to preceding external damage.

A schematic summary of the presented modes of action is illustrated in **Figure 6**.

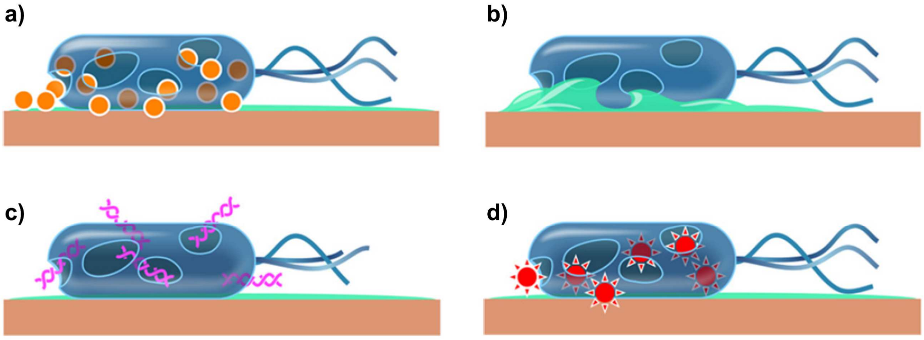

Figure 6: Schematic illustration of the different proven modes of action: a) Agglomeration of dissolved Cu ions on the cell membrane affection respiration and membrane integrity by ionic depletion and the catalyzation of ROS generation via Fenton-type reactions. b) leaking of cytoplasm and loss of bacterial integrity due to increased membrane damage. c) destruction of DNA and d) metabolic proteins. Adapted according to [16].

Each of these mechanisms poses a potential threat to individual pathogens already at low Cu levels, whereby an effective and complete degradation of an entire bacterial contamination requires a certain minimal copper concentration. Presumably, only the complex interaction of several mechanisms of action might lead to rapid cell death, especially in the mutual combination of extra- and intracellular modes of action. In this light, the USEPA specified a minimum alloy content of 60 wt.% copper for the classification of antimicrobial metallic materials, where a 99,9% reduction of viable bacterial cell count must be achieved within 2h of exposure [16].

Antiviral efficiency of Cu

The antiviral effect of Cu has been tested on bacteriophages and pathogenic eukaryotic viruses, so far, where many studies were able to confirm a high antiviral efficiency of Cu [182–185]. This involves the SARS-CoV-2 virus related to the 2020-2023 COVID-19 pandemic, whereas Ag surfaces reportedly do not exhibit antiviral capacities [186]. In murine and human noroviruses, Cu has been shown to cause destruction of the genome and viral disintegration where in case of the human coronavirus HUCoV-229E also a shrinking effect was reported [184,185]. In cross-study agreement, a 60% to 70% Cu content in both brass and Ni-bronze is already sufficient for effective virus elimination, closely matching the USEPA specification of antibacterial Cu based material. Higher contents also lead to an increase in antiviral activity [185].

The mechanism of Cu mediated elimination of viruses as majorly been traced back to the surface release of Cu^+ and Cu^{2+} ions inducing similar molecular interactions like the ones reported in bacteria. Formation of ROS was determined to not play a particular role in antiviral activity, by which Cu ions are considered to rather act directly on viral particles. It has been shown that copper ions are able to aggregate to pathogenic virions effectively limiting a potential health impact of viral infections. This effect is currently utilized in water decontamination combined with silver and small concentration of chlorine to further amplify the chemical activity of Cu ions [187]. A virus specific mode of action is reported to involve chemical interaction with cysteines in viral surface proteins and aggregation. The resulting modification of molecular folding and disintegration of the viral envelope deactivates key viral proteins impacting their virulence [182]. In addition, a destruction of viral genome was observed under involvement of Cu similar to bacterial DNA deactivation, whereas the underlying physicochemical mechanisms are still under investigation [185,188].

Antifungal efficiency of Cu

Similar to many metazoic organisms, eukaryotic filamentous fungi utilize Cu as micronutrient and trace element for growth and proliferation. One of the most investigated Cu transport system in eukaryotes is that of the baker's yeast *Saccharomyces cerevisiae*, where certain intracellular mechanisms were found to efficiently detoxify an overrepresented amount of intracellular Cu. This involves, e.g., metallothioneins (copper sequestrating proteins) [189]. In early studies, fungal capabilities to absorb heavy metals like Cu to utilize them as nutrients without harm has been reported [190]. Within further research, this process was denoted as bioremediation, describing the potential of filamentous fungal biomass to act as agents for biosorption of heavy metals from contaminated sediments [191]. Aside of this, an actually antifungal application of copper complexes [192] and copper nanoparticles [193] has been considered, as well, where however fungal sensitivity to copper complexes and nanoparticles was shown to be highly dependent on the tested fungal species.

The low Cu sensitivity of filamentous fungi can be traced back to effectively protective intracellular mechanisms involving, e.g., ATP-dependent heavy metal translocators, which are deeply conserved from archaea to mammals [194]. These molecular Cu extrusion pumps represent the main eukaryotic heavy metal detoxification mechanism also found in prokaryotic bacteria [195]. Based on this, research on the effects of Cu on filamentous fungi is still at an early stage, especially including potential modes of action in an antifungal contact surface application.

2.3.2 | Potential decrease in antimicrobial efficiency

Since Cu is a widely natural available and partly essential element for microorganisms, they have developed effective mechanisms to regulate its intracellular levels and protect themselves from potentially toxic effects. In humans, Cu is an important trace element as it is involved in many fundamental mechanisms, including, e.g., immune defense [39]. Macrophages have been shown to be equipped with enzymes that enable the control of intracellular Cu storage and release in order to fight intrusive bacteria [40]. Due to this, opportunistic human pathogens such as *S. aureus* and *E. coli* are forced to develop defense and resilience mechanisms against increased environmental Cu levels to maintain viability within the host organism. Previously discovered mechanisms of Cu resistance in bacteria include ATP-dependent and chaperone-mediated efflux of Cu ions as well as detoxification by oxidation of Cu^+ to the less toxic Cu^{2+} or binding in proteins [16,57,180,195]. These systems represent targeted modifications of the general bacterial heavy metal homeostasis [196] that is available in the majority of the yet investigated bacterial strains, either in single or combined form. A schematic illustration of the Cu homeostasis cycle of gram-positive and gram-negative bacteria is provided in

Figure 7. The triggering of a Cu regulatory response has been shown to be related to ion-induced stress levels leading to an upregulation of chaperone and efflux pump related genes [40].

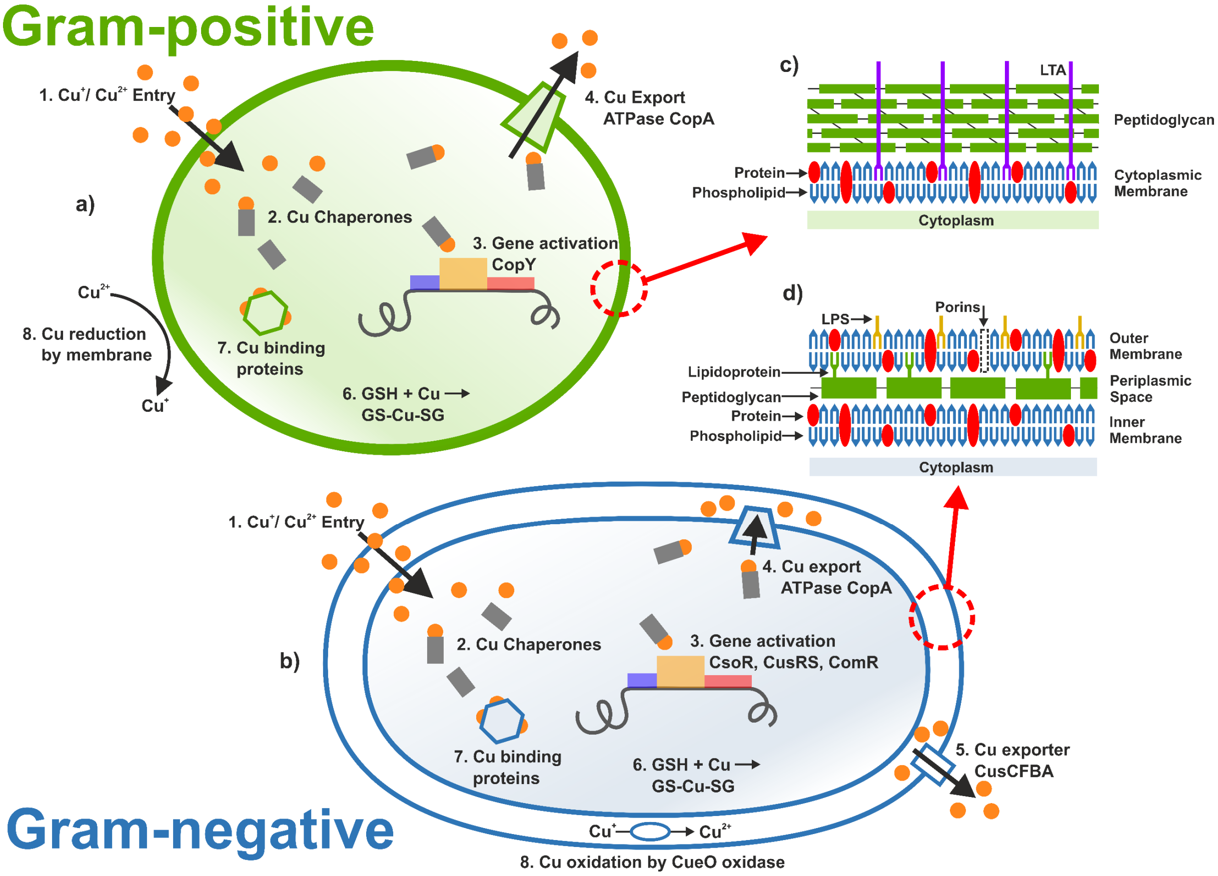

Figure 7: Cu homeostasis of a) gram-positive and b) gram-negative bacteria separated into the following elements: 1. Cu entry into the bacterium, 2. Cu chaperones sequester cytoplasmic Cu for detoxification and routing to places of export or regulations, 3. Several genes are triggered in response to elevated cytoplasmic Cu upregulating key elements of Cu leveling, 4. Cu is pumped through the cytoplasmic membrane by Cu ATPase (powered by ATP), 5. CusCFBA transporter pumps transport periplasmic Cu across the outer membrane (only in gram-negative bacteria), 6. Glutathione (GSH) can bind Cu for detoxification, 7. Cu binding proteins buffer excess cytoplasmic Cu, 8. Extra-cellular/periplasmic modification of Cu ionization state. The membrane structures of both c) gram-positive and d) gram-negative bacteria furthermore exhibit the physiologic differences, e.g., by the protective role of the thick outer peptidoglycan layer in case of gram-positive strains. Modified according to [197].

In addition, the bacterial physique might already induce a decreased Cu sensitivity, as through a thicker cell membrane in gram-positive bacterial strains, spore- or EPS forming bacteria, where the organic extracellular substance have been shown to absorb environmental Cu ions [174,176,198–200]. Gonzalez et al. [201] observed a triggering of EPS production under metal stress in *P. aureofaciens*, which increased cell viability due to lower cellular absorption of Cu. EPS molecules are negatively charged and tend to form metal complexes with increased rates in pH > 6 conditions leading to a depletion of environmental metal ions in proximity to the bacteria, where the overall biomass is however still agglomerating between 80% up to 99.9% of the available environmental Cu [200,201]. An increased Cu binding affinity of EPS has also been considered to induce higher Cu ion release rates effecting reduced bacterial viability in case of an overproduction [202], where EPS defective mutants of *P. aeruginosa* were shown to be more resistant to contact killing. In comparison between different membrane molecules and appendage classes, overproduction of LPS and EPS was linked to an increased bacterial Cu sensitivity, while CA capsule rather induced resistance [202]. Flagella/Pili had no effect on Cu sensitivity.

Experiments in multi passage exposure of *P. fluorescens* [202], *S. aureus* and *E. coli* [56] to sub-lethal Cu doses has been shown to lead to increased bacterial survival rates under laboratory conditions. This effect was especially pronounced in *S. aureus* and *E. coli* where the multi passage mutants were reported to be 12 to 60-fold less susceptible to contact killing. In the final stage, bacterial viability could be retained up to 60 min of direct Cu exposure versus 1-3 min in case of the wild types with a stabilization of Cu resilience over 250 generations. Increased Cu resilience could not be explained by genome sequencing, but rather included a slight adaptation of the membrane setup with a reduced amount of fatty acids that grew along continuous exposure and effectively delayed membrane damage [56].

As a result of artificially elevated environmental Cu concentrations, e.g., due to the use of copper salts for fungal control in agriculture and as a food additive for fattening pigs, an increase in copper resistance beyond natural levels has been observed in soil and gut related bacterial strains [16,200,203]. These isolates are remaining viable in contact to alloys with 70% Cu content, which should entirely deactivate bacteria after 2h of exposure according to the USEPA classification [16]. Increased copper resistance, e.g., in *Streptococcus pneumoniae* and *M. tuberculosis*, is discussed to correlate with the virulence of the corresponding strain (Cu resistant pathogens are considered to exhibit better survival in macrophages) [204,205]. By this, the course of disease in patients infected with heavy metal-resistant strains may be additionally worsened by emerging cross- or co-resistance with antibiotics [206]. In this context, the term "hyper-resistance" was coined, which occurs primarily in *S. aureus* strains [207].

Wilks and Michels et al. [32,58] furthermore reported on environmental impacts on bactericidal Cu efficiency in both *E. coli* and *S. aureus*. On alloys with high Cu content, contact killing of *E. coli* was achieved after 90 min at 20°C, while it took up to 3h to observe the same effect at 4°C on the same Cu substrate [32]. A similar impact can be observed in lowered humidity levels, whereas Cu was shown to retain a certain bactericidal capacity against MRSA while the antibacterial modes of action have not been activated on Ag already in ambient conditions [58]. Similar relations between Cu killing efficiency and environmental temperature have been reported in viruses, as well, where low temperatures of 4°C decrease, while temperatures of 37°C enhance the speed of viral elimination [208]. In the case of viruses, several resilience mechanisms towards Cu have also been shown for different types of bacteriophages, where the least resistant were lipid envelope or single-stranded genome phages [188]. The highest resistance was monitored in dsDNA phages lacking a lipid envelope, which is probably linked to the prevention of lipid Cu aggregation also involved in membrane disintegration in bacteria. Differences in Cu resilience between the phage types were expressed in deviating deactivation rates where nevertheless all phages were effectively deactivated, over time.

In summary, Cu represents an essential element for microorganisms and they have developed several mechanisms to protect themselves from toxic effects in excessive availability. Anyhow, direct exposure to Cu surfaces generally induces environmental Cu levels that overwhelm the regulatory microbial capacities leading to an effective deactivation via “contact killing” [53,209]. In several studies, Cu containing surfaces have been successfully applied in clinical environments [169,210–212]. The replacement of standard materials like stainless steel on frequent-touch surfaces by Cu alloys reportedly reduced the overall microbial burden significantly, which also lead to a decline in antibiotic resistant microorganism contamination including vancomycin resistant *enterococci* and MRSA [213].

2.3.3 | Substrate impact on contact killing

Preliminary work has shown that direct contact between bacteria and substrate plays a supportive role in effective bacterial deactivation [53]. In close relation to this phenomenon, early theories suggested a direct corrosive interaction between bacteria and the substrate surface, whereas more recent studies were able to show that the bacterial uptake of Cu is a rather passive process [214,215]. Corrosion of the Cu substrate is induced by the surrounding medium or atmosphere effecting an emission of Cu ions which might be absorbed in respiratory activity or directly agglomerate on bacterial cells in proximity to the corroded surface [54,214–216]. It was observed that Cu extensively agglomerates in *E. coli* adherent to copper surfaces, which also continues hours after complete bacterial deactivation, where the draining of dissolved Cu ions prevents the formation of passivating oxide layers [54,217]. The resulting preservation of an elevated Cu ion release gives rise to fast intoxication and bacterial killing and is directly linked to the close contact between bacteria and substrate surface enabling the bacterial scavenging of dissolved Cu ions [54]. Although amplified by averted surface passivation, the material inherent capacities of contact killing remain related to quantitative corrosive interaction, which is highly dependent on substrate and environmental properties. Alloying with Ag was shown to catalytically increase Cu ion release (which similarly works for Ag+Pt in antimicrobial Ag applications) [52,186], whereas in the case of pure Cu substrates, Cu emission might be modified by environmental impacts or microstructure engineering.

Corrosion related to biofouling

Alasvand Zarasand et al. [172] investigated on the microbial impact on the corrosion of metals and its potential inhibition dependent on material and environmental conditions. Active microbial involvement in corrosion processes is related to either sulfate-reducing, manganese/iron-oxidizing, iron-reducing or acid-producing bacterial activity in the case of certain strains. Bacterial activity impacting substrate corrosion might furthermore involve the generation of corrosive substances, alteration of anion ratios and the inactivation of corrosion inhibitors, where the actual influence depends on whether metabolic activities contribute to active corrosion mechanisms within the exposed environment. A more uniform microbial impact can be traced back to the active or passive formation of differential concentration cells in liquid environment, subdivided in oxygen, metal ion as well as active-passive concentration cells. In patchy heterogeneous covering, a microbial surface layer may either act as separation to the medium also blocking off the access of oxygen to the surface or directly induce localized decrease of oxygen via cell respiration. In both cases, covered metal surface compartments are anodic due to the inability to form protective oxide layers, while uncovered surface compartments with access to oxygen act as cathodes. In the case of metal ion concentration cells, high affinity of bacterial substances (like, e.g., EPS or the bacterial body itself) to metal ions induces an anodic behavior to covered surface compartments, whereas uncovered or lesser exposed areas act as cathodes. An inversive relation in the formation of both oxygen and metal ion concentration cells is also possible, if preexisting passivation layers below the bacterial covering layer stay intact. An active breaking of mostly oxidic passivation layers (e.g., by bacterial production of metal-chelating agents) furthermore induces the formation of active-passive cells, where the active (metallic) areas as anodes while passive (oxide passivated) areas act as cathodes. How the overall interaction is pronounced in quantitative surface corrosion has been shown to be very sensitive to environmental factors, by which corrosion effects influenced by bacteria appear contradictory in most cases [172].

Considering corrosion as a natural return to the energetically more favorable ore-state of an artificially purified metal, the corrosive effects of biofouling on technical surfaces might be traced back to the early bacterial contribution in mineral formation [218]. Bacteria are involved in mineralization processes since the early stages of life on Earth and are considered as an essential part in natural biogeochemical cycles. The underlying mechanisms of biomineralization are not mineral- or bacteria-specific but rather depend on the environmental conditions and exhibit universal applicability. Biomineralization reportedly involves the precipitation of phosphates, carbonates, sulphates, chlorides, oxalates and silicates [218–220]. The biomineralization of phosphates, e.g., has been shown to form by nucleation and growth on the outer membrane of gram-negative bacteria which effects the formation of kidney and urinary stones commonly accompanying urinary infection [218]. Phosphate precipitation appears to solely require the presence of bacterial organic matrix without a need of metabolic activity, since it was observed on both living and dead bacterial cells [219]. Bacterial membranes have been shown to provide heterogeneous nuclei for phosphate crystallization, which was found in several gram-positive and negative strains, as well as dead bacterial cells of *Pseudomonas* and *Azotobacter* strains [220]. Metallic phosphates have mainly been linked to both extracellular polysaccharide and the cell membrane itself, involving Cu species like cupric phosphate $Cu_3(PO_4)_2$ [54,221]. This has also been described for Ag, where up to 75% of dissolved Ag was found to be bound to cell bodies [222]. Similar to the previously discussed antimicrobial modes of action in Cu, Ag-accumulation on bacteria was described to involve a primary precipitation to membrane polysaccharides and intracellular aggregation in a second step. Uniformly, bacterial biomass exhibits a high metal-binding and mineralization capacity, where viable cell activity and integrity might as well favor decreased metal uptake rates applying metabolic mechanisms of intracellular metal regulation and self-protection [218,219,222]. However, respiratory bacterial activity was also discussed to phosphate precipitation by the formation of a catalytic microenvironment in the vicinity of the bacterial cell [220].

Each of these interactions deplete the dissolved amount of metal ions independent of active or passive bacterial involvement effecting a prevailing electrochemical potential towards the dissolution of bulk metal sources by the formation of metal-ion concentration cells [172], corresponding to the Cu scavenging mechanism described in Luo et al. [54]. The quantitative release of metal ions again depends on the corrosion mechanism present and the mutual influence by substrate properties, which will be considered in more detail with respect to Cu and its antimicrobial properties.

Impact of Cu microstructure on corrosive interaction

In human environment, Cu corrosion mostly involves the exposure to saline fluids, e.g., originating from perspiration that exhibit NaCl levels of up to 20 g/l [223]. These conditions are well reproduced in artificial reagents like Hank´s solution and phosphate buffered saline (PBS) containing between 0.5 M (27 g/l) and 0.137 M (7.4 g/l) NaCl. Under these conditions, dissolved chloride ions (Cl^-) have been shown to promote pitting corrosion of Cu both by the generation of CuCl as well as the catalysis of oxygen-mediated Cu degradation into Cu_2O, $Cu(OH)_2$, e.g., by further enhancing the surface diffusion of Cu ions [215]. Surface passivation of Cu occurs by the epitaxial growth of a Cu_2O layer, which forms an additional passivation layer of CuO under the involvement of $Cu(OH)_2$, both in liquid and humid aqueous environment [224]. Pitting corrosion is electrochemically driven and involves matter redistribution between sacrificial anodic and accepting cathodic surface sites on a heterogeneous surface. Weak spots for anodic pitting corrosion are mostly related to an increased surface energy like in grain boundaries, dislocations or favorable atomic lattice orientation within polycrystalline Cu substrates [217,225]. Lapeire et al. [225] investigated on the grain orientation effect in preferential pitting corrosion of cold-rolled polycrystalline Cu exposed to 0.1 M NaCl saline, where Cu 100 grains were found rather unaffected while neighboring grains underwent corrosive degradation. Between the different orientation arrangements, Cu 100/Cu 111 contacts exhibited the highest overall pitting effect towards the 111 oriented grains. The deviation in neighboring crystal orientation appears to induce a difference in surface potential leading to pronounced localized cathodic/anodic behavior. For the low index planes, the ranking of surface energies is reported to be (111) < (100) < (110) < (210) [225]. In comparison to corrosion experiments, the actual surface energy related to packing density however appears to be of lesser importance in heterogeneous polycrystalline Cu corrosion. Instead, Luo et al. [217] reported a correlation between localized corrosion/passivation in PBS and the befitting of Cu/Cu_2O grain orientation, following a similar orientation neighboring relation like in [225]. The highest thickness of Cu_2O layers was assessed on both Cu 100 and Cu 113 grains, which were therefore better passivated than neighboring grains and lesser exposed to degradation. These observations correlate to early findings of Lawless and Gwathmey [226] who investigated on thermally induced epitaxial oxide growth on single crystal Cu planes. On Cu 100, Cu_2O grew into thicknesses more than double as high as on Cu 111 and Cu 110 planes, which was linked to the available degrees of freedom for single domain oxide nucleation. Cu 100 enables Cu_2O nucleation in five possible orientations, while oxide growth in both Cu 111 and Cu 110 is limited to either two or only one possible orientation. The higher degree of freedom on Cu 100 is discussed to effect a higher density of grain boundaries within the oxide layer, enabling a higher Cu ion diffusion and therefore quicker passivation [226]. In terms of electrochemical interaction, higher passivation capacities induce rather cathodic behavior towards lesser passivated neighboring surface sites, thus potentially causing the corresponding role of Cu 100 grains in saline environment.

Under saline exposure, the orientation dependent intragranular corrosion observed by Lapeire et al. [225] was found to originate from the grain boundaries, where pitting corrosion expands towards anodic grain orientations, finally inducing an anodic role of Cu 111 against most of the other orientations [217]. Localized weak spots of high energetic state, which are related to crystallographic defect sites are therefore considered as the key driving force in saline Cu corrosion [227,228], by which an increased grain boundary/dislocation density is indicative for high Cu ion release rates that potentially enhances antimicrobial efficiency. High dislocation densities have furthermore been shown to induce a positive electrostatic surface charge impacting both corrosive and bacterial interaction [229]. Correlating results on antibacterial efficiency comparing different crystallographic substrate states of Cu materials have been reported, where, e.g., cold-worked Cu sheets exhibited higher antibacterial activity compared to casted parts [32]. In fact, most of the recent reporting on improved antimicrobial Cu surface properties by the application of different surface coating or processing methods can directly be connected to the correlating impact on Cu microstructure favoring higher corrosivity:

Razavipour et al. [230] observed increased inhibition of *P. aeruginosa* biofilm formation and antiviral capacities against the SARS-CoV-2 lentivirus surrogate model on both cold sprayed and shot peened Cu surfaces compared to as-received references. Although a higher initial killing effect was assessed for cold sprayed surfaces, shot peened Cu exhibits a prolonged efficiency increase, which correlates to the applied peening intensity effecting µm-scaled surface roughening, decreased grain sizes and higher dislocation density. The hence increased surface diffusion of Cu ions was found to exhibit the main effect in overall antimicrobial efficiency. A similar increase of bacterial killing on wire arc/cold sprayed Cu coatings was also described by Sharifahmadian et al. [231], discussing a multiscale impact by surface roughening and the fine-grained porous microstructure, as well as Zeiger et al. [232], mostly attributing increased bacterial killing to the rougher topography. Parmar et al. [229] compared the antimicrobial activity of pure Cu in cold-rolled and cryo-rolled condition exhibiting a 14 up to 28 times enhanced dislocation density, where increased killing of *S. aureus* was directly linked to the corresponding increase in Cu ion release via inductively coupled plasma mass spectroscopy (ICP-MS).

With further increasing severe plastic substrate deformation, the earlier described localized pitting corrosion that focusses grain boundaries and dislocations is reported to turn into a rather homogeneous corrosive surface degradation. This is linked to ultra-fine grain sizes (UFG) and high density dislocation networks induced by, e.g., equal-channel angular pressing (ECAP) [233,234] or cold-rolling [235,236], where a clear separation between cathodic and anodic surface sites in an electrochemical microcell formation is no longer possible [237]. The impact of a UFG Cu microstructure on quantitative corrosion varies depending on the corrosive environment, where either decreased [234] or increased corrosion rates [233] have been reported in saline environment. However, under ambient conditions at <0.5 M NaCl levels, a rather general increase of corrosion resistance by UFG was reported in cross-study comparison [237] and linked to a higher and more stable passivation

[236]. A similar microstructure state was achieved by Zhang et al. [238] by grain-fining and implantation of supersaturated dislocation networks via pulsed high-current E-Beam irradiation of Cu. Interestingly, they reported on a dependency of corrosion resistance on pulse accumulation, where corrosivity initially increases up to 5 pulses until it decreases after 10 overlapped pulses marking the set-point of a critical deformation state for the transition from pitting to homogeneous Cu corrosion in saline environment.

A schematic summary of the different impacts on Cu corrosion in <0.5 M NaCl saline discussed in this chapter is provided in **Figure 8**.

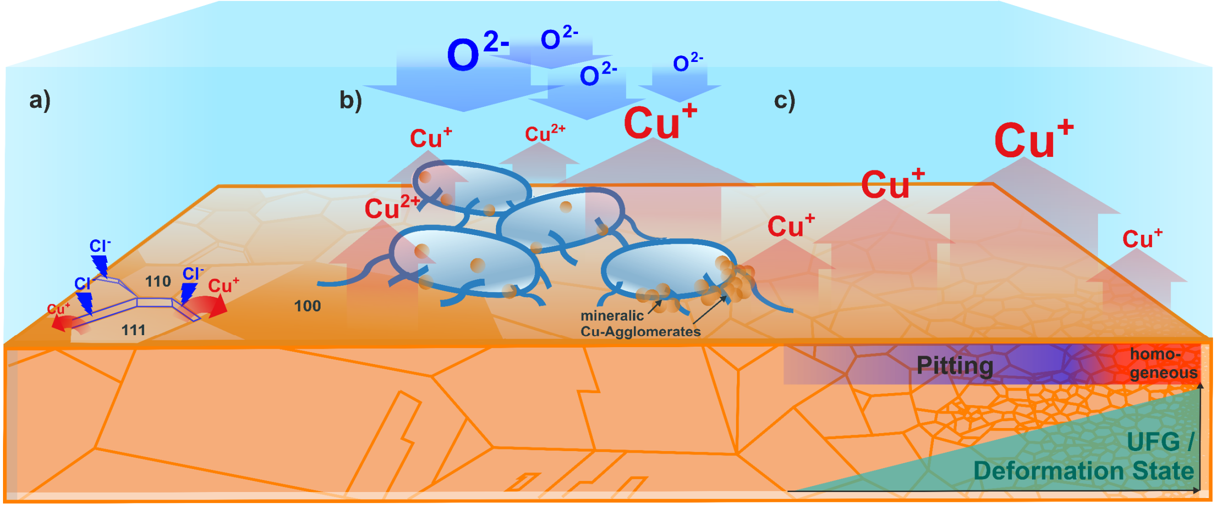

Figure 8: Schematic summary of the Cu corrosion mechanisms and respective impacts in <0.5 NaCl saline as discussed in the current state of literature: a) Cu corrosion in saline mainly involves Cl^- catalyzed pitting corrosion focussing energetic weak spots like grain boundaries and lesser passivated grains within a polycrystalline microstructure. b) Impact of Cu corrosion in the presence of bacteria involves the formation of differential concentration cells and potential membrane precipitation of mineralic Cu compounds like, e.g., cupric phosphate. c) Increase of corrosive interaction by grain fining/ dislocation density enhancement up to a critical point, where pitting tilts into homogeneous corrosion effecting improved passivation.

2.3.4 | Strategies to increase antibacterial Cu efficiency

Although Cu itself exhibits potent antibacterial activity, environmental [58] and microbial impacts [57] might attenuate its killing capacity leading to a critical decline in bacterial deactivation rates [54]. Approaches to enhance the antibacterial efficiency of Cu therefore focus on the amplification of the material inherent modes of action or the complementation of additional, e.g., topographically induced bactericidal capacities. Amongst the readily applied spray coating of Cu materials in decontamination of health care environments [210,211] that is discussed regarding the beneficial microstructural impacts on Cu ion release in the previous chapter, several strategies of Cu efficiency amplification are currently considered.

Cu application in NP distributions as coating, composite or in liquid solution is aiming to increase both bacterial Cu uptake suggesting an increased membrane permeability as well as cell membrane disintegration by quantitative Cu NP agglomeration. In fact, several studies report on both increased membrane agglomeration as well as visible cell rupturing in *P. aeruginosa* and *S. aureus* strains including MRSA, which have been exposed to Cu NP in liquid solution [60,239,240]. A potential driving force behind the membrane agglomeration of Cu NP has been associated with the positive surface charge of the primarily oxide particles due to electrostatic interaction with the negatively charged bacterial surface [240–242]. Comparing the impact of particle size, membrane damage exhibits an earlier onset for nm-scaled compared to µm-scaled Cu particles, whereas the overall impact on bacterial cell integrity equals after 4h of exposure [175]. Cu NP are mostly related to 10-150 nm-scaled particles of either pure Cu, Cu_2O, CuO, $Cu(OH)_2$ as well as CuS, where in the case of pure

Cu NP a considerable content of surface oxide have to be considered in the actual particle composition [60,64,175,241,243,244]. Each of these NP compositions is characterized by a different binding strength of the Cu within the particle, which has a direct effect on the antimicrobial functionality. Comparison in between pure Cu and CuO NP, e.g., assessed a higher antimicrobial efficiency of the former type, which was directly linked to the effective Cu ion release rate [61,175]. However, the comparably low antibacterial effect of CuO NPs was shown to be potentially enhanced against *B. subtilis, S. pneumoniae* and *Morganella morganii* by the addition of Ag [245]. CuS exhibits a low but steady Cu release due to the strong bond, achieving 95% bacterial killing after 5h and 99.9% after 24h of exposure [243]. Based on these observations, the antimicrobial efficiency of Cu NP appear to be subject to the same basic restrictions like bulk Cu materials [51,64]. Aside of the predominant impact of Cu ion release, Ananth et al. [59] were able to show that particle morphology might also play a role in antibacterial efficiency in the case of CuO NPs, where plate-like particles shapes exhibited higher killing efficiency against several gram-positive and negative strains than granular of needle-like particles. Independent of the application, bacterial deactivation by Cu NP ranges close to or below 95% within the first 2h of exposure in most of the reported cases, by which an effective bactericidal capacity befitting the USEPA demands can hardly be achieved.

More recent works discuss laser-based routes to enhance the bacterial contact killing rates on solid Cu surfaces by nanosecond pulsed irradiation [65,246]. Here, the exposure to lowly focused irradiation leads to thermally induced formation of sharp asperities of CuO resembling the topographic blueprint of *cicada* and *dragonfly* wings [69]. Appropriately, increased antibacterial properties by mechanically induced membrane rupturing was reported in liquid environment, where bacteria were pierced on the CuO surface crystallites. Within the first three days after production, these surfaces exhibit increased hydrophilicity enabling a high fluid drag into the surface cavities that agitates the bacteria towards the sharp surface asperities. However, these surfaces turn into super-hydrophobic surface wetting after a certain storage time following a time-dependent surface passivation under the involvement of agglomerating atmospheric carbon-groups, by which the additional mechanistic mode of action is deactivated [80,247]. Furthermore, the thick Cu oxide layer leads to considerably decreased Cu ion release, by which the antibacterial capacities of these surfaces fall below the reference values [66,68].

A similar topographic/mechanistic approach recently introduced by Smith et al. [62] considerably increased bactericidal efficiency against *S. aureus* by structural modification of bulk Cu. Selective etching of a precursor Cu Mn composite material induced an open-porous Cu substrate morphology with considerably increased surface/volume ratio. In combination with fluid drag forces towards the super-hydrophilic porous surface mesh, topographically induced bacterial membrane stretching was discussed as a possible mode of action, whereas the considerably increased initial dissolution of Cu in PBS due to the high surface/volume ratio probably exhibits an even more potent effect. However, Cu ion release was observed to drop after approx. 1h of exposure due to electrochemical surface passivation, also depleting the initial bactericidal capacities.

3 | Ultrashort Pulsed Laser processing

The term “ultrashort laser pulses” comprises single pulse durations τ_p that range below the upper threshold value of 10 picoseconds (ps, 10^{-12} s), which furthermore includes the yet technically realized femto- (fs, 10^{-15} s) and attosecond (as, 10^{-18} s) pulse durations. On this time scale intramolecular and -atomic processes involving low mass elementary particles take place, while micro-/macroscopic interactions of the bulk substrate such as solid-state or solid/liquid/gas phase changes involving multiple atomic domains interactions require longer periods of time, up to the nanosecond (ns, 10^{-9} s) range. By this, USP irradiation in the fs regime has been well applied in molecular analytics, where Ahmed H. Zewail as one of the pioneers has been awarded with the Nobel prize of chemistry in 1999, while recently Ferenc Krausz, Pierre Agostini and Anne L'Huillier have been granted with the Nobel prize of physics in 2023 for the analysis of electron behavior applying attosecond laser pulses. Higher pulse energies and beam intensities for quantitative material processing have been enabled in the late 20th century by the development of chirped pulse amplification (CPA), where a further increase of yet low initial seed beam intensities is conducted in a secondary active crystal by means of a temporary expanded pulse profile to avoid destruction of the active medium. For this invention, Artur Ashkin, Gérard Morou and Donna Strickland - also involved in early investigation of solid state material interaction in response to USP irradiation [248] - have been awarded with the Nobel prize of physics in 2018. Today, ultrashort laser pulses found their way in many applications involving molecular and sub-atomic analysis, surgery as well as micro-scaled industrial processing [249].

3.1 | Specifications of USP laser/material interaction

When laser irradiation strikes solid matter, the laser beam´s intensity is separated into partitions that get either reflected, absorbed or transmitted. In opaque materials non-reflected photons are readily absorbed by electron or electron-hole excitation, followed by a transfer of the energy to the atomic lattice of the bulk substrate by the formation of a thermal equilibrium τ_{eq} between the carrier and the lattice sub-system via electron-phonon relaxation. This initial interaction occurs by the coupling between charge carriers (either electrons or electron-holes) and the electric field of the beam. Laser/material interaction is therefore governed by the mutual physical parameters/properties including the laser wavelength λ, pulse duration τ_p and fluence of the laser pulse as well as optical, mechanical and thermal substrate properties. The time-scale to achieve τ_{eq} alters between 10^{-12} and 10^{-11} s dependent on the material specific electron-phonon coupling strength, also marking the upper temporal threshold of the USP regime [250]. An energy transfer to the lattice induces thermal material responses involving, e.g., phase changes up to ablation, whereby electron removal might similarly be induced by excess excitation effecting ionization and potential atomic bond breaking. The time-frame of these lattice interaction finally scales up to milliseconds including melt-expansion, ablation up to solidification processes (see **Figure 9** for an overview). Material interaction upon USP irradiation has widely been approached by physical modelling, whereas the individual time-frames of substrate response could be assured by pump-probe analysis and time of flight spectroscopy in various studies [251–254].

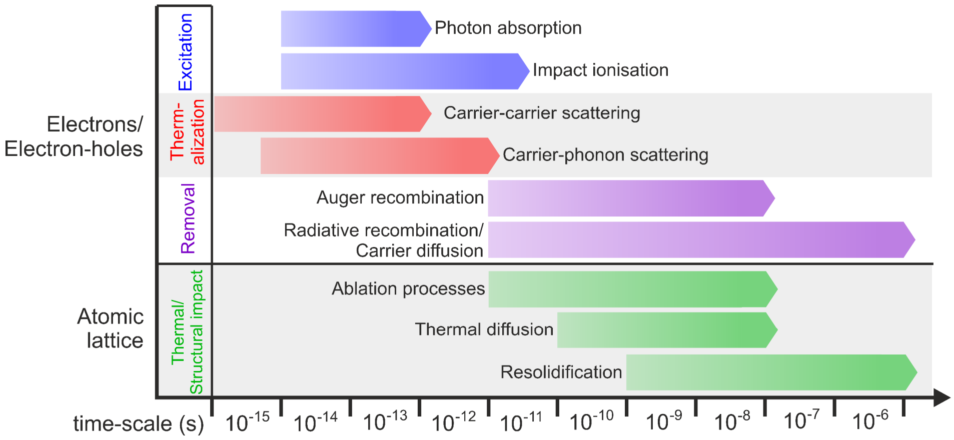

Figure 9: Time-scales of atomic level substrate response on laser irradiation, where sub-atomic scaled processes mostly take place within the initial 1-10 ps after irradiation, while atomic/substrate scaled processes are starting to be effective after several ps. Modified according to [250].

The relation between τ_{eq} and the pulse duration τ_p decides which route further material interaction in response to the deposited energy might take dependent of the time frame of energy implantation. In case of $\tau_p \gg \tau_{eq}$, a thermal equilibrium between the carrier and lattice sub-system is established throughout the majority of the irradiation time-frame leading to predominantly thermal substrate responses involving melting, evaporation and the formation of a heat affection zone via thermal diffusion. At $\tau_p > \tau_{eq}$, structural changes occurring on lower time-scales potentially impact the absorption of the rear temporal flank of the laser pulse. Here, a certain formation of a heat affection zone might still take place, especially in highly conductive materials. For $\tau_p < \tau_{eq}$, the energy implantation is concluded before a considerable energy transfer to the substrate lattice system can be initiated inducing a pronounced thermal carrier/lattice disequilibrium. The corresponding pulse durations in the USP regime are associated with specific ablation mechanisms involving low rates up to no thermal substrate affection coining the term of “cold ablation” [249]. The slightly extended range of initiated substrate response between 1-10 ps indicates a potential deviation of material specific interaction within the upper USP regime dependent on individual electron-phonon relaxation times, where a $\tau_p > \tau_{eq}$ relation might still occur within the boundaries of $\tau_p < 10$ ps. Dependent on the material´s atomic bonding type (metallic, covalent, ionic) and the respective impact of USP laser irradiation on its carrier system, substrate response involves either photochemical (especially in dielectrics and highly ionic semi-conductors) or photothermal interaction (predominant in metals but also relevant in semi-conductors).

Experimental investigation of material specific ablation mechanisms has been conducted since the late 2000´s with the availability of the first CPA-based USP systems to deduce the peculiarities of USP laser material processing dependent on pulse duration and irradiated/absorbed laser fluence. Here, Nolte et al. [255] were able to evidence the occurrence of two separable regimes of altering ablation behavior on metals dependent to either fs or ps pulse duration as well as fluence ranging between 0.1 to 10 J/cm². This initial observations already led to targeted process fine tuning for micromachining via fs-pulsed laser ablation [256]. Simon et al. [257] in parallel showed that a certain amount of surface melting appears to be still involved in ultrashort ablation processes for Cu and Si despite the USP pulse durations, which impacts the surface morphology of the processed substrates. In fact, ablation behavior in response to USP irradiation was later been shown to deviate considerably with a variation of processing laser parameters even within a single material class in response to the grave electron disequilibria states initiated by the elevated pulse intensities [258,259]. Early substrate response in the sub-ps to ps time-frame includes considerable electron emission alongside carrier system heating that induces surface charging of the substrate. Whereas ablation dynamics in dielectrics might involve considerable ion-emission and bond breaking in response to electron depletion leading to specific ionization related ablation mechanisms like coulomb-explosion [260], semi-conductors and metals have been shown to exhibit weaker surface charging due to higher carrier mobility [261]. Both material classes exhibit either thermomechanical (spallation) or thermodynamical (phase explosion) ablation under the involvement of ultrafast homogeneous or heterogeneous formation of a sub- or supercritical fluidic state that is highly compressed due to the yet pending physical expansion in these short time scales [261–263].

Spallation vs. phase explosion

In the case of spallation, the unloading of thermally induced stress in the further relaxation process generates mechanic shockwaves within the super-heated semi-fluidic substrate compartment that get refracted at the solid/fluid phase boundary. Alongside the hence effected acoustic relaxation of the mechanic shockwaves, internal yield is generated that can range above the substrate inherent tensile strength leading to a boiling-like void formation at the solid/fluid boundary that potentially detaches the super-heated substrate compartments from the surface. More recent approaches to model spallative ablation furthermore consider the additional involvement of sub-surface boiling under the formation of a gaseous phase alongside localized acoustic stress relaxation [261]. Although being mainly discussed under theoretical assumption, a hint to the acoustic unloading of internal stresses within confined initial fluidic substrate compartments has been experimentally observed by the formation of “newton rings” within the melt-dome of USP irradiated Si, which are generated by the interference of reflection on the dome surface and the physically separated phase front below [264]. The generated crater depth of spallative ablation has been shown to be mostly related to optical intrusion depths independent of pulse duration at < 10 ps, indicating a rather uniform USP ablation mechanism. Spallation is triggered by laser fluences at the material specific ablation threshold F_{abl} and up to 1.5× above, enabling the formation of yet subcritical melting [265].

Applying further increased fluences, the elevated heating of the ultrafast generated molten substrate compartments in turn induces a supercritical fluid state where temperatures of the yet confined matter considerable scale over the material specific melting or vaporization temperatures. Unloading of the accumulated internal energies follows the same time-scale of acoustic relaxation like spallation but rather involves the heterogeneous precipitation of gaseous phase compartments due to higher internal pressure from the elevated matter temperatures. The onset of quantitative internal expansion after a few ps induces an explosive ablation under the involvement of a hydrodynamic lift-off of the liquid/gas mixture accompanied by the generation of high pressures up to 10^2-10^3 GPa [261]. On this behalf, phase explosion was discussed to be related to fluences that induce substrate heating above the material-specific phase explosion threshold T_{PE} scaling at $0.9T_{cr}$ (T_{cr} = 7696 K in the case of Cu) [266]. A schematic comparison between ablation kinetics of spallation and phase explosion is illustrated in **Figure 10**.

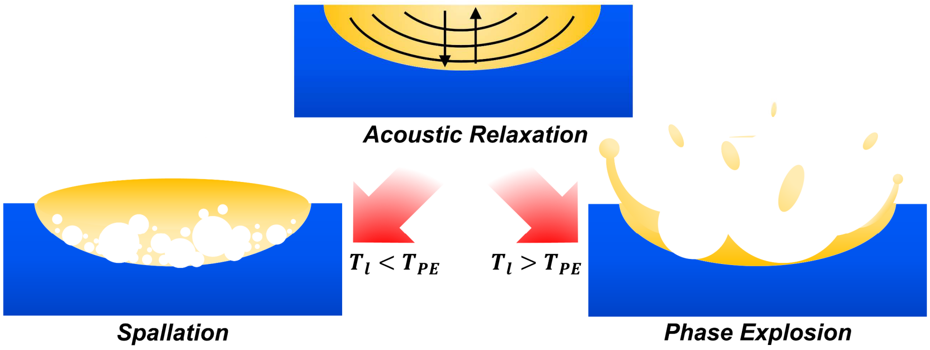

Figure 10: Schematic illustration of the two mechanisms of USP induced thermal ablation following the acoustic relaxation of confined stress within a sub- or supercritical fluid, involving either thermomechanical spallation or thermodynamic phase explosion, dependent on substrate heating $\boldsymbol{T_l}$ in relation to the material specific phase explosion threshold temperature $\boldsymbol{T_{PE}}$. Modified according to [261].

It has been shown that electron-phonon coupling strength might impact the expression of the phase explosion mechanism, where weaker coupling (like in Au, Ag and Cu) leads to a more pronounced explosive ablation, while stronger coupling might reduce the critical overheating by continuous evaporative cooling alongside early ion emission for higher pulse durations in the ps regime, as observed for iron [267]. A similar dependency between the observed ablation mechanisms and τ_p in relation to the effected lattice heating was reported by Winter et al. [265] for Cu, Al and stainless steel. Here, a predominantly thermodynamic ablation via phase explosion was assessed at higher pulse durations up to 20 ps also involving an increase in F_{abl}, where thermomechanical stress confinement involved in spallative ablation appears to be attenuated at $\tau_p > \tau_{eq}$. In fact, a mixed state of thermomechanical spallation and thermodynamic phase explosion have been shown to be involved in effective USP ablation, where a purposeful tuning of the ablation process enables both high processing efficiency and feature quality [250]. Here, Schille et al. [268] defined a mid-fluence regime between 1.5 to 4 J/cm² exhibiting the highest matter removal rates at a yet comparably mild surface yield by phase explosion for the majority of technical materials. Within the fluence range from 0.1 to 10 J/cm² relevant for USP micromachining, the low-fluence regime < 1.5 J/cm² is considered to be rather related to predominant spallation exhibiting low ablation rates, while the high-fluence regime > 4 J/cm² is dominated by ablation via phase explosion, where both ablation rate and surface quality might be impaired by agitated hot matter dynamics.

With the onset of ablation processes in the time-frame above 10 ps, both the physical expansion as well as the quantitative removal of hot matter compartments from the surface induces a strong convective cooling effect, which eventually freezes dynamically agitated melt-fronts and impedes thermal diffusion into the bulk substrate [254]. The superficial substrate modification by USP irradiation can hence involve the material specific formation of ablation related surface morphologies, whereas high pressure applied by acoustic stress relaxation as well as the explosive expansion might similarly lead to deformation and defect implantation into the substrate surface. To further increase the understanding of internal substrate processes involved in the modification of surface morphology as well as the internal substrate structure, experimental investigation is usually supplemented by numerical modelling or simulation of the thermal substrate responses.

3.2 | Modelling the substrate response on USP irradiation

The time-scales of USP material interaction majorly range below the temporal resolution limit of most relevant analytical methods, by which physical modelling has become a well-applied tool in the investigation of USP material processing. To account for the considerable initial thermal carrier/lattice disequilibria upon USP irradiation in the early time-frames below 1-10 ps, Anisimov et al. introduced the two-temperature model (TTM) allowing for a separate consideration of the electron gas (carrier) and the lattice temperatures T_e and T_l within one-dimensional heat implantation and conduction [269,270]:

$$C_e(T_e)\frac{\partial T_e}{\partial t} = \left[k_e(T_e)\frac{\partial T_e}{\partial z}\right] - G(T_e - T_l) + S_{Laser} \tag{3}$$

$$C_l(T_l)\frac{\partial T_l}{\partial t} = \left[k_l(T_l)\frac{\partial T_l}{\partial z}\right] + G(T_e - T_l) \tag{4}$$

Within the TTM, both thermal sub-systems are fully described by individual heat capacities (C_e, C_l) and thermal conductivities (k_e, k_l), whereby energy implantation by laser irradiation occurs in the electron sub-system (implemented by the source term S_{Laser}), which is considered a Fermi-gas according to the Drude-Sommerfeld model. Lattice heating is induced by an energy transfer between electron gas and lattice under the involvement of electron-phonon coupling represented by the material specific coupling coefficient G. Each of the parameters represented in the TTM exhibit a certain dynamic alongside USP energy implantation, where especially the properties of the electron sub-system have been shown to be highly dependent on T_e (C_e) or the T_e/T_l gradient (k_e, G) [271–273]. Due to the ultrafast excitation of the electron sub-system, optical material properties have been shown to be affected within the time-frame of single pulse laser irradiation, as well, by which the rear pulse flank couples into a hot electron gas that exhibits modified absorptivity, even within fs pulse durations [266,274,275]. Considering a one-dimensional depth dependent absorption of laser energy according to the Beer-Lambert Law, the corresponding source term S_{Laser} has to be complement accordingly by the implementation of a functional relation between optical substrate properties and T_e, where α is the material specific absorptivity, R the reflectivity and $I\ (x,t)$ the temporal and spatial laser intensity distribution.

$$S_{Laser}\,(\mathrm{x,z,t}) = \alpha(T_e)\left(1 - R(T_e)\right) I(x,t)^{-\alpha z} \tag{5}$$

Embedded in numerical analyzation, finite element modelling (FEM) or molecular dynamics (MD) simulations, the TTM has emerged into a common tool to model ultrafast material interaction, which allows further understanding of experimental results as well as the investigation of specific substrate responses to USP irradiation on an ultrashort time-scale.

Zhigilei et al. [276] have been able to reproduce pulse width specific ablation via MD-Simulation on Ni represented by three different ablation regimes involving surface melting, spallation, phase explosion in the single digit ps range, whereas stress confinement leading to spallation and higher ablation yield is averted at 50 ps pulse duration. In fact, MD-modelling allows to grasp the ablation kinetics related to USP-irradiation, which supported in the refining of early theories on the thermodynamics of USP ablation processes including the verification of a parallel occurrence of both spallative and phase explosion ablation mechanisms dependent on the implanted energy [250]. This includes the studying of excessively excited electron states and the correlating lattice interaction via electron-phonon coupling, which has been shown to impact the dynamic variation of optical material properties as well as lattice stability [262,277,278]. Based on this, ultrafast homogeneous melting due to non-thermal substrate responses has been evidenced [278,279], which physically enable the thermomechanical relevant mechanisms of stress confinement as well as acoustic shock wave propagation. Lately, these results have been further validified by a combined approach of numerical simulation and X-ray diffraction (XRD) analysis [263,280]. In similar means, the alteration of optical absorptivity alongside USP irradiation due to ultrafast carrier excitation is assessed to allow for further tuning of modelling precision [266,281,282].

Dependent on the scientific approach, the application of modeling means in the investigation of USP related material interaction focusses on either a deeper understanding of inter-atomic processes and solid state physics on an ultrashort time scale [258,279,283–285], or rather ablative substrate interaction to fine tune material processing strategies [286,287]. This might involve the determination of localized heating [78] as well as kinetic ablation processes [288,289] involved in the formation of deterministic surface patterns by periodic spatial intensity distributions. The refinement of the modeling possibilities through the research of the first naturally benefits the second, since material specific parameters to design an applicable TTM are yet scarce and often imprecise [290].

Aside of the investigation of hot matter kinetics involved in topographic substrate processing, the actual thermomechanical impact on the internal substrate structure is similarly assessable by means of physical modelling, as exemplarily illustrated in **Figure 11**. Here, Xiong et al. [291] have been able to determine deviating thermal diffusion, ablation rate as well as thermomechanical crystal defect implantation for polycrystalline Cu, where ablation/defect implantation scales as 111 > 110 >> 100 for low indexed plane orientations. This has been related to higher thermomechanical coupling for 111 and 110 orientations, by which a deeper melting zone and higher dislocation agglomeration up to void formation was induced. Comparable impacts of USP induced thermalization on the microstructure of Cu were modelled by other groups, as well [284,285,289].

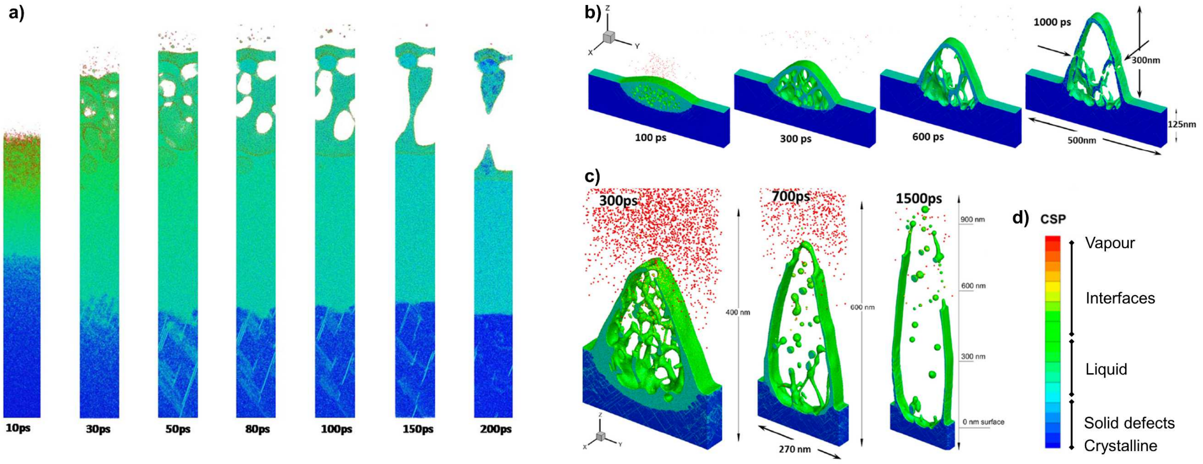

Figure 11: atomistic MD-simulation plots exhibiting a) a classic slab-design [250] and b, c) a local surface features within a periodic arrangement, where scale of MD-simulation dimensions is limited to computing capacity. Each plot displays the time resolved substrate response on USP irradiation of either a) Cu exhibiting energy implantation corresponding to a wavelength of 800 nm, pulse duration of 100 fs and fluence of 1.16 J/cm² as well as Au at a wavelength of 248 nm, pulse duration of 1.6 ps at b) 0.16 J/cm² and c) 0.25 J/cm². d) The atomistic state within the MD-plots is color-indicated, which represents a centro-symmetric parameter that indicates the local phase state. Adapted from [291] and [289].

In summary, TTM based modelling of the substrate response to USP irradiation has been proven to majorly support the understanding of substrate interaction as such, as well as to improve parametrization especially under involvement of processing strategies aiming for µm- down to nm-scaled precision. Especially for advanced USP application an implementation of modelling can therefore highly support process design.

3.3 | Substrate modification alongside multi-pulse USP processing

3.3.1 | Incubation

Since material interaction in response to USP-irradiation does not involve significant heat diffusion into the bulk substrate, single pulse ablation is limited to scales around the optical penetration or absorption depth of $\delta = 1/\alpha$, where the irradiated laser intensity drops to $1/e$ ranging around a few 10 nm for most metals. To achieve a quantitative impact on substrate topography, USP surface processing requires the application of multiple pulses within a confined area effecting higher ablation volumes. Similar to the impact of excited carrier states during single pulse irradiation [266], the continuous modification of the substrate topography, surface chemistry and internal structure alongside consecutive irradiation potentially impacts optical absorptivity of the substrate surface and in turn laser/material interaction. Jee et al. [292] have evidenced an impact of multi-pulse accumulation on the effective ablation threshold of single crystal metals applying laser pulses of 10 ns pulse duration at a wavelength of 1064 nm. The ablation threshold decrease was traced back to both damage accumulation and surface roughening, where the initial preparation of samples has already been shown to have an impact due to the resulting initial surface deformation state. A higher defect accumulation was found on 111 compared to 110 plane orientations for Cu, where also a formation of LIPSS could be assessed, which is actually rather associated with USP pulse durations [293]. Based on these observations, Jee et al. formulated a universal incubation law, where the effective ablation threshold F_N after N pulses is related to the initial threshold F_0 and the material specific incubation coefficient S:

$$F_N = F_0 N^{S-1} \tag{6}$$

The estimation of S is related to a correlation of experimental data between single ablation spot development over consecutive pulse accumulation, as exemplarily illustrated in **Figure 12**.

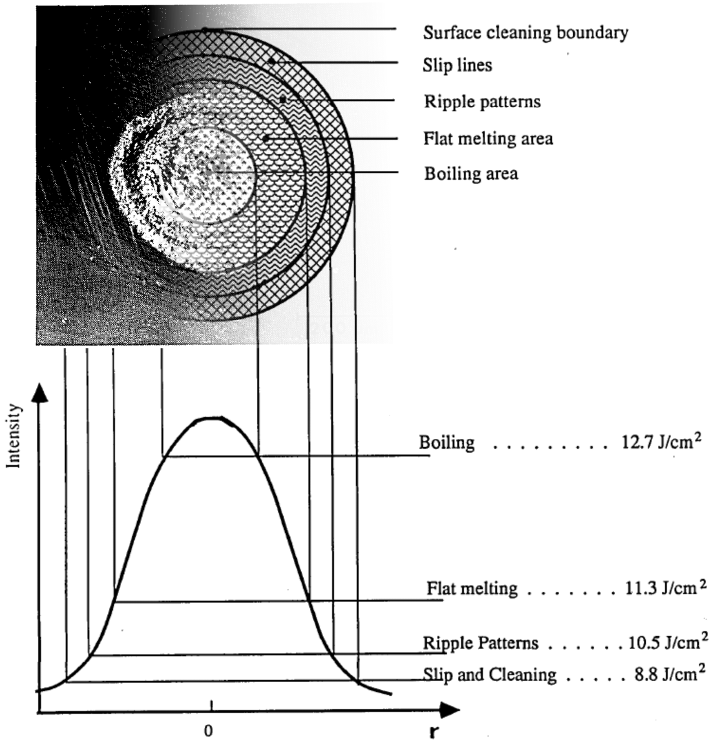

Figure 12: Exemplary illustration of damage threshold fluences F_D related to various morphologies induced by multi-pulse laser irradiation of chemically polished 110 Cu surfaces at 10 ns and a wavelength of 1064 nm. Adapted from [292].

Here, a modification of the formation threshold of specific surface features F_D is related to spot expansion based on multi-pulse irradiation with a Gaussian intensity profile at a peak fluence of F_{max} via the spot diameter of surface modification x_D and the beam width w_d. As a consequence of incubation, F_D is declining with increasing pulse count.

$$F_D = {F_{max}}^{-2x_D^2/{w_d}^2} \tag{7}$$

The incubation coefficient S correlates to the slope of accumulated fluence and the corresponding pulse count, which can be related to the pulse wise expanding area of quantitative surface damage. In [292], F_D was related to the occurrence of visible surface damages scaling in the range between flat melting and ripple pattern (LIPSS) formation. Based on this, the estimation of S is not always straight forward and might in turn strongly depend on the visible amount of material specific interaction on laser irradiation. The peculiarities of material specific incubation alongside multi-pulse processing were already highlighted within the same study, where S varied between the 111 and 110 plane orientation of Cu [292].

Based on Jee´s law of incubation, investigation of surface incubation alongside multi-pulse processing has been conducted in a focused manner for various parameter constellations in USP processing of Cu surfaces, while also adaptations have been made, e.g., to enable an application for dielectrics and semi-conductors [294]. Mannion et al. [295] investigated damage accumulation on several metals alongside USP irradiation with a pulse duration of 150 fs and a wavelength of 775 nm after 5, 10, 15 and 100 pulses also involving polycrystalline Cu sheets. Based on the relation of x_D to applied fluence F and the ablation threshold F_{abl} in equation (8), a direct connection to the incubation wise expanse of single spot ablation craters was formulated including Jee´s law of incubation.

$$ {x_D}^2 = 2{w_d}^2 \ln\left(\frac{F}{F_{abl}}\right) \tag{8}$$

$$x_D = w_d \sqrt{2 \ln\left(\frac{F}{F_0 N^{S-1}}\right)} \tag{9}$$

In [295], the reduction of F_{abl} by incubation is discussed to be traceable to the accumulation of laser induced thermal stress fields within the substrate. The expanse of x_D alongside multi-pulse USP-irradiation was shown to follow a steep slope within the first 10 pulses and gradually attenuate up to 100 pulses highlighting a particularly strong expression of the incubation effect in the initial phase of material processing. A transition between spallation and phase explosion with increasing pulse count at a constant fluence was related to the modification of surface morphology of the ablation craters, while also LIPSS were observed alongside “gentle” fluence regimes on Cu. The incubation coefficient $S = 0.87$ calculated by [295] corresponds to the values of Jee et al. [292] with $S = 0.92$ for 110 and $S = 0.85$ for single crystal Cu, despite the differences in pulse duration, where the scaling of ablation threshold should be assumed as ${\tau_p}^{0.5}$. In contrast, Kirkwood et al. [296] found $S = 0.76$ on clean Cu foils and thin films for almost similar laser parameters (120 fs, 800 nm), where however the individual Cu single pulse ablation thresholds calculated already exhibit a certain deviation with $F_{0\,Mannion} = 0.58$ J/cm² and $F_{0\,Kirkwood} = 1.06$ - 1.1 J/cm². This highlights both the limitations in accessibility of incubation by experimental means, where the experimental setup might modify the beam shape hence affecting readability of x_D (in [295] diffraction rings were formed by a pin hole aperture, while in [296] the beam profile was not circular but elliptical), as well as a potential impact of initial Cu surface properties of the different substrate states on early state laser/material interaction.

In fact, after extended aging under ambient condition, a decrease of F_0 was also observed for thin film Cu samples in [296].

Further investigation on the incubation of Cu involved modified pulse durations up to 10 ps, where both higher F_0 and F_N ablation thresholds were observed in [297] compared to fs-based ablation consistent with ${\tau_p}^{0.5}$. In [265], an increase of F_{abl} with τ_p is paralleled with a decrease in ablation efficiency attributed to reduced compartments of thermomechanical ablation involving stress confinement at pulse durations > 5 ps. Alongside an alteration in ablation kinetics, incubation in multi-pulse processing was similarly been found to be highly dependent on pulse duration, as well as the applied fluence, where the pulse wise increase of F_N exhibits a slope steepening from 0.4 J/cm² up to 3 J/cm² alongside further pronouncing phase explosion. Above this fluence levels, incubation does not increase significantly, anymore befitting the mid-fluence regime considerations of [268].

Different impacts of laser induced surface modification have been discussed in connection to incubation, which are highly dependent on the mutual interaction of thermomechanical/-dynamical substrate response and the laser parameters applied. Potential mechanisms of incubation include the modification of topography, chemistry and the internal substrate structure, by which they might similarly impact functional Cu surface properties related to microbial responses that have been discussed in the **Chapter 1** and **2**. In the following sections, the modification of Cu surface and substrate properties by multi-pulse USP laser processing is therefore considered both in its influence on laser/material interaction in terms of incubation as well as application related surface functionalization within in the scope of this work.

3.3.2 | Impact of topography

The modification of topography is yet considered to exhibit the strongest impact on optical surface properties related to incubation. Independent of the material, USP induced ablation causes surface roughening in the nm- up to the µm-scale depending on the ablation mechanism taking place. Here, ablation induced roughening on metals exhibiting a low electron-phonon coupling strength like Cu is more pronounced than, e.g., on Steel, due to the deviating ablation behavior with higher compartments of phase explosion, as visible for single pulse irradiation at τ_p = 525 fs or 20 ps and $3 \times F_{abl}$ in **Figure 13** [265].

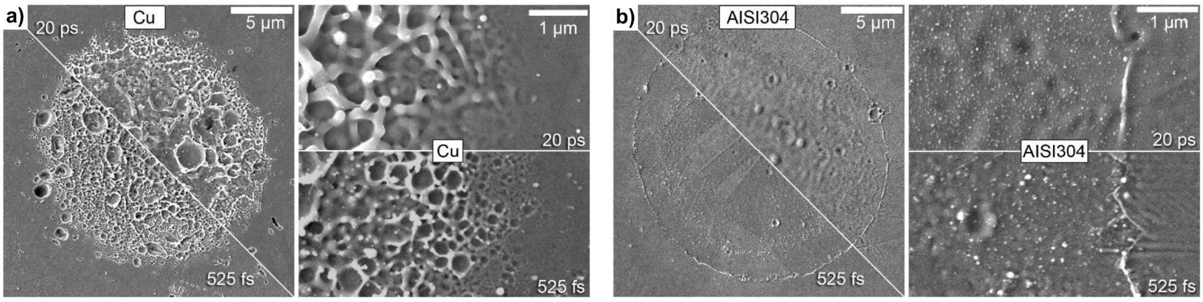

Figure 13: Comparison of nm-scaled surface roughening on a) Cu and b) AISI 304 stainless steel via melt agitation induced by ablation at fluences of $\mathbf{3 \times F_{abl}}$ and pulse durations of either 525 fs or 20 ps majorly related to phase explosion. Phase explosion as well as the related crated formation is more pronounced at longer pulse durations as well as lower electron-phonon coupling strength. Adapted from [265].

Vorobyev et al. [298] monitored the pulse wise modification of surface reflectivity on mechanically polished Ar$^+$-etched Cu surfaces after irradiation at a pulse duration of 66 fs and 800 nm wavelength dependent on the fluence applied. To involve the potential amplification of absorption by excited surface electron states in combination with the nm-scaled roughening of the topography, reflectivity was measured both for processing relevant as well as sub-ablative fluences. In fact, reflectivity was shown to deviate dependent on the monitoring fluence applied, where higher fluences exhibited lower reflectance alongside increased surface roughening already after few pulses. The decrease in reflectivity was also found to be more pronounced for higher fluences, where initial reflectivity is already lowered, which might be linked to higher excited electron temperatures as well as a stronger modification of topography alongside enhanced phase explosion kinetics. The crater-like surface morphology of Cu induced by phase explosion ablation exhibits a general behavior of pulse wise increase in crater diameter as well as stochastic surface roughening [299]. The related topographic features that scale below the applied wavelength generally lead to increased absorptivity due to a graded refractive index (antireflection effect) [79] and plasmonic absorption (also related to LIPSS formation [300]). A more pronounced cavity formation might similarly lead to trapping via diffusive scattering similar to the key-hole effect in laser welding. According to [298] ablation induced surface roughening on Cu appears to have the highest effect in case of high-intensity irradiation both by electron excitation as well as effective surface roughening. By this, initial absorptivity was found to be increased two- up to three-fold already after the first pulse [301].

Laser-Induced Periodic Surface Structures (LIPSS)

With a more pronounced topography modification, absorption of laser irradiation might become sensitive to beam polarization, which was barely observable in [298] but found for USP irradiation of Cu at incidence angles above 45°[248,251]. This might give rise to laser-induced self-organizing surface morphologies like LIPSS that have been found to be highly dependent on a certain amount of initial surface roughening combined with preferential ablation/melt-dynamics influenced by laser beam polarization. In recent theories of LIPSS formation, an irradiating laser pulse is interfering with surface plasmon polaritons (SPP) that are generated in response to photon absorption from the preceding pulse edge, which leads to a periodically modified laser intensity pattern in perpendicular orientation to the electric-field polarization of the laser pulse that photothermally interacts with the substrate surface [302]. In case of a nm-roughened topography, the interaction between the external electric field of the irradiating laser pulse, as well as the internal SPP field is facilitated due to the diffuse surface boundary layer of the substrate surface effecting a higher overlap of both fields [303]. The SPP based mechanism of self-interference is linked to the availability of free carriers in the vicinity of the substrate surface, which is characteristic for metals and some semi-conductors, although LIPSS formation can also be observed on dielectrics [304]. Here, electron excitation via multi photon absorption is assumed to contribute to a filling of the conduction band in semi-conductors and dielectrics according to the Sipe-Drude Modell by which they gain metal-like properties [305]. LIPSS are separated in either low spatial frequency LIPSS (LSFL, $> \lambda/2$) or high spatial frequency LIPSS (HSFL, $< \lambda/2$) by feature size and pattern orientation in relation to beam polarization. Although especially LSFL are highly bound to pattern periodicities slightly below the laser wavelength, LIPSS periodicity was found to depend on the incidence angle, where also scale relations $> \lambda$ have been observed [303].

Several theories on the underlying mechanisms of topographic surface modification are under debate that might be active in a combined or separate manner in LIPSS formation involving preferential ablation and/or dynamic melt kinetics. Marangoni convection within superficial melt pools is considered to be majorly involved in HSFL formation, while especially the depth development of LSFL additionally requires a certain amount of ablative interaction [302]. Currently, a transformation of the active mechanism alongside multi-pulse response is considered most likely, where initial surface modification is modulated by SPP interference potentially including melt dynamics driven by acoustic or capillary waves as well as Marangoni convection, while further pattern pronunciation follows a heterogeneous energy implantation modulated by surface roughness or localized defect formation [304].

Although LIPSS formation is majorly related to USP laser processes, observations on Cu have also been made for short pulse durations in the ps- [306] and ns-regime [292]. Alongside USP irradiation, LIPSS formation on Cu is majorly linked to high pulse accumulation of several 100 up to 1000 pulses [303,307], while other metals might already exhibit LIPSS formation after less than 20 pulses [302,304]. Due to the potential relation on early state melt dynamics, LIPSS formation is commonly related to low fluence regimes, where phase explosion kinetics are majorly attenuated. The need for an initial melt reorganization via, e.g., Marangoni convection might similarly cause the lesser expressed LIPSS formation on Cu exhibiting agitated melt dynamics alongside USP processing. On this behalf a potential involvement of process-induced surface oxidation including particle redeposition might be assumed [303,308], since both Cu_2O and CuO exhibit a considerably higher affinity to LIPSS formation due to their semi-conduction properties [309]. In fact, an accumulation of surface oxide might similarly contribute to overall Cu incubation due to increased photon absorption at near-infrared (NIR) wavelengths.

3.3.3 | Surface oxidation

With a normalization in pulse wise topographic modification by phase explosion kinetics found on Cu surfaces after USP irradiation at pulse counts > 20 in the high- and mid-fluence regime, a decrease in incubation would furthermore be suggested in case of a predominant topographic impact on optical surface absorptivity, which is however not observed in [298]. Alongside a further increase in crater depth, additional impacts of structural defect implantation and oxide agglomeration have therefore been assumed to be similarly involved in USP Cu incubation. In this context, Jee et al. [292] already discussed a potential defect implantation mechanism by laser ablation of surface oxides at fluences below F_D.

Early investigations on the role of surface oxide in the absorption of infrared wavelengths including CO_2 laser sources showed that multiple internal reflections and interference inside the oxide layer can in fact increase absorptivity of the Cu surface [310]. However, oxide thickness needed to range above 100 nm to enable this effect. Oxide thickness on Cu surfaces was found to be highly related to the substrate´s microstructure with a higher expression on polycrystalline Cu that scales with decreasing grain size. Since ambient surface oxidation is related to surface passivation against external chemical potentials it follows similar driving forces of surface energy and ion diffusion like in liquid environment [224]. Fujita et al. [311,312] found a passivation layer thickness relation of 111 > 110 > 100 on single crystal Cu surface under low-temperature conditions, where the highest diffusion mobility was similarly assessed for 111 plane orientations in [313]. Nevertheless, a polycrystalline substrate state was consistently found to exhibit higher oxide thicknesses compared to single crystal surfaces [224,313], where surface oxidation scales with the density of grain boundaries and surface defects [217]. In a relatable study, Porteus et al. [314] investigated the effect of Cu surface preparation on the damage threshold in the development of damage-resistant mirrors for high-power pulsed infrared laser applications using a similar laser system. Different types of damage (topographically relevant crater formation and melting as well as structural defects like slip-band/dislocations) were observed after short pulsed irradiation using a train of 20 ns pulses with 100 ns envelope duration at fluences up to 300 J/cm² under vacuum. They found a F_D relation for crater formation and melting that scales as *111 single crystal UHV etched > polycrystalline electro-polished > polycrystalline mechanically polished >> polycrystalline electro-polished oxidized.* A decrease of approx. 30% in F_D between “fresh” and passivation oxidized electro-polished samples for both damaging processes highlights the impact of Cu surface oxide on optical absorptance at this wavelength spectrum.

Aside of potential coupling effects at defect states within the oxide as well as the boundary layer between oxide and substrate, the band structure of the two predominant Cu oxide phases of cuprous

Cu_2O and cupric CuO might similarly contribute to a decrease in reflectivity of Cu surfaces. Both oxide species represent p-type semi-conducting properties, where Cu_2O exhibits a direct band gap of 2.02 - 2.17 eV corresponding to electro-magnetic wavelengths between 571 nm and 613 nm, which is further decreased to 1.2 – 1.9 eV representing a NIR spectrum from 653 nm to 1033 nm in the case of CuO [315]. The relation between band gap energy and photon absorption for semi-conductors are directly linked to the color of both oxides in their mineral state where cuprite (Cu_2O) exhibits a brownish red close to the original color of metallic Cu due to increased absorption in the yellow and green spectrum of visible light, while tenorite (CuO) represents absorption capacities up to the NIR spectrum resulting in an almost black coloring [316]. These low band gap values might be the cause in the significant variation of Cu reflectivity at an electro-magnetic spectrum around 800 nm measured in early studies [251,281,295,296], where an impact of sample preparation was barely considered. In [296], thin film reflectance was measured as approx. 94 % for cleaned and 77.4 % for aged samples e.g., whereas literature states a reflectance of approx. 96.5 % on metallic Cu for this wavelength [317]. In fact, both Cu_2O and CuO formation have been shown to be involved in atmospheric aging of Cu surfaces [224]. Under consideration of the USP-specific absorption mechanisms in semiconductors via coupling at defect states and multi-photon absorption, surface oxidation might in fact play an important role both in incubation as well as initial photon absorption within USP-processing of Cu considerably increasing the low metallic absorptance within the NIR first harmonic emission spectra of USP laser sources (800 nm for Ti:Sapphire and 1030/1060 nm for ytterbium based fiber lasers).

Oxide formation alongside laser processing of Cu that is potentially linked to incubation mechanisms might take place by thermally induced epitaxial bulk growth as well as redeposition of ablated matter that gets oxidized during atmospheric interaction supported by elevated particle temperatures and surface/volume ratio. Taking both the ultrafast thermal interactions as well as the strong conductive cooling alongside eruptive ablation into account [261,265], redeposition might actually play a more dominant role, here. In fact, Anderson et al. [318] observed a significant variation of process induced surface oxidation on Cu alongside mid-fluence ablation between fs and ps pulse durations within the USP regime. Pulse durations of 4 ps induced thick oxide layers accompanied by pronounced oxidic sub-pattern formation, while pulse durations of 35 fs exhibit low and non-uniform oxide agglomeration. In both cases, redeposition of nanoclusters from ablated matter was identified as the driving oxidation mechanism [318], where the difference in quantitative redeposition between the two pulse durations might be linked to differently expressed ablation dynamics based on the observations of [265]. Quantitative oxide agglomeration might finally lead to partial surface shielding like observed in excessive irradiation with short pulse durations [69], whereas surface morphology modification might be driven by material specific USP laser/material interaction of the oxides including, e.g., LIPSS formation [309].

Due to the predominant mechanism of redeposition in USP processing related surface oxidation, the oxide layer formed might be considered as an agglomerate of oxidic NP in a sinter-like matrix state. NP particle size and properties linked to processing parameters have been investigated for laser irradiation applying $\tau_p = 50$ fs, $\lambda = 800$ nm and fluences within the mid- and high-fluence USP processing regime between 1 and 10 J/cm² in [319]. Here, the NP size was found to be equally distributed within 1-20 nm and in few cases up to 50 nm independent from the fluence applied, whereby NP formation is discussed to relate to decomposing mechanisms in the trace of material ablation, where the fluences within this regime mainly influences the ablation volume and lesser the ablation mechanism [319]. Surface agglomeration alongside multi-pulse processing at similar laser parameters have been investigated by Anoop et al. [299], where oxidic structures were shown to grow in size with increasing pulse overlap and become coarser with higher fluences. Due to the vortex-shaped intensity profile, localized spots of oxide agglomeration were formed within the central low- to zero-intensity spot area indicating a potential impact of modified intensity profiles on localized oxide distribution. Similar to the observations on pulse wise topography modification [298], the morphology of agglomerated oxide was reported to not exhibit significant changes after a pulse count between 20 and 50 [299]. Since the band gap related absorptivity of Cu_2O and CuO was shown to be highly dependent on defect density in relation to the oxide formation mechanism [315], the porous NP structure of process induced Cu oxidation might further impact optical absorptivity. In addition, the high surface/volume ratio of metallic NP at the size scale below 20 nm was found to affect the internal energy balance leading to a decrease in melting temperature [320], which potentially further agitates the oxidic impact on incubation.

3.3.4 | Crystallographic defect implantation

Incubation during USP processing of Cu surfaces can be considered to involve a combined impact on multiple types of surface modification based on the state of research reviewed in the previous chapters, especially at NIR wavelengths. Here, ablation dynamics have shown to impact optical surface properties both by topographic modification as well as oxidic redeposition of previously expulsed matter. The explosive kinetics of thermomechanical substrate interaction might include high expansive internal pressure formation of up to several hundred GPa [261], that potentially exerts mechanic stress upon deformation of the substrate microstructure. In MD simulation, slip bands, dislocations and up to void formation was observed alongside thermomechanical ablation due to acoustic stress propagation into the irradiated bulk Cu substrate [289,291]. The introduced stress field relates to deliberately applied superficial substrate deformation via laser shock peening [321], however with predominantly tensile stresses within closer proximity to the surface [291].

Damage accumulation within the crystalline microstructure of single crystal Cu substrates in response to consecutive ps pulsed NIR laser irradiation was experimentally investigated in [322] by means of scanning and transmission electron microscopy (SEM, TEM). Here, initial defect sites like scratches and voids were found to induce a localized increase in thermal substrate interaction. USP induced crystallographic substrate modification involves nm-scaled grain refining originating from ultrafast solidification processes as well as twin and void formation, even at fluences below detectable damaging thresholds F_D. The observed cooling rates would suggest the formation of an amorphous microstructure, which is however not stabilized in pure Cu due to the lack of stabilizing alloy compartments. Instead, previously molten surface compartments exhibit grain precipitation with deviating orientation from the bulk microstructure. The mechanism of crystallographic defect implantation might lead to an increase in optical absorptance similar to the observations comparing F_D of electro- and mechanically polished Cu surfaces in [314]. Interestingly, F_D for slip band formation was found to be increased for pre-deformed substrate surfaces despite a lower crater and melt formation threshold, where consecutive substrate deformation appears to enhance resistance against further mechanical defect implantation similar to the mechanism of work hardening [314]. Directly applying USP micromachining in a SEM environment, microstructure modification of 111 oriented single crystal Cu including twinning and dislocation formation was found to penetrate up to a depth of 5 μm, where high dislocation densities are concentrated at depths of 1 – 4 μm from the substrate surface [323]. Multi-pulse USP irradiation at increased incidence angles was furthermore found to induce a higher incubation impact for p- versus s-polarized pulses, which was related to differently expressed surface plasmon excitation along elevated superficial defect densities [324]. In [325], low-fluence LIPSS formation on fcc Ni surfaces was discussed to be linked to microstructure modification by twinning and slip band formation.

Based on this, the defect state of the near surface Cu microstructure and its further modification alongside multi-pulse USP processing might in fact influence quantitative absorptance of laser energy, at least by a decrease in the free electron path length with increased grain boundary and lattice defect density. Due to the parallel occurrence and mutual relation of the individual mechanisms of incubation discussed in the previous chapters, a clear separation and quantification of their respective effect on optical surface properties however is hardly possible. Within sophisticated concepts of surface modification, the individual mechanisms of incubation need to be included into the USP processing strategy to allow for high accuracy.

3.3.5 | Incubation vs. antimicrobial functionality of Cu surfaces

Incubation related substrate modification might potentially influence functional surface properties in a similar manner. A high defect density in vicinity to the substrate surface has been shown to potentially effect increased Cu ion emission rates [238] as well as physicochemical surface properties tailoring bacterial adhesion and the bacteria/substrate response [83,138]. In similar relation, the ablation-related modification of topographic morphology as well as surface chemistry are very likely to exhibit an influence on how bacteria sense and respond to the USP processed metallic substrate [82,132,148]. Topographic surface modification including the self-assembly of either stochastic or deterministic sub-µm-scaled surface morphologies might impair quantitative bacteria/surface contact, which is considered in antimicrobial surface concepts, already [71,146]. Chemical surface modification involving an increase in surface oxidation has been observed to potentially interfere with antimicrobial capacities due to decreasing Cu ion release rates [51,69,77,80]. However, the existing knowledge majorly involves considerable oxide layer thicknesses induced via quantitative epitaxial oxide growth, whereas oxidic nano-cluster redepositing alongside USP processing might exhibit a deviating behavior due to its close relation to NP-based strategies of Cu application [59]. Based on these considerations, surface functionalization via USP laser irradiation aiming for increased antimicrobial efficiency of Cu surfaces need to include an understanding of material specific response mechanisms alongside multi-pulse processing to enable a purposeful surface design.

4 | Direct Laser Interference Patterning (DLIP)

Topographic surface modification by means of USP processing can be achieved by both ablative micromachining as well as the generation of self-assembling sub-patterns like, e.g., LIPSS, whereas a potential variation of bacteria/surface interaction is most likely achieved by pattern sizes in the low µm- and sub-µm regime [25,132]. Although LIPSS already exhibit potential applicability for the design of antimicrobial metal surfaces due to a predominant $P <$ Bacterium size relation [71], their material specific formation and accompanying chemical impact on substrate properties do not favor a more targeted application in the case of Cu [303,308,309]. Hence, topographic surface design in the scale-range of single bacteria cells preserving the actively antimicrobial Cu properties are more likely to be attained by micromachining approaches. In the case of conventional direct laser writing (DLW), the minimal achievable pattern size P scales with the focus diameter d_{Focus} in relation to the focal length of the lens system f as well as the laser wavelength λ, the diffraction index M^2 and seed beam diameter d_L.

$$d_{Focus} = \frac{\lambda\, f\, M^2}{d_L} \tag{10}$$

Applying the seed laser parameters of a common Ti:Sapphire USP laser system ($\lambda = 800$ nm, $M^2 = 1.3$, $d_L = 8$ mm [326,327]), the focal length f would need to be adjusted at 30 to 10 mm to enable $P \approx$ Bac pattern sizes, while smaller patterns can barely be achieved with this technique [328,329]. Furthermore considering processing speed and application relevant spatial surface sizes, DLW is nowadays majorly involving galvanometer or polygon-scanners, where the applied Theta-lenses are rather tuned to $f > 100$ mm with spot sizes ranging in the scale of several tens of µm [297].

A generation of topographic surface patterns below this diffraction limit can in turn be realized by spatial modulation of the irradiating intensity profile by laser interference. Overlapping two or more coherent partial beams on the substrate surface leads to the formation of periodic intensity modulations dependent in periodicity and geometry on the number, wavelength and irradiation angle of the overlapping partial beams. First experiments on the modification of metallic surfaces by means of direct laser interference have been conducted in the late 20th and early 21st century [330–334] coining the term laser interference metallography [335–337], which was later transformed into direct laser interference patterning (DLIP) [338,339]. Although early works majorly utilized short pulse durations in the nanosecond regime, USP interference was also readily applied in lithographic [340,341] and direct patterning approaches [257,342,343]. After more than twenty years of applied research, DLIP has been formed into a readily applicable tool for µm- and sub-µm scaled deterministic surface patterning enabling advanced surface functionalities that follow manifold natural blue prints like the lotus leave, shark skin and butterfly wings [74]. Optimization of technical surface properties via DLIP enables reduced friction and wear in various tribological systems [344–346], increased solar absorption [79,347], tailored interaction with liquid media [348,349] and different cell types of the human body [333,350–352] as well as the generation of diffractive color gratings [353] amongst many other applications.

4.1 | Theory of laser interference

In a simplified approximation, light can be described as a plane electromagnetic wave represented by the linearly polarized amplitude of the e-field $E(x,t)$ in space and time.

$$E_i\,(x,t) = E_{0i}\, sin(\, \omega_i t - (k_i\, x + \,\varphi_i)) \tag{11}$$

where $\omega_i t$ represents the temporal and $k_i x + \varphi_i$ the spatial phase with ω_i as the circular frequency, k_i as the wave-number and φ_i as the initial phase constant of a single wave “i”. In case of laser light that is characterized by monochromatism, temporal and spatial coherence, the properties of a single wave can be approximated to similarly apply for larger wave bundles up to a whole laser pulse. The spatial intensity distribution in relation to the electromagnetic wave-nature of laser light is directly linked to the amplitude of E.

$$I = \frac{c\,\varepsilon_0}{2}\,|E|^2 \tag{12}$$

An overlap of two monochromatic waves effects a summarization of E_i, whereas the corresponding intensity modulation depends on the phase relation δ between the two waves.

$$E_{res}\,(x,t) = \sum_{i=1}^{2} E_i\,(x,t) = E_1\,(x,t) + E_2\,(x,t) \tag{13}$$

$$I_{res}(x,t) = \frac{c\,\varepsilon_0}{2}\,|E_{res}\,|^2 = \frac{1}{2}\,(E_1^2 + E_2^2) + 2E_1E_2\cos(\delta) = I_1 + I_2 + 2\sqrt{I_1I_2}\,\cos(\delta) \tag{14}$$

Here, $2\sqrt{I_1I_2}\,\cos(\delta)$ is defined as the interference term inducing a spatial modulation of $I_{res}(x,t)$. With $E_1 = E_2 = \frac{1}{2}E_0$ and $I_1 = I_2 = \frac{1}{2}I_0$, $I_{res}(x,t)$ varies between $2I_0$ and 0 alongside constructive and destructive interference in response to $\cos(\delta)$.

$$\cos(\delta) = \begin{cases} \mathbf{1}, \text{ if } \delta = 2n\pi & \Longrightarrow I_{res} = I_1 + I_2 + 2\sqrt{I_1I_2} = 2I_0 \quad \textbf{constructive} \text{ interference} \\ \mathbf{0}, \text{if } \delta = n\,\frac{\pi}{2} & \Longrightarrow I_{res} = I_1 + I_2 = I_0 \quad \text{neutral} \\ \mathbf{-1}, \text{if } \delta = (2n+1)\pi & \Longrightarrow I_{res} = I_1 + I_2 - 2\sqrt{I_1I_2} = 0 \quad \textbf{destructive} \text{ interference} \end{cases} \tag{15}$$

A schematic illustration of the interference between two coherent laser beams complemented by the corresponding modulation of $I_{res}(x,t)$ is displayed in **Figure 14**.

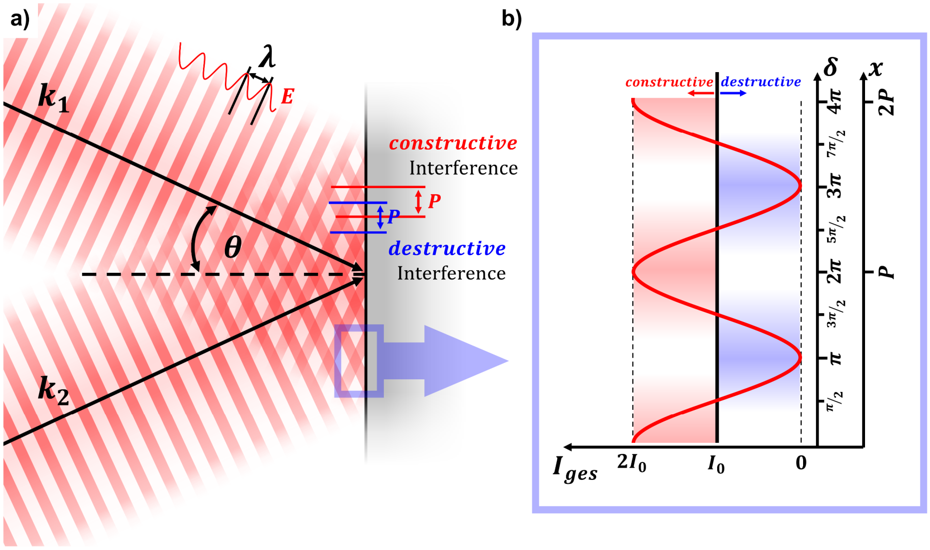

Figure 14: a) overlapping of two coherent laser beams on a substrate surface leads to a sinusoidal spatial modulation of the e-field generating a one-dimensional pattern of alternating constructive and destructive interference. b) modulation of the e-field similarly varies the spatial intensity distribution where $\boldsymbol{I_{res}(x,t) = 2I_0}$ or **0** in case of fully constructive or destructive interference, respectively.

Implementing $k_1 = k_2 = \frac{2\pi}{\lambda}$ for the wavenumbers, the one-dimensional spatial intensity modulation of *I(x)* by two-beam interference can be rewritten as

$$I(x) = 2I_0\, cos\left(\frac{2\pi x}{\lambda}\sin(\theta)\right)^2 \tag{16}$$

with θ as the single beam incidence angle and λ as the wavelength, which parallelly allows to calculate the pattern periodicity P achieved in relation to both [336]:

$$P = \frac{\lambda}{2\sin(\theta)} \tag{17}$$

The numerical derivation of the basic equations of two-beam laser interference, which are well known from the relevant literature, provides the most relevant information to design a given optical setup in order to achieve distinctive primary pattern parameters. A slight modification of equation 17 furthermore allows the design of hexagonal pattern arrangements by three-beam interference, whereas calculations of both the pattern scale as well as the intensity modulation itself are increasing in complexity with rising beam count.

$$P = \frac{\lambda}{\sqrt{3}\sin(\theta)} \tag{18}$$

Schematic examples of the spatial intensity modulation corresponding to two- and three-beam interference are provided in **Figure 15a** and **b**. By this technique, patterns exhibiting a high resolution down to sub-µm scales can be generated within a single laser spot and transferred to the substrate surface via photothermal or photochemical interaction. Here, the thermal substrate interaction in response to the properties of the irradiating laser governs the shape and geometry of the topographic patterns generated, which can range from microstructure rearrangement to melt-pool dynamics during short-pulse up to explosive ablation in response to USP irradiation in the case of metals, as illustrated in **Figure 15c-f**.

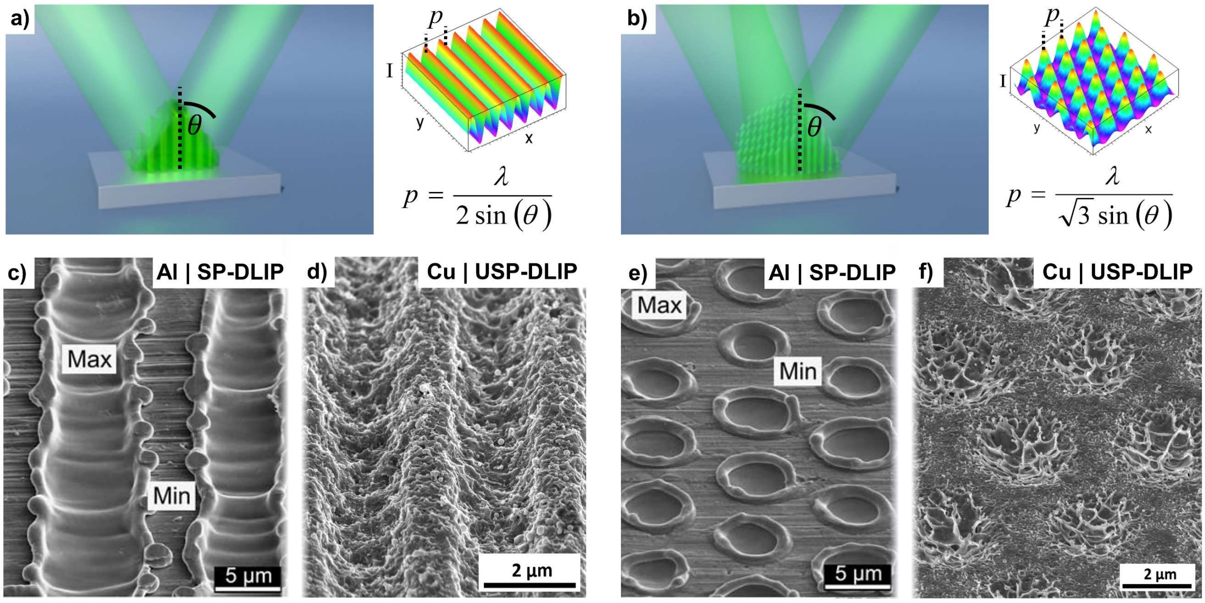

Figure 15: topographic surface modification of metallic substrates by a) two- and b) three-beam interference inducing characteristic pattern morphologies related to either melt-pool dynamics in the case of short pulsed DLIP (SP-DLIP) in c) and e) (adapted from [354]) or eruptive ablation kinetics induced by USP-DLIP in d) and f).

With a reduction in pulse duration, the edge definition of the DLIP-pattern increases. Hence, a precise topographical mapping of local beam intensity modulations can be achieved with USP-DLIP, whereas with short-pulse DLIP (SP-DLIP) topographical structure formation are particularly related to and limited by melt kinetics. However, USP specific material interaction similarly has to be considered in overall pattern morphology alongside USP-DLIP as well as technical restrictions in beam guidance.

4.2 | Applying DLIP with USP

Compared to SP-DLIP applying either nanosecond or two- up to three-digit picosecond pulse durations, beam handling and guidance enabling full spatial interference of USP laser pulses exhibit considerable difficulties due to the comparably low coherence length (e.g., approx. 30 µm in the case of 100 fs pulse durations [336]). Due to this, USP-DLIP needs to imply imaging optical setups [355], whereas group velocity dispersion by optical elements might cause further restrictions in the lower threshold of applicable pulse durations. In the case of pulse durations close to 10 ps, the use of prisms for partial beam collimation has been shown to still be feasible [78]. However, with a further decrease in τ_p, the deviating optical path lengths between the interior and external spot compartments inside the refracting medium induce a critical distortion of the spatial coherence between the respective spot edges. An interference of single-digit down to sub-picosecond pulses was realized by Simon et al. [257,289] for UV wavelengths by the application of Schwarzschild optics, in turn. Both setups allow to modify P solely by repositioning the beam splitting device (1). Another optical setup, which is currently the most frequently used in USP-DLIP, comprises of a multi-lens imaging system involving either passive or active adaption of the partial beam optical path lengths applicable for wavelengths in the visible up to the IR spectrum [340,343,355–358]. Here, the precise adjustment of the optical arrangement between the collimating and focusing lens ((2) and (3) in **Figure 16c**) however is limited to a fixed interference setup and pattern periodicity, where an alteration of P would require a replacement of at least one of the optical elements. The three imaging optical systems applied in USP-DLIP so far are illustrated in **Figure 16**.

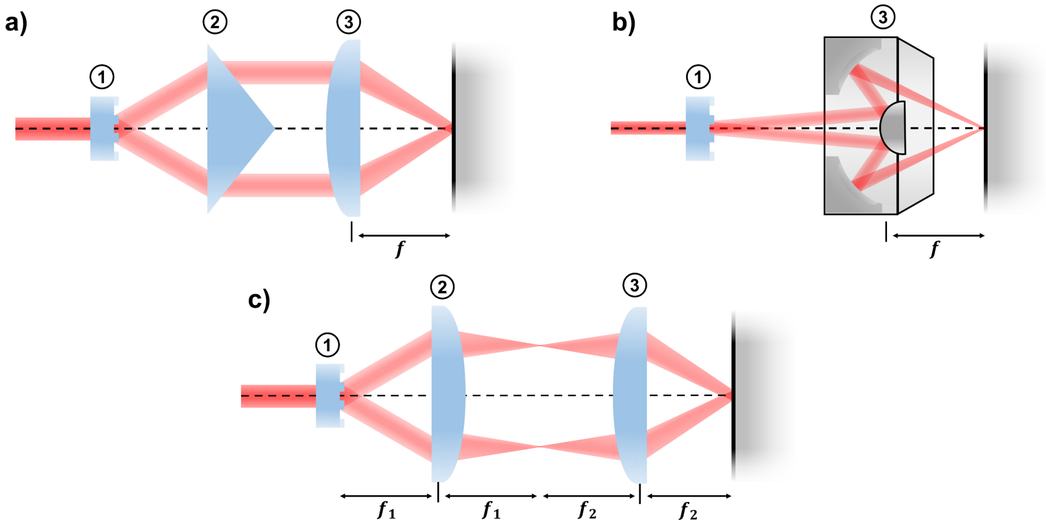

Figure 16: schematic illustration of the three imaging optical setups most frequently applied in USP-DLIP comprising a (1) beam splitter (e.g., a DOE or SLM), (2) a collimating optic, which can be a) a prism, or c) a compressor lens and finally a focusing optic, which might be either a),c) a compressor lens or b) a Schwarzschild optic.

Apart from spatial coherence, the actual pulse duration similarly affects the thermal interaction of the substrate medium, where thermal conductivity as well as material specific ablation mechanisms have been shown to interfere lesser with sub-µm pattern sizes in case of USP pulse durations. Nevertheless, Simon et al. [257,289] showed that melt kinetics still appear to play a dominant role in sub-µm pattern formation after irradiation with ps and sub-ps pulse durations. In parallel, Bieda et al. [78] observed an instability of sub-µm patterning on Cu after dual-pulse irradiation with a pulse duration of 35 ps, which remained stable on lesser conductive stainless steel and Ti, in contrast. The thermal diffusion length l_T restricting minimal spatial pattern sizes can be approximated involving the thermal diffusivity α, where in the case of Cu, l_T in the upper SP regime at 10 ns was previously estimated at approx. 2 µm vs. 1.3 µm for steel [359].

$$l_T = \sqrt{\alpha\,\tau_p} \tag{19}$$

With a reduction of the applied pulse duration τ_p from ns down to ps and fs, l_T should be assumed to decrease by orders of magnitude according to equation 19. However, thermal substrate interaction does not necessarily occur in the same time frame as the applied pulse duration, where substrate thermalization up to phase transitions and ablation might cover time scales several orders of magnitude above τ_p in case of USP irradiation still allowing for a certain amount of thermal diffusion [250,265]. In parallel, material specific ablation dynamics leading to sub-patterns like, e.g., LIPSS that might additionally interfere with primary pattern formation also need to be considered in USP-DLIP.

In more recent works, LIPSS formation alongside primarily DLIP patterning was deliberately used for the generation of hierarchical surface patterns involving both LSFL and HSFL [360–364]. In accordance to the current theories on the mechanism of LIPSS formation [304], hierarchical pattern design involves an adaptation of the beam polarization to allow for LIPSS alignment in certain orientations to the primary DLIP pattern. Here, an additional impact of single beam polarization on the actual intensity modulation by interference was shown to similarly lead to a modified primary pattern formation. In the case of two-beam laser interference lithography, Ellman et al. [365] found a considerable impact of modified single beam polarization on the modulation contrast of line-like intensity patterns. Similar observations have been made in the comparison between s- and p-polarized interference with increasing incidence angle θ, where p-polarization induces a decreasing contrast in intensity modulation, while s-polarized intensity modulation was not affected by an increase in θ [366]. In case of the interference of three or more beams, a deliberate individual adjustment of partial beam polarization has been shown to enable an inversion between intensity maxima and minima areas [367,368], as well as an increase in periodic patterns complexity [369].

4.3 | DLIP processing aiming to impact bacterial interaction

Deterministic surface patterning via DLIP has yet been considered for antimicrobial and antifouling surface designs in a number of studies. Applying SP-DLIP with wavelengths mostly in the UV spectrum, the impact of pattern scale on bacterial adhesion and biofilm formation on polymer surfaces was investigated under involvement of different pattern geometries and 5 µm down to 0.5 µm periodicities. Valle et al. [26] monitored the interaction of *S. aureus* in response to line- and pillar-like as well as hierarchical lamellar DLIP patterns between 5 µm and 1 µm periodicity on polystyrene. Adhesion of *S. aureus* was found to be reduced on more complex hierarchical topographies, while it was enhanced on line- and pillar-like patterns both under static and continuous flow conditions (after 2h and 6h hours of exposure, respectively). Testing of the hierarchical patterns at 2 µm periodicity was also conducted in vivo in mice, where *S. aureus* was injected at log8 cell density two days after implantation followed by another three days of exposure. In summary, overall bacterial adhesion increased with pattern sizes between 3 µm and 1 µm on both line and pillar-like patterns, while adhesion on the hierarchical patterns is reduced, which similarly accounts for static and continuous flow in vitro as well as in vivo in mice (where however only a single hierarchical pattern type with P = 2 µm have been tested). In an extension of [26], Guenther et al. [70] additionally implemented a further decrease of line- and pillar-like pattern sizes down to 0.5 µm, where the latter also showed a decrease in *S. epidermidis* adhesion while bacteria density remained elevated in comparison to flat reference surfaces for the other pattern types. In Helbig et al. [25], the group finally expanded their investigation to the combined impact of pattern scale and geometry on initial adhesion of *S. epidermidis* and *E. coli* on line-like, pillar and dimple DLIP patterns with 5 µm, 1 µm and 0.5 µm periodicity. Both bacteria exhibit a clear preference of 1 µm (closest to single bacterial cell size) and reduced overall adhesion on 0.5 µm pattern sizes. A parallel monitoring of the influence of exposure to different polymers exhibited differences in preferential adhesion between the two strains, where *S. epidermidis* preferred hydrophilic and *E. coli* rather hydrophobic surface properties for attachment. In contrast, a more recent study applying comparable laser parameters on polyimide found reduced adhesion of *P. aeruginosa* on both 1 µm and 2 µm line-like patterns [152].

With a scope on biomedical application, Zwahr et al. [362] combined crater like structures of 50 µm periodicity applied by SP-DLW with 5 µm dimple patterns applied via DLIP at 70 ps pulse duration on Ti6Al2V, where the hierarchical overlay of the smaller pattern aims for a reduction in bacterial accumulation. In fact, *E. coli* adhesion was found to be reduced by 30% via SEM imaging, where however an additional impact by LIPSS formation in the scale of approx. 400 nm might also be involved, taking previous findings into account. A comparably high reduction of bacterial adhesion accounting to 99.4% - 99.8% for *E. coli* and 70.6% – 79.1% for *S. aureus* after 2h of exposure was found on pillar and dimple patterns at a periodicity of 850 nm on stainless steel patterned [72]. Here, DLIP patterning at 8 ps pulse duration parallelly impacted surface wettability leading to a water contact angle (WCA) of 148°to 154°.

In each of the presented cases of DLIP patterning of either polymer of metallic substrates, bacterial interaction closely followed the systematic correlation between topographical and physicochemical surface properties, which have previously been discussed in **Chapter 1** and summarized in **Figure 5**. These investigations exclusively involved inert surfaces and SP-DLIP applications, whereas the highest impact on bacterial adhesion has been achieved by USP-DLIP on stainless steel. First investigations on a potential utilization of DLIP patterning of Cu to improve the antimicrobial properties revealed an unfavorable modification of the substrate surface with increased formation of CuO in the case of SP-DLIP [77]. In a very recent study of a cooperating group, the impact of SP-DLIP using 10ns pulse duration on antimicrobial surface properties of Cu was investigated further exhibiting a low to reduced impact on the viability of *E. coli* and *Variovorax sp*. [370]. The observed variance between both a slightly positive and negative influence of SP-DLIP on antibacterial Cu efficiency might be related to both the unfavorable chemical surface modifications and limitations in the minimal pattern scale by the thermal impact of SP pulse durations, highlighting the potentially beneficial effect of USP laser/material interaction.

III | Objectives

Based on the presented state of research regarding the driving forces behind bacterial surface interaction in **Chapter II 1**, as well as the effective antimicrobial modes of action of Cu materials in **Chapter II 2.3**, a link between several indicative surface properties that benefit both quantitative bacterial surface adhesion as well as the antibacterial efficiency of Cu surfaces can be drawn:

- Topographically increased surface contact appears to enable high bacterial adhesion rates with a parallel influence of physicochemical surface properties, while a direct bacterial/surface contact on Cu was related to a bactericidal contact killing effect.
- A positive surface charge is considered rather beneficial for the attachment of bacteria exhibiting a predominantly negative membrane potential that similarly facilitates Cu^{2+} and Cu^{+} agglomeration.
- In contrast, a rather hydrophilic wetting of Cu surfaces that potentially benefits corrosive interaction linked to Cu ion emission was shown to be less preferential for bacterial adhesion for most bacterial strains exhibiting rather hydrophobic membrane properties.
- Cu corrosion was shown to be similarly dependent on crystallographic substrate properties like grain boundary and dislocation density providing an additional degree of freedom for the tuning of Cu ion release.

By following these guidelines, it may be possible to increase the efficacy of antimicrobial Cu surfaces through targeted surface functionalization using pulsed laser irradiation. Here, the design of the processing strategy should avoid any negative impact on the substrate's inherent capacities and the interaction between bacteria and substrate. On this regard, the application of ultrashort pulse durations combined with spatial intensity modulation by laser interference was considered to allow for both a reduced thermal impact as well as a realization of single-digit µm to sub-µm pattern sizes on the Cu substrates. This dissertation follows an integrated scope that includes the primary development of a suitable DLIP-based processing methodology for Cu based and inert substrates using USP durations (A) followed by an in-depth investigation of the process-related influence on functional surface properties (B) and the resulting integrated influence of DLIP-induced surface modification on antimicrobial efficiency (C):

(A) Process Development:

The basic requirement to allow for a targeted investigation on how altered bacterial contact impacts the antimicrobial efficacy of Cu surfaces is the technical ability to equip these surfaces with deterministic surface topographies in the scale of single bacterial cells. The first objective of this work therefore involves:

- The design of an optical setup for the interference of ultrashort pulsed laser beams based on a DLIP approach.
- Realization of periodic surface patterns on Cu, Cu alloys, and inert substrates by the as-developed Ultrashort Pulsed Direct Laser Interference Patterning (USP-DLIP) methodology that are in the order-of-magnitude of individual bacterial cells (~1 µm), as well as slightly above and below.

- Understanding the underlying laser/material interaction to selectively control the topographic properties on the different substrates being processed, which may be supplemented by a suitable simulation methodology.

(B) Targeted Substrate Modification:

Surface functionalization by ultrashort pulsed laser processing has been shown to involve a parallel modification of surface chemistry and the substrate´s microstructure alongside topographical patterning. To disclose the actual mechanisms behind a potential modification of bacteria/substrate interaction via USP-DLIP, the second objective aims to investigate the integrated impact of this methodology on surface and substrate modification subdivided into:

- Determination of the chemical and microstructure modification of the substrate surface during USP-DLIP, as well as their impact on both
- the laser/material interaction alongside multi-pulse processing and
- their individual and combined influence on application relevant functional properties of the substrate surface such as wettability and corrosion behavior that is coupled with topographic surface modification.

(C) Antibacterial Properties:

Finally, the third objective of this work examines the impact of topographical, chemical, and structural substrate modifications generated by USP-DLIP on the antimicrobial properties of pure Cu surfaces. This may identify key mechanisms that further drive the antimicrobial efficiency of Cu based surfaces. Within the frame of this work, modifications of the antimicrobial properties are monitored by an indicative approach using a standardized experimental design involving the bacterial strains *E. coli* K12 (BW25113) and *S. aureus* SA113. Based on this, the investigation comprises:

- The evaluation of the impact of the chemical and microstructure modification on the active killing mechanism of Cu surfaces alongside topographical patterning via USP-DLIP.
- Determination of the parallel effect of functional surface properties on the overall interaction of bacteria with the substrate surface and the resulting antimicrobial properties.
- The investigation of the actual topographic influence on the antimicrobial effect of Cu surfaces by selectively increasing and decreasing the bacteria/substrate contact area via USP-DLIP.

IV | Overview

The following sections provide a summary of the scientific activities of this dissertation that are presented in detail in the seven papers listed in **Chapter V**, which have been published in international peer review journals. This chapter interlinks the contributions of the individual papers and displays their assignment to the Objectives (A), (B) and (C) to illustrate the full scope of this work. For a more detailed presentation and discussion of the results connected with an introduction into the applied methodology, please refer to the individual publications in the subsequent chapter.

Conceptual structure of the experimental progress

The overall experimental progress of this work is divided into two phases as displayed in **Figure 17**. In **Phase I**, a proof of concept was initially elaborated to assure that the intended objectives can be achieved within the framework of the USP-DLIP process development. Based on the proven feasibility an in-depth understanding of the individual aspects of said objectives enabling further optimization was approached in **Phase II**. In parallel to the works executed in pursuit of the objectives (A) to (C), the ISS space flight experiments Space Biofilms, BIOFILMS and Touching Surfaces were designed and conducted, which represent an extension of the scope specified in the objectives due to the additional introduction of space-associated and in particular gravitational influences on bacteria/surface interaction. In representation of these works, the BIOFILMS introduction paper (**Paper VII**) is included.

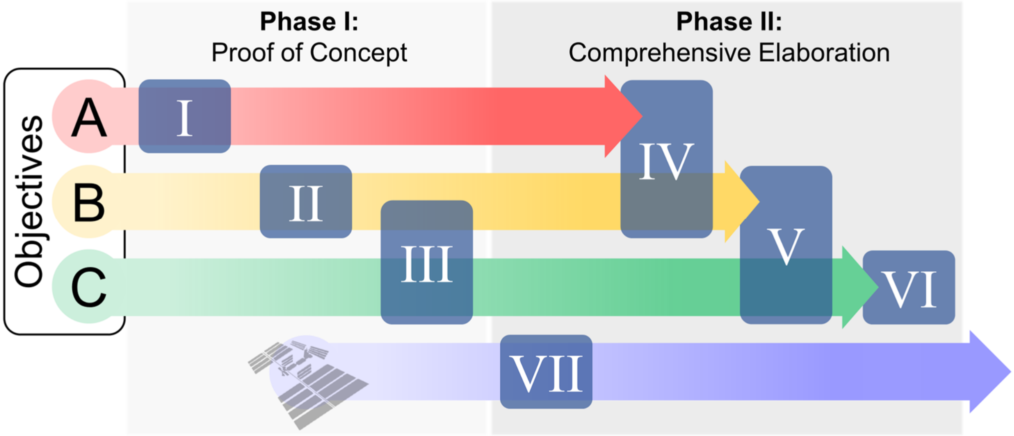

Figure 17: Conceptional structure of the dissertation with assignment of the included papers I-VII to the initial proof of concept or the comprehensive elaboration phase as well as the Objectives (A), (B) and (C).

The initial division of the scope of the work into the three objectives intends a clear allocation of subject-specific research content involving specific experimental methodologies, which at first glance may appear to be separable: Objective (A) focusses on interference-based laser process engineering and thermodynamic laser/material interaction to realize topographic surface patterning in the lower µm and sub-µm scale. Objective (B) involves the application of a broad range of characterization methodology to monitor the multiple aspects of chemical and structural surface and substrate modification by the developed USP-DLIP methodology. Finally, Objective (C) investigates the integrated effect of USP-DLIP with pattern sizes in the scale of single bacterial cells on bacteria/surface interaction and its potential impact on the antimicrobial efficacy of Cu surfaces using microbial screening methods. However, it turned out that the integrated interaction of the initially individually considered aspects forms an inseparable cross-relationship that affects not only bacteria/surface interaction, but also surface processing itself. This was considered in the experimental study design, which in **Paper III** and especially in **Papers IV** and **V** purposefully connect the topics of the respective Objectives (A) and (C) with the in-depth analyses assigned to Objective (B). The integral scope of this work is illustrated in **Figure 18** divided into the individual Objectives (A) Process Development, (B) Targeted Substrate Modification and (C) Antimicrobial Properties.

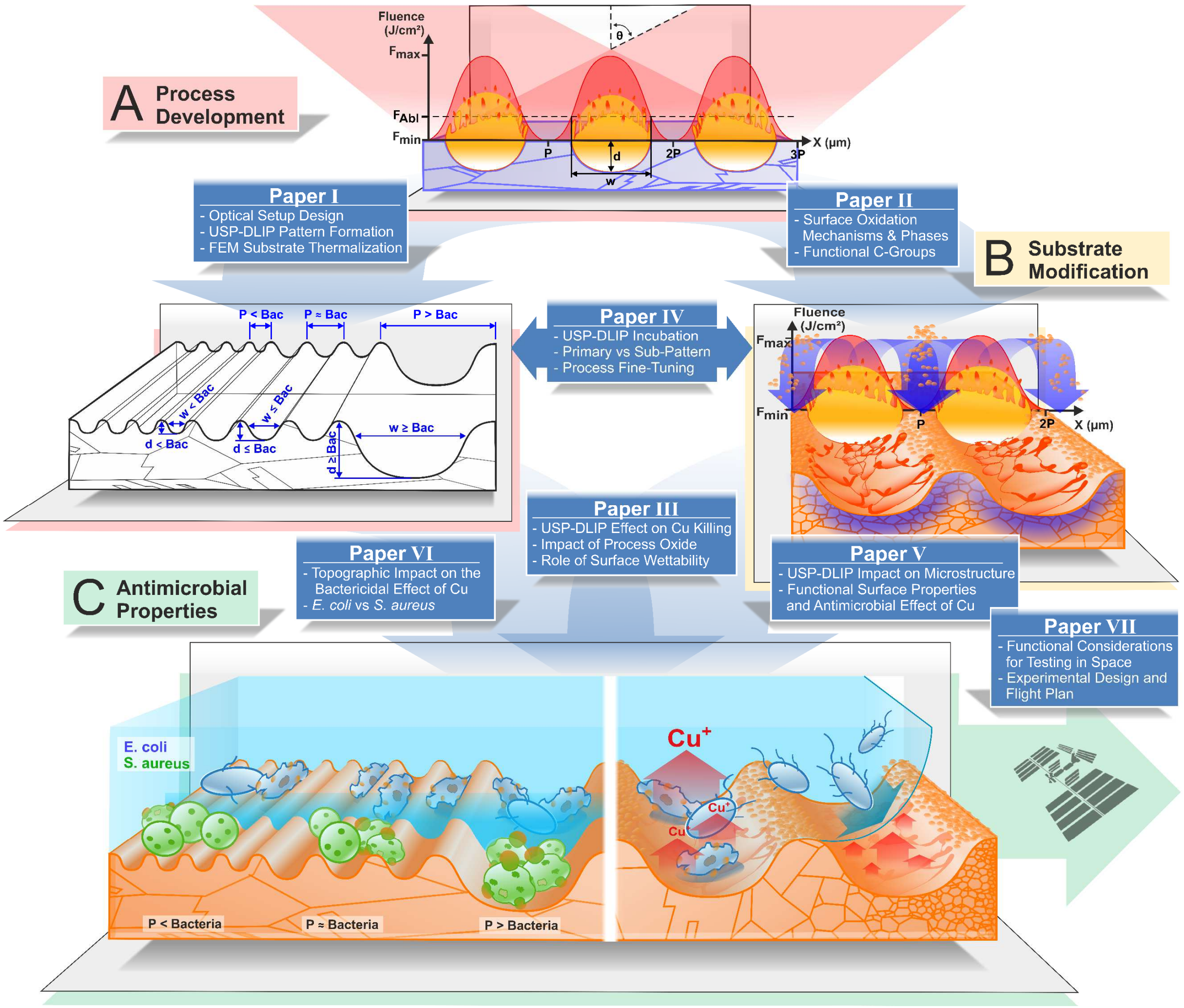

Figure 18: Schematic overview of the experimental progress of the dissertation.

In the following, the conducted research allocated to the three objectives will be presented subdivided into the individual contributions within the seven papers. Within this, the work included in **Paper I, II, VI** and **VII** can clearly be assigned to either Objective (A), (B) or (C), while in the case of **Paper III-V**, the respective proportions are individually highlighted.

Objective (A):
Process Development

As an initial step, a laser interference-based processing methodology using ultrashort pulse durations was developed based on the specifications of a readily available Ti:Sapphire laser system (*Spitfire, Spectra Physics*, generating pulse durations of 100 fs to 4 ps at a centered wavelength of 800 nm). The optical concept of the as-developed USP-DLIP processing technique was designed according to the following basic requirements:

- Maintaining sufficient spatial coherence between the individual overlapping beams within the processing spot to enable comparably high interference spot sizes at the lowest feasible pulse duration.
- Enabling the adjustment of the spatial pattern periodicity within a scale of single digit µm to sub-µm to allow for pattern dimensions from slightly above down below single bacterial cell size.

In case of pulse durations below the picosecond regime, beam guidance within the optical system needs to include a correction between preceding and delayed edges of the beam cross-section to avoid a limitation of spatial interference in the working spot due to the small coherence length (approx. 30 µm in the case of 100 fs pulse duration). In the examples provided by literature, the dual lens imaging optical setup (4f setup) illustrated in **Figure 16, example (3)** was shown to fit best for these requirements, however with limitation in the adjustment of pattern periodicity as well as working spot size using a given set of optics. On this behalf, the designed optical setup uses a Diffractive Optical Element (DOE) and single ($L1$) or dual lens ($L1 + L2$) combination that allows for pattern scale adjustment by DOE repositioning, as displayed in **Figure 19**. The low number of optical elements applied furthermore reduces pulse stretching by positive group velocity dispersion (GVD) within the optical media at approx. < 25% of the seed pulse duration.

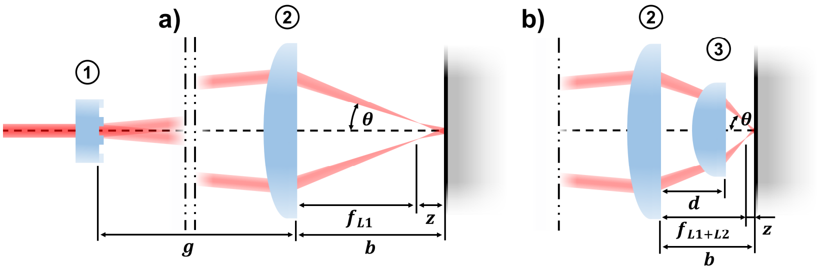

Figure 19: Schematic illustration of the imaging optical setup enabling line-like interference pattern periodicities of a) 3 µm up to >10 µm and b) down to 0.7 µm. (1) DOE, (2) lens 1 ($\boldsymbol{L1}$), (3) lens 2 ($\boldsymbol{L2}$).

Due to the uncollimated individual beam trajectory after separation by the DOE, the individual beams are focused before overlapping in the interference working spot. This compensates proportionally for the deviation in spatial coherence between the inner and outer beam edges due to different path lengths within the focusing lens. The single beam incidence angle θ that defines pattern periodicity is directly linked to the distance g between DOE and the lens system in relation to the single beam separation angle after DOE as well as the distance b between lens system and the working spot. b includes the focal length of either $L1$ or the $L1 + L2$ combination and z, which is accounting for the distance between the single beam foci and the working spot. Pattern periodicity is adjustable between 3 µm and > 10 µm in the single and down to 0.7 µm in the dual-lens setup under application of the systems base wavelength of 800 nm.

To decrease negative impacts on spatial coherence by astigmatism, the incidence angle on $L1$ is reduced by choosing a low DOE separation angle and $L1$ lens curvature, which is compensated by an extended overall beam path. The dual lens setup is applied to further decrease pattern scale by reducing the focal length, which increases θ. To maintain spatial coherence alongside increasing incidence angles, the collimated seed beam diameter is adjusted between 3 mm for single to 1 mm for the dual lens setup. Initial focusing in $L1$ reduces the incidence angle of the individual beams on the curved $L2$ interface, while the modification of the inter-lens spacing d allows to fine-adjust pattern periodicity and control astigmatism in the processing spot. This similarly enables to elongate the spot shape elliptically in perpendicular orientation to the line-like interference pattern within the boundaries of spatial coherence and modified intensity modulation to increase processing efficiency. Spatial laser interference was achieved at a pulse duration of 100 fs (at FWHM) for both setup variations enabling processing spot diameters of up to 200 µm, which allowed an unrestricted application of this pulse duration in USP-DLIP within the full scope of this work.

Contributions in Paper I

The presented imaging optical setup is briefly introduced in **Paper I**, combined with further elaboration of the resulting interference modulation and the actual USP laser/material interaction involved in pattern formation during USP-DLIP. The process development and methodology integrated in this publication builds the backbone for further detailed research in the following studies.

Laser surface processing using pulse durations in the femtosecond regime is related to ablation dominated substrate interaction in most engineering materials including, e.g., polymers, ceramics and metals. The actual dynamics and kinetics of substrate ablation vary significantly depending on the individual laser/material interaction, resulting in material specific pattern characteristics. On this behalf, topography modification by USP-DLIP has been analyzed for the different material classes ceramic (zirconium), polymer (PLLA) and metals (Cu, CuZn37 and AISI 304 stainless steel), separating between primary (DLIP) and secondary sub-pattern formation (e.g., LIPSS).

Substrate thermalization that potentially triggers ablation is achieved at fluences surpassing the material specific ablation threshold, which might change during multi-pulse accumulation due to incubation effects. Based on this consideration, a numerical approach was introduced to either design the pattern´s topographic maxima and minima surface area ratio or determine the material specific ablation thresholds based on processing results. In further elaboration, calculation of the localized intensity modulation was involved in a TTM-based numerical methodology to simulate the local heat input into the superficial substrate volume during USP-DLIP processing. The FEM simulation covers the period of USP laser irradiation until thermal equilibrium between electrons and phonons is reached to determine substrate thermalization linked to melt formation up to thermomechanical ablation in the further course of the material interaction. By supplementing experimental parameter studies on Cu, CuZn37 and AISI 304, the numerical simulations supported in the formation of an initial understanding of the thermomechanical substrate interaction involved in pattern formation during USP-DLIP. Based on this, pattern periodicities of 3 µm and 0.7 µm could be realized on each of the metallic substrates, which corresponds to the scale relevant for the aspired application in this work.

In the course of this initial study, an essential part of **Objective A** was achieved by realizing laser interference processing that enables both ultrashort laser pulse durations down to 100 fs and pattern sizes in the intended scale of single bacterial cells. However, the laser/material interaction involved in pattern formation was shown to induce an additional topographic surface modification by the generation of substrate specific sub-patterns, which potentially impact the real single cell surface contact of adhering bacteria. Furthermore, multi-pulse processing of the metallic substrates was shown to deviate from USP incubation behavior reported in literature suggesting additional impacts of the DLIP-specific process characteristics.

Contributions in Paper IV

The impact of the aforementioned aspects on purposeful topography design was considered in an in-depth investigation of the integrated influences on topography modification during USP-DLIP processing of pure Cu, summarized in **Paper IV**. This study contributes to both Objective (A) and (B), since the process driven impact on topography formation during USP-DLIP was found to be closely linked to a multi-level substrate modification.

To further improve the processing methodology as allocated to Objective (A), an investigation involving the influence of single beam polarization on the spatial intensity modulation by laser interference, localized absorptance and pattern formation for 6 µm, 3 µm and 0.75 µm pattern sizes was conducted. Aside of a deviation in the intensity modulation contrast with increasing incidence angle θ, polarization dependent energy absorption is shown to has an at least similarly important effect on pattern formation with similar relation to the single beam incidence angle θ as well as the effectively resulting pattern scale. Including the individual incubating effects in numerical calculation, the TTM simulation model introduced in **Paper I** was further complemented, which allowed for the derivation of the underlying thermomechanical mechanisms involved in characteristic primary and sub-pattern modulation. In fact, primary and secondary pattern formation on Cu occurs in mutual influence with increasing impact at lower pattern size. Including the knowledge gained on overall surface modification, it was shown that multi-pulse processing by USP-DLIP is strongly influenced by material-specific incubation effects, which deviate from the usual incubation behavior of conventional single-beam micromachining according to Jee [292] that is widely applied in the current state of the art.

Improved process design based on these findings includes a breakdown of pattern scale-specific maximum fluences to avoid a negative interaction between primary and secondary sub-patterns in multi-pulse USP-DLIP processing. In general, high precision USP-DLIP processing was found to require sweet spot conditions at the borderline between the low- and mid-fluence regime defined for USP micromachining. The in-depth investigation of the feedback influence of USP laser/material interaction on USP-DLIP processing in **Paper IV** finally enables a targeted process design with comprehensive access to essential surface morphology elements, which was exploited in the subsequent in-depth studies in **Paper V-VII** on functional surface modification.

Objective (B):
Targeted Substrate Modification

Although the term 'cold ablation' coined for USP laser processing suggests a negligible modification of the substrate properties, a potential impact on physicochemical surface properties has to be considered as inevitable during thermomechanical USP-DLIP processing. Against this background, process-related substrate modification is considered in detail in Objective (B) with application-relevant reference to functional surface properties potentially being involved in bacteria/surface interaction and antimicrobial Cu efficacy, as discussed in **Chapter III**. A fixed USP-DLIP parameter setup generating pattern geometries of 3 µm periodicity, approx. 2.1 µm ablation width and 1 µm ablation depth (close to the single cell-size of *E. coli*) was chosen to assure cross-comparability between the individual studies related to this objective that are published in **Paper II-V**.

Contributions in Paper II:

Based on the laser interference methodology introduced in **Paper I**, the chemical modification of Cu surfaces induced by USP-DLIP processing was analyzed in a high-resolved complementary methodic approach in the initial phase of this thesis. The examination published in **Paper II** was conducted by SEM involving focused ion beam (FIB) cross-sectioning and energy dispersive X-ray spectroscopy (EDS), scanning tunneling microscopy (STM) and spectroscopy (STS) as well as X-ray photoelectron spectroscopy (XPS). To account for passivation/relaxation effects on surface chemistry that are potentially related to functional surface properties, the surface state was analyzed within 24h after processing and after three weeks of exposure to ambient environment.

Within the published study, a comprehensive understanding of chemical surface modification could be elaborated. The predominant process-induced modification of surface chemistry was evidenced to relate to a ballistic mechanism of oxidic particle redeposition. Favoring topographic peaks for accumulation, this mechanism leads to a heterogeneous oxide distribution on the USP-DLIP topography impacting both localized surface chemistry and morphology due to a flake-like particle shape. XPS analysis revealed Cu_2O as the dominant oxide phase, which is in favor of the intended application [51]. Surface properties were furthermore shown to undergo a significant shift from metallic to p-type semiconductor characteristics with a potential impact of surface charge due to the Cu oxide agglomeration. Oxidic surface modification was found to be limited to a layer of a few nm of thickness, which can be undone by a readily developed wet-chemical procedure, achieving a rather native oxidic surface state. USP-DLIP surfaces were furthermore found to undergo chemical surface alteration under extended exposure to ambient environment. This passivation process was shown to involve deviating levels of oxidic phase changes and a preferential agglomeration of functional carbon groups between the two different surface states with and without oxidic surface agglomerates that potentially impacts function surface properties [371].

These results highlight a non-negligible impact of USP-DLIP processing on Cu surface chemistry in view of the aspired application. This aspect was considered in the consecutive investigations regarding a potential influence on functional surface properties and their impact on bacterial interaction and antimicrobial Cu efficiency aside of topography modification itself using the knowledge gained here.

Contributions in Paper III:

A subsequent investigation of the functional impact of topographical and chemical surface modification by USP-DLIP processing on Cu surfaces properties was included in **Paper III**. The study establishes a correlation between the properties of modified surface wettability and ion release resulting from the previously determined chemical surface modification and the approach, interaction, and deactivation of *E. coli* including interlinked aspects of Objective (B) and (C). The experiments furthermore intended to evaluate the suitability of the aspired wet plating methodology for microbial monitoring including further optimization with respect to the high levels of hydrophobicity found on USP-DLIP processed Cu surfaces.

The wetting of USP-DLIP surfaces was shown to exhibit a characteristic change from initially hydrophilic to a pronounced hydrophobic behavior during ambient exposure for more than one week, where hydrophobization follows a logarithmic pace. After three weeks of aging, surface passivation reaches a meta-stable state, where further increase in hydrophobicity is barely detectable. The flake-like oxidic surface agglomeration from USP-DLIP processing tends to boost surface hydrophobicity over a native oxide state, which appears to be attributed to both the higher nm-scale surface roughness as well as a higher proportion of C-C/C-H carbon groups in the superficial adsorption layer.

Based on this, a potential influence of the elevated surface hydrophobicity on bacterial surface approach from a droplet volume during wet plating was considered and investigated in more detail. On this behalf, a specified experimental setup was developed using CLSM and the fluorescent *E. coli* strain ClearColi BL21(DE3) to examine drop edge mobility in the course of progressive wetting. This allowed for both, the detection of either Wenzel or Cassie Baxter wetting states being involved in the restraint of droplet spreading in case of elevated surface hydrophobicity as well as a quantitative impact of planktonic bacteria in vicinity to the drop edge on surface wetting. In fact, wetting is considerably improved in the presence of bacteria. This includes a destabilization of pinned wetting states and an acceleration of the droplet front propagation on all Cu surfaces, which indicates bacterial surface conditioning. USP-DLIP surfaces with and without process-related surface oxide exhibit differences in the initial surface approach of *E. coli* due to deviating fluidic sheer forces at the liquid/air boundary originating from varying surface wetting behavior. Apart from surface wetting, the two distinct USP-DLIP surface states also exhibit unique Cu ion release rates during wet plating with a counterintuitive contribution of the process-induced flake-like oxide agglomerates. Here, the presence of bacteria was shown to play a dominant role on quantitative ion release, which will be further addressed in Objective (C).

In summary, the initial investigation of process-induced impacts by USP-DLIP on the antimicrobial capacity of Cu surfaces presented in **Paper II** and **III** highlight a non-negligible chemical surface modification, which notably contributes to functional surface properties. Based on an adapted wet plating methodology, a suitability of the USP-DLIP process for improving antimicrobial properties could be proved within the scope of these studies. Based on this, the proof of concept on a potential improvement of antibacterial Cu surface properties could be achieved, which is further addressed in the contributions to Objective (C).

Contributions in Paper IV

In addition to potential influences on functional surface properties, an incubating effect of the integrated process-induced modification of Cu surfaces during USP-DLIP was considered in **Paper IV**. The investigation involved interference-induced spatial laser intensity modulation to account for DLIP-specific incubation effects closely interlinked with further improvement of the processing methodology and the TTM simulation model, as outlined in Objective (A). The specific incubation for (USP-)DLIP has been analyzed distinguishing between the individual influences of surface chemistry, superficial microstructure and defect implantation as well as continuous topography modification by laser processing.

Between these three aspects, the modification of surface chemistry was found to exhibit the predominant impact on incubation for the specific material/laser parameter combination used in this thesis. Elevated levels of surface oxidation - either process-induced or in a native state - could be directly correlated with increased broadband absorptance by UV-Vis spectroscopy due to the difference between Cu and Cu_2O/CuO photonic interaction, which is especially emphasized in the NIR spectrum. Consequently, quantitative incubation was traced back to the process-induced agglomeration of oxidic particles evidenced in **Paper II**, which was shown to alter dependent on ablation kinetics.

The continuously modified surface topography was shown to be lesser involved in an overall increase of optical absorptance during incubation, where a measurable effect in UV-Vis spectroscopy is solely related to sub-wavelength feature scales. Instead, an interlinked interaction with beam polarization is found that contributes to primary and sub-pattern geometry shaping. The latter aspect was further investigated by morphological segmentation using a watershed algorithm. In combination with modulated surface chemistry, USP-DLIP related topography modification in scales above the laser wavelength was found to induce a unique incubation behavior characterized by a superposition of the intensity modulation by interference and polarization dependent spatial laser energy implantation.

Similar to topography, the quantitative independent effect of the superficial Cu microstructure on absorptance levels significantly below the impact of surface chemistry. Instead, the microstructure appears to majorly play a mediating role, where e.g., higher deformation in the case of mechanically polished substrates could be linked to a thicker passivating oxide layer, which increases the initial absorption approx. 3-fold over literature values. In a specified set of experiments applying low fluences on deoxidized surfaces, an increased incubation could be evidenced on mechanically deformed compared to annealed microstructure. This indicates a potential incubating effect of microstructure defects involving a reduced free path length of electrons that might further impact electron-phonon coupling. Incubation on deformation free Cu surfaces was furthermore found to deviate between low indexed grain orientations, which might be related to both a difference in photon intrusion depth and damage accumulation.

Aside of the improvement of the USP-DLIP processing methodology, the elaborated investigations of laser induced surface modification and their impact on laser/material interaction in **Paper IV** provides a deeper insight in the mutual interaction of the different mechanisms involved in topography formation during USP processing of Cu. These findings allow to include the surface morphology formed alongside the primary DLIP pattern in surface design and form a valuable basis for the optimization of other USP and/or DLIP-based processes and substrates. (USP-)DLIP specific incubation has not been considered and investigated so far to the best of our knowledge, where this approach constitutes a novelty in the field.

Contributions in Paper V

The impact of USP-DLIP processing on the superficial Cu microstructure was further investigated in a consecutive set of experiments published in **Paper V** including a potential effect on functional surface properties relevant for the antimicrobial application of Cu. The study links process related microstructure modification determined by crystallographic analysis applying FIB/SEM, XRD and EBSD with its impact on wettability and corrosion behavior in saline environment that builds the back bone of the antimicrobial mode of action on Cu surfaces.

It could be verified that USP-DLIP significantly contributes to the superficial defect density of the Cu microstructure, superimposing previous deformations, e.g. by polishing. Adjusting the processing routine by the introduction of additional annealed steps allows for partial or complete removal of the related defect compartments while remaining the USP-DLIP induced topography. This enables a separated and combined investigation of the individual influences of the microstructure states related to annealing, mechanical polishing and USP-DLIP processing both in the case of flat and 3 µm line-like pattern topographies.

Similar to photonic interaction in **Paper IV**, USP-DLIP related defect implantation could be shown to exert an indirect effect on antimicrobial surface properties mediated by altered functional surface properties, which involves surface wettability and corrosion behavior in saline environment. Hydrophobicity in the passivated surface state is found to scale with process-related defect accumulation between the Cu surfaces with similar line-like topography, which provides a direct indication of a subtle effect of USP-DLIP related microstructure modification on physicochemical Cu surface properties. In parallel, USP-DLIP related superficial deformation states induce a tilt in corrosion behavior from heterogeneous localized pitting focusing grain boundaries to a rather homogeneous surface deterioration allowing for a more seamless formation of surface oxide. Both the passivated oxide layer thickness and measured Cu ion release in PBS exposure point out a passivating effect of the increased defect densities after USP-DLIP processing that surpasses polished or undeformed Cu microstructure.

The summarized findings achieved in the previously introduced **Papers II-IV** highlight a multi-level nature of the integrated impact of USP-DLIP processing on physicochemical Cu surface properties alongside of the actually aspired topographic remodeling. These were in fact found to exert a grave influence on the bactericidal efficacy of Cu surfaces, with reference to the state of knowledge about the delicate nature of bacteria/surface interaction and the antimicrobial mode of action of Cu surfaces summarized in **Chapter II1** and **II2.3**, as further addressed in the contributions to Objective (C).

Objective (C):
Antimicrobial Properties

Within the individual contributions to Objective (B), it could be shown that USP-DLIP involves a multi-level effect on functional Cu surface properties that potentially influences antimicrobial efficacy aside from modifying the topography-mediated bacteria/surface contact. This was further investigated in detail in the respective **Papers III** and **V** to allow for a better evaluation of the actual topographic impact on the antimicrobial properties of USP-DLIP processed surfaces with pattern sizes in the scale of single bacterial cells that were ultimately addressed in **Paper VI**.

Contributions in Paper III:

The combined effect of topographical and chemical surface modification of USP-DLIP on active antimicrobial properties of Cu surfaces has been initially investigated in **Paper III**. The experimental design of this study aimed to gain a deeper understanding of the individual impact of modified wettability and surface oxidation on the specific mode of action and effective antimicrobial properties of Cu surfaces. The presented results parallelly mark the conclusion of the initial phase of this thesis by successfully providing the proof of concept for an improvement of antimicrobial surface properties by USP-DLIP in the scale range of single bacteria cells.

In fact, an increase of bacterial killing of *E. coli* K12 (BW25113) could be shown on all USP-DLIP processed Cu surfaces compared to references that exhibit smooth surface topographies. A more detailed examination reveals a significant correlation between the functional surface properties that are parallelly modified by USP-DLIP and the level of enhancement in antimicrobial efficiency. Hydrophobic surface properties appear to further contribute to increased bacterial deactivation rates compared to hydrophilic surfaces despite exhibiting the same topography. Based on the relationships of bacteria/surface interaction discussed in **Chapter II1**, a hydrophobic wetting character might be linked to a more favorable molecular conditioning of the metal surface for the adhesion of microorganisms with hydrophobic membrane properties, such as the *E. coli* strain used here [117].

Surprisingly, quantitative Cu emission on as-processed samples levels higher under bacterial exposure compared to surfaces that underwent deoxidation, despite exhibiting a thicker passivation layer by oxidic process agglomerates. The presence of bacteria appears to play a dominant role here, since these samples in fact display considerably lower Cu release rates combined with rapid surface passivation under exposure to pure PBS solution. It was found that bacterial killing on USP-DLIP surfaces is not necessarily related to the amount of Cu ions emitted, but rather appears to be influenced by bacterial contact conditions. This might indicate an increase in bacterial Cu sensitivity due to surface properties that promote bacterial adhesion, including both topographical and physiochemical factors.

Within these initial experiments published in **Paper III**, a difference in killing efficiency of Cu surfaces depending on the age of the bacteria colonies used for monitoring was observed. This aspect was further investigated in unpublished experiments that aim to better understand the influence of bacteria and their interaction as living organisms on the wet plating methodology used in this work.

Unpublished work related to Paper III

The experiments conducted and published in this thesis employ bacteria as a means of measuring the antimicrobial effect of the functionalized surfaces. Being living organisms (at least in the initial experimental phase) their vitality and ability to interact with the exposed Cu surfaces may exert an impact on the results of the study. On this behalf, further external influences aside of USP-DLIP processing that potentially effect bacterial activity were evaluated in advance of the in-depth studies in **Papers V** and **VI** to improve the determination of actual sample related impacts on antimicrobial efficacy. The experiments were carried out according to the sample preparation and wet plating methodology used in **Papers III**, **V** and **VI**, which are referenced in the respective method sections.

The influence of bacteria colony age

The first of the two unpublished experiments aimed to determine a potential influence of bacterial colony age on the developed deactivation rate in contact with Cu surfaces that was previously hypothesized in **Paper III**. *E. coli* were either cultivated directly from cryopreservation or remained for two and six weeks in a cultivated state on agar plates at 4°C. Exposure was carried out on mirror-polished Cu surfaces to exclude additional topographical or physicochemical influences due to USP-DLIP processing. The data presented in **Figure 20a** suggests that a higher cultivation duration of the bacteria leads to a slower deactivation rate when exposed to Cu. This phenomenon is not related to a difference in the release of Cu ions, which shows similar emission rates, as demonstrated in **Figure 20b**.

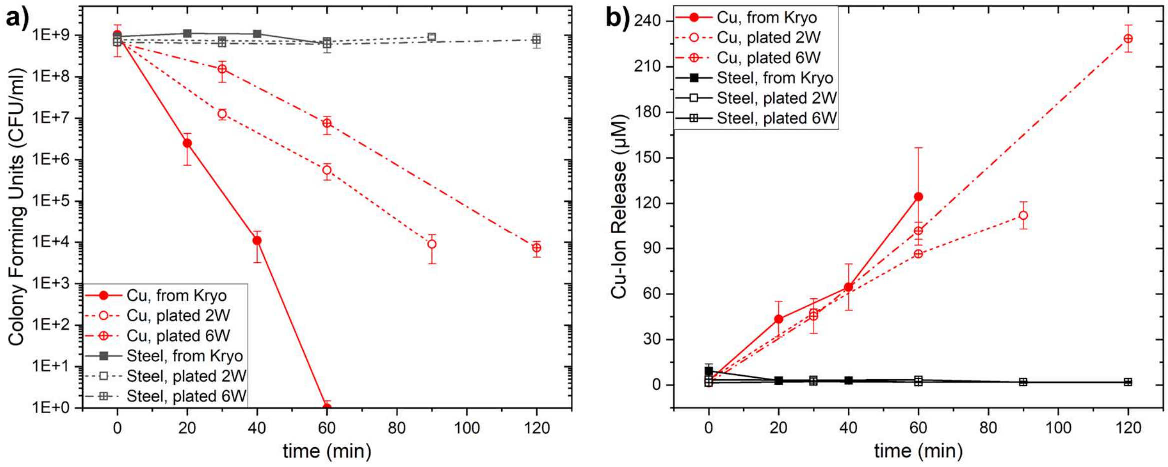

Figure 20: The influence of bacterial cultivation time on antimicrobial efficacy of mirror-polished Cu surfaces. a) Reduction in colony forming units (CFU) of *E. coli* during extended exposure related to three different cultivation times fresh from cryopreservation (from Kryo), plated for two (2W) and sic weeks (6W) . b) Cu ion release parallelly measured via ICP-MS.

With respect to similar external experimental influences in ambient environment, the decreasing bacterial killing rate appears to be related to the duration of the plated colony state. In a mature biofilm, the supply of space and nutrients to individual bacteria is reduced, which results in a reduction in their metabolic activity and reproduction rate. This leads to a shift towards a more static state. As colony age increases, bacteria with lower metabolism are more likely to survive, resulting in the selection of less active individuals. A reduced metabolism potentially decreases the uptake of environmental toxins, such as Cu ions, which might slow down Cu accumulation inside the bacteria and associated deactivation. The results presented here indicate a selection of lesser active bacteria within the matured colonies that furthermore exhibit lower deactivation rates due to decreased metabolic activity and hence active Cu uptake. This suggests that a stimulated bacterial metabolism could also lead to increased Cu uptake and a higher antimicrobial Cu efficiency, in turn.

The influence of ambient temperature

Previous research has shown that low ambient temperatures can inhibit the antimicrobial efficiency of Cu surfaces [44]. This is likely due to either a reduced bacterial metabolic activity under non-optimal growth conditions or decreased Cu release by decelerated corrosion processes. *E. coli*, a human-associated bacterium, typically thrives at the human body temperature of approximately 37°C. As the temperature decreases, its activity is expected to decrease as well. It is possible that slight fluctuations in room temperature just below this range could affect bacterial activity and therefore impact the results of microbial experiments. To investigate this, the antimicrobial effectiveness of mirror-polished reference and USP-DLIP treated Cu surfaces was compared at both 20°C and 30°C ambient temperature using 3 µm line-like pattern geometries also applied in **Paper III**, **V** and **VI**. Complete bacterial deactivation was achieved on the USP-DLIP surfaces for both ambient temperatures after 120 minutes of exposure (refer to **Figure 21a**). At this time, viable bacteria were only detected on the mirror-polished Cu reference measured at 20°C ambient temperature.

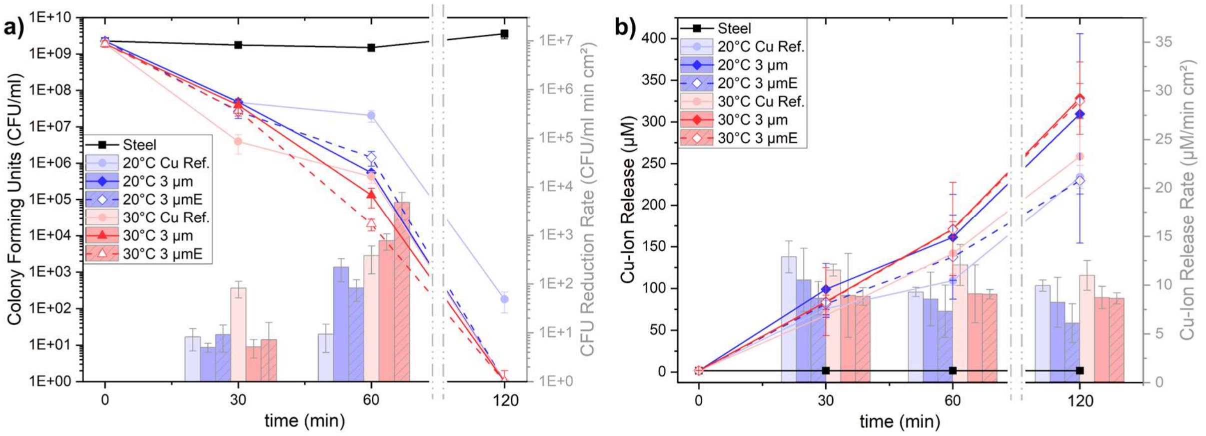

Figure 21: The influence of ambient temperature on the antimicrobial efficacy of both mirror-polished reference and USP-DLIP processed Cu surfaces (the E marks a deoxidized surface state). a) Reduction in colony forming units (CFU) of *E. coli* exposed to the different surface types at either 20°C or 30°C ambient temperature. b) the corresponding Cu ion release measured via ICP-MS.

Higher bacterial deactivation on Cu surfaces at 30°C compared to 20°C can already be found after 30 min of exposure with an increasing trend over time. The most significant contrast in antimicrobial efficiency between the different setups can be observed after 60 minutes of exposure following an almost uniform complete bacterial deactivation after 120 min. The increased bacterial deactivation under 30°C ambient conditions applies to both the USP-DLIP optimized surfaces and the mirror-polished Cu reference. Despite providing a smaller bacterial contact area, the 30°C reference even exhibits a slightly higher antimicrobial efficiency than both USP-DLIP surfaces at 20°C after 60 minutes of exposure.

With regard to Cu ion release, a distinction can be made between almost identical values for the USP-DLIP surfaces at 30°C and the as-processed USP-DLIP surface at 20°C and slightly lower values for the two references and the deoxidized USP-DLIP surface at 20°C. Apart from the deoxidized surfaces, identical sample types show approximately the same ion release at both temperatures indicating a minor thermal influence on corrosion kinetics. Similar to the observation made in **Paper III**, the bacterial deactivation ratio between the samples does not necessarily correspond to Cu emission, where differences in antimicrobial efficiency between the individual sample types cannot be attributed exclusively to quantitative Cu ion release. E.g., the Cu emission rates on three of the USP-DLIP surfaces are almost identical, while bacterial deactivation deviates. This similarly applies to the comparison between the deoxidized USP-DLIP surface at 20°C and the 30°C reference. Furthermore, the Cu reference surface at 30°C exhibits the highest bacterial deactivation rate after 30 minutes, despite releasing the lowest amount of Cu ions.

Based on these results, a notable influence of varying ambient temperature on the antimicrobial efficiency of the Cu surfaces can be assumed corresponding to the general van't Hoff's law [372]. Parallel monitoring of the quantitative Cu ion release suggests an impact of bacterial interaction as the underlying driving force rather than increased Cu intoxication by enhanced corrosion kinetics. In parallel, USP-DLIP surfaces show a significant increase in antimicrobial efficiency compared to the respective reference surfaces under both temperature conditions, where the antimicrobial effect of 20°C USP-DLIP surfaces is similar to the 30°C Cu reference.

The knowledge obtained in the unpublished experiments presented has been involved in the design of the wet plating experiments in **Papers V** and **VI** to improve bacterial monitoring. E.g., an adjustment of the time frame for achieving complete bacterial deactivation based on the bacterial cultivation time was used to improve temporal monitoring resolution.

Contributions in Paper V

Based on the functional considerations on the antimicrobial effect of Cu presented in **Chapter III**, it can be postulated that the antimicrobial mechanism of action of Cu materials by quantitative Cu ion release is linked to the substrate microstructure. An investigation of the potential impact of USP-DLIP processing induced Cu microstructure modification on antibacterial efficacy against *E. coli* in connection to the corrosion related Cu ion release was therefore investigated in a customized experimental setup and published in **Paper V**.

In the experimental approach, the microstructure defect states related to the sub-steps of sample preparation involving mechanical polishing and USP-DLIP processing are selectively generated to investigate their individual and combined impact on functional and antimicrobial surface properties. It could be shown that functional surface properties as well as corrosion behavior is closely linked to the superficial microstructure state, where USP-DLIP specific superficial microstructure modification exerts the most significant impact on each of the individual aspects.

Cu corrosion behavior was found to be majorly dominated by the superficial microstructure, which highly impacts the formation of stable passivating oxide layers as well as quantitative Cu ion release. Here, USP-DLIP induced deformation of the superficial microstructure was shown to reduce localized pitting in saline environment, which allows for a more rapid and stable surface passivation. An additional introduction of *E. coli* into the saline environment accelerates Cu corrosion by the prevention of surface passivation, where the microstructure dominated corrosion mechanisms and respective Cu emission ratios prevail. Aside of corrosion behavior and Cu emission, the microstructure state of Cu furthermore appears to impact physicochemical surface properties as indicated by a differently expressed surface wettability. Although a significant deviation in Cu ion release can be found on USP-DLIP surfaces with different microstructure states, bacterial deactivation does not necessarily follow this trend but appears to be more affected by physicochemical surface properties as indicated by altered wettability. Under the catalytic impact of bacteria on Cu corrosion, USP-DLIP induced surface oxide agglomerations were furthermore found to additionally boost Cu ion release and antimicrobial efficiency through dissolution, while they remain stable and support surface passivation in the absence of bacteria.

Up to this, the integrated combination of surface modification effects by USP-DLIP, including topography, chemistry, and microstructure, could be evidenced to induce the most significant increase in antimicrobial efficiency. Independently, it was be shown that USP-DLIP-modified surfaces consistently exhibits an enhanced antimicrobial effect against *E. coli* compared to the Cu reference surfaces that was individually boosted by functional surface properties.

Contributions in Paper VI

After successful assessment of the parallel influence of superficial chemistry and microstructure modification by USP-DLIP processing, the actual effect of bacterial contact mediation on the antibacterial properties of Cu surfaces by topographic pattern size was finally examined in **Paper VI**.

Applying the knowledge of targeted process parameterization from **Papers I** and **IV**, line-like patterns with size ratios of P > Bac (P = 3 µm), P ≈ Bac (P = 1 µm), and P < Bac (P = 0.75 µm) based on the statistical single cell size variance of the tested bacterial strains *E. coli* K12 (BW25113) and *S. aureus* SA113 were generated on Cu. The pattern topography geometrically allowed for the access of single cells and clusters (P = 3 µm), singular cells (P = 1 µm) and no access (P = 0.75 µm) into concave pattern valleys, which modulates quantitative bacterial/surface contact. Antimicrobial monitoring on Cu involved the consideration of additional functional impacts of process induced oxidic agglomerations as demonstrated in **Paper III** and **V**, while a very small direct influence of varying microstructure modification on antimicrobial efficacy between the different topographies can be assumed based on the findings in **Paper V**. In fact, both hydrophobicity and Cu ion release were shown to be increased on as-processed compared to deoxidized surfaces independent of the pattern scale, which correlates to the previous findings.

The investigations demonstrate a significant relation between pattern scale and antimicrobial efficiency, where however strain specific inter-cell interaction induces a difference in pattern specific bacterial deactivation between *E. coli* and *S. aureus*. High deactivation rates are closely linked to the capability of the bacteria to establish quantitative surface contact either as single cells or in clusters in relation to the topographic boundaries of the individual pattern geometries. In turn, antimicrobial efficacy appears to be decreased in the case of an impaired surface contact. Geometrically induced contact conditions by pattern scale and surface morphology both appeared to induce a higher impact on antimicrobial efficacy than a different level of hydrophobicity as assessed by WCA measurement and quantitative Cu ion release.

In addition to the strain specific response to the different pattern scales, the study also focused on the chemical surface interaction of both bacterial strains with the Cu substrates. The Cu damaging mechanisms of the Gram-positive *S. aureus* involve a higher accumulation of Cu phosphate on the bacterial membrane, as well as leakage of cytoplasm due to advanced membrane damage, in contrast to buckling without extracellular agglomerates observed for the Gram-negative *E. coli*. Bacterial exposure under the saline environment of the PBS solution furthermore exhibits a deviating catalytic impact on Cu corrosion compared to *E. coli*. This results in different Cu ion release kinetics under PBS exposure exhibiting increased passivation levels on the USP-DLIP surfaces, which can directly be attributed to a higher membrane stability of *S. aureus* effecting a decreased transitivity towards Cu ions.

The results of this study highlight a considerable impact of strain specific characteristics on the antimicrobial mechanism of action of Cu surfaces, which involves a deviation of both the topographic effect on antimicrobial efficacy of specific pattern sizes as well as bacterial catalysis of Cu corrosion. Applying USP-DLIP on Cu surfaces could be evidenced to benefit both the antimicrobial efficacy by an exponential increase of bacterial deactivation on contact mediating topographies as well as corrosion resistance of Cu by increasing passivation stability. Surprisingly, these features do not counteract, whereas bacterial deactivation does not necessarily scale by increased Cu ion release, but rather appears to involve a triggering of enhanced bacterial Cu sensitivity on the USP-DLIP surfaces.

In summary, USP-DLIP was shown to improve the antimicrobial properties of Cu surfaces independent of the bacterial strain by a multi-layered modification of both topographic and functional surface properties that each benefit the application.

Contributions in Paper VII

Based on the successful USP-DLIP process development and the initial proof of concept of a potential enhancing effect of USP-DLIP surface functionalization on the antimicrobial efficacy of Cu surfaces in the initial phase of this work, further accompanying research projects have been initiated. Amongst these, research activities in the field of Cu based antimicrobial surfaces and bacterial surface interaction included the ISS projects “Space Biofilms”, “BIOFILMS” and “Touching Surfaces” with reference to human spaceflight (the respective mission batches are displayed in **Figure 22**). The BIOFILMS experiment represents the first study on Cu materials for antimicrobial applications on the ISS. In parallel, samples involved in the Touching Surface experiment have been used in the first ever conducted series of investigations using electron microscopy combined with X-ray spectroscopy in space by means of the as-introduced “Mochii” facility.

Figure 22: Mission batches of the three ISS experiments conducted in the extended scope of this dissertation. Left to right: Space Biofilms (Flight in 2019), BIOFILMS (Flight 1 in 2021, Flight 2 in 2022, Flight 3 in 2023, estimated Flight 4 in 2025), Touching Surfaces (On board the ISS from 09.2021 to 08.2022).

At the time of the submission, the extensive sample material from both the BIOFILMS and Touching Surfaces flight experiments was still under investigation, where the results have yet to be published. In representation of these activities, the first paper of the ISS project BIOFILMS that introduces in the conceptual structure of the flight experiment has been integrated in this thesis as **Paper VII**, which also offers an outlook for research activities beyond this work.

In addition to the increased cosmic radiation outside the Earth's protective atmosphere, bacteria are exposed to various external influences under space conditions that can affect their behavior and viability. Due to the lower level of mixing and the absence of convection or sedimentation, the nutrient supply of bacteria in a liquid medium is subject to different dynamics. Such differences in material transport can also affect vital functions of the bacteria as well as driving forces involved in bacterial surface interaction introduced in **Chapter II 1**. At the same time, the release and diffusion of bactericidal Cu ions on actively antimicrobial Cu surfaces may be subject to similarly altered kinetics.

Previous human spaceflight experience has shown that controlling the microbial environment in spacecraft and space stations is essential to maintain astronaut health and the technical functionality of life support systems. The USP-DLIP functionalized metal surfaces studied in this experiment could potentially contribute to the control and/or containment of the surface microbiome on the space station. By observing bacterial interactions under the modified conditions of space, it may also be possible to draw important conclusions about specific interactions observed on Earth.

The USP-DLIP based concept of topographically functionalized antimicrobial surfaces established in **Papers I-III** builds the technology platform for modified bacterial contact in BIOFILMS. Contact-promoting or -inhibiting conditions with P > Bac and P < Bac are realized by structure sizes of 3 µm and 800 nm. In BIOFILMS, the ability of three space flight relevant bacterial strains[3] to colonize and form biofilms on USP-DLIP functionalized antimicrobial and inert metal surfaces from a planktonic initial state is investigated under different gravity conditions within space station environment. Using the two KUBIK incubation modules with integrated centrifuge installed on the ISS, the experiment simulates the microgravity (µg) on the space station, the gravity of Mars (0.38 g, approximated with 0.4 g) and Earth (1 g). In total, BIOFILMS comprises four flight experiments with a flight interval of several years and a total of 135 parameter modifications tested on 960 individual samples. The in-depth investigation of bacterial behavior on the different surfaces under the environmental conditions of extraterrestrial habitats aims towards a better understanding of the nature and adaptation strategies of bacteria and the evaluation of a potential applicability in contamination control.

---

[3] • *Staphylococcus capitis* subsp. *capitis*, which has previously been exposed to space conditions on the ISS.
• *Acinetobacter radioresistens*, exhibiting high resilience towards increased levels of radiation.
• *Cupravidus metallidurans*, which has shown notable resistance capacities to Cu and heavy metals.

V | Included Papers and Manuscripts

Paper I

Applying Ultrashort Pulsed Direct Laser Interference Patterning for Functional Surfaces

In this study, the Direct Laser Interference Patterning methodology applying ultrashort laser pulses (USP-DLIP) developed in the scope of this work is introduced. This includes approval of the feasibility to generate hierarchical surface structures in the micro- as well as the sub-micrometer scale on ceramic, polymer and metallic materials. Coupled with an elaborated investigation of thermodynamic mechanisms involved in pattern formation especially on metallic substrate materials, this technique enabled an extended research in several fields of application involving the topic of this thesis.

Paper II

In-Depth Investigation of Copper Surface Chemistry Modification by Ultrashort Pulsed Direct Laser Interference Patterning

Surface patterning in the micro- and nanometer-range by means of pulsed laser interference was shown to modify both the topography and surface chemistry. This work presents an in-depth investigation of the chemical surface modification occurring during surface patterning of Cu by USP-DLIP following a multi-method approach. The detailed quantification of surface morphology as well as composition and distribution of surface chemistry related to both processing and atmospheric aging allows for an improved assessment of the multi-level impacts of USP-DLIP on functional Cu surface properties that potentially influence antibacterial efficacy.

Paper III

Increasing Antibacterial Efficiency of Cu Surfaces by targeted Surface Functionalization via Ultrashort Pulsed Direct Laser Interference Patterning (USP-DLIP)

Building on the results of the previous two papers, this study investigates on how antibacterial properties of Cu surfaces against *E. coli* are influenced by USP-DLIP. This involves the modification of both topographic and functional surface properties by applying surface patterns in the scale range of single bacteria cells. In fact, both topographic and physicochemical influences on bacterial adhesion mutually affect the expressed antibacterial efficacy exhibiting a delicate interplay that allows to factorially enhance the antimicrobial properties of Cu.

Paper IV

Multi-Pulse Agglomeration Effects on Ultrashort Pulsed Direct Laser Interference Patterning of Copper

Bacteria/surface interaction is sensitive to a complex setup of surface properties potentially including an impact of both primary and sub-pattern morphology. In this light, the mutual effect of proceeding surface modification on pattern formation alongside multi-pulse USP-DLIP of Cu is investigated to improve both topographic and functional surface tailoring. The in-depth insight into the dynamic physical Cu surface modification by USP-DLIP includes a mutual influence between primary and sub-pattern formation that allows for high precision µm and nm-scaled pattern design.

Paper V

Microstructure versus Topography: The impact of crystallographic substrate modification during Ultrashort Pulsed Direct Laser Interference Patterning on the antibacterial properties of Cu

In antimicrobial applications of Cu surfaces the effective mode of action relies on the quantitative release of Cu ions, by which a modification of the substrate properties related to corrosive interaction might similarly impact bactericidal efficiency. In this regard, the influence of USP-DLIP processing on the superficial microstructure of pure Cu was investigated including its integrated impact on functional surface properties and the bactericidal efficacy on topographic patterns in the scale of single bacterial cells.

Paper VI

Modifying the Antibacterial Performance of Cu Surfaces by Topographic Patterning in the Micro- and Nanometer Scale

Based on the fundamental understanding of the parallel impacts of physicochemical and microstructure modification by USP-DLIP this study investigates the influence of modified bacteria/surface contact conditions by topographic patterning above and below the scale range of single bacteria cells on the antibacterial properties of Cu.. The respective deviation of bacteria/surface interaction for Gram-positive *S. aureus* and Gram-negative *E. coli* is monitored in terms of strain specific bactericidal efficacy and triggering of corrosive driving forces.

Paper VII

Testing laser-structured antimicrobial surfaces under space conditions: the design of the ISS experiment BIOFILMS

Parallel research activities further extended the scope of this thesis from which this paper was included to highlight potential aspects of application of the investigated surface concept. In case of manned space flight, microbial biofilms pose a particular threat due to possible damage to vital technical equipment and systems as well as a general risk to crew health due to potentially increased pathogenicity and resistance development under µG conditions. This paper introduces the cooperative ESA/DLR/UdS FuWe space experiment BIOFILMS, which investigates the decontaminating capacities of USP-DLIP functionalized metallic surfaces under space flight conditions including a variety of G-levels allowing on a view on future extra-terrestrial habitats.

Paper I:

Applying Ultrashort Pulsed Direct Laser Interference Patterning for Functional Surfaces

Daniel Wyn Müller[1,*], Tobias Fox[1], Philipp G. Grützmacher[1], Sebastian Suarez[1], Frank Mücklich[1]

[1]Chair of Functional Materials, Department of Materials Science, Saarland University, 66123, Saarbrücken, Germany.

Published in February 2020 in "Scientific Reports" and accessible online via:

https://doi.org/10.1038/s41598-020-60592-4

Abstract:

Surface structures in the micro- and nanometre length scale exert a major influence on performance and functionality for many specialized applications in surface engineering. However, they are often limited to certain pattern scales and materials, depending on which processing technique is used. Likewise, the morphology of the topography is in complex relation to the utilized processing methodology. In this study, the generation of hierarchical surface structures in the micro- as well as the sub-micrometre scale was achieved on ceramic, polymer and metallic materials by utilizing Ultrashort Pulsed Direct Laser Interference Patterning (USP-DLIP). The morphologies of the generated patterns were examined in relation to the unique physical interaction of each material with ultrashort pulsed laser irradiation. In this context, the pattern formation on copper, CuZn37 brass and AISI 304 stainless steel was investigated in detail by means of a combination of experiment and simulation to understand the individual thermal interactions involved in USP-DLIP processing. Thereby, the pattern's hierarchical topography could be tailored besides achieving higher process control in the production of patterns in the sub-µm range by USP-DLIP.

Own contributions:

Conception and design of the study. Development of the laser setup. Conduction of the experiments including USP-DLIP processing as well as LSM and SEM analyzation of the different substrates processed. Conception of the modelling approach and design of the numerical thermodynamic model including programming of the FEM simulation. Data interpretation, reparation and editing of the manuscript.

www.nature.com/scientificreports

SCIENTIFIC REPORTS
natureresearch

OPEN

Applying Ultrashort Pulsed Direct Laser Interference Patterning for Functional Surfaces

Daniel Wyn Müller*, **Tobias Fox**, **Philipp G. Grützmacher**, **Sebastian Suarez** & **Frank Mücklich**

Surface structures in the micro- and nanometre length scale exert a major influence on performance and functionality for many specialized applications in surface engineering. However, they are often limited to certain pattern scales and materials, depending on which processing technique is used. Likewise, the morphology of the topography is in complex relation to the utilized processing methodology. In this study, the generation of hierarchical surface structures in the micro- as well as the sub-micrometre scale was achieved on ceramic, polymer and metallic materials by utilizing Ultrashort Pulsed Direct Laser Interference Patterning (USP-DLIP). The morphologies of the generated patterns where examined in relation to the unique physical interaction of each material with ultrashort pulsed laser irradiation. In this context, the pattern formation on copper, CuZn37 brass and AISI 304 stainless steel was investigated in detail by means of a combination of experiment and simulation to understand the individual thermal interactions involved in USP-DLIP processing. Thereby, the pattern's hierarchical topography could be tailored besides achieving higher process control in the production of patterns in the sub-µm range by USP-DLIP.

Highly specific surface properties in nature, like the well-known lotus and shark skin effects, are closely related to surface structures in the micrometre and nanometre length scale, often involving hierarchical patterns[1]. In fact, such biomimetic surface patterns have already proven to provide unique properties in several technical systems including the manipulation of contact mechanics and optical properties like light diffraction and absorption[2–4]. Patterns on the threshold between the micro- and the nanometre scale also showed to provide promising surface properties for medical products, as they can tailor the adhesion of both, cells and germs[5–7]. In this context, current research projects investigate the intricacies to prevent biofilm formation by surface patterning of different solid materials on the International Space Station (ISS), which endanger its crew in terms of both, health and damage to critical components[8].

The predominant impact on the unique properties of patterned surfaces is defined by the scale and morphology of the surface features also including sub-patterns, which have to be adjusted specifically for each application. For instance, in antibacterial applications, feature sizes in the sub-µm length scale showed to be most effective against bacterial adhesion[7–10]. The processing methodology, dealing with such delicate surface modification, needs to ensure high machining precision as well as processing speeds and costs, which are able to compete with the classical methods of surface engineering. Besides lithographic methods, laser interference-based techniques have proven their worth in generating precise surface patterns, as they provide high processing speeds with little to no need for preparation and post-processing[11]. Direct Laser Interference Patterning (DLIP) using short pulsed laser sources was successfully applied for the controlled creation of periodic surface patterns in the micrometre scale, but has struggled to obtain sub-µm patterns on conductive materials[3–7,12]. Applying pulse durations close to or below the threshold of 10 ps in DLIP (which defines the ultrashort regime), allows for the generation of smaller pattern periodicities on a wider set of materials, even reaching below the µm scale range on metals[12–16]. When using ultrashort laser pulses (USP), sub-µm patterns can also be applied on several metals, semi-conductors and polymers by the formation of Laser Induced Periodic Sub-Structures (LIPSS)[10,12,17–19]. LIPSS generation is assumed to originate from the superposition of the incident laser pulse and a superficial plasmon wave within the irradiated substrate, inducing line-like sub-structures, which are oriented perpendicular to the laser pulse polarisation and exhibit a periodicity close to the laser wavelength. In addition to their use as primary pattern,

Chair of Functional Materials, Department of Materials Science, Saarland University, 66123, Saarbrücken, Germany. *email: daniel.mueller@uni-saarland.de

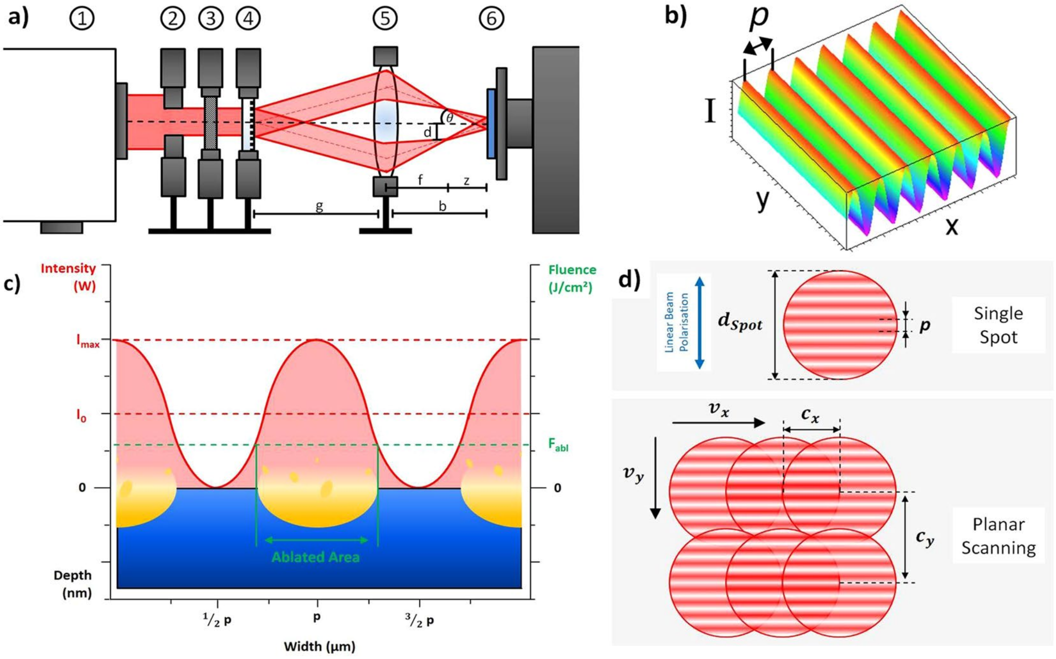

Figure 1. (**a**) Schematic illustration of the optical setup for USP-DLIP. 1 laser source, 2 aperture, 3 wave plate, 4 DOE, 5 lens systeme, 6 automated two axes (x, y) sample mount. (**b**) two beam interference leading to one-dimensional sinusodial intensity patterns. Periodicity p accounts for the distance between two intensity maxima. (**c**) Surface patterning takes place in the areas, where the laser fluence surpasses the material specific ablation threshold F_{abl}. Hence, the pattern parameters can be modified by adjusting p and the seed beam intensity I_0. (**d**) Single spot and planar scanning used for surface patterning also showing the alignment of the linear beam polarisation perpendicular to the pattern orientation. The overlap c_x and c_y were modified by adjusting the horizontal scanning speed v_x and the vertical step size v_y in relation to the pulse frequency of 1 kHz, the laser spot diameter d_{Spot} and the intensity pattern periodicity p.

LIPSS might be used as additional sub-patterns, rendering the morphology of DLIP generated patterns hierarchical[16]. Avoiding their formation, on the other hand, is often hard to achieve, especially on low conductive metals and semi-conductors. Hence, pattern morphologies on different materials generated by USP-DLIP might vary strongly in relation to the physical kinetics involved in topography formation, which need to be understood to efficiently tailor surface functionalities.

The current study investigates the material specific interaction in response to USP-DLIP for the creation of hierarchical structures in the micro- and sub-micrometre scale on ceramic, polymer and metallic materials involving primary pattern formation as well as sub-pattern generation. Since metals showed the most intricate response to processing by USP-DLIP in the experiments, the complex thermal surface kinetics involved in the pattern formation were examined by a combination of experiment and thermal simulation using a Two Temperature Model (TTM). Thus, the thermal and kinetic response of the noble metal copper, as well as the alloys CuZn37 brass and AISI 304 stainless steel on USP-DLIP could be determined in relation to a range of laser fluences and pulse accumulation. The knowledge of the material´s response allows for precise tailoring of the pattern's topographical parameters and the creation of optimised patterns in the sub-µm scale.

Methods

Ultrashort pulsed direct laser interference patterning (USP-DLIP).

For Direct Laser Interference Patterning a *Ti:Sapphire* laser source emitting ultrashort laser pulses with a pulse duration t_p of 100 fs at Full Width Half Maximum (FWHM) and a centred wavelength λ of 800 nm was used. In the optical setup, the seed beam first passes an aperture defining the working beam diameter, as well as altering the intensity profile from Gaussian to a near Top Hat. A wave plate adjusts the polarization angle of the laser beam perpendicular to the generated pattern orientation. The femtosecond pulsed seed beam is divided by a Diffractive Optical Element (DOE), while a lens system causes the coherent beams to overlap on the sample surface. Due to the short coherence length of approx. 30 µm in case of 100 fs laser pulses, deflection of the beam paths is kept as low as possible to still allow for interference across the full spot diameter. The optical setup is schematically shown in Fig. 1a. Overlapping the coherent beams induces an interference pattern modulating the distribution of the laser intensity on the substrate surface. In case of the two-beam interference setup used in these experiments, the pattern shows a one-dimensional sinusoidal distribution of laser intensity illustrated in Fig. 1b.

In the used optical setup, the individual beams are focussed before reaching the substrate's surface. Thus, the interference zone is situated further along the beam path, where both beam diameters are widening again, which enables a faster processing due to the increased spot diameter. The analogy of the beam paths in the interference setup to the setup of the Fresnel mirror test can be utilised to calculate the periodicity p of the generated pattern in correlation to the incident angle θ of a single beam according to:

$$p = \frac{\lambda}{2\,\tan(\theta)} \tag{1}$$

The sinusoidal linear intensity distribution $I(\mathrm{x})$ induced by DLIP can be calculated by[13]

$$I(\mathrm{x}) = 2\,I_0\,cos^2\left(\frac{\pi \mathrm{x}}{p} + 1\right) \tag{2}$$

Patterning of the irradiated substrate happens by physical laser-material-interaction, which depends on the local intensity gradient, as illustrated in Fig. 1c. In this context, the material response mainly corresponds to the material specific ablation threshold F_{abl}[20].

Materials preparation. In the experiments different series of spots, as well as planar patterns with a periodicity p of 3 µm were applied on 10 × 25 mm platelets of the three metallic substrates copper, CuZn37 brass (*Wieland*) and AISI 304 stainless steel (*Brio*). The two ceramic and polymer samples, 3Y-TZP zirconia and Poly-L-Lactide Acid (PLLA), were solely planar patterned, both with 3 µm and 10 µm periodicity. The metallic substrates were first mirror-polished utilising an automated *TegraPol* system (*Struers*). Additionally, patterns of 0.7 µm periodicity were fabricated to investigate the possibility of producing sub-µm periodic structures on metallic substrates by this technique. To achieve this, the focal length of the lens system was changed from 100 mm ($p = 3$ µm) to 23 mm ($p = 0.7$ µm) by introducing an additional lens. The single spot samples were irradiated with different pulse numbers (n = 1, 2 and 5) at different laser fluences. Planar patterning was conducted by scanning the substrate surface in continuous pulsing mode using a pulsing frequency of 1 kHz. The different processing types are schematically shown in Fig. 1d. The overlap of the sequential pulses was tailored by the scanning speed, as well as the vertical spacing of the scanning lines as described in[21]. The laser fluence was altered from 0.5 to 4.6 J/cm² for $p = 3$ µm and from 2.07 to 7.6 J/cm² for $p = 0.7$ µm corresponding to the intensity calculated at FWHM of the DLIP-induced intensity pattern.

Characterisation. Characterisation of the surface topography as well as the modification of the microstructure was conducted by means of confocal laser scanning microscopy (CLSM) utilising a *LEXT OLS4100 3D Measuring Laser Microscope* by *Olympus* as well as scanning electron microscopy (SEM) (*Helios 600* by *FEI*). The CLSM measurements were done using the 50× lens in digitally doubled magnification mode at a laser wavelength of 405 nm. For SEM imaging, secondary electron (SE) contrast was used in addition to a sample tilt of 52° degree, which allows for an improved visualization of topographical features. The acceleration voltage was set to either 10 kV or 5 kV at a current of 0.86 pA.

Modelling the thermal response of metals to USP-DLIP. In case of an irradiation of metals by ultrashort laser pulses, the pulse duration and hence the time needed for a complete energy transfer to the material´s electron system is generally far shorter than the electron-phonon relaxation time[22]. This induces a high thermal gradient between electron gas and lattice leading to a very localized, strong heating. To predict the materials response correctly under these circumstances, the temperatures of both the electron system T_e and the lattice system T_l have to be considered separately in a Two Temperature Model (TTM)[23]. Corresponding to Fourier´s law of heating, the one dimensional distribution of T_e and T_l oriented orthogonal to the substrate surface is defined by the following equations[23,24].

$$C_e(T_e)\frac{\partial T_e}{\partial t} = \left[k_e(T_e)\frac{\partial T_e}{\partial z}\right] - G(T_e - T_l) + S \tag{3}$$

$$C_l(T_l)\frac{\partial T_l}{\partial t} = \left[k_l(T_l)\frac{\partial T_l}{\partial z}\right] + G(T_e - T_l) \tag{4}$$

The parameters C_e and C_l represent the specific heat capacity of the electron and the lattice sub-systems, while k_e and k_l are their thermal conductivities. The energy transfer rate between electron gas and lattice is defined by the electron-phonon coupling coefficient G. The heat input induced by laser irradiation is represented by the source term S.

The electron heat capacity C_e of a Fermi-distributed electron gas is increasing linearly in relation to the electron temperature T_e for temperatures below the Fermi Temperature $T_F = E_F/k_B$. Hence, C_e can be calculated by $C_e = C_{e0}T_e$ where C_{e0} is the specific electron heat capacity at ambient temperature. For electron temperatures close to and higher than T_F, the specific electron heat capacity should be determined by

$$C_e = \frac{N_e k_B}{2} \tag{5}$$

where N_e is the electron density[24].

The heat capacity C_l of the lattice can be estimated as being invariable for temperatures higher than the Debye temperature and hence represents a constant material parameter[25].

Thermal diffusion in the electron system strongly depends on the local electron and lattice temperatures. For electron temperatures below T_F, the thermal conductivity k_e of the electron system is suggested to follow the ratio between T_e and T_l as $k_e \approx k_{e0}(T_e/T_l)$, where k_{e0} is the electron thermal conductivity at ambient temperature[26]. However, recent investigations have shown a more delicate behaviour of the electron thermal conductivity over a wider range of temperature, suggesting an improved term to determine k_e using the specific material constants A and B[27,28].

$$k_e = k_{e0}\frac{BT_e}{AT_e^2 + BT_l} \tag{6}$$

Nevertheless, by using Eq. (6) the electron thermal conductivity gets underestimated, when the electron temperature reaches a temperature much higher than the lattice temperature (by two orders of magnitude)[13,29]. This is most likely the case at high laser fluences and for metals exhibiting a low electron-phonon-coupling, like gold, silver and copper. Here, the electron thermal conductivity is represented more accurately by

$$k_e = C\frac{(\theta_e^2 + 0.16)^{5/4}\ (\theta_e^2 + 0.44)\theta_e}{(\theta_e^2 + 0.092)^{1/2}\ (\theta_e^2 + s\theta_l)} \tag{7}$$

where $\theta_e = T_e/T_F$ and $\theta_l = T_l/T_F$. The two material specific constants C and s can be determined by adjusting the progression of k_e to the behaviour calculated by Eq. (6) at low electron temperature, as described in[27]. In the simulations, Eq. (7) was preferred for copper and CuZn37, since the calculated values for T_e tend to significantly exceed T_l at higher fluences. In the case of steel, Eq. (6) was applicable for all the calculations, as the difference between T_e and T_l remained lower, which can be addressed to higher electron-phonon coupling.

As heat diffusion in metals is related up to 99% to transmissions by collisions within the electron system the contribution of k_l to the thermal diffusion can be neglected[30].

Similar to the electron thermal conductivity, the electron-phonon coupling coefficient G depends on the system temperatures. It can be determined using the following equation[31]

$$G = G_0\left[\frac{A}{B}(T_e - T_l) + 1\right] \tag{8}$$

G_0 is defined here as the electron-phonon coupling at ambient temperature.

The temporal intensity distribution of the laser pulse is following a Gaussian behaviour, defined by the pulse duration t_p at FWHM[32]. In conjunction to the Beer-Lambert Law and the pattern-shaped distribution of $I(x)$ on the target surface defined by Eq. (2), the energy absorption of the irradiated substrate accounting for the source term is defined by[13]

$$S(\mathrm{x},\ \mathrm{z},\ \mathrm{t}) = \Delta_{abs}\ \alpha(1 - R)\frac{I(x)}{\sigma\sqrt{2\pi}}\exp\left[-\frac{(t - t_0)^2}{2\sigma^2} - \alpha z\right] \tag{9}$$

In this term, t_0 is the arrival time of the pulse at maximal intensity and σ the standard deviation defined by

$$\sigma = \frac{t_p}{2\sqrt{2ln2}} \tag{10}$$

The material specific absorptivity α and reflectivity R depend on the wavelength of the laser used to irradiate the substrate and can be calculated using the corresponding refractive index n and extinction coefficient k[33] by

$$\alpha = \frac{4\pi k}{\lambda} \tag{11}$$

and

$$R = \frac{[(n - 1)^2 + k^2]}{[(n + 1)^2 + k^2]} \tag{12}$$

As former works have shown, the optical substrate properties are significantly changed due to strong thermal electron excitation during ultrashort pulsed laser irradiation, which increases the absorption of the laser pulse during irradiation[34–36]. To include this optical behaviour in the simulation of ultrashort pulsed laser-material interaction, n and k were altered according to enhanced electron energy states ΔeV using the data provided for copper and iron in[33]. Alteration of the optical properties was linked to the electron temperature T_e by approximating $\Delta T_e \sim \Delta eV/k_B$.

Aside of the electron temperature, chemical or topographical surface modifications like oxidation or laser induced surface roughening also showed to enhance laser absorption of the substrate surface. In order to include this influence in the numerical calculation the factor Δ_{abs} was implemented in Eq. (9), which is raised from 1 to 2 according to the findings of Vorobyev *et al.*[37] for the calculation of thermal interactions in response to multi pulse irradiation.

The thermal substrate response upon irradiation by USP-DLIP was analysed numerically in a 2D depth profile by solving the introduced thermal model with the simulation software *FlexPDE*. The specific material constants used in the numerical analysis of the thermal behaviour of copper and AISI 304 stainless steel are listed in Table 1.

	Copper	Stainless steel
Absorptivity $\alpha_{(\lambda=800\ nm,\ Te=300\ K)}\left(\frac{1}{m}\right)$[33]	12.8×10^7	5.74×10^7
Reflectivity $R_{(\lambda=800\ nm,\ Te=300\ K)}$[33]	0.9645	0.601
Electron heat capacity $C_{e0}\left(\frac{J}{m^3K^2}\right)$[13,47]	96.6	706.4
Lattice heat capacity $C_l\left(\frac{J}{m^3K^2}\right)$[48]	3.39×10^6	3.66×10^6
Electron thermal conductivity $k_{e0}\left(\frac{W}{mK}\right)$[49,50]	401	15
Electron-phonon coupling coefficient $G_0\left(\frac{W}{m^3K}\right)$[49]	12×10^{16}	130×10^{16}
Material specific constants C and $A\left(\frac{1}{sK}\right)$[13,38]	$C = 386.5$	$A = 0.98 \times 10^7$
Material specific constants s and $B\left(\frac{1}{sK^2}\right)$[13,38]	$s = 0.14$	$B = 2.8 \times 10^{11}$

Table 1. Specific material constants used in the TTM simulation of copper and stainless steel.

For stainless steel, the optical and thermal material parameters of iron were used, only adapting the material specific constants A and B, as well as the electron thermal conductivity k_{e0} to represent the low thermal conductivity of steel[38]. In the case of CuZn37 brass, the main parameters of copper were used, as its characteristics still dominate the metallic properties of this alloy. To specify the model for the alloy´s thermal behaviour, the lower thermal conductivity and heat capacity were implemented by choosing k_{e0} as 120 W/m³K and C_l as 3.17×10^6 J/m³K.

Results

USP-DLIP on insulating materials.

For USP-DLIP on the insulating materials zirconia and PLLA I_0 was adjusted accordingly to ablate an area of 50% of the whole spot area. To obtain continuous line patterns, the substrate surfaces were patterned with a pulse overlap c_x of 90%. The ablation areas on both materials are well defined and exhibit sharp boundaries to the non-ablated areas. The morphology of the ablated areas indicates that in both cases a liquid phase appears to have been present aside of predominant evaporative ablation during thermal interaction in response to USP laser irradiation. In the case of zirconia, the surface in the ablation area exhibits a high porosity accompanied by crack formation illustrated in Fig. 2a,b, which is likely to be induced by thermal stress from fast temperature transitions during laser processing. Similar observations were made on zirconia substrates processed by short pulsed DLIP, in case of a higher number of overlapped pulses[39]. The underlying mechanism leading to the occurrence of porosity could not be unambiguously determined, but it is most likely related to localized explosive vaporization events, which might originate from both inhomogeneity in the bulk material and enhanced localized absorption by laser induced surface roughening[37]. On PLLA the unaffected surface partitions exhibit spots and strands of re-solidified substrate that stretch across the ablation areas, as can be seen in Fig. 2c. In the experiments, remarkably high ablation depths of up to 10 µm were achieved in comparison to the other materials investigated at comparable processing parameters. Since neither zirconia nor PLLA have a band gap that matches the wavelength of the laser radiation used, electron excitation by multiphoton absorption is assumed, as also formerly observed for other ceramics and polymers[14,40]. This absorption mechanism was suggested to be able to induce avalanche ionisation, which is strongly increasing the absorptivity of the substrate in case of sufficiently high irradiation intensities[41]. This might be the reason for the high ablation depths observed for USP-DLIP on PLLA. As thermal interaction for both materials only occurs in case of irradiation intensities surpassing the critical threshold of multiphoton absorption, the sharp borderline between ablated and unimpaired substrate also speaks in favour of the postulated mechanism[29]. The laser fluence at FWHM surpassing the critical ablation threshold for multi photon absorption (leading to an ablation area of 50% of the periodicity p) accounts to 2.4 J/cm² for 3Y-TZP zirconia and 0.58 J/cm² for PLLA. Roitero *et al.*[39] measured a similar ablation threshold F_{abl} for 3Y-TZP in case of short pulse durations of 10 ns, although melt formation clearly dominated the thermal interaction of the material. The comparable ablation thresholds despite the different pulse durations can be traced back to the lower laser wavelength of 355 nm used by Roitero *et al.*, which appear to be energetically closer to the existing band gap of the material.

USP-DLIP on metallic materials.

Examination of the surface topographies on both copper and CuZn37 induced by single pulse USP-DLIP at a fluence of 1.1 J/cm², which is close to the single pulse ablation threshold of copper[42], reveals a morphology formed by superficial melting, as shown in Fig. 3a,b. In the proximity of surface scratches, single craters indicate localised vaporisation events. The craters appear more often and exhibit greater diameters on CuZn37. After dual pulse processing, the ablation rate and surface morphology on both materials is changed significantly. The roughened surface of a strongly agitated liquid phase, illustrated in Fig. 3d,e, is characterised by large craters, which appear to be initiated by explosive removal of molten matter. The affected area on both materials exhibits a significantly increased width in comparison to single pulse patterns, while patterns on copper show slimmer ablation areas in comparison to CuZn37 patterns. Both the extended width of the ablation area as well as the more frequent occurrence of localised vaporisation on CuZn37 might be linked to a reduction of the ablation threshold F_{abl} by alloying.

In comparison to single pulse processing, the ablation of material is significantly enhanced in dual pulsing. In fact, it was shown that consecutive pulsing alters the absorptivity of metals by oxidation as well as surface

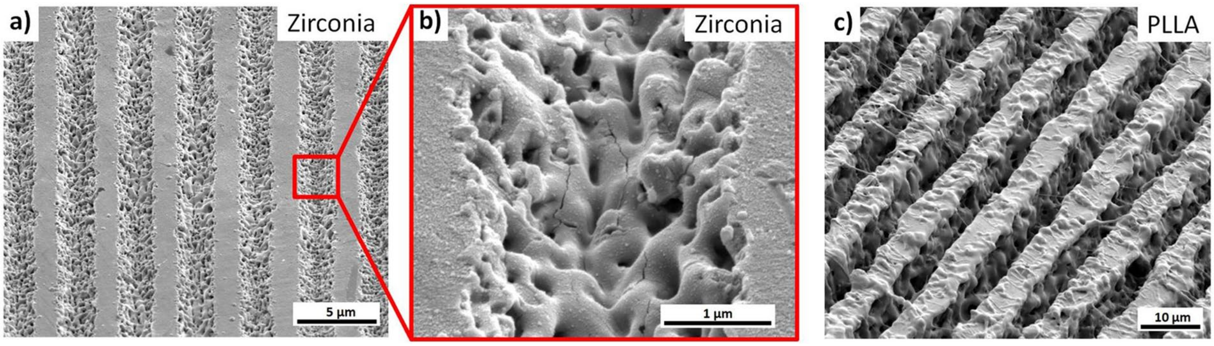

Figure 2. SEM-images of line patterns created by USP-DLIP on (**a**) 3Y-TZP zirconia at periodicity *p* of 3 µm and a fluence of 2.4 J/cm² as well as (**c**) PLLA at periodicity *p* of 10 µm and a fluence of 0.58 J/cm². (**b**) close-up of the ablation area on 3Y-TZP zirconia exhibiting porosity and cracks in the center, where the highest laser intensity was affecting the substrate surface.

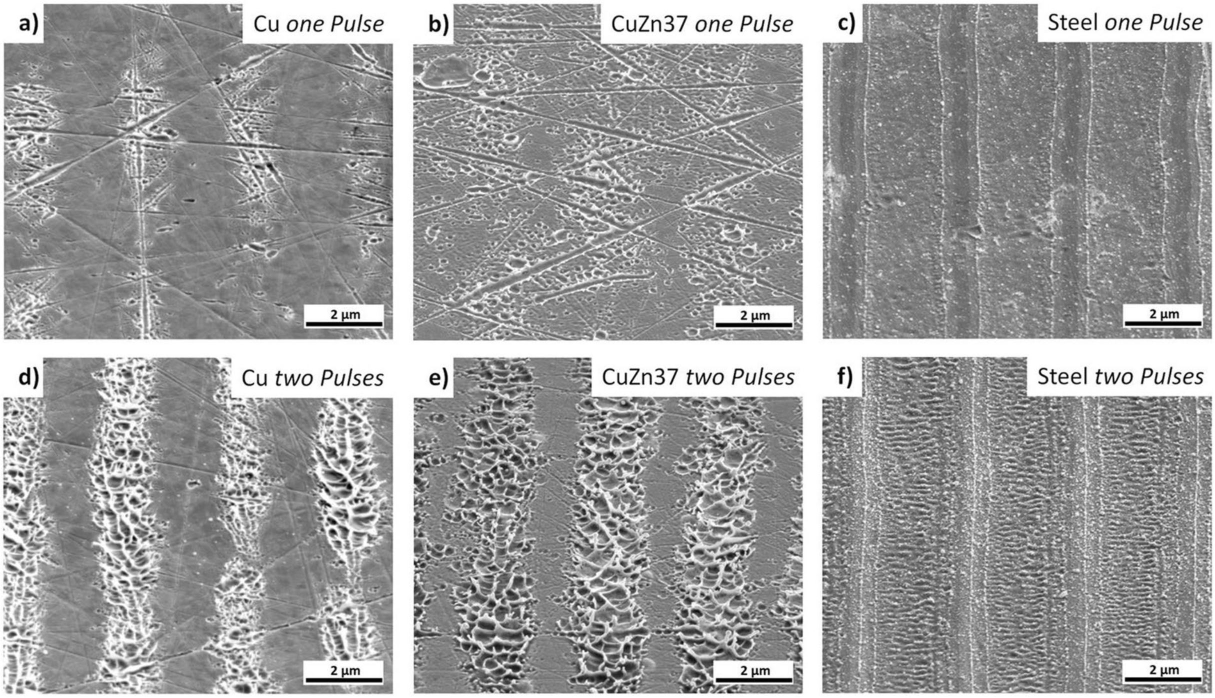

Figure 3. SEM-images of line patterns of 3 µm periodicity applied by USP-DLIP showing the different physical interaction of the three metallic substrates induced by USP-DLIP using a fluence of 1.1 J/cm², which corresponds to the single shot ablation threshold of copper for the utilised laser parameters[42]. (**a**) copper, (**b**) CuZn37, and (**c**) stainless steel after single pulse, (**d**) copper, (**e**) CuZn37, and (**f**) stainless steel after two pulses.

roughening, leading to multiple reflections and absorption of the irradiating laser beam[20,42]. Surface roughness in the nanometre-scale has been proven to effectively enhance the absorptivity up to two-fold[37], which might also be the reason for enhanced thermal interaction at scratches on copper and CuZn37 surfaces, leading to the evaporation induced craters visible in Fig. 3a,b.

The topographies created on stainless steel by USP-DLIP strongly differ in morphology compared to the copper-based metallic substrates, as shown in Fig. 3c,f. The thermally affected area is marked by a clear melt-front. The smooth surfaces resulting from single pulse irradiation are replaced by a slight ripple formation after dual pulse irradiation. Although the pattern morphology does not indicate evaporation, ablation can be detected even for the lowest tested fluence of 0.5 J/cm², which is in good correlation to the USP induced ablation behaviour of iron measured by Artyukov *et al.*[43]. The ablation area width (i.e., line width) slightly increases after the second pulse. In the center of the ablation areas, ripple formation oriented perpendicular to the pattern orientation is visible. As the orientation of these ripples is parallel to the beam polarisation, they should not be related to LIPSS formation as it would be expected from other investigations[16,19]. The enhanced ablation of steel for the second pulse might be linked to higher absorption by laser induced oxidation and minor surface roughening due to the

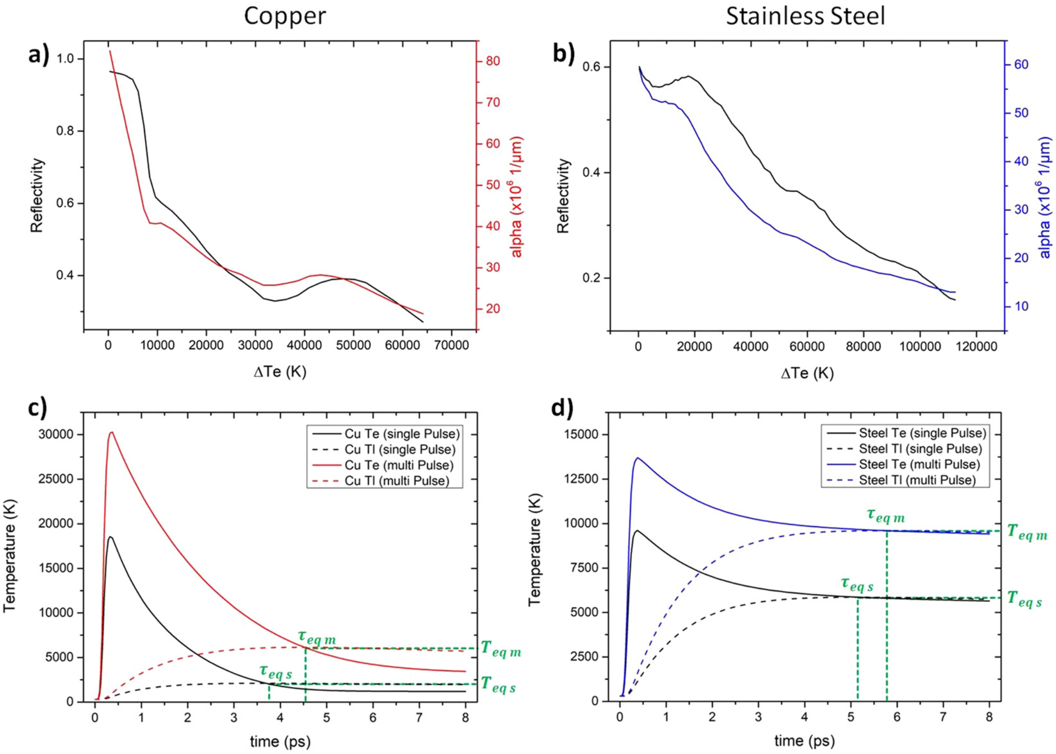

Figure 4. Alteration of the optical parameters of (**a**) copper and (**b**) stainless steel (literature data from iron) by enhanced electron temperatures during the laser pulse. Electron and lattice heating calculated for both (**c**) copper and (**d**) stainless steel at the surface area exposed to the maximum intensity of the DLIP pattern induced by a fluence of 1.1 J/cm² at single and multiple pulse irradiation. The thermal relaxation time τ_{eq} as well as the corresponding equilibrium temperature T_{eq} is marked for both single (*s*) and multi pulse (*m*) irradiation.

agglomeration of redeposited particles marked by a brighter SE contrast in Fig. 3c. Comparing the ablation area width between the illustrated DLIP patterns of the three metallic substrates in Fig. 3 additionally marks out the different ablation thresholds for single and multi-pulse irradiation.

Thermal interaction of metallic substrates on USP-DLIP. In order to study the thermal interaction of the different metallic substrates in response to USP-DLIP in detail, the substrate heating after irradiation by fluences of 0.5 to 4.6 J/cm² was simulated in 2D utilizing the aforementioned TTM. Alteration of surface absorptivity was involved in the calculation in two different ways: Modification of laser absorption due to excited electron states during laser irradiation was accounted for by modifying the optical parameters in relation to electron heating ΔT_e, as mentioned in the Methods section. The approximated relation of reflectivity R and absorption coefficient α to ΔT_e are both shown in Fig. 4a,b. Experimental data achieved for fluence and equilibrium temperature dependent alteration of both parameters show good correlation to referenced experiments[34,36]. The enhanced absorptivity due to laser induced chemical and topographical surface modification was addressed by enhancing the value of the absorption factor Δ_{abs} in Eq. (9). According to the findings of Vorobyev *et al.*[37], the chosen value of Δ_{abs} for the calculation of the thermal substrate interaction on consecutive pulses was 2, while it was kept 1 for single pulse irradiation. The change in thermal response of both copper and stainless steel by altered surface absorptivity is illustrated for an irradiation fluence of 1.1 J/cm² in Fig. 4c,d. Both graphs exhibit a significant rise in the resulting heating of both materials due to enhanced laser absorption, which especially is true for copper.

To estimate the lattice heating induced by USP-DLIP responsible for phase changes and material ablation, the 2D depth profile of the lattice temperature at thermal relaxation τ_{eq} is calculated, marking the highest lattice temperature. As electron-phonon-coupling transitions are assumed to have the main effect on lattice heating in the ultrashort time regime, the influence of heat diffusion in the lattice system after τ_{eq} was neglected[30]. Phase fronts were estimated by following the isothermal frontiers of the threshold temperatures for solid/liquid and liquid/vapour phase transitions. In the context of ultrafast phase transitions within hundreds of femtoseconds, Rethfeld *et al.*[29,44] discussed the stimulation of homogeneous melting of metals and semiconducting materials due to strong electronic in-equilibria in the substrate surface induced by ultrashort laser pulses. In case of copper, the critical lattice temperature leading to homogeneous melting within a pulse duration of 100 fs is assumed as $T_{hm\,100\,fs} = 1.45 \times T_m$, with T_m as the melting temperature of copper[44]. Reduced metallic behaviour of the irradiated material was shown to decrease the threshold and hence the period between irradiation and formation of superheated liquid[44,45]. This effect appears to be triggered by a change in atomic bond forces after intense superficial electron emission[29,45]. According to this theory, threshold temperatures for ultrafast homogeneous melt formation during ultrashort pulsed irradiation of less conductive metals and alloys like CuZn37 and steel can be estimated to

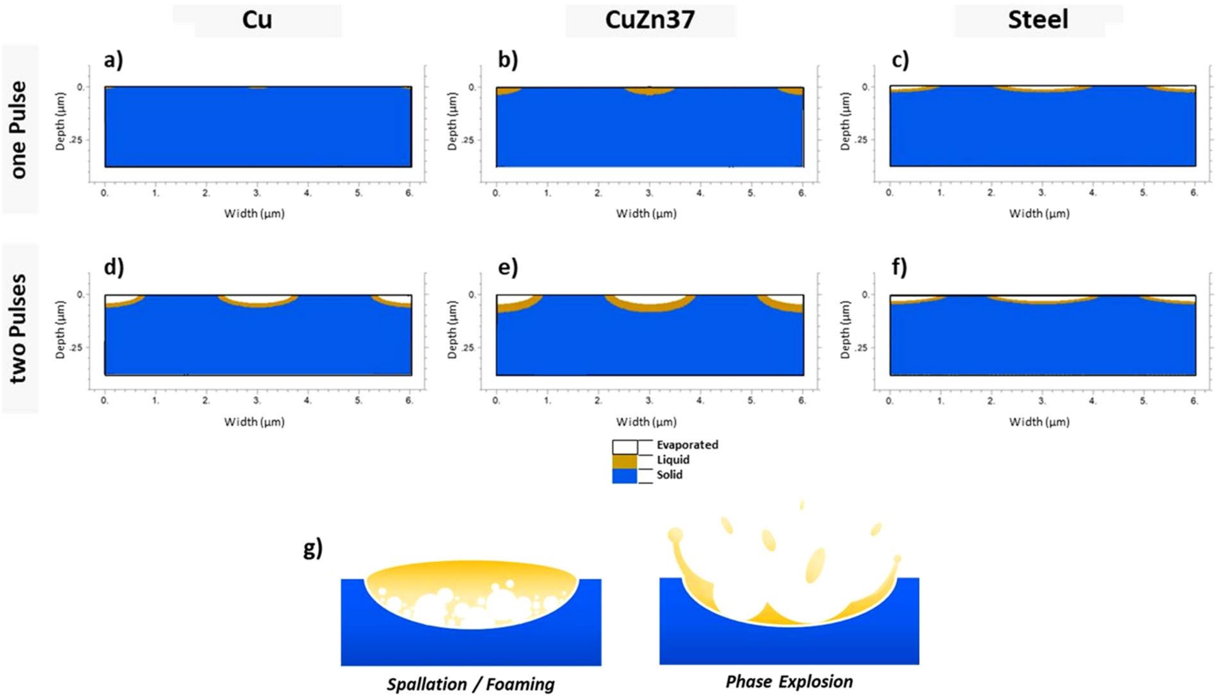

Figure 5. Numerical simulation plots of the phase changes in each of the three metallic substrates induced by lattice heating after single and dual pulse USP-DLIP at a fluence of 1.1 J/cm² and 3 µm periodicity. The utilised parameters correspond to the experimental setup used to fabricate the patterns illustrated in Fig. 3. (**a**) copper, (**b**) CuZn37, and (**c**) stainless steel after a single pulse, (**d**) copper, (**e**) CuZn37, and (**f**) stainless steel after two pulses. (**g**) Illustration of the two mechanisms of USP induced thermal ablation on highly conductive metals[46], involving either expansion of subsurface vapour cavities (spallation) or explosive expansion of a superheated vapour-liquid mixture (phase explosion).

be in a considerable lower relation to T_m compared to copper[45]. Hence, the solid/liquid threshold temperature T_{sl} for copper was chosen at $T_{sl} = 1.45 \times T_m$, while in case of both alloys T_{sl} was approximated to be equal to T_m. The liquid/vapour threshold temperature T_{lv} for all materials was estimated as the boiling temperature T_b. The calculated distribution of the different material states at τ_{eq} after single pulse and dual pulse USP-DLIP irradiation at a fluence of 1.1 J/cm² is illustrated for the three different metallic substrates in Fig. 5a to f corresponding to the patterns displayed in Fig. 3. On both copper and CuZn37 the effect of enhanced surface absorptivity due to altered surface roughness and chemistry on thermal interaction clearly stands out due to the increase of both width and depth of the thermally affected area observed after two pulses. In both cases, the liquid/vapour threshold was not surpassed after single pulse irradiation emphasising the relation of crater formation by evaporation to locally enhanced surface roughness by scratches in Fig. 3a,b. The thermally affected area on stainless steel already exhibits a large width after single pulse irradiation accompanied by a comparably shallow depth, which both increase slightly after dual pulse irradiation. This behaviour might be traced back to both the comparably low surface reflectivity for the irradiating wavelength of 800 nm as well as the smaller change of both surface reflectivity and the absorption coefficient in the present range of electron heating. Thereby, enhanced absorptivity by laser induced surface modification has a less serious effect compared to copper.

The observed ablation of highly conductive metals like copper after ultrashort pulsed irradiation can be separated into two different mechanisms: At fluences slightly higher than the ablation threshold, ablation is linked to *spallation* (or *foaming*), which is denoting heterogeneous vapour nucleation in a subcritical liquid phase[43,46]. Spallation results in minor ablation, as measured after single pulse USP-DLIP. When the fluence significantly surpasses the ablation threshold, the material's ablation is associated with evaporative supercritical fluid expansion, also denoted as *phase explosion*[46]. This mechanism is induced by an adiabatic unloading of a supercritical liquid phase leading to a strong impulse, detaching the vapour/liquid mixture from the surface at high velocities. The explosive removal of hot matter initiates a strong convective cooling effect, which is limiting further heat diffusion and freezes the agitated melt-front, leading to the characteristic topographies of churned up melt[43]. This corresponds well to the morphology visible on the surfaces treated by dual pulse USP-DLIP illustrated in Fig. 3d,e. In case of phase explosion, ablation is significantly enhanced as the kinetic impulse also removes a considerable amount of molten material, while for spallation localized boiling with minor melt mobilisation can be observed, as schematically shown in Fig. 5g.

Wang *et al.*[36] linked the onset of phase explosion on copper to lattice heating surpassing a threshold temperature of $T_{PE} = 0.9 \times T_{cr}$ with a critical temperature T_{cr} of 7696 K. The relation of ablation depths measured by CLSM to the calculated melting and vaporisation depth for single pulses on copper at the different tested laser fluences, illustrated in Fig. 6a, shows a good correlation to the experimental results. Thereby, it can be noted that the measured ablation depth starts to match the calculated melting depth as soon as the maximum lattice temperature

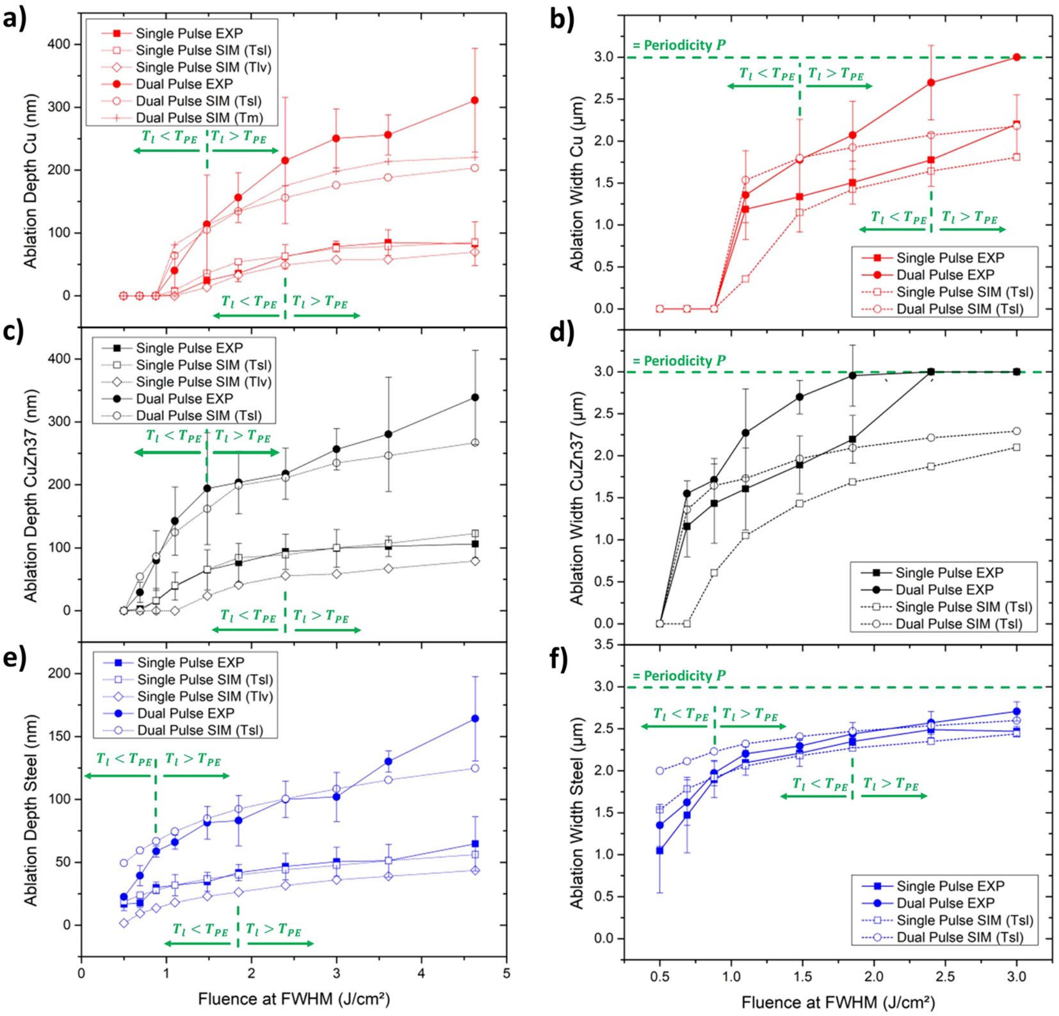

Figure 6. Comparison of the numerically calculated and measured (CLSM) ablation depth and width in relation to laser fluences in the range of 0.5 to 4.6 J/cm² after single and dual pulse USP-DLIP on the three metallic substrates: (**a**) ablation depth and (**b**) ablation area width on copper, (**c**) ablation depth and (**d**) ablation area width on CuZn37, (**e**) ablation depth and (**f**) ablation area width on stainless steel. The parameters, where the lattice temperature exceeds the phase explosion threshold temperature $T_l > T_{PE}$ in the numerical calculations are additionally marked in (**a**–**c**,**e**,**f**).

surpasses T_{PE}. This can be traced back to melt expulsion expected during phase explosion. In case of dual pulse irradiation, T_{PE} is reached at significantly lower laser fluences due to the enhanced laser absorption. Here, experimental values for ablation induced by phase explosion exceed the calculated depth of melt formation for an estimated homogeneous melting threshold of $T_{sl} = 1.45 \times T_m$ for $T_l > T_{PE}$. This also applies if the considered melting threshold is reduced to T_m of copper. This effect appears to be attributed to an accumulation of melt ejections at the edges of the ablation zone. In support of this theory, the experimentally measured ablation width tends to permanently exceed the calculated width of melt induction, as illustrated in Fig. 6b. It should be emphasised that the continuous increase in ablation width on copper leads to an overlap of the ablation areas after the second pulse for fluences higher than 2.4 J/cm². Hence, a complete covering of the substrate surface by expulsed melt can be assumed for multi-pulsed USP-DLIP substrate processing at a periodicity of 3 µm.

In case of CuZn37, the effect of a complete covering of the substrate surface by expulsed melt is already expected for a reduced threshold fluence of 1.88 J/cm² as a result of a lower ablation threshold as visible in Fig. 6d. Here, experimentally measured ablation depth shows a strong correlation to the calculated melting depth for single pulse irradiation without any indication of a change from ablation by spallation to phase explosion (see Fig. 6c), even though, ablation on CuZn37 appears to follow similar kinetics like on copper, judging from the resulting surface morphologies imaged by SEM. A possible reason for the contradictory results could be the stronger, scratch-induced crater formation after single pulses on CuZn37, which can lead to a higher average depth observed in the experiments. A topography-induced influence of the experimental values by scratches at low fluences can also be assumed by the strong correlation between measured single and dual pulse ablation width visible for both copper and CuZn37 in Fig. 6b,d, indicating similar effective ablation thresholds and leading to a strong deviation from the calculated ablation width at low fluences. In case of dual pulse irradiation, a transition from spallation to phase explosion might be assumed between 0.88 J/cm² and 1.1 J/cm² from the comparison of experimental and calculated values. However, this is questionable due to the ambiguous values of single pulse ablation. Neither single nor dual pulse ablation can be linked to the phase explosion threshold temperature T_{PE} of copper, indicating that other ablation mechanisms and/or threshold temperatures need to be considered for the USP thermal interaction for the alloy.

Tsibidis *et al.*[38] indicate a similar relation of phase explosion to the critical temperature for steel as Wang *et al.*[36] using the critical temperature of iron ($T_{cr} = 8500\,K$) for their calculations. However, USP-DLIP patterns produced on stainless steel do not exhibit traces of spallation or phase explosion in our observations, which might be linked to the influence of superficial electron emission on atomic bond strength as discussed by Rethfeld *et al.*[29]. Accordingly, the resulting surface charging in the case of low-conductive steel might favour the formation of low-temperature plasma formation on the substrate surface during thermal interaction after USP irradiation. In this case, removal of superheated material can take place before spallation or phase explosion is induced. Thereby, thermal energy losses by plasma emission could cause a strong freezing effect on the electron subsystem, keeping the overall heating permanently below the threshold of spallation or phase explosion[46]. A similar behaviour was already reported for iron[43]. Consequently, patterns induced by single pulse USP-DLIP on stainless steel surfaces show a similar relation to the calculated melting depth as CuZn37, where changes between ablation mechanisms are not visible, as illustrated in Fig. 6e. Even though, phase explosion is not visible on steel, the melt seems to be displaced out of the ablation area during ablation, which is also indicated by the clear melt throw-ups marking the boundaries of the individual ablation areas in Fig. 3c,f. After dual pulse processing, on the other hand, measured ablation remains below the calculated melting depth until the theoretical phase explosion threshold estimated by Tsibidis *et al.*[38] is surpassed. A similar approximation of the measured and calculated values can be observed for the ablation width of stainless steel in the low fluence regime, illustrated in Fig. 6f. However, the observed ablation behaviour is not equally connected to T_{PE} of iron for both single and dual pulse irradiation. Additionally, surface morphologies in both cases do not indicate phase explosion ablation, by which an actual involvement of this parameter in thermal interaction of steel on USP irradiation is questionable. Comparing the measured ablation depths after single pulse irradiation of copper and stainless steel to the experimental results of Wang *et al.*[36] and Artyukov *et al.*[43] exhibit a good correlation of our own findings to literature data for the investigated range of fluence.

Aside of the different mechanisms involved in ablation and surface morphology formation, all three metallic substrates exhibit a significant increase of the experimentally measured ablation depth in relation to the calculated melting depth at higher fluences, especially for dual pulse processing. This behaviour appears to be related to an increasing overlap of the ablation areas, leading to an accumulation of ejected melt between the ablation areas. For greater pulse numbers, this effect on pattern depth mostly vanishes in case of copper. Here, the ablated volume can be mainly related to evaporation by comparing measured and calculated ablation depth, illustrated in Fig. 7a. On CuZn37, ablation also appears to be related to evaporation for fluences below 2,4 J/cm², but yet exhibits an increasing effect of melt expulsion from 3 to 4.6 J/cm², similar to the additionally enhanced ablation depths measured after dual pulse irradiation, as can be seen in Fig. 7b. Although the surface of steel does not show any characteristics of phase explosion even after five pulses, ablation can again be linked closely to the threshold temperature T_{PE} of iron[38]. This is demonstrated by an increasing involvement of melt expulsion in ablation as soon as the lattice temperature surpasses this threshold, as illustrated in Fig. 7c. At a fluence of 1.48 J/cm², the measured ablation even surpasses the corresponding calculated melt depth, until the measured vales are almost twice as high as the calculated values at 4.6 J/cm². Here, USP-DLIP processing of stainless steel might be benefiting from the smaller expansion of the ablation area during consecutive pulsing in contrast to the enhanced expansion by melt expulsion during phase explosion on copper and CuZn37 (compare Fig. 6b,d,f).

Effect of thermal interaction on surface morphology. The ablation mechanisms observed in the USP-DLIP processing of the different metallic substrates are likely to not only influence ablation, but also the surface morphology of the patterns. This involves the formation of sub-patterns like in particular LIPSS on stainless steel. In case of copper, the two observable ablation mechanisms spallation and phase explosion differ mainly in the amount of melt agitation during the ablation process. The comparison of patterns produced on copper by a fluence of 1.48 J/cm², where the threshold temperature T_{PE} for phase explosion at consecutive pulsing is barely reached in the simulations, and 3 J/cm², where T_{PE} is considerably surpassed, is illustrated in Fig. 7d. The aspect ratio of the patterns was adjusted to be equal by enhancing the pulse overlap for the lower fluence from 90% to 95%, leading to an increase in pulse number from 10 to 20 pulses. The difference in ablation width between the two laser parameters is clearly visible, leading to almost flat pattern peaks at lower fluence, while the peak sharpness at higher fluence is enhanced by the agglomeration of expulsed melt. Aside of the main pattern geometry, the morphology the sub-patterns also differ corresponding to the different ablation mechanisms. In case of 1.48 J/cm², spallation ablation leads to smaller scale feature sizes of the sub-pattern, which is dispersed equally on the whole surface. On patterns processed at a fluence of 3 J/cm², the sub-pattern is formed by re-solidified melt, which was agitated during phase explosion inducing both a bigger feature size of the sub-pattern as well as a difference in surface morphology between the pattern peaks and valleys.

On steel surfaces processed by USP laser irradiation, LIPSS formation dominates the sub-pattern morphology at a fluence of 1.48 J/cm², which is mainly related to an agglomeration of a higher number of pulses at low laser fluence[19,38]. Consequently, LIPSS formation is significantly reduced on stainless steel substrates by applying a lower pulse overlap combined with enhanced laser fluence, as visible in Fig. 7e. The parameters utilised for USP-DLIP processing of the displayed patterns on steel were the same as the ones used on copper. In case of steel, the difference in fluence is only recognizable by the different slopes at the flanks of the peaks, as the main pattern geometries resemble each other closely. Both patterns exhibit a high peak sharpness attributable to melt agglomeration between the ablation areas similar to the pattern formed on copper at higher laser fluence. This might be linked to the fact that

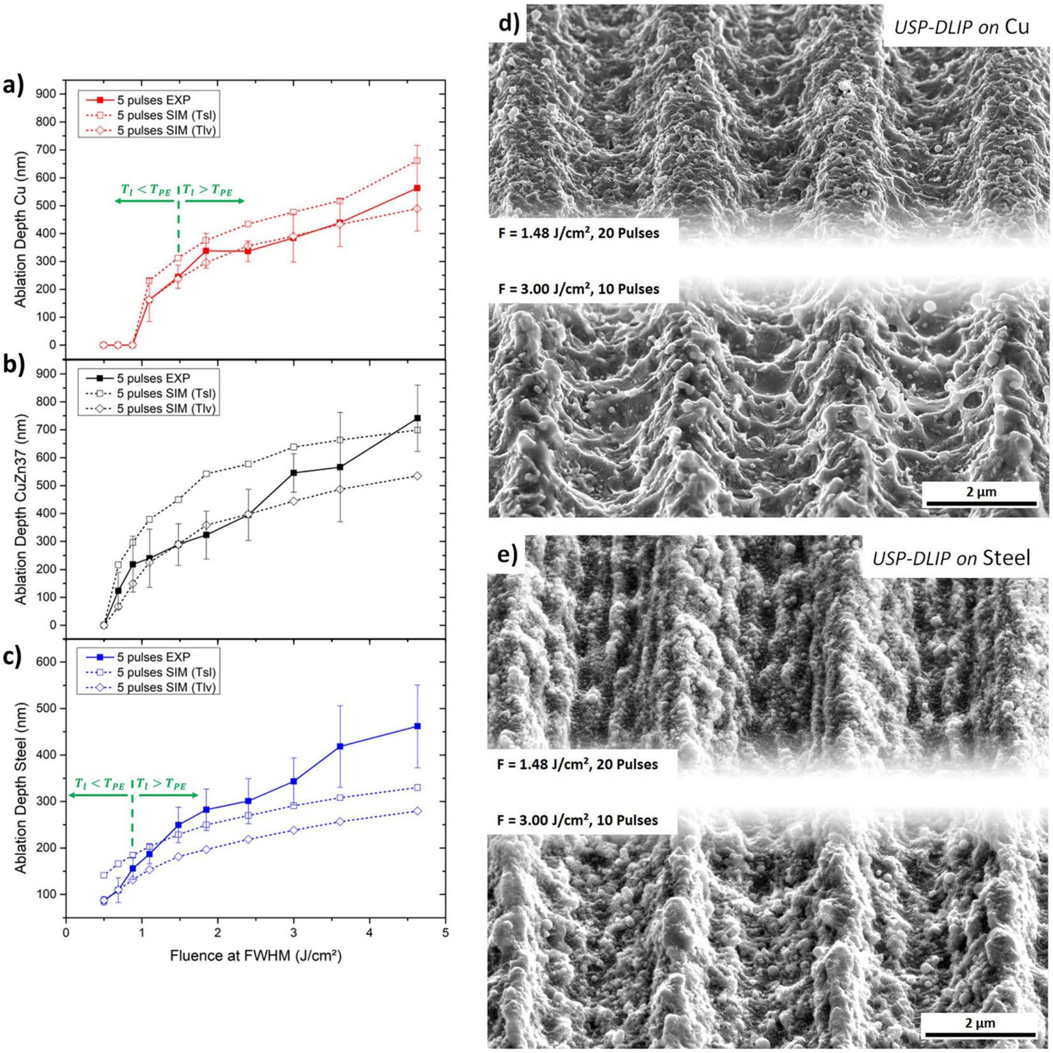

Figure 7. Ablation depth measured by CLSM on USP-DLIP patterns compared to simulated results of melting and vaporisation depth after irradiation by five consecutive pulses at fluences ranging from 0.5 to 4.6 J/cm² on the three metallic substrates (**a**) copper, (**b**) CuZn37 and (**c**) AISI 304 stainless steel. (**d**) Modification of the surface parameters on copper by adaption of the processing parameters in favour of faster processing speed leading to sharper pattern tips and a melt dominated sub-pattern. (**e**) Inhibiting LIPSS-formation on stainless steel by adaption of the processing parameters in favour of both higher laser intensity and lower pulse agglomeration.

in both cases, the threshold temperature T_{PE} was surpassed. As for the patterns produced on copper, similar aspect ratios were achieved by adjusting the pulse overlap accordingly to the alteration of the laser fluence.

In case of lower pattern periodicities, both enhanced absorptivity by laser induced surface modification as well as melt expulsion during ablation might play a crucial role in DLIP processing. Bieda *et al.*[13] for example showed a critical enhanced absorptivity in DLIP processing of copper using near-USP durations, where sub-µm patterns could be applied by single pulses, but vanished after dual pulse irradiation. A similar behaviour was observed in our experiments, after irradiation of copper at a fluence of 7.6 J/cm², where the sub-µm pattern exhibits a significant overlap of the ablation areas already after single pulse irradiation. By reducing the fluence to 3.7 J/cm², a less critical surpassing of T_{PE} was achieved in dual pulse irradiation, whereby the pattern could be maintained for two consecutive pulses, as illustrated in Fig. 8a. Similar results for two pulses were achieved for CuZn37 at a fluence of 2.07 J/cm² and steel at a fluence of 6.1 J/cm², where the difference between the applicable fluences once again highlights the effect of the individual ablation behaviour on USP-DLIP processing of the different metals. The patterns on both alloys corresponding to the mentioned processing parameters are displayed in Fig. 8b,c.

Conclusions

USP-DLIP processing at near-infrared wavelength of the three different material groups ceramics, polymers and metals was achieved using similar laser fluences. The processability of materials showing low absorptivity at this wavelength can be attributed to the altered laser-material interaction during USP irradiation. The influence of the ultrashort pulse duration on the thermal interaction was discussed. Special attention was paid to processability as

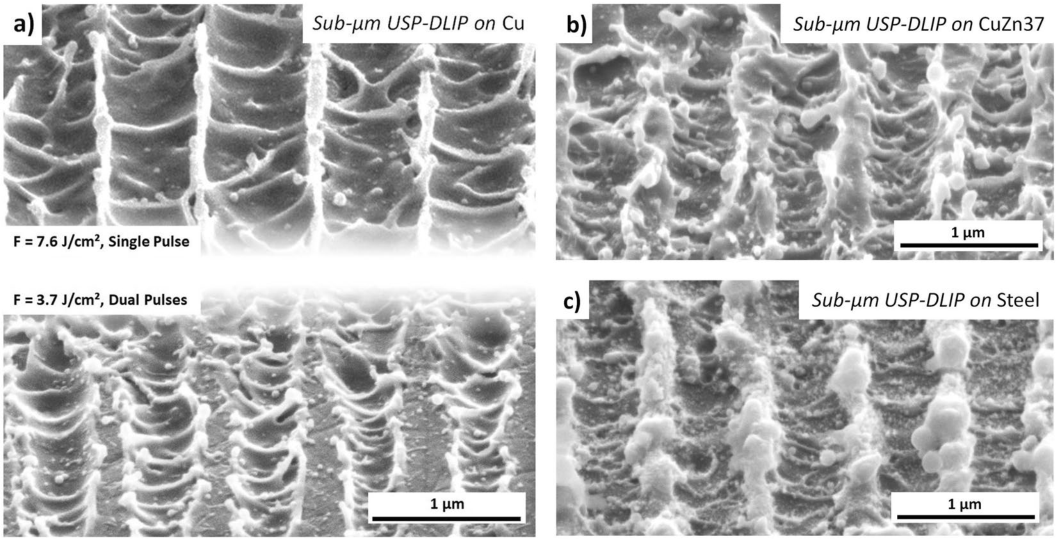

Figure 8. Display of sub-µm patterns on each of the investigated metallic substrates exhibiting a periodicity of 0.7 µm. (**a**) Comparison between sub-µm patterns on copper processed at a fluence of either 7.6 J/cm² or 3.6 J/cm², where pattern preservation was improved at lower fluence. (**b**) sub-µm pattern on CuZn37 processed at a fluence of 2.07 J/cm² by two consecutive pulses. (**c**) sub-µm pattern on AISI 304 stainless steel processed at a fluence of 6.1 J/cm² by two consecutive pulses.

well as to surface morphology for the individual material groups, pointing out the unique specifications, which need to be considered in USP-DLIP.

On insulating materials, ablation is strongly related to the critical threshold fluence inducing multiphoton absorption. Measurable ablation only happens when the laser fluence surpasses this threshold leading to sharply defined pattern features. Thereby, sub-pattern formation within the clear-cut ablation areas represents substrate specific thermal responses involving both melting and evaporation that lead to unique pattern morphologies. Alteration of the processing parameters appears to only influence the amount of ablation without impacting the morphology of the ablation area.

In case of metals, an alteration of the occurring ablation mechanism related to material specific threshold fluences has to be taken into account. At elevated fluences, which induce lattice heating considerably surpassing the material-specific phase explosion threshold temperature T_{PE}, a strong influence of melt agitation on pattern formation has to be considered. Numerically, this also seems to apply to the pattern formation on steel surfaces, although no change in the ablation mechanism has been observed based on surface morphology. At low fluences, pattern geometries on copper are more defined (e.g. exhibiting higher edge sharpness) similar to USP-DLIP patterns on insulating materials, while at fluences inducing lattice heating above T_{PE} melt expulsion appears to dominate pattern formation. On AISI 304 stainless steel, lower fluences mainly result in enhanced LIPSS formation, which can consequently be reduced by increasing the laser fluence. Pattern geometry formation on steel is dominated by melt agitation for all parameters investigated, where it must be noted that the phase explosion threshold temperature T_{PE} of iron was surpassed in each case.

It was shown that laser induced surface roughening and oxidation plays a significant role in USP-DLIP of materials exhibiting low absorptivity for the utilised near-infrared wavelength, as it greatly increases the laser absorption. Thereby, significant enhancement of ablation, as well as a change in ablation mechanism has to be considered on highly conductive metals for consecutive pulsing. This has to be taken into account especially in the creation of sub-µm patterns, where the enhanced laser absorption might lead to a vanishing of the pattern by a single subsequent pulse.

In summary, we were able to show that both pattern geometry as well as hierarchical sub-pattern formation during USP-DLIP processing of different materials can be controlled by taking their individual thermal interaction into account. By this, surface functionalisation for manifold applications including e.g. wettability or bacterial adhesion can be tailored more precisely, thus enhancing the effect of the surface treatment.

Data availability

The experimental data generated in this work can be made available on request.

Received: 28 June 2019; Accepted: 13 February 2020;
Published online: 27 February 2020

References

1. Kamperman, B. M., Kroner, E., Mcmeeking, M. & Arzt, E. Functional Adhesive Surfaces with Gecko Effect: The Concept of Contact Splitting. *Adv. Eng. Mater.* **12**, 335–348 (2010).
2. Ródenas, A. *et al.* Three-dimensional femtosecond laser nanolithography of crystals. *Nat. Photonics* **13**, 105–109 (2019).
3. Rosenkranz, A., Hans, M., Gachot, C., Thome, A. & Bonk, S. Direct Laser Interference Patterning: Tailoring of Contact Area for Frictional and Antibacterial Properties. *Lubricants* **4** (2016).

4. Soldera, B. M., Taretto, K. & Berger, J. Potential of Photocurrent Improvement in m c-Si: H Solar Cells with TCO Substrates Structured by Direct Laser Interference Patterning. *Adv. Eng. Mater.* **18**, 1674–82 (2016).
5. Schieber, R. *et al*. Direct Laser Interference Patterning of CoCr Alloy Surfaces to Control Endothelial Cell and Platelet Response for Cardiovascular Applications. *Adv. Healthc. Mater.* **6**, 1–14 (2017).
6. Zwahr, C., Günther, D., Brinkmann, T., Gulow, N. & Oswald, S. Laser Surface Pattering of Titanium for Improving the Biological Performance of Dental Implants. *Adv. Healthc. Mater.* **6**, 1–9 (2017).
7. Helbig, R. *et al*. The impact of structure dimensions on initial bacterial adhesion. *Biomater. Sci.* **4**, 1074–1078 (2016).
8. Zea, L. *et al*. Design of a space flight biofilm experiment. *Acta Astronaut.* **148**, 294–300 (2018).
9. Lüdecke, C. *et al*. Nanorough titanium surfaces reduce adhesion of Escherichia coli and Staphylococcus aureus via nano adhesion points. *Colloids Surfaces B Biointerfaces* **145**, 617–625 (2016).
10. Lutey, A. H. A. *et al*. Towards laser-textured antibacterial surfaces. *Sci. Rep.* **8**, 1–10 (2018).
11. Lang, V., Roch, T. & Lasagni, A. F. World record in high speed laser surface microstructuring of polymer and steel using direct laser interference patterning. *Laser-based Micro- Nanoprocessing X* **9736**, 1–8 (2016).
12. Paivasaari, K., Kaakkunen, J. J. J., Kuittinen, M. & Jaaskelainen, T. Enhanced optical absorptance of metals using interferometric femtosecond ablation. *Opt. Express* **15**, 13838–13843 (2007).
13. Bieda, M., Siebold, M. & Fabián, A. Applied Surface Science Fabrication of sub-micron surface structures on copper, stainless steel and titanium using picosecond laser interference patterning. *Appl. Surf. Sci.* **387**, 175–182 (2016).
14. Kondo, T., Matsuo, S., Juodkazis, S., Mizeikis, V. & Misawa, H. Multiphoton fabrication of periodic structures by multibeam interference of femtosecond pulses. *Appl. Phys. Lett.* **82**, 2758–2760 (2003).
15. Indrisiunas, S., Voisiat, B. & Raciukaitis, G. Direct Laser Beam Interference Patterning Technique for Fast High Aspect Ratio Surface Structuring. *Proc. SPIE* **9350** (2015).
16. Alamri, S. *et al*. On the Interplay of DLIP and LIPSS Upon Ultra-Short Laser Pulse Irradiation. *Materials (Basel).* **12**, 1–9 (2019).
17. Romano, J., Garcia-giron, A., Penchev, P. & Dimov, S. Triangular laser-induced submicron textures for functionalising stainless steel surfaces. *Appl. Surf. Sci.* **440**, 162–169 (2018).
18. Gnilitskyi, I. *et al*. High-speed manufacturing of highly regular femtosecond laser-induced periodic surface structures: Physical origin of regularity. *Sci. Rep.* **7**, 1–11 (2017).
19. Razi, S. *et al*. Birth of periodic Micro/Nano structures on 316L stainless steel surface following femtosecond laser irradiation; single and multi scanning study. *Opt. Laser Technol.* **104**, 8–16 (2018).
20. Ionin, A. A. *et al*. Electron emission and ultrafast low-fluence plasma formation during single-shot femtosecond laser surface ablation of various materials. *JETP Lett.* **101**, 308–312 (2015).
21. Aguilar-morales, A. I., Alamri, S., Kunze, T. & Fabián, A. Influence of processing parameters on surface texture homogeneity using Direct Laser Interference Patterning. *Opt. Laser Technol.* **107**, 216–227 (2018).
22. Chichkov, B. N., Momma, C., Nolte, S., von Alvensleben, F. & Tünnermann, A. Femtosecond, picosecond and nanosecond laser ablation of solids. *Appl. Phys. A* **63**, 109–115 (1996).
23. Anisimov, S. I., Kapeliovich, B. L. & Perel´man, T. L. Electron emission from metal surfaces exposed to ultrashort laser pulses. *Sov. Phys.-JETP* **39**, 374–400 (1974).
24. Cheng, J. *et al*. Optics & Laser Technology A review of ultrafast laser materials micromachining. *Opt. Laser Technol.* **46**, 88–102 (2013).
25. Anisimov, S. I. & Luk, B. S. Selected problems of laser ablation theory. **45** (2002).
26. Kanavin, A. *et al*. Heat transport in metals irradiated by ultrashort laser pulses. *Phys. Rev. B - Condens. Matter Mater. Phys.* **57**, 14698–14703 (1998).
27. Schaefer, C., Urbassek, H. M. & Zhigilei, L. V. Metal ablation by picosecond laser pulses: A hybrid simulation. *Phys. Rev. B* **66**, 54041–8 (2002).
28. Chen, A. M. *et al*. Modeling of femtosecond laser damage threshold on the two-layer metal films. *Appl. Surf. Sci.* **257**, 1678–1683 (2010).
29. Rethfeld, B., Ivanov, D. S., Garcia, M. E. & Anisimov, S. I. Modelling ultrafast laser ablation. *J. Phys. D. Appl. Phys.* **50**, 01–39 (2017).
30. Zhang, Y. & Chen, J. K. Ultrafast melting and resolidification of gold particle irradiated by pico- to femtosecond lasers. *J. Appl. Phys.* **104**, 1–9 (2008).
31. Hopkins, P. E. & Norris, P. M. Substrate influence in electron – phonon coupling measurements in thin Au films. **253**, 6289–6294 (2007).
32. Daniel, C., Lasagni, A. & Mucklich, F. Stress and texture evolution of Ni y Al multi-film by laser interference irradiation. *Surf. Coatings Technol.* **181**, 478–482 (2004).
33. Berger, L. I. *et al*. *CRC Handbook of Chemistry and Physics*. *CRC press* (2014).
34. Ren, Y., Chen, J. K. & Zhang, Y. Optical properties and thermal response of copper films induced by ultrashort-pulsed lasers. *J. Appl. Phys.* **110**, 1–7 (2011).
35. Cheng, C. W., Wang, S. Y., Chang, K. P. & Chen, J. K. Femtosecond laser ablation of copper at high laser fluence: Modeling and experimental comparison. *Appl. Surf. Sci.* **361**, 41–48 (2016).
36. Wang, S. Y., Ren, Y., Cheng, C. W., Chen, J. K. & Tzou, D. Y. Micromachining of copper by femtosecond laser pulses. *Appl. Surf. Sci.* **265**, 302–308 (2013).
37. Vorobyev, A. Y. & Guo, C. Enhanced absorptance of gold following multipulse femtosecond laser ablation. *Phys. Rev. B* **72**, 1–5 (2005).
38. Tsibidis, G. D. Modelling periodic structure formation on 100Cr6 steel after irradiation with femtosecond-pulsed laser beams. *Appl. Phys. A* **0**, 0 (2018).
39. Roitero, E., Lasserre, F., Anglada, M. & Mücklich, F. A parametric study of laser interference surface patterning of dental zirconia: Effects of laser parameters on topography and surface quality. *Dent. Mater.* **33**, 28–38 (2017).
40. Hirayama, Y., Yabe, H. & Obara, M. Selective ablation of AlN ceramic using femtosecond, nanosecond, and microsecond pulsed laser. *J. Appl. Phys.* **89**, 2943–9 (2001).
41. Rethfeld, B. Unified Model for the Free-Electron Avalanche in Laser-Irradiated Dielectrics. *Phys. Rev. Lett.* **92**, 1–4 (2004).
42. Kirkwood, S. E., Van Popta, A. C., Tsui, Y. Y. & Fedosejevs, R. Single and multiple shot near-infrared femtosecond laser pulse ablation thresholds of copper. *Appl. Phys. A Mater. Sci. Process.* **81**, 729–735 (2005).
43. Artyukov, I. A. *et al*. Relaxation Phenomena in Electronic and Lattice Subsystems on Iron Surface during Its Ablation by Ultrashort Laser Pulses. *JETP Lett.* **99**, 54–58 (2014).
44. Rethfeld, B., Sokolowski-Tinten, K., von der Linde, D. & Anisimov, S. I. Ultrafast thermal melting of laser-excited solids by homogeneous nucleation. *Phys. Rev. B* **65**, 1–4 (2002).
45. Recoules, V., Clérouin, J., Zérah, G., Angalde, P. M. & Mazevet, S. Effect of Intense Laser Irradiation on the Lattice Stability of Semiconductors and Metals. *Phys. Rev. Lett.* **96**, 1–4 (2006).
46. Ionin, A. A., Kudryashov, S. I. & Samokhin, A. A. Material surface ablation produced by ultrashort laser pulses. *Uspekhi Fiz. Nauk* **187**, 159–172 (2017).
47. Yang, L., Wang, C. & Yang, W. Numerical Simulation and Analysis on 3D Temperature Field of the Metal Ablated with Femtosecond Pulse Laser. **276**, 1–5 (2011).

48. Majchrzak, E., Poteralska, J., Science, C., Majchrzak, E. & Poteralska, J. Two-temperature microscale heat transfer model. part ii: determination of lattice parameters. **9**, 109–119 (2010).
49. Wang, Z. G., Dufour, C., Paumier, E. & Toulemonde, M. Se-sensitivity of Metals under Swift Heavy Ion Irradiation. *J. Phys. Condens. Matter* (1994).
50. Callister, W. D. & Rethwisch, D. G. *Materials Science and Engineering - an Introduction*. (Wiley, 2009).

Acknowledgements

The authors want to acknowledge the kind advice of Dr. C. Pauly during SEM analysis, as well as Dr. L. Reinert for proofreading the manuscript. The present work is supported by funding from the European Regional Development Fund (EFRE, Interreg Großregion, Project: "Pulsatec"). We acknowledge support by the Deutsche Forschungsgemeinschaft (DFG, German Research Foundation) and Saarland University within the funding programme Open Access Publishing.

Author contributions

F. Muecklich conceived the idea, while D.W. Müller, T. Fox and P.G. Grützmacher designed the laser setup. The experiments as well as the design and utilisation of the thermal simulation were conducted by D.W. Müller including analysation and interpretation. Design of the thermal simulation was developed by D.W. Müller and S. Suarez. The manuscript was written by D.W. Müller and edited by P.G. Grützmacher and S. Suarez.

Competing interests

The authors declare no competing interests.

Additional information

Correspondence and requests for materials should be addressed to D.W.M.

Reprints and permissions information is available at www.nature.com/reprints.

Paper II:

In-Depth Investigation of Copper Surface Chemistry Modification by Ultrashort Pulsed Direct Laser Interference Patterning

Daniel W. Müller[1], Anne Holtsch[2], Sarah Lößlein[1], Christoph Pauly[1], Christian Spengler[2], Samuel Grandthyll[2], Karin Jacobs[2], Frank Mücklich[1], Frank Müller[2,*]

[1]Chair of Functional Materials, Department of Materials Science, Saarland University, 66123, Saarbrücken, Germany.

[2]Experimental Physics, Functional Materials and Engineering Physics, Saarland University, 66123 Saarbrücken, Germany.

Published in November 2020 in "Langmuir" and accessible online via:

https://doi.org/10.1021/acs.langmuir.0c01625

Abstract:

Surface patterning in the micro- and nanometer-range by means of pulsed laser interference has repeatedly proven to be a versatile tool for surface functionalization. With these techniques, however, the surface is often changed not only in morphology but also in surface chemistry. In this study, we present an in-depth investigation of the chemical surface modification occurring during surface patterning of copper by ultrashort pulsed direct laser interference patterning (USP-DLIP). A multi-method approach of parallel analysis using visualizing, topography-sensitive and spectroscopic techniques allowed a detailed quantification of surface morphology as well as composition and distribution of surface chemistry related to both processing and atmospheric aging. The investigations revealed a heterogeneous surface composition divided into peak and valley regions predominantly consisting of Cu2O, as well as superficial agglomerations of CuO and carbon groups. The evaluation was supported by a novel modelling approach for the quantification of XPS results in relation to heterogeneous surface composition, which was developed by means of a combination of different spectroscopic techniques. The overall results indicate a very good suitability of USP-DLIP for surface functionalization of antimicrobial and (super-) hydrophobic copper surfaces.

Own contributions:

Conception and design of the study. Design of the interference based USP laser setup. Sample preparation and processing via USP-DLIP. Analysation via SEM combined with FIB and EDS. Data interpretation, preparation and editing of the manuscript.

LANGMUIR

pubs.acs.org/Langmuir Article

In-Depth Investigation of Copper Surface Chemistry Modification by Ultrashort Pulsed Direct Laser Interference Patterning

Daniel W. Müller,* Anne Holtsch, Sarah Lößlein, Christoph Pauly, Christian Spengler, Samuel Grandthyll, Karin Jacobs, Frank Mücklich, and Frank Müller*

Cite This: *Langmuir* 2020, 36, 13415−13425

Read Online

ACCESS | Metrics & More | Article Recommendations | Supporting Information

ABSTRACT: Surface patterning in the micro- and nanometer-range by means of pulsed laser interference has repeatedly proven to be a versatile tool for surface functionalization. With these techniques, however, the surface is often changed not only in terms of morphology but also in terms of surface chemistry. In this study, we present an in-depth investigation of the chemical surface modification occurring during surface patterning of copper by ultrashort pulsed direct laser interference patterning (USP-DLIP). A multimethod approach of parallel analysis using visualizing, topography-sensitive, and spectroscopic techniques allowed a detailed quantification of surface morphology as well as composition and distribution of surface chemistry related to both processing and atmospheric aging. The investigations revealed a heterogeneous surface composition separated in peak and valley regions predominantly consisting of Cu_2O, as well as superficial agglomerations of CuO and carbon species. The evaluation was supported by a modeling approach for the quantification of XPS results in relation to heterogeneous surface composition, which was observed by means of a combination of different spectroscopic techniques. The overall results provide a detailed understanding of the chemical and topographical surface modification during USP-DLIP, which allows a more targeted use of this technology for surface functionalization.

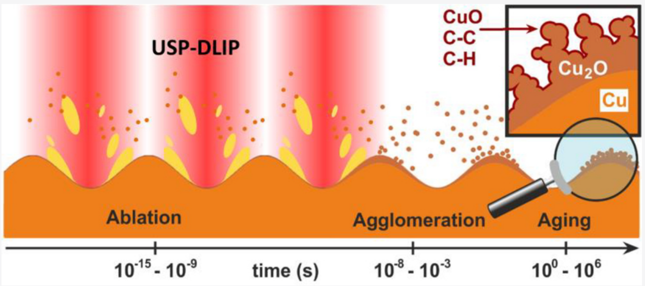

■ INTRODUCTION

Surface functionalization by topographic structuring in the micro- and nanometer range has established itself as a successful technique to tailor surface properties for various applications. It has been shown recently that surface patterning can significantly improve the performance of spot-welding electrodes,[1] conductive heat exchangers,[2] or light absorption,[3] which can be used, for example, to enhance the efficiency of solar cells.[4] Further promising applications are possible by varying the wetting properties since both fluid guiding on hydrophilic and the synthesis of (super)hydrophobic surfaces can be achieved by laser surface structuring.[3,5−9] In addition, cell or bacterial adhesion on technical surfaces has been influenced by adapting the periodicity of the surface pattern to the size of the colonizing organism in order to tune the effective contact area: DLIP-induced periodicities on the same scale as the diameter of cells or bacteria improved the adhesion rate.[10−12] Smaller periodicities decreased the adhesion rate in the case of bacteria,[13] while they provide beneficial anchorage points during proliferation of cells.[14]

To better understand the actual mechanisms for optimal surface functionalization by laser-based techniques, the impact of both, the topographic surface modification as well as the alteration of surface chemistry during processing, must be considered. Especially the latter was shown to be tightly linked to the actual thermal behavior of the irradiated substrate in response to a particular setup of the laser parameters: previous studies on nanosecond pulsed laser processing of copper surfaces showed process-induced oxidation forming a predominant superficial layer of CuO on an interface layer of Cu_2O.[15,16] Although this setup provides copper surfaces with the natural composition of a passivating oxide layer as formed in ambient atmosphere,[17] the distribution of CuO and Cu_2O presented in ref 15 corresponds more to a thermally induced oxide as produced by Hans et al.[18] At this rate of thermal oxide growth, self-assembling superficial oxide structures cover the actual substrate topographies formed by melt kinetics leading to an additional modification of the surface morphology.

In the case of ultrashort laser pulses in the femtosecond regime, as used in the present study, similar mechanisms of self-assembling structures in the nano- and micrometer range have been used in surface functionalization.[6,19] However, investigations of surface chemistry alterations by ultrashort

Received: June 2, 2020
Revised: October 19, 2020
Published: November 3, 2020

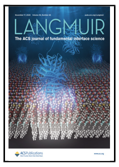

https://dx.doi.org/10.1021/acs.langmuir.0c01625
Langmuir 2020, 36, 13415−13425

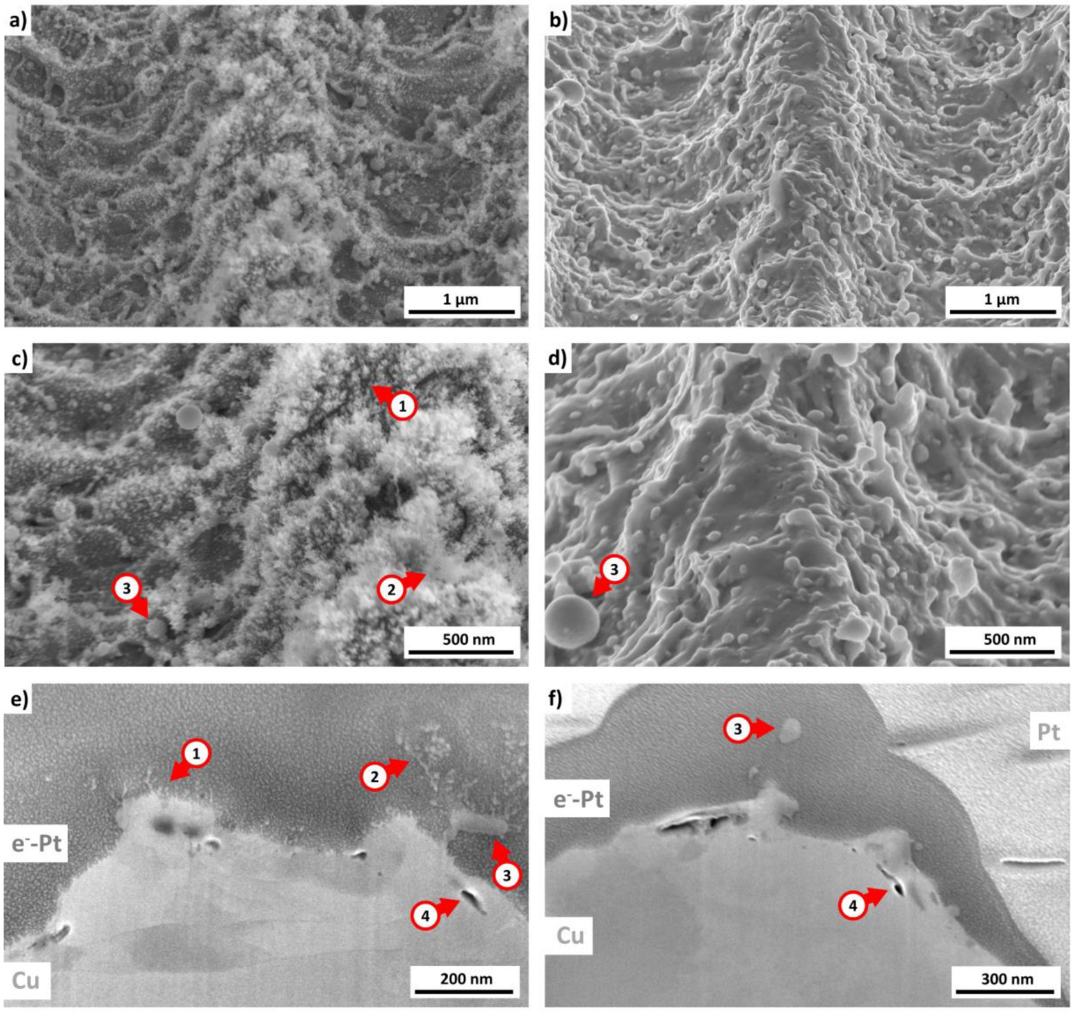

Figure 1. Illustration of the patterned copper surface. (a) As-processed surface with a close-up in panel (c) exhibiting flakelike substructures attached to the substrate surface (1) and forming agglomerations extending several nanometers from the surface (2) as well as redeposited substrate particles (3). (b) Post-treated surface after etching with citric acid with a close-up in panel (d) showing no traces of (1) and (2) but still remaining redeposited droplets (3). A more detailed view on the actual substrate topography reveals sections of melt overlays, which might induce cavities beneath. (e) FIB cross section of as-processed surface showing a pattern peak, where each type of the three previously mentioned surface characteristics is visible. Previously masked cavities (4) are also visible. (f) FIB cross section of post-treated surface, where both remnant droplets (3) as well as cavities (4) are still remaining. All figures were imaged under 52° observation angle.

laser pulses was yet mainly focusing on functional aspects such as altered wettability. Transitions from hydrophilic to hydrophobic wetting due to surface aging in a period of up to several weeks, as it is observed after both short and ultrashort pulsed laser processing, are commonly attributed to a time-dependent alteration in surface chemistry due to carbon group agglomerations.[6,9,19,20] In this context, Long et al.[21] were able to modify the aging related composition of carbon groups by exposing ultrashort pulsed laser processed copper surfaces to atmospheres rich in either organic groups, CO_2 or O_2, which exerted a significant impact on their functional properties.

Both carbon-group agglomeration as well as changes of oxide thickness and composition were shown to be two interdependent attributes in the process of chemical stabilization of copper surfaces during atmospheric aging,[17,22] which finally dictates functional surface properties.[23] Therefore, functionalization of copper surfaces by laser treatment needs to be performed by considering both process-induced as well as aging-induced alterations of surface chemistry. Also in terms of antibacterial activity, surface oxidation has been shown to significantly influence the cytotoxicity of the surfaces. The antibacterial efficiency is reduced in the presence of CuO, while it is lesser affected in case of a predominant content of Cu_2O in the superficial oxide layer.[18]

Against this background, a detailed knowledge of the chemical composition of the USP-DLIP treated surfaces, especially in terms of the distribution of copper and copper oxides, is mandatory to understand and specifically modify functional surface properties by laser treatment.

This work presents an in-depth investigation of the process-related chemical composition of patterned copper surfaces, as fabricated by USP-DLIP. Using complementary experimental techniques such as scanning electron microscopy (SEM) combined with focused ion beam (FIB) cross-sectioning and energy dispersive X-ray spectroscopy (EDS), scanning tunneling microscopy (STM) and spectroscopy (STS), as well as X-ray photoelectron spectroscopy (XPS), a profound understanding of the surface composition is achieved. This provides detailed insight into the resulting chemical surface modifications from material redistributions that occur during

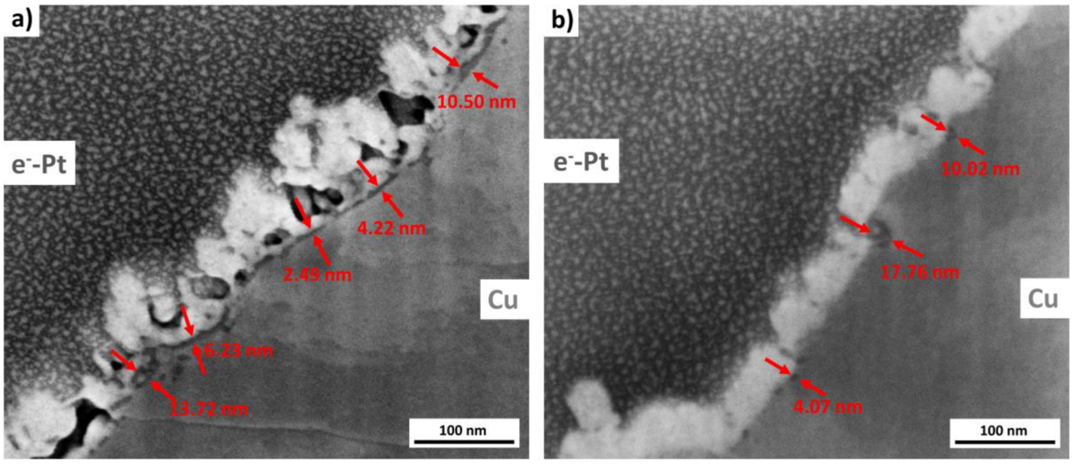

Figure 2. FIB cross sections (observation angle 52°) of the patterned copper surface after Au PVD. (a) As-processed surface with a thin surface layer in between the Au layer and the copper substrate. The overall thickness ranges from 2 to 7 nm, with some localized spots of enhanced thickness. (b) Etched surface with no continuous surface layer of oxide. Localized spots between Au layer and substrate might be attributed to remnants of localized spots of enhanced thickness on the former as-processed surface.

laser patterning. The findings allow one to effectively tailor surface functionalization, e.g., for both wetting and anti-bacterial applications on copper surfaces by USP-DLIP.

EXPERIMENTAL SECTION

Sample Preparation. Platelets of oxygen-free copper (> 99.95%) (Wieland) were laser processed by USP-DLIP applying linear sinusoidal patterns with periodicities of $p = 3$ μm. Before laser treatment, the copper samples (10 mm × 25 mm) were mirror-polished using an automated *TegraPol-21* system (Struers), resulting in a smooth surface exhibiting an RMS roughness smaller than 10 nm. A Ti:sapphire Spitfire laser system (Spectra Physics) with ultrashort laser pulses (pulse duration of $t_p = 100$ fs, full width at half maximum, fwhm) was used for USP-DLIP. The centered wavelength λ was 800 nm. Planar patterning was performed by scanning the substrate surface in continuous pulsing mode (pulse frequency 1 kHz, fluence 3 J/cm^2, pulse overlap 90%). In the optical setup, the seed beam is split by a diffractive optical element (DOE) and focused on the sample's surface by a lens system, causing an overlap of the two beams. This setup provides a sinusoidal intensity distribution causing line-like surface patterns. Details of the USP-DLIP methodology, as well as the thermal interactions involved in pattern formation are described in a previous work.[24]

After USP-DLIP processing, a batch of samples was additionally treated by immersion etching in 3% citric acid in an ultrasonic bath (40 s) to remove process-induced oxide on the patterned surfaces.

Characterization. Characterization of the surface morphology and modifications of the microstructure were performed by means of SEM (FEI Helios Nanolab 600 FIB/SEM). For SEM imaging, secondary electron (SE) contrast was used at an acceleration voltage of either 10 or 5 kV and a current of 86 pA. High-resolution imaging was conducted in immersion mode using the system's in-lens detector. Sample surface morphology was investigated at a tilt of 52° degree for improved visualization of topographical features. For depth-resolved analysis of the microstructure, FIB cross sectioning was carried out at an acceleration voltage of 30 kV after applying an electron-beam-deposited protective Pt layer to preserve the substrate surface from ion-induced degradation. To achieve a better contrast between the carbon-containing Pt-layer and the superficial oxide layers, samples were sputter-coated from a $\mathrm{Au_{80}Pd_{20}}$ target prior to FIB work.

For chemical characterization focusing on individual surface features, energy-dispersive X-ray spectroscopy (EDS) was applied. As the interacting volume in this technique generally exceeds both the thickness of superficial oxide layers and the pattern periodicity on the copper surfaces, a low beam voltage of 5 kV was used for localized probing to allow for a higher signal content of the superficial chemistry as well as a higher spatial resolution in the analysis. Monte Carlo simulations were used to estimate the relationship between signal depth and the actual oxide layer thickness, providing a high accuracy in the representation of the surface oxide distribution by the EDS measurements (see Figure S1).

STM[25,26] and STS[27,28] were performed with a VT STM from Scienta Omicron at room temperature and a pressure less than 3×10^{-9} mbar. Etched, sharp tungsten tips were used for all measurements. The STM tip is on ground potential, and any given voltages refer to the potential of the sample.

XPS was performed (on samples as provided) with an ESCA Mk II spectrometer by Vacuum Generators (base pressure $\sim 3 \times 10^{-10}$ mbar). The spectra were recorded with nonmonochromatic Al Kα radiation (photon energy 1486.6 eV) and a 150° analyzer at a pass energy of 20 eV (energy resolution ∼ 1.4 eV). For calculating the relative amount of Cu, O, and C in terms of atom %, a Shirley background[29] was applied to the Cu-2p$_{3/2}$, the O-1s, and the C-1s peaks and the peak intensities were scaled with the photoemission cross sections by Yeh and Lindau.[30] For depth profiling via Ar$^+$ ion etching a Specs IQE ion source was operated at 3 kV with an ion current of approximately 5 μA at the sample. The calibration of the etching rate was similar to the procedure described in literature[31] (with white light interferometry replaced by atomic force microscopy and with the shadow mask replaced by a razor blade).

RESULTS AND DISCUSSION

Scanning Electron Microscopy. To examine the surface morphology and to reveal possible indications of inhomogeneous surface chemistry of the copper samples after USP-DLIP processing, SEM analysis was applied involving FIB cross sectioning as well as EDS analysis. As ascribed in a previous study, investigating the surface morphology formation of different metallic materials on USP-DLIP processing, copper exhibits a roughened surface alongside the actual pattern characterized by expulsive melt agitation after USP-DLIP.[24] However, the as-processed substrate surface is actually covered by a flakelike substructure, which is merged with redeposited particles partially masking the substrate surface, as shown in Figure 1a and Figure 1c. The bright appearance of these substructures in the secondary electron (SE) detection mode can be attributed to their small size and fine morphology, allowing for high SE emission. The FIB cross section in Figure 1e is revealing a fairly stable connection of these intricate

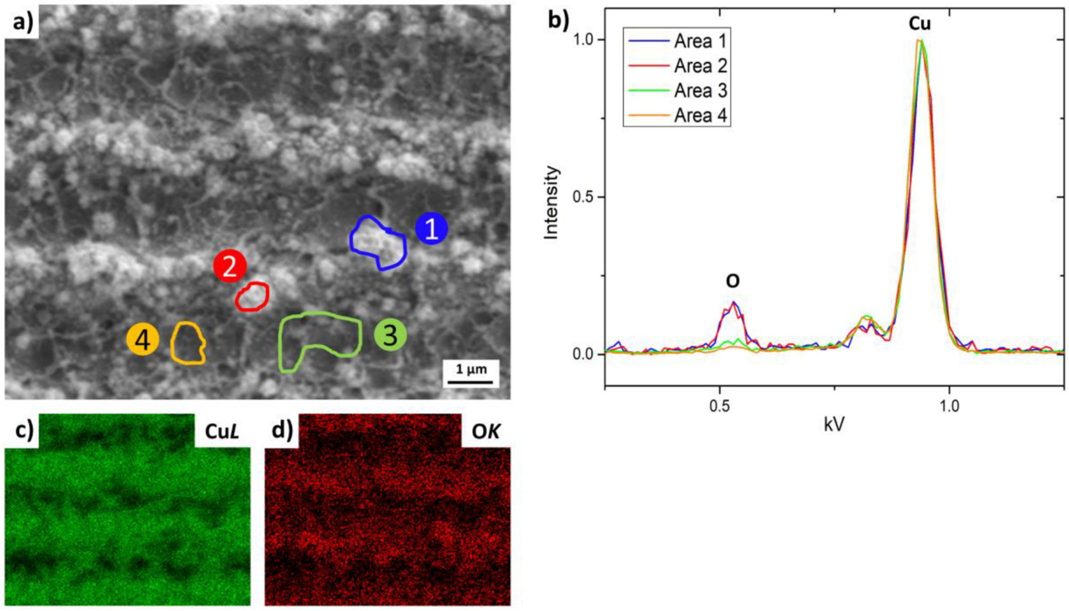

Figure 3. EDS analysis of the as-processed patterned copper surface. (a) SEM image of the analyzed area showing the areas of the localized EDS measurements. The color code links the marked areas to the corresponding spectra in panel (b), which was normalized to the Cu peak intensity. (c) EDS mapping showing the distribution of copper. (d) EDS mapping of the oxygen distribution. Bright areas in the SEM image correspond to higher oxygen content.

structures to the solid substrate surface from where they extend up to several tens of nanometers. Particles of redeposited material were found to be directly fused to the substrate surface via small, sinter-like contact areas. Some of the redeposited particles additionally exhibit porous surfaces, which might be linked to oxidation. FIB cross sectioning also exposes cavities close to the substrate surface. Position and shape of these cavities indicate that they are created by melt inclusions during the ablation process. After post treatment by etching with citric acid, the flakelike partitions are completely removed alongside with a part of the redeposited particles, as shown in Figure 1b,d.

Consequently, FIB cross sections after etching in Figure 1f display no traces of the flakelike substructure but remaining redeposited particles as well as cavities.

In an additional experiment, samples of both batches were sputter-coated with a $Au_{80}Pd_{20}$ capping layer to provide a better contrast between the substrate, superficial oxide layers, and the protective electron-beam deposited Pt layer in FIB cross sectioning. The $Au_{80}Pd_{20}$ layer of approximately 45 nm thickness exhibits a bright contrast in Figure 2 separating the Pt layer (upper left) and the copper substrate (lower right). Compared to the etched samples (Figure 2b), the $Au_{80}Pd_{20}$ layer of the samples in the as-processed state (Figure 2a) shows higher irregularity and higher porosity due to the incomplete deposition on the closely interconnected flakelike substructures. Between the capping layer and the substrate an intermediate layer represented by a darker contrast is visible in Figure 2a, which can be assigned to an oxide layer on top of the surface. The overall thickness of this layer varies between 2 and 7 nm, while localized spots of higher thickness are also detectable. In case of etched samples, a continuous intermediate layer is missing in Figure 2b.

However, localized spots between capping layer and substrate are visible, which might be attributed to either remnants of localized spots that showed enhanced thickness on the as-processed surface or sites of pitting corrosion during atmospheric aging.

To get a first insight on the surface chemistry of both as-processed and etched patterned copper surfaces, EDS analysis was performed both localized and area integrated by focusing on specific topographic features as well as measuring the spatially distributed signal intensity.

In the SEM image in Figure 3a, four areas of local probing on as-processed surfaces are highlighted, where the red and blue area refer to agglomerations of the flakelike substructure mainly found on the pattern peaks while the green and orange areas are taken in the valley. The superposition of the different spectra in Figure 3b shows a significant difference in oxygen content compared to the prominent amount of copper between peak and valley regions of the pattern (intensities have been normalized to the Cu-Peak for comparison). This trend is also visible in the oxygen map in Figure 3d, where a higher oxygen signal is not only attributed to surface peak areas but also especially to spots of stronger agglomeration of the flakelike substructure visible by the brighter SE contrast in Figure 1a. In contrast, no notable amounts of oxygen could be detected in EDS measurements on etched samples.

Although the first overview via FIB/SEM methodology already provides initial indications on the chemical composition of the sample surfaces resulting from USP-DLIP, the possible impact of topographical features on the detected intensity, such as signal amplification at the structural peaks or attenuation in the valleys, has to be considered as well. A good indication of the extent of this influence is provided by the copper mapping in Figure 3c showing gaps in the valley areas where a continuous Cu signal should be expected. The same features are also reflected in the oxygen mapping. These are most likely induced by shadowing, as the gaps are located in the vicinity of prominent topographic features in the exact opposite direction of the tilted EDS detector (positioned upper right image corner, elevation angle 35°, azimuthal angle 43°).

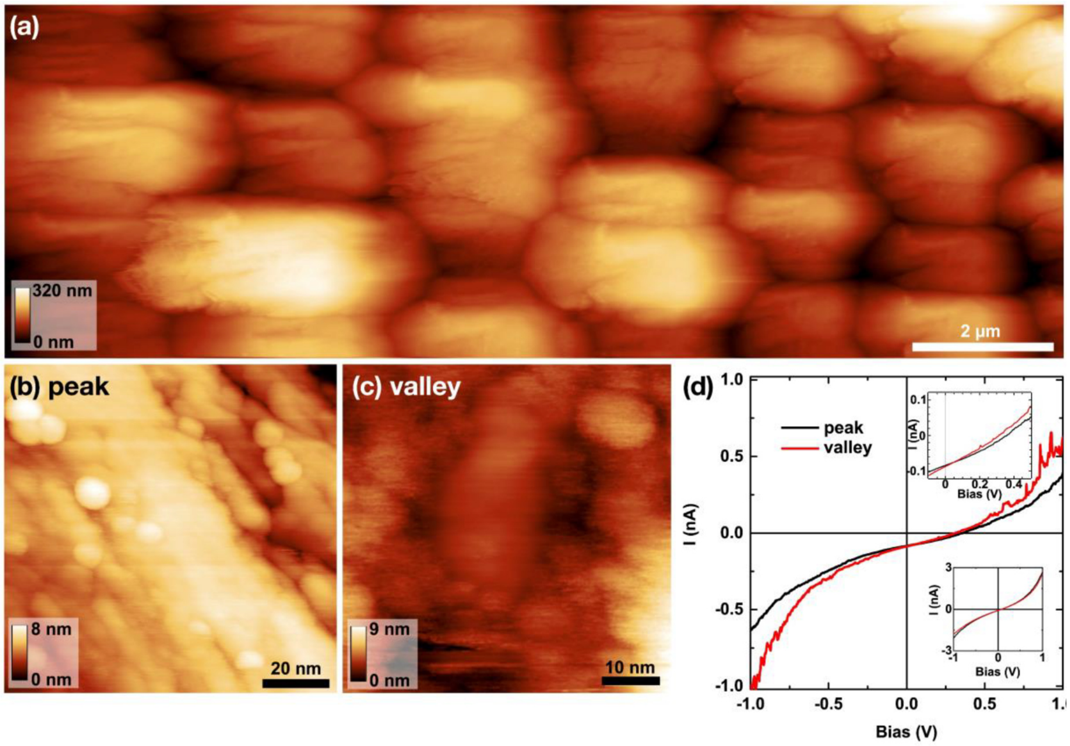

Figure 4. (a) Overview STM image of the structured Cu surface. Tunneling parameters: U = 0.1 V, I = 100 pA. (b) Detailed STM image of the peak areas [as brighter regions in (a)]. Tunneling parameters: U = 0.5 V and I = 100 pA. (c) Detailed STM image of the valleys [as darker regions in (a)]. Tunneling parameters: U = 0.5 V and I= 100 pA. (d) STS data (as averaged over several hundreds of measurements) on the peaks and the valleys. Top insets: detailed image of the region where I = 0 and U = 0. Bottom inset: STS data of peak and valley after sputtering. For clean Cu, the conductivity is increased by more than 1 order of magnitude.

Nevertheless, these results provide a first indication that oxygen and thus most likely copper oxide are not distributed uniformly throughout the surface in the case of as-processed samples, and that the overall oxygen content is significantly reduced on the etched samples.

Scanning Tunneling Microscopy/Spectroscopy. In light of the results from EDS mapping, combined STM/STS experiments were performed in order to obtain the spatial distribution of metallic Cu and Cu oxides.

The wide range STM scan (5 μm × 15 μm) on the as-processed Cu sample in Figure 4a displays the convolution of topography and local density of states after USP-DLIP. STM scans in the nanometer range show a variation of the surface structure between the peaks and the valleys of the topography. The peak region in Figure 4b exhibits a large number of spherical particles (similar to the SEM images in Figure 1), which can be assigned to redeposited droplets of material ejected during USP-DLIP processing. These particles are also found in the valleys in Figure 4c, yet to a much lower extent.

By comparing the $I(V)$ curves in Figure 4d from STS experiments (as averaged over several hundreds of measurements) on the peaks and in the valleys, a slightly reduced conductivity (slope of the $I(V)$ curve) can be observed in the peak region. This gives another evidence that, in accordance to the EDS results, the copper oxides are distributed rather in the peak regions than in the valley regions, either as CuO or Cu_2O.

The material dependency of $I(V)$ curves originates from the local density of states (LDOS)[32] that is proportional to the slope dI/dV. Cu_2O and CuO are both p-type semiconductors with the band gaps varying from approximately 1.2 eV[32] for CuO to approximately 2.2 eV[32] for Cu_2O. Due to the p-type character, the Fermi energy of both oxides is shifted toward the valence band, causing the asymmetry of the $I(V)$ curves in Figure 4d with increased spectral weight at negative voltages.

$I(V)$ curves are separated into two regimes: the ohmic regime[33,34] and the Fowler-Nordheim tunneling regime.[35] The latter is correlated to variations of the work function for various materials.

The ohmic regime ranges from −0.5 to +0.5 V. Here, the tunneling current depends linearly on the voltage via the conductivity.[36] Both $I(V)$ curves display only slight differences in this regime with a conductivity of approximately 0.28 nA/V and a resistance of approximately 3.7 GΩ, respectively.

In the Fowler-Nordheim regime, i.e., $|V| > 0.5$ V, the $I(V)$ curves change to an exponential behavior. For increased voltages, the height of the tunneling barrier correlates stronger with the work function. A larger work function results in a larger tunneling barrier and thus in a decrease of the conductivity. The work functions of CuO (5.5 eV)[37] and Cu_2O (5.0 eV)[38] are larger than the one of Cu (4.5 eV),[39] hence the lower conductivity in the peak region gives strong evidence that copper oxide is depleted in the valley region, both on as-processed and etched samples.

For metals, the linear behavior within the ohmic regime is usually accompanied by zero-crossing at zero voltage. The shifting of the zero-crossing toward positive voltage in Figure 4d represents a p-type doping which is characteristic for both copper oxides.[40] Since the shift is observed in both $I(V)$ curves, copper oxide is distributed in both regions, i.e., valleys and peaks. However, the upper inset in Figure 4d displays a shift of the zero-crossing toward zero voltage for the valley region, giving more evidence that the oxide is enriched in the peak regions.

Combining the variation in conductivity and the overall p-type doping, one can conclude that copper oxide is generally enriched at the peak regions. After removing the oxide by Ar^+-ion etching (i.e., after the XPS depth profiling experiments were performed, see next section), the lower inset in Figure 4d displays nearly symmetrical $I(V)$ curves. The p-type doping induced shift of the zero-crossing disappears, and for both locations, the $I(V)$ curves are identical within the experimental uncertainties. In addition, the slope of the $I(V)$ curve for the clean copper sample is larger by more than 1 order of magnitude compared to the slope of the $I(V)$ curve of the oxide covered sample, giving evidence that the conductivity of the latter is strongly affected by the Cu_2O layer.

X-ray Photoelectron Spectroscopy. Since the STS and the EDS data predict a nonuniform distribution of copper and copper oxides of yet unknown composition, XPS was performed to achieve more detailed information on the actual surface chemistry, especially the distribution of oxide(s). Surface chemistry analysis was performed within 24 h after sample processing and after 3 weeks of storage under ambient conditions to investigate the influence of aging on surface chemistry, which is commonly linked to altered wetting behavior.[6,19] In addition, the analysis of aged samples was combined with Ar^+ etching of the surface to get information on the depth distribution of Cu, CuO, and Cu_2O.

In XPS, Cu and CuO can be easily distinguished by the shape of the Cu-2p spectra since for CuO the 2p spectra display a characteristic satellite structure at higher-binding energies.[41−43] However, the distinction between Cu_2O and Cu is not straightforward since the Cu-2p spectra of both materials display only marginal differences.[41−43] However, for the Cu-LMM Auger spectra the situation is reversed: Cu and Cu_2O display distinct differences in energies and in spectral shape while the Cu-LMM spectra of Cu_2O and CuO display only slight differences.[41−43]

Figure 5 shows the Cu-2p and Cu-LMM spectra of the as-processed and the etched USP-DLIP sample after 3 weeks of aging for different ablation steps by Ar^+ ion etching. The series of Cu-2p spectra in Figure 5a,c give evidence that CuO is present only at the initial surface (cf. the satellite peaks between 940 and 945 eV and between 960 and 965 eV, as being characteristic for CuO). After ablation of about 9 Å, the CuO-like satellites completely disappear and the Cu-2p spectra of both samples display only the Cu- and/or Cu_2O-like intensity distribution. From the Cu-LMM spectra in Figure 5b,d, it is evident that even at the initial surface, i.e., when both oxides, CuO and Cu_2O, are present, the contribution of Cu_2O is much larger than that of CuO (cf. peak position at the Cu_2O specific energy for the spectra at 0 nm).

For the etched sample, the Cu-LMM spectra in Figure 5d are dominated by the Cu-like distribution for all ablation steps. For the as-processed sample, the Cu-LMM spectra in Figure 5b show a smooth change from the Cu_2O-like distribution to the Cu-like distribution via increasing ablation, meaning that the thickness of the oxide is noticeably larger.

The larger oxide thickness of the as-processed sample can be directly observed in the O-1s spectra in Figure 6a,c. For the as-processed sample, the O-1s intensity in Figure 6a decreases smoothly with increased ablation, while for the etched sample, the O-1s intensity in Figure 6c decreases rapidly. According to the C-1s spectra in Figure 6b,d, the as-prepared surfaces are mainly contaminated with hydrocarbons (peak at ∼ 284.5 eV) and with minor amounts of carbon−oxygen species (peak at ∼ 287 eV). For both samples, the latter contribution disappears as soon as Ar^+ ion etching is applied, meaning that all oxygen that is observed after first Ar^+ ion etching can be assigned to Cu_2O because CuO also disappears in Figure 5a,c after the first Ar^+ ion etching.

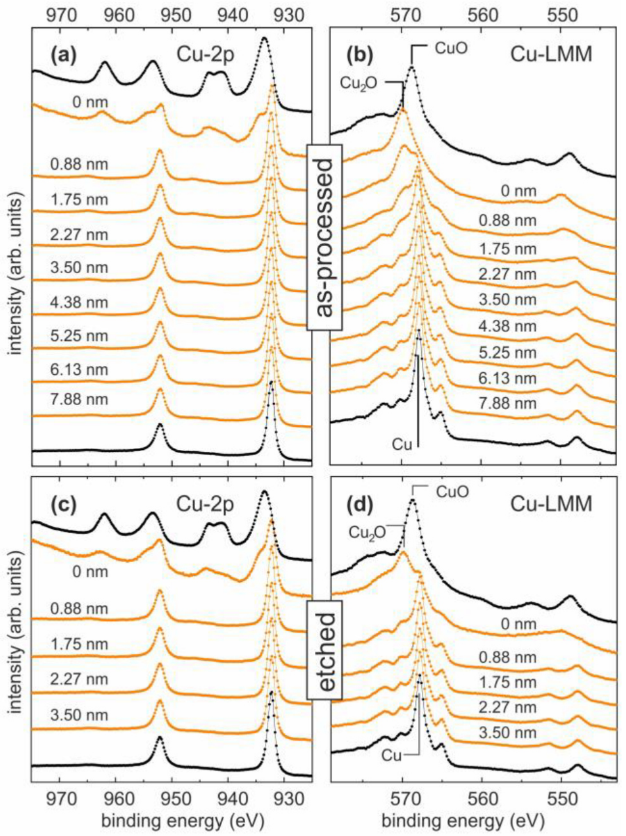

Figure 5. (a) Cu-2p spectra and (b) Cu-LMM spectra of the as-processed sample (after 3 weeks of aging) for different steps of ablation. (c) Cu-2p spectra and (d) Cu-LMM spectra of the etched sample (after 3 weeks of aging) for different steps of ablation. The spectra at the top and the bottom row refer to CuO and Cu reference samples, respectively.

In accordance with the data displayed in Figures 5 and 6, both samples are mainly formed by Cu and Cu_2O after aging, the materials with the largest antibacterial activity.[18] This is well corresponding to the p-doping measured in STS, which was previously observed in relation to the semiconducting properties of Cu_2O. Since CuO is present only at the initial surfaces, it can be regarded as a kind of surface contamination, similar to C.

Comparing the surface composition measured within 24 h and 3 weeks after processing, as shown in the XPS data in Figure 7, as-processed samples exhibit a similar ratio of CuO/Cu_2O in surface composition with a slightly increased CuO content after 3 weeks of aging (see Table S1). Metallic Cu is totally missing in both cases, indicating a dense oxide surface layer.

For etched samples, metallic Cu can still be measured to some extent, while the composition differs more significantly, as upon aging the (CuO + Cu_2O)/Cu ratio appears to shift in favor of the oxides, especially CuO (see Table S1). Platzman et al.[17] linked the formation of CuO in ambient atmosphere on

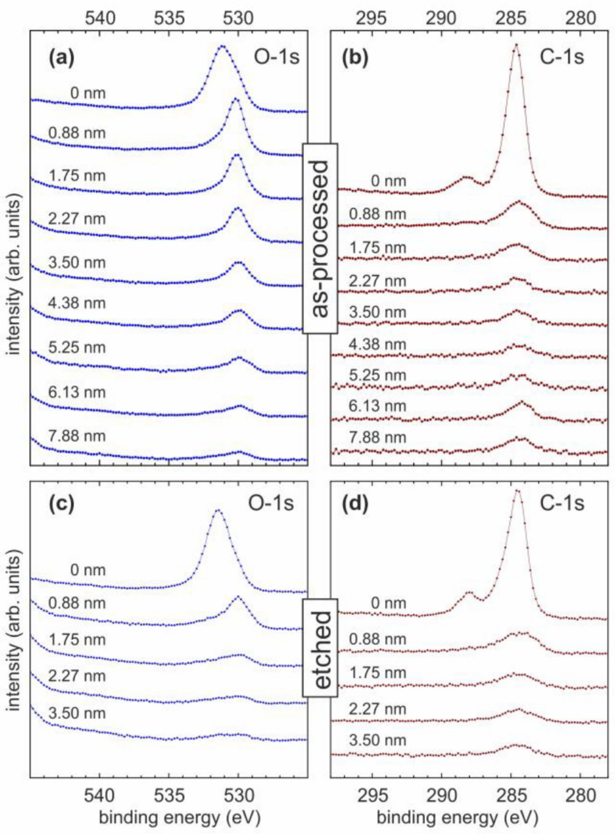

Figure 6. (a) O-1s spectra and (b) C-1s spectra of the as-processed sample (after 3 weeks of aging) for different steps of ablation. (c) O-1s spectra and (d) C-1s spectra of the etched sample (after 3 weeks of aging) for different steps of ablation.

polycrystalline copper surfaces to the interaction of hydrophilic Cu_2O with adherent moisture until passivation is achieved. Both, the formation of Cu_2O and superficial CuO is linked to the energetic state of the substrate and therefore highly influenced by grain boundaries, dislocations, etc.[22] According to the analysis of Cu-$2p_{3/2}$ and Cu-LMM Auger intensities (see Figure S2 and Table S2), the relative amount of CuO increases from 15.2% (= 4.3/28.2 in Table S2) after several hours to 31.5% (= 5.8/18.4 in Table S2) after 3 weeks of aging. This correlates to the results of Platzman et al.,[22] where ∼ 48% (i.e., ∼ 15.2/31.5) of the stable oxide is achieved shortly after exposure of the pristine copper surfaces to ambient atmosphere. In terms of antibacterial activity, etching the samples after USP-DLIP processing benefits in a reduction of the overall amount of CuO with less antibacterial activity.

For the as-processed USP-DLIP samples, the relative amount of CuO is 62% (= 18.2/29.5 in Table S2) and 66% (= 10.5/16.0 in Table S2) for the fresh and for the aged sample, respectively. For the etched samples, the relative amount of CuO is reduced to the smaller values listed above. Hence, etched surfaces appear to undergo oxide growth, while the process-induced oxide layer of as-processed samples remains stable during aging.

Compared to the "fresh" samples, the amount of hydrocarbons is increased compared to the amount of carbo-oxygen species on as-processed surfaces after 3 weeks of aging (see Table S2). This corresponds well with the atmospheric aging observed in relation to significantly reduced wettability, which is mainly linked to enhanced agglomerations of C−C/C−H type carbon groups while carbo-oxygen groups retain hydrophilic behavior.[21] On immersion-etched samples, the overall amount of carbon increases as well during aging. However, the ratio of hydrocarbons and carbo-oxygen species remains nearly constant, in contrast to the as-processed USP-DLIP surfaces.

According to the STS/STM data in Figure 4, both samples display a larger conductivity in the valley region. This may result from a spatial variation of the thickness of Cu_2O, which is also indicated by the reduced oxygen signal in the EDS measurements. Since a sharp Cu_2O/Cu interface is not very likely, it can be assumed that the amount of Cu_2O exponentially decreases into bulk while the amount of metallic Cu exponentially increases to saturation. In both cases, the spatial modulation of the decay $d(x)$ follows the cross section of the topography, i.e.

$$d(x) = \frac{\Delta}{2}\cdot\left\{1 + \cos\left(\frac{2\pi}{3\mu m}\cdot x\right)\right\} + \delta \tag{1}$$

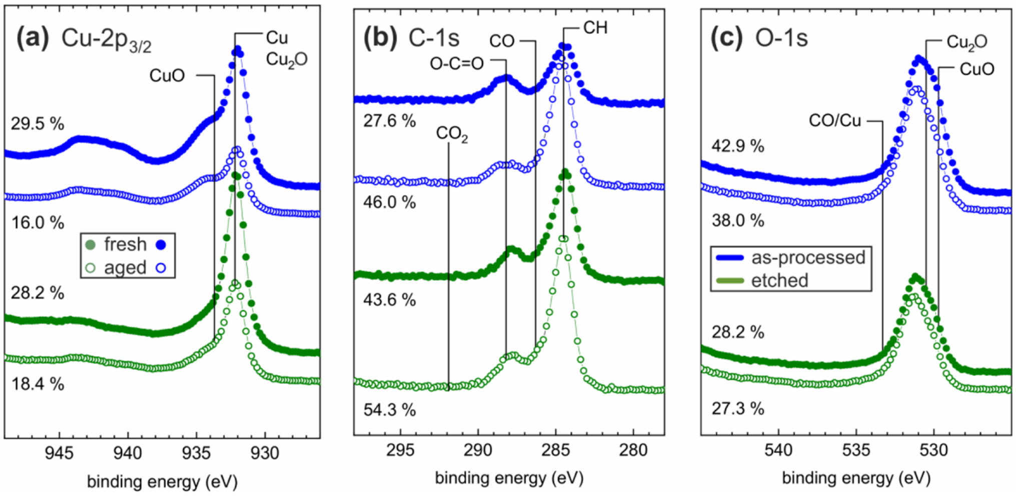

Figure 7. XPS detail spectra of (a) Cu-$2p_{3/2}$, (b) C-1s, and (c) O-1s for fresh (●) and aged (○) USP-DLIP-prepared Cu surfaces as-processed (blue) and after etching (green). The relative amount of Cu, C, and O are given in atom %.

with Δ and δ describing two attenuation lengths, i.e., the attenuation length for Cu_2O is $\Delta+\delta$ at the peaks of the topography, while it is δ in the valleys. Then, the spatial distribution of Cu_2O (as represented by the distribution of O after the first Ar^+ etching, see before) and Cu in the plane of the cross section of the USP-DLIP topography can be written as

$$\rho_{Cu_2O}(x, y) = \rho_{0,Cu_2O} \times \exp\left(\frac{-y}{d(x)}\right) \tag{2}$$

$$\rho_{Cu}(x, y) = \rho_{0,Cu} \times \left\{1 - \exp\left(\frac{-y}{d(x)}\right)\right\} \tag{3}$$

These distributions of atomic densities are used to calculate the atomic O:Cu ratio in dependence on the ablation of the surface (see the model described in section 3 of the Supporting Information). The attenuation lengths Δ and δ can be varied to fit the experimental O:Cu ratio since the XPS-probed amount of oxygen can be assigned to Cu_2O exclusively according to the vanishing carbo-oxygen group contributions in the C-1s spectra in Figure 6.

In Figure 8 the O:Cu ratios, as calculated from the Cu and Cu_2O distributions, i.e., equations (1−3), are compared to the XPS-derived O:Cu ratio for both samples. In Figure 8a,b, the model fits the experimental data for Δ = 4.7 and δ = 0.5 nm for the as-processed sample (see Figure 8c) and Δ = 1.6 and δ = 0.0 nm for the etched sample (see Figure 8d). XPS-derived oxide "thicknesses" ranging from 0.5 to 5.2 nm for the as-processed sample and ranging from 0 to 1.6 nm for the etched sample are in very good agreement with the values observed in the FIB cross sections in Figure 2a and the nearly vanishing oxide layer in Figure 2b, respectively. Therefore, these calculated values represent at least mean values for the thickness of the oxide layers along a patterning period.

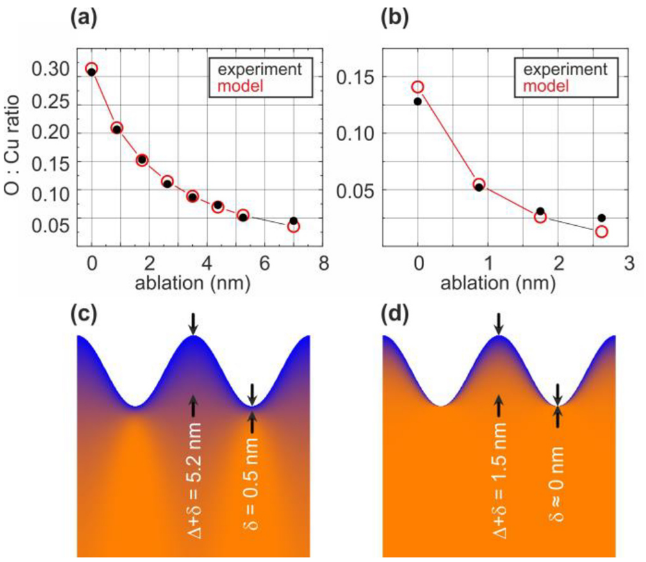

Figure 8. Comparison of the XPS probed O:Cu with the expected O:Cu ratio as calculated in the model described in the appendix for (a) the as-processed sample and (b) the etched sample. Please note that the 0 nm ablation refers to the surfaces that are obtained after the first step of Ar^+ ion etching that removes all CuO and adsorbates. The calculated O:Cu ratio fits the experimental ratio (c) for Δ = 4.7 nm and δ = 0.5 nm for the as-processed sample and (d) for Δ = 1.6 nm and δ = 0 nm for the etched sample. Note that in (c−d), topography and thickness of oxide layers are not scaled.

However, the model described in the Supporting Information just uses a modulation of the oxide "thickness" according to eq 1. It does not give information on how the maxima and minima of the oxide "thickness" are correlated to the peaks and valleys of the topography. Since the STS experiments revealed a reduced conductivity at the peaks of the topography, it can be assumed that here the oxide thickness is largest. This assumption is also confirmed by angular-resolved XPS data: according to Figure 9a, XPS experiments in normal emission mode (ϑ = 0°) probe the whole surface, while in XPS experiments in grazing emission mode (ϑ = 80°), intensity distributions from the valley regions are suppressed. In Figure 9b, the Cu-LMM spectra of the as-processed sample are compared for ϑ = 0° and ϑ = 80° emission with the intensity normalized at the peak position for Cu_2O. Since the spectra taken at ϑ = 80° display reduced intensity at the peak position for Cu, it is evident that the bottom region of the topography has to be enriched with metallic Cu.

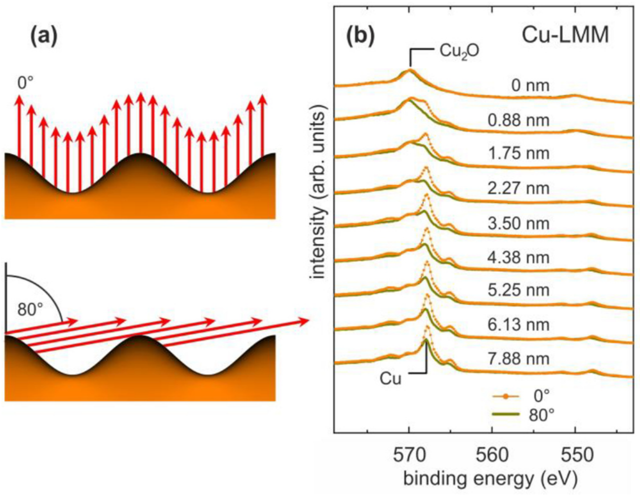

Figure 9. (a) Scheme of the XPS probed part of the surface topography in normal emission (top) and grazing emission (bottom) geometry. (b) Cu-LMM spectra taken at 0° and 80° on the as-processed sample for different steps of ablation.

On the basis of the presented results, it can be assumed that the oxide layer on the as-processed samples mainly forms during USP-DLIP processing by condensation of hot metal vapor and the preferential redeposition of already agglomerating nanoclusters of Cu_2O on the topography peaks, which lead to the flakelike substructure morphology. Oxidation by thermally induced diffusion processes seems to play a secondary role, which is indicated by the low oxide thicknesses determined in the topography minima, where the highest laser intensity and thus the strongest substrate heating is induced. This may be linked to the high convective cooling rates that are observed during ultrashort pulsed laser ablation on metals leading to a very short time scale for diffusion processes.[44] The amount of process-induced oxidation appears to sufficiently passivate the substrate surface, therefore postprocess changes of the oxide composition are limited to superficial CuO formation as it is generally observed under ambient conditions.[17] The expectable characteristics of a self-assembled oxide layer on USP-DLIP-processed copper, in contrast, appear to be characterized by the surface composition of etched samples after aging, which can be assumed to be mainly attributable to substrate properties.[22] The higher ratio of CuO on as-processed samples in comparison to etched samples can be traced back to the highly enlarged surface-to-bulk ratio of the flakelike morphology. According to the results achieved by XPS, they appear to be partly composed of both, CuO and Cu_2O, which can be linked to superficial layers of CuO grown in ambient atmosphere on a Cu_2O backbone. Due to the fragile structure and weak surface bonding of these agglomerates, they are most likely removed within the first Ar^+ ion etching cycle (nominal ablation of 0.8 nm), by which oxide measured in-depth by XPS is more related to the surface layer visible in FIB cross sections of $Au_{80}Pd_{20}$-coated samples than the actual height of the flakelike substructure.

The observed preferential agglomeration of condensing Cu_2O on the peaks during ablation in USP-DLIP processing might be triggered by the topography itself leading to a shadowing of the valleys as well as temperature differences of the substrate surface. As the maximum of laser intensity in USP-DLIP is applied in the center of the topography valleys, substrate heating is highest at this location, while the topography peaks do not experience noticeable heating with the parameters used in this experiment.[24] As a result, the peaks show thermodynamically preferred conditions for a condensation of hot metal vapor and nanoscaled clusters compared to the valley regions. Both mechanisms might have a combined impact on the significant deviation of oxidation between peaks and valleys on as-processed samples.

In the case of the etched samples, oxidation is not detectable by SEM but only STS and XPS show a reduced oxide thickness, even after aging, which is yet still dispersed heterogeneously between peaks and valleys. Considering the influence of substrate condition on oxide formation,[22] this observation might be traced back to the microstructure of the copper substrate: compared to the bulk material, the grain size in the peak region is reduced as visible in Figure 1e,f. The finer grain size originates from sample preparation by mechanical polishing, which induces a deformation area of about 500 nm thickness on the substrate surface (see Figure S4), which is half as deep as the ablated pattern valleys. Due to the low thermal substrate affection by USP-DLIP, the original microstructure is retained leading to heterogeneous properties in the peak and in the valley regions also affecting their corrosive, hence oxidation, behavior.

The heterogeneous oxide distribution appears similar to a former study on surface chemistry modification of stainless steel by DLIP using short laser pulses.[45] However, in the former case the highest oxide thickness of 15.4 nm was detected in the middle of the valleys, which can be attributed to the clearly different thermal effect on the substrate by processing with higher pulse durations. In contrast to USP-DLIP, pattern formation during short-pulsed DLIP is mainly influenced by Marangoni convection causing melt flow from areas exposed to high laser intensity to areas of low laser-induced heating, instead of ablation.[46] According to this previous study, process-related oxidation during short pulsed DLIP is related to actual substrate heating involving diffusion processes, while we were able to show that oxidation during USP-DLIP is predominantly caused by redeposition of ablated matter in the case of USP-DLIP, where laser-induced thermal affection of the substrate appears to play a minor role in chemical surface modification.

■ CONCLUSIONS

By applying a multimethodical approach, we were able to shed light on the chemical modification of copper surfaces by USP-DLIP processing. The results allow for deeper insights in the actual mechanisms leading to the process-induced surface chemistry. (i) USP-DLIP induces a heterogeneous distribution of oxidation, which is more distinct in the peaks than in the valleys. This might be caused by a mechanism of preferential metal vapor condensation and agglomeration of ablated material during processing due to, for example, topographic shadowing and heterogeneous surface temperatures. Aside from a dense oxide layer, this mechanism is leading to mechanically stable flakelike agglomerations of copper oxide, highly affecting the overall surface morphology. In contrast, oxidation by thermally induced diffusion appears to play a minor role in oxide formation during USP-DLIP. (ii) The process-related oxide layer can be almost fully removed by post-treatment via immersion etching in 3% citric acid. While on as-processed surfaces the process-induced oxide layer remains stable during aging and etched surfaces exhibit growth of a self-assembling oxide layer, which is still heterogeneously distributed. The latter can be traced back to heterogeneous crystallographic properties of the copper substrate exhibiting lower grain sizes in the peak areas. (iii) Depth profiling experiments by XPS on as-processed and etched USP-DLIP processed copper surfaces (both after aging for 3 weeks) revealed an inhomogeneous oxide layer of mainly Cu_2O that is covered by a sub-nm layer of CuO and several carbon species. The agglomeration of carbon species is different for the as-processed and the etched surfaces due to the elimination of the USP-DLIP-induced modifications of surface chemistry on the etched Cu surface.

■ ASSOCIATED CONTENT

Supporting Information

The Supporting Information is available free of charge at https://pubs.acs.org/doi/10.1021/acs.langmuir.0c01625.

> Monte Carlo simulation of EDS signal depth; analysis of XPS data; simulation of XPS probed depth distributions of Cu and Cu_2O; and microstructure of the polished Cu-surfaces pre-USP-DLIP (PDF)

■ AUTHOR INFORMATION

Corresponding Authors

Daniel W. Müller − *Chair of Functional Materials, Department of Materials Science, Saarland University, 66123 Saarbrücken, Germany*; Phone: +49 681/302−70545; Email: daniel.mueller@uni-saarland.de; Fax: +49 681/302−70502

Frank Müller − *Experimental Physics and Center for Biophysics, Saarland University, 66123 Saarbrücken, Germany*; orcid.org/0000-0001-8955-5317; Email: f.mueller@mx.uni-saarland.de

Authors

Anne Holtsch − *Experimental Physics and Center for Biophysics, Saarland University, 66123 Saarbrücken, Germany*

Sarah Lößlein − *Chair of Functional Materials, Department of Materials Science, Saarland University, 66123 Saarbrücken, Germany*

Christoph Pauly − *Chair of Functional Materials, Department of Materials Science, Saarland University, 66123 Saarbrücken, Germany*
Christian Spengler − *Experimental Physics and Center for Biophysics, Saarland University, 66123 Saarbrücken, Germany*; orcid.org/0000-0002-0504-1149
Samuel Grandthyll − *Experimental Physics and Center for Biophysics, Saarland University, 66123 Saarbrücken, Germany*
Karin Jacobs − *Experimental Physics and Center for Biophysics, Saarland University, 66123 Saarbrücken, Germany*
Frank Mücklich − *Chair of Functional Materials, Department of Materials Science, Saarland University, 66123 Saarbrücken, Germany*

Complete contact information is available at:
https://pubs.acs.org/10.1021/acs.langmuir.0c01625

Notes

The authors declare no competing financial interest.

■ ACKNOWLEDGMENTS

This work has been funded by the German Research Foundation (DFG) within the project "Controlled bacterial interaction to increase the antimicrobial efficiency of copper surfaces" (project number 415956642) and within the Collaborative Research Center SFB 1027 "Physical Modelling of Non-Equilibrium Processes in Biological Systems" (project number 200049484).

■ REFERENCES

(1) Heilmann, S.; Zwahr, C.; Knape, A.; Zschetzsche, J.; et al. Improvement of the Electrical Conductivity between Electrode and Sheet in Spot Welding Process by Direct Laser Interference Patterning. *Adv. Eng. Mater.* **2018**, *20*, 1700755.

(2) Venkata Krishnan, D.; Udaya Kumar, G.; Suresh, S.; Jubal, M.; Thansekhar, M. R.; Ramesh, R. Wetting Transition in Laser-Fabricated Hierarchical Surface Structures and Its Impact on Condensation Heat Transfer Characteristics. *Int. J. Heat Mass Transfer* **2019**, *140*, 886−896.

(3) Ding, K.; Wang, C.; Zheng, Y.; Xie, Z.; Luo, Z.; Man, S.; Wu, B.; Duan, J. One-Step Fabrication of Multifunctional Fusiform Hierarchical Micro/Nanostructures on Copper by Femtosecond Laser. *Surf. Coat. Technol.* **2019**, *367*, 244−251.

(4) Soldera, M.; Taretto, K.; Berger, J.; Lasagni, A. F. Potential of Photocurrent Improvement in m C-Si: H Solar Cells with TCO Substrates Structured by Direct Laser Interference Patterning. *Adv. Eng. Mater.* **2016**, *18* (9), 1674−1682.

(5) Ta, V. D.; Dunn, A.; Wasley, T. J.; Li, J.; Kay, R. W.; Stringer, J.; Smith, P. J.; Esenturk, E.; Connaughton, C.; Shephard, J. D. Laser Textured Surface Gradients. *Appl. Surf. Sci.* **2016**, *371*, 583−589.

(6) Kietzig, A.-M.; Negar Mirvakili, M.; Kamal, S.; Englezos, P.; Hatzikiriakos, S. G. Laser-Patterned Super-Hydrophobic Pure Metallic Substrates: Cassie to Wenzel Wetting Transitions. *J. Adhes. Sci. Technol.* **2011**, *25* (20), 2789−2809.

(7) Wu, H.; Jiao, Y.; Zhang, C.; Chen, C.; Yang, L.; Li, J.; Ni, J.; Zhang, Y.; Li, C.; Zhang, Y.; et al. Large Area Metal Micro-/Nano-Groove Arrays with Both Structural Color and Anisotropic Wetting Fabricated by One-Step Focused Laser Interference Lithography. *Nanoscale* **2019**, *11*, 4803−4810.

(8) Allahyari, E.; Jjnivas, J.; Oscurato, S. L.; Salvatore, M.; Ausanio, G.; Vecchione, A.; Fittipaldi, R.; Maddalena, P.; Bruzzese, R.; Amoruso, S. Laser Surface Texturing of Copper and Variation of the Wetting Response with the Laser Pulse Fluence. *Appl. Surf. Sci.* **2019**, *470*, 817−824.

(9) Lian, Z.; Xu, J.; Yu, Z.; Yu, P.; Yu, H. A Simple Two-Step Approach for the Fabrication of Bio-Inspired Superhydrophobic and Anisotropic Wetting Surfaces Having Corrosion Resistance. *J. Alloys Compd.* **2019**, *793*, 326−335.

(10) Zwahr, C.; Gunther, D.; Brinkmann, T.; Gulow, N.; Oswald, S.; Grosse Holthaus, M.; Lasagni, A. F. Laser Surface Pattering of Titanium for Improving the Biological Performance of Dental Implants. *Adv. Healthcare Mater.* **2017**, *6*, 1600858.

(11) Schieber, R.; Lasserre, F.; Hans, M.; Fernández-Yagüe, M.; Díaz-Ricart, M.; Escolar, G.; Ginebra, M.; Mücklich, F.; Pegueroles, M. Direct Laser Interference Patterning of CoCr Alloy Surfaces to Control Endothelial Cell and Platelet Response for Cardiovascular Applications. *Adv. Healthcare Mater.* **2017**, *6*, 1700327.

(12) Helbig, R.; Günther, D.; Friedrichs, J.; Rößler, F.; Lasagni, A.; Werner, C. The Impact of Structure Dimensions on Initial Bacterial Adhesion. *Biomater. Sci.* **2016**, *4* (7), 1074−1078.

(13) Spengler, C.; Nolle, F.; Mischo, J.; Faidt, T.; Grandthyll, S.; Thewes, N.; Koch, M.; Müller, F.; Bischo, M.; Klatt, A. Strength of Bacterial Adhesion on Nanostructured Surfaces Quantified by Substrate Morphometry. *Nanoscale* **2019**, *11*, 19713 DOI: 10.1039/c9nr04375f.

(14) Raimbault, O.; Benayoun, S.; Anselme, K.; Mauclair, C.; Bourgade, T.; Kietzig, A. M.; Girard-Lauriault, P. L.; Valette, S.; Donnet, C. The Effects of Femtosecond Laser-Textured Ti-6Al-4V on Wettability and Cell Response. *Mater. Sci. Eng., C* **2016**, *69*, 311−320.

(15) Boinovich, L. B.; Emelyanenko, K. A.; Domantovsky, A. G.; Chulkova, E. V.; Shiryaev, A. A.; Emelyanenko, A. M. Pulsed Laser Induced Triple Layer Copper Oxide Structure for Durable Polyfunctionality of Superhydrophobic Coatings. *Adv. Mater. Interfaces* **2018**, *5*, 1801099.

(16) Hans, M.; Müller, F.; Grandthyll, S.; Hüfner, S.; Mücklich, F. Anisotropic Wetting of Copper Alloys Induced by One-Step Laser Micro-Patterning. *Appl. Surf. Sci.* **2012**, *263*, 416−422.

(17) Platzman, I.; Brener, R.; Haick, H.; Tannenbaum, R. Oxidation of Polycrystalline Copper Thin Films at Ambient Conditions. *J. Phys. Chem. C* **2008**, *112* (111), 1101−1108.

(18) Hans, M.; Erbe, A.; Mathews, S.; Chen, Y.; Solioz, M.; Mücklich, F. Role of Copper Oxides in Contact Killing of Bacteria. *Langmuir* **2013**, *29* (52), 16160−16166.

(19) Kietzig, A. M.; Hatzikiriakos, S. G.; Englezos, P. Patterned Superhydrophobic Metallic Surfaces. *Langmuir* **2009**, *25* (8), 4821−4827.

(20) Jagdheesh, R.; Diaz, M.; Ocaña, J. L. Bio Inspired Self-Cleaning Ultrahydrophobic Aluminium Surface by Laser Processing. *RSC Adv.* **2016**, *6* (77), 72933−72941.

(21) Long, J.; Zhong, M.; Fan, P.; Gong, D.; Zhang, H. Wettability Conversion of Ultrafast Laser Structured Copper Surface. *J. Laser Appl.* **2015**, *27* (S2), S29107.

(22) Platzman, I.; Saguy, C.; Brener, R.; Tannenbaum, R.; Haick, H. Formation of Ultrasmooth and Highly Stable Copper Surfaces through Annealing and Self-Assembly of Organic Monolayers. *Langmuir* **2010**, *26* (1), 191−201.

(23) Israelachvili, J. N. *Intermolecular and Surface Forces*; Elsevier, 2011; Vol. 3rd ed., DOI: 10.1017/CBO9781107415324.004.

(24) Müller, D. W.; Fox, T.; Grützmacher, P. G.; Suarez, S.; Mücklich, F. Applying Ultrashort Pulsed Direct Laser Interference Patterning for Functional Surfaces. *Sci. Rep.* **2020**, *10*, DOI: 10.1038/s41598-020-60592-4.

(25) Binnig, G.; Rohrer, H. Scanning Tunnelling Microscopy. *Surf. Sci.* **1983**, *126*, 236−244.

(26) Binnig, G.; Rohrer, H.; Gerber, C.; Weibel, E. 7 × 7 Reconstruction on Si(111) Resolved in Real Space. *Phys. Rev. Lett.* **1983**, *50* (2), 120−123.

(27) Tersoff, J.; Hamann, D. R. Theory and Application of the Scanning Tunneling Microscope. *Phys. Rev. Lett.* **1983**, *50* (25), 1998−2001.

(28) Tersoff, J.; Hamann, D. R. Theory of the Scanning Tunneling Microscope. *Phys. Rev. B: Condens. Matter Mater. Phys.* **1985**, *31* (2), 805−813.

(29) Shirley, D. A. High-Resolution x-Ray Photoemission Spectrum of the Valence Bands of Gold. *Phys. Rev. B* **1972**, *5* (12), 4709−4714.

(30) Yeh, J. J.; Lindau, I. Atomic Subshell Photoionization Cross Sections and Asymmetry Parameters: 1 < Z < 103. *At. Data Nucl. Data Tables* **1985**, *32*, 1−155.

(31) Müller, F.; Zeitz, C.; Mantz, H.; Ehses, K. H.; Soldera, F.; Schmauch, J.; Hannig, M.; Hüfner, S.; Jacobs, K. Elemental Depth Profiling of Fluoridated Hydroxyapatite: Saving Your Dentition by the Skin of Your Teeth? *Langmuir* **2010**, *26* (24), 18750−18759.

(32) Yin, M.; Wu, C.-K.; Lou, Y.; Burda, C.; Koberstein, J. T.; Zhu, Y.; O'Brien, S. Copper Oxide Nanocrystals. *J. Am. Chem. Soc.* **2005**, *127*, 9506−9511.

(33) Simmons, J. G. Electric Tunnel Effect between Dissimilar Electrodes Separated by a Thin Insulating Film. *J. Appl. Phys.* **1963**, *34* (9), 2581−2590.

(34) Simmons, J. G. Generalized Formula for the Electric Tunnel Effect between Similar Electrodes Separated by a Thin Insulating Film. *J. Appl. Phys.* **1963**, *34* (6), 1793−1803.

(35) Fowler, R. H.; Nordheim, L. Electron Emission in Intense Electric Fields. *Proc. R. Soc. London. Ser. A* **1980**, *119* (781), 173−181.

(36) Stroscio, J. A.; Feenstra, R. M. 4. Methods of Tunneling Spectroscopy. *Methods Exp. Phys.* **1993**, *27*, 95−147.

(37) Koffyberg, F. P.; Benko, F. A. A Photoelectrochemical Determination of the Position of the Conduction and Valence Band Edges of P-Type CuO. *J. Appl. Phys.* **1982**, *53*, 1173−1177.

(38) Lin, J.; Hao, W.; Shang, Y.; Wang, X.; Qiu, D.; Ma, G.; Chen, C.; Li, S.; Guo, L. Direct Experimental Observation of Facet-Dependent SERS of Cu2O Polyhedra. *Small* **2018**, *14*, 1703274.

(39) Gartland, P. O.; Berge, S.; Slagsvold, B. J. Photoelectric Work Function of a Copper Single Crystal for the (100), (110), (111), and (112) Faces. *Phys. Rev. Lett.* **1972**, *28* (12), 738−739.

(40) Wang, Y.; Lany, S.; Ghanbaja, J.; Fagot-Revurat, Y.; Chen, Y. P.; Soldera, F.; Horwat, D.; Mücklich, F.; Pierson, J. F. Electronic Structures of Cu2O, Cu4O3, and CuO: A Joint Experimental and Theoretical Study. *Phys. Rev. B: Condens. Matter Mater. Phys.* **2016**, *94* (24), 1−10.

(41) Tahir, D.; Tougaard, S. Electronic and Optical Properties of Cu, CuO and Cu2O Studied by Electron Spectroscopy. *J. Phys.: Condens. Matter* **2012**, *24*, 175002−175010.

(42) Schedel-Niedrig, T.; Neisius, T.; Böttger, I.; Kitzelmann, E.; Weinberg, G.; Demuth, D.; Schlögl, R. Copper (Sub)Oxide Formation: A Surface Sensitive Characterization of Model Catalysts. *Phys. Chem. Chem. Phys.* **2000**, *2*, 2407−2417.

(43) McShane, C. M.; Choi, K. S. Junction Studies on Electrochemically Fabricated P-n Cu2O Homojunction Solar Cells for Efficiency Enhancement. *Phys. Chem. Chem. Phys.* **2012**, *14* (17), 6112−6118.

(44) Artyukov, I. A.; Zayarniy, D. A.; Ionin, A. A.; Kudryashov, S. I.; Makarov, S. V.; Saltuganov, P. N. Relaxation Phenomena in Electronic and Lattice Subsystems on Iron Surface during Its Ablation by Ultrashort Laser Pulses. *JETP Lett.* **2014**, *99* (1), 51−55.

(45) Rosenkranz, A.; Reinert, L.; Gachot, C.; Aboufadl, H.; Grandthyll, S.; Jacobs, K.; Müller, F.; Mücklich, F. Oxide Formation, Morphology, and Nanohardness of Laser-Patterned Steel Surfaces. *Adv. Eng. Mater.* **2015**, *17* (8), 1234−1242.

(46) D'Alessandria, M.; Lasagni, A.; Mücklich, F. Applied Surface Science Direct Micro-Patterning of Aluminum Substrates via Laser Interference Metallurgy. *Appl. Surf. Sci.* **2008**, *255*, 3210−3216.

Supporting Information for

In-Depth Investigation of Copper Surface Chemistry Modification by Ultrashort Pulsed Direct Laser Interference Patterning

Daniel W. Müller[1], Anne Holtsch[2], Sarah Lößlein[1], Christoph Pauly[1], Christian Spengler[2], Samuel Grandthyll[2], Karin Jacobs[2], Frank Mücklich[1], Frank Müller[2]

[1]Chair of Functional Materials, Department of Materials Science, Saarland University, 66123 Saarbrücken, Germany

[2]Experimental Physics and Center for Biophysics, Saarland University, 66123 Saarbrücken, Germany.

Number of pages: 9

Number of figures: 4

Number of tables: 2

Contents of SI

Figures

Tables

1. *Estimation of EDS signal depth by Monte-Carlo Simulation*

In order to estimate the EDS signal depth in relation to the oxide thickness, a Monte-Carlo simulation (MCS) of the penetration depth of the electrons at a beam voltage of 5 kV was carried out using the software *Casino V2.5.1*. In the simulation, a Cu_2O layer is added to the copper substrate, as Cu_2O has proven to be the dominant process-related oxide from the XPS measurements. The oxide thickness probed in the FIB cross sections mainly varied between 2 nm and 7 nm in case of the as-processed samples, which was again confirmed by the simulation model based on the XPS results. Therefore, the MCS is conducted with an average oxide (Cu_2O) thickness of 4.5 nm. A visualization of individual electron paths in the substrate is shown in Fig. S1a as calculated in the MCS. The interface between oxide layer and Cu substrate is indicated by the red dotted line. The signal depth distribution of non-absorbed Cu-LIII-X-rays contributing to the respective electron absorption depths are plotted in Fig. S1b. The Cu-LIII signal is used in EDS analyzation of the USP-DLIP Cu surfaces to measure the amount of Cu, whereas the latter value is used to estimate the overall signal depth in the experiment. The signal is plotted cumulatively as a function of the sample depth and shows that 90 % of the total signal originate from a sample depth of about 62 nm. Since the average oxide layer thickness on as-processed surfaces accounts to about 7.3 % of the overall signal depth (varying from 3.2 % for 2 nm to 11.3 % for 7 nm), the results achieved during elemental mapping allow for a qualitative estimation of oxide thickness distribution on these surfaces. In case of the lower oxide thickness observed on immersion etched samples on the other hand, the oxygen signal might not stand out sufficiently against the Cu signal to e.g. compare between peak and valley regions, which is also observed in the experiments. Nevertheless, based on the EDS analysis, a clear statement can be made about the difference in surface oxide thickness between the etched and as-processed samples.

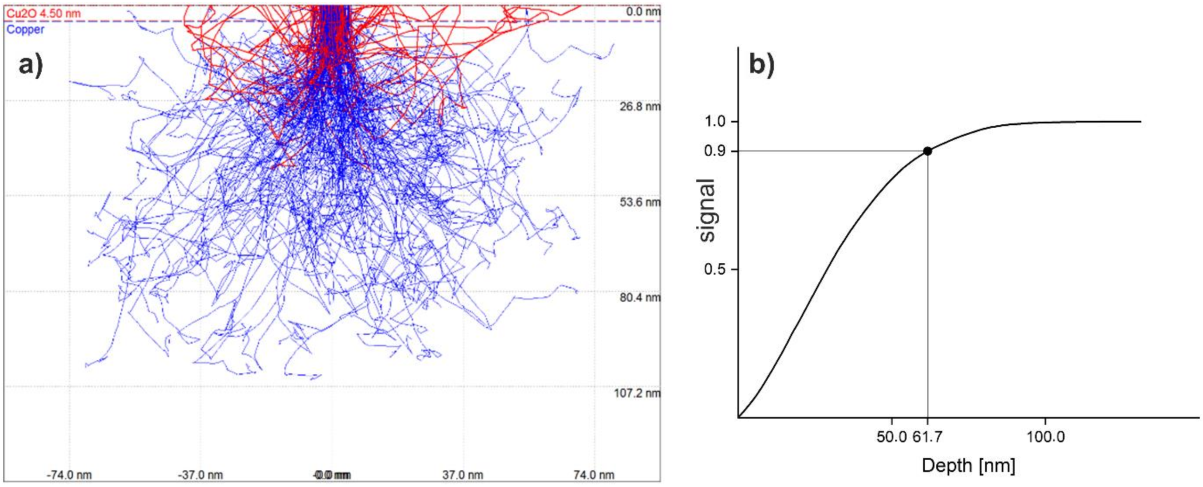

Figure S1: a) Monte-Carlo simulation of a copper sample covered with a 4.5 nm thick process oxide of Cu_2O. b) Cumulated signal of the non-absorbed X-rays of the Cu-LIII line as a function of the sample depth. The results exhibit that 90% of the detected signal originate from a depth of <62 nm from the sample surface.

2. Analysis of XPS data

In order to reveal the distribution of Cu, Cu_2O and CuO of the as-processed and etched USP-DLIP Cu samples (as presented in Fig. 7) a combined analysis of the Cu-$2p_{3/2}$ spectra and the Cu-LMM Auger spectra was performed. Since the satellite of the Cu$2p_{3/2}$ spectra of CuO cannot be approximated by a simple line profile (i.e. Gaussian, Lorentzian or mixture of both) the Cu$2p_{3/2}$ spectra in Fig. 7a (as well as the corresponding Cu-LMM Auger spectra, not shown) were approximated by a combination of model spectra. The reference spectra for Cu were obtained from a clean Cu surface after Ar^+ ion etching whereas the reference for CuO were obtained from a Cu sample that was oxidized under ambient conditions by heating with a heat gun. The refence spectra for Cu_2O were taken from literature. In ref. 1, the Cu-$2p_{3/2}$ and Cu-LMM Auger spectra of Cu and CuO are nearly identical with our data. Therefore, the Cu-$2p_{3/2}$ and Cu-LMM Auger spectra of Cu_2O were digitized with the energy step width adapted to our data.

Fig. S2 shows the result of the fitting procedure exemplarily for the fresh USP-DLIP sample after etching. The distribution of Cu, Cu_2O and CuO, as averaged from the distributions obtained from the fitting of the Cu-$2p_{3/2}$ spectra and the fitting of the Cu-LMM Auger spectra, are listed in table S1.

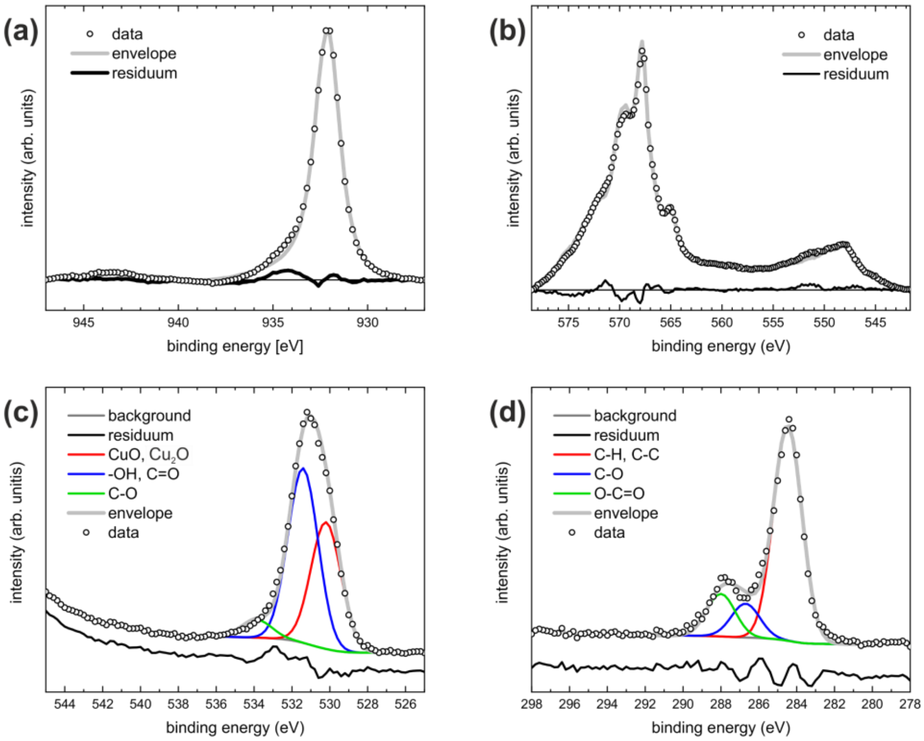

Figure S2. Example for fitting XPS data from the fresh USP-DLIP sample after etching. (a) Cu-2p$_{3/2}$, (b) Cu-LMM, (c) O-1s and (d) C-1s. In (a) and (b) the envelope represents the combination of reference spectra from Cu, Cu_2O and CuO. In (c)-(d) the envelope represents the superposition of three Gaussians and a Shirley background (the residuum is shifted downwards for better visibility).

In addition, the C-1s and O-1s data from Fig. 7 were fitted by three Gaussians (the minimal number of lines needed to simulate the data), as exemplarily shown in Fig. S2c-d for the fresh USP-DLIP sample after etching. In Fig. S2c, the distribution from CuO and Cu_2O could not be resolved and are represented by a common contribution. For O-1s, the peaks represent contributions from CuO, Cu_2O, -OH, C=O and C-O like bonding. For C-1s, the peaks represent C-H, C-C, C-O and O-C=O like bonding.

	etched	**as-processed**
aged	Cu 35 CuO 25 ½ Cu_2O 40	Cu 0 CuO 49 ½ Cu_2O 51
fresh	Cu 44 CuO 12 ½ Cu_2O 44	Cu 1 CuO 45 ½ Cu_2O 54

Table S1. Distribution of Cu, CuO and Cu_2O for the USP-DLIP samples from Fig. 7 in at-% (please note, that for Cu_2O, the amount refers to one Cu atom per formula unit).

The overall compositions of the samples from Fig. 7 are listed in Table S2. The overall amount of Cu, O and C is calculated from the overall Cu-2$p_{3/2}$, O-1s and C-1s intensities as described in the experimental section. The distribution of the different bonding types refers to their relative amount as obtained from the fitting procedures described above.

	Cu			**C**			**O**		
	Cu	CuO	Cu_2O	C-C, C-H	C-O	O-C=O	CuO, Cu_2O	-OH, C=O	C-O
as processed, fresh	**29.5**			**27.6**			**42.9**		
	0.4	18.2	10.9	17.9	2.5	7.2	21.0	20.0	1.9
as processed, aged	**16.0**			**46.0**			**38.0**		
	0	10.5	5.5	35.6	4.8	5.6	14.5	22.1	1.4
etched, fresh	**28.2**			**43.6**			**28.2**		
	15.9	4.3	8.0	31.8	5.6	6.2	11.2	15.4	1.6
etched, aged	**18.4**			**54.3**			**27.3**		
	8.0	5.8	4.6	40.4	7.2	6.7	7.0	18.9	1.4

Table S2. Distribution of bonding types for the USP-DLIP samples from Fig. 7 in at-% (please note, that in the Cu column the amount of Cu in Cu_2O now refers to both Cu atoms per formula unit). For comparison, the colors of the lines refer to the colors used in Fig. 7.

3. *Simulation of XPS probed depth distributions of Cu and Cu_2O*

Fig. S3a displays the cross section of the laser patterned topography with a period of 3 µm and a bottom-top distance of about 1 µm. Since the thickness of the oxide is expected to be in the range of only a few nanometers, it is sufficient to regard photoemission contribution from a subsurface range of some tens of nanometers. Since the modulation of topography exceeds the oxide thickness by 2-3 orders of magnitude, an overall extension of the sample along the y-direction of > 1 µm would be necessary. However, in XPS the atomic O : Cu is probed in normal emission mode, i.e. the momentum of the photoelectron is parallel to the y-direction. Therefore, the sample can be cut in slices (Fig. S3b) which are shifted along the y-direction to form a flat surface (Fig. S3c).

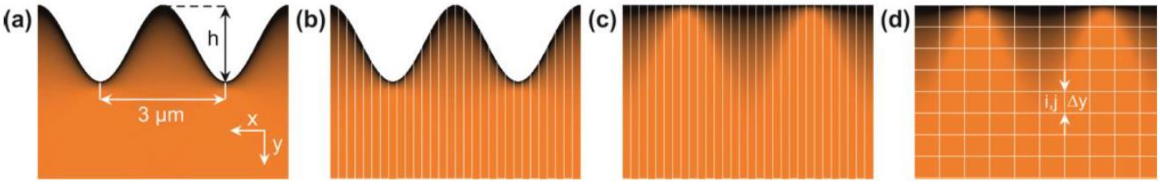

Figure S3. (a) Cross section of the laser-patterned samples with 3 µm periods along the x-axis and a height of h ~ 1 µm with oxide distribution (dark regions) according to eqn. 3. (b)-(c) In normal emission XPS experiments only the projection of the topography is probed and the oxide distribution can be regarded relative to a flat surface. (d) The cross section is dived in cells of uniform height Δy. For details, see text.

The cross section is divided in N x M cells (x_i, y_j) of uniform height Δy (Fig. S3d) and in each cell the distribution of Cu, Cu^+ and O^{2-} atoms/ions is given according to the oxide thickness in eqn. (1), i.e.

$$\rho_{Cu^+}\left(x_i, y_j\right) = \rho_{0,Cu^+} \cdot exp\left(\frac{-y_j}{d(x_i)}\right)$$

$$\rho_{O^{2-}}\left(x_i, y_j\right) = \rho_{0,O^{2-}} \cdot exp\left(\frac{-y_j}{d(x_i)}\right)$$

$$\rho_{Cu}\left(x_i, y_j\right) = \rho_{0,Cu} \cdot \left\{1 - exp\left(\frac{-y_j}{d(x_i)}\right)\right\},$$

with the densities ρ_0 = 0.143 mol/l, 0.084 mol/l and 0,042 mol/l for Cu, Cu^+ and O^{2-}, respectively (when taking a mass density of 9 g/cm^3 for Cu und 6 g/cm^3 for Cu_2O).

From table 1 and equation 8 in ref. 2, the electron mean free paths for Cu-$2p_{3/2}$ and O-1s photoelectrons with kinetic energies of 555 eV and 957 eV, respectively, can be calculated as

$$\lambda_{Cu}^{Cu2p} = 1.16nm \quad \lambda_{Cu_2O}^{Cu2p} = 1.62nm$$

$$\lambda_{Cu}^{O1s} = 1.69nm \quad \lambda_{Cu_2O}^{O1s} = 24.1nm$$

The electron mean free paths for Cu-2p$_{3/2}$ and O-1s photoelectrons in cell (i, j) is then given according to the overall material distribution in this cell

$$\lambda^{Cu2p}\left(x_i, y_j\right) = \frac{\varrho_{Cu}\left(x_i, y_j\right)}{\varrho_{0,Cu}} \cdot \lambda_{Cu}^{Cu2p} + \frac{\varrho_{Cu^+}\left(x_i, y_j\right)}{\varrho_{0,Cu^+}} \cdot \lambda_{Cu^+}^{Cu2p}$$

$$\lambda^{O1s}\left(x_i, y_j\right) = \frac{\varrho_{Cu}\left(x_i, y_j\right)}{\varrho_{0,Cu}} \cdot \lambda_{Cu}^{O1s} + \frac{\varrho_{Cu^+}\left(x_i, y_j\right)}{\varrho_{0,Cu^+}} \cdot \lambda_{Cu^+}^{O1s}$$

The contribution of an Cu-2p$_{3/2}$ photoelectron, as emitted in cell (i,j), to the detected overall Cu2p$_{3/2}$ intensity is given by the attenuation of all cells that are passed on the path to the surface, i.e. (i, j), (i ,j-1), …, (i, 1). The overall attenuation factor for cell (i, j) is

$$D^{Cu2p}\left(x_i, y_j\right) = \prod_{n=1}^{j} exp\left(\frac{-\Delta y}{\lambda^{Cu2p}\left(x_i, y_n\right)}\right).$$

Similar, for O-1s photoelectrons, the overall attenuation factor for cell (i, j) is

$$D^{O1s}\left(x_i, y_j\right) = \prod_{n=1}^{j} exp\left(\frac{-\Delta y}{\lambda^{O1s}\left(x_i, y_n\right)}\right).$$

The overall intensity of Cu-2p$_{3/2}$ and of O-1s photoelectrons is given by taking the sums over all cells via

$$I(Cu) = \sum_{allcells} D^{Cu2p}(x_i, y_j) \cdot \{\varrho_{Cu}(x_i, y_j) + \varrho_{Cu^+}(x_i, y_j)\},$$

$$I(O) = \sum_{allcells} D^{01s}(x_i, y_j) \cdot \varrho_{O^{2-}},$$

finally providing the atomic ratio $\frac{I(O)}{I(Cu)}$ that can be compared with the experimental ratio.

4. *Microstructure of the polished Cu-surfaces pre USP-DLIP*

In the main article, heterogeneous oxidation behavior of Cu samples processed by USP-DLIP and etched by citric acid during three weeks of aging was linked to differences in the microstructure between peak and valley regions of the pattern. The finer grains visible in the FIB cross sections of topography peaks in Fig. 1e and Fig. 1f are linked to the original substrate microstructure mechanically induced during preparation of the Cu samples by polishing. This microstructure comprises of a superficial deformation zone exhibiting a thickness of approx. 500 nm as visible in Fig. S4. This microstructure remains unchanged during laser processing due to the minimal thermal substrate affection by this ultrashort laser pulsed technique. Hence, localized ablation during USP-DLIP down to a depth of approx. 1 µm leads to inhomogeneous microstructure properties between peak and valley regions as illustrated in Fig. S4, which strongly influences corrosion resistance and alongside the thickness of locally forming passivating oxide layers.[3]

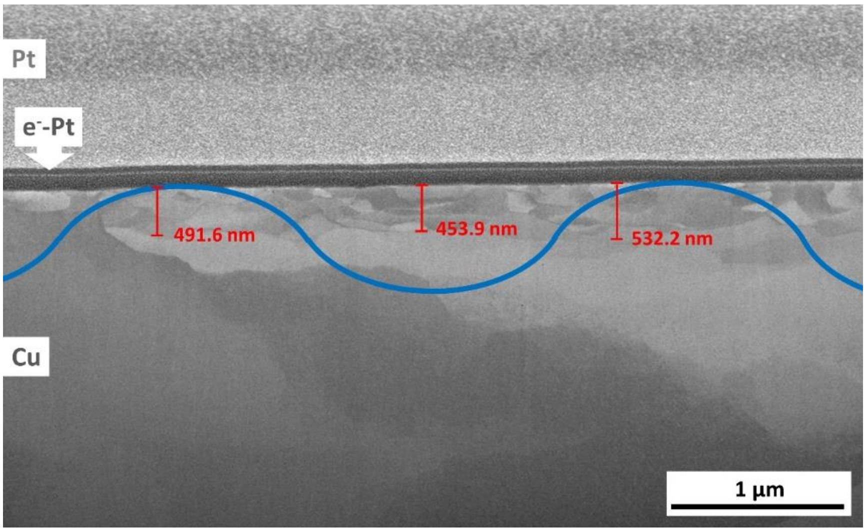

Figure S4. FIB Cross section of the polished substrate surfaces exhibiting a superficial deformation layer of ~ 500 nm thickness. Localised ablation during USP-DLIP having a minimal thermal effect on the substrate then induces a heterogeneous microstructure distribution between peak and valley regions, as illustrated by the blue line showing the final pattern. In the peaks, the mechanically induced fine-grained microstructure remains, while in the valleys, the larger grained microstructure of the mechanically unaffected substrate is present.

References

(1) Schedel-Niedrig, T.; Neisius, T.; Böttger, I.; Kitzelmann, E.; Weinberg, G.; Demuth, D.; Schlögl, R. Copper (Sub)Oxide Formation: A Surface Sensitive Characterization of Model Catalysts. *Phys. Chem. Chem. Phys.* **2000**, *2*, 2407–2417.

(2) Lesiak, B.; Jablonski, A.; Zemek, J.; Jiricek, P. Determination of the Inelastic Mean Free Paths of Electrons in Copper and Copper Oxides by Elastic Peak Electron Spectroscopy (EPES). *Surf. Interface Anal.* **1998**, *26*, 400–411. https://doi.org/10.1016/S0039-6028(02)01369-9.

(3) Platzman, I.; Brener, R.; Haick, H.; Tannenbaum, R. Oxidation of Polycrystalline Copper Thin Films at Ambient Conditions. *J. Phys. Chem. C* **2008**, No. 111, 1101–1108.

Paper III:

Increasing Antibacterial Efficiency of Cu Surfaces by targeted Surface Functionalization via Ultrashort Pulsed Direct Laser Interference Patterning

Daniel W. Müller[1,*], Sarah Lößlein[1], Emmanuel Terriac[2], Kristina Brix[3], Katharina Siems[4], Ralf Moeller[4], Ralf Kautenburger[3], Frank Mücklich[1]

[1]Chair of Functional Materials, Department of Materials Science, Saarland University, 66123, Saarbrücken, Germany.

[2]Leibniz Institute for New Materials, Dynamic Biomaterials. Saarbrücken 66123, Germany.

[3]Department of Inorganic Solid-State Chemistry, Elemental Analysis, Saarland University, Saarbrücken 66123, Germany.

[4]Aerospace Microbiology, Radiation Biology Department, Institute of Aerospace Medicine, German Aerospace Center (DLR e.V.), Cologne 51147, Germany.

Published in March 2021 in "Advanced Materials Interfaces" and accessible online via:

https://doi.org/10.1002/admi.202001656

Abstract:

Copper (Cu) exhibits great potential for application in the design of antimicrobial contact surfaces aiming to reduce pathogenic contamination in public areas as well as clinically critical environments. However, current application perspectives rely purely on the toxic effect of emitted Cu ions, without considering influences on the interaction of pathogenic microorganisms with the surface to enhance antimicrobial efficiency. In this study, it is investigated on how antibacterial properties of Cu surfaces against Escherichia coli can be increased by tailored functionalization of the substrate surface by means of ultrashort pulsed direct laser interference patterning (USP-DLIP). Surface patterns in the scale range of single bacteria cells are fabricated to purposefully increase bacteria/surface contact area, while parallel modification of the surface chemistry allows to involve the aspect of surface wettability into bacterial attachment and the resulting antibacterial effectivity. The results exhibit a delicate interplay between bacterial adhesion and the expression of antibacterial properties, where a reduction of bacterial cell viability of up to 15-fold can be achieved for E. coli on USP-DLIP surfaces in comparison to smooth Cu surfaces. Thereby, it can be shown how the antimicrobial properties of copper surfaces can be additionally enhanced by targeted surface functionalization.

Own contributions:

Conception and design of the study. Design of the interference-based USP laser setup. Sample preparation and surface characterisation via LSM and SEM including bacterial imaging. CA measurement and wet plating for antibacterial monitoring. Conception and design of the wetting experiment involving fluorescent bacteria in inverted LSM. Data interpretation, preparation and editing of the manuscript.

Included Cover Art related to this article: https://doi.org/10.1002/admi.202170027

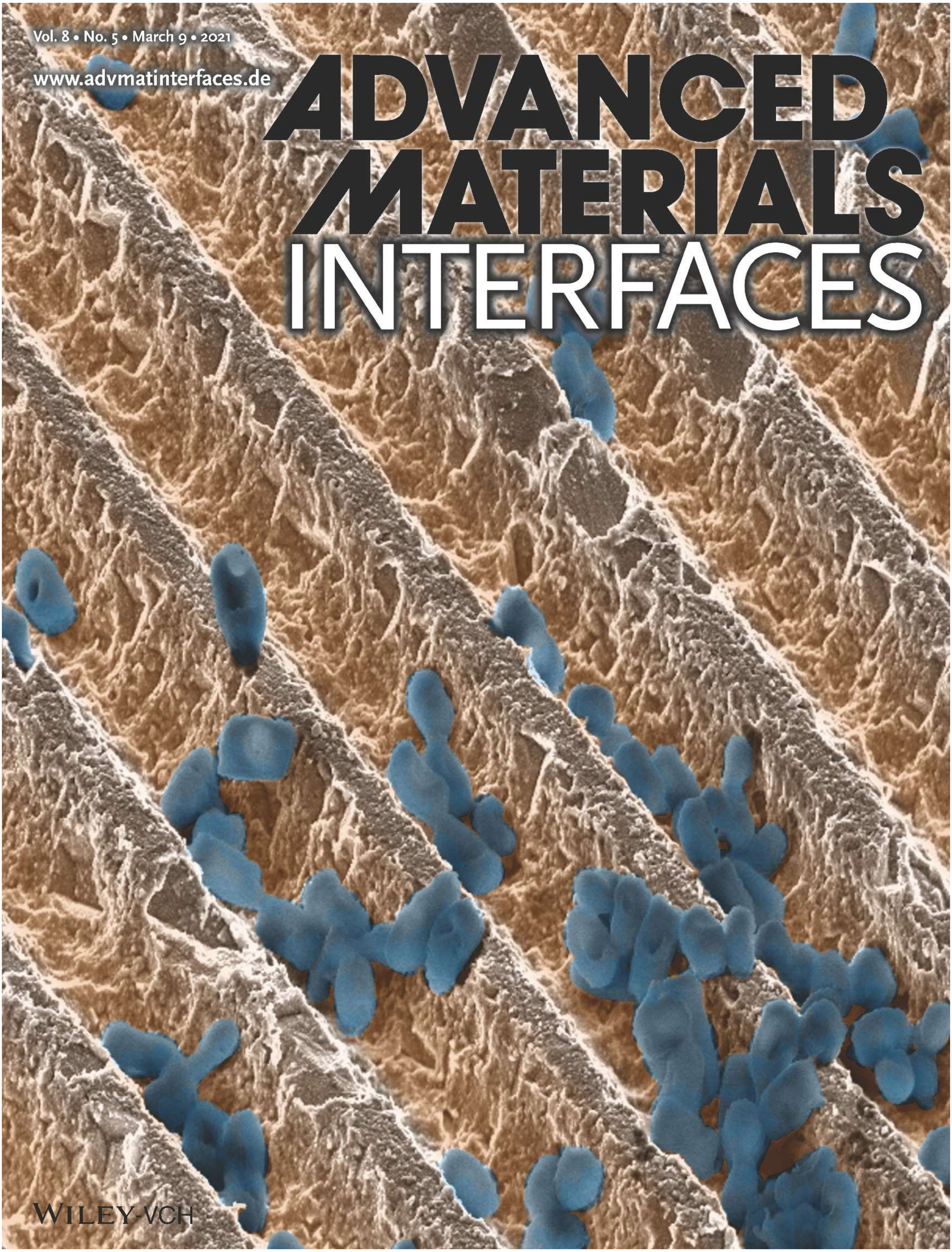

Vol. 8 • No. 5 • March 9 • 2021
www.advmatinterfaces.de

ADVANCED MATERIALS INTERFACES

WILEY-VCH

ADVANCED MATERIALS INTERFACES
www.advmatinterfaces.de

Increasing Antibacterial Efficiency of Cu Surfaces by targeted Surface Functionalization via Ultrashort Pulsed Direct Laser Interference Patterning

Daniel W. Müller, Sarah Lößlein, Emmanuel Terriac, Kristina Brix, Katharina Siems, Ralf Moeller, Ralf Kautenburger, and Frank Mücklich*

Copper (Cu) exhibits great potential for application in the design of antimicrobial contact surfaces aiming to reduce pathogenic contamination in public areas as well as clinically critical environments. However, current application perspectives rely purely on the toxic effect of emitted Cu ions, without considering influences on the interaction of pathogenic microorganisms with the surface to enhance antimicrobial efficiency. In this study, it is investigated on how antibacterial properties of Cu surfaces against *Escherichia coli* can be increased by tailored functionalization of the substrate surface by means of ultrashort pulsed direct laser interference patterning (USP-DLIP). Surface patterns in the scale range of single bacteria cells are fabricated to purposefully increase bacteria/surface contact area, while parallel modification of the surface chemistry allows to involve the aspect of surface wettability into bacterial attachment and the resulting antibacterial effectivity. The results exhibit a delicate interplay between bacterial adhesion and the expression of antibacterial properties, where a reduction of bacterial cell viability of up to 15-fold can be achieved for *E. coli* on USP-DLIP surfaces in comparison to smooth Cu surfaces. Thereby, it can be shown how the antimicrobial properties of copper surfaces can be additionally enhanced by targeted surface functionalization.

1. Introduction

The decreasing effectiveness of antibiotics in fighting infectious diseases is a growing problem not only in hospitals and public spaces, but even on the International Space Station, where biofilms might also induce hazardous system failure by biofouling.[1] Current estimates by the World Health Organization (WHO) suggest that the number of deaths caused by multidrug-resistant bacteria worldwide could rise to ten million per year by 2050, if the current trend continues.[2] One way to fight both critical biofilm formation as well as the spreading of infectious diseases is to reduce the survivability of bacteria on technically and frequently touched contact surfaces, by using actively antimicrobial materials like copper (Cu) and silver (Ag) that are not based on pharmaceutical antibiotics. Here, Cu shows great potential for a wider application,[3,4] looking back to a multi-millennial history of repeated rediscovery of its aseptic properties,[5] while it is also involved as a trace element in central processes of human metabolism.[6] In contrast, Ag exhibits toxicity at low quantities,[7] by which dosing has to be precisely adjusted in case of antimicrobial application to avoid a negative immune response.[8] Due to the toxic effect of released Cu ions, bacteria[9,10] as well as viruses[11] are rapidly killed in both dry and moist environments, when adhering to Cu surfaces. The antimicrobial properties of Cu are closely linked to both the amount of ions released and absorbed by the attacked microorganism, whereby specific effects have to be considered when using Cu as an antimicrobial agent: 1) It

---

D. W. Müller, S. Lößlein, Prof. F. Mücklich
Chair of Functional Materials
Department of Materials Science
Saarland University
Saarbrücken 66123, Germany
E-mail: daniel.mueller@uni-saarland.de

The ORCID identification number(s) for the author(s) of this article can be found under https://doi.org/10.1002/admi.202001656.

DOI: 10.1002/admi.202001656

Dr. E. Terriac
Leibniz Institute for New Materials
Dynamic Biomaterials
Saarbrücken 66123, Germany

Dr. K. Brix, Dr. R. Kautenburger
Department of Inorganic Solid-State Chemistry
Elemental Analysis
Saarland University
Saarbrücken 66123, Germany

K. Siems, Prof. R. Moeller
Aerospace Microbiology
Radiation Biology Department
Institute of Aerospace Medicine
German Aerospace Center (DLR e.V.)
Cologne 51147, Germany

has been shown that close contact to the Cu surface is mandatory to achieve a high antimicrobial effectiveness.[12] Since bacteria act as reservoirs for released Cu ions, close contact to the surface might reduce the self-passivation of the copper surfaces through oxide formation, whereby the ion release can be kept constantly high.[13] 2) Cu surfaces might face reduced antimicrobial efficiency in certain cases of corrosion/aging, as its stabilizing oxides CuO and Cu_2O show either less, or similar antimicrobial efficiency as the pure metal, respectively.[14] 3) Bacteria have to be exposed for sometimes up to 3 h to the Cu surface to achieve a sufficient reduction of 99.9% of viable cell count.[11,13] Against this background, it is essential to understand how the antimicrobial capacity of copper-based materials can be both increased and maintained to allow for an efficient adaptation of its functional properties for different kinds of antimicrobial application.

Attempts to enhance the antibacterial properties and especially the speed of bacterial reduction of Cu mainly focused on its application as nanoparticles distributed in liquid or solid matter for several years, similar to Ag.[8,15–20] However, recent results suggest a negligible antibacterial impact of the low particle sizes, as bacterial killing by Cu nanoparticles was actually shown to be mainly linked to Cu ion release rate instead of absorption of the nanoparticles.[21] Another promising approach involves the functionalization of the Cu substrate surfaces, as it has been shown that bacteria respond quite sensitively to chemical and topographic surface properties, where especially wettability and features in the micro- and nanometer range appear to exhibit the highest effect: Using bacterial probe atomic force microscopy, Maikranz et al.[22] were recently able to determine a significantly enhanced adhesion force of *Staphylococcus aureus* on Si substrates, which were chemically modified to exhibit hydrophobic wetting behavior, compared to unmodified hydrophilic Si. Similar behavior was observed in previous studies, where different bacterial strains showed higher adhesion on hydrophobic polymer surfaces compared to hydrophilic glass and metal surfaces.[23,24] In contrast, Lutey et al.[25] detected a stronger reduction of bacterial retention on hydrophobic compared to hydrophilic steel surfaces, where both were treated by ultrashort laser pulses to form laser-induced periodic surface structures (LIPSS). In this context, they claimed that surface topography actually plays a more significant role on bacterial adhesion than wetting properties, as a parallel sample group exhibiting higher topographic feature size showed even increased adhesion in case of *Escherichia coli*.[25] The actual relation between topographic roughness/structuring to bacterial size was indeed proven to play a major role in bacterial adhesion in various studies, where topographic features matching the size of the tested bacteria enhance attachment, while lower feature sizes reduce it, which lead to sometimes contrary effectivity of a specific surface topography against different bacterial strains.[26–31]

Following the approach of topographically induced antimicrobial surface properties further on, a number of natural blueprints like the *Cicada* and *Dragonfly* wings are available where prevention of adhesion alters into mechanically triggered killing of bacteria by piercing and structurally damaging the bacterial cell wall when micro- and nanometer-scaled surface structures exhibit high aspect ratios.[32,33] This functional approach was successfully applied many times, so far, also involving more technically oriented surfaces like, for example, black silicon[34] and oxidic nanostructures on Ti surfaces.[35,36] However, the bactericidal interaction of these types of surfaces is tightly connected to chemically induced attractive forces between bacteria and surface to enable mechanical damage of the cell walls.[32] It was also proven that particular structure types are highly effective for certain bacterial strains, while others may not be affected to a similar extent.[37]

First approaches involving functional surface properties on antimicrobial copper surfaces highlighted the possibility to reduce bacterial transmission by hydrophobic wetting similar to the lotus effect.[18,19] In more recent studies, both Boinovich et al.[38] and Selvamani et al.[39] achieved antibacterial efficiency exceeding the copper-based reference material by the coupled effect of surface roughening and enhanced wettability induced by short pulsed laser treatment. Here, soaking of the deposited liquid into the porous surface structure forces the bacteria against the hierarchically scaled surface features resulting in structural cell membrane damage,[38–40] similar to the killing mechanism of bacteria piercing surface topographies on *Cicada* or *Dragonfly* wings.[32,33] Unfortunately, antibacterial efficiency decreases strongly as soon as the surfaces stabilize at hydrophobic wetting,[38,41] which is most likely linked to the dense superficial layer of CuO initiated during short pulsed laser processing[42] showing reduced antimicrobial capacities due to reduced Cu ion release.[14] Therefore, it is important to include all functional aspects of their antiseptic effectiveness when specifically optimizing antimicrobial copper surfaces in order to maintain the positive effects over a longer period of time.

As former research has proven the impact of functional surface properties on the bacteria/surface interaction,[25,28] a suitable modification of the surface properties might positively affect the antibacterial efficiency of copper surfaces. Here, we introduce a novel methodology to enhance antimicrobial properties of Cu surfaces by topographic as well as chemical modification using ultrashort pulsed direct laser interference patterning (USP-DLIP). By adjusting the pattern parameters in the size of the tested bacterial strain *E. coli* K12 WT(BW25113) to allow for increased bacteria/surface contact area, bacterial viability could be significantly reduced in comparison to smooth reference surfaces. In addition, aging-related alteration of wettability of the patterned surfaces allowed for detailed investigation of the combined influences of molecular surface condition and contact favoring topography on the antimicrobial properties of Cu. The presented results form a suitable basis for the targeted optimization of copper-based antimicrobial contact surfaces by surface functionalization using ultrashort pulsed laser irradiation.

2. Results

2.1. Surface Characterization

The morphology as well as the topographic parameters of surface patterns induced by USP-DLIP on metals have been previously shown to be tailorable by adjusting the fluence in respect to the individual thermal substrate interaction.[43] Here, an

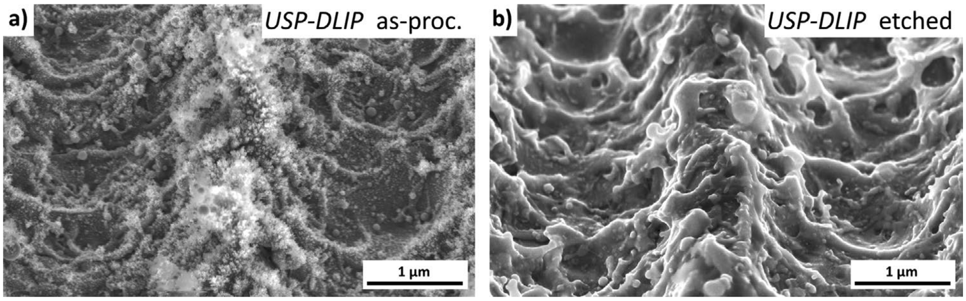

Figure 1. SEM images of pattern peaks on USP-DLIP-processed Cu surfaces representing the individual topographies before and after post-treatment by immersion etching. a) Cu surface processed by 3 J cm^{-2} in as-processed state; b) Cu surface processed by 3 J cm^{-2} after immersion etching using 3 % citric acid.

alteration of the occurring ablation mechanisms by increasing the applied laser fluence has to be considered as well, since it prominently affects both primary pattern and sub-structure parameters. In the case of Cu, ablation behavior changes between spallation and phase explosion, as soon as substrate heating surpasses the threshold temperature of $T_{PE} = 0.9 \times T_{cr}$ with a critical temperature T_{cr} of 7696 K,[44] which is shown to affect both peak geometry as well as surface morphology.[43] To create line pattern geometries befitting the scale of single cells of the tested *E. coli* K12 strain, laser parameters were adjusted to a fluence of 3 J cm^{-2} and pattern periodicity of 3 µm, which lead to ablation in the phase explosion regime on the utilized oxygen free Cu (OF-Cu) material.[43] The resulting surface morphologies both in as-processed as well as post-treated state are illustrated in **Figure 1**.

The USP-DLIP patterns exhibit narrow peaks framed by spatially expanded valleys where material ablation during processing took place. The ratio of the total surface area distributed between the two topographic features corresponds ≈29%/71% (peaks/valleys). In the as-processed state, these surfaces contain flake-like nanostructures, which concentrate mainly on the peak regions, as visible in Figure 1a. In a former study, these sub-structures could be identified as agglomerations of Cu_2O formed by re-deposition of ablated matter during USP-DLIP processing.[45] Post-processing by immersion etching in 3% citric acid was shown to fully remove surface oxide revealing both the metallic substrate material as well as a surface morphology mainly induced by mobilized and rapidly cooled melt fronts resulting from the phase explosion ablation mechanism (see Figure 1b). Consequently, the surface roughness *Rq* is highest in the peak area of the as-processed surfaces, which can be attributed to the flake-like sub-structure, since in case of the immersion etched samples peak roughness almost equals the roughness measured in the valleys, as presented in **Table 1**. In contrast to the peak regions, roughness in the valley areas shows no alteration before and after chemical post-processing.

In USP-DLIP processing, pattern depth was set to 1 µm, which leads to an increase of surface area by factor 1.6 (*S*-value) in comparison to the flat surface topography of polished Cu samples. Minor alteration of the *S*-value in between as-processed and etched surfaces can be attributed to surface roughening induced by the oxidic sub-structures.

2.2. Wettability

The wetting behavior of the different Cu surfaces was measured in relation to the duration of storage in ambient environment starting from 24 h after processing (Week 0) and repeating the measurement every 7 days on a yet unused sample. Wetting behavior of all patterned samples followed a similar trend of rapidly enhancing hydrophobicity during aging within the first week starting from low contact angles (CA) that is followed by leveling at slightly higher CA within 2 more weeks of aging as visible in **Figure 2**. This effect has been reported for Cu surfaces processed by ultrashort pulsed laser irradiation before and can be traced back to a prominent agglomeration of functional carbon groups of C-C/C-H bonding type,[46,47] which

Table 1. Surface parameters of USP-DLIP patterns applied on Cu surfaces in the as-processed and immersion etched state.

	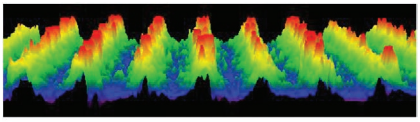 **USP-DLIP as-proc.**	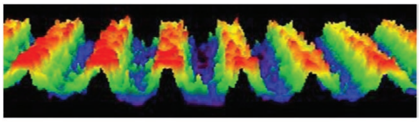 **USP-DLIP etched**
Valley width [µm]	$2.19^{+/-0.12}$	
Depth [µm]	$1.055^{+/-0.084}$	$1.016^{+/-0.058}$
Rq peak [nm]	$188.5^{+/-30.5}$	$97.3^{+/-28.3}$
Rq valley [nm]	$90.3^{+/-12.3}$	$94.2^{+/-12.2}$
S-value	1.61	1.57

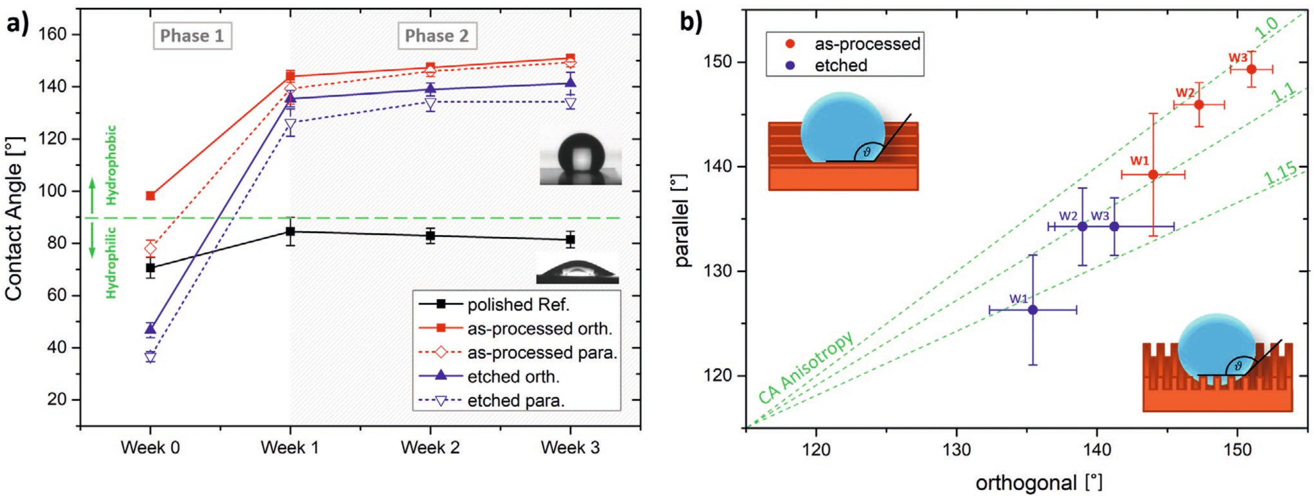

Figure 2. Modification of surface wetting behavior on Cu samples processed by USP-DLIP in relation to aging under ambient atmosphere: a) Aging-related alteration of CA in orthogonal and parallel orientation to the line-like pattern also highlighting the two different phases of either rapid CA increase or CA leveling; b) development of droplet shape anisotropy during atmospheric aging in Phase 2.

was also recently verified for the surfaces investigated in this study.[45] However, the rapid increase in CA has to be emphasized especially for as-processed USP-DLIP surfaces where elevated values around 90° could be detected already 24 h after laser processing (see Figure 2a,b).

The quick attainment of high CA values in the first aging phase indicates a prominent effect of sticking on the droplet spreading by the rough surface topography alongside the chemical modification during aging, which also leads to higher drop shape anisotropy as spreading is less suppressed parallel to the line pattern orientation (compare Figures 2a and 2b). Besides the minor overall CA increase, the second aging phase highlighted in Figure 2a is characterized by further approximation of the CA values measured in orthogonal and parallel orientation of the line patterns leading to reduced drop shape anisotropy. As soon as this approximation reaches a stable level, falling droplets would bounce off the patterned surfaces in horizontal alignment, while they tend to stick on the surface before. This change indicates a transition between Wenzel and Cassie–Baxter like wetting of the surfaces, where sufficient sticking by penetration of the pattern grooves is no longer possible. This assumption is supported by measured values of advancing and receding contact angles that are less than 15° in case of the non-sticking surfaces, while on sticking surfaces they are significantly higher. On as-processed surfaces, this state is reached already after 2 weeks, while 3 weeks of aging are needed in case of immersion etched samples.

The higher CA reached for as-processed surfaces (illustrated in Figure 2a), as well as the low droplet shape anisotropy stabilized already after the second week of aging (see Figure 2b) appear to be linked to the roughness values *Rq* measured on the peak areas of the different surfaces, indicating an enhancing effect of the process-induced flake-like sub-structure on hydrophobic wetting behavior. A similar increase of CA was also observed on micrometer patterns by Allahyari et al.,[48] which was traced back to a more pronounced nanoparticle decoration of the surfaces during processing with higher laser fluence. It has to be noted that the ratio of agglomeration between hydrophilic carbo-oxygen and hydrophobic C-C/C-H bonding species was shown to vary in favor of the latter type on as-processed surfaces during aging in a recent study, while a similar ratio was already stabilized after 24 h of aging on immersion etched samples.[45] Hence, wetting of as-processed surfaces would be expected to show a more pronounced hydrophilic behavior in comparison to etched surfaces slightly after processing from a chemical aspect. However, CA measurements show the opposite, which highlights the significant influence of the difference in surface roughness.

2.3. Antibacterial Properties

2.3.1. Antibacterial Effect of USP-DLIP Processing

The previous results show a prominent impact of the process-related flake-like sub-structure on topographical and wetting properties of USP-DLIP Cu surfaces. To involve the influence of the oxidic sub-structure on antibacterial properties in the investigation of the actual impact of topographic patterning in the scale range of single bacteria cells, wet plating tests were conducted on both as-processed and immersion etched USP-DLIP Cu surfaces. Testing was conducted after 3 weeks of aging of each the USP-DLIP as well as the polished reference surfaces, by which the patterned samples showed distinctive (super-)hydrophobic wetting, while the references were slightly hydrophilic (Figure 2a). A uniform droplet/metal contact area on all samples was achieved by applying the wet plating methodology involving hydrophobic adhesive tape rings described in more detail in Experimental Section.

The results of the wet plating tests illustrated in **Figure 3**a show a considerable reduction of viable bacteria detectable on the different tested Cu surfaces with increasing exposure time. Although the polished Cu reference already shows high antibacterial efficiency against the tested *E. coli* strain, the USP-DLIP surfaces patterned in the scale range of single bacteria

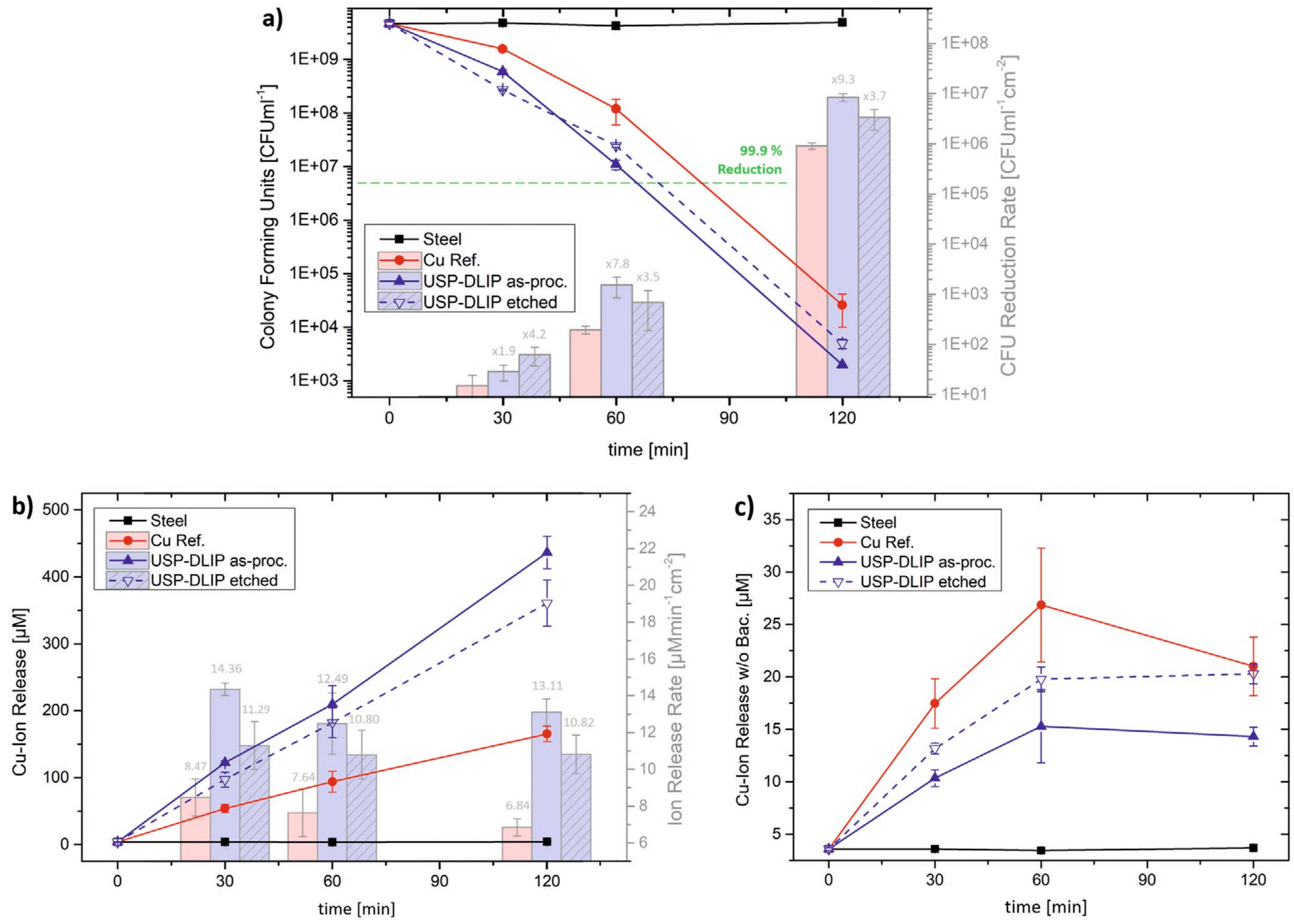

Figure 3. Illustrations showing the results of wet plating tests on USP-DLIP surfaces after 3 weeks of aging: a) CFU reduction of *E. coli* on the different Cu surfaces in relation to an inert steel reference. CFU values normalized to actual surface area show an increase of up to 9.3-fold of USP-DLIP surfaces against polished Cu. b) Cu ion release measured on the individual surfaces alongside CFU reduction. c) Cu Ion release in case of PBS application without bacteria.

cells exceed these values both in the case of as-processed and immersion etched state. While on polished Cu, viable cell count reduction reaches a critical amount of 99.9%[13] after ≈85 min, the same level is reached on the USP-DLIP surfaces already between 60 and 70 min. Surprisingly, the antibacterial properties of as-processed surfaces seem to exceed those of immersion etched samples after 60 min despite a significantly higher amount of surface oxidation,[14,45] whereas the post-treated surfaces dominate in bacterial killing in the first 30 min. Comparison of the colony forming units (CFUs) reduction rate in relation to the smooth Cu reference reveal a 4.5-fold enhancement on immersion etched surfaces in this early phase, which decreases to ≈3.6-fold during further exposure. On as-processed surfaces, this trend is reversed as CFU reduction rate continuously increases up to 9.3-fold of the values measured on the Cu reference after 120 min exposure while starting at 1.9-fold in the first phase.

Parallel examination of the Cu ion release during the experiment, as displayed in Figure 3b, reveals a considerable increase of Cu emission in comparison to the Cu reference on both USP-DLIP surfaces. Despite the presence of a dense oxide layer, ion release of the as-processed surfaces exhibits the highest values, which appears to be the reason for the high CFU reduction observed. Here, the dominance of Cu_2O in the chemical composition of the oxidic sub-structure[45] seems to induce an overall positive effect on the antibacterial properties, as it shows minor reduction of Cu ion release in relation to pure Cu.[14] In combination with the increased surface/area ratio of the flake-like sub-structure expressed by the *Rq* values presented in Table 1, the overall balance appears to be in favor of an additional enhancement of Cu emission and hence antibacterial efficiency on as-processed in comparison to immersion etched USP-DLIP surfaces. The thin superficial layer of CuO that was determined on both surfaces via XPS depth profiling does not appear to affect Cu ion release, here.[45] In addition to the overall increase of Cu emission, the ion release rate of both USP-DLIP surfaces remain on a stable high level after a peak during the first 30 min of exposure, while on the Cu reference ion release rate continuously drops throughout the whole experiment as presented in Figure 3b. It must be emphasized that the discussed CFU reduction rate as well as the Cu ion release rate are directly related to the real surface and include the surface enlargement on USP-DLIP surfaces by involving the S-value. The actual enhancement of CFU reduction determined on immersion etched and as-processed USP-DLIP Cu surfaces in relation to the smooth reference accounts to 6- and 15-fold. Therefore, the observed enhancement of these two properties cannot be attributed to the increase in surface area caused by laser structuring but seems to be related to a beneficial bacteria/surface interaction, instead.

Analyzation of Cu ion release under exposure to PBS without bacteria on the other hand reveals a comparably low Cu emission on all surfaces, as displayed in Figure 3c: Both polished Cu and immersion etched USP-DLIP surfaces reach almost equal emission values after 120 min of exposure, which might be traced back to a similar surface chemistry mainly consisting of a native oxide layer leading to analogous passivation behavior. However, the etched USP-DLIP surfaces show a more leveled gradient of Cu emission also visible in case of the as-processed surfaces, which indicates a slightly different passivation process of the laser processed samples. Cu ion release on as-processed USP-DLIP surfaces stagnates at a considerably lower level related to a higher passivating effect of the process-related Cu_2O layer. Here, the high surface/area ratio of the flake-like oxide topography does not appear to increase Cu ion release in contrast to the behavior observed in the presence of bacteria.

Bacteria have been recently reported to affect Cu ion release during wet plate testing using PBS as they act as drains for Cu ions, which prevents chemical surface passivation by oxide formation and leads to the maintenance of a constantly high corrosion-induced ion emission rate.[13] Against this background, USP-DLIP surface modification appears to additionally enhance this effect leading to a significant increase in Cu ion release in the presence of bacteria compared to flat Cu surfaces, while corrosion resistance is actually enhanced after laser treatment, as indicated by the reduced emission values without bacteria. This especially accounts for as-processed samples exhibiting the highest difference of Cu ion release with and without bacteria as well as the highest killing efficiency.

It has been reported before that dead cells are accumulating more copper in the cytosol than living cells, where membrane damage might induce the increased uptake of copper ions from the medium due to concentration gradients.[41,49] Furthermore, dead cells cannot discard the copper ions via efflux pumps which might also be a factor for increased Cu accumulation inside dead bacterial cells. Thereby it has to be questioned if the increase in antibacterial efficiency and Cu ion release on as-processed surfaces might be affected by additional mechanical damaging of the bacteria by the flake-like oxidic sub-structure, like, for example, on *Cicada* and *Dragonfly* wing surfaces[32,33] and short pulsed laser treated Cu surfaces.[38,39] In order to investigate this more closely, scanning electron microscopy (SEM) imaging of formaldehyde-fixated bacteria after wet plating was conducted to get a hint on the dominant mode of action in bacteria killing on as-processed USP-DLIP surfaces. Since formaldehyde has a low pH value, bacteria fixation is accompanied by intense corrosive attack of the Cu surfaces, especially visible in the peak areas of USP-DLIP patterns, whereby this statement must be made primarily by observing the morphology of adhering bacteria.

The distribution of the bacteria over the surface area shows a clear preference of the valleys for adhesion, as displayed in **Figure 4**a, where peak regions appear to be mainly occupied by greater clusters expanding out of neighboring valleys. Bacteria morphology in the valleys shows no change compared to conspecifics adhering to flat reference surfaces (see Figure 4c), while single bacteria cells attached to peak areas often exhibit a shortened cell body, in contrast. No indication of topography-induced membrane damage is visible on most of the imaged bacteria cells aside of individual specimen that appeared to be collapsed due to leaking (see Figure 4b). However, relating to the low level of visible cell damage which can be observed likewise on polished reference surfaces as visible in Figure 4c, membrane damage is more likely to be caused by interaction with Cu ions, here.[9]

In the light of these investigations, the major mode of action leading to increased antibacterial efficiency of the USP-DLIP surfaces appears to be an amplification of Cu ion induced toxic stress. It was shown that bacteria have mechanisms for sensing if they are attached to a surface which include cell appendages (flagella, pili, curli) or envelope deformations resulting in envelope stress.[50] After sensing the surface attachment, phenotypic changes from the planktonic life form toward a sessile state appear to be initiated, where metabolism alters to now focus on the formation of biofilms.[50] Compared to previous results, these phenotypic changes in relation to surface contact might influence the uptake of ions such as copper ions and hence the efficiency of copper mediated killing, even though the exact mechanisms are not completely understood yet.[12,51]

2.3.2. Influence of Wetting Behavior on Antibacterial Efficiency

The significant enhancement of the antibacterial properties of Cu surfaces by USP-DLIP processing, in parts also despite increased surface oxidation, indicates a pristine bacteria/surface interaction on the laser-induced topographies. In case of ultrashort pulsed laser processing, chemical surface modification also involves an aging related change in wettability, which is also observed here (see Figure 2). As surface wettability is shown to have a huge effect on bacterial adhesion,[22,25] possible changes of bacteria/surface interaction might also lead to an alteration of the antibacterial efficiency of USP-DLIP surfaces. To further investigate this, wet plating tests were conducted on as-processed and immersion etched USP-DLIP samples after 24 h and 3 weeks of aging under ambient atmosphere. With reference to the results presented in Figure 2a, the different aging periods lead to either hydrophilic wetting after 24 h or (super-) hydrophobic wetting after 3 weeks.

Bacterial viability of the tested *E. coli* K12 strain on both Cu reference and the USP-DLIP surfaces aged for 3 weeks show a similar relation like in the previous experiment, exhibiting a predominant antibacterial efficiency of the laser-treated samples with increased bacterial killing rates on as-processed samples after 60 and 120 min exposure (see **Figure 5**a). CFU reduction on USP-DLIP samples after 24 h of aging show a comparable relation between as-processed and immersion etched samples after 120 min, although bacterial viability appears to be less decreased here. However, the etched surfaces of the hydrophilic samples remain more efficient in bacterial killing even after

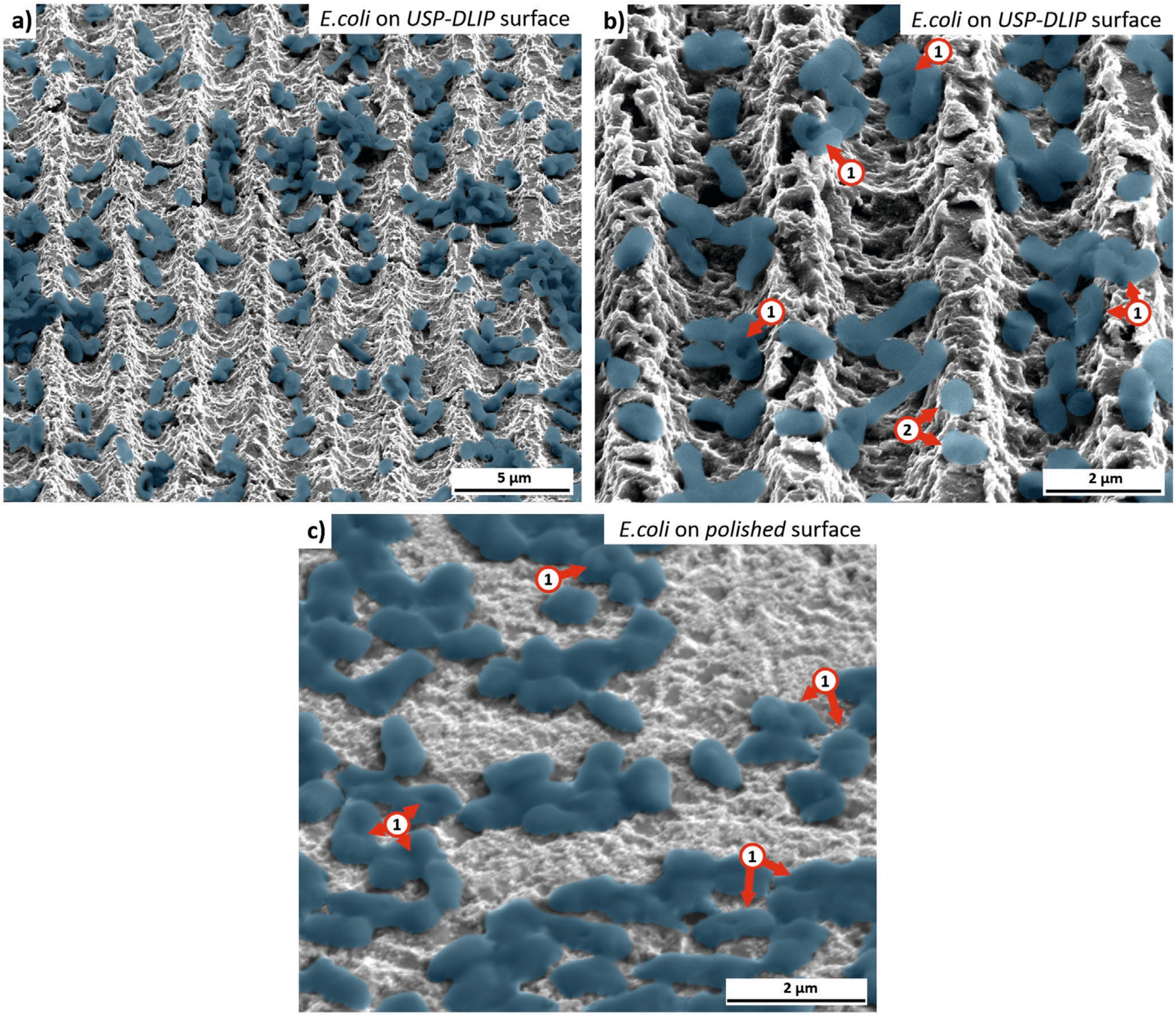

Figure 4. SEM images of *E. coli* (blue) on as-processed USP-DLIP and polished Cu surfaces fixated by 4% formaldehyde. a) Overview showing single bacteria cells and clusters. b) Close-up revealing several collapsed cells (1). Bacteria in peak areas show a more shortened morphology (2) compared to bacteria in valley regions. c) Bacteria on polished Cu surfaces showing similar collapsing (1) compared to cells on USP-DLIP surfaces. The visible surface roughening is due to corrosive attack during fixation after the wet plating experiment and not related to bacteria/surface interaction.

60 min of exposure compared to as-processed surfaces despite significantly lower Cu ion release (compare Figure 5b). In addition, CFU reduction in relation to surface area falls below the values of the copper reference in the first two measuring points on both hydrophilic USP-DLIP surfaces. The slightly decreased overall bacterial viability after 120 min of exposure might be linked rather to increased Cu ion release instead of favorable bacteria/surface interaction, here.

By directly comparing hydrophobic and hydrophilic USP-DLIP samples, a clearly lower antibacterial efficiency can be determined for the hydrophilic laser treated surfaces, although Cu ion release does not deviate noteworthy from the values measured on the hydrophobic surfaces, as displayed in Figure 5b. The almost identical course of the Cu emission on etched samples both after 24 h and after 3 weeks of aging is particularly striking when related to the significantly different CFU reductions measured in parallel. A similar trend can be observed between the different as-processed USP-DLIP surfaces, whereas it must be emphasized that bacterial killing on the hydrophilic as-processed samples still falls below the values of etched hydrophobic samples after 120 min despite significantly higher Cu ion release. This illuminates the grave influence of surface chemistry on the bacteria/surface interaction, which in turn has a significant effect on the antimicrobial effectiveness of Cu surfaces. It appears that both increased Cu ion release and bacteria/surface contact area in case of the as-processed surfaces only lead to an improved efficiency in bacterial killing, if bacteria are facing wetting properties that might be preferential for adhesion. The same relation accounts to immersion etched samples, whereas it has to be noted that Cu

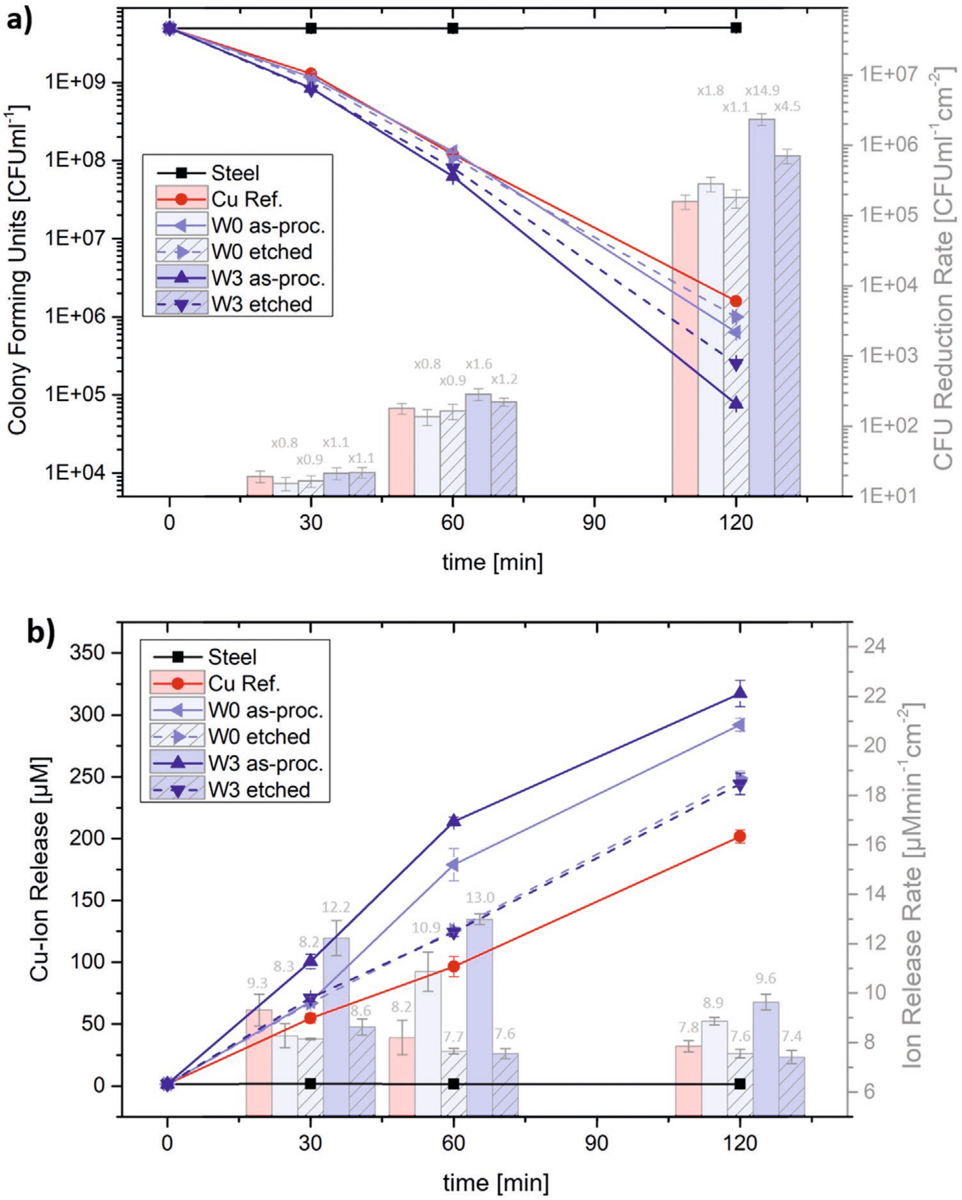

Figure 5. Results of the wet plating tests in correlation to surface wetting properties: a) Reduction of detectable CFU count of *E. coli* K12 during wet plating tests on either hydrophilic (W0) or (super-)hydrophobic (W3) USP-DLIP surfaces in relation to a smooth Cu reference; b) Cu ion release on the different tested surfaces measured alongside CFU reduction.

ion release rate in relation to surface area of both hydrophobic and hydrophilic surfaces run lower than the values of the Cu reference in this experiment. However, the lower ion emission does not appear to affect antibacterial efficiency of the two different surfaces as much as the differences in wetting properties, where hydrophobic etched samples again exhibit increased bacterial killing, even despite low ion release, while the antimicrobial properties of the hydrophilic sample approximate the Cu reference when related to the relative surface.

From these results, the hydrophilic etched samples actually appear to reflect the antibacterial properties of the Cu reference surface transmitted to an increased ratio of surface area, while hydrophobic wetting induces bacteria/surface interaction on the very same surface topography that enhances the antibacterial effect of Cu even without an actual increase of Cu ion release, in contrast. In case of as-processed USP-DLIP surfaces, increased bacteria killing rates in comparison to etched surfaces are linked to a prominently enhanced Cu ion release rate, which however still needs to be coupled with preferential wetting properties to reach its full potential in bacteria killing.

It has to be noted here that bacteria killing as well as Cu ion release showed an overall decrease compared to the previous experiment as visible by comparing Figures 3 and 5, where especially a lower relative CFU reduction on hydrophobic USP-DLIP samples after 60 min of exposure as well as lower Cu ion release on both of the etched surfaces stand out. The underlying reason might be aging of the bacterial culture during storage at 4 °C for 2 months between both experiments leading to a reduced metabolic activity of the bacteria. Warnes and Keevil showed that the DNA of dead cells denatures much more slowly on Cu surfaces, suggesting that metabolic activity is involved in the expression of the initial superoxide-mediated killing.[52] By this, a significant antibacterial effect on Cu surfaces might be delayed in case of reduced metabolic activity.

2.3.3. Bacterial Attachment during Surface Wetting

Aside of the significantly increased Cu ion release, as-processed USP-DLIP surfaces exhibit a characteristic lag phase, where bacterial killing remains below the values of etched samples despite higher Cu ion release. In the case of hydrophobic samples, this phase includes the first sampling time after 30 min, while it seems to still continue after 60 min for hydrophilic samples (compare Figures 3a and 5a). A possible reason for this behavior might be reduced bacteria/surface interaction, for example, by reduced adhesion during the initial contact phase due to the increased nano-scale roughness of surfaces exhibiting the flake-like sub-structure.[28] To investigate bacterial mobility and adhesion alongside propagating surface wetting on the different tested surfaces in situ investigations were conducted by means of confocal laser scanning microscopy (LSM). The specified setup used in the investigation, where the wetting front propagation of PBS with and without bacteria between the tilted sample surface and a glass substrate is imaged, is described in detail in the experimental section. To facilitate a detection of bacteria and their activity in LSM, a strain of *E. coli* (ClearColi BL21(DE3)) expressing green fluorescent protein (GFP) and exhibiting similar properties as *E. coli* K12 WT(BW25113) was utilized. Propagation of the wetting front was recorded in situ by imaging the reflection signal of wetted partitions of the sample surface, while the location of bacteria in relation to the surface and wetting front was recorded through alternating imaging of the fluorescence signal (see **Figure 6**a). In order to determine the surface-specific wetting behavior in relation to the various topographical surface characteristics with parallel inclusion of a possible bacterial influence, the drop spreading velocity of PBS with and without bacteria was measured in parallel orientation of the line patterns. The presented results focus on USP-DLIP samples after 3 weeks of aging as well as the Cu reference, since the pronounced hydrophilic wetting behavior of samples aged for 24 h leads to elevated drop expansion speeds too high to perform imaging of the drop front. Videos of the drop edge propagation alongside bacterial attachment on the different surfaces referring to the images shown in Figure 6 are provided in Supporting Information.

The main influence on bacterial mobility turned out to be sedimentation, through which the majority of bacteria are detected on or in close proximity to the glass substrate below the sample surfaces after 20 min without additional fluid dynamics involved. The additional drag induced by capillary forces in the utilized testing method on the other hand leads to fluid currents by which the planktonic bacteria gets flushed between the sample surface and glass substrate. Most of the bacteria still continue sedimentation, whereas individual cells or clusters in the vicinity of the sample surfaces might adhere in case the attractive surface forces surpass both fluid drag and gravity force.

In case of the smooth topography of the polished Cu reference samples, the propagation speed of the drop edge was too fast to allow for continuous switching between the two signal channels, whereas imaging was either focusing one or the other signal, as illustrated in Figure 6a. Records of the droplet propagation reveal a straight wetting front spreading at a speed of either 10.41 μms^{-1} without and 11.38 μms^{-1} with bacteria. Imaging the fluorescence signal emitted by the bacteria shows a slightly increased density of bacteria along the wetting front, which are getting pushed over the surface without adhering, while bacteria from the subsequent medium flow manage to adhere instead. The adhering units appear to mainly be composed of clusters instead of single cells, especially in closer vicinity to the wetting front pointing out that fluid drag in this area represents a major obstacle to the adhesion of bacteria. However, attractive forces appear to induce interaction between the bacteria and the surface enabling adhesion as soon as fluid drag gets reduced. From the data received, the bacteria approach to the Cu surface appears to be mainly due to currents in the media, while self-motion capability of individual cells might additionally contribute to the final contacting in close vicinity to the substrate.

On USP-DLIP surfaces, imaging using the reflection contrast shows the pattern valleys as bright lines separated by dark areas attributed to the peak regions where surface inclination significantly weakens the signal (illustrated in Figure 6b). In case of immersion etched USP-DLIP surfaces, the wetting front exhibits a slightly less straight progression along the pattern compared to the Cu reference both with and without bacteria. Wetting propagation speed is significantly reduced to ≈159.59 nms^{-1} without and 877.22 nms^{-1} with bacteria that marks out both a decreasing effect of the hydrophobic surface properties on wetting propagation as well as a significant alteration of surface wetting in the presence of bacteria on this type of surface. Adhesion of bacteria mainly takes place in the vicinity of the droplet edge, which is most likely linked to a lower fluid drag due to the lower wetting propagation speed in comparison to the Cu reference. Adhering bacteria occupy both peak and valley regions but are detected more frequently in the valleys (see Figure 6b) indicating a positive effect of concave topography features on bacteria/surface interaction.

Droplet propagation on as-processed samples is significantly reduced compared to both the Cu reference as well as immersion etched samples. Imaging of surfaces exposed to PBS without bacteria exhibits a weak reflection signal alongside a distorted course of the wetting front along the surface pattern. The propagation speed of the drop edge runs at a very slow level of ≈51.61 nms^{-1} until droplet intrusion is finally stopped by pinning of the wetting front a few tens of micrometer after the sample edge, where the water-repellent forces of the hydrophobic surface seem to come into equilibrium with the counteracting forces induced by the measurement setup. As soon as bacteria are present in the medium, droplet propagation is slightly increased to a speed of ≈61.39 nms^{-1} also showing a continuous wetting front expansion although localized pinning is still apparent, as visible in Figure 6c. Planktonic bacteria detected in the medium appear solely in the wetting front

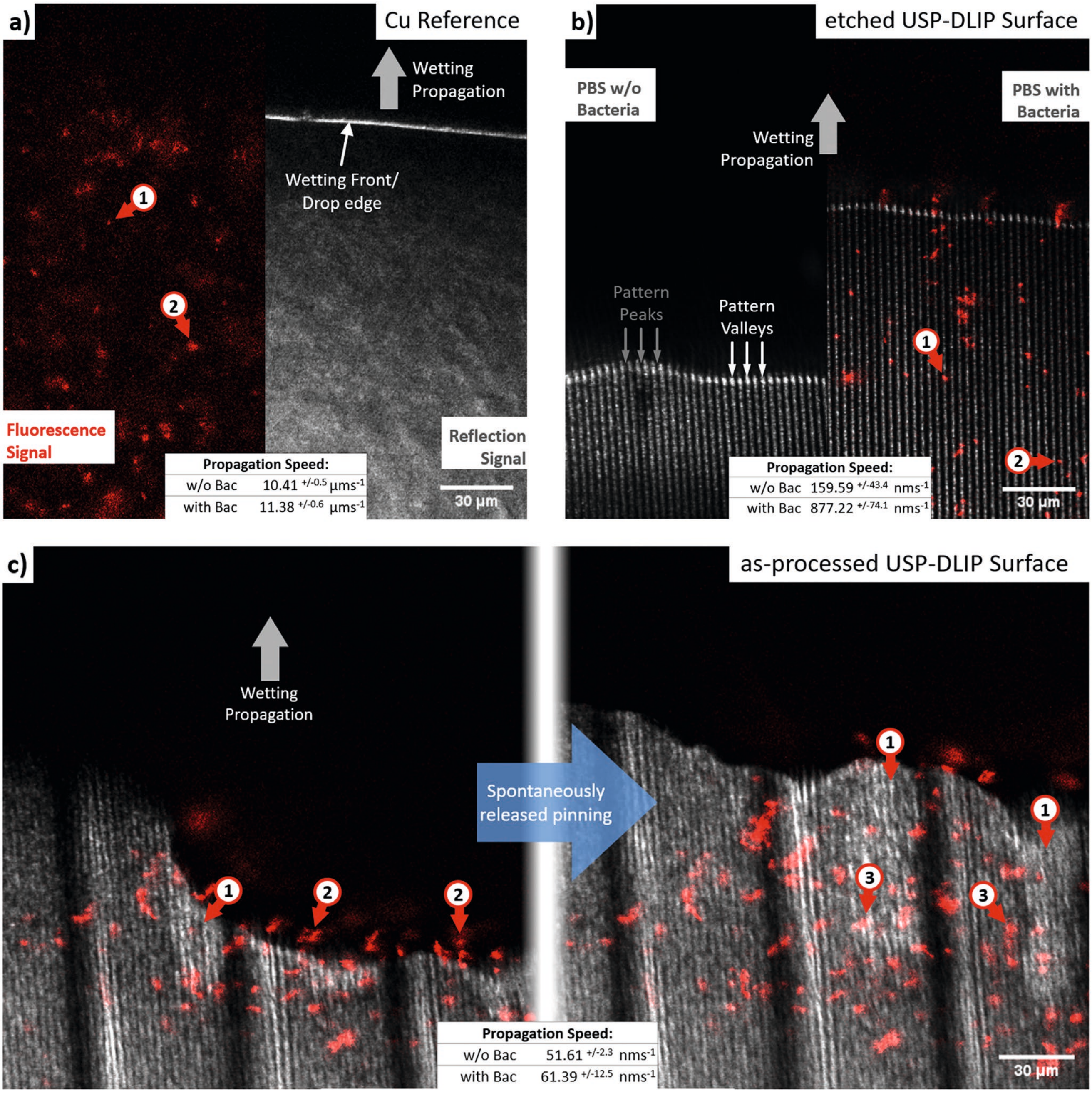

a)

Propagation Speed:	
w/o Bac	10.41 $^{+/-0.5}$ µms^{-1}
with Bac	11.38 $^{+/-0.6}$ µms^{-1}

b)

Propagation Speed:	
w/o Bac	159.59 $^{+/-43.4}$ nms^{-1}
with Bac	877.22 $^{+/-74.1}$ nms^{-1}

c)

Propagation Speed:	
w/o Bac	51.61 $^{+/-2.3}$ nms^{-1}
with Bac	61.39 $^{+/-12.5}$ nms^{-1}

Figure 6. Imaging of the wetting propagation on the different Cu samples: a) wetting front propagation on a smooth Cu reference surface imaged parallel to bacterial attachment by LSM using fluorescent *E. coli* separated in reflection signal showing the substrate surface, as well as the fluorescent signal showing single cells (1) and clusters of bacteria (2). b) Wetting of an immersion-etched USP-DLIP surface by PBS with and without bacteria. Adhering bacteria are found in the valley (1) as well as the peak areas (2). c) Wetting on as-processed USP-DLIP surface showing areas of altered wetting state (1) alongside local pinning and release events related to adhesion of bacteria (3) that were previously floating close to the drop edge (2).

pointing out a rather low fluid drag, but a predominant influence of propagation induced currents near the drop interface on bacteria dispersed within the droplet volume close to the substrate surface. Bacteria leaving the droplet edge directly attach to the substrate surface, where they are fully immobilized leading to adhesion observed solely along the wetting front. In case of single bacteria cells and smaller clusters, attached bacteria are predominantly located within the pattern valleys, while larger clusters also manage to cover peak areas. However, initial attachment points of these clusters are also located within the valley regions indicating preferential bacterial adhesion in these areas, which might be attributed to the difference in nanoscaled surface roughness *Rq* in between the two areas.[28] These observations correspond very well with the distribution of the bacteria visible in Figure 4a,b. It has to be emphasized that in several events a spontaneous release of localized pinning could be observed in relation to the presence of bacteria close to the drop edge, which appeared to contribute to further propagation of surface wetting (displayed in Figure 6c). Here, attractive forces between patterned surface and bacteria seem to form an additional antipole to the hydrophobic properties, which shifts the balance of forces at the wetting front in favor of a progressive wetting. Alongside these events, changes in the reflection contrast of the valley areas point out localized changes of the wetting state.

Considering these observations in the in situ LSM investigations, a clear influence of specific surface features on bacterial adhesion and surface wetting on the different examined surfaces can be determined:

On as-processed USP-DLIP surfaces, wetting involving bacteria is expressed less by an increase in wetting propagation speed but moreover by the destabilization of localized droplet pinning. Wetting without bacteria appears to stabilize in a Cassie–Baxter state, where the pattern valleys are not penetrated by the liquid and contribute to a pinning of the drop edge. Once bacteria are involved, this state gets destabilized allowing both medium as well as bacteria to enter the valleys, which also reduces the previously observed pinning in the peak areas. Bacteria are predominantly attached to valley regions pointing out a low suitability of the peak regions for adhesion, whereas bacterial attachment can be assumed to be locally suppressed until full surface wetting is achieved. In fact, previous literature has already pointed out the repelling effect of surface topographies exhibiting feature sizes smaller than the scale of single bacteria cells.[28,31] These results complement the SEM observations discussed earlier which are illustrated in Figure 4.

On immersion etched surfaces, instead, wetting observed via LSM appears to exhibit a low stability of a Cassie–Baxter and rather the appearance of a Wenzel state, which is further enhanced in the presence of bacteria. These examinations fit to the late change between sticking and bounce off behavior during wetting tests involving falling droplets after 3 weeks of atmospheric aging, as discussed earlier. In contrast to the as-processed surfaces, bacteria attach to pattern peaks more often showing a higher suitability for adhesion of these regions after post-processing.

In that regard, the deviation of the overall wetting behavior and bacterial adhesion between the two types of USP-DLIP samples appears to be mainly contributable to the filigree morphology of the flake-like sub-structure found on the peaks of as-processed surfaces effecting reduced wettability[48] and bacterial adhesion[28] due to increased nano-scale roughness. Alongside the preliminary Cassie–Baxter wetting state, especially the suppressed adhesion of bacteria on the rough surface peaks in the early state of surface wetting on as-processed USP-DLIP surfaces appear to be the reason for the lower bacterial killing rates measured after 30 min in the wet plating experiments in relation to immersion etched surfaces even despite higher Cu ion release rates. This illustrates the necessity of a direct and pronounced contact between bacteria and Cu surface, as already postulated by Mathews et al.[12] to enable a strong expression of antibacterial properties. In this context, the reduced bacterial killing on hydrophilic USP-DLIP surfaces, as displayed in Figure 5a, might be attributed to lower adhesion forces between bacteria and the surface, similar to the results of Maikranz et al.[22]. This is particularly evident in the prolonged lag phase of hydrophilic as-processed samples, where increased surface roughness and reduced adhesion forces between bacteria and surface appear to negatively interact. However, the exact mechanism of bacterial adhesion alongside altered sensitivity against Cu ions has to be clarified more precisely. Contrary to the *S. aureus* used in ref. [22], *E. coli* has a significantly lower hydrophobicity of the cell surfaces, which might be reflected in a weaker surface adhesion.[53] Therefore, preceding protein attachment preferring hydrophobic surfaces could also play a role here.[54]

3. Conclusion

We were able to show that surface functionalization via USP-DLIP treatment has a significant effect on the antibacterial properties of Cu surfaces. The results allow for a better understanding of the role of bacteria/surface interaction in the expressed Cu sensitivity of bacteria as well as an improved design of contact surfaces to enhance antibacterial properties of copper surfaces:

- Reduction of viable cell count of *E. coli* on Cu surfaces in wet conditions is enhanced by USP-DLIP patterning in the scale range of single bacteria cells leading to a relative increase of up to ≈ 6-fold in case of post-processed and 15-fold in case of as-processed surfaces. The enhancement of killing efficiency surpasses the capacities of sole enlargement of available surface area indicating a beneficial effect on bacteria/surface interaction, which induces higher sensitivity of the bacteria against Cu intoxication.
- Cu ion release is increased in the presence of bacteria, which especially accounts for USP-DLIP surfaces in as-processed condition. In contrast, Cu emission falls below the smooth Cu reference in exposure to PBS without bacteria. Hence, increased Cu ion release can be directly connected to bacterial Cu draining which was previously reported,[13] however with a much stronger effect on the laser structured surfaces. As-processed USP-DLIP surfaces exhibit the greatest differences in Cu ion release indicating an opposite corrosion behavior of the oxidic flake-like substructure with and without bacteria.
- Although increased Cu ion release exhibits a beneficial influence on antibacterial efficiency, the reduction of viable cell count appears to be influenced to a larger extent through quality and quantity of contact to the surface. This predominantly involves surface wettability, where hydrophilic USP-DLIP surfaces exhibit significantly lower effectiveness against *E. coli* compared to hydrophobic USP-DLIP surfaces, even despite higher Cu ion release.
- Furthermore, reduced bacterial attachment on the peaks of the as-processed samples was observed compared to immersion etched samples, indicating a repelling effect of the nanoscale substructure.[28]. Together with a lower bacterial contact in the initial phase of the wet plating experiments, reduced bacterial killing on these surfaces can be observed despite high Cu ion emission. This effect is particularly noticeable on the hydrophilic sample, which further illustrates the strong influence of

topographic and chemical surface properties on the antibacterial effectiveness of Cu surfaces.

The presented results show the possibilities of targeted surface functionalization to increase the antibacterial effectiveness of Cu contact surfaces to the same extent as they illustrate the necessity of a precise knowledge of the dominant influencing factors in order to achieve a maximum increase in efficiency. By this, they allow for a more targeted approach to the design of copper-based antibacterial surfaces that increases their effectivity beyond the toxic effect of emitted Cu ions itself.

4. Experimental Section

Sample Preparation: Sheets of OF-CU (>99.95%) (Wieland) and AISI 304 stainless steel (Brio) of the dimensions 10 × 25 mm^2 were mirror-polished on an automated TegraPol-21 system (Struers). Shares of the polished Cu samples as well as the steel samples were deducted for their later use as references in the wet plating experiments.

The remaining Cu samples were laser processed by USP-DLIP utilizing a Ti:Sapphire Spitfire laser system (Spectra Physics) emitting a pulse duration of $t_p = 100$ fs (full width at half maximum) at a centered wavelength λ of 800 nm and 1 kHz pulse frequency. Two beam laser interference was achieved by using the optical setup previously introduced in ref. [43] consisting of a diffractive optical element to divide and a lens system to overlap the individual beams on the sample surfaces. The periodicity p of the generated pattern in correlation to the incident angle θ can be calculated by Equation (1) utilizing the analogy of the beam paths in the interference setup to the setup of the Fresnel mirror test:

$$p = \frac{\lambda}{2\tan(\theta)} \qquad (1)$$

Planar patterning was conducted in continuous pulsing mode at a fluence of 3 J cm^{-2} and 90% pulse overlap. The periodicity of the applied patterns was set to 3 µm, by which the achieved topography closely fits the bacterial size of the tested *E. coli* K12 strain. A batch of samples was subsequently selected to undergo immersion etching in 3% citric acid for 40 s in an ultrasonic bath to remove process-induced oxidic substructures on the pattern surfaces.[45]

Wetting Tests: CA measurements were conducted to examine aging-related alterations of surface wettability of the different sample surfaces by means of a Drop Shape Analysator DSA 100 (Krüss GmbH) using distilled water at a fixed droplet volume of 3 µL. Due to the anisotropic surface patterns, the CA was detected in orthogonal and parallel orientation to the pattern on the USP-DLIP samples. In a parallel experiment, falling droplet tests are conducted by releasing the droplets at a height of 100 mm above horizontally aligned USP-DLIP treated surfaces leading to either sticking or bouncing off.

For the investigation of wetting front propagation and bacterial adhesion LSM experiments were performed on an inverted Zeiss LSM 880 with a 40× Fluar N.A 1.30 oil immersion objective. The patterned (or smooth for reference) Cu sample was held upside down in a glass-bottom dish by means of a sticking 300 µm thick spacer. The topography of the surface was imaged in reflection mode using a 20% reflection/80% transmission beam splitter and the detection of bacteria was achieved in the 530 nm range of the emitted light (emission of GFP). For both signal, 488 nm laser light was used as excitation.

The fluorescent bacteria are derived from the *E. coli* strain ClearColi BL21(DE3) from Lucigen. The strain was transduced with a pBAD-sfGFP plasmid in order to produce super-folder Green Fluorescent GFP (sfGFP) in the presence of arabinose. For each experiment, cells were freshly thawed 24 h, and arabinose was added 2 h before image acquisition. Short before imaging, the bacteria were diluted in PBS similar to the wet plating tests. A drop of 500 µL of the solution was deposited in close proximity of the metal sample and image acquisition was started immediately with a frequency of one image per 3 s. Capillary forces as well as fluid pressure would lead to a penetration of the solution into the narrow space between sample and glass surface due to hydrophilic wetting properties of the glass substrate exhibiting a CA of 62°. The experimental setup is schematically illustrated in **Figure 7**.

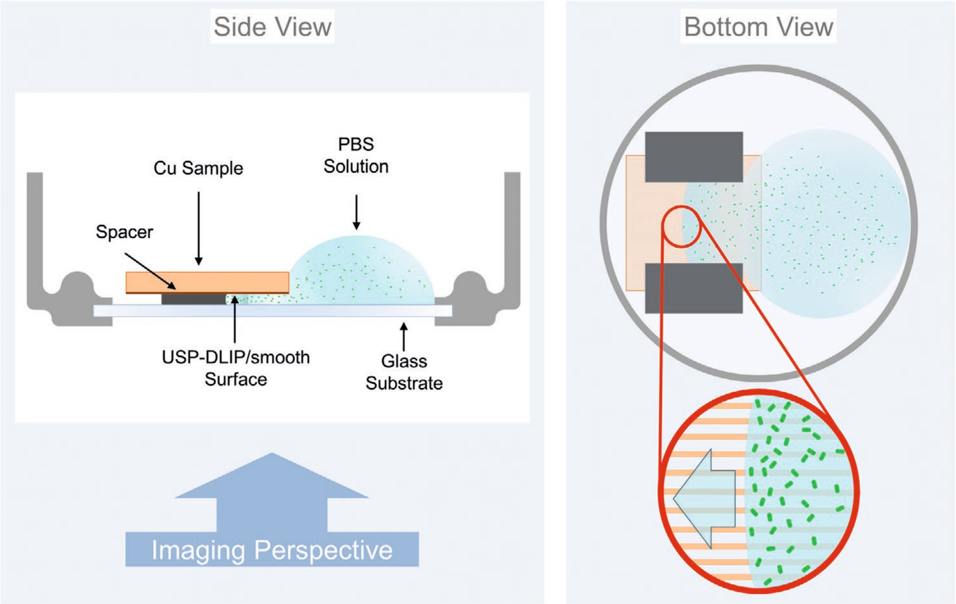

Figure 7. Schematic illustration of the experimental setup used to investigate wetting propagation on the smooth and USP-DLIP-processed Cu surfaces. Cu samples are mounted upside down to allow for imaging in the inverse LSM forming a cavity of 300 µm spacing with the glass substrate of the sample holder below. Droplets of PBS solution with and without bacteria that are applied aside of the copper sample penetrate the cavity with a wetting front speed related to the wettability of the sample surface.

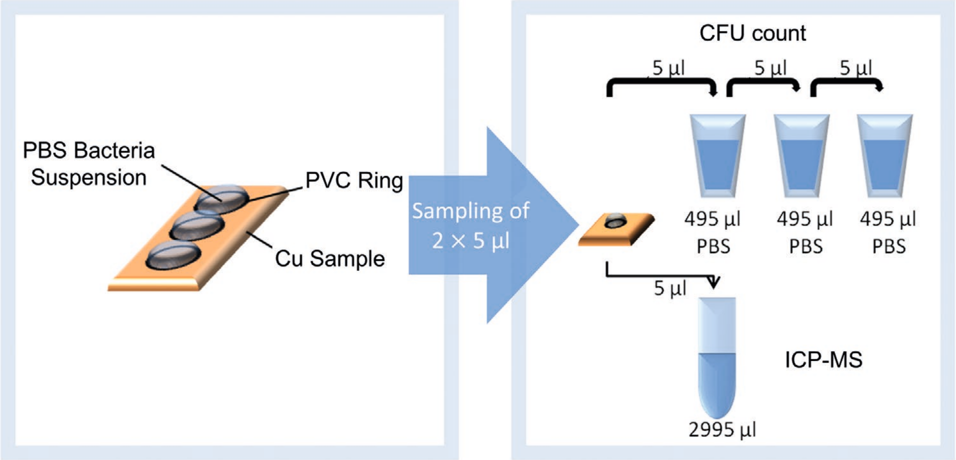

Figure 8. Schematic illustration of the wet plate testing setup used in the experiments involving surfaces of different wetting properties utilizing rings of polyvinyl chloride (PVC) adhesive tape to predefine the exposed surface area. Both colony forming units (CFU) and Cu ion released are measured in parallel.

Antibacterial Properties: *E. coli* K12 WT(BW25113) was cultured following the protocol of Molteni et al.[55] by aerobic overnight growth in Lysogeny broth (LB) medium at 37 °C with a shaking speed of 220 rpm. The stationary cells were collected from 5 mL culture medium by centrifugation for 15 min at 5000 × *g*, followed by three consecutive PBS washing steps involving the same centrifugation parameters. The final bacteria testing solution (BTS) was gained by resuspension in 5 mL of PBS. The initial average cell count following this routine ranges from 3×10^9–5×10^9 CFU mL^{-1}. Bacteria of the *E. coli* K12 WT(BW25113) strain were provided on Agar plates by the group of Prof. Rolf Müller from the Helmholtz Centre of Infection Research, Saarbrücken and stored at 4 °C.

Following the wet plating method, three droplets of 40 µL of the BTS were applied on each sample stored in water saturated environment from which two doses of each 5 µL were withdrawn after individual exposure intervals (30 min, 60 min, and 120 min). Resuspension of settled bacteria was conducted by vigorous pipetting where a parallel orientation of the tip to the surface pattern avoids shadowing of the bacteria attached in the pattern valleys. The cell count of bacteria was determined via the standard plate count method, whereby one of the 5 µL doses was serially diluted in PBS and spread on LB agar plates, which were incubated at 37 °C and 80% moisture overnight to enable counting of the remaining CFUs after the individual exposure intervals. The second 5 µL dose was diluted 600-fold in 0.1% HNO_3 and used to determine the corresponding Cu ion concentrations in the BTS by inductively coupled plasma mass spectrometry (Agilent 7500cx).

The wet plating experiments aimed to compare the antibacterial properties of USP-DLIP patterned samples to polished flat Cu surfaces, as well as patterned samples with different surface characteristics involving both topography and chemistry. To allow for comparability in between samples of different wetting properties, a novel wet plating routine was developed where the contact area between BTS and the sample surface was predefined by rings of polyvinyl chloride (PVC) adhesive tape exhibiting an inner diameter of 5 mm. Due to their hydrophobic wetting behavior, the PVC rings prevent the droplets from further expansion in case of hydrophilic sample surfaces, while they can be used to expand the droplet over the whole area inside the rings in case of (super-) hydrophobic surfaces using the adhesive tape as anchorage for the edges of the droplets, as schematically illustrated in **Figure 8**.

Surface Characterization: Characterization of the topographical properties of the differently processed USP-DLIP Cu samples was conducted by means of both confocal laser scanning microscopy (CLSM) utilizing a LEXT OLS4100 3D Measuring Laser Microscope by Olympus and SEM (Helios 600 by FEI). The CLSM measurements were done utilizing the 50× lens and altering the digital post-magnification between 2× and 6× at a laser wavelength of 405 nm and focusing the detection of topographic surface parameters including, for example, roughness and surface/projected area ratio (S-value). SEM imaging was conducted in secondary electron (SE) contrast mode while the samples were tilted 52° degree to allow for better visualization of topographical features. The acceleration voltage was set to either 10 or 5 kV at a current of 0.86 pA. To allow investigation of bacterial cell morphology alongside the detection of preferential contacting areas on the surface, samples that underwent wet plating for 60 min were immersed in 4% formaldehyde for 12 h to assure stabilization of the cell shape in vacuum followed by immersion in sterilized distilled water for another 10 min to wash off remnants from PBS.

Supporting Information

Supporting Information is available from the Wiley Online Library or from the author.

Acknowledgements

The authors would like to thank Prof. Rolf Müller and his group from the Helmholtz Institute for Pharmaceutical Research Saarland (HIPS) for providing the *E. coli* K12 strain used in the wet plating experiments, as well as Shardul Bhusari from the Leibniz Institute for New Materials (INM) for his help in cultivating the fluorescent *E. coli* bacteria culture. The authors also want to acknowledge the help of the INM by enabling access to their LSM facility. This work was funded by the German Research Foundation (DFG) within the project “Controlled bacterial interaction to increase the antimicrobial efficiency of copper surfaces” (project number 415956642) and SFB1027 Collective Research Center as well as the German Aerospace Center – Space Administration (DLR) within the project “Investigation of antimicrobial metal surfaces under space conditions—An effective strategy to prevent microbial biofilm formation“ (project number 50WB1930). K.S. and R.M were supported by the DLR grant FuE-Projekt “ISS LIFE” (Programm RF-FuW, TP 475) while their contributions are part of the ESA project BIOFILMS (No. ESA-HSO-ESR-ILSRA-2014-054).

Open access funding enabled and organized by Projekt DEAL.

Conflict of Interest

The authors declare no conflict of interest.

Keywords

antimicrobial copper surfaces, laser surface structuring, ultrashort pulsed direct laser interference patterning

Received: September 21, 2020
Revised: November 22, 2020
Published online: December 9, 2020

---

[1] L.-Y. Sobisch, K. M. Rogowski, J. Fuchs, W. Schmieder, A. Vaishampayan, P. Oles, N. Novikova, E. Grohmann, *Front. Microbiol.* **2019**, *10*, 543.

[2] E. P. Lesho, M. Laguio-Vila, *Mayo Clin. Proc.* **2019**, *94*, 1040.

[3] M. Colin, E. Charpentier, F. Klingelschmitt, C. Bontemps, C. De Champs, F. Reffuveille, S. C. Gangloff, *J. Hosp. Infect.* **2020**, *104*, 283.

[4] E. A. Bryce, B. Velapatino, H. A. Khorami, T. Donnelly-Pierce, T. Wong, R. Dixon, E. Asselin, *Biointerphases* **2020**, *15*, 011005.

[5] J. J. Hostýnek, H. I. Maibach, *Copper and the Skin*, Informa Healthcare, New York **2006**.

[6] S. Krupanidhi, A. Sreekumar, C. B. Sanjeevi, *Indian J. Med. Res.* **2008**, *128*, 448.

[7] S. Kim, J. E. Choi, J. Choi, K. H. Chung, K. Park, J. Yi, D. Y. Ryu, *Toxicol. In Vitro* **2009**, *23*, 1076.

[8] M. Croes, S. Bakhshandeh, I. A. J. van Hengel, K. Lietaert, K. P. M. van Kessel, B. Pouran, B. C. H. van der Wal, H. C. Vogely, W. Van Hecke, A. C. Fluit, C. H. E. Boel, J. Alblas, A. A. Zadpoor, H. Weinans, S. A. Yavari, *Acta Biomater.* **2018**, *81*, 315.

[9] G. Grass, C. Rensing, M. Solioz, *Appl. Environ. Microbiol.* **2011**, *77*, 1541.

[10] M. Hans, S. Mathews, F. Mücklich, M. Solioz, *Biointerphases* **2016**, *11*, 018902.

[11] N. van Doremalen, T. Bushmaker, D. H. Morris, M. G. Holbrook, A. Gamble, B. N. Williamson, A. Tamin, J. L. Harcourt, N. J. Thornburg, S. I. Gerber, J. O. Lloyd-Smith, E. de Wit, V. J. Munster, *N. Engl. J. Med.* **2020**, *382*, 1564.

[12] S. Mathews, M. Hans, F. Mücklich, M. Solioz, *Appl. Environ. Microbiol.* **2013**, *79*, 2605.

[13] J. Luo, C. Hein, J. Ghanbaja, J. Pierson, F. Mücklich, *Micron* **2019**, *127*, 102759.

[14] M. Hans, A. Erbe, S. Mathews, Y. Chen, M. Solioz, F. Mücklich, *Langmuir* **2013**, *29*, 16160.

[15] C. Sun, Y. Li, Z. Li, Q. Su, Y. Wang, X. Liu, *J. Nanomater.* **2018**, *2018*, 6546193.

[16] J. Al-Haddad, F. Alzaabi, P. Pal, K. Rambabu, F. Banat, *Clean Technol. Environ. Policy* **2020**, *22*, 269.

[17] A. Ananth, S. Dharaneedharan, M. S. Heo, Y. S. Mok, *Chem. Eng. J.* **2015**, *262*, 179.

[18] A. Tripathy, A. Kumar, S. Sreedharan, G. Muralidharan, A. Pramanik, D. Nandi, P. Sen, *ACS Biomater. Sci. Eng.* **2018**, *4*, 2213.

[19] E. Ozkan, C. C. Crick, A. Taylor, E. Allan, I. P. Parkin, *Chem. Sci.* **2016**, *7*, 5126.

[20] M. Polívková, T. Hubáček, M. Staszek, V. Švorčík, J. Siegel, *Int. J. Mol. Sci.* **2017**, *18*, 419.

[21] C. A. P. Bastos, N. Faria, J. Wills, P. Malmberg, N. Scheers, P. Rees, J. J. Powell, *NanoImpact* **2020**, *17*, 100192.

[22] E. Maikranz, C. Spengler, N. Thewes, A. Thewes, F. Nolle, P. Jung, M. Bischoff, L. Santen, K. Jacobs, *Nanoscale* **2020**, *12*, 19267.

[23] M. C. M. van Loosdrecht, W. Norde, J. Lyklema, A. J. B. Zehnder, *Aquat. Sci.* **1990**, *52*, 103.

[24] J. H. Pringle, M. Fletcher, *Appl. Environ. Microbiol.* **1983**, *45*, 811.

[25] A. H. A. Lutey, L. Gemini, L. Romoli, G. Lazzini, F. Fuso, M. Faucon, R. Kling, *Sci. Rep.* **2018**, *8*, 10112.

[26] C. Díaz, M. C. Cortizo, P. L. Schilardi, S. S. G. G. de, M. M. A. F. L. de, *Mater. Res.* **2007**, *10*, 11.

[27] A. K. Epstein, A. I. Hochbaum, P. Kim, J. Aizenberg, *Nanotechnology* **2011**, *22*, 494007.

[28] R. Helbig, D. Günther, J. Friedrichs, F. Rößler, A. Lasagni, C. Werner, *Biomater. Sci.* **2016**, *4*, 1074.

[29] D. Guenther, J. Valle, S. Burgui, C. Gil, C. Solano, A. Toledo-Arana, R. Helbig, C. Werner, I. Lasa, A. F. Lasagni, in *SPIE 9736, Laser-based Micro- and Nanoprocessing X*, SPIE, Bellingham, WA **2016**.

[30] K. Schwibbert, F. Menzel, N. Epperlein, J. Bonse, J. Krüger, *Materials* **2019**, *12*, 3107.

[31] A. Peter, A. H. A. Lutey, S. Faas, L. Romoli, V. Onuseit, T. Graf, *Opt. Laser Technol.* **2020**, *123*, 105954.

[32] A. Tripathy, P. Sen, B. Su, W. H. Briscoe, *Adv. Colloid Interface Sci.* **2017**, *248*, 85.

[33] A. Elbourne, R. J. Crawford, E. P. Ivanova, *J. Colloid Interface Sci.* **2017**, *508*, 603.

[34] S. Ghosh, S. Niu, M. Yankova, M. Mecklenburg, S. M. King, J. Ravichandran, R. K. Kalia, A. Nakano, P. Vashishta, P. Setlow, *Sci. Rep.* **2017**, *7*, 17768.

[35] T. Sjöström, A. H. Nobbs, B. Su, *Mater. Lett.* **2016**, *167*, 22.

[36] J. V. Wandiyanto, T. Tamanna, D. P. Linklater, V. K. Truong, M. Al Kobaisi, V. A. Baulin, S. Joudkazis, H. Thissen, R. J. Crawford, E. P. Ivanova, *J. Colloid Interface Sci.* **2020**, *560*, 572.

[37] J. Hasan, H. K. Webb, V. K. Truong, S. Pogodin, V. A. Baulin, G. S. Watson, J. A. Watson, R. J. Crawford, E. P. Ivanova, *Appl. Microbiol. Biotechnol.* **2013**, *97*, 9257.

[38] L. B. Boinovich, V. V. Kaminsky, A. G. Domantovsky, K. A. Emelyanenko, A. V. Aleshkin, E. R. Zulkarneev, I. A. Kiseleva, A. M. Emelyanenko, *Langmuir* **2019**, *35*, 2832.

[39] V. Selvamani, A. Zareei, A. Elkashif, M. K. Maruthamuthu, S. Chittiboyina, D. Delisi, Z. Li, L. Cai, V. G. Pol, M. N. Seleem, R. Rahimi, *Adv. Mater. Interfaces* **2020**, *7*, 1901890.

[40] A. M. Emelyanenko, V. V. Kaminskii, I. S. Pytskii, A. G. Domantovsky, K. A. Emelyanenko, A. V. Aleshkin, L. B. Boinovich, *Bull. Exp. Biol. Med.* **2020**, *168*, 488.

[41] A. M. Emelyanenko, I. S. Pytskii, V. V. Kaminsky, E. V. Chulkova, A. G. Domantovsky, K. A. Emelyanenko, V. D. Sobolev, A. V. Aleshkin, L. B. Boinovich, *Colloids Surf., B* **2020**, *185*, 110622.

[42] L. B. Boinovich, K. A. Emelyanenko, A. G. Domantovsky, E. V. Chulkova, A. A. Shiryaev, A. M. Emelyanenko, *Adv. Mater. Interfaces* **2018**, *5*, 1801099.

[43] D. W. Müller, T. Fox, P. G. Grützmacher, S. Suarez, F. Mücklich, *Sci. Rep.* **2020**, *10*, 3647.

[44] S. Y. Wang, Y. Ren, C. W. Cheng, J. K. Chen, D. Y. Tzou, *Appl. Surf. Sci.* **2013**, *265*, 302.

[45] D. W. Müller, A. Holtsch, S. Lößlein, C. Pauly, C. Spengler, S. Grandthyll, K. Jacobs, F. Mücklich, F. Müller, *Langmuir* **2020**, *36*, 13415.

[46] A. M. Kietzig, M. N. Mirvakili, S. Kamal, P. Englezos, S. G. Hatzikiriakos, *J. Adhes. Sci. Technol.* **2011**, *25*, 2789.

[47] J. Long, M. Zhong, P. Fan, D. Gong, H. Zhang, *J. Laser Appl.* **2015**, *27*, S29107.

[48] E. Allahyari, J. J. J. Nivas, S. L. Oscurato, M. Salvatore, G. Ausanio, A. Vecchione, R. Fittipaldi, P. Maddalena, R. Bruzzese, S. Amoruso, *Appl. Surf. Sci.* **2019**, *470*, 817.

[49] M. Köller, N. Ziegler, C. Sengstock, T. A. Schildhauer, A. Ludwig, *Biomed. Phys. Eng. Express* **2018**, *4*, 055002.

[50] T. E. P. Kimkes, M. Heinemann, *FEMS Microbiol. Rev.* **2020**, *44*, 106.

[51] R. Nandakumar, C. E. Santo, N. Madayiputhiya, G. Grass, *BioMetals* **2011**, *24*, 429.

[52] S. L. Warnes, C. W. Keevil, *Appl. Environ. Microbiol.* **2011**, *77*, 6049.

[53] V. Kochkodan, S. Tsarenko, N. Potapchenko, V. Kosinova, V. Goncharuk, *Desalination* **2008**, *220*, 380.

[54] G. B. Sigal, M. Mrksich, G. M. Whitesides, *J. Am. Chem. Soc.* **1998**, *120*, 3464.

[55] C. Molteni, H. K. Abicht, M. Solioz, *Appl. Environ. Microbiol.* **2010**, *76*, 4099.

ADVANCED
MATERIALS
INTERFACES

Supporting Information

for *Adv. Mater. Interfaces,* DOI: 10.1002/admi.202001656

Increasing Antibacterial Efficiency of Cu Surfaces by targeted Surface Functionalization via Ultrashort Pulsed Direct Laser Interference Patterning

Daniel W. Müller, Sarah Lößlein, Emmanuel Terriac, Kristina Brix, Katharina Siems, Ralf Moeller, Ralf Kautenburger, and Frank Mücklich*

Supporting Information

Increasing Antibacterial Efficiency of Cu Surfaces by targeted Surface Functionalization via Ultrashort Pulsed Direct Laser Interference Patterning (USP-DLIP)

Daniel W. Müller*, Sarah Lößlein, Emmanuel Terriac, Kristina Brix, Katharina Siems, Ralf Moeller, Ralf Kautenburger, Frank Mücklich

Aside of the images shown in **Figure 6** in the main article, videos where recorded during LSM investigation of the wetting propagation of PBS with and without fluorescent Escherichia coli on the different Cu surfaces, which are accessible here. Following the order displayed in **Figure 6**, the videos are arranged according to the following parameter sequence:

Video 1: Wetting of smooth Cu_Fluorescence Signal

Video 2: Wetting of smooth Cu_Reflection Signal

Video 3: Wetting of USP-DLIP surface immersion etched without Bacteria

Video 4: Wetting of USP-DLIP surface immersion etched with Bacteria

Video 5: Wetting of USP-DLIP surface as-processed without Bacteria

Video 6: Wetting of USP-DLIP surface as-processed with Bacteria

Due to recording times, where single images on the surfaces could be taken every 3 seconds in single channel (fluorescence or reflection signal) and every 10 seconds in dual channel imaging mode (fluorescence and reflection), the recorded processes on the surfaces are displayed in fast motion in the videos (which are set to a frame rate of one image per second). The real duration of the individual processes shown in the videos as well as the utilized imaging frequency (recording time, showing the real temporal distance between the single images) are provided in **Table S1**.

Table S1.

Parametrization of imaging during LSM investigation.

Video Nr.	Real duration [s]	Image frequency [s]
1	27	3
2	21	3
3	813	3
4	520	10
5	498	3
6	3320	10

Paper III:

Increasing Antibacterial Efficiency of Cu Surfaces by targeted Surface Functionalization via Ultrashort Pulsed Direct Laser Interference Patterning

Daniel W. Müller[1,*], Sarah Lößlein[1], Emmanuel Terriac[2], Kristina Brix[3], Katharina Siems[4], Ralf Moeller[4], Ralf Kautenburger[3], Frank Mücklich[1]

[1]Chair of Functional Materials, Department of Materials Science, Saarland University, 66123, Saarbrücken, Germany.

[2]Leibniz Institute for New Materials, Dynamic Biomaterials. Saarbrücken 66123, Germany.

[3]Department of Inorganic Solid-State Chemistry, Elemental Analysis, Saarland University, Saarbrücken 66123, Germany.

[4]Aerospace Microbiology, Radiation Biology Department, Institute of Aerospace Medicine, German Aerospace Center (DLR e.V.), Cologne 51147, Germany.

Published in March 2021 in "Advanced Materials Interfaces" and accessible online via:

https://doi.org/10.1002/admi.202001656

Abstract:

Copper (Cu) exhibits great potential for application in the design of antimicrobial contact surfaces aiming to reduce pathogenic contamination in public areas as well as clinically critical environments. However, current application perspectives rely purely on the toxic effect of emitted Cu ions, without considering influences on the interaction of pathogenic microorganisms with the surface to enhance antimicrobial efficiency. In this study, it is investigated on how antibacterial properties of Cu surfaces against Escherichia coli can be increased by tailored functionalization of the substrate surface by means of ultrashort pulsed direct laser interference patterning (USP-DLIP). Surface patterns in the scale range of single bacteria cells are fabricated to purposefully increase bacteria/surface contact area, while parallel modification of the surface chemistry allows to involve the aspect of surface wettability into bacterial attachment and the resulting antibacterial effectivity. The results exhibit a delicate interplay between bacterial adhesion and the expression of antibacterial properties, where a reduction of bacterial cell viability of up to 15-fold can be achieved for E. coli on USP-DLIP surfaces in comparison to smooth Cu surfaces. Thereby, it can be shown how the antimicrobial properties of copper surfaces can be additionally enhanced by targeted surface functionalization.

Own contributions:

Conception and design of the study. Design of the interference-based USP laser setup. Sample preparation and surface characterisation via LSM and SEM including bacterial imaging. CA measurement and wet plating for antibacterial monitoring. Conception and design of the wetting experiment involving fluorescent bacteria in inverted LSM. Data interpretation, preparation and editing of the manuscript.

Included Cover Art related to this article: https://doi.org/10.1002/admi.202170027

Applied Surface Science 611 (2023) 155538

Contents lists available at ScienceDirect

Applied Surface Science

journal homepage: www.elsevier.com/locate/apsusc

Full length article

Multi-pulse agglomeration effects on ultrashort pulsed direct laser interference patterning of Cu

Daniel Wyn Müller [a,*], Sarah Lößlein [a], Christoph Pauly [a], Max Briesenick [b], Guido Kickelbick [b], Frank Mücklich [a]

[a] Chair of Functional Materials, Department of Materials Science, Saarland University, 66123 Saarbrücken, Germany
[b] Department of Inorganic Solid-State Chemistry, Elemental Analysis, Saarland University, 66123 Saarbrücken, Germany

ARTICLE INFO

Keywords:
Direct laser interference patterning
Ultrashort laser pulses
Biomimetic surface structures
Functional surfaces

ABSTRACT

Surface functionalization by biomimetic patterns in the micro- and nanometer scale is well-established in a wide range of applications. The finely tuned surface properties are directly related to both primary and sub-pattern morphology of the applied topographies, which must be well-adjusted for maximum functionalization efficiency. In this light, the role of proceeding surface modification and its effect on pattern formation alongside multi-pulse ultrashort pulsed direct laser interference patterning (USP-DLIP) of Cu are investigated in detail by applying a multi-method characterization approach. It was shown that aside of topographical remodeling, USP-DLIP processing parallelly affects chemistry and the mechanical deformation state of the substrate surface, which in turn considerably influences laser/material interaction via incubation. An in-depth investigation of the individual and combined impacts of these substrate alterations on localized optical absorptance reveals how primary and sub-pattern formation dynamically respond to process induced surface modification. The DLIP-specific incubation impact on pattern morphology increases with inverted relation to pattern scale. The findings of this study provide a profound insight in the predominant physical interactions involved in pattern formation arising from the mutual influence between laser irradiation and substrate modification during USP-DLIP-processing of Cu allowing for high precision micro- and nanometer scaled pattern design.

1. Introduction

Surface patterning in the micro- and nanometer scale mimicking natural blue prints found in manifold variation in the flora and fauna has been well-applied and developed to improve technical surface properties in the last two decades [1]. The envisaged application areas cover a broad spectrum from optical effects and photonics [2],[3], to technically utilized surface functionalization including wetting, friction and wear [4–6], as well as biomedical surface optimization to enhance cell colonization or antibacterial surface properties in the civil and aerospace sector [7–10]. Here, a close connection between sophisticated pattern design and effectiveness of the surface functionalization was demonstrated across the different applications studied, which is highlighting the necessity to understand and precisely control the process of pattern formation.

Among the technologies applied in this field, pulsed laser irradiation in the pico- and femtosecond regime involving purposefully induced interference has proven to be particularly versatile in terms of precision and variety of pattern geometries that can be created [11],[12]. In direct laser interference patterning (DLIP), the primary geometry of the topographical pattern applied is controlled by the design of the laser setup involving beam count and incidence angle, the wavelength as well as single beam polarization [13],[14]. Pattern formation itself is influenced by the material specific physical response to laser irradiation e.g. involving melt formation, vapor recoil pressure and Marangoni convection in case of pulse durations of several tens of picoseconds and higher [15], while ultrashort pulse durations <10 ps (USP) induce surface modifications dominated by varying material specific ablation mechanisms, which are closely related to individual threshold fluences [16]. Applying USP-DLIP, high aspect ratios as well as the formation of sophisticated pattern geometries can be achieved via multi-pulse overlap. However, material specific accumulation effects on pattern formation have to be considered, which might also lead to pattern deterioration as previously shown for pattern scales in the sub-µm range

---

* Corresponding author at: Chair of Functional Materials, Saarland University, Post Office Box 151150, 66041 Saarbruecken, Germany.
E-mail address: daniel.mueller@uni-saarland.de (D.W. Müller).

https://doi.org/10.1016/j.apsusc.2022.155538
Received 18 August 2022; Received in revised form 27 October 2022; Accepted 28 October 2022

[16],[17]:

Alongside primary pattern formation, multi-pulse USP processing involves sub-pattern alteration, e.g. by self-assembly of laser induced periodic sub-structures (LIPSS) on metals, semi-conductors and dielectrics [18]. LIPSS are divided in two subspecies with different relation to beam polarization: While the formation of high spatial frequency LIPSS (HSFL, oriented parallel to beam polarization and scaling $< \lambda/2$) have been shown to mainly involve melt kinetics like Marangoni convection, low spatial frequency LIPSS (LSFL, oriented perpendicular to beam polarization and scaled $> \lambda/2$) are shaped in multi-pulse overlaps by a combination of the interference between the incident laser beam and excited surface plasmon polaritons (SPP) on a roughened surface and further increased absorption in the resulting pits, according to current theories [19],[20]. Alongside USP-DLIP, LIPSS formation can even be purposefully superimposed with the primary DLIP pattern [21],[22]. Overlying process mechanisms may suppress LIPSS formation in some cases, resulting in other forms of sub-patterns, like e.g. crater-like morphologies in the case of Cu as a result from ablation kinetics, which are also subject to change during multi-pulse processing [23].

In parallel, substrate modification during pulse accumulation alongside laser processing modifies the optical surface properties resulting in decreasing ablation thresholds denoted as incubation [24],[25]. Incubation itself describes a sum-up of different effects involving the alteration of surface topography and chemistry as well as the disruption of internal order by defect-formation inside the substrate that altogether result in increasing laser absorption. To which extend the individual laser-induced substrate modifications contribute to incubation might differ significantly depending on the material and the laser parameters used. Incubation has not been considered in DLIP-processing so far. Especially in USP-DLIP, where pattern formation involves precise tailoring of threshold-related material response [16], the reduction of effective ablation thresholds in direct relation to the overlapping pulse count might considerably affect the resulting pattern morphologies.

In this work, multi-pulse effects on pattern formation during USP-DLIP processing are investigated for Cu using femtosecond laser pulses and a near-infrared wavelength, exhibiting a pronounced incubation behavior in previous studies [26],[27]. To monitor the individual impacts of surface chemistry and topography modification as well as defect implantation on overall incubation, a complementary multi-method approach is applied including confocal laser and scanning electron microscopy, electron back-scatter diffraction, UV–Vis spectroscopy, statistic image segmentation and numerical analysis. To include parametrization related influences into the investigation, altering DLIP setups as well as an application relevant fluence spectrum spanning the different ablation regimes observed on USP processed Cu are applied in the experiments. The combined evaluation of the different examination methods in mutual complementation allows for the determination of the individual USP-DLIP specific incubation mechanisms and their effect on pulse-wise primary and sub-pattern formation during multi-pulse processing. Following this approach, our investigation shed light on the predominant incubation mechanisms as well as their interplay in multi-pulse USP-DLIP of Cu and how they can be purposefully applied in targeted process parameterization.

2. Materials and methods

2.1. Material preparations and USP-DLIP

Sheets of cold rolled oxygen-free Cu (>99.95% purity, thickness 1 mm, *Wieland*, Germany) were cut into coupons of 10 × 25 mm size. Fine grinding on 1200 Grid Silicon Carbide paper followed by three polishing steps (6 µm, 3 µm, 1 µm suspension with reducing pressure of 15 to 10 N) results in a mirror finish with a roughness $R_a < 10$ nm of the Cu samples. Mechanical preparation is followed by thorough cleaning with distilled water and ethanol to remove suspension remnants. To investigate the influence of microstructure on laser-material interaction during the experiments, one batch of samples underwent annealing for 12 h at 450 °C and 10^{-7} mbar in a vacuum furnace. Said samples underwent electropolishing to avoid mechanical surface deformations, as described in [28].

Cu develops a native oxidation layer of Cu_2O and CuO by atmospheric storage, whereas process related agglomeration of oxidic redepositions also occurs during USP-DLIP [29]. Low concentrations of citric acid have been shown to remove both types of oxide [29],[30] and are therefore used to assess the influence of oxidation layers on optic surface properties. Deoxidized samples are produced by immersion in 3% citric acid for one minute in an ultrasonic bath directly before USP-DLIP processing or characterization.

USP-DLIP was conducted using a *Ti:Sapphire* laser source emitting ultrashort laser pulses with a pulse duration t_p of 100 fs at Full Width Half Maximum (FWHM) and a centered wavelength λ of 800 nm. An optical setup primarily containing a wave plate, diffractive optical element (DOE) and multi-lens system allows for the formation of two-beam interference patterns in µm and sub-µm scale on the sample surface [16]. While the wave plate is adjusted to alter the orientation of linear beam polarization in relation to the inference pattern to either s- or p-polarization, the setup of both DOE and multi-lens system defines the pattern periodicity P by adjusting the single beam incidence angle Θ according to Eq. (1).

$$p = \frac{\lambda}{2\, sin(\theta)} \tag{1}$$

In the experiments, pattern periodicity was varied between 6 µm, 3 µm and 750 nm. Cu surfaces were either processed by multi-pulse overlaps of $N = 1$, 2, 5 and 10 pulses on a single spot or planar patterning by scanning the sample surface in continuous pulsing mode at a pulse frequency of 1 kHz. In the latter case, pulse overlap is controlled by adjusting the x- and y- hatching distances in relation to the laser spot diameter of 70 µm. The applied fluences ranged from 0.31 J/cm^2 to 4.0 J/cm^2 partly including the low to the middle-fluence processing regime of Cu [31]. Fluences denoted in the results section are corresponding to the mean fluence at Full Width Half Maximum (FWHM) of the interference modulation, which has been calculated applying the mentioned spot diameter and pulse frequency as well as the measured seed beam power and 22.2% power loss of the optical system.

2.2. Characterization

2.2.1. Confocal laser scanning and scanning electron microscopy (LSM, SEM)

Characterization of the alteration in surface topography by USP-DLIP was conducted by means of confocal laser scanning microscopy (LSM) utilizing a *LEXT OLS4100 3D Measuring Laser Microscope* by *Olympus* (50× lens, 2× and 6× increased magnification, laser wavelength 405 nm) and scanning electron microscopy (SEM) (*Helios Nanolab600* by *FEI* and *Helios PFIB G4 CXe* by *Thermo Fisher*). Six individual samplings have been conducted for topographic characterization in relation to individual USP-DLIP parameters to include statistical dispersion. High resolution SEM imaging and characterization involved both secondary and back-scatter electron contrast (SE, BSE) combined with electron back-scatter diffraction (EBSD). High-resolution SE imaging was performed in immersion mode using the in-lens detector, while BSE imaging utilized a single segment retractable solid-state detector to visualize the grain orientations and surface topography of the sample. In both cases, an acceleration voltage of 5 kV was used, while in SE imaging, a beam current of 86 pA and in BSE imaging a beam current of 1.4 nA was applied. SEM imaging in SE contrast additionally involved a sample tilt of 52° degree to improve the visualization of topographical features. EBSD measurements were carried out using a high-speed CMOS camera (*Velocity Super* by *EDAX*) at 20 kV acceleration voltage and a beam current of 26 nA. The step size on a hexagonal grid was set to 250 nm. Lattice planes parallel to the sample surface of selected grains were extracted using *OIM Analysis 8.6* software by *EDAX* in order to correlate their response to the laser irradiation.

2.2.2. UV–Vis spectroscopy

A *PerkinElmer Lambda 750* UV–Vis spectrometer was used to determine the optical absorptance of the differently prepared initial state Cu surfaces as well as absorptance increase due to pulse agglomeration alongside USP-DLIP processing. The measurement was performed for electro-magnetic wavelengths of 800 to 200 nm (1.55 to 6.2 eV) with 1 nm increments and 0.2 s integration time utilizing a 100 mm InGaAs integration sphere to guide the non-absorbed part of probing radiation to the detector. Due to the optical beam path involving several gratings and mirrors, the probing beam polarization is altered from circular to partly linear before it irradiates the samples. This feature is purposefully used in this study to allow for a qualitative assertion of polarization and topographic effects during multi-pulse processing by measuring the line-like patterned surfaces both in s- and p-polarization orientation to the probing beam. Multi-pulse agglomeration effects on absorptance have been monitored after irradiation with 1, 2, 5 and 10 pulse overlaps at a fluence of 2.1 J/cm^2 and 3 µm pattern geometry.

2.2.3. Numerical analysis

Material processing using ultrashort laser pulse durations in the femtosecond regime involves complex physical laser-material interactions like e.g. multi-photon absorption in dielectrics and ceramics as well as considerable thermal non-equilibria between the electron and lattice sub-systems in metals. These different physical interactions altogether result in ablation dominated material response closely linked to fluence levels surpassing the material specific ablation threshold F_{abl}, allowing to precisely tailor surface feature sizes down to the sub-µm scale. In case of USP-DLIP, this relation can be utilized to define the targeted width of the ablated area in order to design primary pattern geometries as illustrated in Fig. 1a [16]. However, in case of multi-pulse surface processing the optical properties of the substrate surface change due to incubation leading to a reduction of F_{abl} that has to be considered in process parametrization, which is especially the case for Cu [32].

Alongside the previously described characterization methods, numerical analysis of the thermal response of Cu surfaces to USP-DLIP irradiation was therefore utilized to further assess the different accumulation effects on line-like primary pattern formation that contribute to incubation in multi-pulse processing. The 2D two-temperature model (TTM) for USP-DLIP irradiation of Cu surfaces previously introduced in [16] was modified to include single beam polarization as well as pulse-wise increase of surface absorptance during multi-pulse processing. The key influences of altering laser-material interaction are fully described by the thermal heat source term S in the TTM denoted by Eq. (2),

$$S(\mathrm{x,z,t}) = \alpha A_x \frac{I(x)}{\sigma\sqrt{2\pi}} exp\left[-\frac{(t-t_0)^2}{2\sigma^2} - \alpha z\right] \tag{2}$$

which involves the energy absorption correlating to the Beer-Lambert Law, where α is the absorption coefficient and A_x the localized optical absorptance. The spatial distribution of laser intensity correlating to the interference pattern is denoted by $I(x)$ while the temporal distribution of laser power in relation to the arrival time t_0 of the pulse at maximal intensity is defined by the standard deviation σ involving the pulse duration t_p:

$$\sigma = \frac{t_p}{2\sqrt{2ln2}} \tag{3}$$

Optical absorptance of Cu surfaces varies depending on initial surface condition as well as multi-pulse agglomeration. Hence, the energy absorption in S is modelled to enable the inclusion of experimental values from UV–Vis spectroscopy. Here, absorptance A_0 at different states of pulse agglomeration during surface processing is taken as the mean value between s- and p-pol from UV–Vis data for $N = 1, 2, 5$ and 10 at a wavelength of 800 nm (1.55 eV). The increase of energy absorption alongside ultrashort pulsed irradiation due to thermally enhanced electron excitation states ΔeV [33] is involved for both A_0 and α in the numerical calculation of the TTM by approximating $\Delta T_e \sim \Delta eV/k_B$, where T_e is the electron temperature and k_B the Boltzmann constant. This approach introduced in an earlier study shows good correlation to referenced experiments [33],[34].

Since optical absorptance of USP irradiation alters with incidence angle between s- and p-pol [36], the topographic influence on optical absorptance during multi-pulse pattern formation was additionally involved. Localized absorptance A_x involves the alteration of irradiation incidence angle Θ_x perpendicular to the line-like surface pattern. The ablation area geometry of the primary surface pattern is approximated as a circular segment as illustrated in Fig. 1b where the slope of Θ_x can be determined by Eq. (4) using the individual ablation width w and depth d from topographic characterization.

$$\theta_x = arcsin\left(x\frac{8d}{4d2 + w2}\right) \tag{4}$$

The polarization dependent absorptance $A_{s,p}$ in response to surface topography can be determined as (1-$R_{s,p}$) either for s- or p-polarization by calculating the Fresnel equations for R_s or R_p in relation to Θ_x utilizing the optical properties of Cu from literature data [35]. To enable the determination of overall localized absorptance A_x including topographic absorption modelling, UV–Vis data and electron excitation in numerical analyzation, the calculated literature values for $A_{s,p}$ are approximated by

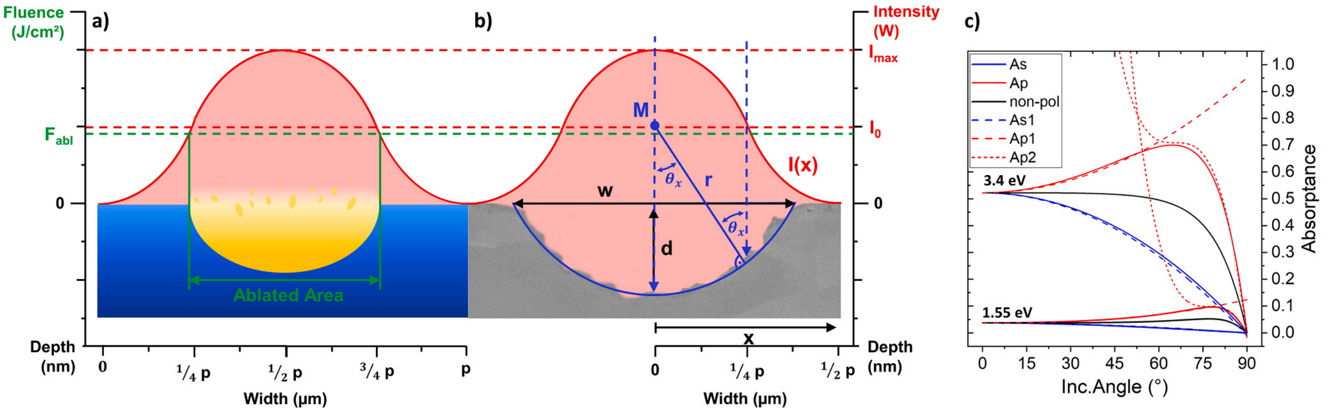

Fig. 1. Schematic illustration of a) the relation between interference intensity pattern, ablation threshold F_{abl} and laser-material interaction and b) the influence of surface inclination to the localized irradiation incidence angle Θ_x due to advanced material ablation below the intensity maxima. c) alteration of optical absorptance for 1.55 eV and 3.4 eV in relation to beam polarization and incidence angle calculated from literature values (A_s, A_p, *non-pol*) [35] and approximated (A_{s1}, A_{p1}, A_{p2}).

a set of equations relating to $A_0(\Delta T_e)$ and $\Theta_x(x,w,d)$, as well as the pseudo-Brewster angle *BA* for Cu corresponding to A_0. Depending on beam polarization, A_x is either represented by A_s or A_{p1} (for $A_{p1} < A_{p2}$) | A_{p2} (for $A_{p1} > A_{p2}$).

$$A_x \begin{cases} A_s = A_0\left(1 - \theta_x^2 \bullet 10^{-3.9}\right) & (5) \\ A_{p1} = A_0 + \theta_x^{(2.53 - A_0)}\left(\dfrac{A_0 \bullet 10^{-3}}{-45 \bullet A_0 + 33.7}\right) & (6) \\ A_{p2} = (1.3 \bullet A_0 + 0.05) - 5(\theta_x - (A_0 + BA - 2)\,)3 \bullet 10^{-5} & (7) \end{cases}$$

The comparison between polarization dependent absorptance $A_{s,p}$ calculated by eqs. (5–7) and literature values in relation to Θ_x is illustrated in Fig. 1c for A_0 at 1.55 eV and 3.4 eV showing a high level of conformity.

Aside of absorptance alteration in response to topography, beam polarization also influences intensity modulation in laser interference, which was shown to have a significant effect on pattern formation [37]. In case of two-beam interference, the modulation of intensity *I(x)* in relation to the electrical field amplitudes E_1 and E_2 and incidence angle Θ of the individual partial beams is described by Eqs. (8) and (9) for either s- or p-polarization.

$$\text{S} - \text{polarization}: \quad I_s(x) = \frac{1}{2}\left(E_1^2 + E_2^2\right) + E_1E_2 \bullet cos\left(\frac{4\pi}{\lambda}sin(\theta)x\right) \tag{8}$$

$$\text{P} - \text{polarization}: \quad I_p(x) = \frac{1}{2}\left(E_1^2 + E_2^2\right) + E_1E_2cos(2\theta)cos\left(\frac{4\pi}{\lambda}sin(\theta)x\right) \tag{9}$$

Assuming equal distribution of initial laser intensity I_0 between both partial beams with $I_1 = I_2 = \frac{1}{2}I_0$ and $E_1 = E_2 = \sqrt{\frac{I_0}{K}}$, where $K = 1$ is approximated, Eqs. (8) and (9) can be transformed to:

$$I_s(x) = I_0 + I_0 \bullet cos\left(\frac{4\pi}{\lambda}sin(\theta)x\right) \tag{10}$$

$$I_p(x) = I_0 + I_0 \bullet cos(2\theta)cos\left(\frac{4\pi}{\lambda}sin(\theta)x\right) \tag{11}$$

Replacing F_0 for I_0 and $w/2$ for x, where w corresponds to the ablation width, either the effective ablation threshold F_{abl} can be calculated from experimental data or the estimated ablation width for predefined F_{abl} can be determined involving polarization dependent pattern modulation.

$$F_{abl\ s} = F_0 + F_0 \bullet cos\left(\frac{4\pi}{\lambda}sin(\theta)\frac{w}{2}\right) \tag{12}$$

$$F_{abl\ p} = F_0 + F_0 \bullet cos(2\theta)cos\left(\frac{4\pi}{\lambda}sin(\theta)\frac{w}{2}\right) \tag{13}$$

Numerical analyzation of the thermal substrate response on USP-DLIP during multi-pulse processing was conducted by solving the TTM in a 2D depth profile utilizing the simulation software *FlexPDE*, where initial A_o, A_x and *I(x)* are modified corresponding to pulse count *N* and beam polarization. Lattice heating corresponding to phase changes and material ablation is calculated at thermal relaxation τ_{eq} between the electron and lattice sub-systems of the TTM, where isothermal frontiers of the threshold temperatures for solid/liquid and liquid/vapor phase transitions mark the phase fronts.

2.2.4. Morphologic segmentation

Alterations in sub-pattern formation and geometry during multi-pulse processing via USP-DLIP have been monitored using the *MorphoLibJ* Plugin [38] of *ImageJ* (*FiJi*) [39] for the segmentation and morphological characterization of individual particles. In order to enable a targeted segmentation distinguishing between the individual crater-like sub-pattern features (in the following: craters), SEM images were taken in SE mode with increased topographic contrast allowing to separate the individual craters via watershed boundary conditions. Segmentation fragments are filtered out by size and shape filters (minimal particle size and aspect ratio) whereas each segmentation result was carefully monitored for left-over fragments or falsely filtered craters. Using the morphologic segmentation, the alterations in size, shape and orientation of the crater-like features in response to multi-pulse agglomeration were statistically evaluated to quantify the effect of beam polarization, laser fluence and pattern scale on the development of sub-pattern geometry during USP-DLIP processing within the first ten consecutive laser pulses.

3. Results and discussion

3.1. Effect of incubation on multi-pulse USP-DLIP

3.1.1. Pattern formation in response to periodicity

To investigate a possible effect of pattern scale on multi-pulse USP-DLIP processing of Cu surfaces, the three different periodicities 6 µm, 3 µm and 750 nm have been applied in multi-pulse overlaps of $N = 1$, 2, 5 and 10 on a single spot. The pattern geometry in terms of peak/valley surface ratio has previously been shown to be directly linked to the ablated area defined by the material specific ablation threshold F_{abl} in response to the fluence utilized, as visible in Fig. 1a. Here, the effect of incubation during multi-pulse processing must be included, which might vary significantly depending on the material processed and the laser parameters used. To investigate a broader range of laser/material interaction involving both spallative and phase explosion ablation, fluences for USP-DLIP have been chosen in both the low-fluence regime below 1.5 J/cm^2 and the mid-fluence regime ranging between 1.5 and 4 J/cm^2, where femtosecond pulsed ablation for Cu shows the highest efficiency according to Schille et al. [31]. This also fits to the $F_{max} = 7.4\ F_{abl}$ referenced in [25] taking the $N = 10$ and $N = 100$ multi-pulse ablation thresholds of 0.581 J/cm^2 and 0.307 J/cm^2 measured by Kirkwood et al. [26] into account. In a previous study, low-fluence USP-DLIP exhibited an ablation behavior mainly involving thermomechanical spallation, while in the mid-fluence regime photothermal phase explosion could be traced back as the dominant ablation mechanism after the second consecutive laser pulse [16].

In terms of localized laser/material interaction in response to the DLIP intensity pattern, the modulation depth induced by laser interference has to be considered, which decreases in case of p-polarization with enhancing incidence angle Θ [37]. In Fig. 2a, the sinusoidal intensity modulation for either s- or p-polarized two-beam interference calculated by Eqs. (10) and (11) is plotted for the pattern periodicities 6 µm, 3 µm and 750 nm. While the modulation depth for p-polarized (p-pol) interference does not alter significantly for both µm-scaled patterns of 6 µm ($I_0 \pm 99.2\%$) and 3 µm ($I_0 \pm 96.4\%$), a considerable difference occurs for high incidence angles as used for 750 nm pattern periodicity with a low intensity pattern contrast ($I_0 \pm 43{,}2\%$). Consequently, varying beam polarization can already be considered to influence pattern formation during multi-pulse USP-DLIP processing of Cu from interference modulation alone. In fact, a more pronounced increase of ablation area during consecutive pulsing is visible comparing both SEM images and the fluence dependent ablation plots in Fig. 2b, c and d in case of p-pol, which applies to a different extent on the individual pattern scales.

In 6 µm USP-DLIP processing, the difference between s- and p-polarized ablation width mainly becomes prominent in the low-fluence regime after a pulse count of five (see Fig. 2b). Here, p-pol ablation width surpasses the range, which would be estimated by applying the $N = 10$ ablation threshold from [26], while s-pol ablation width continuously stays below that threshold. Entering the mid-fluence regime, the slope of ablation width tends to drop with increasing pulse count *N* after

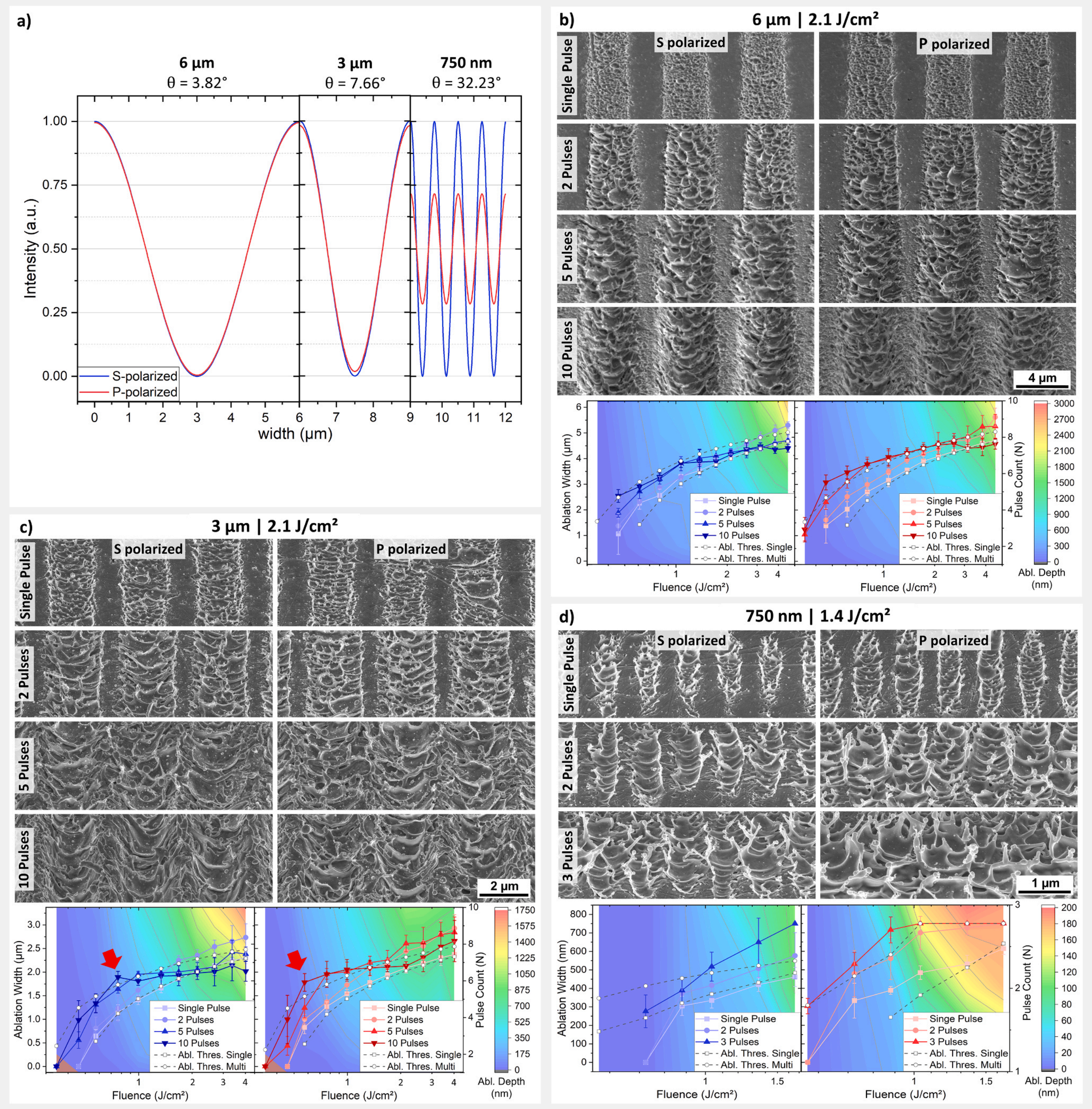

Fig. 2. Line-like USP-DLIP processing of the pattern periodicities 6 µm, 3 µm and 750 nm on Cu involving interference pattern modulation by altering linear single-beam polarization. a) Difference in two-beam interference pattern modulation between s- and p-polarization for each periodicity. b) SEM-imaging of 6 µm patterns applied by increasing multi-pulse overlap at 2.1 J/cm^2 for either s- or p-polarization followed by a combined plot of ablation width (line graph) vs ablation depth (underlaying heat map). c) SEM-imaging of 3 µm patterns applied by increasing multi-pulse overlap at 2.1 J/cm^2 for either s- or p-polarization followed by a combined plot of ablation width (line graph) vs ablation depth (underlaying heat map). The red arrows mark the individual setting points for s- and p-pol, where ablation area expansion is restricted for further increasing fluence and pulse-count. d) SEM-imaging of 750 nm patterns applied by increasing multi-pulse overlap at 1.4 J/cm^2 for either s- or p-polarization followed by a combined plot of ablation width (line graph) vs ablation depth (underlaying heat map). The ablation thresholds marked in b), c) and d) are corresponding to the single and $N = 10$ pulse ablation threshold of 1.06 J/cm^2 (Single) and 0.581 J/cm^2 (Multi) from [26] calculated by Eqs. (12) and (13). SEM images have been taken at a sample tilt of 52°. (For interpretation of the references to colour in this figure legend, the reader is referred to the web version of this article.)

a strong increase for the second pulse. This trend is more pronounced for s-pol pattern formation where this trend already involves $N = 5$. For both polarization orientations a pulse count of $N = 10$ exhibits a kink at 3.13 J/cm^2 (s-pol) and 2.68 J/cm^2 (p-pol), where a developed state of topographic pattern formation might get involved with laser/material interaction. In contrast to the ablation width ratio between the USP-DLIP patterns generated with different beam-polarization, s-pol processing induces a greater pattern depth than p-pol at similar fluence and pulse count, especially in the mid-fluence regime.

In case of 3 µm pattern periodicity, the previously observed kink in ablation width increase for higher pulse counts during multi-pulse processing can already be observed in the low-fluence regime at 0.76

J/cm^2 (s-pol) and 0.57 J/cm^2 (p-pol), as highlighted in Fig. 2c. For s-pol this point marks the onset of a plateau-like slope exhibiting constant ablation width for increasing fluences at both $N = 5$ and $N = 10$ pulse counts, which also continues into the mid-fluence regime. A difference between low- and mid-fluence regime s-pol ablation width is only visible for dual pulse irradiation, where the referenced $N = 10$ multi-pulse ablation threshold is increasingly surpassed. In contrast, the plateau-like slope of ablation width during multi-pulse p-pol processing can only be exhibited for $N = 10$ in the low-fluence regime, although it remains below the values for $N = 5$ from this point on. In parallel to s-pol, p-pol dual pulse ablation width also exceeds the range denoted by the referenced multi-pulse ablation threshold in the mid-fluence regime. Including the findings in [16], the second consecutive pulse applied in the mid-fluence regime induces a growing proportion of phase explosion in ablation, which leads to increasing melt-agitation and hence additional pressure mediated expansion of the ablation area. The observed stagnation up to reduction of the ablation area width with elevated pulse count suggests an effect of the pattern topography on laser/material interaction during multi-pulse USP-DLIP processing of 3 μm patterns, which considerably depends on beam polarization. Similar to the observations at 6 μm pattern periodicity, s-pol ablation depth surpasses the values of p-pol but on a significantly higher scale. The maximum s-pol ablation depth of 1.71 μm after 10 pulses at 4.02 J/cm^2 is almost double as high as the p-pol ablation depth of 0.88 μm with the same parameters. It is noteworthy that the actual maximum ablation depth of 0.99 μm for p-polarization was measured at a lower fluence of 2.1 J/cm^2, instead. Directly comparing overall ablation depth between 6 μm and 3 μm periodicities shows a similar depth vs fluence and pulse count ratio for s-pol, while ablation depth on p-pol 3 μm patterns fall below the values of 6 μm with an additional decrease after 2.1 J/cm^2. This might be related to partial ablation of the 3 μm peak areas in the course of reduced multi-pulse F_{abl} due to the less modulated p-pol interference pattern, which points out a polarization and pattern scale specific threshold fluence to achieve high pattern aspect ratio and quality that lies lower than the general mid-fluence range in case of p-polarized USP-DLIP.

Comparing the SEM images of both 6 μm and 3 μm patterns after different pulse counts applied at a fluence of 2.1 J/cm^2 in Fig. 2b and c, a difference in sub-pattern formation originating from melt agitation during ablation can be observed. Where the ablation areas on 6 μm patterns remain separated and the peak surface and geometry indicate minor thermal affection, overlapping structures of resolidified melt cover the peak areas on 3 μm patterns, which appear to have been ejected from the neighboring topographic minima in the course of ablation. Agitated liquified substrate has been shown to expand from the ablation site up to a certain range before it resolidifies due to enhanced convective cooling in the process of material expulsion in relation to the amount of super-critical lattice heating and the parallel pile-up of internal pressure during femtosecond pulsed laser irradiation of Cu [40]. Measuring the fluence-dependent quantitative pulse-wise increase of ablation width for both periodicities, pattern valley expansion ranges in the same order of magnitude in the low-fluence regime and for $N < 5$ in the lower mid-fluence range, where ablation starts to be dominated by phase explosion [16]. Based on this ablation kinetics, agitated melt originating from the further expanding ablation areas appears to completely cover previously unimpaired pattern peaks in case of lower pattern periodicities after a certain fluence-dependent pulse count in the mid-fluence regime, with a potential impact on further laser/material interaction from surface modification.

A significant alteration of the previously observed polarization/ablation depth relation can be determined for a pattern periodicity of 750 nm. In contrast to μm-scaled pattern formation, p-pol pattern depths exceed the ones measured for s-pol processing up to two-fold. In parallel, p-pol ablation width exhibits a rapid increase, where an overlap of neighboring ablation areas can be observed within only three consecutive pulses at low fluences close to the referenced single pulse ablation threshold of 1.06 J/cm^2 [26]. It is noteworthy that for fluences in the mid-fluence regime, this overlap already happens after the second pulse, which fits to the effect of phase explosion on melt-agitation previously discussed for 3 μm pattern scale. In a previous work, higher fluences induced a melt-overlap already after the first pulse, where pattern stability could not be retained for two consecutive pulses highlighting the negative effect of mid-fluence processing in this pattern scale [16]. In close relation, the highest ablation depth is measured for 1.4 J/cm^2 right below the mid-fluence regime. As also visible in the SEM images in Fig. 2d, further irradiation after melt-overlap leads to the destruction of pattern integrity by the formation of a stoichiometric topography of a randomized sub-pattern originating from phase explosion ablation kinetics, which has already been reported for sub-μm USP-DLIP patterning in earlier works [16],[17]. Taking the polarization dependent interference modulation into account, the moderately decreased laser intensity within the p-pol interference pattern minima (approx. 0.8 J/cm^2 in case of 1.4 J/cm^2) might suffice to induce surface melting up to ablation already after a low pulse agglomeration due to incubation, while the reduced peak intensity should cause lower ablation in comparison to s-pol, in contrast. By this, the increased pattern depth of p-pol might result from beneficial melt kinetics, similar to previous works, where melt pile-ups during sub-μm USP-DLIP of highly conductive metals have been shown to be usable as an effective mechanism in the formation of line-like topography patterns [41],[42]. However, in direct comparison the p-pol ablation values exceed the ones measured for the more sharply defined s-pol patterns already after the first pulse, where melt-overlap is not observed in both cases. In addition to decreased ablation depth, s-pol ablation width tends to undercut the single and multi-pulse ablation threshold boundaries, especially for low fluences. In contrast, p-pol ablation width constantly surpasses single and multi-pulse ablation threshold and even shows ablation on lower fluences than s-pol, which is not consistent with the difference in interference pattern modulation indicating additional effects on sub-μm USP-DLIP processing.

In direct comparison, the investigated pattern periodicities can be divided relating to the effect of material specific ablation kinetics on pattern formation during multi-pulse USP-DLIP: 6 μm shows an almost linear relation between both ablation depth and width to both fluence and pulse count with low dependency on the fluence regime, where however p-pol seems to have a slightly higher effect on ablation width compared to the comparably low interference modulation. On 750 nm patterns, an increase of melt agitation from altering ablation kinetics due to incubation leads to melt pileups covering the peak areas especially in case of p-pol, where the topographic patterns are not stable for a higher number of overlapping pulses. In the case of 3 μm periodicity an intermediate behavior can be observed, where especially the formation of pattern geometry but also ablation related sub-patterns during multi-pulse processing can be divided by the involvement of either spallation or phase explosion. For mid-fluences on one hand, pattern peaks appear to be increasingly eroded during p-pol multi-pulse processing at fluences higher than 2.1 J/cm^2 as visible in the reducing pattern depth at $N = 10$, while they remain less affected aside of the visible melt overlap in case of s-pol. In the low-fluence range, a mostly parallel pattern formation behavior between s-pol and p-pol USP-DLIP can be observed suggesting a fluence/pulse count relation of pattern formation fitting closer to F_{abl} values from literature according to previously described incubation behavior of Cu [26]. Due to the intermixed relation between ablation kinetics and pattern formation, further investigation on the effect of incubation in multi-pulse USP-DLIP processing of Cu mainly focus on 3 μm pattern periodicity.

3.1.2. *Pattern formation in response to altering ablation mechanism*

In Fig. 3, topographies of 3 μm patterns generated by planar surface scanning with an absolute agglomeration of 21 ± 0.78 J/cm^2 are visualized by both SEM imaging and a comparison of the achieved topographic parameters. Between the individual patterns, the effect of s-pol versus p-pol USP-DLIP on pattern morphology is investigated using different fluences in the low- and mid-fluence regime at adjusted pulse

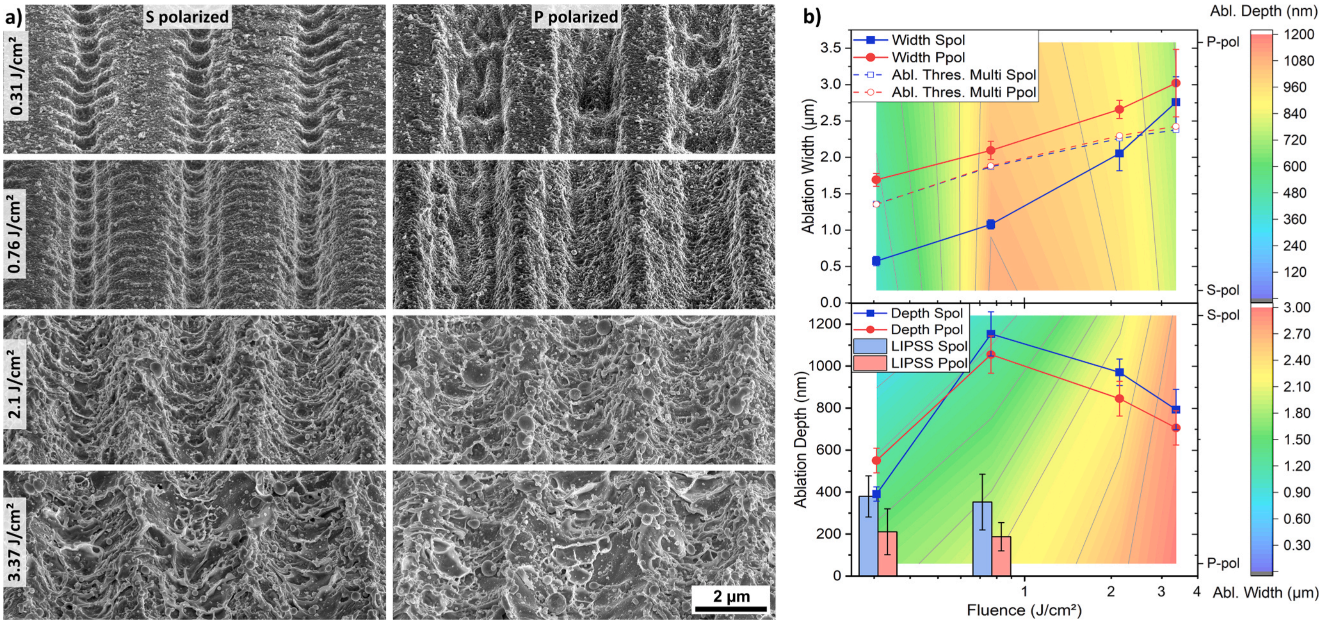

Fig. 3. a) SEM imagines and b) corresponding plotting of topographic parameters of line-like 3 µm patterns generated on Cu via USP-DLIP in planar scanning utilizing different fluences, x/y pulse overlaps and polarization parameters individually resulting in an agglomerated fluence of 21 ± 0.78 J/cm^2. The multi-pulse ablation thresholds in b) have been calculated applying $F_{abl}(N) = F_{abl}(1)N^{(S\text{-}1)}$ [24] with $S = 0.76$ [26] for both s- and p-pol interference pattern modulation. SEM images have been taken at a sample tilt of 52°.

overlap (0.31 J/cm^2, $N = 70$, scanning speed $\Delta x = 1$ mm/s | 0.76 J/cm^2, $N = 28$, $\Delta x = 2.5$ mm/s | 2.1 J/cm^2, $N = 10$, $\Delta x = 7$ mm/s | 3.37 J/cm^2, $N = 6$, $\Delta x = 11.5$ mm/s). A differentiation between low- and mid-fluence regime USP-DLIP can directly be applied comparing the individual sub-patterns, where the involvement of melt-agitation in pattern formation is clearly visible after mid-fluence processing and appears to be absent on low-fluence patterns. This can be linked back to the dominating ablation mechanisms in the different fluence regimes, where in case of low fluence thermomechanical spallation can be assumed, whereas phases explosion prevails at mid-fluence within the first two pulses. While the sub-pattern morphology seems to be independent of beam polarization in case of mid-fluence ablation, patterns generated by low-fluence irradiation differ significantly in both primary and sub-pattern formation between s- and p-polarization. Most obvious is the difference in the peak/valley ratio where ablation width is significantly higher on p-pol and increases to a much lower extend with further enhanced fluences compared to s-pol. Secondly, both fluences in the low-fluence regime exhibit LSFL formation in perpendicular orientation to the beam polarization adding to the difference between s-pol and p-pol patterns. Relating the measured ablation widths to the individual pulse count dependent ablation thresholds $F_{abl}(N)$ according to Jee et al. [24] (calculated by applying the incubation coefficient $S = 0.76$ provided in [26]) in Fig. 3b additionally points out the significant difference in multi-pulse ablation between s- and p-polarization via 3 µm USP-DLIP. Ablation width of p-pol patterns constantly surpass the estimated values with an additionally increasing ratio in the mid-fluence regime. In contrast, ablation width of s-pol patterns significantly undercuts the width corresponding to $F_{abl}(N)$ in the low-fluence regime until the measured values are approaching the ones of p-pol with increasing contribution of phase explosion ablation in the mid-fluence regime, where the ablation threshold estimated pattern width is finally surpassed for 3.37 /cm^2. Since intensity pattern modulation does not alter to that extend in case of $\Theta = 7.66°$ for 3 µm periodicity, topography-induced effects on absorptance for s- and p-polarization appear to be involved, here.

Ablation depth shows a steady increase with decreasing pulse-energy undergoing a sudden drop in the case of 0.31 J/cm^2. This behavior points out a reducing efficiency in the achievement of high pattern aspect ratio with accumulating fluence in direct relation to the extent of phase explosion in the mid-fluence regime, which appears to also affect s-pol in case of planar patterning in contrast to the previously shown behavior during single spot ablation. However, the overall polarization related dominance in either ablation width (p-pol) or depth (s-pol) development for µm-scaled pattern periodicities still applies, as visible in the comparison plots in Fig. 3b.

On low-fluence patterns, LSFL depth has been measured to allow for the evaluation of additional effects of LIPSS-formation that overlaps with the actual DLIP-patterning. Interestingly, LSFL depth is inverse to the measured ablation width for the different polarizations, suggesting a mutual influence between DLIP and LIPSS pattern, similar to recent findings [21]. If LSFL depth is subtracted, the corrected ablation depths of s- and p-pol at 0.76 /cm^2 are approx. on par with 2.1 J/cm^2, while overall formation of s-pol patterns at a fluence of 0.31 J/cm^2 appear to majorly dependent on the LSFL mechanism due to corresponding pattern and LSFL depths. The calculated multi-pulse ablation threshold equals to 0.38 J/cm^2 for this parametrization setup, which still undercuts the interference modulated peak fluence of approx. 0.61 J/cm^2 for both s- and p-pol, showing a significant overestimation of the incubation effect for s-pol USP-DLIP. Concurrently, the reduced energy absorption favors LSFL formation linked to sub-ablative threshold fluences on Cu [18] over ablative substrate interaction, probably leading to the different extent of LSFL depth between s-pol and p-pol. By this, the substrate response to 3 µm USP-DLIP with different polarization corresponds to the previously observed behavior for 750 nm, where s-pol ablation exhibited sub-threshold widths, while topographic patterning was achieved for sub-threshold fluences in case of p-pol, in contrast.

3.2. Impact of individual incubation effects during USP-DLIP

In the previously described topographic characterization, multi-pulse USP-DLIP pattern formation on Cu was shown to be influenced by incubation in differing response to both pattern scale and beam polarization in contrast to homogeneous incubation previously described for spot ablations utilizing gaussian intensity distribution [24],[26],[27]. This might be due to a differing individual impact of chemical, topographical and thermomechanical surface modification in case of

USP processing with an intensity distribution altered by DLIP, which will be further analyzed in the following sub-sections.

3.2.1. Overall incubation

The overall incubation during multi-pulse processing with 1, 2, 5 and 10 consecutive pulses utilizing a fluence of 2.1 J/cm^2 and 3 µm pattern periodicity was analyzed by measuring the alteration of optical absorptance via UV–Vis spectroscopy. The individual samples have been processed utilizing adjusted pulsing frequency and scanning speed to allow for spatially patterning at specified pulse accumulation (N = 1: 250 Hz, Δx = 17.5 mm/s | N = 2: 500 Hz, Δx = 17.5 mm/s | N = 5: 1 kHz, Δx = 14 mm/s | N = 10: 1 kHz, Δx = 7 mm/s). A partly linearly polarized probing beam allowed for the parallel qualitative investigation of the effect of polarization orientation in relation to the line-like pattern topography on overall surface absorptance. In Fig. 4a, a continuous enhancement of absorptance alongside increasing pulse count for the whole spectrum of probed wavelengths is apparent especially for N = 5 and N = 10 pulses in case of as-processed Cu surfaces (left graph of Fig. 4a). Tilting the orientation of beam polarization to the pattern geometry exhibits a minor total effect on overall absorptance with slightly higher values for p-pol, which additionally increases for higher pattern depths in case of N = 10 pulses in the Near IR spectrum. Since the probing beam was only partly linear polarized, this effect can be assumed to increase for fully linear polarized irradiation. For low pulse counts, the difference in absorptance between one and two consecutive pulses is minor and lies below the measured differences of s- and p-polarization at 800 nm, corresponding to the utilized laser wavelength. As soon as deoxidation via immersion etching in citric acid is applied, absorptance drops significantly exhibiting an increasing magnitude scaling with N (from N = 1 with approx. -16.8 ± 0.8% up to N = 10 with

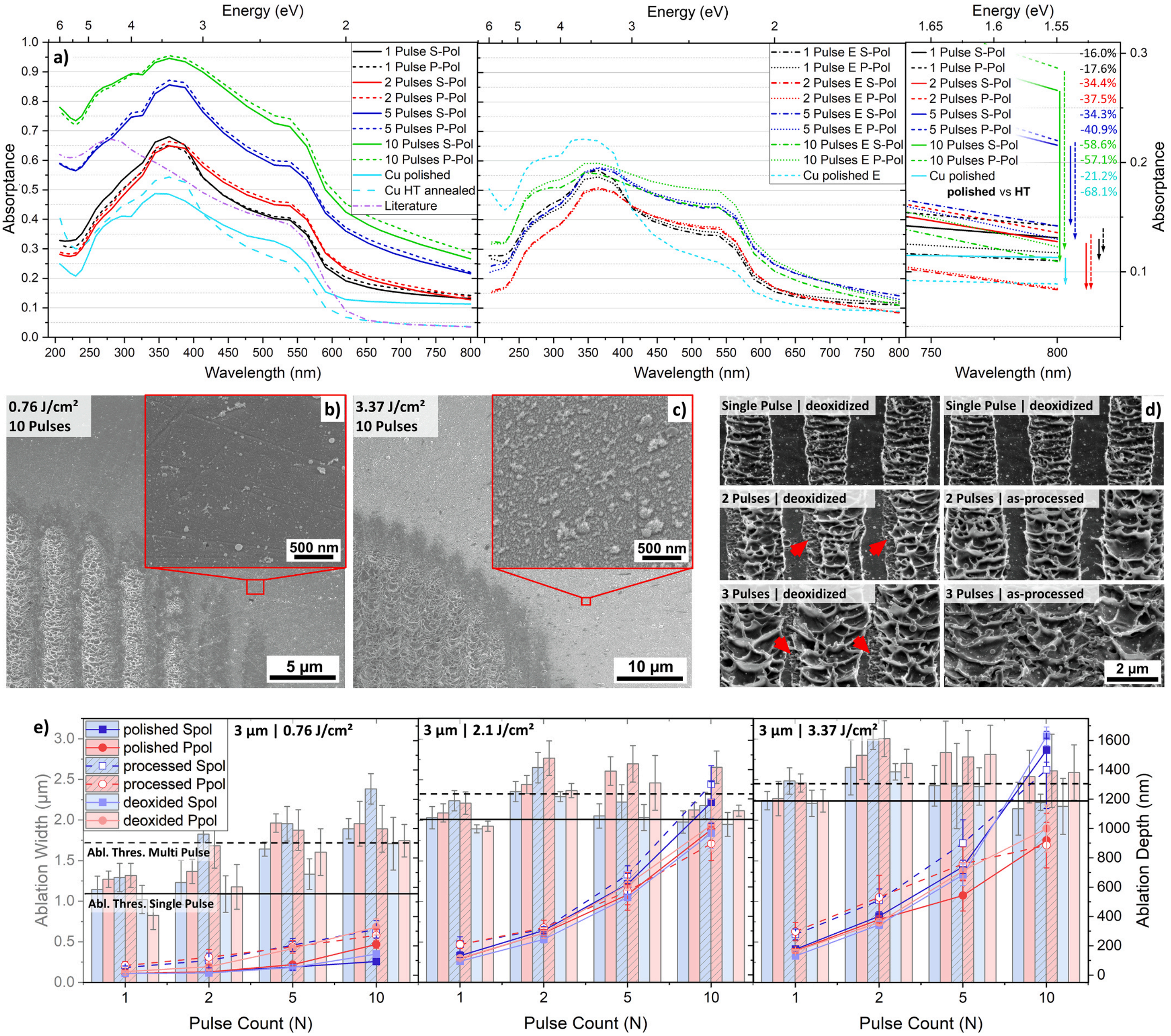

Fig. 4. Investigation of the effect of overall absorptance on USP-DLIP processing at a pattern periodicity of 3 µm. a) UV–Vis spectroscopy on USP-DLIP surfaces with a pulse overlap of N = 1, 2, 5 and 10, as well as polished and high temperature annealed Cu reference surfaces. Left graph: as-processed/−polished state. Middle graph: after immersion etching. Right graph: comparison between the optical absorptance at the laser wavelength of 800 nm. b) process-related redepositions after 10 pulses at 0.76 J/cm^2. c) process-related redepositions after 10 pulses at 3.37 J/cm^2. d) comparison of increasing ablation width/reducing ablation threshold at 2.1 J/cm^2 with and without intermediate deoxidation starting from deoxidized initial surface conditions. e) effect of initial surface state of either polished, as-processed and deoxidized on pattern geometry formation in the course of ten consecutive pulses. SEM images have been taken at a sample tilt of 52°.

approx. -57.9 ± 0.8%). By this, the difference in absorptance between increasing pulse counts gets significantly reduced, where in case of near-infrared wavelengths, the *N*-relation of absorptance is canceled out (see middle and right graph in Fig. 4a). The drop in absorptance indicates a dominant contribution of oxidic redepositions in overall increase of the surface absorptance. In the course of continuous ablation via USP laser processing, a fraction of the ablated material tends to redeposit on the substrate surface covering both already processed and non-processed surface areas. In a recent study, the redeposited matter related to USP-DLIP processing of Cu was determined to predominantly consist of Cu_2O with a smaller ratio of superficial CuO [29]. Both oxide phases exhibit semi-conducting properties with optical bandgaps ranging from 2.02 to 2.62 eV for Cu_2O and 1.2 to 1.9 eV for CuO depending on interstitial defect density [43]. Especially the bandgap of CuO is in close relation to the photon energies of the utilized laser wavelength while the Cu_2O bandgap facilitates two-photon absorption. By this, both oxide phases exhibit an increased absorptance in comparison to metallic Cu, hence impacting overall surface absorptance. An additional effect on both optical and thermal interaction might as well be induced by the nano-scaled morphology of the oxidic surface agglomerates exhibiting a high surface/volume ratio [29],[44],[45], where the single particle size of 10 up to 40 nm does not appear to change in the mid-fluence regime [46]. In fact, USP-DLIP ablation on thermally oxidized Cu substrates corresponding to [47] showed a significantly reduced single pulse ablation thresholds of approx. 0.12 J/cm^2.

Alongside USP-DLIP induced incubation, the comparably high initial absorptance of mechanically polished Cu surfaces in relation to literature data [35] has to be emphasized, which still ranges more than two-fold higher after immersion etching. Due to a negligible topographical influence on the mirror-polished surfaces, increased absorptance can predominantly be related to either chemistry + crystallographic defects for the as-polished sample and crystallographic defects alone after etching. It has been shown that the crystallography of Cu influences oxidic passivation layer formation, with a direct relation between grain boundary density and oxide thickness [48], by which the superficial mechanical deformation from polishing appears to cause a double effect on absorptance, both by crystallographic surface defects and increased oxide layer thickness. Consequently, the absorptance of reference samples, which have been annealed at high temperatures inducing excessive grain-growth (HT) exhibit a significantly closer relation to the literature values for ideal single crystal states. Comparable deviations of initial absorptance between differently pre-treated Cu surfaces have also been observed in previous studies [26],[27].

Since immersion etching solely causes the removal of surface oxide [29], the incubating effects of both modified topography and crystallographic defect formation during USP-DLIP remain active on the post-processed surfaces. Against this background, the inverted difference in absorptance between $N = 1$ and $N = 2$ before and after immersion etching exhibits different facets of incubation at the initial phase of multi-pulse USP-DLIP: Comparing the absorptance at both pulse counts after etching indicates a higher topography related absorptance-increase by the smaller scaled sub-pattern of $N = 1$ (compare Fig. 2c) for the utilized wavelength of 800 nm. Absorptance of $N = 2$ patterns matches mechanically polished Cu surfaces after etching, instead, indicating both a neglectable topographic influence of the $N = 2$ sub-pattern and similar defect related incubation. This suggests that additional defect implantation after the second consecutive laser pulse has not yet surpassed the crystallographic deformation of mechanical polishing. In addition, the more pronounced decrease in absorptance for $N = 2$ indicates significant oxidic agglomeration already after the second pulse, which might be linked to the alteration of ablative interaction from spallation to phase explosion [16]. Comparing the quantitative agglomeration of oxidic particles between spallative (Fig. 4b) and phase explosion ablation (Fig. 4c) in vicinity to the ablation site of single laser spots further underlines the reinforcing influence of the more eruptive ablation mechanism, fitting to literature data on fluence related ion-release [49]. The increase of absorptance related to $N = 5$ and $N = 10$ can mainly be linked to oxide agglomeration by comparison of the as-processed and etched values, as well, whereas enhancing sub-pattern perturbation, primary pattern geometry as well as defect formation seem to play a subordinate role in overall incubation on Cu according to UV–Vis examination with partly linear polarized probing beam.

3.2.2. *Incubation effects of surface oxide*

To further assess the pulse-to-pulse effect of oxide agglomeration on USP-DLIP incubation, a series of consecutive pulses at 2.1 J/cm^2 in p-polarization was overlapped on single spots starting from a deoxidized initial state of the Cu surface, where a part of the samples was etched while mounted between each consecutive pulse. Comparing pattern formation within the first three pulses in Fig. 4d with and without process-related oxide agglomeration reveal a reduced enhancement of ablation width on continuously deoxidized samples. Here, the ablation areas remain separated after three pulses in contrast to as-processed surfaces, while a lesser ablated outer region is visible. The latter indicates an intermixture of ablation mechanisms with spallation in the outer lower fluence and phase explosion in the central higher fluence area of the intensity pattern. Even though oxide agglomeration was removed, widening of the ablation area can be determined on both sample series due to melt-mobility aside of oxide-agglomeration, which is however still less expressed after deoxidation. It can be noted that melt-covering of the peak-areas already takes place after the third consecutive pulse in as-processed state traced back to enhanced melt-mobilization alongside more pronounced phase explosion ablation, which is also indicated by increasing crater size of the sub-pattern.

The predominant impact of surface oxidation on optical absorptance of Cu surfaces especially in the near-infrared regime might additionally be effective at the initial state of USP-DLIP processing, when pre-decoration of Cu surfaces with oxidic redepositions is considered before irradiation, as visible in Fig. 4b and c. Alteration of ablation behavior is therefore compared in relation to beam polarization and fluence after $N = 1$, 2, 5 and 10 pulse overlap on a single spot for the different initial states as-polished, deoxidized and processed. In the latter case, the ablation spot was localized in direct vicinity to previously applied surface patterns, which were processed at an accumulated fluence of 21 ± 0.78 J/cm^2 applying the same pulse fluence as used in the single spot investigation. A clear difference in ablation width between the three different initial surface states can be determined in both the low- and mid-fluence regime in Fig. 4e. Parallel comparison to estimated ablation width from single and $N = 10$ multi-pulse ablation thresholds emphasize an enhancing impact of initial oxide decoration with increased fluence, where the multi-pulse ablation threshold is reached after two pulses at low-fluence and even surpassed in the mid-fluence regime. Deoxidizing appears to reduce not only initial ablation width, but also ablation area expansion rate in case of 0.76 J/cm^2 indicating a reducing effect on overall incubation in the low-fluence regime. In both 2.1 J/cm^2 and 3.37 J/cm^2 multi-pulse processing, differences between the varying initial surface states become leveled after $N = 5$ showing the previously described variation between s-pol and p-pol patterns with only one outlier in case of 2.1 J/cm^2 at $N = 10$, in previously processed state. Here, higher melt-agitation with increasing expansion forces during phase explosion might play the predominant role in pattern formation with lesser dependency on the initial state of the Cu surface. The effect of this ablation mechanism in the mid-fluence regime is already visible after the second pulse where ablation width generally surpasses the multi pulse threshold mark. Ablation depth follows the same trend with higher values for pre-processed initial sample states that start to be dominated by polarization dependent effects after $N = 5$ in the mid-fluence regime, where at 2.1 J/cm^2 an inverse trend between s- and p-pol can be observed. In case of 3.37 J/cm^2, reduced initial ablation appears to be involved with higher ablation depths after $N = 10$ indicating an important effect of surface conditioning within the first consecutive pulses on further processing. In the case of low-fluence regime ablation, preconditioning remains the dominant factor within the first 10 pulses, where however deoxidized p-pol appears to be particularly suitable for high ablation rates.

From these results an enhancing effect of surface oxide on absorptance that directly influences USP-DLIP pattern formation can be stated, which leads either to increased ablation efficiency in the low-fluence regime or tends to affect pattern aspect ratio and quality in the mid-fluence regime on Cu surfaces. Based on these observations, the varying results of planar patterning at accumulated 21 J/cm^2 illustrated in Fig. 3 can be assumed to be co-triggered by altering fluence-dependent response on process-related oxide agglomerations, which also affect initial surface absorptance.

3.2.3. Crystallographic defects

The comparison of the absorptance between mechanically polished Cu reference and USP-DLIP patterned surfaces after immersion etching in Fig. 4a points out a low impact of mechanical substrate alteration on incubation over the amount of already existing deformation from polishing. Defect formation from USP processing on Cu is mainly linked to thermomechanical substrate response on laser irradiation, which is getting more pronounced with decreasing pulse duration and increasing fluence [40]. In direct comparison between the two ablation regimes observed for Cu, increasing melt-kinetics during phase explosion aggravates a correct interpretation of effective ablation threshold in response to USP-DLIP pattern modulation at 3 µm pattern periodicity, while patterns achieved by spallation exhibit high ablation contrast (see Fig. 3a). Further investigation of the incubating effect of Cu crystallography and defect formation during USP-DLIP therefore focusses low-fluence regime thermomechanical spallative ablation at 0.31 J/cm^2. Single scan lines have been applied utilizing an accumulated fluence of approx. 9.9 J/cm^2 ($N = 32$ at $\Delta x = 2.2$ mm/s), where the corresponding calculated multi-pulse ablation threshold of 0.65 J/cm^2 ranges slightly above the peak values of the interference modulation. The initial crystallographic surface state of the Cu substrate condition was altered between the originally intrinsic cold rolled Cu sheet microstructure exhibiting a superficial deformation zone of approx. 500 nm depth from mechanical polishing [29] and a deformation free state by annealing the sample for 12 h in 450 °C under vacuum atmosphere at a pressure of 10^{-7} mbar followed by electro polishing. Deoxidation via immersion etching was additionally included, to compare the combined and single initial incubation effects of surface chemistry and crystallography.

The crystal orientation sensitive BSE contrast utilized for SEM imaging reveals the difference of both initial substrate states as visible in Fig. 5a and b, where the original substrate grain structure can hardly be distinguished on cold rolled mechanically polished Cu, while clear grain differentiation is possible on annealed samples. The mechanically predeformed surfaces exhibit localized ablation sites from USP-DLIP processing, however with less expression on deoxidized samples. Clear effects of differing beam polarization on overall ablation can be found in sub-pattern formation, where LSFL perpendicular to the polarization angle appear to contribute to localized ablation for both s-pol and p-pol. Aside of a more pronounced LSFL formation in case of s-pol, clear differences of ablation rate between s- and p-polarization cannot be determined unambiguously due to the unsteady ablation. Stripes of brightened contrast are framing ablation areas in the intensity maxima of the interference patterns that exhibit an identical width on all samples, which might be linked to laser surface cleaning. On annealed surfaces, ablation is considerably reduced in comparison to the pre-deformed substrate state and cannot be detected on deoxidized samples at all, which is finally fitting to the fluence/ablation threshold estimation for the chosen parameter setup from literature data [26]. Ablation on as-polished annealed surfaces appears to be related to crystal orientation with contrasting results for individual neighboring grains also exhibiting a more pronounced substrate interaction in the case of p-pol irradiation (see Fig. 5b).

Further investigation of this phenomenon was conducted tracing individual p-pol USP-DLIP scan lines utilizing a combination of BSE and EBSD analysis to link local crystal orientation to laser induced substrate interaction. Detected surface morphology ranged between three interaction regimes, where the measured width of the interaction area was used to calculate the locally effective threshold linked to that phenomenon by utilizing Eq. (13). Threshold values below 0.58 J/cm^2 did not induce ablation but rather rippling of the Cu surfaces (visible in the dark contrasted twins in Fig. 5b, s-pol and p-pol, as-polished), which appears to be related to HSFL formation considering both the small sub-pattern scale below λ/2 and orientation relative to the beam polarization [19], [20]. Since HSFL are mainly linked to melt-resolidification, they also might affect the crystal state of the substrate after sub-ablative irradiation in size scales below EBSD sensitivity [50],[51]. Above 0.56 J/cm^2 spallative ablation was induced on the entire interaction area, whereas crater morphology and ablation width increase with decreasing threshold (visible in the bright contrasted grains and twin in Fig. 5b, s-pol and p-pol, as-polished) also exhibiting first traces of LSFL formation. In the transition range, the rippled topography exhibits intermediate interaction characterized by widening HSFL morphology with incipient spallation in the central area highlighting a preconditioning incubation effect of the melt-induced surface reorganization. A mixture of non-ablative and transition range interaction can be detected for the majority of identified crystal orientations as visible in the orientation triangle in Fig. 5c, where corresponding interaction is marked by a heat map colour code ranging from blue to green. Ablative interaction is concentrated close to the {110} and {111} planes with significantly

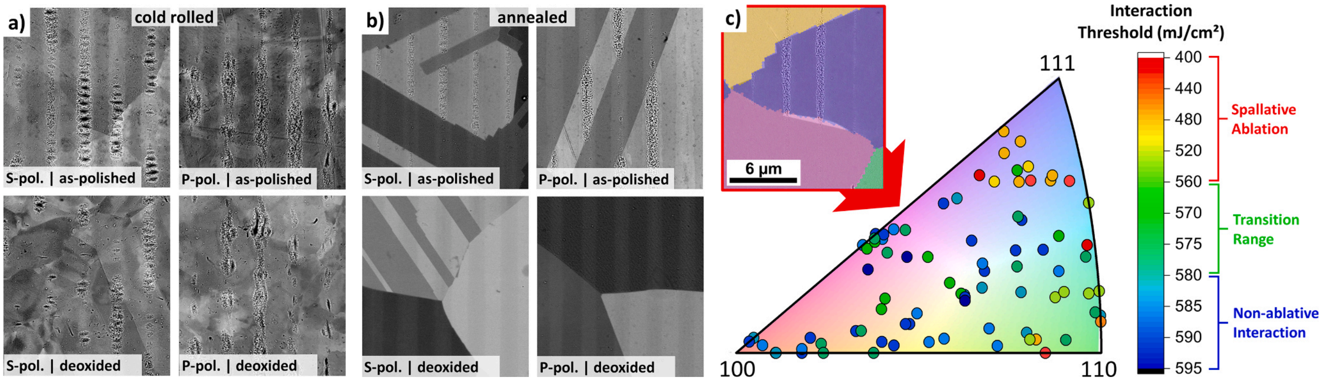

Fig. 5. Investigation of the effect of initial Cu crystallography on USP-DLIP ablation and incubation by single scan line patterning utilizing a fluence of 0.31 J/cm^2 and $N = 32$. a) SEM images in BE contrast of USP-DLIP patterns on mechanically pre-deformed Cu surfaces in as-polished and deoxidized state. b) SEM images in BSE contrast of USP-DLIP patterns on deformation free Cu surfaces in as-polished and deoxidized state. c) SEM analysis on annealed Cu samples utilizing BSE and EBSD in a complementary approach to link thermomechanical substrate interaction after USP-DLIP irradiation to local crystal orientation.

stronger expression of ablative behavior around {111}. According to this, thermomechanical defect implantation and agglomeration faces the lowest crystallographic resistance in ⟨111⟩ direction, corresponding to the early findings of Porteus et al. [52] who stated a comparably low threshold fluence for slip band formation on {111} oriented single crystal Cu mirrors in high power IR laser systems. Further increased ablation could be detected in the vicinity of grain boundaries. In more recent MD simulations on single crystal fcc Ni, {111} plane twinning was directly related to the formation of HSFL [51]. In another MD simulation study, single pulse USP irradiation of Cu showed altering thermal response in relation to crystal orientation as well, where melting and ablation depth is increased for {111} and {110} in comparison to {100} also involving a higher amount of defect formation in shape of voids and dislocations [53]. Here, the quantity of thermomechanical defect formation scales with {111} > {110} > > {100}, which fits the incubation gradient experimentally determined in this analysis. Crystallographic defects induce electron scattering, which affect surface plasmon formation and hence the reflection of laser irradiation, which is also highlighted by the observed increase in ablation interaction in the vicinity of grain boundaries. The physical course of surface modification however also involves HSFL formation as a preceding step before actual ablation, by which incubation by crystallographic defect implantation might involve nano-scaled surface roughening, as well [54].

3.2.4. *Topographic impact of primary pattern formation*

Alongside varying pulse accumulation and laser intensity, considerable topographic influences on absorptance corresponding to both primary and sub-pattern morphology in response to beam polarization have been apparent on USP-DLIP processed Cu in the previously described analysis. The effect of beam polarization on localized absorptance alongside topography modification on primary pattern formation was investigated numerically also applying FEM simulation of USP-DLIP induced substrate thermalization utilizing a specified 2D TTM.

Parallel to interference modulation, beam polarization influences localized absorption of radiation as soon as the incidence angle $\Theta \neq 0°$ [36],[44], which can either result from beam tilting on flat surfaces or by increasing topographic surface slopes. While the first case can be well

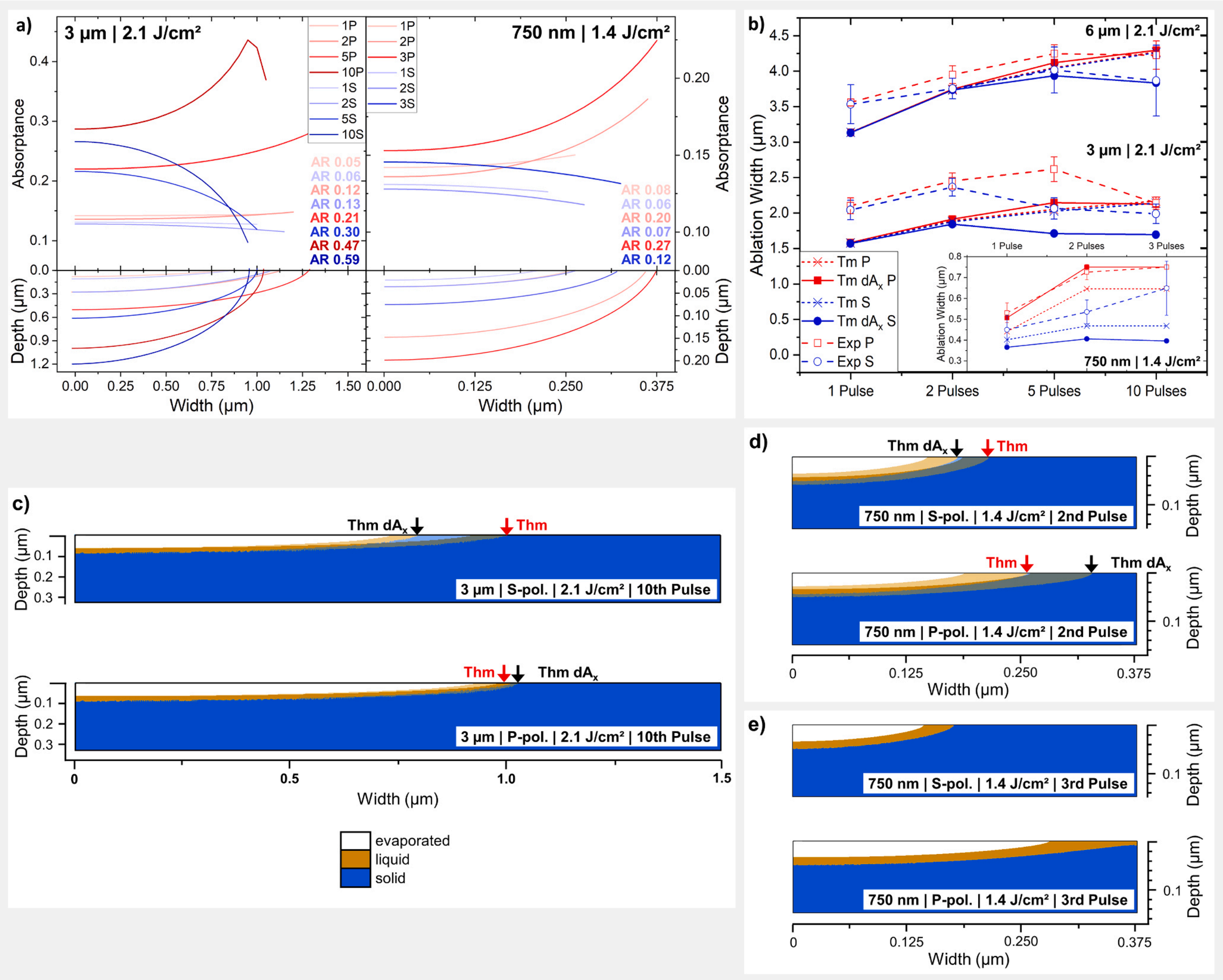

Fig. 6. Combined influence of topography development and beam polarization on multi-pulse USP-DLIP pattern formation with 6 µm and 3 µm at 2.1 J/cm^2 as well as 750 nm at 1.4 J/cm^2. a) localized alteration of absorptance in response to beam polarization and increasing pattern aspect ratio AR of USP-DLIP with 3 µm and 750 nm pattern periodicity. b) ablation width corresponding to substrate thermalization up to T_m calculated by numerical TTM simulation of USP-DLIP at 6 µm, 3 µm and 750 nm pattern periodicity and $N = 1$, 2, 5 and 10 with and without inclusion of topographically altered absorptance A_x in response to beam polarization. The calculated values are compared to experimental data. c) numerically calculated substrate thermalization corresponding to T_{hm} at τ_{eq} (=1.37 × T_m [55]) in response to USP-DLIP with s- and p-polarization of 3 µm periodicity at $N = 10$ with and without the inclusion of A_x. d) numerically calculated substrate thermalization corresponding to T_{hm} in response to USP-DLIP with s- and p-polarization of 3 µm periodicity at $N = 2$ and e) $N = 3$ with and without the inclusion of A_x.

described by the Fresnel equations, localized alteration of Θ_x in response to surface topography additionally requires full knowledge of mostly complex surface geometries. Taking advantage of the uni-directional periodic character of the line-like patterns, the local change in absorptance relative to Θ_x is characterized in direct correlation to the pulse-wise development of a single ablation site, which can be scaled up to the entire pattern. Utilizing the experimental data of fluence + pulse count specific ablation width and depth illustrated in Fig. 2, individual Θ_x slopes for intermediate processing steps can be calculated via Eq. (4). In Fig. 6a, the alteration of polarization dependent localized absorptance A_x correlating to increasing pulse counts is plotted in relation to the corresponding ablation area geometries for 3 µm and 750 nm at 2.1 J/cm^2 and 1.4 J/cm^2. A_0 at $\Theta = 0°$ is taken as a mean value from UV–Vis data for s-pol and p-pol of as-polished Cu at $\lambda = 800$ nm and $N = 1, 2, 5, 10$ in the as-processed state. Alongside a significant pulse wise increase of absorptance A_0 due to oxide agglomeration, an inverse trend of localized absorptance A_x is obvious between s-pol and p-pol. Beam polarization perpendicular to the line-like pattern induces further enhancing localized absorptance along the pattern slope in case of p-pol, while maximum localized absorptance can only be achieved in the ablation area center with decreasing gradient along the edge for s-pol. This polarization dependent absorptance modulation by altering surface topography determines the local uptake of the interference modulated laser intensity. By this, the actual substrate response involves the superposition of both the laser intensity and the absorptance modulation pattern. Consequently, ablation area width is shrinking for s-pol after $N > 2$ closely linked to the pronounced drop in absorptance, while it is increasing for p-pol along the further steepening slope of the ablation site. In the case of 3 µm, the increasing pattern aspect ratio finally induces incidence angles above the pseudo-Brewster angle for Cu at the outer edge of the ablation area at $N = 10$, where absorptance starts to drop for p-pol as well. Likewise, ablation area width starts to decrease similar to s-pol from this point on. The pseudo-Brewster angle for Cu ranges around 78.6° for 1.55 eV but tends to fall with increasing A_0 alongside incubation even below 70°. Applying Eq. (4), one can calculate an approximated pattern aspect ratio of 0.4, where localized absorptance tends to drop for p-pol, as visible for $N = 10$ with an aspect ratio of 0.47. Since aspect ratio/pulse count inversely scales with pattern size in case of USP-DLIP, the threshold aspect ratio for 6 µm is not achieved within $N = 10$, while on 750 nm patterns, aspect ratio does also not reach this critical value, however due to preliminary pattern disruption, in contrast.

For the sub-µm pattern scale, the slope in A_x increases stronger for p-pol in direct comparison to 3 µm, which can be related to the higher impact of melt-kinetics on primary pattern geometry already after two pulses. In the previously described topographic characterization, a significant deviation between estimated and measured ablation in relation to polarization specific intensity pattern modulation was apparent for 750 nm periodicity. Here, the modulated minimum fluence still ranging at approx. 56.8% of F_0 must be considered to interpret ablation area expansion alongside incubation and topographic absorption amplification of p-pol in comparison to s-pol USP-DLIP. However, the distinctive difference in ablation rate already apparent after the first pulse cannot be explained by the effects mentioned above, but rather indicates a preferential initial absorption of p-pol irradiation induced by the considerable partial beam incidence angle of $\Theta = 32.23°$ [36]. Involving a corresponding initial offset of Θ_x in the calculation of A_x induces differing absorptance between s-pol and p-pol even without topography involvement, which additionally increases with incubation (see Fig. 6a). This indicates that polarization specific initial absorption involved in USP-DLIP processing potentially counter balances the reduced fluence amplification by interference modulation in case of p-pol inducing ablation in inverse relation to the actual intensity pattern modulation between s- and p-pol at 750 nm periodicity. A similar but lesser pronounced polarization relation of initial ablation can also be exhibited for 3 µm and 6 µm pattern periodicity whereas this effect appears to still be valid with decreasing partial beam incidence angles.

Involving interference pattern modulation as well as chemically and topographically increased absorptance in numerical FEM simulation of the ultrafast substrate heating allows to identify the combined effects on substrate response in USP-DLIP. Since overall incubation was mainly related to oxidic agglomeration with an insignificant contribution of both defect formation and topography in the UV–Vis examination, the achieved spectroscopic data was utilized to model chemically related absorption increase. To allow differentiation between the single effects of interference modulation and topographic pattern formation alongside chemical incubation, numerical simulation has been conducted with and without inclusion of locally altered A_x. Due to lattice temperatures above the phase explosion threshold temperature T_{PE} [56] achieved in numerical simulation, ablation-kinetics can be considered to involve melt-agitation. Hence, ablation width was related to the thermalization area corresponding to solid/liquid phase transition, where either the melting temperature T_m of Cu (1357.8 K, utilized in Fig. 6b) or the superheating temperature $T_{hm} = 1.37 \times T_m$ associated with ultrafast homogeneous melting within the time period of $\tau_{eq} \approx 4$ ps is considered in numerical simulation [55], to parallelly allow for comparison and evaluation of the applicability of the ultrafast homogeneous melting theory in this study. The course of ablation area expanse in Fig. 6b that is corresponding to substrate thermalization up to T_m without involvement of A_x does not exhibit a significant difference between s- and p-polarization for both 6 µm and 3 µm in case of 2.1 J/cm^2. At 750 nm periodicity, on the other hand, chemical incubation alone suffices to enhance p-pol over s-pol ablation at 1.4 J/cm^2. In contrast to topography insensitive simulation, experimental measurements exhibit characteristic kinks of dropping ablation area width with increasing pulse count, which cannot be mirrored without the involvement of topographical effects on localized absorptance. Consistently, the results achieved by numerical simulation applying A_x follow similar trends like the experimental values even achieving similar results at maximal N for 60% of the patterns, which emphasizes a mutual influence of topographic surface modification and laser/material interaction. The clear deviation between experimental and numerically calculated ablation width in Fig. 6b can be attributed to the pure consideration of the thermalization zone in FEM simulation without including melt-kinetics in the resulting ablation process additionally expanding the melt-affected area.

Pattern scales of 6 µm show a weaker effect of polarization specific absorptance amplification, which is visible in both experimental and calculated ablation width and can be directly linked to lower aspect ratios at similar pulse counts. This accounts to both ablation width enhancement and initial difference in ablation rate between s-pol and p-pol due to a comparably low partial beam incidence angle. Polarization specific ablation is well-expressed for 3 µm, in contrast, exhibiting characteristic kinks in ablation area expansion at $N = 2$ for s-pol and $N = 5$ for p-pol in both experimental and calculated values involving topographic alteration of localized absorptance. The deviation between both numerical calculations of substrate thermalization at $N = 10$ especially for s-pol is additionally highlighted in Fig. 6c, where the difference of thermalization width up to T_{hm} is marked for both s-pol and p-pol. The importance of involving the irradiation incidence angle to correctly model absorptance is especially apparent for 750 nm pattern periodicity, where calculated p-pol ablation width either match or underestimate experimental results depending on the involvement of A_x. Here, the effect of p-pol on ablation area expanse is already apparent after the first pulse, as visible in Fig. 6b with less significance for s-pol. Further processing finally induces melt-overlap for p-pol and shrinking ablation width for s-pol considering substrate thermalization alone. Comparing thermalization between T_m and T_{hm} for 750 nm patter periodicity, it has to be emphasized that only the latter correctly predicts a full overlap of the molten areas corresponding to pattern deterioration in the experimental results at $N = 3$ (compare Fig. 6b, d and e). This indicates a good correlation of T_{hm} with actual ablation related substrate thermalization when combined with incubation related laser/material interaction in numerical calculation. The considerable deviation of both simulated s-pol values from experimental data highlight the additional effect of melt-agitation in ablation area expansion at this pattern scale, as visible in the topographic morphologies displayed in Fig. 2d. As soon as ablation area separation breaks down by melt-overlap, the DLIP induced pattern gets deteriorated, where surface morphology rather exhibits sub-pattern crater features also visible in the ablation area of µm-scaled USP-DLIP patterns. While topography/polarization dependent laser/material interaction has been shown to significantly affect primary topography, sub-pattern formation might similarly be impacted by DLIP alongside multi-pulse processing.

3.2.5. Sub-pattern morphology

The morphology of sub-pattern craters for varying processing parameters has been investigated by means of statistical segmentation based on watershed algorithm utilizing high-contrasted SEM images of 3 µm and 6 µm patterned single laser spots. The investigated morphologic features involving crater size and shape factors (displayed in Fig. 7e) have been chosen to determine multi-pulse response mechanisms in sub-pattern formation alongside primary USP-DLIP. The effect of low- and mid-fluence irradiation has been analyzed for 3 µm periodicity including 0.76 J/cm^2, 2.1 J/cm^2 and 3.37 J/cm^2, while a comparison of 3 µm and 6 µm at 2.1 J/cm^2 involves the influence of pattern scale on crater formation.

Comparing the lower graphs in Fig. 7a-c, initial crater size is showing minor fluence regime specific difference. According to thermal simulation from previous work, spallation ablation can be assumed as the predominant ablation mechanism in first pulse ablation leading to less crater-like ablation features as visible in Fig. 2b-d. In case of mid-fluence regime irradiation, the dominant ablation mechanism changes to phase explosion after the second pulse [16]. Likewise, crater size gets enhanced alongside ongoing pulse accumulation with a shallow slope

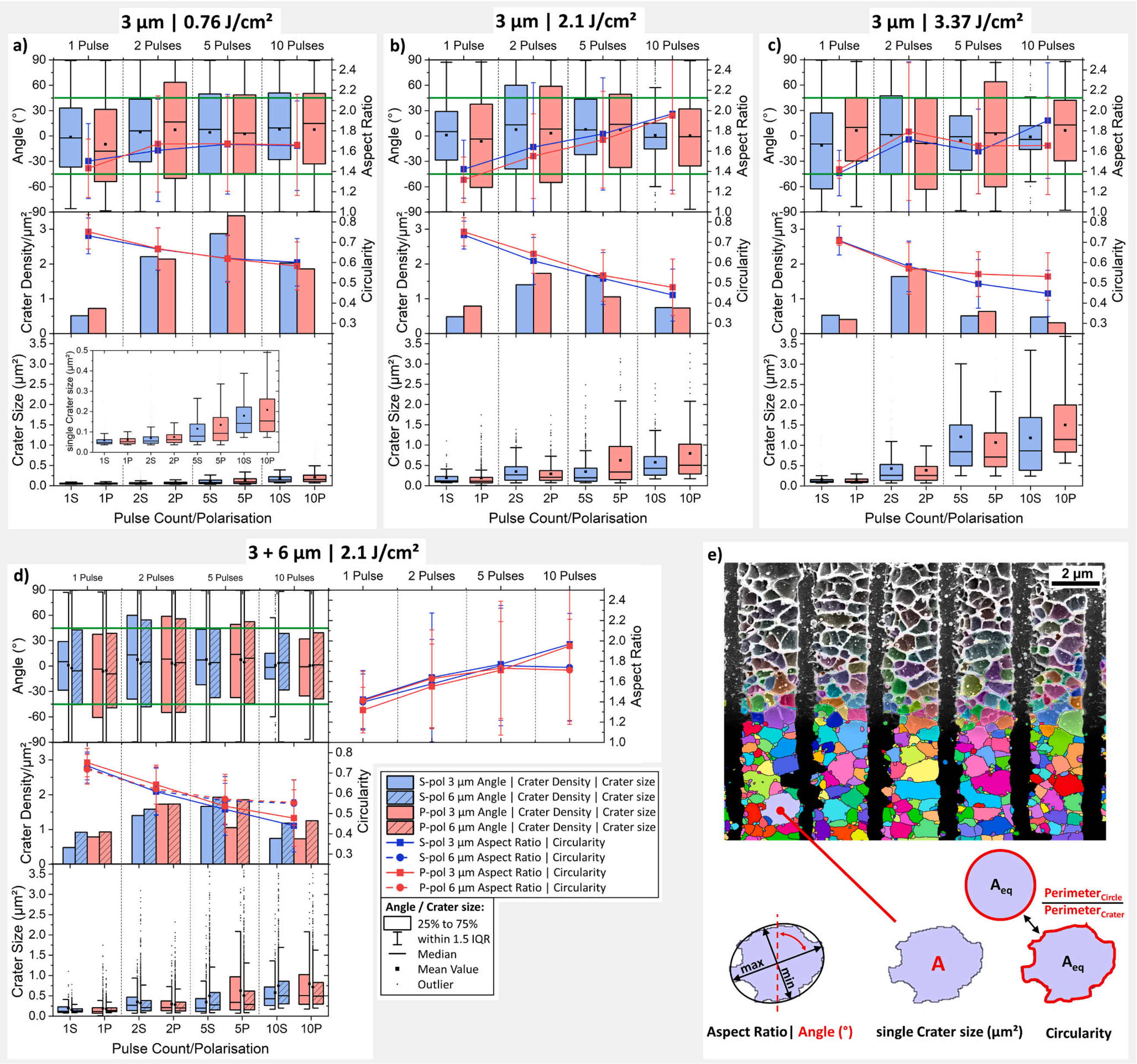

Fig. 7. Statistical segmentation of sub-pattern crater morphology utilizing high contrasted SEM images and watershed algorithm. Crater morphologies are plotted in combined graphs in case of correlated parameters comparing the effect of a) 0.76 J/cm^2, b) 2.1 J/cm^2 and c) 3.37 J/cm^2 fluence at 3 µm periodicity as well as pattern scale between d) 3 µm and 6 µm periodicity at 2.1 J/cm^2 on sub-pattern formation. e) Schematic illustration of the analytical procedure involving the investigated morphological parameters.

for 0.76 J/cm^2 while this behavior is well-pronounced for 2.1 J/cm^2 and especially 3.37 J/cm^2, also indicating a higher pulse-wise increase of absorptance of the modified surfaces. In the mid-fluence regime, the increase in crater size appear to saturate between $N = 5$ and 10 exhibiting higher values for p-pol, while s-pol dominates in crater size after the second pulse. The latter aspect builds an interesting parallel to the inverted absorptance relation between s-pol and p-pol for $N = 2$ in the UV–Vis results after deoxidation. In case of further ablation at 0.76 J/cm^2, crater size increases almost linearly with pulse count on a low scale with consistently higher crater sizes for p-pol, indicating a prevailing dominance of spallation. The falling slope of crater density for increasing pulse agglomeration after $N = 5$ for 0.76 J/cm^2 as well as $N = 2$ for 2.1 J/cm^2 and 3.37 J/cm^2 is directly linked to the continuously increasing crater size, due to the limited space available within the ablation area. Arising from the physical constriction by neighboring craters and the topographical pattern boundaries, radially expanding crater edges merge into a cellular network reducing the circularity of the individual crater shape (visible in Fig. 7e). Further pulsing decreases crater density independent of the utilized laser parameters as soon as circularity falls below 0.6 indicating a recombination of individual craters alongside crater size enhancement in the highly connected sub-pattern mesh. Based on this, the development of crater shape allows to detect preferred expansion/recombination angles depending on primary pattern topography and beam polarization.

Increasing crater aspect ratio is plotted in relation to the orientation angle of the major axis, where 0° is oriented parallel to the line-like pattern and exhibits the preferential orientation angle of crater elongation relative to both beam polarization and the pattern topography. The boxes of the statistical graph represent 50% of the measured values closest related to 0° orientation, by which an overlap with the thresholds of ±45° (highlighted by the green lines) mark preferential perpendicular (90°) overall crater orientation relative to the pattern topography, while no overlap indicates rather parallel (0°) elongation. Closely linked to falling circularity, the aspect ratio of the individual craters increases almost to the same extent for both s- and p-polarization, with higher aspect ratio/lower circularity for s-pol after $N = 10$ in the mid-fluence regime. Here, the elongated s-pol craters are aligned almost parallel to the line-like primary pattern geometry already after the 5th pulse indicating an increasing influence of the lowered ablation area width of the primary pattern at higher pulse counts. A similar effect is also apparent for $N = 10$ in case of p-pol, where the later inset of this behavior follows the same trend as primary pattern formation in relation to localized absorptance A_x. An influence of either the beam polarization or pattern topography on crater orientation is not visible at 0.76 J/cm^2, while slightly higher crater sizes might be linked to preferential p-pol absorption. This might be resulting from both the low pattern aspect ratio and crater expansion at this state of processing for the low fluence regime.

Directly comparing pulse-wise alteration of crater orientation to corresponding primary pattern geometries highlights a paralleled relation between high ablation width and majorly perpendicular crater orientation for p-pol as well as stabilizing lower ablation width and pronounced parallel orientation for s-pol. From this, an influence of polarization related absorptance on topography slopes appears to be effective on sub-pattern features similarly to the already shown impact on primary pattern formation.

To better illuminate this phenomenon, a comparison of crater morphology segmentation was performed on USP-DLIP patterns of 3 μm and 6 μm periodicity with increasing pulse count at a uniform fluence of 2.1 J/cm^2. Here, the slopes of crater density, circularity and aspect ratio alongside increasing pulse count on 6 μm patterns follow a similar trend like the low-fluence regime patterns at 3 μm periodicity, however with higher crater size linked to the fluence. For similar fluence applied, crater size is constantly higher on 3 μm and increases additionally in difference at $N = 5$ for p-pol, whereas the ratio between 3 μm and 6 μm crater size gets inverted at this pulse count for s-pol. In parallel, both crater density and circularity of the 3 μm patterns fall increasingly below the values of 6 μm at this state of pulse agglomeration alongside higher aspect ratio and a more pronounced crater orientation parallel to the pattern geometry. The combined alteration in crater morphology parameters between the two pattern scales after $N = 5$ highlights the significant effect of primary pattern topography on sub-pattern formation: Higher pattern scales exhibit a smaller increase in primary pattern aspect ratio within the ten first consecutive pulses, while at 3 μm periodicity the topography induced alteration in absorptance is already stronger expressed, which appears to also affect sub-pattern formation, as visible by comparison of the s- and p-pol crater size relation between 3 μm and 6 μm. In parallel, the increased topography slope on 3 μm patterns after $N = 5$ focusses surface excitation at the ablation area centers while the steepening topography limits perpendicular crater expanse. However, beam polarization appears to also affect crater morphology at lower pulse counts before it gets affected by the primary pattern topography as visible in the pronounced perpendicular p-pol crater orientation independent of pattern scale. The overall widening of crater diameter appears to be preferentially aligned in perpendicular orientation to the beam polarization, which fits to the polarization relation of localized absorptance A_x and correlates with common LSFL formation theory [19]. Preferential localized absorption within the crater-like network of the initial sub-pattern topography at 0.76 J/cm^2 thus appears to be involved in the transformation to LSFL sub-pattern morphology after higher pulse counts as observed in planar patterning at accumulated 21 J/cm^2 (see Fig. 3).

As an additional effect, 3 μm ablation area width is in lower size-relation to the pulse-wise increasing sub-pattern crater size in the mid-fluence regime, by which the bottom profile of the ablation area at $N = 10$ is majorly related to single craters, especially for s-pol at 2.1 J/cm^2 and 3.37 J/cm^2 (see Fig. 2c). The effect of low primary/sub-pattern feature size relation is further amplified in the case of 750 nm compared to 3 μm periodicity, whereas incubation induced increase in crater size might invert the dominance in topography formation between primary and sub-pattern. The Cu-specific incubation impact on ablation kinetics appears to cause the previously observed low fluence/pulse count threshold for qualitative processing at sub-μm pattern scale observed [16],[17]. This points out the need to consider sub-pattern formation alongside primary DLIP patterning in case of USP-DLIP on Cu for pattern scales <6 μm. Since crater size enhancement depends on laser energy absorption, threshold fluences to avoid negative interplay between primary and sub-pattern formation for USP-DLIP can be interpolated from the experimental results. Involving primary pattern size and the specific incubation behavior, the polarization dependent threshold fluences for high USP-DLIP pattern quality on Cu correspond to $F_s \approx P$ and $F_p \approx 2/3\,P$ (in J/cm^2 and μm). However, additional effects on laser/substrate interaction, like e.g. a reduced absorption of s-pol USP-DLIP irradiation at high single beam incidence angles for sub-μm pattern scales have to be considered in parallel, where higher fluences need to be applied to achieve ablation.

4. Conclusions

The geometry and morphology of USP-DLIP patterns on Cu have been shown to be dependent on different ablation mechanisms in the low- and mid-fluence regime as well as pattern scale in parallel interaction of primary and sub-pattern formation. Within the first 2 to 10 consecutive pulses, pattern geometry formation and chemical surface conditioning is initiated, which predominantly influences further USP-DLIP processing and the resulting pattern morphology. Here, the underlying mechanisms in pattern formation are related to beam polarization involving both interference pattern modulation, as well as altering absorptance by pulse wise substrate modification that play an interconnected role.

Incubation during USP-DLIP processing of Cu turns out to be too complex to allow the application of general methodology based on

Gaussian spot examination. This is mainly due to the combined impact of beam polarization and primary pattern topography on localized absorptance, but also relates to sub-pattern formation mechanisms in case of smaller pattern periodicities scaling close to the sub-pattern feature sizes. To better understand the contribution of incubation mechanisms on multi-pulse USP-DLIP pattern formation, the individual incubation mechanisms have been selectively investigated:

- Between the different individual influences on incubation, surface oxidation, both as passivation layer and process-induced, has the highest impact on initial absorptance and its pulse wise increase during USP-DLIP processing of Cu at a wavelength of 800 nm. The results highlight the impact of initial substrate condition on laser processing also including its deformation state, which must be considered in laser parametrization. Directly related to the extent of ablative interaction, incubation by oxidic agglomeration scales higher in the mid- compared to the low-fluence regime. Since oxide agglomeration also covers previously unprocessed surface compartments, the resulting enhancement of initial absorptance must be considered in pattern formation, as well. In low-fluence processing, oxidic pre-conditioning leads to higher initial aspect ratios, while at mid-fluence processing, pattern formation starts to get negatively affected with raising fluence in the case of 3 μm patterns. Here, melt-agitation during phase explosion is enhanced alongside the increasing surface absorptance, which causes the affection of pattern peaks in both s- and p-pol multi-pulse USP-DLIP processing.
- Incubation by crystallographic defect formation mainly plays a role on deformation free Cu surfaces exhibiting low initial absorptance of 0.036 at 800 nm. In contrast, mechanical polishing already induces a defect related increase of absorptance, which is barely surpassed during multi-pulse USP-DLIP processing. This might be linked to the upper limit of dislocation density in crystallographic deformation of Cu, which appears to be closely approximated in polishing already, whereby sufficient defect formation during laser processing to considerably contribute to incubation cannot be accumulated. Here, the impact of surface oxide on overall absorptance can again be observed, as immersion etched samples exhibit reduced ablative interaction compared to their as-polished counter parts. Low-fluence USP-DLIP was applied at increased pulse counts close to the corresponding multi-pulse ablation threshold to investigate the impact of crystallographic substrate condition on incubation. Here, preferentially enhanced incubation by defect implantation on annealed Cu surfaces could be linked to preferential crystallographic orientations, where ablative interaction scales with a relation of $\{111\} > \{110\} > > \{100\}$. The course of defect related incubation includes HSFL formation, followed by further enhancing spallative ablation, both expanding from the ablation area center outwards along the descending slope of the intensity pattern in case of low-fluence USP-DLIP irradiation. Here, a certain topographic effect on absorptance by HSFL formation might as well be involved alongside further pronouncing sub-pattern formation due to the nano-scaled feature size [54]. In the case of mechanically polished Cu exhibiting significantly increased initial absorptance, ablation induces considerable LSFL formation correlating to low-fluence regime pattern morphology after twice the pulse count. Here, LSFL formation appears to be the main mechanism involved in pattern formation for s-pol at sub-threshold fluence.
- Incubating effects of topography alteration unrelated to beam polarization have mainly been observed for nm-scaled sub-pattern morphologies after the first laser pulse, where the relation between feature size and laser wavelength induce enhanced absorptance [54]. This is visible in both the significant increase of ablation width as well as the drop of measured absorptance in UV–Vis spectroscopy on immersion etched samples after the second consecutive pulse. Increasing sub-pattern feature size, especially related to phase explosion ablation, appear to reduce topography induced overall absorptance, but rather follow polarization sensitive localized absorptance during pulse wise sub-pattern formation similarly to the primary pattern.
- The formation of the primary line-like pattern proves to be predominantly dependent on beam polarization in direct interaction with pulse-wise surface modification. Comparison to experimental data exhibits the applicability of the introduced numerical model to determine pulse wise substrate thermalization corresponding to locally increased absorptance A_x and pattern formation, which allows for a better interpretation of the impact of the different incubation mechanisms. Absorptance is increased alongside topography edges in perpendicular orientation to the beam polarization, which favors ablation area expanse for p-pol and ablation depth increase for s-pol in case of μm-scaled USP-DLIP patterns. Reaching aspect ratios above 0.4, absorptance at the edge of the ablation area also decreases for p-pol inducing a trend of inverted ablation area expanse similar to s-pol ablation. Pattern peaks appear to also suffer partial ablation at higher fluences in case of p-pol at 3 μm pattern periodicity due to the lesser modulated interference minima in combination with a preconditioning of the pattern peaks increasing the local absorptance. In contrast, higher pattern depths are achieved for p-pol at sub-μm pattern scales in inverse relation to intensity modulation, where melt pile-ups can contribute to pattern formation but become destabilized in case of further pulse agglomeration. Multi-pulse sub-μm pattern stability is improved in case of low-fluence regime USP-DLIP processing due to decreased melt-agitation and reduced oxidic agglomeration.
- Sub-pattern formation is predominantly determined by the specific ablation mechanisms induced by USP irradiation of Cu. The initial sub-pattern morphology is characterized by crater-like features, which align into a mesh-like network along consecutive pulsing. Depending on the ablation mechanism prevailing throughout incubation, crater-sizes significantly increase in case of phase explosion, by which they tend to merge with the primary pattern at low primary/sub-pattern feature size ratio especially in the mid-fluence regime. In the case of spallative ablation, the mesh-like sub-pattern may transform into LSFL at higher pulse counts in the low-fluence regime. Alteration of crater morphology is governed by polarization dependent reshaping similar to LSFL formation and alignment along primary pattern scales in case of sufficiently high aspect ratios.
- Alongside primary and sub-pattern formation, beam polarization has been shown to also impact initial absorption in relation to the partial beam incidence angle. This leads to polarization specific ablation efficiency in inverse relation to the actual difference in interference modulation between s-pol and p-pol. This effects scales higher with decreasing pattern scale due to enhanced single beam incidence angles [36], by which single and multi-pulse ablation thresholds effective in USP-DLIP patterning scale above in case of p-pol and below the corresponding values calculated using incubation models relating on Gaussian spot experiments, in case of s-pol. According to these findings, single beam interaction with the substrate surfaces also impacts DLIP processing alongside interference pattern formation, which has not been considered, so far.

In summary, pattern geometry and morphology formation on Cu in response to USP-DLIP underlies a complex interplay of mutually interacting multi-pulse agglomeration effects impacting the development of both primary and sub-pattern. Based on our findings, polarization dependent locally increased absorptance alongside topographic and chemical surface modification plays a similar critical role as intensity pattern modulation by interference. Hence, laser/material interaction in USP-DLIP is defined by the superposition of both intensity and absorptance modulation alongside multi-pulse processing, which as well affects initial surface and partial beam properties. By determining the impact of the individual agglomeration effects related to the specific optical and physical properties of Cu, these findings can be used as a foundation to improve the understanding of multi-pulse USP-DLIP of other metallic materials, as well. Using this knowledge, increased precision in targeted micro- and nanometer scaled surface pattering via laser interference inducing higher impacts of surface functionalization in the manifold application areas previously mentioned can be realized.

Author contributions

D.W. Müller conceived the idea, designed the interference-based laser setup, developed the numerical model and conducted the numerical analyzation. Sample preparation, surface characterization via confocal laser scanning microscopy (LSM) and scanning electron microscopy (SEM) as well as morphologic segmentation were performed by D.W. Müller and S. Lößlein. D.W. Müller and M. Briesenick conducted UV–Vis Spectroscopy. C. Pauly executed electron back-scatter diffraction analysis. Data interpretation and preparation of the manuscript was done by D.W. Müller. S. Lößlein and C. Pauly contributed in editing the manuscript. F. Mücklich and G. Kickelbick supervised the work.

Declaration of Competing Interest

The authors declare that they have no known competing financial interests or personal relationships that could have appeared to influence the work reported in this paper.

Data availability

Data will be made available on request.

Acknowledgements

The authors acknowledge financial support in the project “ZuMat” (supported by the Saarland State Chancellery with resources from the European Fund for Regional Development (EFRE)) and for the project “Pulsatec”(supported as part of the EFRE program Interreg Greater Region). Parts of this work were financially supported by the German Research Foundation (DFG) within the projects “Controlled bacterial interaction to increase the antimicrobial efficiency of copper surfaces” (project number 415956642) and “Influence of surface topography and chemistry on the wetting behavior of laser-structured metallic surfaces” (project number 435334669). The authors acknowledge funding for the PFIB/SEM instrument used for the EBSD measurements by Deutsche Forschungsgemeinschaft (DFG, INST 256/510-1 FUGG).

References

[1] A.F. Lasagni, C. Gachot, K.E. Trinh, M. Hans, A. Rosenkranz, T. Roch, S. Eckhardt, T. Kunze, M. Bieda, D. Günther, V. Lang, F. Mücklich, Direct laser interference patterning, 20 years of development: From the basics to industrial applications, in: Proc. SPIE 10092, Laser-Based Micro- Nanoprocessing XI, 2017, p. 1009211, https://doi.org/10.1117/12.2252595.

[2] H. Heffner, M. Soldera, A.F. Lasagni, Optical enhancement of fluorine-doped tin oxide thin films using infrared picosecond direct laser interference patterning, Adv. Eng. Mater. (2022) 2200266, https://doi.org/10.1002/adem.202200266.

[3] B. Voisiat, W. Wang, M. Holzhey, A.F. Lasagni, Improving the homogeneity of diffraction based colours by fabricating periodic patterns with gradient spatial period using direct laser interference patterning, Sci. Rep. 9 (2019) 7801, https://doi.org/10.1038/s41598-019-44212-4.

[4] A.M. Kietzig, M.N. Mirvakili, S. Kamal, P. Englezos, S.G. Hatzikiriakos, Laser-patterned super-hydrophobic pure metallic substrates: Cassie to Wenzel wetting transitions, J. Adhes. Sci. Technol. 25 (2011) 2789–2809, https://doi.org/10.1163/016942410X549988.

[5] P.G. Grützmacher, A. Rosenkranz, C. Gachot, How to guide lubricants – tailored laser surface patterns on stainless steel, Appl. Surf. Sci. 370 (2016) 59–66, https://doi.org/10.1016/j.apsusc.2016.02.115.

[6] A. Rosenkranz, L. Reinert, C. Gachot, F. Mücklich, Alignment and wear debris effects between laser-patterned steel surfaces under dry sliding conditions, Wear. 318 (2014) 49–61, https://doi.org/10.1016/j.wear.2014.06.016.

[7] R. Schieber, C. Mas-Moruno, F. Lasserre, J.J. Roa, M.P. Ginebra, F. Mücklich, M. Pegueroles, Effectiveness of direct laser interference patterning and peptide immobilization on endothelial cell migration for cardio-vascular applications: an in vitro study, Nanomaterials. 12 (2022) 1217, https://doi.org/10.3390/nano12071217.

[8] J. Minguela, D.W. Müller, F. Mücklich, L. Llanes, M.P. Ginebra, J.J. Roa, C. Mas-Moruno, Peptidic biofunctionalization of laser patterned dental zirconia: a biochemical-topographical approach, Mater. Sci. Eng. C 125 (2021), 112096, https://doi.org/10.1016/j.msec.2021.112096.

[9] D.W. Müller, S. Lößlein, E. Terriac, K. Brix, R. Kautenburger, K. Siems, R. Möller, F. Mücklich, Increasing antibacterial efficiency of Cu surfaces by targeted surface functionalization via ultrashort pulsed direct laser interference patterning (USP-DLIP), Adv. Mater. Interfaces 8 (2021) 2001656, https://doi.org/10.1002/admi.202001656.

[10] K. Siems, D.W. Müller, L. Maertens, A. Ahmed, R. Van Houdt, R.L. Mancinelli, S. Baur, K. Brix, R. Kautenburger, N. Caplin, J. Krause, R. Demets, M. Vukich, A. Tortora, C. Roesch, G. Holland, M. Laue, F. Mücklich, R. Moeller, Testing laser-structured antimicrobial surfaces under space conditions: the design of the ISS experiment BIOFILMS, Front. Sp. Technol. 2 (2022) 1–18, https://doi.org/10.3389/frspt.2021.773244.

[11] S. Indrišiūnas, B. Voisiat, M. Gedvilas, G. Račiukaitis, New opportunities for custom-shape patterning using polarization control in confocal laser beam interference setup, J. Laser Appl. 29 (2017), 011501, https://doi.org/10.2351/1.4976679.

[12] F. Fraggelakis, G.D. Tsibidis, E. Stratakis, Tailored sub-micrometer periodic surface structures via ultrashort pulsed direct laser interference patterning, Phys. Rev. B 103 (2021), 054105, https://doi.org/10.1103/physrevb.103.054105.

[13] F. Mücklich, A. Lasagni, D. Claus, Laser interference metallurgy – using interference as a tool for micro / nano structuring, Int. J. Mater. Res. 97 (2006) 1337–1344.

[14] B. Voisiat, C. Zwahr, A.F. Lasagni, Growth of regular micro-pillar arrays on steel by polarization-controlled laser interference patterning, Appl. Surf. Sci. 471 (2019) 1065–1071, https://doi.org/10.1016/j.apsusc.2018.12.083.

[15] B. Voisiat, S. Milles, A.F. Lasagni, Impact of molten pool dynamics on resultant surface structures during direct laser interference patterning, J. Laser Micro Nanoeng. 16 (2021) 1–6, https://doi.org/10.2961/jlmn.2021.01.2006.

[16] D.W. Müller, T. Fox, P.G. Grützmacher, S. Suarez, F. Mücklich, Applying ultrashort pulsed direct laser interference patterning for functional surfaces, Sci. Rep. 10 (2020) 3647, https://doi.org/10.1038/s41598-020-60592-4.

[17] M. Bieda, M. Siebold, A. Fabián, Applied Surface Science Fabrication of sub-micron surface structures on copper, stainless steel and titanium using picosecond laser interference patterning, Appl. Surf. Sci. 387 (2016) 175–182, https://doi.org/10.1016/j.apsusc.2016.06.100.

[18] Y. Fuentes-Edfuf, J.A. Sánchez-Gil, C. Florian, V. Giannini, J. Solis, J. Siegel, Surface plasmon polaritons on rough metal surfaces: role in the formation of laser-induced periodic surface structures, ACS Omega. 4 (2019) 6939–6946, https://doi.org/10.1021/acsomega.9b00546.

[19] J. Bonse, S. Gräf, Maxwell meets marangoni—a review of theories on laser-induced periodic surface structures, Laser Photonics Rev. 14 (2020) 1–25, https://doi.org/10.1002/lpor.202000215.

[20] A. Rudenko, A. Abou-Saleh, F. Pigeon, C. Mauclair, F. Garrelie, R. Stoian, J. P. Colombier, High-frequency periodic patterns driven by non-radiative fields coupled with Marangoni convection instabilities on laser-excited metal surfaces, Acta Mater. 194 (2020) 93–105, https://doi.org/10.1016/j.actamat.2020.04.058.

[21] A. Sikora, M. Faucon, L. Gemini, R. Kling, G. Mincuzzi, LIPSS and DLIP: from hierarchical to mutually interacting, homogeneous, structuring, Appl. Surf. Sci. 591 (2022), 153230, https://doi.org/10.1016/j.apsusc.2022.153230.

[22] F. Fraggelakis, G.D. Tsibidis, E. Stratakis, Ultrashort pulsed laser induced complex surface structures generated by tailoring the melt hydrodynamics, Opto-Electron. Adv. 5 (2022), 210052, https://doi.org/10.29026/oea.2022.210052.

[23] K.K. Anoop, R. Fittipaldi, A. Rubano, X. Wang, D. Paparo, A. Vecchione, L. Marrucci, R. Bruzzese, S. Amoruso, Direct femtosecond laser ablation of copper with an optical vortex beam, J. Appl. Phys. 116 (2014), 113102, https://doi.org/10.1063/1.4896068.

[24] Y. Jee, M.F. Becker, R.M. Walser, Laser-induced damage on single-crystal metal surfaces, J. Opt. Soc. Am. B. 5 (1988) 648–659, https://doi.org/10.1364/josab.5.000648.

[25] G. Raciukaitis, Ultra-short pulse lasers for microfabrication: a review, IEEE J. Sel. Top. Quantum Electron. 27 (2021) 1100112, https://doi.org/10.1109/JSTQE.2021.3097009.

[26] S.E. Kirkwood, A.C. Van Popta, Y.Y. Tsui, R. Fedosejevs, Single and multiple shot near-infrared femtosecond laser pulse ablation thresholds of copper, Appl. Phys. A Mater. Sci. Process. 81 (2005) 729–735, https://doi.org/10.1007/s00339-004-3135-7.

[27] A.Y. Vorobyev, C. Guo, Reflection of femtosecond laser light in multipulse ablation of metals, J. Appl. Phys. 110 (2011), 043102, https://doi.org/10.1063/1.3620898.

[28] S.M. Lößlein, M. Kasper, R. Merz, C. Pauly, D.W. Müller, M. Kopnarski, F. Mücklich, Patience alone is not enough - a guide for the preparation of low-defect sections from pure copper Geduld allein reicht nicht! - Ein Leitfaden zur Herstellung defektarmer Schliffe von Reinkupfer, Prakt. Metallogr. Metallogr. 58 (2021) 388–407, https://doi.org/10.1515/pm-2021-0031.

[29] D.W. Müller, A. Holtsch, S. Lößlein, C. Pauly, C. Spengler, S. Grandthyll, K. Jacobs, F. Mücklich, F. Müller, In-depth investigation of copper surface chemistry modification by ultrashort pulsed direct laser interference patterning, Langmuir. 36 (2020) 13415–13425, https://doi.org/10.1021/acs.langmuir.0c01625.

[30] N. Habbache, N. Alane, S. Djerad, L. Tifouti, Leaching of copper oxide with different acid solutions, Chem. Eng. J. 152 (2009) 503–508, https://doi.org/10.1016/j.cej.2009.05.020.

[31] J. Schille, L. Schneider, U. Loeschner, Process optimization in high-average-power ultrashort pulse laser microfabrication: how laser process parameters influence efficiency, throughput and quality, Appl. Phys. A Mater. Sci. Process. 120 (2015) 847–855, https://doi.org/10.1007/s00339-015-9352-4.

[32] P.T. Mannion, J. Magee, E. Coyne, G.M. O'Connor, T.J. Glynn, The effect of damage accumulation behaviour on ablation thresholds and damage morphology in ultrafast laser micro-machining of common metals in air, Appl. Surf. Sci. 233 (2004) 275–287, https://doi.org/10.1016/j.apsusc.2004.03.229.

[33] C.W. Cheng, S.Y. Wang, K.P. Chang, J.K. Chen, Femtosecond laser ablation of copper at high laser fluence: modeling and experimental comparison, Appl. Surf. Sci. 361 (2016) 41–48, https://doi.org/10.1016/j.apsusc.2015.11.055.

[34] Y. Ren, J.K. Chen, Y. Zhang, Optical properties and thermal response of copper films induced by ultrashort-pulsed lasers, J. Appl. Phys. 110 (2011) 1–7, https://doi.org/10.1063/1.3662897.

[35] A.D. Rakic, A.B. Djuris, J.M. Elazar, M.L. Majewski, Optical properties of metallic films for vertical-cavity optoelectronic devices, Appl. Opt. 37 (1998) 5271–5283.

[36] S. Amoruso, X. Wang, C. Altucci, C. De Lisio, M. Armenante, R. Bruzzese, R. Velotta, Thermal and nonthermal ion emission during high-fluence femtosecond laser ablation of metallic targets, Appl. Phys. Lett. 77 (2000) 3728–3730, https://doi.org/10.1063/1.1329869.

[37] S. Indrišiūnas, B. Voisiat, M. Gedvilas, G. Račiukaitis, Polarisation control in direct laser interference ablation setup for flexible generation of periodic patterns, Proc. LPM2017 (2017) 1–5. http://www.jlps.gr.jp/lpm/lpm2017/.

[38] D. Legland, I. Arganda-Carreras, P. Andrey, MorphoLibJ: integrated library and plugins for mathematical morphology with ImageJ, Bioinformatics. 32 (2016) 3532–3534, https://doi.org/10.1093/bioinformatics/btw413.

[39] C.A. Schneider, W.S. Rasband, K.W. Eliceiri, NIH image to ImageJ: 25 years of image analysis, Nat. Methods 9 (2012) 671–675, https://doi.org/10.1038/nmeth.2089.

[40] J. Winter, M. Spellauge, J. Hermann, C. Eulenkamp, H.P. Huber, M. Schmidt, Ultrashort single-pulse laser ablation of stainless steel, aluminium, copper and its dependence on the pulse duration, Opt. Express 29 (2021) 14561, https://doi.org/10.1364/oe.421097.

[41] P. Simon, J. Ihlemann, Ablation of submicron structures on metals and semiconductors by femtosecond UV-laser pulses, Appl. Surf. Sci. 109–110 (1997) 25–29, https://doi.org/10.1016/S0169-4332(96)00615-0.

[42] A. Blumenstein, M.E. Garcia, B. Rethfeld, P. Simon, J. Ihlemann, D.S. Ivanov, Formation of periodic nanoridge patterns by ultrashort single pulse UV laser irradiation of gold, Nanomaterials. 10 (2020) 1998, https://doi.org/10.3390/nano10101998.

[43] C. Gattinoni, A. Michaelides, Atomistic details of oxide surfaces and surface oxidation: the example of copper and its oxides, Surf. Sci. Rep. 70 (2015) 424–447, https://doi.org/10.1016/j.surfrep.2015.07.001.

[44] P.P. Rajeev, S. Sengupta, A. Das, P. Taneja, P. Ayyub, P.K. Kaw, G.R. Kumar, Laser absorption in short-lived metal and nanoplasmas, Appl. Phys. B Lasers Opt. 80 (2005) 1015–1019, https://doi.org/10.1007/s00340-005-1827-0.

[45] P. Buffat, J.P. Borel, Size effect on the melting temperature of gold particles, Phys. Rev. A 13 (1976) 2287–2298, https://doi.org/10.1103/PhysRevA.13.2287.

[46] N. Tsakiris, K.K. Anoop, G. Ausanio, M. Gill-Comeau, R. Bruzzese, S. Amoruso, L. J. Lewis, Ultrashort laser ablation of bulk copper targets: dynamics and size distribution of the generated nanoparticles, J. Appl. Phys. 115 (2014), 243301, https://doi.org/10.1063/1.4885196.

[47] M. Hans, A. Erbe, S. Mathews, Y. Chen, M. Solioz, F. Mücklich, Role of copper oxides in contact killing of bacteria, Langmuir. 29 (2013) 16160–16166, https://doi.org/10.1021/la404091z.

[48] I. Platzman, R. Brener, H. Haick, R. Tannenbaum, Oxidation of polycrystalline copper thin films at ambient conditions, J. Phys. Chem. C 1101–1108 (2008).

[49] A.A. Ionin, S.I. Kudryashov, S.V. Makarov, P.N. Saltuganov, L.V. Seleznev, D. V. Sinitsyn, V.A. Lednev, S.M. Pershin, Electron emission and ultrafast low-fluence plasma formation during single-shot femtosecond laser surface ablation of various materials, JETP Lett. 101 (2015) 308–312, https://doi.org/10.1134/S0021364015050112.

[50] J. Vincenc Oboňa, V. Ocelík, J.C. Rao, J.Z.P. Skolski, G.R.B.E. Römer, A.J. Huis In 't Veld, J.T.M.D. Hosson, Modification of Cu surface with picosecond laser pulses, Appl. Surf. Sci. 303 (2014) 118–124, https://doi.org/10.1016/j.apsusc.2014.02.104.

[51] X. Sedao, M.V. Shugaev, C. Wu, T. Douillard, C. Esnouf, C. Maurice, S. Reynaud, F. Pigeon, F. Garrelie, L.V. Zhigilei, J.P. Colombier, Growth twinning and generation of high-frequency surface nanostructures in ultrafast laser-induced transient melting and resolidification, ACS Nano 10 (2016) 6995–7007, https://doi.org/10.1021/acsnano.6b02970.

[52] J.O. Porteus, D.L. Decker, J.L. Jernigan, W.N. Faith, M. Bass, 17.7 evaluation of metal mirrors for high-power applications by multi-threshold damage analysis, IEEE J. Quantum Electron. 14 (1977) 896–897, https://doi.org/10.1109/JQE.1977.1069587.

[53] Q. Xiong, Z. Li, T. Kitamura, Effect of crystal orientation on femtosecond laser-induced thermomechanical responses and spallation behaviors of copper films, Sci. Rep. (2017) 1–14, https://doi.org/10.1038/s41598-017-09559-6.

[54] A.Y. Vorobyev, C. Guo, Enhanced absorptance of gold following multipulse femtosecond laser ablation, Phys. Rev. B 72 (2005) 1–5, https://doi.org/10.1103/PhysRevB.72.195422.

[55] B. Rethfeld, K. Sokolowski-Tinten, D. von der Linde, S.I. Anisimov, Ultrafast thermal melting of laser-excited solids by homogeneous nucleation, Phys. Rev. B 65 (2002) 1–4, https://doi.org/10.1103/PhysRevB.65.092103.

[56] S.Y. Wang, Y. Ren, C.W. Cheng, J.K. Chen, D.Y. Tzou, Micromachining of copper by femtosecond laser pulses, Appl. Surf. Sci. 265 (2013) 302–308, https://doi.org/10.1016/j.apsusc.2012.10.200.

Paper V:

Microstructure versus Topography: The impact of crystallographic substrate modification during Ultrashort Pulsed Direct Laser Interference Patterning on the antibacterial properties of Cu

Daniel Wyn Müller[1,2*], Ben Josten[1], Sebastian Wältermann[1,2], Christoph Pauly[1], Sebastian Slawik[1], Kristina Brix[3], Ralf Kautenburger[3], Frank Mücklich[1]

[1]Chair of Functional Materials, Department of Materials Science, Saarland University, 66123 Saarbrücken, Germany.

[2]SurFunction GmbH, 66123 Saarbrücken, Germany

[3]Department of Inorganic Solid-State Chemistry, Elemental Analysis, Saarland University, 66123 Saarbrücken, Germany.

Published in July 2024 as an invited paper in the collection "Antimicrobial surface treatments for applications on confined space stations and bioburden reduction" in "Frontiers in Materials" and accessible online via: https://doi.org/10.3389/fmats.2024.1397937

Abstract:

Topographic surface patterning in the micro- and nanometer scale has evolved into a well applied approach in surface functionalization following biomimetic blueprints from nature. Depending on the production process an additional impact of process-related substrate modification has to be considered in functional surface optimization. This is especially true in case of antimicrobial applications of Cu surfaces where a modification of the substrate properties might impact bactericidal efficiency. In this regard, the effect of ultrashort pulsed direct laser interference patterning on the microstructure of pure Cu and resulting antimicrobial properties was investigated alongside line-like patterning in the scale of single bacterial cells. The process-induced microstructure modification was shown to play an important role in corrosion processes on Cu surfaces in saline environment, whereas the superficial microstructure impacts both corrosive interaction and ion emission. Surprisingly, antimicrobial efficiency is not predominantly following deviating trends in Cu ion release rates but rather depends on surface topography and wettability, which was shown to be impacted by the substrate microstructure state, as well. This highlights the need of an in-depth understanding on how different surface properties are simultaneously modulated during laser processing and how their interaction has to be designed to acquire an effective surface optimization e.g. to agitate active antimicrobial surface functionalization.

Own contributions:

Conceptualization, Data curation, Formal Analysis, Funding acquisition, Investigation, Methodology, Project administration, Software, Validation, Visualization, Writing–original draft, Writing–review and editing.

frontiers | Frontiers in Materials

TYPE Original Research
PUBLISHED 30 July 2024
DOI 10.3389/fmats.2024.1397937

Microstructure versus topography: the impact of crystallographic substrate modification during ultrashort pulsed direct laser interference patterning on the antibacterial properties of Cu

Daniel Wyn Müller[1,2]*, Ben Josten[1], Sebastian Wältermann[1,2], Christoph Pauly[1], Sebastian Slawik[1], Kristina Brix[3], Ralf Kautenburger[3] and Frank Mücklich[1]

[1]Department of Materials Science, Saarland University, Saarbrücken, Germany, [2]SurFunction GmbH, Saarbrücken, Germany, [3]Department of Inorganic Solid-State Chemistry, Elemental Analysis, Saarland University, Saarbrücken, Germany

OPEN ACCESS

EDITED BY
Malgorzata Holynska,
European Space Research and Technology Centre (ESTEC), Netherlands

REVIEWED BY
Omid Sharifahmadian,
Alexander Dubcek University in Trencin, Slovakia
Sivashankar Krishnamoorthy,
Luxembourg Institute of Science and Technology (LIST), Luxembourg

*CORRESPONDENCE
Daniel Wyn Müller,
daniel.mueller@uni-saarland.de

RECEIVED 08 March 2024
ACCEPTED 04 July 2024
PUBLISHED 30 July 2024

CITATION
Müller DW, Josten B, Wältermann S, Pauly C, Slawik S, Brix K, Kautenburger R and Mücklich F (2024), Microstructure versus topography: the impact of crystallographic substrate modification during ultrashort pulsed direct laser interference patterning on the antibacterial properties of Cu.
Front. Mater. 11:1397937.
doi: 10.3389/fmats.2024.1397937

Introduction: Topographic surface patterning in the micro- and nanometer scale has evolved into a well applied approach in surface functionalization following biomimetic blueprints from nature. Depending on the production process an additional impact of process-related substrate modification has to be considered in functional surface optimization. This is especially true in case of antimicrobial applications of Cu surfaces where a modification of the substrate properties might impact bactericidal efficiency.

Methods: In this regard, the effect of ultrashort pulsed direct laser interference patterning on the microstructure of pure Cu and resulting antimicrobial properties was investigated alongside line-like patterning in the scale of single bacterial cells.

Results and Discussion: The process-induced microstructure modification was shown to play an important role in corrosion processes on Cu surfaces in saline environment, whereas the superficial microstructure impacts both corrosive interaction and ion emission. Surprisingly, antimicrobial efficiency is not predominantly following deviating trends in Cu ion release rates but rather depends on surface topography and wettability, which was shown to be impacted by the substrate microstructure state, as well. This highlights the need of an in-depth understanding on how different surface properties are simultaneously modulated during laser processing and how their interaction has to be designed to acquire an effective surface optimization e.g., to agitate active antimicrobial surface functionalization.

KEYWORDS

direct laser interference patterning, antimicrobial surfaces, biomimetic surface structures, ultrashort laser pulses, antibacterial Cu

1 Introduction

While the need for improved decontamination measures has become painfully aware to the public during the recent pandemic, biofilm prevention has already been an increasing issue in numerous technical and medical applications before. In 2019, the damage caused by biofilms was estimated to run up to 4,000 billion USD, majorly comprising technical impairment with a share of approx. 66% solely related to corrosion and 20% to the health sector (Cámara et al., 2022). In parallel, biofilm related health issues become increasingly severe with the ongoing emerge of antimicrobial resistances in pathogenic microorganisms, where multi-resistant bacteria have even been found in the most remote habitats (Sobisch et al., 2019).

Concepts to control the microbial load of technical and hygienic surfaces has been in the focus of research for decades aiming to prevent severe material deterioration as well as a spread of pathogens in multiple environments (Mikolay et al., 2010; Zea et al., 2020; Siems et al., 2022). The most common approaches on antimicrobial surfaces are following a strategy of either contact guiding up to repulsion to avoid initial microbial seeding or active killing mechanisms. Periodic surface patterns that scale slightly below single bacterial cells have been found to reduce the overall bacterial surface loads for certain tested bacteria strains (Peter et al., 2020). This has been shown to be most effective against several gram-negative bacteria species, whereas a universal applicability of the repelling topography effect cannot be established (Fadeeva et al., 2011; Epperlein et al., 2017). Following the natural blueprints of topographies found on dragonfly and cicada wings, nm-scaled surface asperities can also be designed to induce a rupture of bacterial cell membranes (Tripathy et al., 2017). However, a supporting role of secondary functional surface properties such as wettability, which introduces attractive forces or external drag has to be considered here to drive the mechanical mode of action (Tripathy et al., 2017; Boinovich et al., 2018). Such physico-chemical surface properties have in fact repeatably been shown to be highly involved in bacteria/surface interaction (Pratt and Kolter, 1998; Kimkes and Heinemann, 2020; Maikranz et al., 2020).

Applying active antimicrobial agents like Copper (Cu) and Silver (Ag), the state of the surface has to be similarly considered since the deactivation of adherent microorganisms is directly related on the quantitative emission of toxic ions (Hans et al., 2014; Meister et al., 2022). On Cu surfaces, effective ion emission has been shown to be negatively affected by thermally induced oxide layers, with a corresponding decrease in antimicrobial efficiency against *Escherichia coli* (Hans et al., 2013). A similar effect was observed on Cu based surfaces after different methods of laser processing, whereas a change in alloy stoichiometry could also be determined to play an important role (Boinovich et al., 2019; Ahmed et al., 2023). Variations in surface finishing on pure Cu surfaces has been shown to cause different states of surface deformation and grain fining down to nm-scales where antimicrobial efficiency could be impacted by enhanced Cu ion release. Here, the superficial microstructure of Cu has been shown to be modified by polishing routines (Luo et al., 2019a), surface processing via spray-coating and shot peening (Razavipour et al., 2022). Consequently, rapid bacterial killing rates on Cu surfaces have recently been achieved by an significant increase of initial Cu emission by means of a porous surface design that aims for a high surface/volume ratio (Smith et al., 2022).

Further approaches to improve antimicrobial properties of Cu surfaces aim for a combination of the active toxicity induced killing effect with e.g., mechanical surface functionalization by involving the surface concepts of dragonfly or cicada wings (Emelyanenko et al., 2020; Yi et al., 2021). However, the gain of the additional mechanic killing effect is associated with losses in Cu ion release due to the chemical surface modification of the structuring methodology used (Hans et al., 2013; Boinovich et al., 2019).

In a recent study, the antimicrobial efficiency of Cu surfaces against *E. coli* have been improved by applying periodic surface patterns in the scale of single bacteria cells via ultrashort pulsed direct laser interference patterning (USP-DLIP) (Müller et al., 2021). Increased bactericidal activity was associated with both topographic and physico-chemical surface modification, where a process-induced impact on the substrate properties was also evident. This antimicrobial surface concept is currently investigated in the ISS flight experiments BIOFILMS and Touching Surfaces (Siems et al., 2022). In this context, the objective of this study is to provide a detailed analysis of how USP-DLIP processing alters the functional surface properties of Cu surfaces, which may be associated with their active antimicrobial mechanisms with a particular focus on crystallographic substrate modification. Analyzation involves X-ray diffraction (XRD), energy dispersive X-ray spectroscopy (EDS) and electron back-scatter diffraction (EBSD) aside of different imaging modes of scanning electron microscopy (SEM) including focused ion beam cross-sectioning (FIB-SEM). Assessment of the resulting functional surface properties is conducted via contact angle (CA) measurement and wet plating experiments monitoring the antimicrobial properties against *E. coli*. The dissection of process-induced influences on the superficial microstructure and related antimicrobial activity allows for an improved comprehension of the complementing effects of the various functional surface properties impacted by USP-DLIP to further enhance antimicrobial efficiency of Cu surfaces.

2 Materials and methods

2.1 Material preparations and USP-DLIP

Oxygen-free Cu (>99.95% purity, provided in sheets of 1 mm thickness from *Wieland*, Germany) was cut to coupon sizes of $10 \times 25\ \mathrm{mm}^2$. Surface finishing of the Cu samples was executed following a stepwise procedure involving fine grinding on 1200 grit silicon carbide paper and polishing by three consecutive steps (6 µm, 3 µm, 1 µm diamond suspension with decreasing pressure of 15 to 10 N) that results in a roughness $R_a < 10$ nm. Between each polishing step, a thorough cleaning with distilled water and ethanol is conducted to remove suspension remnants. At this point, one share of the as-polished samples additionally underwent annealing for 12 h at 450°C and 10^{-7} mbar in a vacuum furnace followed by electropolishing [as described in (Lößlein et al., 2021)] to provide Cu substrates without microstructure deformation from cold-roll processing of the Cu sheets and mechanical surface deformations from polishing. Another share of both as-polished and annealed

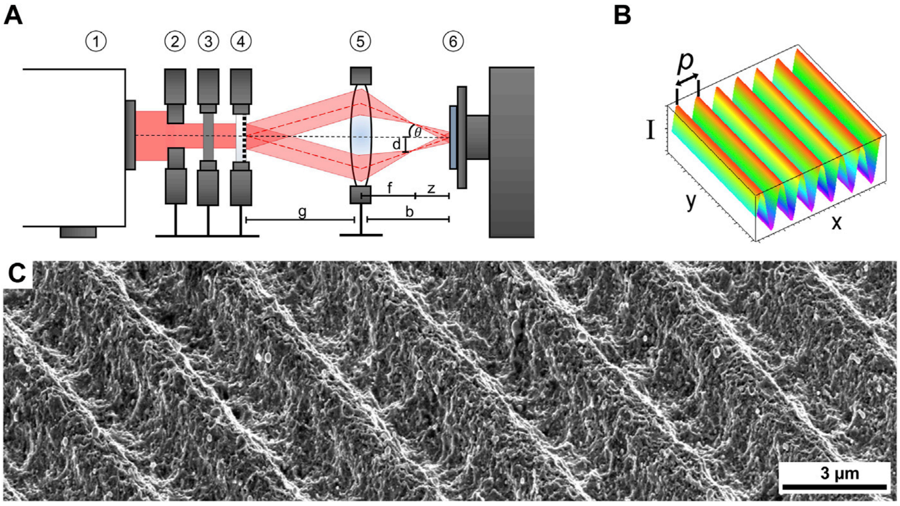

FIGURE 1
(A) optical Setup used for USP-DLIP: 1 laser source, 2 aperture, 3 waveplate, 4 DOE, 5 lens system, 6 sample on x-, y- motion stage. **(B)** intensity pattern resulting from two beam interference. **(A, B)** have been adapted with permission from Müller et al. (2020a). **(C)** SEM image of USP-DLIP patterned surface in SE contrast at 52° sample tilt.

samples is held back to be used as refence surfaces in the further experiments.

Topographic surface patterning was conducted via USP-DLIP at a pulse duration τ_p of 100 fs at Full Width Half Maximum (FWHM) and centered wavelength λ of 800 nm using a *Ti:Sapphire* laser system (*Spitfire, Spectra Physics*). In the optical DLIP setup illustrated in Figure 1A (Müller et al., 2020a), a wave plate is used to adjust the polarization of the seed beam, which is further separated into two partial beams by a diffractive optical element (DOE). A multi-lens system finally superimposes the separated partial beams on the substrate surface. This induces two-beam laser interference in which the individual beams are p-polarized in orientation to the line-like interference pattern (illustrated in Figure 1B). The setup of both the DOE and multi-lens system adjusts the single beam incidence angle Θ, by which the pattern periodicity P can be defined according to Eq. 1.

$$p = \frac{\lambda}{2\sin(\theta)} \tag{1}$$

In this study, a partial beam incidence angle of $\Theta = 7.66°$ was applied resulting in a fixed pattern periodicity of 3 µm. Cu surfaces were processed by scanning the sample surface in continuous pulsing mode at a fluence of 2.1 J/cm^2 and 1 kHz pulse frequency. The pulse overlap was tuned to a spatially agglomeration pulse count of N = 10 by adjusting x- and y-hatching according to (Müller et al., 2020a). The resulting surface topography is shown in Figure 1C).

Both as-polished as well as annealed Cu samples underwent USP-DLIP processing (laser structured LS and heat treated before laser structuring HT-LS), from which a third share of LS samples is extracted to be annealed as described above. This results in topographically patterned surfaces without mechanically deformed microstructure (laser structured, then heat treated, LS-HT). Process-induced surface oxidation of the USP-DLIP samples was removed for half of the sample batches via immersion etching in 3% citric acid for 1 minute in an ultrasonic bath [according to (Müller et al., 2020b)]. This further allows analyzation in an as-processed and naturally passivated surface state after etching (LS-E, HT-LS-E, and LS-HT-E).

From this procedure, a matrix of Cu surface states is gained that vary in topography, microstructure and the oxidic passivation layer (listed in Table 1), which allows for investigation on their individual impact on antimicrobial surface properties.

2.2 Surface wettability

Contact angle (CA) measurements were conducted on each sample type listed in Table 1 after 3 weeks of aging in ambient conditions. In this passivation state, surface wettability alteration after surface treatment via mechanical/electro-polishing, annealing or USP-DLIP processing can be considered as mostly stabilized (Lößlein et al., 2022). The static contact angle of distilled water was monitored in triplicates at a fixed droplet volume of 3 µL by means of a Drop Shape Analysator DSA 100 (*Krüss GmbH*). The CA was measured both in orthogonal and parallel sample orientation to also include anisotropic droplet propagation in case of the line-like surface patterns.

2.3 Wet plating

Escherichia coli K12 WT(BW25113) was cultured according to the protocol provided by Molteni et al. (2010) by aerobic overnight growth in Lysogeny broth (LB) medium at 37°C and 220 rpm shaking speed. The stationary cells were collected from 5 mL culture medium by centrifugation for 15 min at 5000 × g. The final bacteria testing solution (BTS) was gained by washing the collected cells in three similar consecutive centrifugation steps followed by resuspension, each in 5 mL of phosphate buffered saline (PBS) with

TABLE 1 Surface states of the different sample types.

Sample type	Topography	Microstructure	Passivation layer
polished	flat	cold-roll + polishing deformation	natural
annealed		without microstructure deformation	natural
LS	patterned in relation to single bacterial cell size	cold-roll + polishing deformation + USP-DLIP induced surface defects	USP-DLIP induced
LS-E			natural
HT-LS		only USP-DLIP induced surface defects	USP-DLIP induced
HT-LS-E			natural
LS-HT		without microstructure deformation	after annealing (10^{-7} bar)
LS-HT-E			natural

a pH value of 7.4. The initial average cell count following this routine ranges in the scale of 9 log CFU/mL. Prior to wet plating, the bacteria were stored at 4°C on Agar plates, which were provided by the group of Prof. Rolf Müller from the Helmholtz Centre of Infection Research, Saarbrücken.

To enable a homogeneous exposure area on the individual samples despite heterogeneous surface wetting properties, droplets of 40 µL of the BTS were applied in predefined areas within polyvinyl chloride (PVC) rings exhibiting an inner circular diameter of 5 mm (Müller et al., 2021). The slightly hydrophobic PVC prevents BTS from spreading on hydrophilic and facilitates droplet covering of the predefined area on hydrophobic surfaces. During the experiment, the samples were stored in water saturated environment at ambient temperature. After three exposure intervals of 30, 60, and 90 min, two doses of 5 µL were withdrawn probing a different droplet for each interval. Surface adherent bacteria were resuspended by vigorous pipetting in parallel orientation to the surface pattern to avoid bacterial retention by topographic shadowing within the pattern valleys. Assessment of the viable bacterial cell numbers was conducted by the standard plate count method following serial 2 log dilution of a single 5 µL BTS dose in PBS and spreading on LB agar plates. To enable counting of the remaining colony forming units (CFU), the inoculated agar plates were incubated overnight at 37°C and 80% moisture. The second 5 µL dose was diluted 600-fold in 0.1% HNO_3 followed by analyzation via inductively coupled plasma triple quadrupole mass spectrometry (ICP-QQQ, *Agilent 8900*) to determine the Cu ion concentration within the BTS corresponding to the parallelly monitored CFU values.

Complementary to BTS exposure, a second set of wet plating experiments was conducted utilizing PBS solution without *E. coli* to assess differences in corrosion behavior of the individual surface states related to the presence of bacteria.

2.4 Characterization

Characterization of the USP-DLIP surface topography was conducted by means of confocal laser scanning microscopy (LSM) utilizing a *LEXT OLS4100 3D Measuring Laser Microscope* by *Olympus* (50× lens, 2x and 6x increased magnification, laser wavelength 405 nm) to assure conformity of the patterned sample types. Detailed analysis of the individual surfaces was applied via scanning electron microscopy (SEM) including characterization in both secondary and back-scatter electron contrast (SE, BSE) as well as focused ion beam cross-sectioning (FIB) and electron back-scatter diffraction (EBSD). High-resolution SE imaging in immersion mode was used for both surface and cross-section imaging using the system´s in-lens detector (*Helios Nanolab600* by *FEI*). Analyzation involved both the initial surface state as well as corrosion damage and passivation layer formation after exposure within the wet plating experiments. For FIB cross-sectioning, the investigated surface site was covered with a protective layer of electron and ion beam induced Pt-deposition to prevent ion-induced degradation of the substrate surface. An additional contrast layer of ~10 nm $Au_{80}Pd_{20}$ was previously applied via sputter coating to distinguish between original surface features and the Pt-layers (highlighted in Figure 2A). Measurement of passivation layer thickness was conducted using *ImageJ* (*FiJi*) (Schneider et al., 2012). BSE imaging by means of a solid-state detector was used in combination with EBSD to visualize the sub-surface microstructure within single cross-sections (*Helios PFIB G4 CXe* by *Thermo Fisher*). For both SE and BSE, an acceleration voltage of 5 kV was applied. Surface imaging in SE contrast was conducted at a sample tilt of 52° degree for improved visualization of topographical features. FIB cross-sectioning was executed at 30 kV beam current for both Ga- and Xe-ion beams. EBSD measurements were carried out at 20 kV acceleration voltage and a beam current of 26 nA using a high-speed CMOS camera (*Velocity Super* by *EDAX*) set to a 4 × 4 binning. For EBSD analysis, neighboring domains were measured on a hexagonal grid with a step size of 50 nm. EBSD patterns were recorded and processed using the Neighbor Pattern Averaging and Reindexing (NPAR) algorithm in *OIM Analysis 8.6* software by *EDAX* to improve indexing rate and reduce orientation noise. Thereafter, lattice planes oriented parallel to the cross-section surface were extracted. From the data, both Inverse Pole Figure (IPF) maps in relation to the sample normal of the analyzed surface

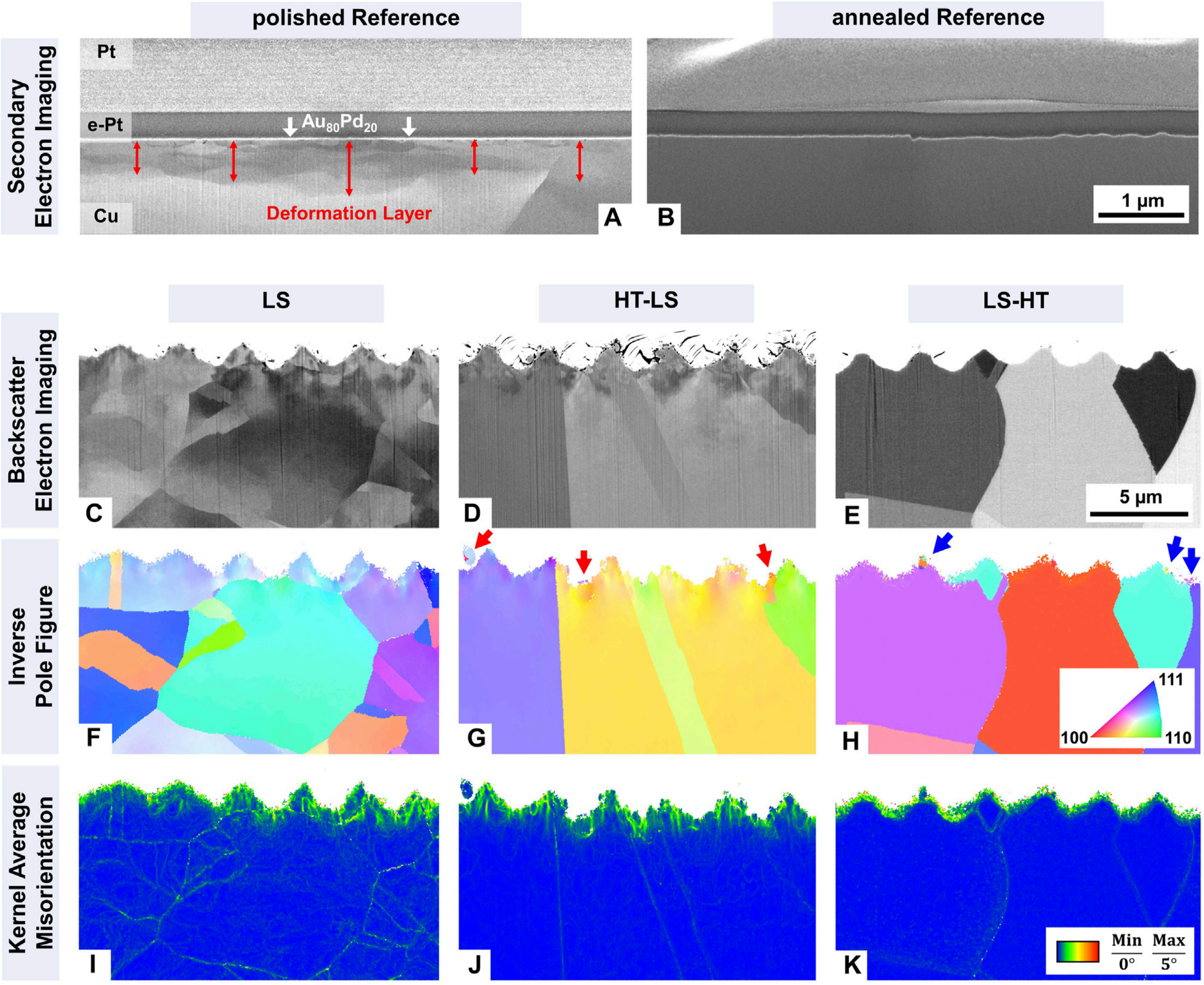

FIGURE 2
SEM analysis of sample microstructure for the different surface states via FIB cross-sectioning, utilizing SE imaging for **(A)** as-polished and **(B)** annealed reference surfaces, as well as BSE imaging for **(C)** LS, **(D)** HT-LS and **(E)** LS-HT samples. Both IPF-Maps and KAM-maps from EBSD analysis are displayed in **(F, I)** for LS, **(G, J)** for HT-LS and **(H, K)** for LS-HT. Red and blue arrows in **(G, H)** highlight superficial domains of rearranged crystal orientation. The scale bars in **(B, E)** apply uniformly to the reference and USP-DLIP surfaces, respectively.

and Kernel Average Misorientation (KAM) relative to the next neighbors were taken for depth related analyzation of superficial deformation states.

To assess the initial as well as the post-exposure phase and grain deformation state of the different surface types, X-ray diffraction (*PANalytical X'Pert PRO-MPD*) utilizing Cu K_α radiation was applied in both Bragg-Brentano (BB-XRD) and grazing incidence (GI-XRD) geometry at a grazing angle of 1° with a Goebel mirror as primary optics. In these parametrizations, 95% of the measured signal is originating from substrate depths of approx. 12 µm (Cu 111) to 24 µm (Cu 311) in case of BB-XRD and <1.1 µm for GI-XRD according to Cullity and Stock (2001). The diffraction plane was oriented parallel to the line-like patterns to avoid topographic shadowing of the valley surface compartments.

3 Results and discussion

3.1 Initial surface state

The initial surface state of the individual sample types was analyzed by means of SEM/FIB - USP-DLIP processed samples additionally underwent EBSD analysis - as well as BB-/GI-XRD and CA measurement to determine both crystallographic and functional surface properties. In case of the reference surfaces, SE imaging of FIB cross-sections displays a deformation layer of approximately 500 nm depth (496 ± 238 nm) in case of the mechanically polished Cu surface, which is absent on the additionally annealed samples (see Figures 2A, B).

Based on the DLIP parametrization chosen, line-like surface patterns have been generated on the differently pretreated Cu surfaces that exhibit trench widths of approx. 2.13 ± 0.09 µm and depths of approx. 0.97 ± 0.1 µm. The applied fluence of 2.1 J/cm^2 induces substrate ablation dominated by phase explosion kinetics, which was previously been shown to impact the superficial substrate crystallography by mechanically as well as thermally induced defect implantation (Xiong et al., 2017; Müller et al., 2023). The resulting laser induced modification of the substrate microstructure was visualized via FIB cross-sectioning by means of the orientation contrast in BSE imaging as well as EBSD. Cross-sections of LS samples exhibit intragranular orientation gradients that can be related to the cold-rolled state of the Cu sheets. The annealed sample types HT-LS and LS-HT do not show variations in intragranular orientation contrast but a marginally increased grain size, instead (compare Figures 2C–E). In the surface vicinity of HT-LS samples, a deformation layer originating from USP-DLIP processing is exhibited, which intersects with the intragranular contrast alterations of the cold-rolled substrate in case of LS. Accordingly, a comparable microstructure state can be observed in the micropatterned surface areas for LS and HT-LS surface types via EBSD examination. This is indicated both by color-gradients in IPF-mapping, as well as low angle orientation misorientations visualized in KAM-maps that can be related to geometrically necessary dislocations (GND) (displayed in Figures 2F, G, I, J). In contrast, ultimately annealed LS-HT surfaces do not exhibit misorientations within the bulk substrate. Here, EBSD analysis of both LS and HT-LS samples indicates a predominant impact of laser processing on the superficial microstructure state that additionally adds to preexisting deformation layers. In superficial areas, minor domains of crystallographic reorientation can additionally be observed in IPF-mapping (examples marked in Figure 2G with red arrows). Smaller domains of rearranged crystal orientation of previously deformed surface compartments during annealing are visible within the topographic surface features of the LS-HT sample type in Figure 2H (blue arrows). In the LS-HT cross-sections, misorientations determined via KAM are limited to the pattern surfaces without loop shaped progressions into the substrate interior, which indicates a possible link to boundary artifacts of the misorientation measurement on the intersection between substrate surface and covering layers of Pt (Figure 2H).

Monitoring the texture state of the differently processed near surface volumes via BB-XRD reveals a predominant peak intensity for 200 oriented lattice planes parallel to the surface that is linked to the cold-rolled initial Cu surface state (see Figure 3A). Annealing does not impact this characteristic texture, whereas a slight increase of the Cu 111 integral intensities can be observed in comparison to the LS and polished reference surfaces. Based on these observations, USP-DLIP processing does not appear to have a significant effect on the state of bulk Cu microstructure in depths >12 µm. A process-related impact on functional substrate properties might therefore be predominantly related to superficial defect implantation in smaller depths. With a shallower signal depth of approx. 1.1 µm (95% of the signal intensity), peak dominance shifts to Cu 220 in GI-XRD with a more pronounced deviation between the different surface states (visible in Figure 3B). For both polished and LS samples, Cu peak integral intensities scale as 111 < 200 < 220 in similar magnitude. This characteristic relation is amplified after annealing with a preferential increase of the 220 intensity as visible for LS-HT samples as well as the annealed reference. Since the sample irradiation angle is fixed in GI-XRD, the measured spectrum does not show grain orientation distribution in parallel orientation to the sample surface, whereas different mostly complex indicated orientations contribute to the individual peaks. However, in the GI-parametrization applied here, Cu grains with a preferred crystal orientation 111 parallel to the substrate surface exhibit a 220 plain orientation that might contribute to the GI-Cu 220 signal due to a close angle relation. By this, the increase of the Cu 111 peak in BB-XRD analysis might at least partially contribute to the increasing Cu 220 dominance in GI-XRD for annealed Cu surfaces. USP-DLIP processing of annealed surfaces in case of HT-LS again induces higher 111 and 200 signals in GI-XRD, however with inverted relation in comparison to polished and LS surfaces, which might be linked to crystallographic adaption mechanisms like twinning following plastic deformation (Vincenc Oboňa et al., 2014; Zhao et al., 2014; Xiong et al., 2017).

Comparing the individual laser processed surface states before and after immersion etching exhibits a neglectable impact of post-processing on Cu substrate crystallography, while the previously visible Cu_2O 111 peak related to process-induced oxidation vanishes for LS and HT-LS samples (visible in Figure 3B). Peak broadening can already be observed visually for polished in comparison to annealed reference surfaces in Figure 3B with relation to a higher deformation state, similarly applicable in LS, HT-LS vs. LS-HT comparison. Considering the peak width deviation at FWHM between the individual deformed surfaces states, peak broadening can be observed for the USP-DLIP processed sample types LS and HT-LS compared to the polished reference indicating a higher overall deformation state (see Figure 3C). The annealed USP-DLIP samples LS-HT and LS-HT-E exhibit higher peak broadening than the respective annealed reference sample as well, but scale below the polished reference.

The impact of microstructure modification aside of topographic remodeling during USP-DLIP on functional surface properties was assessed by CA measurements after 3 weeks of aging under ambient conditions. At this stage, surface passivation involving monolithic oxide growth and agglomeration of carbon species can be assumed to have reached mostly stabilized conditions. In case of the line-like USP-DLIP surface topographies, wetting behavior can be assessed by both the quantitative CA values and droplet shape anisotropy. Due to the pattern geometry, droplets tend to get pinned on the pattern peaks, while they can extend along the pattern trenches with lesser topographic resistance leading to an elongation parallel to pattern orientation in case of higher hydrophilicity. Accordingly, a mild CA drop in orthogonal orientation to the pattern is always accompanied by increasing droplet anisotropy, since the simultaneous decrease in parallelly oriented CA is more significant. Comparing surface wettability of the different patterned surface states indicates a dominant impact of laser-induced substrate modification, whereas both the LS and HT-LS sample types exhibit high CA and low anisotropy close to the super-hydrophobic wetting regime, while LS-HT surfaces exhibit lower hydrophobicity accompanied by increasing droplet anisotropy, as visible in Figure 3D. Immersion etching also affects surface wettability indicated by decreasing CA, however with a lower impact compared to laser-induced substrate deformation. The effect of

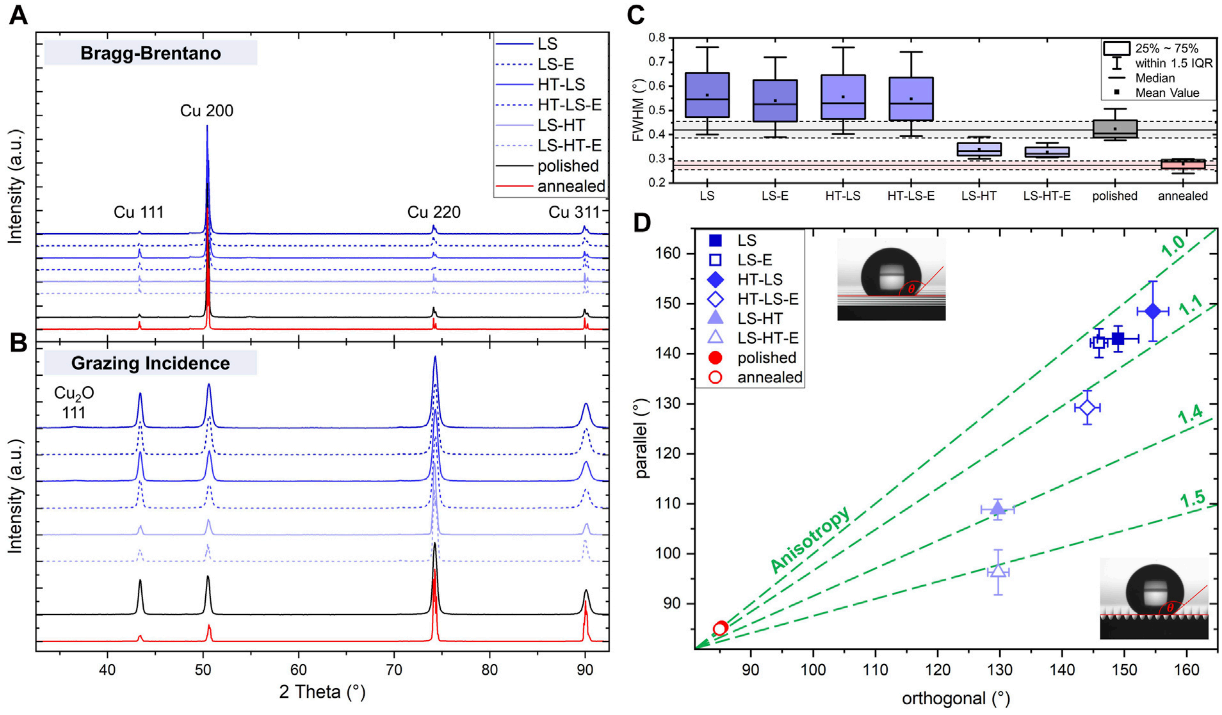

FIGURE 3
Results of the XRD analysis of initial crystallographic surface and substrate states via **(A)** Bragg-Brentano and **(B)** Grazing Incidence. **(C)** comparison of peak broadening in GI-XRD between the different surface types represented by peak width data at FWHM. **(D)** surface wettability of the individual surface types monitored via CA measurement.

crystallographic defect density on CA can also be seen for the reference surfaces, however on a significantly lower scale. Based on this, process induced microstructure modification alongside USP-DLIP appears to play an at least similarly important role in modifying surface wettability than the actual topographic surface modification. A recent study observed similar relations between the superficial defect state of Cu substrate microstructure and surface wetting in case of polished surface topographies where a quicker increase in hydrophobicity was linked to higher chemical activity of surfaces that exhibit higher defect densities (Lößlein et al., 2023).

3.2 Antibacterial efficiency against *E. coli*

Wet plating was conducted on samples that underwent 3 weeks of aging under ambient conditions corresponding to the functional surface properties previously described. The intervals for probing were selected to enable continuous monitoring of the reduction in bacteria viability, while still detecting a count of viable bacteria after the longest exposure duration on most surfaces. This approach intends to enable a better comparison of antimicrobial efficiency between the different Cu surfaces despite deviating interaction under BTS exposure.

Each of the Cu surfaces exhibit high antimicrobial properties, with a >99.9% reduction of viable bacteria cell count already being assessed after 60 min of exposure independent of the surface preparation routine (see the line graph in Figure 4A). Within this time interval, contact killing on USP-DLIP surfaces is surpassing the references leading to final CFU reduction rates after 90 min that scale between one and three orders of magnitude higher (indicated by the bar graph in Figure 4A). Comparison of CFU reduction between as-processed and immersion etched samples exhibit higher antimicrobial efficiency of the former within the differently processed USP-DLIP surface types. LS and immersion etched HT-LS samples exhibit an initial lag phase within the first 30 min of exposure that shows an inverted relation to their respective CA-values. A similar effect was previously monitored in a comparable experiment, where lower initial CFU reduction was linked to yet developing surface wetting on highly hydrophobic surfaces which delays initial bacteria/surface contact (Müller et al., 2021). Both LS-HT sample types do not show this initial lag phase, where lower CA values and high droplet anisotropy indicate an early initial surface wetting in the Wenzel state. However, the as-processed HT-LS samples do not seem to follow this relationship. They exhibit initial killing rates that indicate well-expressed initial surface wetting in contrast to the high CA values measured. Considering the different bacteria/surface contact states in the initial experiment phase due to a still developing surface wetting of the BTS droplet on USP-DLIP samples, CFU values after 90 min of exposure might provide the most suitable indication of actual differences in bacterial killing of the different surface states. Here, CFU reduction levels are of the same order of magnitude between the majority of laser processed surface types, with reduction rates normalized to similar surface/area ratio that scale between 2.5 and 7.5 times higher than the reference surfaces (bar graph in Figure 4A).

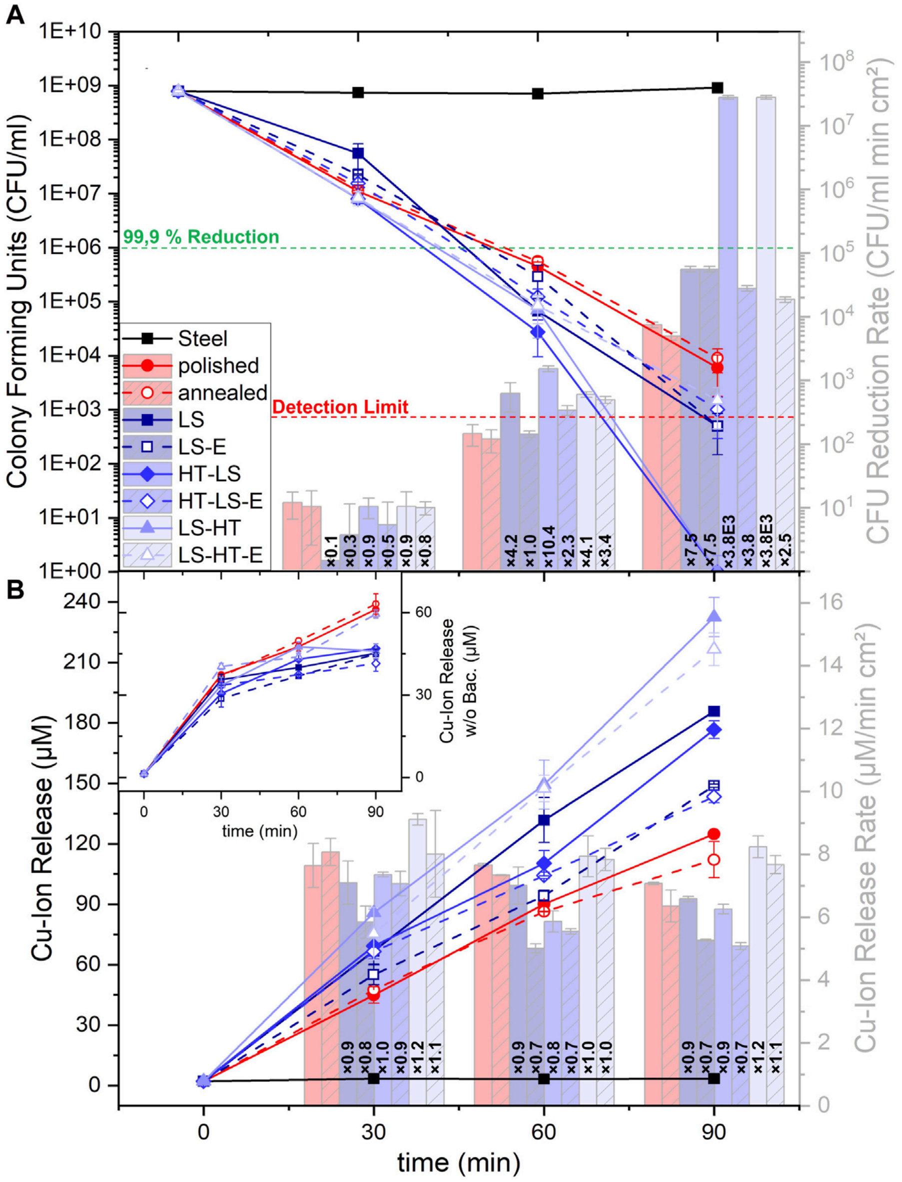

FIGURE 4
Graphical reproduction of the results from the wet plating experiments on the different sample types: **(A)** Bacterial killing monitored via the assessment of the viable cell count (CFU) after 30, 60 and 90 min of exposure (line graph), with a normalization of the assessed data to homogeneous surface ratios representing the time dependent killing rate (bar graph). **(B)** parallelly detected Cu ion release (line graph), also normalized in surface area and time dependency (bar graph). The inlay graph represents Cu ion release measured for PBS exposure without inoculated bacteria.

Between the immersion etched surface states, the highest killing efficiency measured is shifted from LS-HT to LS between 60 and 90 min of exposure, which is however not observed for the as-processed samples. It has to be mentioned that the abrupt decrease of measured CFU for both HT-LS and LS-HT after 90 min of exposure is most likely linked to the close vicinity of the measured values to the detection limit of the CFU counting methodology for low amounts of viable bacteria. Thereby, the actual viable bacterial count might range closer to the values of the LS surface type in a similar relation like the deviation range between the final CFU values of the immersion etched USP-DLIP surface types.

In contrast to the variable progression of the CFU values, Cu ion release exhibits an almost stable ratio between the different surface types throughout extended exposure. Normalizing the measured values to surface area ratio and exposure time, a slight decline in the Cu release rate over time can be uniformly visualized which is most pronounced for HT-LS samples after 30 min of exposure (see Figure 4B). The quantitative Cu emission throughout BTS exposure scales higher on USP-DLIP surfaces in comparison to the smooth references (represented in the line graph in Figure 4B). Here, as-processed USP-DLIP surfaces tend to exhibit a higher Cu ion release compared to their immersion etched counterpart, where in each case ion emission measured on LS and HT-LS surfaces appear to be closely related. The normalized values presented in the bar graph of Figure 4B reveal a lower μM/cm^2 relation of both USP-DLIP surface types to the reference surfaces. LS-HT surfaces in turn exhibit the highest overall ion release values both with and without surface/area ratio normalization, by which Cu ion release in μM/cm^2 scales as LS-HT > references > LS, HT-LS.

Surface exposure to PBS without inoculated bacteria exhibits an inverted relation of Cu emission between the USP-DLIP and reference samples, whereas LS-HT surfaces retain high release values close to the references (visible in Figure 4B inlay). The Cu ion release measured on the as-polished and annealed reference samples is inverted, as well. The barely observable decline in Cu ion release after 30 min of exposure to BTS is well pronounced in case of PBS exposure, especially on LS and HT-LS surfaces. The overall quantity of ion release accumulated after 90 min of exposure remains below the values of BTS exposed surfaces with a two-fold decrease for the reference and a 3.3 to 5 fold decrease for the USP-DLIP surface types.

The monitored difference in Cu emission with and without bacteria inoculation highlights a catalytic effect of bacterial presence on corrosive processes on Cu surfaces, independent of the deformation state of the superficial microstructure or surface wettability. Similar observations have previously been made (Luo et al., 2019b; Emelyanenko et al., 2020), where Luo et al. (2019b) stated that bacteria play an active role in Cu corrosion by draining the solution of Cu ions, which impairs the formation of oxides and thus surface passivation. This has also been linked to an alteration in quantitative ion release in a previous work, where USP-DLIP samples exhibits a higher surface passivation than mirror-polished surfaces under exposure to pure PBS (Müller et al., 2021). A similar relation can be found in the results presented in Figure 4B, where Cu ion release measured under exposure to PBS with and without bacteria inoculation exhibits an alteration that is more pronounced for USP-DLIP surfaces than the corresponding behavior on reference surfaces. Quantitative Cu emission is similar between USP-DLIP surfaces, but in inverted relation to the reference surfaces. Here, Cu ion release between LS and HT-LS samples can be assumed to follow similar corrosion mechanisms due to closely related values in both experiments. The combination of a lower Cu ion release rate under BTS exposure, as well as continuously reduced emission in contact to pure PBS observed on these surfaces indicates increased passivation capacities in comparison to both LS-HT and the reference surfaces.

Aside of a uniform increase, bacterial killing does not present a clear relation to actual Cu ion release on the topographically patterned surfaces. Although having the second highest Cu emission, immersion etched LS-HT samples exhibit the lowest CFU reduction rate after 90 min of exposure. On the other hand, the relation of bacterial killing between LS and HT-LS in the immersion etched state is closely linked to the corresponding ion emission slopes, while the overall difference in contact killing between as-processed and immersion etched surface states extends in the same way to their ion release ratios, as well. Here, the high initial killing on as-processed HT-LS also corresponds to a peaking Cu ion release rate within the first 30 min of BTS exposure. In similar relation, the higher killing rates on as-polished in comparison to annealed reference surfaces are paralleled by a slightly higher Cu ion release. The differences in bacterial killing after 90 min of exposure appear to be more consistently related to the corresponding CA values measured for the initial surface properties, rather than to quantitative Cu ion release, apart from the LS-HT outlier. In fact, hydrophobic wetting properties have previously been shown to have a considerable impact on the antibacterial properties of USP-DLIP surfaces (Müller et al., 2021).

3.3 Characterization of corrosion induced surface modification

Surface modification has been investigated via SEM/FIB after 90 min of exposure to assess the differences in corrosive interaction under exposure to either BTS or pure PBS between the individual surface types related to the variation of Cu ion release. Within the FIB cross-sections, separation between the contrast of bulk Cu and the $Au_{80}Pd_{20}$ layer allows to determine the localized thickness of oxidic passivation layers, while surface deterioration by corrosion is parallelly related to the underlying microstructure.

Corrosive surface modification of the reference surfaces has been investigated prior to the USP-DLIP surfaces to gain a basic understanding of the corrosion mechanisms occurring in relation to the differences in the Cu microstructure. Surface deterioration on polished reference surfaces exposed to BTS includes the formation of elongated pits along surface scratches and grain boundaries, as well as smaller localized pits that are randomly distributed on the surface (big/small red arrow in Figures 5A, C). FIB cross-sectioning reveals a thin and unevenly distributed passivation layer, which is locally interrupted at dominant corrosion sites. Localized pitting appears to be linked to individual units of rearranged crystal orientation within the superficial deformation layer of the as-polished reference surfaces. Annealed reference surfaces exhibit similar elongated corrosion pits, but an absence of randomly localized pitting. Here, corrosive interaction appears to focus on grain boundaries eventually including an intragranular attack of single grains (red arrow in Figures 5B, D). The passivation layer formed on annealed reference surfaces is slightly thicker with a higher homogeneity compared to the polished references, but similarly impaired at pitting corrosion sites.

Corrosion under PBS exposure without bacterial involvement follows similar damaging mechanisms of scratch related and randomized pitting in case of polished reference surfaces, while grain boundaries are attacked on both surface types (red arrows in Figures 5E, F, H, I). In both cases, the oxidic passivation layer is thicker, but not homogeneously distributed. Protrusions of the passivation layer are located within single grain domains and especially on localized corrosion sites like grain boundaries. A homogeneous oxide film can solely be determined for single grain domains on annealed surfaces, where a pronounced intragranular pitting can be determined on neighboring grains, as visible in Figures 5F, I (well passivated grain domain is marked by light blue arrows). On both surfaces, clusters of spherical particles can be detected, which do not appear in similarly high concentration during BTS exposure. EDX analysis reveals increased contents of both oxygen and phosphorus (displayed in Figure 5G) indicating the formation of cupric phosphate ($Cu_3(PO_4)_2$) on Cu surfaces due to the combined availability of dissolved oxygen, chloride and phosphate-ions under PBS exposure in ambient conditions, according to literature (He et al., 2015).

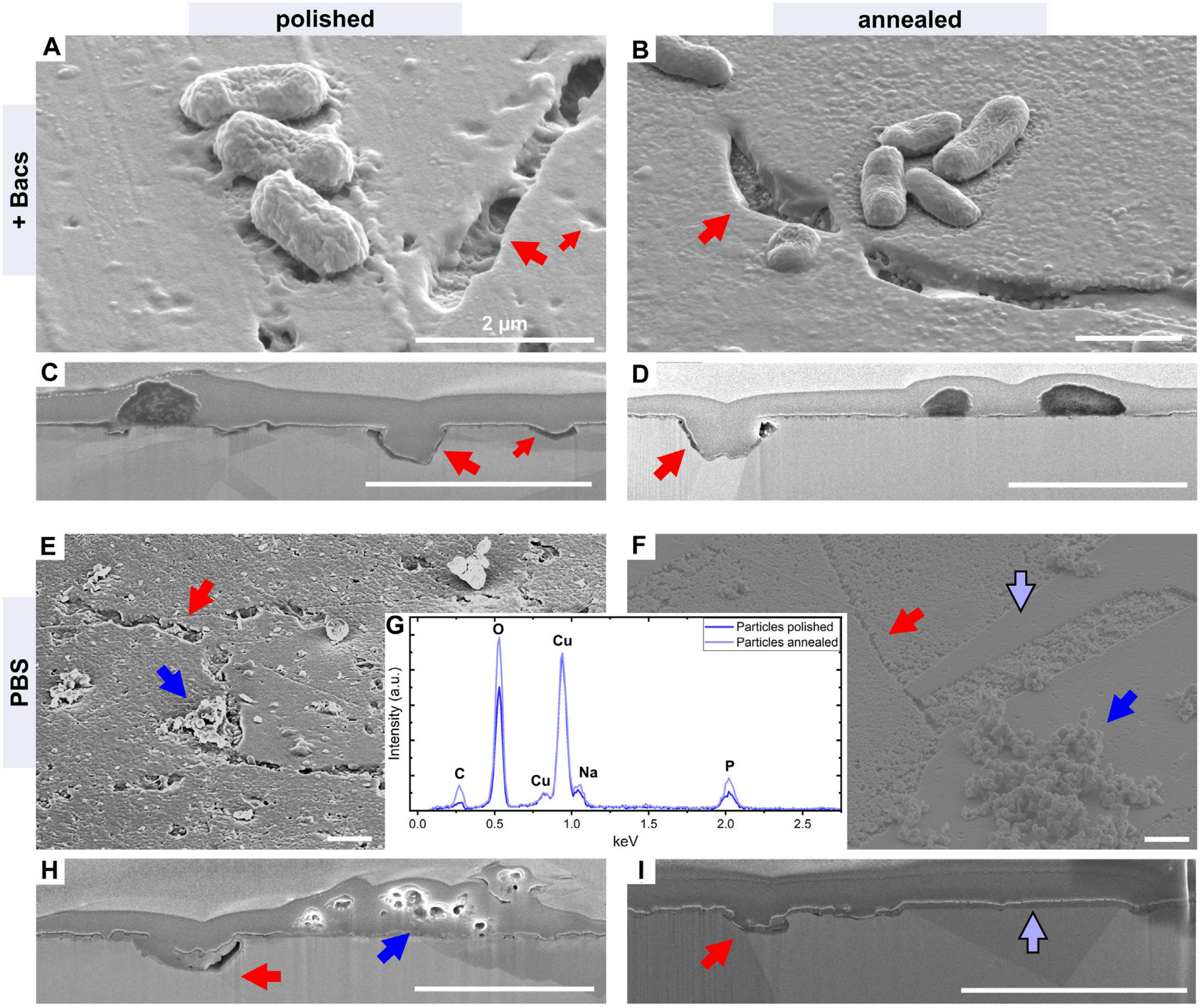

FIGURE 5
SEM analysis of the surface modification on smooth Cu surfaces after 90 min exposure to BTS and PBS: **(A)** polished and **(B)** annealed Cu surfaces exposed to BTS that are supplemented by FIB cross-sections of the surface areas marked by the red arrows **(C)** polished, **(D)** annealed. **(E)** polished and **(F)** annealed Cu surfaces exposed to PBS that are supplemented by cross-sections of individual surface features indicated by the different arrows **(H)** polished, **(I)** annealed, red = pitting sites, blue = agglomeration of corrosion products, light blue = grain domain of annealed surfaces forming dense passivation layers. **(G)** EDX analysis of the spherical corrosion products found on both polished and annealed surfaces after PBS exposure indicating cupric phosphate formation. SEM images have been taken under 52° sample tilt. The dimension bars in each image account to 2 µm.

The grain specific corrosion behavior observed on annealed surfaces indicates the formation of galvanic microcells with anodic and cathodic grain domains. This mechanism can be driven by orientation related differences in corrosion resistance or preferential epitaxial oxide growth as well as a combination of both (Lapeire et al., 2013; Luo et al., 2019a). In case of annealed Cu surfaces under PBS exposure, 100 oriented grain domains have been observed to majorly act as cathodic sites, by which neighboring grains undergo corrosive erosion where 111 oriented grains were observed to exhibit the most pronounced degradation (Lapeire et al., 2013). The deformed superficial microstructure state of polished samples impairs the formation of such clearly defined heterogeneous conditions, by which corrosion is rather focusing localized weak spots of high defect energy (Nikfahm et al., 2013; Miyamoto, 2016). Similar observations have previously been made on ground and electro-polished Cu surfaces, where the surface deformation state of the former increased localized pitting corrosion, while grain orientation specific corrosion could be observed on the latter surface type (Luo et al., 2019a). Under exposure to BTS, microcell formation on the Cu surfaces appears to be modified by the presence of bacteria, where no grain specific passivation behavior can be observed on the annealed surfaces, while the overall passivation layer exhibits lower thickness for both surface types. Former studies have shown that the re-accumulation of dissolved Cu ions within protective oxide layers on smooth Cu surfaces is largely suppressed by bacterial Cu scavenging (Luo et al., 2019b). Thus, higher Cu release values measured alongside BTS exposure can directly be related to both, a sustained high corrosive activity by prevention of surface passivation and parallelly increased Cu levels bound within bacterial cells, which are withdrawn by pipetting. The increased formation of cupric phosphate clusters in pure PBS furthermore indicates an excess availability of free Cu ions in vicinity to the substrate surface in the absence of bacteria.

The passivation layer formed on USP-DLIP samples under BTS exposure exhibit low thicknesses akin to the refence samples indicating similar impairment of surface passivation in the presence of bacteria. In contrast, surface deterioration is less obvious on USP-DLIP surfaces, where superficial pitting corrosion can only be observed on LS and HT-LS sample types under BTS exposure. Here, pitting corrosion sites are located within both the topographic peaks as well as the valley regions mostly related to grain boundaries or complete corrosive removal of superficial grain domains. The comparison between Figures 6A, C reveals that pitting sites in valley regions tend to be covered by a superficial passivation layer, while peak related pitting might also be detectable without cross-sectioning mostly due to their exposed location (corrosion sites are indicated by red arrows, the white arrows mark the position of the cross-section taken). Small amounts of spherical Cu phosphate particles can be observed on USP-DLIP surfaces as well with a predominant relation to bacterial remnants (see blue arrows in Figures 6A, C).

The impact of bacterial presence on surface passivation is further emphasized by comparison to surface modification on corresponding samples exposed to pure PBS, displayed in Figures 6E–H. Both LS and HT-LS samples form a dense passivation layer, which is homogeneously covering the surface. Pitting corrosion sites cannot be determined in SEM analyzation but are revealed by FIB cross-sectioning (an example is provided in Figure 7E). In contrast, surface passivation appears to be heterogeneously distributed on LS-HT surfaces. Here, surface oxide agglomerates appear in separated rather spherical particles that tend to connect by growth instead of a homogeneous layer. The localized accumulations of surface oxide exhibit an increased thickness in comparison to PBS-related passivation layers formed on LS and HT-LS surfaces. Higher quantitative accumulation is observed on peaks compared to valley regions, where yet non-passivated areas of the Cu surface remain uncovered between the agglomerated oxide clusters (red arrows in Figures 6F, H).

An extended comparison between surface passivation under BTS and PBS exposure as well as the initial surface state of the different sample types was conducted by means of FIB cross-section analysis. Representative outtakes of the USP-DLIP related data used in this investigation are illustrated in Figure 7 and summarized in Figure 8A. Aside of both the as-processed LS and HT-LS surfaces, initial oxide thickness of the different surface types ranges below 10 nm with slightly higher values on the USP-DLIP samples. Thickness of the oxide layers on these surfaces further increases alongside BTS and PBS exposure with a clear dominance in PBS due to an unimpaired surface passivation, which is especially striking for the LS-HT samples. These surfaces exhibit the largest gap between BTS and PBS related oxide thicknesses. The high values and standard deviation under PBS exposure are directly linked to the heterogeneous passivation layer formed. The deviating distribution of surface oxide indicates cathodic and anodic surface sites that potentially form galvanic microcells, where resulting impairment of surface passivation can be estimated to account for the continuously high Cu ion release rate measured via ICP-QQQ. Full passivation might be finally attained on a later point after further oxide growth but is not reached within the experimental time frame applied here. The formation of oxide clusters is majorly suppressed in the presence of bacteria.

In case of PBS exposure, the passivation layer of HT-LS samples is similar to the reference surfaces, The oxide thickness of LS samples tend to range higher but in similar scale to single cathodic grain domains of annealed reference surfaces. Here, the reduced Cu ion release measured on USP-DLIP surfaces indicates higher surface passivation in comparison to the corresponding Cu emission of the reference samples, although the measured oxide thickness accounts to similar values after 90 min of PBS exposure. In parallel, a deviating passivation behavior is observed on as-processed LS and HT-LS surfaces between BTS and PBS exposure. The high initial values measured for these samples are related to the localized surface extension of the flake-like surface oxide accumulated during laser processing (compare Figures 7A, B, M, N). Destabilization of these oxide agglomerations might be assumed to occur during annealing and under BTS exposure, where both as-processed LS and HT-LS surfaces exhibit a decline in oxide layer thickness, while remnants of this oxide structures could not be observed in SEM-analysis after each treatment (see Figures 7A–D, M–P and as-processed HT-LS in Figures 7Y, Z). A dissolution of the flake-like surface oxide structures under BTS exposure might be related to the difference in Cu ion release between the as-processed and etched surface types, as well as the high initial Cu release peak after 30 min of exposure on as-processed HT-LS samples. It can be assumed that the rapid removal of these substructures has a parallel effect on functional properties such as surface wettability, which is emphasized by the extended gap between CA of HT-LS surfaces in as-processed and immersion etched surface state. The resulting accelerated surface wetting appears to account for the absence of a CFU reduction lag on as-processed HT-LS samples within the first 30 min of exposure. In the case of PBS exposure, a strong increase of oxide thickness especially on the peak regions indicates an opposing role in surface corrosion, where the flake-like oxide structures appear to act as nuclei for epitaxial oxide growth, in turn.

Complementary observations are made via GI-XRD regarding the development of Cu oxide thickness represented by comparison of the Cu_2O 111 peaks as displayed in Figures 8B–D. Cu_2O has been determined as the stabilizing oxide phase predominantly involved in surface passivation of Cu substrates exposed to saline solutions (Luo et al., 2019a), whereas CuO plays a minor role within the interface between Cu_2O and moist/aqueous environments (Platzman et al., 2008). Corresponding to the results of FIB cross-section analysis, the integral intensity of Cu_2O 111 peaks on the USP-DLIP surfaces increases alongside surface exposure to both BTS and PBS, which furthermore indicates a certain amount of oxide formation in the presence of bacteria, as well. This indication of minor surface passivation can be linked to the slight decline in Cu ion release rate after 30 min of exposure, especially on both LS and HT-LS samples. Between these two surface types, oxide thickness continuously ranges higher on LS samples which is accompanied by a slightly higher Cu ion release rate under BTS exposure and quicker passivation in pure PBS. Quantitative oxide formation on LS-HT appears to level in similar magnitude compared to both LS and HT-LS surfaces in spatial distribution. The

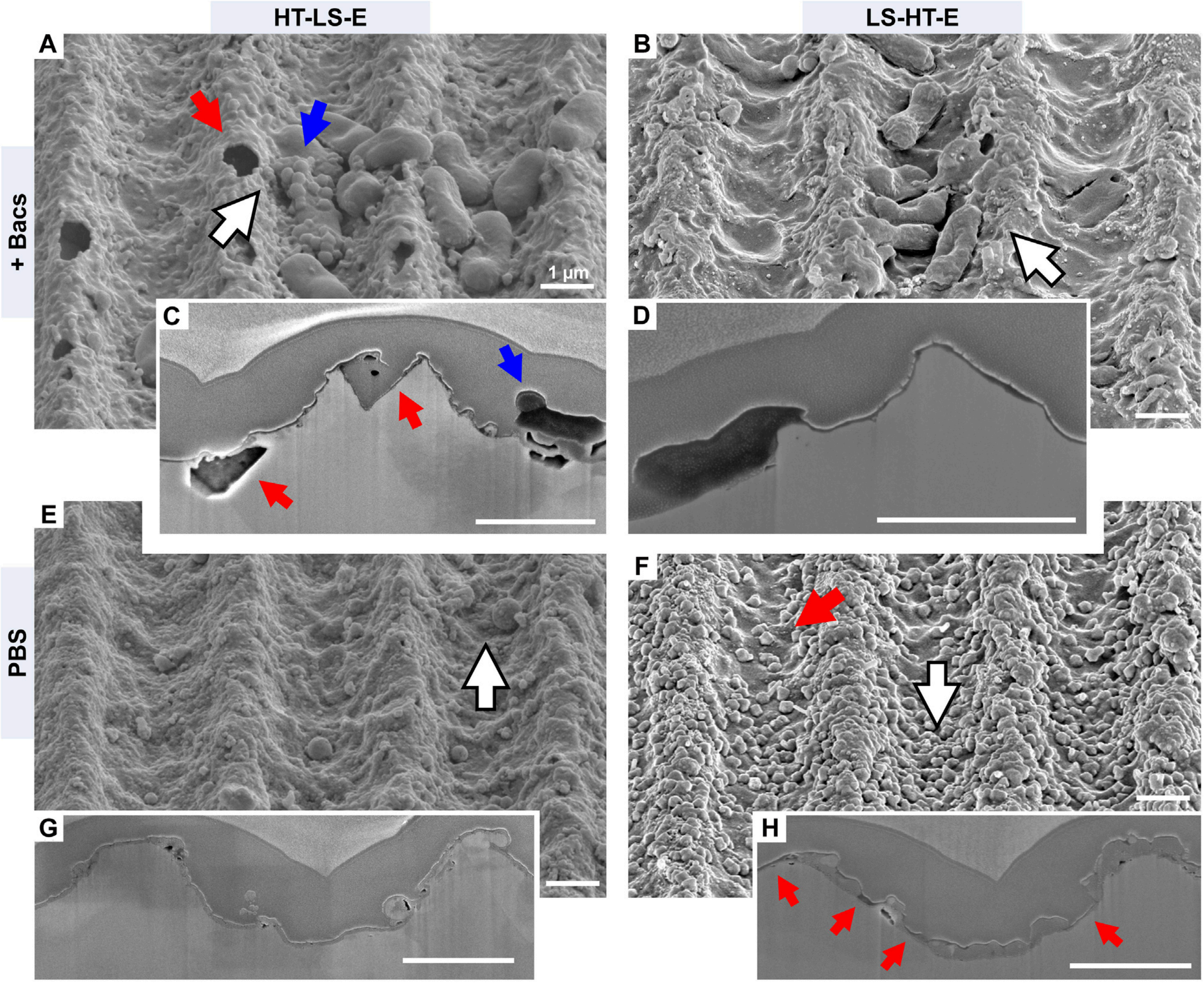

FIGURE 6
SEM imaging of the surface modification of immersion etched HT-LS and LS-HT samples induced after 90 min exposure to BTS and pure PBS that are supplemented by FIB cross-sections in the areas are marked by white arrows: **(A)** HT-LS-E in BTS, where red arrows mark pitting corrosion sites (grain boundary in the valley, full grain removal in the peak) and blue arrows highlight the agglomeration of spherical Cu phosphate particles. **(B)** LS-HT-E in BTS, with corresponding cross-section in **(D)**. **(C)** cross-section of **(A)** according to arrow indications. **(E)** HT-LS-E in PBS with corresponding cross-sectioning in **(G)**. **(F)** LS-HT-E in BTS. The red arrow highlights uncovered Cu regions. **(H)** cross-section of **(F)**, where red arrows highlight protrusions in the passivation layer. Imaging was done under 52° sample tilt. The dimension bars in each image account to 1 µm.

high oxide cluster thickness and uncovered surface compartments tend to level out in an overall oxide growth rate closely related to as-processed HT-LS samples.

The observed deviations in surface passivation between the different surface types seem to correspond to the process-induced surface deformation states. Surface deformation by USP-DLIP processing can be linked to rapid and stable surface passivation under PBS exposure as well as reduced Cu release rates per surface area in the presence of bacteria. Previous deformation from polishing additionally appears to impact surface passivation considering the slight difference in oxide thicknesses between LS and HT-LS surfaces after 90 min of PBS exposure. The reference as well as the annealed LS-HT surfaces exhibit lower superficial deformations states, whereas higher Cu release rates under pure PBS exposure indicate a reduced passivation capability in comparison to both LS and HT-LS surfaces. This differentiation in corrosion behavior is counterintuitive according to Ralston`s rule, since surface defects including grain boundaries and dislocations are points of attack for Cl^- driven pitting corrosion in saline solutions and should increase the corrosion rate with higher densities (Vinogradov et al., 1999; Miyamoto, 2016; Luo et al., 2019a). However, an alteration of passivation behavior in saline environment was previously described at a certain state of crystallographic deformation that inhibits a clear differentiation between neighboring cathodic and anodic surface sites alongside microcell formation (Miyamoto et al., 2008; Miyamoto, 2016). Corrosion behavior of the Cu surfaces was observed to switch from grain boundary focused and intergranular pitting to uniform surface corrosion, after sufficiently high substrate deformation that results in enhanced surface passivation (Nikfahm et al., 2013). This

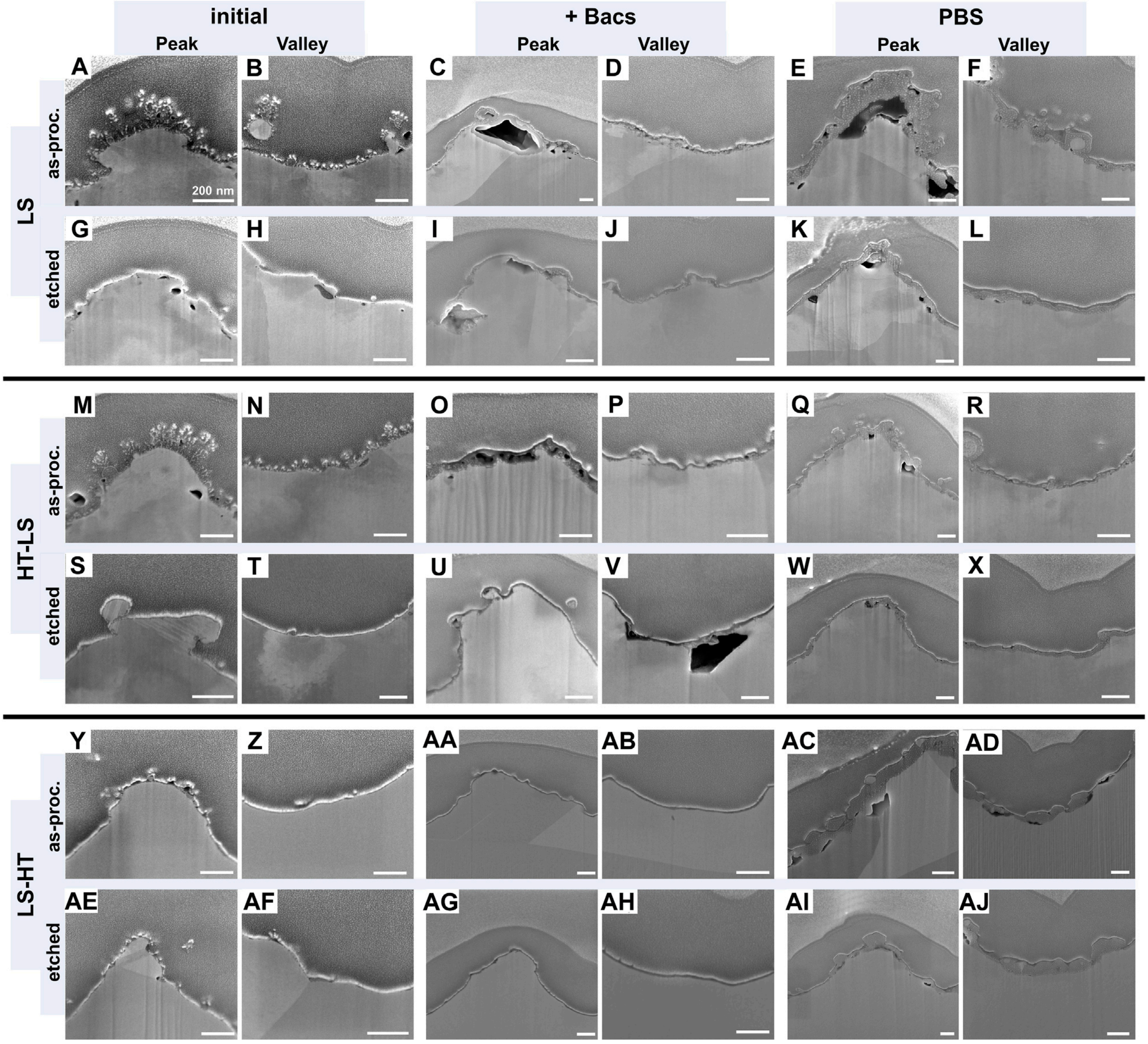

FIGURE 7
FIB cross-sections of the three USP-DLIP processed Cu surface types (LS, HT-LS and LS-HT). Both as-processed and post-processed by immersion etching are listed as analyzed in initial state as well as after exposure to BTS (+Bacs) or pure PBS. The provided image matrix displays the different processing routines as listed in Table 1 of the manuscript in vertical orientation and alters the initial/exposed surface state in horizontal orientation. E.g., the initial as-processed (etched) LS surface condition is provided in **(A, B, G, H)**, where the surface modification by exposure to either BTS or PBS is displayed in **(C, D, I, J)** or **(E, F, K, L)**. This applies similarly for HT-LS **(M-X)** and LS-HT **(Y-AJ)**. For each surface condition, a high resolved SE image of both topographic maxima and minima is provided that focusses on the superficial area to identify corrosive surface modification as well as passivating oxide layer thickness and spatial distribution.

is most likely linked to a higher mobility of Cu ions within the dense dislocation network in vicinity to the surface that enables a homogeneous surface passivation, where the lack of breaches prevent further corrosive attack (Miyamoto et al., 2008; Zhao et al., 2014). In Zhang et al. (2014) a comparably high deformation state was reached by high-current electron beam irradiation. The parallelly increased corrosion resistance was linked to the formation of supersaturated dislocation networks alongside short-termed surface melting and crater formation similar to the processing characteristics of USP-DLIP on Cu (Müller et al., 2023). The role of processed induced surface defects is especially emphasized by comparing corrosion on LS and HT-LS sample types to LS-HT samples, sharing similar topographies but deviating superficial deformation states.

A differentiation between Cu surface types undergoing homogeneous or microcell corrosion is similarly visible when comparing the GI-XRD spectra in Figure 9 before and after exposure to both BTS and PBS. Here, peaks related to the Cu 200, 220 and 311 orientations get weakened for both LS-HT and the annealed reference samples, while a minor decline of Cu 220 can also be

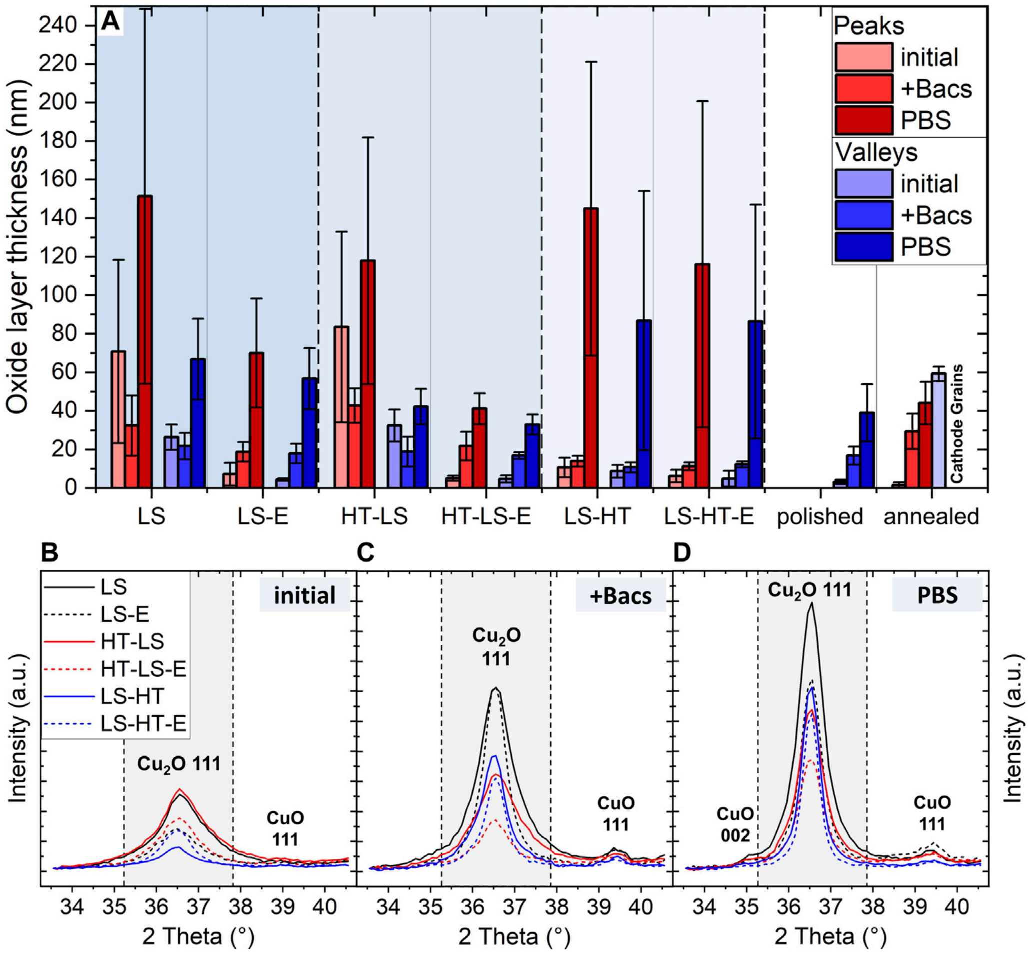

FIGURE 8
Examination of the passivation layer development on the different Cu surfaces under BTS and PBS exposure. **(A)** layer thickness measurement within FIB cross-sections and GI-XRD analysis of USP-DLIP surfaces focusing the characteristic oxide peaks at low diffraction angles for **(B)** initial surface states, **(C)** after BTS and **(D)** after PBS exposure.

observed for the polished reference. The deviations between initial and as-exposed XRD-spectra indicates a shift in the texture of the near-surface microstructure by corrosive erosion of anodic grain domains. This reduction is most expressed in BTS exposure, where impaired passivation induces a higher corrosive rate, but can also be observed in PBS exposure for LS-HT and annealed surfaces. The Cu 220 signal undergoes the most pronounced decline during exposure, which might be linked to its relation to the Cu 111 surface oriented microstructure compartments exhibiting the highest erosion within microcell corrosion between neighboring grain domains (Lapeire et al., 2013). Aside from HT-LS-E that also shows a mild change of the GI-XRD spectrum under BTS exposure, LS and HT-LS surfaces do not exhibit deviants of superficial crystallography after BTS and PBS exposure, which indicates a corrosion mechanism that is rather indifferent of grain orientation.

Independent of the deformation state of the substrate surface, the line-like surface topography generated via USP-DLIP processing appears to impact localized surface passivation, since oxide thickness is found to be constantly higher on peak compared to valley regions. This might be influenced by topographic effects with different possible underlying mechanisms: On the one hand, valley regions tend to be shadowed in case of galvanically induced material flows. On the other hand, the higher surface/volume ratio in the peak regions rather exposes grain subdivisions and might influence the local electric fields leading to topographically induced microcell formation. Grains located within the pattern peaks additionally exhibit an enlarged and convex shaped surface leading to an exposure of differing crystallographic orientations of the same grain to corrosive attack. This might drive the increase of pitting corrosion in the peak regions on LS and HT-LS samples partly inducing topographic erosion in case of BTS exposure, while unimpaired passivation leads to thicker passivation layers.

4 Conclusion

The influence of microstructure modification on the antimicrobial properties of Cu surfaces has been investigated by means of a dissemination of the different surface deformation sources throughout sample preparation including topographical patterning via USP-DLIP.

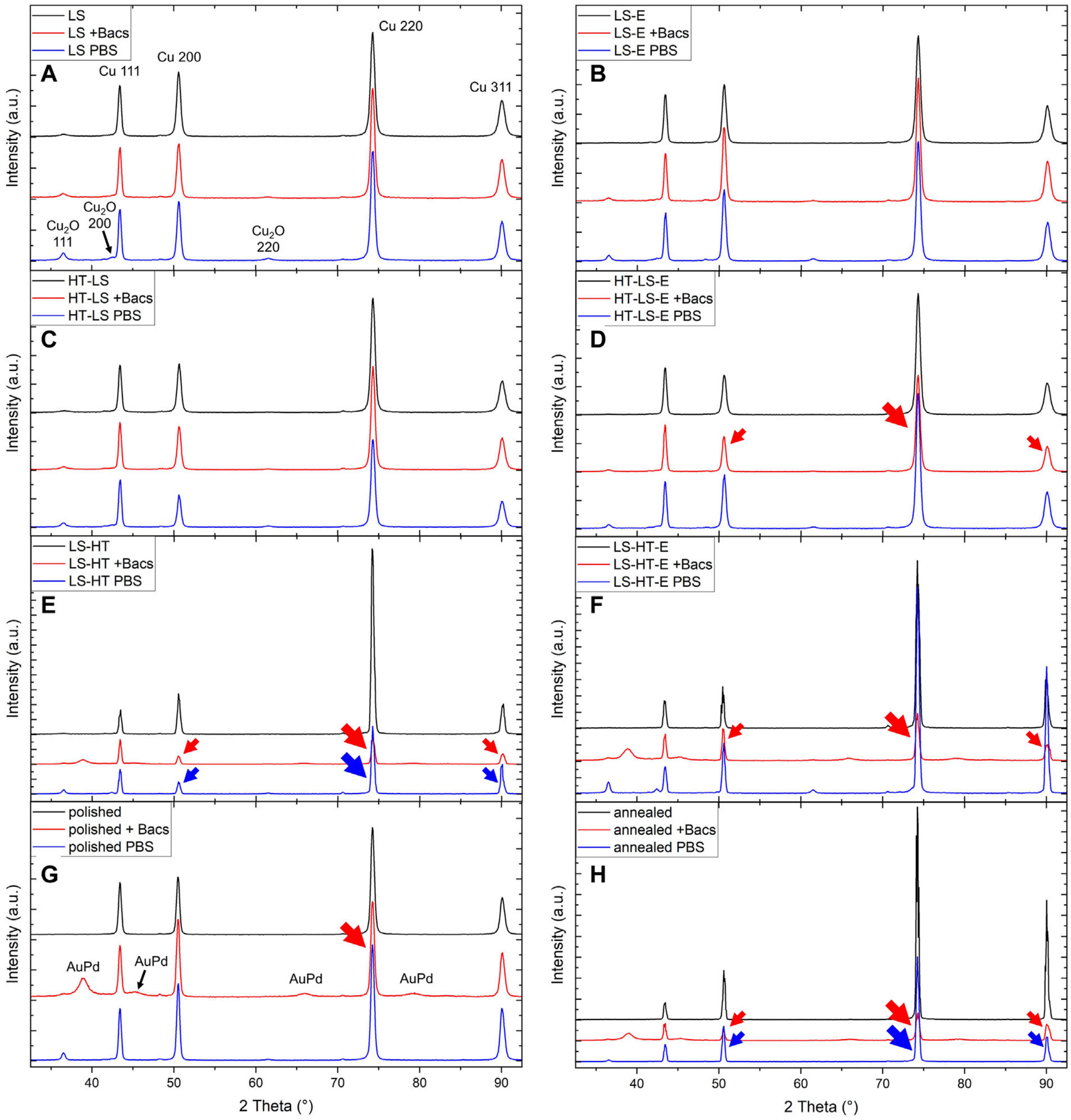

FIGURE 9
Comparison of the GI-XRD spectra between the initial and the BTS/PBS exposed Cu surface types for **(A)** LS, **(B)** LS-E, **(C)** HT-LS, **(D)** HT-LS-E, **(E)** LS-HT, **(F)** LS-HT-E, **(G)** polished and **(H)** annealed surfaces. Red and blue arrows mark a reduction of peak intensities for either BTS or PBS exposed samples. In case of **(E-H)** the BTS samples additionally exhibit side peaks from the 10 nm Au80Pd20 coating.

- **Initial state of the superficial microstructure:** The initial microstructure of the Cu substrate exhibits a characteristic cold-rolled texture with a dominance of grain domains in 100 orientation parallel to the surface. Annealing induces a mild increase of 111 domains. USP-DLIP processing does not affect the texture of bulk or superficial microstructure in case of LS and LS-HT, whereas the superficial texture of previously annealed Cu surfaces gets modified in the case of HT-LS samples. Regarding overall deformation state, the surface types can be subdivided in LS > HT-LS >> polished >> LS-HT > annealed. Different impacts of the microstructure deformation state on functional surface properties are observed:
- **Surface wettability corresponding to topography and microstructure state:** The wetting behavior of the different Cu surface types appears to be highly impacted by surface topography befitting to the Wenzel law (Wenzel, 1949). The near-surface microstructure modification by USP-DLIP processing appears to additionally impact the level of the developed hydrophobicity. This is especially emphasized comparing the CA of the different immersion etched USP-DLIP

surface types that exhibit identical surface topography. Near-surface defect density furthermore seems to influence surface passivation, which might similarly include quantitative carbon-group absorption, according to recent findings (Lößlein et al., 2023). A higher hydrophobicity can consistently be observed on as-processed surface states, which is related to process-induced oxidic sub-structures in the case of LS and HT-LS surfaces. A dissolution of the delicate oxide structures in BTS solution might lead to a rapid increase in surface wettability, in turn, that appears to facilitate early state bacteria/surface contact on HT-LS samples.

- **Impact on corrosive interaction:** Exposure to PBS solution with and without bacteria induces surface corrosion that alters between the different surface types directly dependent on superficial microstructure deformation. Corrosive interaction in pure PBS is subdivided into homogeneous oxide growth leading to stabilizing passivation for LS and HT-LS samples and heterogeneous surface degradation alongside minor surface passivation in the case of the reference and LS-HT surfaces. The driving mechanism behind heterogeneous surface corrosion is galvanic microcell formation between cathodic low energetic and anodic high energetic surface sites, linked to surface defects like scratches as well as grain boundaries and neighboring grain orientations. A sacrificial erosion of certain grain orientation is further suggested by a deviation in GI-XRD signal distribution after both BTS and PBS exposure. On LS and HT-LS samples, a clear spatial separation between cathodic and anodic surface sites appears to be impeded due to the high superficial defect densities, which leads to homogeneous corrosion and oxide growth that enables stabilizing passivation. Surface passivation is inhibited in the presence of bacteria, whereby the acting corrosion mechanisms might slightly deviate from pure PBS, also enabling localized pitting. Quantitative Cu ion release is found to be directly linked to the passivation capabilities of the different surface types in either BTS or PBS environment. Cu emission of LS and HT-LS samples solely surpasses the reference surfaces because of their higher surface/area ratio. Aside from the mentioned indications of microcell formation, an additional impact of surface topography on localized oxide agglomeration is apparent independent on the superficial microstructure.
- **Antimicrobial efficiency:** Bacterial viability on the different Cu surfaces is found to be indirectly influenced by the process-induced deformation state of the superficial microstructure due to its impact on functional surface properties like surface wettability and corrosive interaction. Overall bacterial deactivation assessed after 90 min of exposure exhibits an enhanced reduction of viable bacteria on all tested USP-DLIP surfaces than ranges between 4 and >12 times below CFU-values of the smooth references. A consistently high killing efficiency is achieved on LS surface types independent of their post-processing state, whereas HT-LS levels above LS-HT both in the as-processed and immersion etched state. Probably due to increased Cu ion release by dissolution of the flake-like surface agglomerations, as-processed samples exhibit higher bacterial killing than their immersion etched counter parts. Nevertheless, the bactericidal efficiency against *E. coli* appears to correlate more with surface wettability than quantitative Cu release, since CFU-decrease on the individual Cu surfaces scales inversely with their respective initial state CA-values, aside of the LS-HT outlier. Here, surface hydrophobicity and antimicrobial efficiency is supported by USP-DLIP induced defect implantation in contrast to the parallelly increased surface passivation capabilities that reduce the quantitative Cu emission. In accordance with previous findings (Müller et al., 2021), this indicates that physio-chemical surface properties and their influence on bacterial surface interaction play a similarly important role in the antimicrobial efficiency of Cu surface as the actual quantity of Cu ion release.

The presented results illustrate how integrated Cu surface properties are influenced by USP-DLIP processing, achieving complementing functional features that benefit the application scope. In the case of antimicrobial Cu surfaces, the USP-DLIP induced modification of both superficial chemistry and microstructure alongside surface topography were found to improve bactericidal efficiency in mutual interaction, whereby neutralization of one or two of these impacts decreases bactericidal efficiency against *E. coli*. This is a good example of how targeted surface optimization involving multi-level substrate modification can be tailored to provide the greatest benefit for a specific application.

Data availability statement

The raw data supporting the conclusions of this article will be made available by the authors, without undue reservation.

Author contributions

DM: Conceptualization, Data curation, Formal Analysis, Funding acquisition, Investigation, Methodology, Project administration, Software, Validation, Visualization, Writing–original draft, Writing–review and editing. BJ: Investigation, Writing–review and editing. SW: Investigation, Writing–review and editing. CP: Data curation, Formal Analysis, Investigation, Methodology, Software, Writing–review and editing. SS: Data curation, Formal Analysis, Investigation, Methodology, Software, Writing–review and editing. KB: Data curation, Formal Analysis, Investigation, Methodology, Software, Writing–review and editing. RK: Funding acquisition, Resources, Supervision, Writing–review and editing. FM: Funding acquisition, Resources, Supervision, Writing–review and editing.

Funding

The author(s) declare that financial support was received for the research, authorship, and/or publication of this article. This work has been funded by the German Research Foundation (DFG) within the project "Controlled bacterial interaction to increase the antimicrobial efficiency of copper surfaces" (project number 415956642) as well as the German Aerospace Center—Space Administration (DLR) within the project "Investigation of antimicrobial metal surfaces under space conditions—An effective strategy to prevent microbial biofilm formation" (project number 50WB1930). The authors acknowledge financial support in the project "MatInnovat" supported by the Saarland State Ministry of Economics with resources from the European Fund for Regional Development (EFRE) and funding by the German Research Foundation for the PFIB/SEM instrument used for the EBSD measurements (DFG, INST 256/510-1 FUGG) and for the ICP-QQQ instrument used for elemental quantification (DFG, INST 256/553-1 FUGG).

Acknowledgments

We would like to acknowledge the support of Prof. Rolf Müller and his group from the Helmholtz Institute for Pharmaceutical Research Saarland (HIPS) by providing the *E.coli* K12 strain, which was used to assess the antimicrobial properties of the differently treated Cu surfaces via wet plating.

Conflict of interest

Authors DM and SW were employed by SurFunction GmbH.

The remaining authors declare that the research was conducted in the absence of any commercial or financial relationships that could be construed as a potential conflict of interest.

Publisher's note

References

Ahmed, A. S., Müller, D. W., Bruyere, S., Holtsch, A., Müller, F., Barrirero, J., et al. (2023). Surface modification of brass via ultrashort pulsed direct laser interference patterning and its effect on bacteria-substrate interaction. *ACS Appl. Mat. Interfaces* 15, 36908–36921. doi:10.1021/acsami.3c04801

Boinovich, L. B., Kaminsky, V. V., Domantovsky, A. G., Emelyanenko, K. A., Aleshkin, A. V., Zulkarneev, E. R., et al. (2019). Bactericidal activity of superhydrophobic and superhydrophilic copper in bacterial dispersions. *Langmuir* 35, 2832–2841. doi:10.1021/acs.langmuir.8b03817

Boinovich, L. B., Modin, E. B., Aleshkin, A. V., Emelyanenko, K. A., Zulkarneev, E. R., Kiseleva, I. A., et al. (2018). Effective antibacterial nanotextured surfaces based on extreme wettability and bacteriophage seeding. *ACS Appl. Nano Mat.* 1, 1348–1359. doi:10.1021/acsanm.8b00090

Cámara, M., Green, W., MacPhee, C. E., Rakowska, P. D., Raval, R., Richardson, M. C., et al. (2022). Economic significance of biofilms: a multidisciplinary and cross-sectoral challenge. *Npj Biofilms Microbiomes* 8, 42–48. doi:10.1038/s41522-022-00306-y

Cullity, B. D., and Stock, S. R. (2001). *Elements of X-ray diffraction*.

Emelyanenko, A. M., Pytskii, I. S., Kaminsky, V. V., Chulkova, E. V., Domantovsky, A. G., Emelyanenko, K. A., et al. (2020). Superhydrophobic copper in biological liquids: antibacterial activity and microbiologically induced or inhibited corrosion. *Colloids Surfaces B Biointerfaces* 185, 110622. doi:10.1016/j.colsurfb.2019.110622

Epperlein, N., Menzel, F., Schwibbert, K., Koter, R., Bonse, J., Sameith, J., et al. (2017). Influence of femtosecond laser produced nanostructures on biofilm growth on steel. *Appl. Surf. Sci.* 418, 420–424. doi:10.1016/j.apsusc.2017.02.174

Fadeeva, E., Truong, V. K., Stiesch, M., Chichkov, B. N., Crawford, R. J., Wang, J., et al. (2011). Bacterial retention on superhydrophobic titanium surfaces fabricated by femtosecond laser ablation. *Langmuir* 27, 3012–3019. doi:10.1021/la104607g

Hans, M., Erbe, A., Mathews, S., Chen, Y., Solioz, M., and Mücklich, F. (2013). Role of copper oxides in contact killing of bacteria. *Langmuir* 29, 16160–16166. doi:10.1021/la404091z

Hans, M., Támara, J. C., Mathews, S., Bax, B., Hegetschweiler, A., Kautenburger, R., et al. (2014). Laser cladding of stainless steel with a copper-silver alloy to generate surfaces of high antimicrobial activity. *Appl. Surf. Sci.* 320, 195–199. doi:10.1016/j.apsusc.2014.09.069

He, G., Hu, W., and Li, C. M. (2015). Spontaneous interfacial reaction between metallic copper and PBS to form cupric phosphate nanoflower and its enzyme hybrid with enhanced activity. *Colloids Surfaces B Biointerfaces* 135, 613–618. doi:10.1016/j.colsurfb.2015.08.030

Kimkes, T., and Heinemann, M. (2020). How bacteria recognise and respond to surface contact. *FEMS Microbiol. Rev.* 44, 106–122. doi:10.1093/femsre/fuz029

Lapeire, L., Martinez Lombardia, E., Verbeken, K., De Graeve, I., Kestens, L. A. I., and Terryn, H. (2013). Effect of neighboring grains on the microscopic corrosion behavior of a grain in polycrystalline copper. *Corros. Sci.* 67, 179–183. doi:10.1016/j.corsci.2012.10.017

Lößlein, S. M., Kasper, M., Merz, R., Pauly, C., Müller, D. W., Kopnarski, M., et al. (2021). Patience Alone is not Enough - A Guide for the Preparation of Low-Defect Sections from Pure Copper Geduld allein reicht nicht! - Ein Leitfaden zur Herstellung defektarmer Schliffe von Reinkupfer. *Prakt. Metallogr. Metallogr.* 58, 388–407. doi:10.1515/pm-2021-0031

Lößlein, S. M., Merz, R., Müller, D. W., Kopnarski, M., and Mücklich, F. (2022). An in-depth evaluation of sample and measurement induced influences on static contact angle measurements. *Sci. Rep.* 12, 19389–19416. doi:10.1038/s41598-022-23341-3

Lößlein, S. M., Merz, R., Müller, D. W., Kopnarski, M., and Mücklich, F. (2023). The influence of adventitious carbon groups on the wetting of copper: a study on the effect of microstructure on the static contact angle. *Langmuir* 39, 12020–12031. doi:10.1021/acs.langmuir.3c01060

Luo, J., Hein, C., Ghanbaja, J., Pierson, J., and Mücklich, F. (2019b). Bacteria accumulate copper ions and inhibit oxide formation on copper surface during antibacterial efficiency test. *Micron* 127, 102759. doi:10.1016/j.micron.2019.102759

Luo, J., Hein, C., Pierson, J., and Mücklich, F. (2019a). Localised corrosion attacks and oxide growth on copper in phosphate-buffered saline. *Mat. Charact.* 158, 109985. doi:10.1016/j.matchar.2019.109985

Maikranz, E., Spengler, C., Thewes, N., Thewes, A., Nolle, F., Jung, P., et al. (2020). Different binding mechanisms of *Staphylococcus aureus* to hydrophobic and hydrophilic surfaces. *Nanoscale* 12, 19267–19275. doi:10.1039/d0nr03134h

Meister, T. L., Fortmann, J., Breisch, M., Sengstock, C., Steinmann, E., Köller, M., et al. (2022). Nanoscale copper and silver thin film systems display differences in antiviral and antibacterial properties. *Sci. Rep.* 12, 7193–7210. doi:10.1038/s41598-022-11212-w

Mikolay, A., Huggett, S., Tikana, L., Grass, G., Braun, J., and Nies, D. H. (2010). Survival of bacteria on metallic copper surfaces in a hospital trial. *Appl. Microbiol. Biotechnol.* 87, 1875–1879. doi:10.1007/s00253-010-2640-1

Miyamoto, H. (2016). Corrosion of ultrafine grained materials by severe plastic deformation, an overview. *Mat. Trans.* 57, 559–572. doi:10.2320/matertrans.M2015452

Miyamoto, H., Harada, K., Mimaki, T., Vinogradov, A., and Hashimoto, S. (2008). Corrosion of ultra-fine grained copper fabricated by equal-channel angular pressing. *Corros. Sci.* 50, 1215–1220. doi:10.1016/j.corsci.2008.01.024

Molteni, C., Abicht, H. K., and Solioz, M. (2010). Killing of bacteria by copper surfaces involves dissolved copper. *Appl. Environ. Microbiol.* 76, 4099–4101. doi:10.1128/AEM.00424-10

Müller, D. W., Fox, T., Grützmacher, P. G., Suarez, S., and Mücklich, F. (2020a). Applying ultrashort pulsed direct laser interference patterning for functional surfaces. *Sci. Rep.* 10, 3647. doi:10.1038/s41598-020-60592-4

Müller, D. W., Holtsch, A., Lößlein, S., Pauly, C., Spengler, C., Grandthyll, S., et al. (2020b). In-depth investigation of copper surface chemistry modification by ultrashort pulsed direct laser interference patterning. *Langmuir* 36, 13415–13425. doi:10.1021/acs.langmuir.0c01625

Müller, D. W., Lößlein, S., Pauly, C., Briesenick, M., Kickelbick, G., and Mücklich, F. (2023). Multi-pulse agglomeration effects on ultrashort pulsed direct laser interference patterning of Cu. *Appl. Surf. Sci.* 611, 155538. doi:10.1016/j.apsusc.2022.155538

Müller, D. W., Lößlein, S., Terriac, E., Brix, K., Kautenburger, R., Siems, K., et al. (2021). Increasing antibacterial efficiency of Cu surfaces by targeted surface functionalization via ultrashort pulsed direct laser interference patterning. *Adv. Mat. Interfaces.* 8, 2001656. doi:10.1002/admi.202001656

Nikfahm, A., Danaee, I., Ashrafi, A., and Toroghinejad, M. R. (2013). Effect of grain size changes on corrosion behavior of copper produced by accumulative roll bonding process. *Mat. Res.* 16, 1379–1386. doi:10.1590/S1516-14392013005000135

Peter, A., Lutey, A. H. A., Faas, S., Romoli, L., Onuseit, V., and Graf, T. (2020). Direct laser interference patterning of stainless steel by ultrashort pulses for antibacterial surfaces. *Opt. Laser Technol.* 123, 105954. doi:10.1016/j.optlastec.2019.105954

Platzman, I., Brener, R., Haick, H., and Tannenbaum, R. (2008). Oxidation of polycrystalline copper thin films at ambient conditions. *J. Phys. Chem. C* 112, 1101–1108. doi:10.1021/jp076981k

Pratt, L. A., and Kolter, R. (1998). Genetic analysis of *Escherichia coli* biofilm formation: roles of flagella, motility, chemotaxis and type I pili. *Mol. Microbiol.* 30, 285–293. doi:10.1046/j.1365-2958.1998.01061.x

Razavipour, M., Gonzalez, M., Singh, N., Cimenci, C. E., Chu, N., Alarcon, E. I., et al. (2022). Biofilm inhibition and antiviral response of cold sprayed and shot peened copper surfaces: effect of surface morphology and microstructure. *J. Therm. Spray. Technol.* 31, 130–144. doi:10.1007/s11666-021-01315-7

Schneider, C. A., Rasband, W. S., and Eliceiri, K. W. (2012). NIH Image to ImageJ: 25 years of image analysis. *Nat. Methods.* 9, 671–675. doi:10.1038/nmeth.2089

Siems, K., Müller, D. W., Maertens, L., Ahmed, A., Van Houdt, R., Mancinelli, R. L., et al. (2022). Testing laser-structured antimicrobial surfaces under space conditions: the design of the ISS experiment BIOFILMS. *Technol.* 2, 1–18. doi:10.3389/frspt.2021.773244

Smith, J. L., Tran, N., Song, T., Liang, D., and Qian, M. (2022). Robust bulk micro-nano hierarchical copper structures possessing exceptional bactericidal efficacy. *Biomaterials* 280, 121271. doi:10.1016/j.biomaterials.2021.121271

Sobisch, L.-Y., Rogowski, K. M., Fuchs, J., Schmieder, W., Vaishampayan, A., Oles, P., et al. (2019). Biofilm forming antibiotic resistant gram-positive pathogens isolated from surfaces on the international space station. *Front. Microbiol.* 10, 543–616. doi:10.3389/fmicb.2019.00543

Tripathy, A., Sen, P., Su, B., and Briscoe, W. H. (2017). Natural and bioinspired nanostructured bactericidal surfaces. *Adv. Colloid Interface Sci.* 248, 85–104. doi:10.1016/j.cis.2017.07.030

Vincenc Oboňa, J., Ocelík, V., Rao, J. C., Skolski, J. Z. P., Römer, G. R. B. E., Huis In 'T Veld, A. J., et al. (2014). Modification of Cu surface with picosecond laser pulses. *Appl. Surf. Sci.* 303, 118–124. doi:10.1016/j.apsusc.2014.02.104

Vinogradov, A., Mimaki, T., Hashimoto, S., and Valiev, R. (1999). On the corrosion behaviour of ultra-fine grain copper. *Scr. Mat.* 41, 319–326. doi:10.1016/S1359-6462(99)00170-0

Wenzel, R. N. (1949). Surface roughness and contact angle. *J. Phys. Colloid Chem.* 53, 1466–1467. doi:10.1021/j150474a015

Xiong, Q., Li, Z., and Kitamura, T. (2017). Effect of crystal orientation on femtosecond laser-induced thermomechanical responses and spallation behaviors of copper films. *Sci. Rep.* 7, 9218–9314. doi:10.1038/s41598-017-09559-6

Yi, G., Riduan, S. N., Armugam, A., Ong, J. T., Hon, P. Y., Abdad, M. Y., et al. (2021). Nanostructured copper surface kills ESKAPE pathogens and viruses in minutes. *ChemMedChem* 16, 3553–3558. doi:10.1002/cmdc.202100504

Zea, L., Mclean, R. J. C., Rook, T. A., Angle, G., Carter, D. L., Delegard, A., et al. (2020). Potential biofilm control strategies for extended space flight missions. *Biofilm* 2, 100026. doi:10.1016/j.bioflm.2020.100026

Zhang, Z., Yang, S., Lv, P., Li, Y., Wang, X., Hou, X., et al. (2014). The microstructures and corrosion properties of polycrystalline copper induced by high-current pulsed electron beam. *Appl. Surf. Sci.* 294, 9–14. doi:10.1016/j.apsusc.2013.12.178

Zhao, Y., Cheng, I. C., Kassner, M. E., and Hodge, A. M. (2014). The effect of nanotwins on the corrosion behavior of copper. *Acta Mater* 67, 181–188. doi:10.1016/j.actamat.2013.12.030

Paper VI:

Modifying the Antibacterial Performance of Cu Surfaces by Topographic Patterning in the Micro- and Nanometer Scale

Daniel Wyn Müller[1,2*], Christoph Pauly[1], Kristina Brix[3], Ralf Kautenburger[3], Frank Mücklich[1]

[1]Chair of Functional Materials, Department of Materials Science, Saarland University, 66123 Saarbrücken, Germany.

[2]SurFunction GmbH, 66123 Saarbrücken, Germany.

[3]Department of Inorganic Solid-State Chemistry, Elemental Analysis, Saarland University, 66123 Saarbrücken, Germany.

Submitted in September 2024 in "Biomaterials Advances"

Abstract:

Antimicrobial surfaces are a promising approach to reduce the spread of pathogenic microorganisms in various critical environments. To achieve high antimicrobial functionality, it is essential to consider the material-specific bactericidal mode of action in conjunction with bacterial surface interactions. This study investigates the effect of altered contact conditions on the antimicrobial efficiency of Cu surfaces against *Escherichia coli* and *Staphylococcus aureus*. The fabrication of line-like periodic surface patterns in the scale range of single bacterial cells was achieved utilizing ultrashort pulsed direct laser interference patterning. These patterns create both favorable and unfavorable topographies for bacterial adhesion. The variation in bacteria/surface interaction is monitored in terms of strain-specific bactericidal efficiency and the role of corrosive forces driving quantitative Cu ion release. The investigation revealed that bacterial deactivation on Cu surfaces can be either enhanced or decreased by intentional topography modifications, independent of Cu ion emission, with strain-specific deviations in effective pattern scales observed. The results of this study indicate the potential of targeted topographic surface functionalization to optimize antimicrobial surface designs, enabling strain-specific decontamination strategies.

Own contributions:

Conception and design of the study. Design of the interference based USP laser setup and sample preparation. Conduction of the surface characterisation via LSM, SEM, GI-XRD and WCA also involving bacterial imaging via FIB cross-sectioning, STEM and EDS. Investigation of antibacterial properties via wet plating experiments. Data interpretation, preparation and editing of the manuscript.

Modifying the Antibacterial Performance of Cu Surfaces by Topographic Patterning in the Micro- and Nanometer Scale

Authors

Daniel Wyn Müller[1,2*], Christoph Pauly[1], Kristina Brix[3], Ralf Kautenburger[3], Frank Mücklich[1]

[1]Chair of Functional Materials, Department of Materials Science, Saarland University, 66123 Saarbrücken, Germany.

[2]SurFunction GmbH, 66123 Saarbrücken, Germany.

[3]Department of Inorganic Solid-State Chemistry, Elemental Analysis, Saarland University, 66123 Saarbrücken, Germany.

Contact:

Chair of Functional Materials
Saarland University
Post Office Box 151150
66041 Saarbruecken

daniel.mueller@uni-saarland.de
Phone: +49 681 / 302 – 70545
Fax: +49 681 / 302 – 70502

Abstract

Antimicrobial surfaces are a promising approach to reduce the spread of pathogenic microorganisms in various critical environments. To achieve high antimicrobial functionality, it is essential to consider the material-specific bactericidal mode of action in conjunction with bacterial surface interactions. This study investigates the effect of altered contact conditions on the antimicrobial efficiency of Cu surfaces against *Escherichia coli* and *Staphylococcus aureus*. The fabrication of line-like periodic surface patterns in the scale range of single bacterial cells was achieved utilizing ultrashort pulsed direct laser interference patterning. These patterns create both favorable and unfavorable topographies for bacterial adhesion. The variation in bacteria/surface interaction is monitored in terms of strain-specific bactericidal efficiency and the role of corrosive forces driving quantitative Cu ion release. The investigation revealed that bacterial deactivation on Cu surfaces can be either enhanced or decreased by intentional topography modifications, independent of Cu ion emission, with strain-specific deviations in effective pattern scales observed. The results of this study indicate the potential of targeted topographic surface functionalization to optimize antimicrobial surface designs, enabling strain-specific decontamination strategies.

Keywords: Active antimicrobial surfaces, Biomimetic Surface Structures, Ultrashort Laser Pulses, Direct Laser Interference Patterning

Introduction

Diseases related to bacterial infections are considered as one of the major future threats for public health, which caused one out of eight deaths worldwide in 2019[1]. In the same year, biofilm induced economic damage was estimated at more than 4000bn USD, where approx. 30% are directly related to biofilm burden in the healthcare sector and food production[2]. In close relation, a considerable and ongoing hazard by the increase of bacterial resistance against antibiotic agents is reported. This also affects remote habitats such as the international space station (ISS)[3,4]. In case of bacterial spread in public and remote environments, contact surfaces represent one of the dominant distribution routes. This has recently been demonstrated by microbial tracking on the ISS, where the overall space station microbiome was shown to be dominated by bacterial strains associated with the human skin[5]. Multiple strategies to reduce the formation of biofilms and the viability of pathogenic microorganisms on technical as well as frequently contacted surfaces have therefore been investigated in the recent two decades. A variety of acting mechanisms can be utilized, here, without the need to involve antibiotic agents.

The two most investigated and applied strategies are active antimicrobial substrate materials like silver (Ag) and copper (Cu) and bactericidal or contact guiding surface topographies[6–9]. The antimicrobial activity of Ag- and Cu based substrates is directly linked to the quantity of electrochemically emitted ions, which are toxic to most microorganisms[10,11]. Here, Cu proves to be particularly interesting due to extended environmental applicability[12], its higher broadband effect[11], lower human toxicity threshold[13,14] as well as economically more favorable and broad availability in technically applicable alloy systems. Cu mediated bacterial deactivation is related to several modes of action including membrane damage, formation of reactive oxygen species (ROS) via Fenton-type reaction and structural damage against DNA as well as protein molecules due to its high thiophilicity[15,16]. Certain guidelines need to be followed to achieve high antimicrobial efficiency of Cu surfaces. This includes a close contact between bacteria and Cu emitting agent[17], as well as the avoidance of chemical surface contamination[18].

Biomimetic surface patterns on inert substrates utilize self-cleaning and bactericidal surface properties based on the functionality of µm- and nm-scaled topographies found, e.g., on *lotus* leaves[19] or *cicada* and *dragonfly* wings. How bacterial surface interaction is modulated on these surfaces relates to the topographic pattern scale. Pillar like patterns at a scale below 200 nm following the design of *cicada* or *dragonfly* wings have been shown to exhibit bactericidal properties where adherent bacterial cells are deactivated by mechanical membrane rupture[8,20]. On surface patterns with topographic feature sizes in the upper sub-µm range, bacterial interaction was found to switch from bactericidal to contact inhibition[21,22]. Further enlargement of the pattern scales up to the size of a single bacterial cell and beyond ultimately leads to improved bacterial adhesion and retention[9,23,24]. Here, contact guidance impacting cell orientation and initiation of biofilm formation can be achieved by targeted surface design[9,25]. How the actual scale of topographic surface patterns affects bacterial response may vary significantly between different bacterial strains[21,26], indicating a very complex interaction between the bacterium and the patterned surface. In fact, secondary surface properties were shown to play an important role in antimicrobial surface functionality, since mechanically induced killing or the attachment/repulsion of individual bacteria is driven by attraction and bonding forces. These forces depend, e.g., on environmental conditions[27], surface charge[28] and wettability[29,30].

More recently, antimicrobial surface design aims to agitate or combine the previously mentioned modes of action[31,32] which has already been shown to potentially improve inherent bactericidal surface properties. Functional coatings on topographically patterned inert surfaces have been proven to reduce bacterial viability either by inducing a positive surface charge that affects membrane integrity[33], or by adding the active killing capacities of Ag and Cu[34]. The application of Cu has also been investigated as nanoparticles (NP) in surface decoration or as a complementing composite in coatings, where the NP shape aims to facilitate aggregation on bacterial membranes up to intrusion[35,36]. More recently, it has been found that the antibacterial effect of Cu NP is closely linked to the quantitative release of Cu ions, while an actual intrusion into bacterial cells does not occur[37]. Recent functionalization to enhance the antimicrobial efficacy of Cu surfaces involves the combination with mechanically induced antimicrobial properties of *cicada* and *dragonfly* wing, such as nm-scale surface features piercing bacterial cell walls[38,39]. Depending on the methodology used, Cu ion release might however be negatively affected by excessive oxide formation, here[40,41]. In another approach, the surface/area ratio of bulk Cu is exponentially increased by inducing a super-hydrophilic mesh-like porous morphology, which in parallel enhances the initial Cu ion release and bactericidal activity[42]. In another study, topographic surface patterns at the scale of a single bacterium were shown to enhance antimicrobial efficacy with lesser dependence on quantitative Cu ion release[43]. Here, the decrease of bacterial viability was discussed to be related to functional properties of the substrate surface, including both topography and wettability, which affect bacteria/surface bonding and, in parallel, the bacterial sensitivity against Cu.

The current state of research on bactericidal surfaces highlights the complexity of the underlying mechanisms being involved in the actual expression of antimicrobial effects within the different surface design strategies. To achieve a sustained high decontamination efficiency, the actual bacteria/surface interaction must be actively tailored to agitate the focused mode of action by surface design. In this context, the aim of the presented study is to investigate how bacterial contact modulation by topographical surface design impacts the antibacterial efficacy of Cu surfaces. Line-like periodic surface patterns are generated using ultrashort pulsed direct laser interference patterning (USP-DLIP), which topographically modulate the contact surface available for the adhesion of individual bacterial cells. The resulting impact on the antimicrobial efficacy of Cu surfaces against rod-shaped gram-negative *Escherichia coli* K12 (BW25113) and spherical gram-positive *Staphylococcus aureus* SA113 is investigated in a complementary approach applying water contact angle measurement (CA) confocal laser scanning microscopy (LSM), high resolution electron beam analysis (FIB/SEM/EDS), grazing incidence X-ray diffractometry (GI-XRD) and wet plating. Improved comprehension of the influence of modified bacterial contact conditions on bactericidal efficacy of actively antimicrobial substrate surfaces potentially allows for a better conception of decontamination measures in various partly critical environments[6,7,31].

Results and Discussion

Initial Surface State

Line-like surface structures exhibiting pattern periodicities of 3 µm ($P > Bac$), 1 µm ($P \approx Bac$) and 750 nm ($P < Bac$) are generated on pure Cu surfaces via USP-DLIP with respect to the single cell dimensions of the two bacterial strains involved in this study (see Figure 1). The actual bacterial contact conditions on these surfaces result from the individual surface geometries including concave (valley areas) and convex (peak areas) sections. The primary pattern geometry with a periodicity of 3 µm exhibits a valley width of 2.08 ± 0.14 µm and depth of 1.1 ± 0.15 µm, which enables complete intrusion of single cells and clusters. On 1 µm patterns, the valley width of 0.81 ± 0.07 µm approximates the single cell dimensions of both parallelly aligned *E. coli* and *S. aureus*, which facilitates single cell contact combined with the low pattern depth. The valley width of approx. 0.54 µm on 750 nm patterns finally ranges below the single bacterial cell diameter, by which the valley floor is not fully accessible for adherent bacteria at the present pattern depth. In parallel to the described primary pattern geometry, the surface design involved tailoring of the sub-pattern formation by material specific thermodynamic response according to the aspired contact conditions[44].

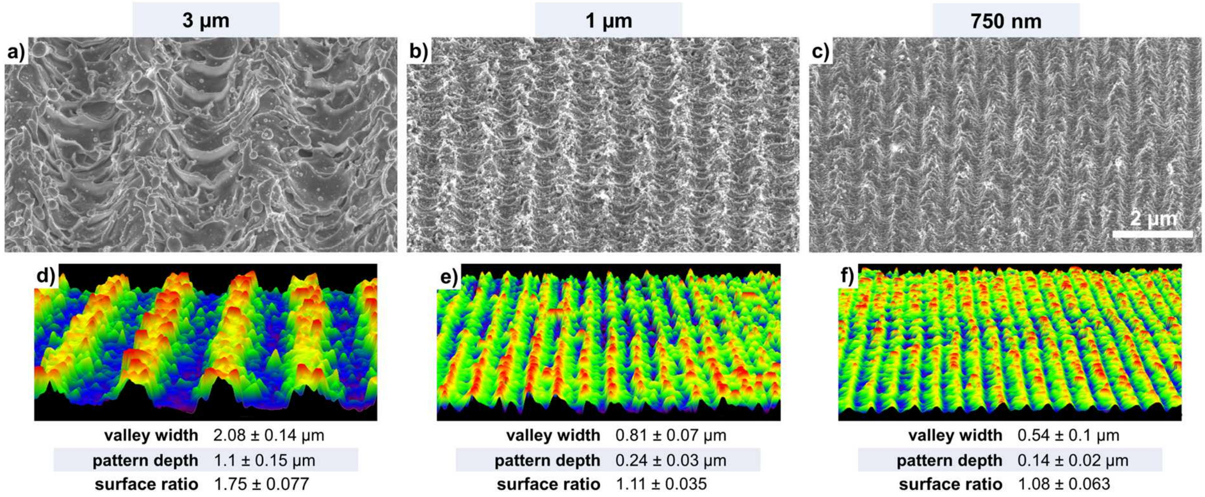

Figure 1: SEM images of line-like periodic surface patterns in the scale of 3 µm ($P > Bac$), 1 µm ($P \approx Bac$) and 750 nm ($P < Bac$) applied on the Cu surfaces: a-c) SEM imaging, where the 3 µm pattern was previously immersion etched, while 1 µm and 750 nm represent the as-processed state. d-f) representative topographic profiles of 3 µm, 1 µm and 750 nm patterns detected via CLSM also listing the deviation of corresponding pattern geometry parameters relevant for bacterial contact investigation between the different substrates.

In parallel to topographic surface modification, an agglomeration of nm-scaled oxidic redepositions during USP-DLIP processing was previously described on Cu[45]. The redeposited oxide particles have been shown to mainly consist of Cu_2O and scale with the amount of ablated matter as well as the fluence applied[44]. Accordingly, the Cu_2O (111) signal measured by grazing incidence X-ray diffraction (GI-XRD) indicates a more pronounced agglomeration of process-induced surface oxides on as-processed 3 µm patterns in comparison to 1 µm and 750 nm (see Figure 2a) corresponding to the respective ablated volume. Post-processing by immersion etching in citric acid induces a reduction of the oxide signal as visible in Figure 2a, which can be attributed to the removal of oxidic process agglomerates[45]. The stable but low CuO signal intensity fits to the previously suggested oxidation mechanism, where this oxide phase is mainly formed as a superficial layer during consecutive atmospheric passivation[45].

In bacterial adhesion to technical surfaces, physicochemical surface properties were shown to play a parallel role to surface topography and might furthermore impact bactericidal efficacy[29,43,46]. This includes e.g. surface wettability corresponding to acid-base interactions[47]. Wettability of laser processed metallic surfaces is impacted by atmospheric aging as well as hierarchical pattern morphologies[48], which is confirmed by comparison of the contact angles (CA) measured on as-processed and immersion etched USP-DLIP Cu surfaces after three weeks of aging (displayed in Figure 2b). Wettability is consistently reduced on the USP-DLIP surfaces, while the hydrophobic wetting behavior is enhancing alongside increasing pattern scale. In between similar pattern periodicities, the as-processed surfaces exhibit elevated hydrophobic surface properties over the immersion etched topographic counterparts suggesting an additional contribution of the nm-scaled oxide particles.

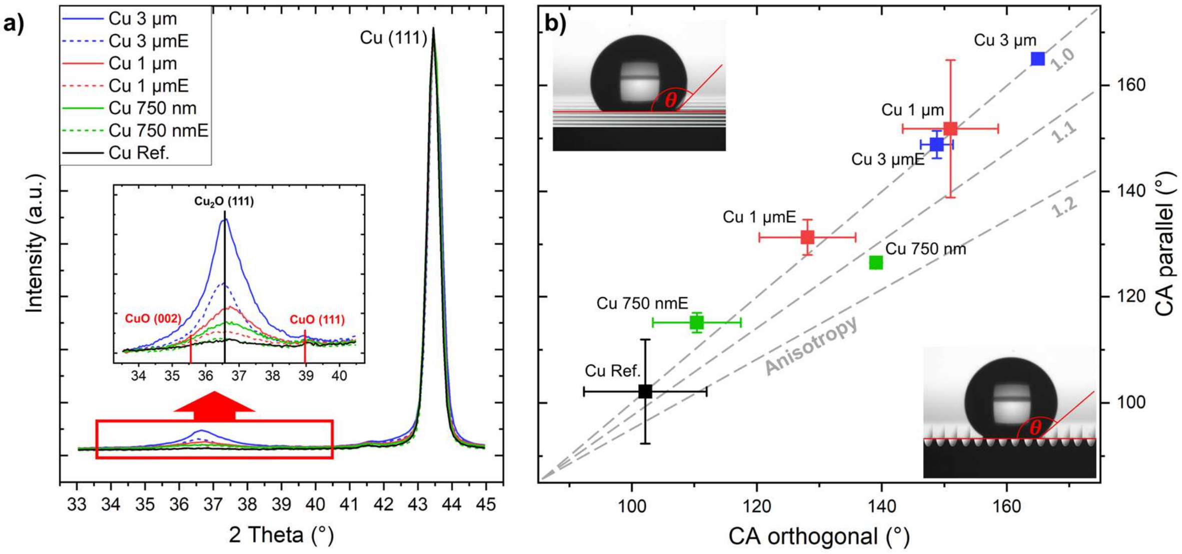

Figure 2: Process related modification of surface chemistry impacting functional aspects: a) alteration of surface oxidation after USP-DLIP patterning in as-processed and immersion etched state (E). b) stabilized surface wettability of the polished reference (Steel Ref., Cu Ref.) and USP-DLIP patterned Cu and stainless steel surfaces at 3 µm, 1 µm and 750 nm pattern periodicity after three weeks of aging under ambient atmosphere. Cu USP-DLIP surfaces are represented both in as-processed and immersion etched state.

Both, the high CA values, as well as the roll-off/sticking behavior on the 3 µm samples are consistent with previous results indicating a Cassie-Baxter wetting state on as-processed and Wenzel wetting on immersion etched surfaces[43]. A pronounced difference between CA on as-processed and immersion etched samples can be observed for less hydrophobic 1 µm and 750 nm patterns. CA anisotropy on the isotropic surface patterns remains close to 1.0 along reducing CA for 3 µm and 1 µm indicating a low pinning effect on droplet propagation. Surface wetting on 750 nm patterns exhibits a deviating behavior, where increased CA anisotropy in the as-processed state indicates pinning along the structure peaks, which is eliminated after immersion etching.

Antimicrobial Properties vs. Bacteria/Pattern Scale Ratio

Both gram-negative *E. coli* and gram-positive *S. aureus* have been exposed to as-processed and immersion etched USP-DLIP Cu surfaces by wet plating using mirror-polished samples of both bactericidal Cu and inert steel as topographically smooth reference surfaces. Strain specific exposure times were chosen to allow for the determination of topography related differences in bacterial viability with respect to the individual survival rates. The time-resolved reduction of viable bacterial cell count for both *E. coli* (blue) and *S. aureus* (green) is illustrated in Figure 3 and 4, each complemented by the corresponding Cu ion release. The line graphs represent experimentally measured bacterial viability/dissolved Cu while the bar graphs represent the respective time- and area-dependent killing rates normalized by the surface ratio measured in LSM analysis. The factor of in- or decrease in relation to the smooth Cu reference is stated for each data-point of the USP-DLIP patterned surfaces in the bar graphs.

Bacterial cells of both strains were found to be rapidly killed on Cu surfaces with a reduction in viable cell count of more than 3 log already after 60 minutes of exposure, affecting the majority of the USP-DLIP surfaces as well as the Cu reference surfaces tested. Extended exposure times of up to 120 minutes resulted in complete inactivation of bacterial cells on all tested surfaces, which was also found in additional test series after 90 minutes of exposure. Deviations in bacterial viability between the different USP-DLIP patterned Cu surfaces are well displayed after 60 minutes of exposure, before complete bacterial deactivation is initiated universally. USP-DLIP surface modification is found to exhibit a significant impact on bacterial viability, where both agitation and depletion of the bactericidal capacities of smooth Cu surfaces can be observed on the different pattern scales with varying dependency on the bacterial strain tested.

In case of *E. coli* initial bacterial killing on USP-DLIP patterned surfaces consistently levels above topographically smooth Cu within the first 40 minutes of exposure (see Figure 3a). The observed differences between individual USP-DLIP surfaces do not follow a clear dependency on pattern scale or post-processing state, where the highest initial killing rates are distributed between immersion etched 3 µm followed by as-processed 1 µm and 750 nm. This is however altered after 60 minutes, where the post-processed surface state appears to play an additional dominant role aside of actual primary pattern scales. Here, bacterial inactivation is consistently higher on immersion etched surfaces compared to their as-processed counterparts of similar primary surface pattern. This is particularly evident for 3 µm and 1 µm structures with primary pattern geometries that are geometrically favorable for increased bacterial contact area: No remaining viable bacteria could be determined on etched surfaces, while the viable cell count still ranges close to the experimental detection limit on as-processed samples. In the case of 750 nm pattern scales, bacterial deactivation lies either within or below the range of the smooth Cu reference throughout 60 minutes of exposure. Independent of the post-processing state, samples of 750 nm pattern periodicity exhibit considerably lower bactericidal activity compared to 3 µm and 1 µm on which the bacterial killing rate ranges three to four orders of magnitude above the smooth reference (displayed Figure 3b). On as-processed 3 µm and 1 µm USP-DLIP surfaces, a higher antibacterial efficacy of 1 µm (2 log increase of killing rate) over 3 µm (1 log increase of killing rate) against *E. coli* is observed. Overall, the bactericidal effect of the different surface topographies against *E. coli* scale as 1 µm ($P \approx Bac$) > 3 µm ($P > Bac$) >> 750 nm ($P < Bac$) ≈ smooth. The post-processing state appears to have a similarly pronounced impact as the primary DLIP pattern size, scaling with immersion etched > as-processed in antibacterial efficacy.

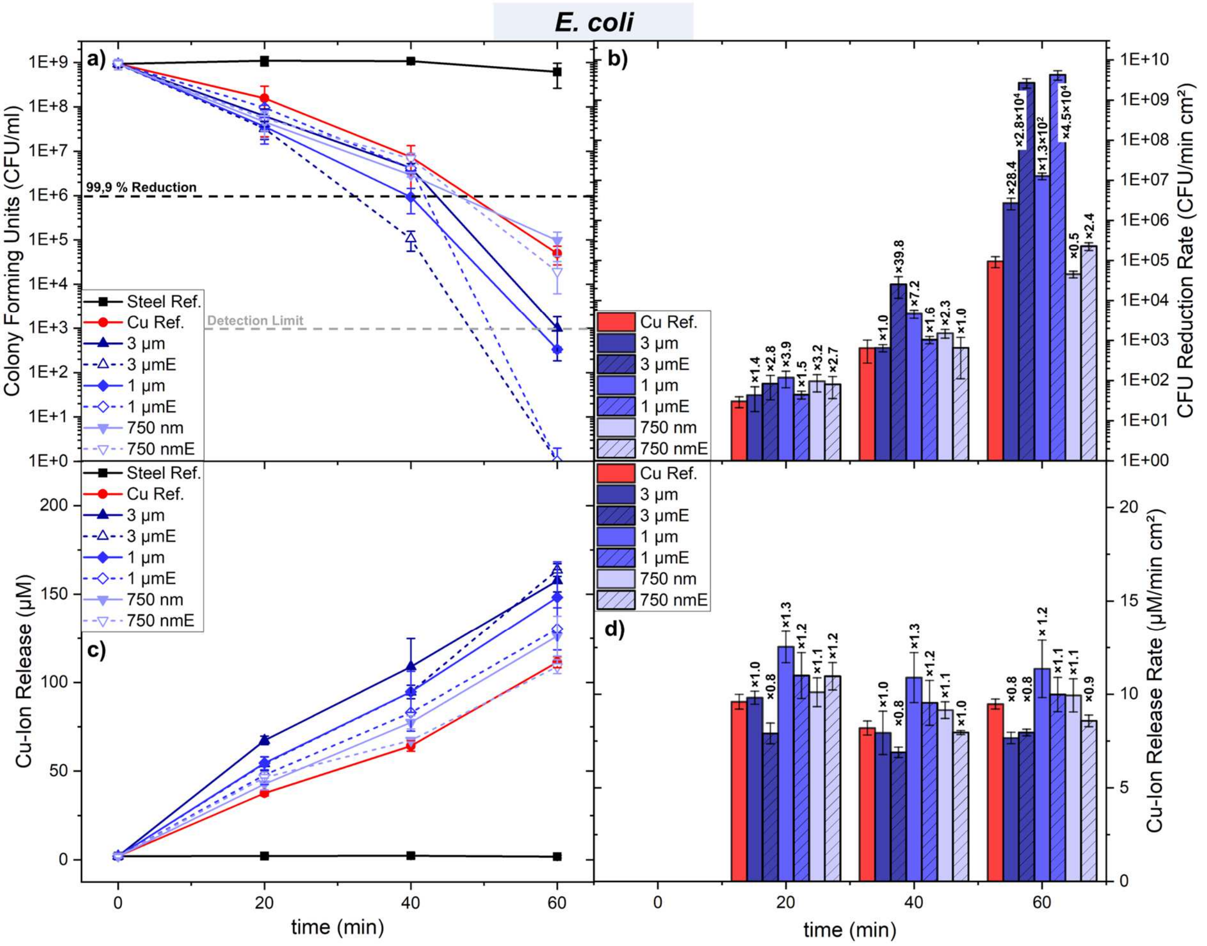

Figure 3: a, b) Bacterial viability and c, d) respective Cu ion release rates measured via wet plating and inductively coupled plasma triple quadruple mass spectrometry (ICP-QQQ) for *E. coli.* Exposure times were chosen as 20, 40 and 60 minutes. Line graphs represent the measured a) colony forming units (CFU) and c) quantitative Cu ion release. The bar graphs in show the time dependent development of b) bacterial killing and d) Cu emission rates per area, corrected for the topography related increase in surface ratio complemented by the factor of in- or decrease observed on USP-DLIP surfaces in comparison to the smooth Cu reference surfaces.

Initial bacterial killing within the first 30 minutes of exposure exhibits a pronounced lag phase for *S. aureus*, where CFU reductions remains below the values of smooth Cu on most USP-DLIP surfaces (see Figure 4a and 4b). Similar to *E. coli*, differences in topography mediated bactericidal efficacy between the surfaces tested are most evident after 60 minutes. In case of contact promoting surface topographies, post-processing by immersion etching also leads to higher bacterial deactivation within similar pattern scales, which is however inverted at 750 nm. In contrast to *E. coli*, the primary pattern scale appears to have a higher effect on bactericidal efficacy than the post-processing state. The highest bacterial inactivation rate is observed on 3 µm surface patterns exhibiting bacterial viability close to the detection limit. A 1 log increase of bacterial killing compared to smooth reference surfaces can furthermore be detected on immersion etched 1 µm patterns. Bactericidal efficacy is not promoted by USP-DLIP processing in case of as-processed 750 nm patterns and even reduced on as-processed 1 µm as well as etched 750 nm surface patterns. In summary, the antibacterial efficacy of the tested surface topographies against *S. aureus* scales as 3 µm (*P* > *Bac*) >> 1 µm (*P* ≈ *Bac*) >/< smooth >/=

750 nm (*P* < *Bac*). The post-processing state shows a similar relation of immersion etched > as-processed like for *E. coli*, but with a lower overall impact on bactericidal activity.

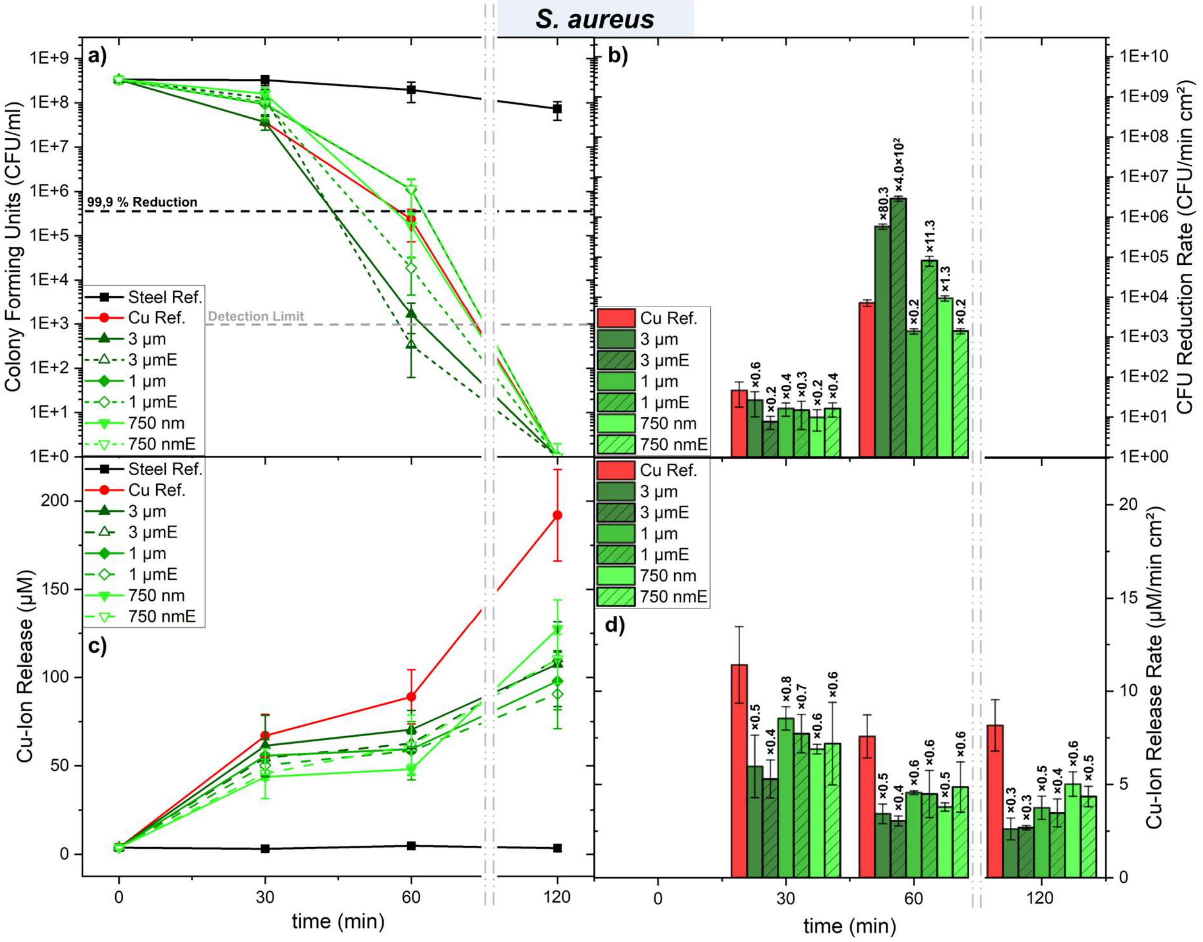

Figure 4: a, b) Bacterial viability and c, d) respective Cu ion release rates measured via wet plating and inductively coupled plasma triple quadruple mass spectrometry (ICP-QQQ) for *S. aureus*. exposure times were chosen as 30, 60 and 120 minutes, displayed with a shortened time axis. Line graphs represent the measured a) colony forming units (CFU) and b) quantitative Cu ion release. The bar graphs show the time dependent development of b) bacterial killing and d) Cu emission rates per area, corrected for the topography related increase in surface ratio complemented by the factor of in- or decrease observed on USP-DLIP surfaces in comparison to the smooth Cu reference surfaces.

The Cu ion release parallelly monitored during Cu exposure of *E. coli* exhibits a clear relation to surface area enhancement by USP-DLIP where the Cu emission rate appears to level with increasing pattern scale (displayed in Figure 3c). The surface ratio equalization of Cu ion release in Figure 3d shows an almost similar release rate of Cu ions between the different Cu surfaces, with only 3 µm textured surfaces showing lower values compared to the Cu references. Between similar pattern sizes Cu ion release tends to be higher on as-processed surfaces, which appears to be linked to the dissolution of the process-induced oxide particles as recently shown in a preliminary study[49]. In contrast, the relation of Cu ion release between USP-DLIP and smooth reference surfaces is inverted in the case of *S. aureus*, where the reference surfaces exhibit the highest Cu emission (compare Figure 3c, d and 4c, d). Nevertheless, bacterial killing rates of *S. aureus* on 3 µm and immersion etched 1 µm patterns are one to two orders of magnitude higher than the reference surfaces. In fact, bacterial viability is found to not necessarily correlate to the amount of Cu emission for both tested strains. E.g., Cu ion release on immersion etched 3 µm and 1 µm usually falls below the values of as-processed surfaces, while the corresponding killing rates after 60 minutes exposure against *E. coli* and *S. aureus* exhibit an inverse relation. Cu release from immersion etched 1 µm surfaces exposed to *E. coli* inoculated bacteria testing solution (BTS) remains at similar magnitudes like as-processed 750 nm, whereas bacterial killing rates of both sample types occupy the opposite ends of the bactericidal efficiency spectrum after 60 minutes of exposure. Likewise, the bactericidal efficiency of the smooth Cu reference surfaces against *E. coli* surpasses that of the as-processed 750 nm patterns, although the respective Cu ion release is lower.

In parallel to the lower Cu emission on USP-DLIP surfaces exposed to *S. aureus*, the total amount of dissolved Cu appears to stagnate between 30 and 60 minutes of exposure, while bacterial viability undergoes a significant decline within this period. After 120 minutes of exposure, a further increase in the dissolved Cu content can be observed in Figure 4c, coupled with complete bacterial inactivation of *S. aureus*. Here, the release of Cu ions on the 750 nm patterns shows an altered trend, eventually surpassing the values of the other USP-DLIP patterns despite a lower surface ratio. These combined observations indicate both, a different bacteria/surface interaction between the tested bacterial strains and a modulation of antibacterial efficacy by USP-DLIP, which is not necessarily linked to Cu ion release rates. Aside of a potentially beneficial effect of hydrophobic surface wetting[43], differences in CA between the tested surface types do not appear to allow a direct correlation to bactericidal activity.

In view of the topography specific deviation in antibacterial efficacy, a closer look is taken on the individual contact conditions established alongside Cu exposure by post-mortem SEM analysis of bacterial allocation on the different topographies.

Impact of Topographic Contact Conditions on Bacteria/Surface Interaction

To gain insight into the actual bacterial contact conditions involved in the expression of Cu sensitivity on the different surface topographies, SEM analyzation of the bacterial interaction with the Cu surfaces was conducted after either 60 minutes (*E. coli*) or 90 minutes (*S. aureus*) of exposure. A capability of cell-cluster agglomeration can be determined on 3 µm patterned surfaces ($P > Bac$) for both *E. coli* (blue) and *S. aureus* (green) due to the increased valley dimensions, as visible in Figure 5a and b. On both 1 µm ($P \approx Bac$) and 750 nm ($P < Bac$), surface attachment was found to be more likely to occur in the single cell domain in case of *E. coli*, while *S. aureus* remains clustered. Single cells of *E. coli* are frequently aligned in parallel orientation to the line-like surface pattern on 1 µm (Figure 5c), while they are more randomly oriented and less elongated on 750 nm (Figure 5e), which might indicate unfavorable bacteria/surface contact conditions for these pattern scales, similar to previous findings[23]. Individual *S. aureus* cells appear to be torn between increasing their surface contact area and maintaining connections with neighboring cells on both 1 µm and 750 nm surface patterns, where individual cells also adhere to pattern peaks due to spatial restrictions within the small interconnected cell clusters (Figure 5d and f). The cell-cluster size on the mirror-polished reference surfaces is similar to 3 µm for *E. coli*, while it is increased for *S. aureus* compared to the topographic surface patterns, highlighting the strain's preference for cell-cell connectivity. In fact, cell-wall associated macromolecules involved in surface adhesion of *S. aureus* have been reported to be similarly related to cell-cell connectivity and biofilm formation[50], where intercellular connectivity might be considered to be of similar importance as quantitative surface contact for single cell viability. Depending on the combination of topographical and chemical surface properties present, intercellular bond strength may outweigh the bacteria/surface bond strength[29,51].

Surface contact conditions have been shown to influence bacterial response mechanisms involving, e.g., the triggering of biofilm formation and stimulated metabolic activity[28]. In parallel, quantitative Cu uptake by viable bacteria has previously been discussed as being facilitated by respiratory activity, which leads to an accelerated cell-damaging rate[16]. In fact, bacterial killing was found to be significantly enhanced on surface patterns where an increased bacterial contact was observed for both strains independent from quantitative Cu ion release. In view of the bactericidal activity measured, cavity dimensions that allow for cell-cluster adhesion on 3 µm patterns seems to be effective to increase antimicrobial efficiency against both *E. coli* and *S. aureus*. An elevated Cu sensitivity on 1 µm patterns was in turn solely found for *E. coli,* which predominantly showed single cell adhesion that allows for increased single cell contact on this surface type. A low up to inverted impact on bactericidal effectivity can finally be observed on the 750 nm pattern scale for both strains. In previous studies, reduced biofilm growth after extended exposure times could be ascertained for *E. coli* on comparable sub-µm topographies, which was however not the case for *S. aureus* that rather exhibited a higher adaptivity[21,26]. A recent publication linked surface adhesion of *S. aureus* to functional membrane sites, which are heterogeneously distributed across the cell envelope and display a characteristic patchiness that appears to befit this pattern periodicity[52]. This might improve surface adhesion of *S. aureus* on line-like 750 nm patterns in an extended time frame, whereas initial bacterial adhesion related to the rapid onset of the antibacterial mechanism of Cu surfaces might still be restrained within the time scales of the wet plating experiments.

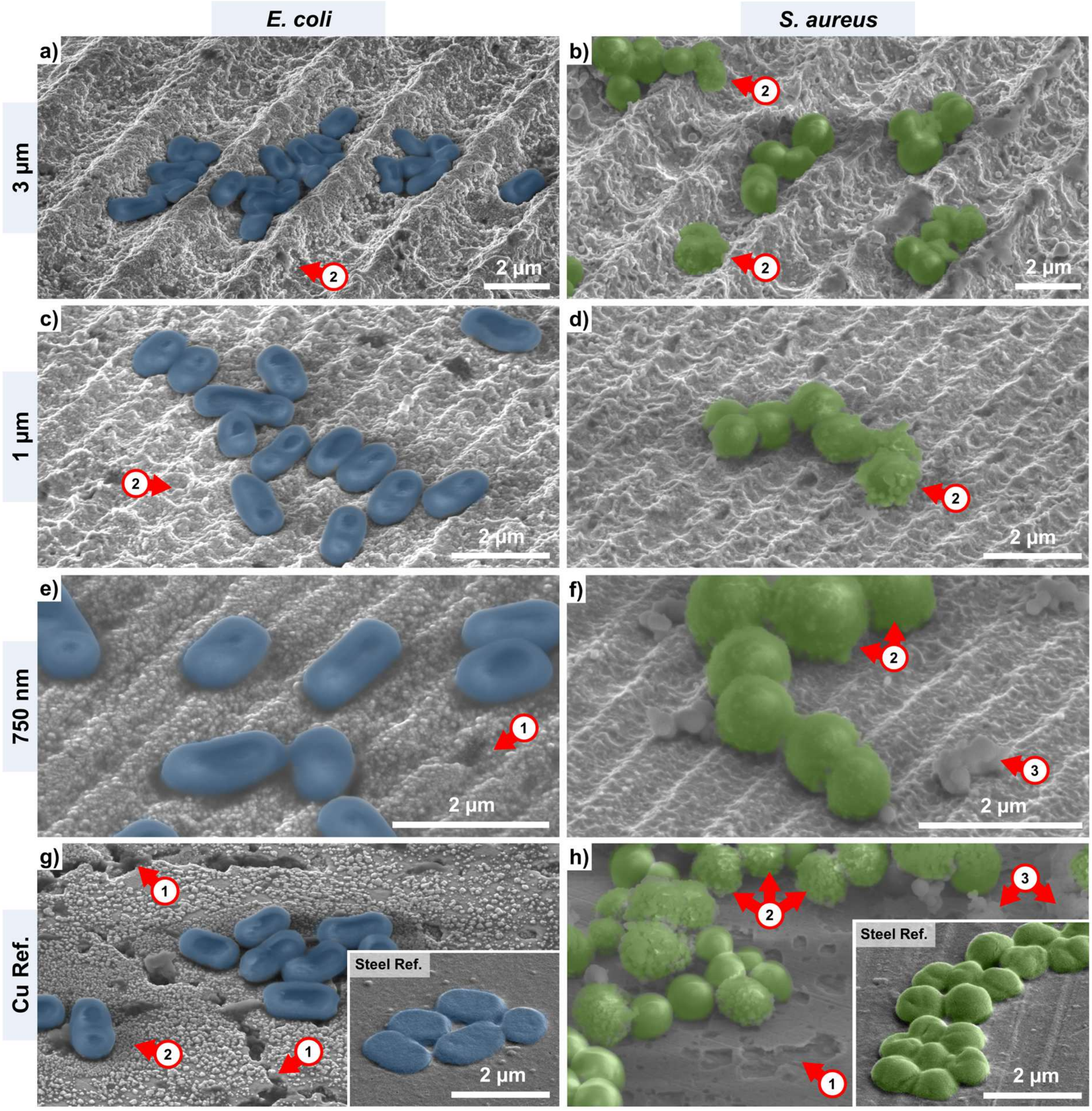

Figure 5: Representative images of the SEM analysis on topography related contact conditions for single bacterial cells and cell-clusters on immersion etched USP-DLIP and polished Cu reference surfaces. Single cells of *E. coli* (blue) and *S. aureus* (green) are shown in exposure to a, b) 3 µm ($P > Bac$), c, d) 1 µm ($P \approx Bac$) and e, f) 750 nm ($P < Bac$) pattern scale as well as g, h) Cu Ref. surfaces exhibiting varying impact on cell-adhesion. The bacterial cell morphology observed on inert stainless steel references is provided by an inset in both g) and h) for each strain. Several modifications on the substrate surfaces arising from chemical interaction during BTS exposure are highlighted in the images corresponding to (1) corrosive surface deterioration, (2) redepositions in the vicinity (*E. coli*) or attached (*S. aureus*) to bacterial cells, (3) weakly attached globular particle clusters. Imaging was done utilizing SE contrast on uncoated samples under 52° tilt.

Bactericidal Interaction with the Cu Substrate

The notable deviation of Cu ion emission between *E. coli* and *S. aureus* with inverse relation of USP-DLIP patterned to smooth surfaces indicates a different chemical surface interaction of the two bacterial strains (compare Figure 3c and 4c). Quantitative ion release on Cu surfaces exposed to bacteria inoculated PBS has previously been shown to be majorly dependent on the corrosive interaction between the Cl^--containing medium and substrate, where bacteria might act as corrosion catalysts due to the impairment of surface passivation by Cu ion scavenging[53]. This mechanism has been shown be enhanced in case of lysed bacterial cells[40,53] indicating a protective role of intact cell membranes. In the absence of bacterial cells, USP-DLIP Cu surfaces form a stabilized oxide layer preventing further surface degradation and Cu dissolution within 1 h of exposure to PBS indicated by a reduced Cu ion release rate[43].

In this study, the Cu ion release from USP-DLIP patterned Cu surfaces exposed to *E. coli* inoculated PBS exhibits a constant Cu release above the level of mirror-polished Cu, befitting the previously described catalytic behavior[53]. Under exposure to *S. aureus* inoculated PBS, Cu ion emission exhibits a closer correlation to stabilizing passivation without a bacterial impact on corrosion behavior presenting a similar relation between USP-DLIP patterns and the smooth reference surfaces[43]. This observation might be related to different cellular response mechanisms involved in the higher Cu resistance reported for gram-positive bacteria[6]. This may also be linked to the stagnation of Cu ion release between 30 and 60 minutes, as well as the lower bacterial inactivation rates of *S. aureus* within the first 60 minutes of exposure.

Comparing the corrosive degradation of Cu surfaces alongside BTS exposure, pitting corrosion sites related to grain boundaries or intragranular corrosion are evident on mirror-polished surfaces, while localized corrosion is less evident on USP-DLIP treated surfaces (indicated by (1) arrows in Figure 5). This corresponds to previous investigation of corrosion kinetics of USP-DLIP processed Cu surfaces [49]. In the case of *E. coli*, corrosion products appear to agglomerate preferentially in the form of a condensing layer of Cu oxide particles close to cell clusters, surrounded by an outer ring of corrosion sites ((2) arrows in Figure 5a, c and g). The pH value of *E. coli* inoculated PBS has been shown to undergo an alkaline shift favorable for Cu_2O formation[53] alongside Cu surface exposure, whereas preferential agglomeration sites in vicinity to *E. coli* clusters are potentially related to electrochemical microcell formation and mass transport under involvement of the bacterial cells[54]. Regarding *S. aureus*, USP-DLIP patterned Cu surfaces exposed to BTS exhibit considerably less degradation of the substrate surface and thicker oxide layers, indicating better surface passivation when combined with the comparably low Cu ion release rates measured[49]. Instead, particulate adsorbates on bacterial cells can be observed ((2) arrows in Figure 5b, d, f and h) which vary in quantity and size. Further agglomerations of circular particles can be found with loose connection to the substrate surface ((3) arrows in Figure 5f and h), which are more likely to be suppressed under *E. coli* BTS exposure.

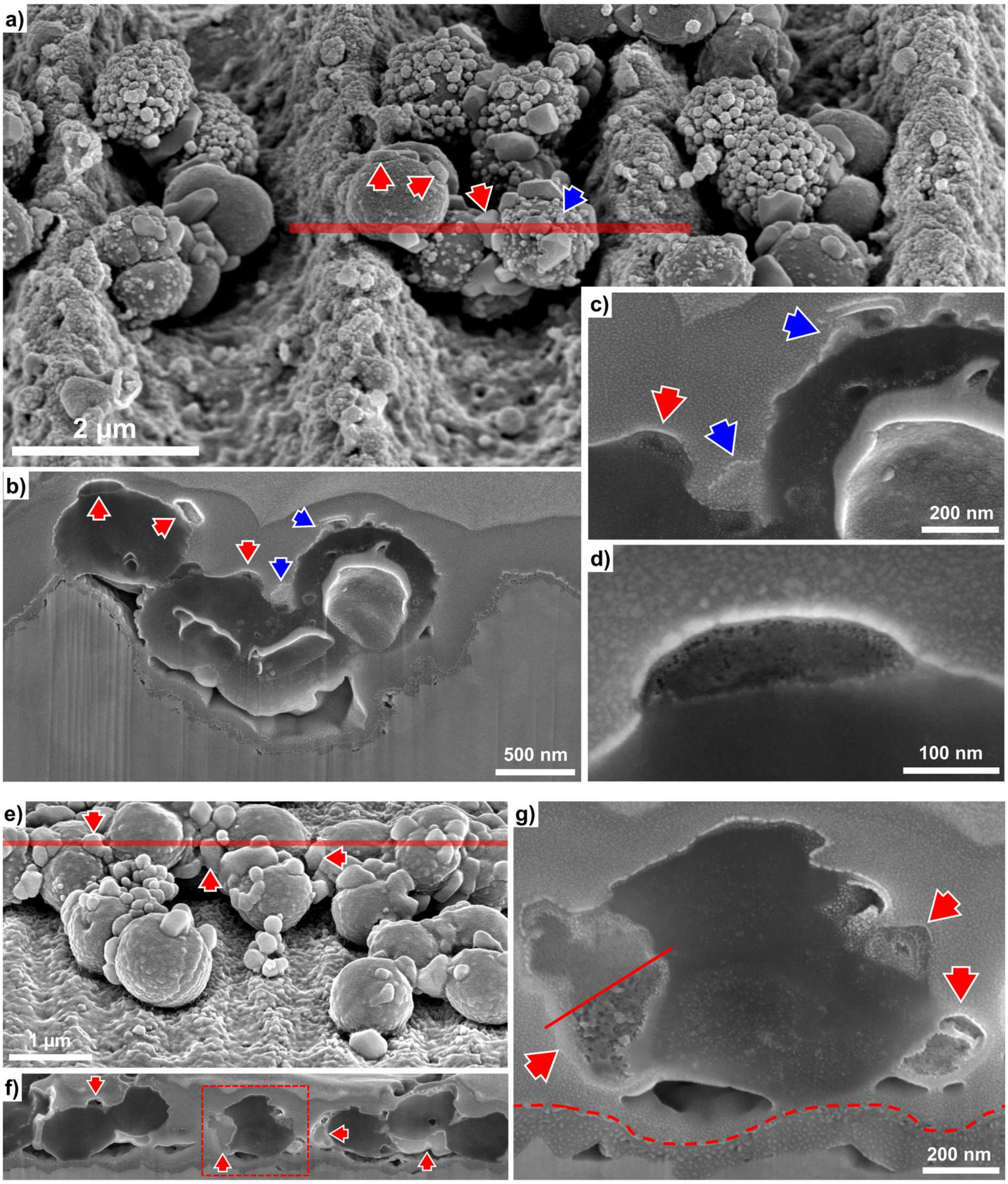

Figure 6: SEM-imaging of *S. aureus* cells after 90 minutes of exposure on Cu surfaces. a) Cell-clusters on a 3 µm pattern exhibiting different types of particle agglomerations marked with red (large single particles) and blue arrows (small spherical particle accumulations). The red line indicates the location of the FIB cross-section displayed in b-d). e) Cell-cluster on a 750 nm pattern mainly exhibiting large particle agglomerations, which appear to affect bacterial integrity further highlighted via FIB cross-sectioning in f) and g). Particles are not stable under electron beam irradiation as indicated by structural alteration of the left particle in g) after single (upper part) and multiple imaging (lower part). Imaging was conducted in SE-contrast at 52° sample tilt.

Comparative consideration of both the difference in corrosive surface deterioration and Cu ion release between *E. coli* and *S. aureus* suggests a deviation in the chemical bacteria/surface interaction for the gram-positive strain from the previously described involuntary Cu drainage of *E. coli*[40,53].

Corrosion catalysis by Cu scavenging of *E. coli* was similarly determined on USP-DLIP Cu surfaces in saline environment in a recent study, where USP-DLIP was also found to increase the corrosion resistance of Cu surfaces by severe mechanical defect implantation[49].

To gain a better understanding of the underlying mechanisms in bacteria/surface interaction occurring alongside deactivation of *S. aureus*, alteration of bacterial cell morphology has been investigated in SEM analysis after 90 minutes of exposure to the Cu surfaces. Prior to SEM analysis a nm-thick sputter-coating of $Au_{80}Pd_{20}$ was applied on one sample batch to enable high resolution (HR) analyzation and to provide a contrasting layer to distinguish the original sample surface from the deposited Pt-cover layer in FIB cross-sections. HR imaging of *S. aureus* cells exhibits a considerable agglomeration of particles on and partially around bacterial cells (displayed in Figure 6a and e). These can be separated by morphology and local concentration into two groups, where small spherical particles (SP, blue arrows) tend to fully cover single bacterial cells, while larger particles (LP, red arrows) vary in shape and size without local reference to each other. FIB cross-sectioning reveals varying surface contact angles of SP to the bacterial cell as well as a bright SEM contrast that points towards heavy, non-organic element composition (illustrated in Figure 6b and highlighted in Figure 6c). LP in turn constantly exhibit low contact angles to the bacterial surface and a dark SEM contrast similar to the bacterial cell (Figure 6d). However, in case of further enhanced particle sizes, also the previously dark contrasted LP begin to display an increasing contrast brightening in FIB cross-sectioning indicating the agglomeration of heavier elements (see Figure 6e and f). LP show a weak structural stability against electron beam irradiation (visible in the cross-section of the particle in Figure 6g), indicating a partly organic composition.

EDS analysis under low acceleration voltage reveals that both types of particles contain considerable amounts of Cu combined with trace elements C, N and Na originating from the bacterial matrix. An increased Cu content is additionally indicated by a bright Z-contrast in backscatter electron (BSE) imaging that deviates from the bacterial cell envelopes, as displayed in Figure 7a and c. Both particle types appear in different sizes, suggesting a continuous particle growth after nucleation onto the bacterial cell membranes. Aside of morphology, the two identified particle types differ in composition, where SP exhibit increased intensities of both O and P (see Figure 7a). This composition implies the formation of cupric phosphate ($Cu_3(PO_4)_2$) on the bacterial membrane, whereas the unconnected spherical particle clusters at the periphery of the bacterial cells can also be assigned to this particle group according to their EDS spectrum (compare Figure 7b)[55]. Cu phosphate has previously been identified as a corrosion product formed on Cu surfaces under PBS exposure[55], whereas its formation might be decreased in the presence of *E. coli* due to the reduced availability of free Cu ions in solution and allocated to destroyed bacterial cells[53]. Phosphate formation has been shown to be triggered in the vicinity of bacteria under certain conditions, where the membrane acts as a nucleation site through the catalytic effect of specific membrane molecules and metabolites[56], which may cause the spatial correlation between bacteria and phosphate formation observed here. Further particle growth on *S. aureus* cells indicates a predominant activity of the Cu phosphate formation driving force with an involuntary role of the subjected bacteria, where phosphate formation has been shown to potentially involve chemical dissolution of bacterial biomass[57].

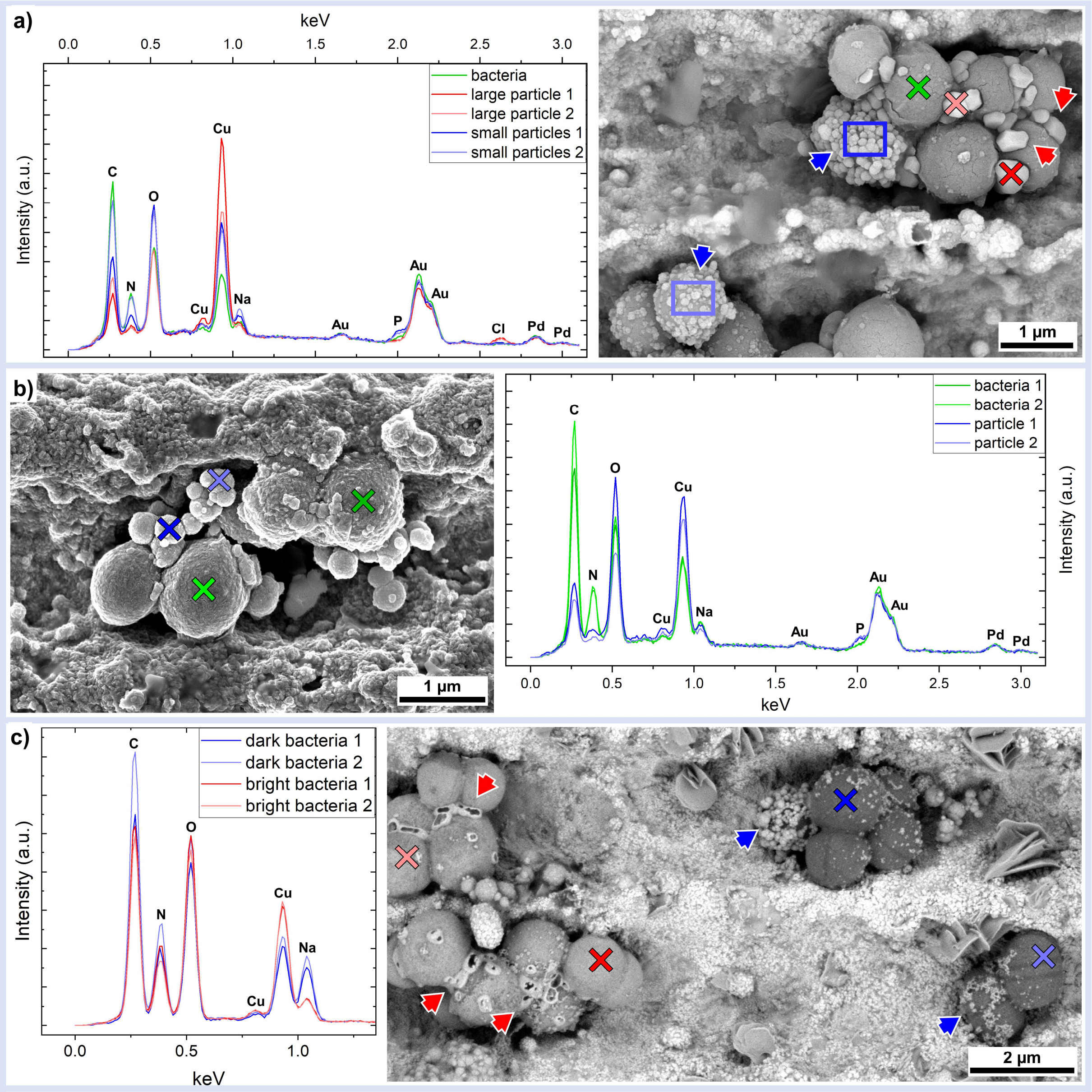

Figure 7: EDS analysis of a) different particles found attached to *S. aureus* bacterial cells on coated samples imaged in BSE-contrast at 10 kV, b) spherical particle clusters in the periphery of bacterial cells imaged in SE-contrast, c) uncoated bacteria exhibiting different Z-contrast in BSE-imaging at 1.5 keV acceleration voltage. Large and small particle types are exemplarily marked by red and blue arrows in a) and c).

In contrast, LP exhibit increased Cu levels combined with traces of Cl, whereas P is completely absent. Considering the shape and imaging contrast at early formation stages and after further growth, Cu particle formation on *S. aureus* might be linked to defects in the bacterial cell membrane, where exposed cytoplasm triggers a localized agglomeration of Cu (further analysis of Cu particle formation is provided as Supporting Information). Both bacterial Cu scavenging and phosphate formation were found to be enhanced in the case of previously lysed bacteria, where accessible cytoplasm appears to play the major role within the underlying chemical processes of bacterial Cu uptake with membrane integrity as the limiting factor[40,53,56,57]. Nucleation and growth of Cu based agglomerates has previously been found to disrupt bacterial cell wall integrity due to the opposing charging between Cu ions and the membrane that leads to a reduction in membrane Zeta-potential. The resulting avalanching cell wall collapse exposes the bacterial cytoplasm and allows for elevated intracellular Cu ingress[36,58]. Accordingly, *S. aureus* bacterial cells that show increased agglomeration of LP present both a brightened Z-contrast and higher levels of intracellular Cu monitored by EDS in comparison to bacteria lacking LP accumulation (displayed in Figure 7c). Therefore, the increasing Cu ion release between 60 and 120 minutes in case of *S. aureus* inoculated BTS visible in Figure 4c may potentially be linked to an increase in Cu uptake by the exposure of the cytoplasm, accompanying cell wall disruption and cell death after extended contact to the Cu surfaces, which was previously averted by a more rigid cell wall of the gram-positive bacteria.

Based on these considerations, the deviation in measured Cu ion release between gram-positive *S. aureus* and gram-negative *E. coli* appears to be mainly related to strain-specific differences in membrane integrity, which affects Cu scavenging and thus Cu surface corrosion. In fact, the thickened surface oxide layer formation as well as the reduced Cu ion release of USP-DLIP Cu surfaces under exposure to *S. aureus* befits previous observations of increased surface passivation in PBS by defect implantation alongside USP-DLIP in a recent study[49]. This shows a considerably lower Cu scavenging effect of *S. aureus,* which results in lower Cu ion release rates on USP-DLIP compared to smooth surfaces. However, this does not appear to limit an enhancement of bactericidal activity by contact promoting topographies.

Conclusions

The impact of topographically modified contact conditions on antibacterial efficacy of Cu surfaces has been investigated for gram-negative *E. coli* and gram-positive *S. aureus*. The conclusions of the study can be summarized as follows:

- **Increased Bacteria/Substrate Contact and Antibacterial efficacy:** Topographic surface modification by USP-DLIP that allows for a larger contact area between bacteria and the substrate is associated with increased bactericidal activity. Bacterial killing rates on these surfaces might level several orders of magnitude higher than the smooth reference surfaces. The USP-DLIP topography that exhibit the highest bactericidal efficacy varies between the two tested strains. In the case of *S. aureus*, the bacteria-specific tendency to cluster formation appears to reduce the capability of individual bacterial cells to achieve high surface contact within the topographic trenches close to single bacterial scale. Instead, an increased cavity scale that allows intrusion of whole cell clusters was shown to be highly effective in increasing bactericidal efficacy against *S. aureus*. This results in higher pattern scales that are associated with increased bactericidal activity despite lower statistical cell diameters compared to *E. coli*, which is most efficiently killed on surfaces allowing high single cell contact. Pattern scales below the single bacterial cell size rather tend to decrease both antibacterial efficacy and Cu sensitivity for both strains.

- **Antimicrobial Efficacy and Cu Ion Release:** Antimicrobial efficacy of Cu surfaces against *E. coli* and *S. aureus* is found to be less dependent on the quantity of Cu ion release, but rather scales with the extend of contact area between individual adherent cells and substrate. Surface topographies that provide high single cell contacts appear to trigger an increased sensitivity for environmental Cu, where bactericidal activity is enhanced independent from quantitative Cu emission. Based on this, contact dependent Cu sensitivity appears to be the main driving force behind deviating antimicrobial activity between the different tested surface topographies.
- **Strain specific Cu Interaction:** Wet plating in PBS was found to involve Cu scavenging mechanisms in both bacterial strains that catalyzes Cu ion release over natural passivation. This effect is more pronounced in *E. coli*, where the bacterial cells seem to be less protected against involuntary Cu uptake due to the weaker cell membrane, while Cu accumulation may be additionally driven by chemical microcell formation. In the case of *S. aureus*, Cu scavenging is reduced, which additionally results in higher surface passivation of USP-DLIP processed samples. Initial Cu accumulation in *S. aureus* involves the agglomeration of extracellular Cu phosphate particles via membrane nucleation. Increased membrane stress finally appears to induce a step-wise collapse of the cell wall followed by an exposure of cytoplasm and a quantitative increase in Cu uptake under further extended Cu exposure.

The chemical affinity of the bacterial cytoplasm for Cu ions combined with their high thiophilicity is a dominant driving force for the bactericidal properties of Cu substrates, with killing rates being directly related to the quantitative Cu uptake and associated damage to the bacterial cell. Up to now, this killing mechanism has been mainly driven by the quantitative Cu ion emission of the applied Cu based material. Here, it has been demonstrated that targeted surface design by USP-DLIP, involving topographic and chemical surface modification, can potentially increase antimicrobial surface efficiency with less dependency on quantitative Cu ion release. A higher Cu sensitivity could be linked to topographies that provide improved bacterial contact conditions, which might trigger bacterial activity by downstream response mechanisms[28]. An inverse effect on Cu sensitivity was similarly ascertained on rather contact inhibiting surfaces. These results show both the potential to increase the efficiency of functional surfaces by targeted surface design, as well as the peculiarities of strain specific surface interactions that need to be considered in parallel to enable targeted surface tailoring. This provides a valuable foundation to further investigate and potentially incorporate bacterial interactions into advanced decontamination concepts including strain-specific adaptation strategies for critical environments[6,7,31].

Methods

Sample Preparation

For further surface modification and testing, single samples of the dimensions 10 x 25 mm² have been charted from 1 mm sheets of oxygen free Cu (>99,95%) (*Wieland*) and AISI 304 stainless steel (*Brio*) In case of stainless steel, the material was purchased in mirror-polished condition (Ra < 10nm), while Cu samples underwent polishing on an automated *TegraPol-21* system (*Struers*) to reach equivalent initial surface roughness[59]. Shares of the polished samples are deducted to provide reference surfaces of flat topography (denoted as Steel Ref. and Cu Ref.).

Mirror-polished samples of Cu are subjected to USP-DLIP inducing line-like periodic surface patterns in the scale of either 3 µm ($P > Bac$), 1 µm ($P \approx Bac$) or 750 nm ($P < Bac$). In the USP-DLIP setup a Ti:Sapphire *Spitfire* laser system (*Spectra Physics*) is utilized, operating at $t_p = 100$ fs pulse duration (FWHM), 1 kHz repetition rate and a centered wavelength λ of 800 nm. Line-like surface patterns are generated by two beam laser interference using a previously introduced optical setup[60] consisting of a diffractive optical element (DOE) to split and a lens system to recombine the partial beams on the substrate surface. To create the different pattern periodicities P the optical setup has been modified to adjust the single beam incident angle Θ according to equation (1):

$$P = \frac{\lambda}{2\sin(\theta)} \tag{1}$$

With $P = 3$ µm → $\Theta = 7.66°$, $P = 1$ µm → $\Theta = 23.58°$ and $P = 750$ nm → $\Theta = 32.23°$. Planar patterning was conducted by scanning the substrate surface in continuous pulsing mode adjusting the fluence and pulse overlap according to the individual material ablation threshold and pattern scale specific impact of ablation kinetics in pattern formation using p-polarized two-beam USP-DLIP[44]: 3 µm patterns have been produced with an overlapping pulse count of $N = 10$ at 2.14 J/cm², while for 1 µm and 750 nm patterns reduced pulse counts of $N = 3$ and 2 at fluences of 1.38 J/cm² were applied. One batch of Cu samples subsequently underwent ultrasonic assisted immersion etching in 3% citric acid for 40 seconds to remove process-induced oxidic substructures[45]. The other batch of the Cu samples remained unaffected (as-processed samples).

Surface Characterization

Surface characterization of the different samples with and without USP-DLIP treatment was conducted by means of both confocal laser scanning microscopy (CLSM) (*LEXT OLS4100* by *Olympus*) and scanning electron microscopy (SEM) (*Helios Nanolab 600* by *FEI* and *Helios PFIB G4 CXe* by *Thermo Fisher*) also including the system's focused ion beam (FIB) and energy-dispersive X-ray spectroscopy (EDS) modules.

The CLSM analysis involved a 50× objective (NA 0.95) with altered digital magnification of either 2x or 6x at a laser wavelength of 405 nm. The surface geometry of the various topographies applied using USP-DLIP was quantified based on periodicity, valley/peak ratio, valley width and depth, and surface ratio, defined as the ratio between the actual surface and an idealized smooth reference surface. Each parameter was measured on six individual spots on three different samples per topography for statistical evaluation.

High resolution SEM imaging was conducted in secondary electron (SE) contrast mode at an acceleration voltage of 5 kV and a current of 86 pA at 52° sample tilt for improved visualization of topographic morphology. High resolution imaging was conducted using the in-lens detector in immersion mode. Furthermore, low voltage backscatter electron (BSE) images of uncoated samples were acquired using a solid state detector at 0° sample tilt. To assess the initial state of surface oxide composition high resolution grazing incidence X-ray diffraction (GI-XRD, *PANalytical X'Pert PRO-MPD*) was applied utilizing Cu K_α radiation with a Goebel mirror at a 1° grazing angle in parallel orientation to the line-like patterns to avoid shadowing of the valley surface compartments. Within this setup 95% of the measured signal can be estimated to originate from an interaction volume within a depth of < 1.11 µm from the substrate surface[61].

After surface exposure during wet plating, the bacteria/substrate contact as well as the induced damage on both bacterial cells and Cu substrate were investigated by SEM imaging, FIB cross-sectioning, and EDS analysis at an acceleration voltage of 1.5 kV to 10 kV (BSE-SEM), 30 kV (Ga-ion beam) and 5 kV (EDS), respectively. The low acceleration voltage chosen for EDS was shown to enable a more surface sensitive spectroscopic assessment of element composition, in a previous study[45]. For FIB cross-sectioning, an additional contrast layer of ~10 nm $Au_{80}Pd_{20}$ was applied by sputter coating before covering the investigated site with a protective layer of electron and ion beam induced Pt-deposition to preserve the substrate surface from ion-induced degradation. For EDS measurements, the sample was rotated to align the line pattern on the surface with the azimuth angle of the detector to avoid shadowing. SE imaging to investigate bacterial contact condition has been conducted at ten different locations on samples of immersion etched USP-DLIP Cu surfaces and both the Cu and stainless steel references, whereas in-depth investigation of chemical surface modification for *S. aureus* was executed on representative locations chosen from this.

Surface Wettability

Contact angle (CA) measurements were conducted to monitor the parallel influx of wettability on bacteria/surface interaction aside of surface topography. The samples have been tested after three weeks of aging in ambient condition, where surface wettability alteration after USP-DLIP processing can be considered as stabilized[43]. The static contact angle was monitored in triplicates for each surface by means of a Drop Shape Analysator *DSA 100* (*Krüss GmbH*) using distilled water at a fixed droplet volume of 3 µl. The CA was detected both in orthogonal and parallel orientation to also include anisotropic droplet propagation on the line-like surface patterns.

Wet Plating

E. coli K12 (BW25113) was cultured via aerobically overnight growth in lysogeny broth (LB) medium for 12 h at 37 °C with a shaking speed of 220 rpm according to Molteni et al.[62]. Bacterial cells in the stationary growth phase were collected from 5 ml culture medium by centrifugation for 15 minutes at 5000 × g, which is followed by three consecutive PBS washing steps involving identical centrifugation parameters. Finally, the bacteria testing solution (BTS) was gained by resuspension in 5 mL of PBS. The hence achieved initial average cell count ranges in the scale of 9 log CFU/ml. Prior to cultivation, the *E. coli* bacteria have been stored for two weeks at 4 °C on agar plates after cultivation from cryo-storage at -81 °C, which have been provided by the Helmholtz Institute for Pharmaceutical Research Saarland (HIPS).

For the preparation of BTS containing *S. aureus* a single bacterial colony from a previously prepared blood agar plate was added to 5 ml tryptic soy broth (TSB). The bacterial solution was cultivated for 16 hours at 37 °C and 150 rpm in an incubator. Afterwards, 40 µl of the bacterial solution was transferred into 4 ml of TSB. To obtain bacteria in the exponential phase this suspension was placed for 2.5 hours at 37 °C and 150 rpm in the incubator. Subsequently, washing and centrifugation was performed, where 1 ml of the bacterial suspension was centrifuged for 3 minutes at 17000 g, followed by three washing steps in PBS. Before cultivation, the *S. aureus* bacteria have been stored on blood agar plates at 4 °C for less than two weeks after cultivation from a cryo-storage in glycerol stock at -20 °C. The utilized *S. aureus* wild-type strain SA113 (ATCC 35556) was provided by the Institute of Medical Microbiology and Hygiene of the Saarland University medical center.

Following the wet plating method for heterogeneous surface wetting properties described in a previous work[43], three droplets of 40 µl of the BTS were applied to individual exposure areas predefined by polyvinyl chloride (PVC) rings exhibiting an inner circular diameter of 5 mm. The slightly hydrophobic PVC prevent BTS spreading in case of hydrophilic and provide anchoring edges to facilitate complete droplet covering of the exposure area in case of (super-)hydrophobic surfaces. Each sample was stored in water saturated environment at ambient temperature during BTS exposure. Two doses of 5 µl each were withdrawn after three individual exposure intervals, each time probing a different droplet. Bacterial survival on the Cu surfaces was initially monitored to define suitable exposure durations that allow for a comparative assessment of bacterial viability on the different surfaces, where complete killing of both bacterial strains could be initially ascertained after 120 min of exposure. Due to the varying resilience of the tested bacterial strains, *E. coli* cells were exposed for 20 minutes, 40 minutes and 60 minutes, while *S. aureus* survival was monitored for 30 minutes, 60 minutes and 120 minutes. Bacteria adhering to the surface were resuspended by vigorous pipetting with a parallel tip orientation to the surface pattern to avoid shadowing of the pattern valleys. The number of viable bacteria was assessed using the standard plate count method by serial dilution of one of the 5 µl doses in PBS followed by plating on LB/blood agar plates. The inoculated agar plates were incubated overnight at 37 °C and 80% moisture followed by counting of the remaining colony forming units (CFU) after the individual exposure intervals. The second 5 µl was diluted 600-fold dilution in 0.1% HNO_3 for further determination of the corresponding Cu ion concentrations in the BTS by inductively coupled plasma triple quadrupole mass spectrometry (ICP-QQQ, *Agilent 8900 ICP-QQQ*). The experiments were conducted in triplicates on separate dates for each bacterial strain, where statistical variation of both CFU and Cu-ion release is determined via standard deviation.

In order to exclude the effect of surface enlargement by USP-DLIP on bacterial viability as well as quantitative Cu ion release, the CFU and ICP-QQQ results determined were normalized to a standardized surface area and exposure duration, thus allowing for a more accurate comparison. The corresponding CFU reduction and Cu ion release rate were defined by equation (2) and (3).

$$\text{CFU reduction rate} = \frac{CFU}{t_{exp}\,A\,S} \quad \text{in} \quad \left(\frac{\text{CFU}}{\text{min cm}^2}\right) \tag{2}$$

$$\text{Cu ion release rate} = \frac{Cu_{emitted}}{t_{exp}\,A\,S} \quad \text{in} \quad \left(\frac{\mu\text{M}}{\text{min cm}^2}\right) \tag{3}$$

Here, *CFU* accounts to the viable colony forming units per ml and $Cu_{emitted}$ to the release of Cu in µM detected after a defined exposure interval t_{exp}. *A* is the exposed surface area of 0.196 cm^2 defined by the circular PVC rings and *S* corresponds to the individual surface ratio denoted in Figure 1, where *S* = 1 in the case of the smooth reference surfaces.

Acknowledgements

We would like to acknowledge the support of Hannah Heintz from the group of Prof. Karin Jacobs (Department of Experimental Physics, Saarland University) in the wet plating experiments including *S. aureus* as well as Dr. Flavio Soldera in SEM analyzation and further discussion. This work has been funded by the German Research Foundation (DFG) within the project “Controlled bacterial interaction to increase the antimicrobial efficiency of copper surfaces” (project number 415956642) and the German Aerospace Center – Space Administration (DLR) within the project “Investigation of metal surfaces under space conditions - An effective strategy to prevent microbial biofilm formation“(project number 50WB1930). The authors acknowledge financial support in the project “MatInnovat” supported by the Saarland State Ministry of Economics with resources from the European Fund for Regional Development (EFRE) and funding by the German Research Foundation for the PFIB/SEM system (*Helios PFIB G4 CXe* by *Thermo Fisher*) used in SEM analysis (DFG, INST 256/510-1 FUGG) and for the ICP-QQQ instrument used for elemental quantification (DFG, INST 256/553-1 FUGG).

Author Contributions:

D.W. Müller conceived the idea, designed the interference-based laser setup used in this study and conducted sample preparation, surface characterization via confocal laser scanning microscopy (LSM), CA measurement, GI-XRD-analysis, scanning electron microscopy (SEM) for bacterial imaging and the wet plating experiments with additional support in the S2 level experiments involving the *S. aureus* strain. Post-mortem SEM-analysis of *S. aureus* cells including FIB cross-sectioning, STEM and EDS was carried out by D.W. Müller and C. Pauly. K. Brix and R. Kautenburger performed the inductively-coupled-plasma mass-spectrometry (ICP-QQQ) analysis. Data interpretation and preparation of the manuscript was done by D.W. Müller and C. Pauly. F. Mücklich supervised the work.

Competing Interests:

The authors declare no competing interests.

References

[1] M. Naghavi, Global mortality associated with 33 bacterial pathogens in 2019: a systematic analysis for the Global Burden of Disease Study 2019, The Lancet 6736 (2022) 02185. https://doi.org/10.1016/S0140-6736(22)02185-7.

[2] M. Cámara, W. Green, C.E. MacPhee, P.D. Rakowska, R. Raval, M.C. Richardson, J. Slater-Jefferies, K. Steventon, J.S. Webb, Economic significance of biofilms: a multidisciplinary and cross-sectoral challenge, Npj Biofilms and Microbiomes 8 (2022) 1–8. https://doi.org/10.1038/s41522-022-00306-y.

[3] C.J. Murray, K.S. Ikuta, F. Sharara, L. Swetschinski, G. Robles Aguilar, A. Gray, C. Han, C. Bisignano, P. Rao, E. Wool, S.C. Johnson, A.J. Browne, M.G. Chipeta, F. Fell, S. Hackett, G. Haines-Woodhouse, B.H. Kashef Hamadani, E.A.P. Kumaran, B. McManigal, R. Agarwal, S. Akech, S. Albertson, J. Amuasi, J. Andrews, A. Aravkin, E. Ashley, F. Bailey, S. Baker, B. Basnyat, A. Bekker, R. Bender, A. Bethou, J. Bielicki, S. Boonkasidecha, J. Bukosia, C. Carvalheiro, C. Castañeda-Orjuela, V. Chansamouth, S. Chaurasia, S. Chiurchiù, F. Chowdhury, A.J. Cook, B. Cooper, T.R. Cressey, E. Criollo-Mora, M. Cunningham, S. Darboe, N.P.J. Day, M. De Luca, K. Dokova, A. Dramowski, S.J. Dunachie, T. Eckmanns, D. Eibach, A. Emami, N. Feasey, N. Fisher-Pearson, K. Forrest, D. Garrett, P. Gastmeier, A.Z. Giref, R.C. Greer, V. Gupta, S. Haller, A. Haselbeck, S.I. Hay, M. Holm, S. Hopkins, K.C. Iregbu, J. Jacobs, D. Jarovsky, F. Javanmardi, M. Khorana, N. Kissoon, E. Kobeissi, T. Kostyanev, F. Krapp, R. Krumkamp, A. Kumar, H.H. Kyu, C. Lim, D. Limmathurotsakul, M.J. Loftus, M. Lunn, J. Ma, N. Mturi, T. Munera-Huertas, P. Musicha,

M.M. Mussi-Pinhata, T. Nakamura, R. Nanavati, S. Nangia, P. Newton, C. Ngoun, A. Novotney, D. Nwakanma, C.W. Obiero, A. Olivas-Martinez, P. Olliaro, E. Ooko, E. Ortiz-Brizuela, A.Y. Peleg, C. Perrone, N. Plakkal, A. Ponce-de-Leon, M. Raad, T. Ramdin, A. Riddell, T. Roberts, J.V. Robotham, A. Roca, K.E. Rudd, N. Russell, J. Schnall, J.A.G. Scott, M. Shivamallappa, J. Sifuentes-Osornio, N. Steenkeste, A.J. Stewardson, T. Stoeva, N. Tasak, A. Thaiprakong, G. Thwaites, C. Turner, P. Turner, H.R. van Doorn, S. Velaphi, A. Vongpradith, H. Vu, T. Walsh, S. Waner, T. Wangrangsimakul, T. Wozniak, P. Zheng, B. Sartorius, A.D. Lopez, A. Stergachis, C. Moore, C. Dolecek, M. Naghavi, Global burden of bacterial antimicrobial resistance in 2019: a systematic analysis, The Lancet 399 (2022) 629–655. https://doi.org/10.1016/S0140-6736(21)02724-0.

[4] L.-Y. Sobisch, K.M. Rogowski, J. Fuchs, W. Schmieder, A. Vaishampayan, P. Oles, N. Novikova, E. Grohmann, Biofilm Forming Antibiotic Resistant Gram-Positive Pathogens Isolated From Surfaces on the International Space Station, Front Microbiol 10 (2019) 1–16. https://doi.org/10.3389/fmicb.2019.00543.

[5] C. Urbaniak, M.D. Morrison, J.B. Thissen, F. Karouia, D.J. Smith, S. Mehta, C. Jaing, K. Venkateswaran, Microbial Tracking-2, a metagenomics analysis of bacteria and fungi onboard the International Space Station, Microbiome 10 (2022) 1–19. https://doi.org/10.1186/s40168-022-01293-0.

[6] E.A. Bryce, B. Velapatino, H. Akbari Khorami, T. Donnelly-Pierce, T. Wong, R. Dixon, E. Asselin, In vitro evaluation of antimicrobial efficacy and durability of three copper surfaces used in healthcare , Biointerphases 15 (2020) 011005. https://doi.org/10.1116/1.5134676.

[7] M. Colin, E. Charpentier, F. Klingelschmitt, C. Bontemps, C. De Champs, F. Reffuveille, S.C. Gangloff, Specific antibacterial activity of copper alloy touch surfaces in five long-term care facilities for older adults, Journal of Hospital Infection 104 (2020) 283–292. https://doi.org/10.1016/j.jhin.2019.11.021.

[8] A. Tripathy, P. Sen, B. Su, W.H. Briscoe, Natural and bioinspired nanostructured bactericidal surfaces, Adv Colloid Interface Sci 248 (2017) 85–104. https://doi.org/10.1016/j.cis.2017.07.030.

[9] L. Pellegrino, L.S. Kriem, E.S.J. Robles, J.T. Cabral, Microbial Response to Micrometer-Scale Multiaxial Wrinkled Surfaces, ACS Applied Materials and Interfaces 14 (2022) 31463–31473. https://doi.org/10.1021/acsami.2c08768.

[10] M. Hans, J.C. Támara, S. Mathews, B. Bax, A. Hegetschweiler, R. Kautenburger, M. Solioz, F. Mücklich, Laser cladding of stainless steel with a copper-silver alloy to generate surfaces of high antimicrobial activity, Applied Surface Science 320 (2014) 195–199. https://doi.org/10.1016/j.apsusc.2014.09.069.

[11] T.L. Meister, J. Fortmann, M. Breisch, C. Sengstock, E. Steinmann, M. Köller, S. Pfaender, A. Ludwig, Nanoscale copper and silver thin film systems display differences in antiviral and antibacterial properties, Scientific Reports 12 (2022) 1–10. https://doi.org/10.1038/s41598-022-11212-w.

[12] H.T. Michels, J.O. Noyce, C.W. Keevil, Effects of temperature and humidity on the efficacy of methicillin-resistant *Staphylococcus aureus* challenged antimicrobial materials containing silver and copper, Letters in Applied Microbiology 49 (2009) 191–195. https://doi.org/10.1111/j.1472-765X.2009.02637.x.

[13] S. Krupanidhi, A. Sreekumar, C.B. Sanjeevi, Copper & biological health, 2008. https://doi.org/10.1080/10937400600755911.

[14] S. Kim, J.E. Choi, J. Choi, K.H. Chung, K. Park, J. Yi, D.Y. Ryu, Oxidative stress-dependent toxicity of silver nanoparticles in human hepatoma cells, Toxicology in Vitro 23 (2009) 1076–1084. https://doi.org/10.1016/j.tiv.2009.06.001.

[15] M. Hans, S. Mathews, F. Mücklich, M. Solioz, Physicochemical properties of copper important for its antibacterial activity and development of a unified model, Biointerphases 11 (2016) 018902. https://doi.org/10.1116/1.4935853.

[16] M. Solioz, Copper disposition in bacteria, in: Clinical and Translational Perspectives on WILSON DISEASE, 2019: pp. 101–113. https://doi.org/10.1016/B978-0-12-810532-0.00011-2.

[17] S. Mathews, M. Hans, F. Mücklich, M. Solioz, Contact killing of bacteria on copper is suppressed if bacterial-metal contact is prevented and is induced on iron by copper ions, Applied and Environmental Microbiology 79 (2013) 2605–2611. https://doi.org/10.1128/AEM.03608-12.

[18] M. Hans, A. Erbe, S. Mathews, Y. Chen, M. Solioz, F. Mücklich, Role of copper oxides in contact killing of bacteria, Langmuir 29 (2013) 16160–16166. https://doi.org/10.1021/la404091z.

[19] E. Fadeeva, V.K. Truong, M. Stiesch, B.N. Chichkov, R.J. Crawford, J. Wang, E.P. Ivanova, Bacterial retention on superhydrophobic titanium surfaces fabricated by femtosecond laser ablation, Langmuir 27 (2011) 3012–3019. https://doi.org/10.1021/la104607g.

[20] A. Elbourne, R.J. Crawford, E.P. Ivanova, Nano-structured antimicrobial surfaces: From nature to synthetic analogues, Journal of Colloid and Interface Science 508 (2017) 603–616. https://doi.org/10.1016/j.jcis.2017.07.021.

[21] N. Epperlein, F. Menzel, K. Schwibbert, R. Koter, J. Bonse, J. Sameith, J. Krüger, J. Toepel, Influence of femtosecond laser produced nanostructures on biofilm growth on steel, Applied Surface Science 418 (2017) 420–424. https://doi.org/10.1016/j.apsusc.2017.02.174.

[22] D. Guenther, J. Valle, S. Burgui, C. Gil, C. Solano, D. Guenther, J. Valle, S. Burgui, C. Gil, C. Solano, A. Toledo-arana, R. Helbig, C. Werner, I. Lasa, F. Andrés, Direct laser interference patterning for decreased bacterial attachment, in: SPIE 9736, Laser-Based Micro- and Nanoprocessing X, 2016. https://doi.org/10.1117/12.2216065.

[23] R. Helbig, D. Günther, J. Friedrichs, F. Rößler, A. Lasagni, C. Werner, The impact of structure dimensions on initial bacterial adhesion, Biomater. Sci. 4 (2016) 1074–1078. https://doi.org/10.1039/C6BM00078A.

[24] J. Valle, S. Burgui, D. Langheinrich, C. Gil, C. Solano, A. Toledo-Arana, R. Helbig, A. Lasagni, I. Lasa, Evaluation of Surface Microtopography Engineered by Direct Laser Interference for Bacterial Anti-Biofouling, Macromol Biosci 15 (2015) 1060–1069. https://doi.org/10.1002/mabi.201500107.

[25] L.C. Hsu, J. Fang, D.A. Borca-Tasciuc, R.W. Worobo, C.I. Moraru, Effect of micro- and nanoscale topography on the adhesion of bacterial cells to solid surfaces, Applied and Environmental Microbiology 79 (2013) 2703–2712. https://doi.org/10.1128/AEM.03436-12.

[26] A.H.A. Lutey, L. Gemini, L. Romoli, G. Lazzini, F. Fuso, M. Faucon, R. Kling, Towards laser-textured antibacterial surfaces, Scientific Reports 8 (2018) 1–10. https://doi.org/10.1038/s41598-018-28454-2.

[27] C. Berne, C.K. Ellison, A. Ducret, Y. V. Brun, Bacterial adhesion at the single-cell level, Nature Reviews Microbiology 16 (2018) 616–627. https://doi.org/10.1038/s41579-018-0057-5.

[28] T. Kimkes, M. Heinemann, How Bacteria Recognise and Respond to Surface Contact, FEMS Microbiology Reviews 44 (2020) 106–122.

[29] E. Maikranz, C. Spengler, N. Thewes, A. Thewes, F. Nolle, P. Jung, M. Bischoff, L. Santen, K. Jacobs, Different binding mechanisms of Staphylococcus aureus to hydrophobic and hydrophilic surfaces, Nanoscale 12 (2020) 19267–19275. https://doi.org/10.1039/d0nr03134h.

[30] L.B. Boinovich, E.B. Modin, A. V. Aleshkin, K.A. Emelyanenko, E.R. Zulkarneev, I.A. Kiseleva, A.L. Vasiliev, A.M. Emelyanenko, Effective Antibacterial Nanotextured Surfaces Based on Extreme Wettability and Bacteriophage Seeding, ACS Applied Nano Materials 1 (2018) 1348–1359. https://doi.org/10.1021/acsanm.8b00090.

[31] K. Siems, D.W. Müller, L. Maertens, A. Ahmed, R. Van Houdt, R.L. Mancinelli, S. Baur, K. Brix, R. Kautenburger, N. Caplin, J. Krause, R. Demets, M. Vukich, A. Tortora, C. Roesch, G. Holland, M. Laue, F. Mücklich, R. Moeller, Testing Laser-Structured Antimicrobial Surfaces Under Space Conditions: The Design of the ISS Experiment BIOFILMS, Frontiers in Space Technologies 2 (2022) 1–18. https://doi.org/10.3389/frspt.2021.773244.

[32] P. Flores, R. Schauer, S.A. McBride, J. Luo, M. Cortesão, C. Hoehn, S. Doraisingam, D. Widhalm, J. Chadha, H. Meyerson, E. Mitzak, V. Hurd, L. Selman, M. Vellone, S. Floyd, S. Tozer, M. Rupert, S. Gorti, S. Reagan, K.K. Varanasi, F. Muecklich, R. Moeller, L. Stodieck, S. Countryman, L. Zea, Preparation for and Performance of a Pseudomonas aeruginosa Biofilm Experiment On Board the International Space Station, Acta Astronautica (2021). https://doi.org/10.1016/j.actaastro.2022.07.015.

[33] C. Chen, A. Enrico, T. Pettersson, M. Ek, A. Herland, F. Niklaus, G. Stemme, L. Wågberg, Bactericidal surfaces prepared by femtosecond laser patterning and layer-by-layer polyelectrolyte coating, Journal of Colloid and Interface Science 575 (2020) 286–297. https://doi.org/10.1016/j.jcis.2020.04.107.

[34] A. Tripathy, S. Sreedharan, C. Bhaskarla, S. Majumdar, S.K. Peneti, D. Nandi, P. Sen, Enhancing the Bactericidal Efficacy of Nanostructured Multifunctional Surface Using an Ultrathin Metal Coating, Langmuir 33 (2017) 12569–12579. https://doi.org/10.1021/acs.langmuir.7b02291.

[35] V. Gopinath, S. Priyadarshini, A.R. Al-Maleki, M. Alagiri, R. Yahya, S. Saravanan, J. Vadivelu, In vitro toxicity, apoptosis and antimicrobial effects of phyto-mediated copper oxide nanoparticles, RSC Advances 6 (2016) 110986–110995. https://doi.org/10.1039/c6ra13871c.

[36] A.L. Ulloa-Ogaz, H.A. Piñón-Castillo, L.N. Muñoz-Castellanos, M.S. Athie-García, M.D.L. Ballinas-Casarrubias, J.G. Murillo-Ramirez, L.Á. Flores-Ongay, R. Duran, E. Orrantia-Borunda, Oxidative damage to Pseudomonas aeruginosa ATCC 27833 and Staphylococcus aureus ATCC 24213 induced by CuO-NPs, Environmental Science and Pollution Research 24 (2017) 22048–22060. https://doi.org/10.1007/s11356-017-9718-6.

[37] C.A.P. Bastos, N. Faria, J. Wills, P. Malmberg, N. Scheers, P. Rees, J.J. Powell, Copper nanoparticles have negligible direct antibacterial impact, NanoImpact 17 (2020) 100192. https://doi.org/10.1016/j.impact.2019.100192.

[38] A.M. Emelyanenko, V. V. Kaminskii, I.S. Pytskii, A.G. Domantovsky, K.A. Emelyanenko, A. V. Aleshkin, L.B. Boinovich, Antibacterial Properties of Superhydrophilic Textured Copper in Contact with Bacterial Suspensions, Bulletin of Experimental Biology and Medicine 168 (2020) 488–491. https://doi.org/10.1007/s10517-020-04737-5.

[39] G. Yi, S.N. Riduan, A. Armugam, J.T. Ong, P.Y. Hon, M.Y. Abdad, S. Vasoo, B.S.P. Ang, Y. Zhang, Nanostructured Copper Surface Kills ESKAPE Pathogens and Viruses in Minutes, ChemMedChem 16 (2021) 3553–3558. https://doi.org/10.1002/cmdc.202100504.

[40] A.M. Emelyanenko, I.S. Pytskii, V. V. Kaminsky, E. V. Chulkova, A.G. Domantovsky, K.A. Emelyanenko, V.D. Sobolev, A. V. Aleshkin, L.B. Boinovich, Superhydrophobic copper in biological liquids: Antibacterial activity and microbiologically induced or inhibited corrosion, Colloids Surf B Biointerfaces 185 (2020) 110622. https://doi.org/10.1016/j.colsurfb.2019.110622.

[41] L.B. Boinovich, K.A. Emelyanenko, A.G. Domantovsky, E. V. Chulkova, A.A. Shiryaev, A.M. Emelyanenko, Pulsed Laser Induced Triple Layer Copper Oxide Structure for Durable Polyfunctionality of Superhydrophobic Coatings, Adv Mater Interfaces 5 (2018) 1–10. https://doi.org/10.1002/admi.201801099.

[42] J.L. Smith, N. Tran, T. Song, D. Liang, M. Qian, Robust bulk micro-nano hierarchical copper structures possessing exceptional bactericidal efficacy, Biomaterials 280 (2022) 121271. https://doi.org/10.1016/j.biomaterials.2021.121271.

[43] D.W. Müller, S. Lößlein, E. Terriac, K. Brix, R. Kautenburger, K. Siems, R. Möller, F. Mücklich, Increasing Antibacterial Efficiency of Cu Surfaces by targeted Surface Functionalization via Ultrashort Pulsed Direct Laser Interference Patterning (USP- DLIP), Advanced Materials Interfaces 8 (2021) 2001656. https://doi.org/10.1002/admi.202001656.

[44] D.W. Müller, S. Lößlein, C. Pauly, M. Briesenick, G. Kickelbick, F. Mücklich, Multi-pulse agglomeration effects on ultrashort pulsed direct laser interference patterning of Cu, Applied Surface Science 611 (2023) 155538. https://doi.org/10.1016/j.apsusc.2022.155538.

[45] D.W. Müller, A. Holtsch, S. Lößlein, C. Pauly, C. Spengler, S. Grandthyll, K. Jacobs, F. Mücklich, F. Müller, In-Depth Investigation of Copper Surface Chemistry Modification by Ultrashort Pulsed Direct Laser Interference Patterning, Langmuir 36 (2020) 13415–13425. https://doi.org/https://doi.org/10.1021/acs.langmuir.0c01625.

[46] L.B. Boinovich, V. V. Kaminsky, A.G. Domantovsky, K.A. Emelyanenko, A. V. Aleshkin, E.R. Zulkarneev, I.A. Kiseleva, A.M. Emelyanenko, Bactericidal Activity of Superhydrophobic and Superhydrophilic Copper in Bacterial Dispersions, Langmuir 35 (2019) 2832–2841. https://doi.org/10.1021/acs.langmuir.8b03817.

[47] Y. Cheng, G. Feng, C.I. Moraru, Micro-and nanotopography sensitive bacterial attachment mechanisms: A review, Frontiers in Microbiology 10 (2019) 1–17. https://doi.org/10.3389/fmicb.2019.00191.

[48] S. Marie Lößlein, R. Merz, Y. Rodríguez-Martínez, F. Schäfer, P.G. Grützmacher, D. Horwat, M. Kopnarski, F. Mücklich, Influence of chemistry and topography on the wettability of copper, Journal of Colloid and Interface Science 670 (2024) 658–675. https://doi.org/10.1016/j.jcis.2024.04.212.

[49] D.W. Müller, B. Josten, S. Wältermann, C. Pauly, S. Slawik, K. Brix, R. Kautenburger, F. Mücklich, Microstructure versus topography : the impact of crystallographic substrate modification during ultrashort pulsed direct laser interference patterning on the antibacterial properties of Cu, Frontiers in Materials 11 (2024) 1397937. https://doi.org/10.3389/fmats.2024.1397937.

[50] C. Formosa-Dague, C. Feuillie, A. Beaussart, S. Derclaye, S. Kucharíková, I. Lasa, P. Van Dijck, Y.F. Dufreîne, Sticky Matrix: Adhesion Mechanism of the Staphylococcal Polysaccharide Intercellular Adhesin, ACS Nano 10 (2016) 3443–3452. https://doi.org/10.1021/acsnano.5b07515.

[51] Y.F. Dufrêne, A. Persat, Mechanomicrobiology: how bacteria sense and respond to forces, Nature Reviews Microbiology 18 (2020) 227–240. https://doi.org/10.1038/s41579-019-0314-2.

[52] C. Spengler, E. Maikranz, B. Glatz, M.A. Klatt, H. Heintz, M. Bischoff, L. Santen, A. Fery, K. Jacobs, The adhesion capability of Staphylococcus aureus cells is heterogeneously distributed over the cell envelope, Soft Matter 20 (2024). https://doi.org/https://doi.org/10.1039/D3SM01045G.

[53] J. Luo, C. Hein, J. Ghanbaja, J. Pierson, F. Mücklich, Bacteria accumulate copper ions and inhibit oxide formation on copper surface during antibacterial efficiency test, Micron 127 (2019) 102759.

[54] K. Alasvand Zarasvand, V.R. Rai, Microorganisms: Induction and inhibition of corrosion in metals, International Biodeterioration and Biodegradation 87 (2014) 66–74. https://doi.org/10.1016/j.ibiod.2013.10.023.

[55] G. He, W. Hu, C.M. Li, Spontaneous interfacial reaction between metallic copper and PBS to form cupric phosphate nanoflower and its enzyme hybrid with enhanced activity, Colloids and Surfaces B: Biointerfaces 135 (2015) 613–618. https://doi.org/10.1016/j.colsurfb.2015.08.030.

[56] M.T. González-Muñoz, C. Rodriguez-Navarro, F. Martínez-Ruiz, J.M. Arias, M.L. Merroun, M. Rodriguez-Gallego, Bacterial biomineralization: New insights from Myxococcus-induced mineral precipitation, Geological Society, London, Special Publication 336 (2010) 31–50. https://doi.org/10.1144/SP336.3.

[57] N. Ben Omar, M.M. Nez-canamero, J.M. Arias, F. Huertas, Myxococcus xanthus' killed cells as inducers of struvite crystallization, Its possible role in the biomineralization processes., Chemosphere 30 (1995) 2387–2396.

[58] P. Wang, T.B. Kinraide, E. Smolders, D.M. Zhou, N.W. Menzies, S. Thakali, W.W. Xia, X.Z. Hao, W.J.G.M. Peijnenburg, P.M. Kopittke, An electrostatic model predicting Cu and Ni toxicity to microbial processes in soils, Soil Biology and Biochemistry 57 (2013) 720–730. https://doi.org/10.1016/j.soilbio.2012.09.002.

[59] S.M. Lößlein, M. Kasper, R. Merz, C. Pauly, D.W. Müller, M. Kopnarski, F. Mücklich, Patience Alone is not Enough - A Guide for the Preparation of Low-Defect Sections from Pure Copper Geduld allein reicht nicht! - Ein Leitfaden zur Herstellung defektarmer Schliffe von Reinkupfer, Praktische Metallographie/Practical Metallography 58 (2021) 388–407. https://doi.org/10.1515/pm-2021-0031.

[60] D.W. Müller, T. Fox, P.G. Grützmacher, S. Suarez, F. Mücklich, Applying Ultrashort Pulsed Direct Laser Interference Patterning for Functional Surfaces, Scientific Reports 10 (2020) 3647. https://doi.org/10.1038/s41598-020-60592-4.

[61] B.D. Cullity, S.R. Stock, Elements of X-Ray Diffraction, 2001.

[62] C. Molteni, H.K. Abicht, M. Solioz, Killing of Bacteria by Copper Surfaces Involves Dissolved Copper, Applied and Environmental Microbiology 76 (2010) 4099–4101. https://doi.org/10.1128/AEM.00424-10.

Supporting Information for

Modifying the Antibacterial Performance of Cu Surfaces by Topographic Patterning in the Micro- and Nanometer Scale

Daniel Wyn Müller[1,2*], Christoph Pauly[1], Kristina Brix[3], Ralf Kautenburger[3], Frank Mücklich[1]

[1]Chair of Functional Materials, Department of Materials Science, Saarland University, 66123 Saarbrücken, Germany.

[2]SurFunction GmbH, 66123 Saarbrücken, Germany.

[3]Department of Inorganic Solid-State Chemistry, Elemental Analysis, Saarland University, 66123 Saarbrücken, Germany.

STEM analysis on particles observed on *S. aureus* cells after Cu exposure

In the manuscript "Modifying the Antibacterial Performance of Cu Surfaces by Topographic Patterning in the Micro- and Nanometer Scale" high resolved SEM investigation of particle agglomerations observed on the cell surface of *S. aureus* bacteria after exposure to Cu in PBS was conducted. Differences in morphology, Z-contrast and stability under electron beam irradiation are observed including FIB-cross sectioning (displayed in Figure 6), while top-down EDS analysis (summarized in Figure 7) reveals differences in element composition between particle groups of different size. Singular particles of increased scale could be linked to enhanced compositions of intracellular Cu concentrations, which indicates a triggering of the agglomeration of environmental Cu by exposed cytoplasm. Further investigation of this phenomenon was conducted by means of scanning transmission electron microscopy (STEM).

Sample preparation

Sample preparation was conducted on a Ga-FIB equipped *Helios Nanolab 600* (*FEI*) workstation that allows for high precision lamella extraction and thinning, while imaging and EDS analysis was executed on a *Helios PFIB G4 CXe* (*Thermo Fisher*) workstation due to better imaging and EDS detector area. STEM EDS was applied in addition to high-resolved STEM imaging to allow further reduction in background signals due to the signal depth. Both imaging and EDS analysis were conducted at an acceleration voltage of 20 kV.

Target preparation was executed on a surface partition of an immersion etched 3 µm USP-DLIP patterned sample that exhibits *S. aureus* at different stages of cell deterioration in three neighboring topographic trenches, as shown in Figure SI1a) and b). Prior to SEM/STEM, the sample was sputter-coated by several nm of $Au_{80}Pd_{20}$ to allow for both high resolved SEM imaging and a clear identification of the sample/Pt-coat interface in cross section view. Three sections were defined for further analysis each representing a specified cross section within the individual trenches that represent different states of bacterial deterioration and membrane particle agglomeration (highlighted in Figure SI1b). The particles investigated by STEM EDS are marked in Figure SI1c)-d), while the corresponding sample partition chosen for lamella extraction is illustrated in Figure SI1a).

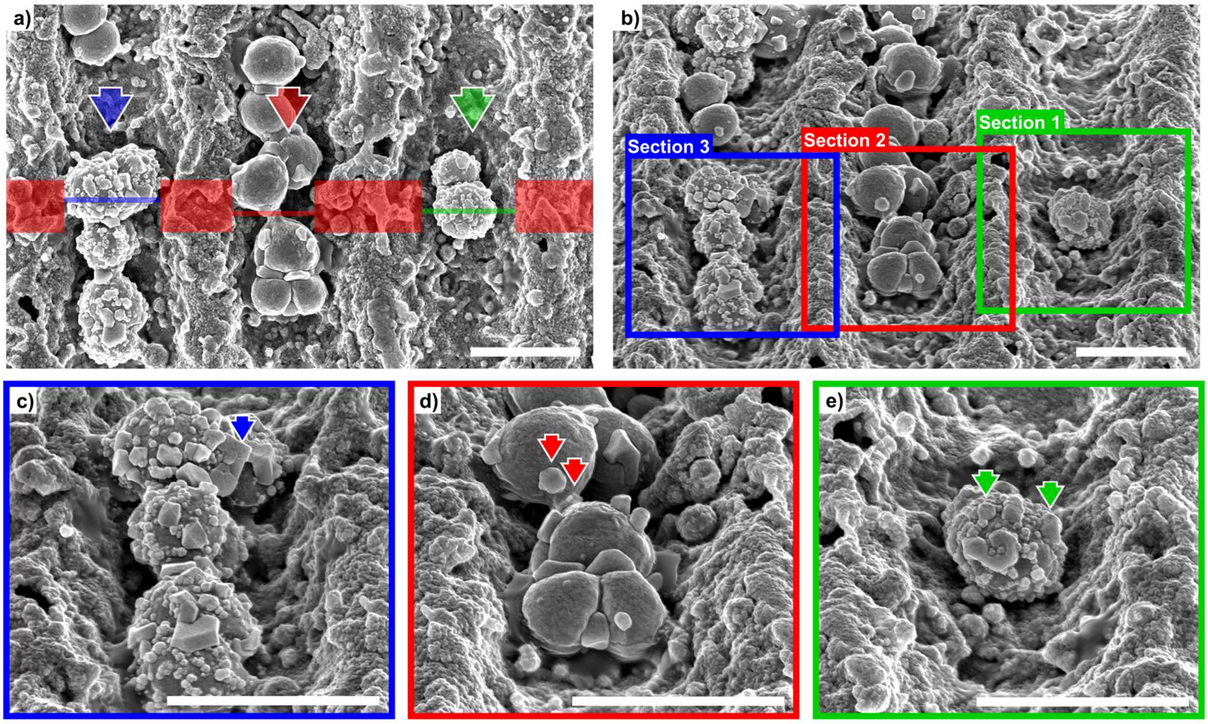

Figure SI1: SEM imaging of the sample partition investigated via STEM. a) top-down image of the three different trenches, where the colored overlay indicates the lamella extracted in a further step as well as the respective location of the thinned sections 1(green), 2 (red) and 3(blue). The three arrows indicate the STEM imaging perspective. b) Section 1-3 in 52° tilted perspective with close-ups in c)-e). The arrows in c), d) and e) highlight the bacterial membrane associated particles analyzed via STEM EDS and indicate the imaging/analysis perspective in STEM. The scale bar corresponds to 2 µm on each image.

Target preparation and lamella extraction involved the application of protective Pt layers (Figure SI2a) followed by the extraction of the targeted sample partition as a several 100 nm thick lamella, which was attached to a grid-holder (Figure SI2b). Further thinning was conducted via ion beam polishing upon electron beam transparency at an acceleration voltage of 30 kV, focusing on the three sections highlighted in Figure SI1a).

Results and discussion

Bright field imaging of the targeted sections and particles marked in Figure SI1c)-e) after thinning is displayed in Figure SI2c)-e). The inverted Z-contrast indicates bacterial cell matrix (mainly composing of the light elements C, N, O and Na) by a bright contrast, while the Cu substrate surface and protective $Au_{80}Pd_{20}$-coating both exhibit a dark imaging contrast. Particles adherent to bacterial cells exhibit a light gray Z-contrast indicating an average Z-value of the overall element composition between the bacterial matrix and Cu/ $Au_{80}Pd_{20}$. At the interface between the bacterial cell and adherent particles, small (Figure SI2c) up to elevated (Figure SI2e) protrusion of bright contrast areas into the particles can be observed, potentially indicating cytoplasm exposure at defects of the bacterial membrane. This is especially pronounced for the bacterial cells in section 3 that exhibit the highest state of cell deterioration, as displayed in Figure SI2e).

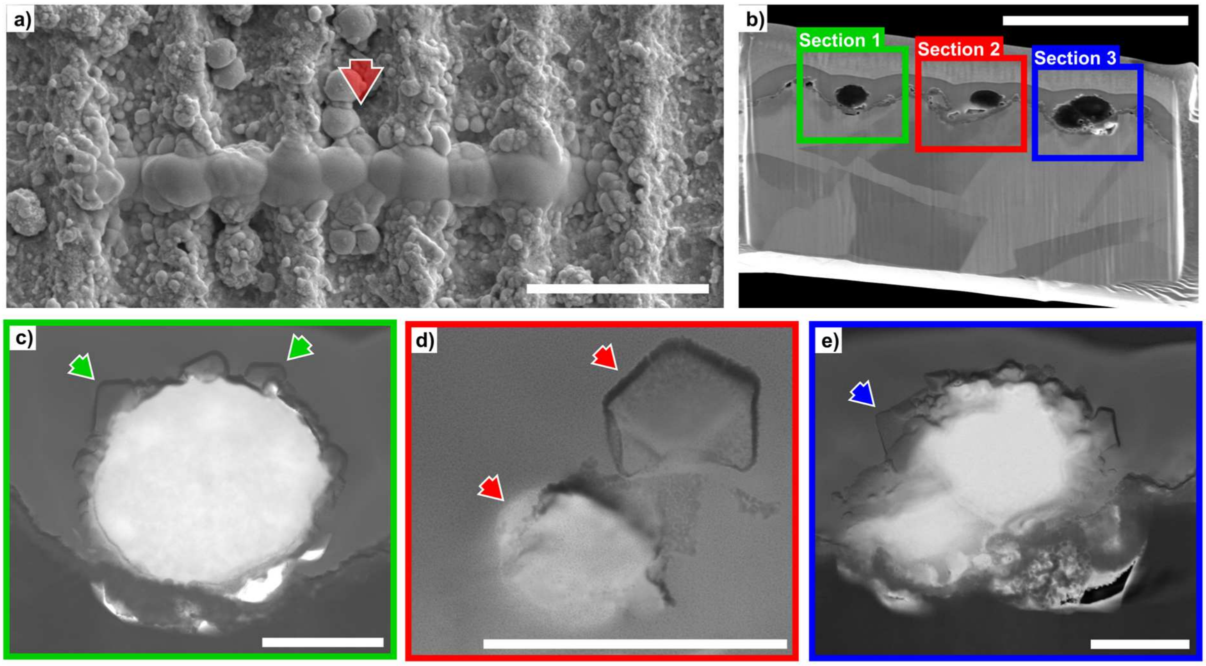

Figure SI2: Lamella preparation of the targeted sample partition. a) top-down image after Pt-coating, where the red arrow indicates the imaging perspective of b)-e). b) the extracted lamella after transfer to the grid before thinning with marking of the three investigated sections. c)-e) bright field imaging of section 1-3 where the particles marked by colored arrows correspond to the markings in Figure SI1c)-d).

The two particles highlighted in section 1 deviate slightly in size and morphology whereas both exhibit contrast broadening at the interface to the bacterial cell. STEM EDS reveals a higher proportion of Cu accompanied by contents of Cl in the case of particle 1 (displayed in Figure SI3), which corresponds to the composition of large particles (LP) determined by top-down EDS in the manuscript (see Figure 7). Particle 2 exhibits slightly lower levels of Cu, O and almost no traces of Cl. However, a clear allocation of particle 2 to the small particle (SP) group is not possible due to the dominant Pt signal in the neighboring spectrum that prevents a clear identification of a phosphorus signal (indicated by the EDS spectrum of the bacterial cell center). Both particles exhibit a similar signal in Au, Pd and Pt contributing to the interfacial composition of the particle surface as well as neighboring or underlying partitions of the Pt-layer. The increased C signal in the Pt coating results from carrier gas remnants that have been implanted in parallel to the Pt coating process. Both particles exhibit similar levels of C, which are however accompanied by increased levels of N and Na that point towards a contribution of bacterial matter to the particle composition.

The spectrum of the Pt layer furthermore displays a Cu signal peak, which results from background signals of the nearby Cu grid holder. The distance to the grid holder is increasing from section 1 to section 3, corresponded by a decreasing Cu/Pt ratio in the Pt spectrum, where the respective Cu signal intensity might be considered as a comparative offset for the interpretation of the other sampling spectra.

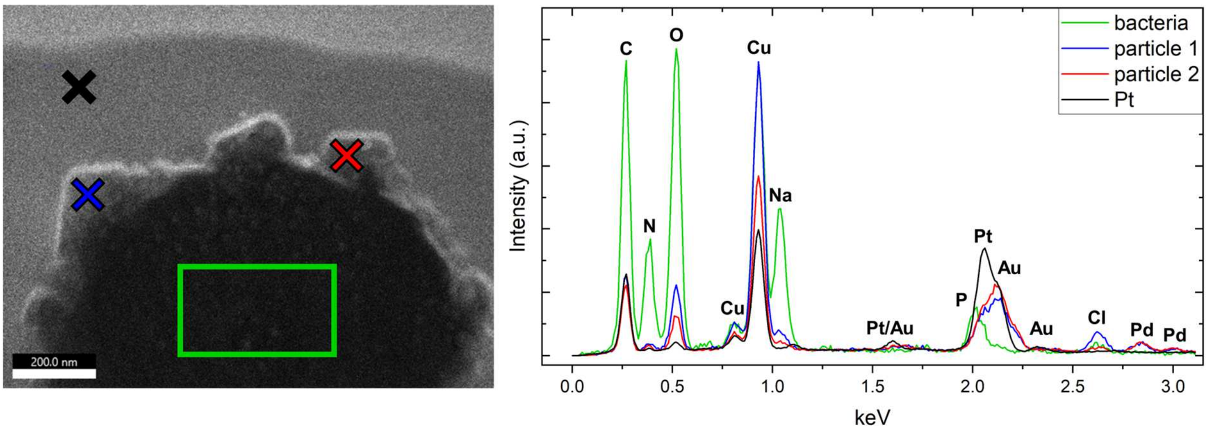

Figure SI3: STEM EDS analysis of the bacterial cell as well as of the marked adherent particles in section 1.

STEM EDS analysis of the dissected particles 1 and 2 in section 2 exhibits a similar composition of C, N, O and Na with a dominant proportion of Cu as well as interface related Au, Pd and Pt in comparison to particle 1 and 2 in section 1 (see Figure SI4). The dominance in C and O as well as the relative signal intensity of N and Na correspond to the bacterial cell spectrum in Figure SI3 in parallel to a similar dark imaging contrast in the case of particle 2. As visible in Figure SI1, particle 2 forms a connection between two individual *S. aureus* cells whereas it might not necessarily represent agglomerated matter but a direct link between the two cells containing bacterial cell matter. This is emphasized by higher C, N, O and Na as well as abundant Au and Pd signals representing a lack of interfacial areas that are well expressed in the spectrum of particle 1, instead.

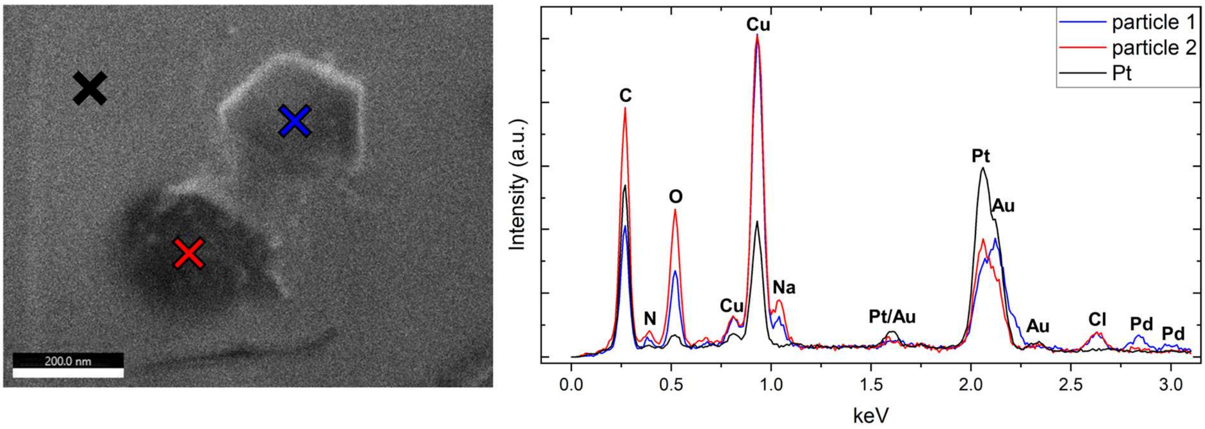

Figure SI4: STEM EDS analysis of the two particles marked in section 2.

Although being completely separated from bacterial cell matter, particle 1 exhibits C, N, O and Na levels that are closely related to particle 2 also exhibiting a similar intensity ratio between the individual signals. It is worth mentioning that the Cu and Cl signal also exhibit a similar intensity ratio between particle 1 and 2, where considerable amounts of Cu are also observed in particle 2 although it potentially represents bacterial matter.

In section 3, analysis via STEM EDS focused on the largest particle adherent to a deteriorated bacterial cell. Similar to the particles monitored in section 1 and 2, a certain level and ratio of C, N, O and Na signal intensity could be identified, however with a limited proportion compared to a predominant Pt signal. This indicates that the analyzed particle was sectioned at the outer volume close to the backward surface including a signal of background Pt in the thinned lamella section. Correspondingly, the Cu signal of particle 1 levels below the intensity observed within the bacterial cell of section 3. The high C to Cu ratio measured in the bacterial cell center points towards a considerable ingress of Cu, whereas the similar C to Cu ratio of particle 1 potentially involves an additional C signal from the Pt coat in the background.

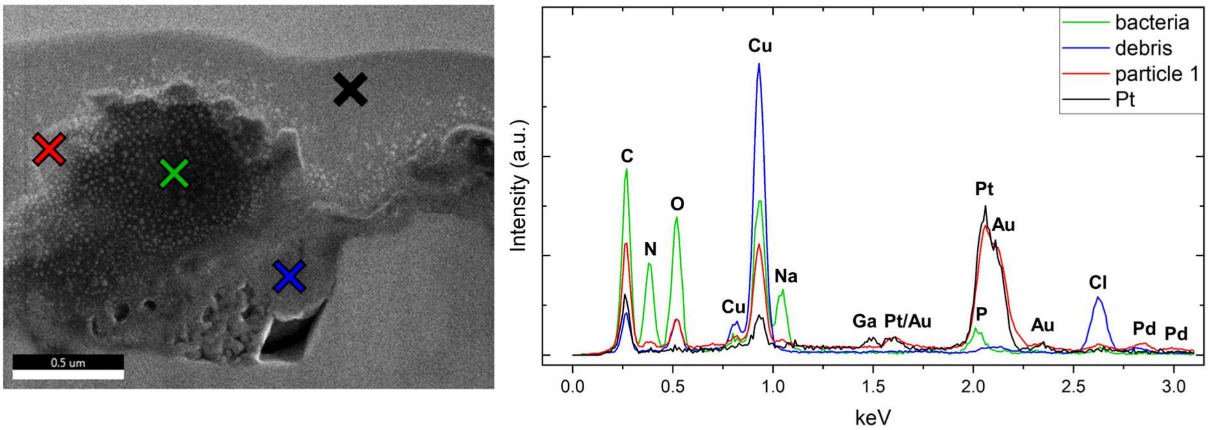

Figure SI5: STEM EDS analysis of the bacterial cell, the marked particle as well as debris at the interface between the bacterial cell and the Cu substrate.

An increased amount of debris was found at the interface between the bacterial cells and the Cu surface and in close vicinity that deviates in morphology and layer thickness to oxidic passivation layers displayed in Figure 6. STEM EDS reveals predominant levels of Cu, aside of C, O and an elevated proportion of Cl. With regard to the low O signal, the debris does not appear to contain significant amounts of Cu oxide that might contribute to surface passivation. Instead, the high levels of Cl point toward an unpassivated pitting corrosion site in correspondence to preliminary findings[1,2]. This is further supported by the Cu surface profile below the bacterial cell that represents the morphology of a grain boundary, where the cavity partly filled with debris might represent a former grain that was dissolved due to anodic interaction[3].

Summarizing the results of STEM investigation in the three different sections, a connection between localized particle agglomeration and potential exposure of bacterial cell matter could be determined. Independent of their size, increased levels of C, N, O and Na are found for each particle where at least the N/Na and in some cases the overall signal intensity ratio corresponds to the element spectrum of the parallelly analyzed bacterial cells. Above a certain scale, Cu particles adherent to bacterial cells contain increased amounts of Cl, which is similarly observed in the debris at potential pitting corrosion sites of the Cu substrate. In parallel, these particles exhibit a crystal morphology of straight edges and corners, which is especially visible by the hexagonal symmetry of particle 1 in section 2.

Based on these findings, the underlying mechanism of Cu particle formation and growth observed on *S. aureus* cells appears to follow a course of localized nucleation on the bacterial membrane and further accumulation of Cu that was dissolved by Cl induced pitting. Both the localized nucleation as well as the growth of Cu particles appear to be catalyzed by exposed bacterial cell matter as indicated by the particle element composition and morphology transformation of bacterial cells. This corresponds to the current state of literature, which ambiguously demonstrate the catalytic impact of bacterial matrix on copper agglomeration [4–9]. An increasing content of Cu and Cl combined with the crystalline morphology of larger scaled particles point towards the formation of preferential Cu agglomeration site within the galvanic microenvironment, that might induce a Cu scavenging impact.

References

[1] Luo J., Hein C., Pierson J., Mücklich F., *Mater. Charact.* **2019**, *158*, 109985.

[2] Luo J., Hein C., Pierson J.F., Mücklich F., *Surfaces and Interfaces* **2020**, *20*, 100630.

[3] Müller D.W., Josten B., Wältermann S., Pauly C., Slawik S., Brix K., Kautenburger R., Mücklich F., *Front. Mater.* **2024**, *11*, 1397937.

[4] Ulloa-Ogaz A.L., Piñón-Castillo H.A., Muñoz-Castellanos L.N., Athie-García M.S., Ballinas-Casarrubias M.D.L., Murillo-Ramirez J.G., Flores-Ongay L.Á., Duran R., Orrantia-Borunda E., *Environ. Sci. Pollut. Res.* **2017**, *24*, 22048.

[5] Emelyanenko A.M., Pytskii I.S., Kaminsky V. V., Chulkova E. V., Domantovsky A.G., Emelyanenko K.A., Sobolev V.D., Aleshkin A. V., Boinovich L.B., *Colloids Surfaces B Biointerfaces* **2020**, *185*, 110622.

[6] Luo J., Hein C., Ghanbaja J., Pierson J., Mücklich F., *Micron* **2019**, *127*, 102759.

[7] González-Muñoz M.T., Rodriguez-Navarro C., Martínez-Ruiz F., Arias J.M., Merroun M.L., Rodriguez-Gallego M., *Geol. Soc. London, Spec. Publ.* **2010**, *336*, 31.

[8] Ben Omar N., Nez-canamero M.M., Arias J.M., Huertas F., *Chemosphere* **1995**, *30*, 2387.

[9] Wang P., Kinraide T.B., Smolders E., Zhou D.M., Menzies N.W., Thakali S., Xia W.W., Hao X.Z., Peijnenburg W.J.G.M., Kopittke P.M., *Soil Biol. Biochem.* **2013**, *57*, 720.

Paper VII:

Testing Laser-Structured Antimicrobial Surfaces Under Space Conditions: The Design of the ISS Experiment BIOFILMS

Katharina Siems[1,*], **Daniel W. Müller[2,*]**, Laurens Maertens[3,4], Aisha Ahmed[2], Rob Van Houdt[3], Rocco L. Mancinelli[5], Sandra Baur[6], Kristina Brix[6], Ralf Kautenburger[6], Nicol Caplin[7], Jutta Krause[7], Rene Demets[7], Marco Vukich[7], Alessandra Tortora[8], Christian Roesch[9], Gudrun Holland[10], Michael Laue[10], Frank Mücklich[2] and Ralf Moeller[1]

[1]Department of Radiation Biology, Institute of Aerospace Medicine, German Aerospace Center (DLR), Cologne, Germany.

[2]Department of Materials Science and Engineering, University of Saarland, Saarbrücken, Germany.

[3]Microbiology Unit, Interdisciplinary Biosciences, Belgian Nuclear Research Centre (SCK CEN), Mol, Belgium. [4]Research Unit in Microorganisms Biology (URBM), Narilis Institute, University of Namur, Namur, Belgium. [5]NASA Ames Research Center/Bay Area Environmental Research Institute, Petaluma, CA, United States.

[6]Department of Inorganic Solid State Chemistry, Elemental Analysis, University of Saarland, Saarbrücken, Germany.

[7]ESA, European Space Research and Technology Centre (ESTEC), Noordwijk, Netherlands.

[8]Kayser Italia Srl, Livorno, Italy.

[9]Biotechnology Space Support Center (BIOTESC), Lucerne University of Applied Sciences and Arts, Lucerne, Switzerland.

[10]Robert-Koch-Institute, Berlin, Germany.

Published in January 2022 in "Frontiers in Space Technologies" and accessible online via:

https://doi.org/10.3389/frspt.2021.773244

Abstract:

Maintaining crew health and safety are essential goals for long-term human missions to space. Attaining these goals requires the development of methods and materials for sustaining the crew's health and safety. Paramount is microbiological monitoring and contamination reduction. Microbial biofilms are of special concern, because they can cause damage to spaceflight equipment and are difficult to eliminate due to their increased resistance to antibiotics and disinfectants. The introduction of antimicrobial surfaces for medical, pharmaceutical and industrial purposes has shown a unique potential for reducing and preventing biofilm formation. This article describes the development process of ESA's BIOFILMS experiment, that will evaluate biofilm formation on various antimicrobial surfaces under spaceflight conditions. These surfaces will be composed of different metals with and without specified surface texture modifications. *Staphylococcus capitis* subsp. *capitis*, *Cupriavidus metallidurans* and *Acinetobacter radioresistens* are biofilm forming organisms that have been chosen as model organisms. The BIOFILMS experiment will study the biofilm formation

potential of these organisms in microgravity on the International Space Station on inert surfaces (stainless steel AISI 304) as well as antimicrobial active copper (Cu) based metals that have undergone specific surface modification by Ultrashort Pulsed Direct Laser Interference Patterning (USP-DLIP). Data collected in 1 x g has shown that these surface modifications enhance the antimicrobial activity of Cu based metals. In the scope of this, the interaction between the surfaces and bacteria, which is highly determined by topography and surface chemistry, will be investigated. The data generated will be indispensable for the future selection of antimicrobial materials in support of human- and robotic-associated activities in space exploration.

Own contributions:

Conduction of the pre-flight experiments. USP-DLIP sample preparation and characterization including SEM of the bacterial strains. Data interpretation, preparation and editing of the manuscript.

frontiers in Space Technologies

ORIGINAL RESEARCH
published: 03 January 2022
doi: 10.3389/frspt.2021.773244

Testing Laser-Structured Antimicrobial Surfaces Under Space Conditions: The Design of the ISS Experiment BIOFILMS

Katharina Siems[1†], Daniel W. Müller[2†], Laurens Maertens[3,4], Aisha Ahmed[2], Rob Van Houdt[3], Rocco L. Mancinelli[5], Sandra Baur[6], Kristina Brix[6], Ralf Kautenburger[6], Nicol Caplin[7], Jutta Krause[7], Rene Demets[7], Marco Vukich[7], Alessandra Tortora[8], Christian Roesch[9], Gudrun Holland[10], Michael Laue[10], Frank Mücklich[2] and Ralf Moeller[1]*

[1]Department of Radiation Biology, Institute of Aerospace Medicine, German Aerospace Center (DLR), Cologne, Germany, [2]Department of Materials Science and Engineering, University of Saarland, Saarbrücken, Germany, [3]Microbiology Unit, Interdisciplinary Biosciences, Belgian Nuclear Research Centre (SCK CEN), Mol, Belgium, [4]Research Unit in Microorganisms Biology (URBM), Narilis Institute, University of Namur, Namur, Belgium, [5]NASA Ames Research Center/Bay Area Environmental Research Institute, Petaluma, CA, United States, [6]Department of Inorganic Solid State Chemistry, Elemental Analysis, University of Saarland, Saarbrücken, Germany, [7]ESA, European Space Research and Technology Centre (ESTEC), Noordwijk, Netherlands, [8]Kayser Italia Srl, Livorno, Italy, [9]Biotechnology Space Support Center (BIOTESC), Lucerne University of Applied Sciences and Arts, Lucerne, Switzerland, [10]Robert-Koch-Institute, Berlin, Germany

OPEN ACCESS

Edited by:
Cosimo Buffone,
Tianjin University of Commerce, China

Reviewed by:
Po Bian,
Hefei Institutes of Physical Science (CAS), China
Sheila Nielsen,
Montana State University, United States

***Correspondence:**
Ralf Moeller
ralf.moeller@dlr.de

†These authors have contributed equally to this work

Specialty section:
This article was submitted to Microgravity, a section of the journal Frontiers in Space Technologies

Received: *09 September 2021*
Accepted: *29 November 2021*
Published: *03 January 2022*

Citation:
Siems K, Müller DW, Maertens L, Ahmed A, Van Houdt R, Mancinelli RL, Baur S, Brix K, Kautenburger R, Caplin N, Krause J, Demets R, Vukich M, Tortora A, Roesch C, Holland G, Laue M, Mücklich F and Moeller R (2022) Testing Laser-Structured Antimicrobial Surfaces Under Space Conditions: The Design of the ISS Experiment BIOFILMS. Front. Space Technol. 2:773244. doi: 10.3389/frspt.2021.773244

Maintaining crew health and safety are essential goals for long-term human missions to space. Attaining these goals requires the development of methods and materials for sustaining the crew's health and safety. Paramount is microbiological monitoring and contamination reduction. Microbial biofilms are of special concern, because they can cause damage to spaceflight equipment and are difficult to eliminate due to their increased resistance to antibiotics and disinfectants. The introduction of antimicrobial surfaces for medical, pharmaceutical and industrial purposes has shown a unique potential for reducing and preventing biofilm formation. This article describes the development process of ESA's BIOFILMS experiment, that will evaluate biofilm formation on various antimicrobial surfaces under spaceflight conditions. These surfaces will be composed of different metals with and without specified surface texture modifications. *Staphylococcus capitis* subsp. *capitis, Cupriavidus metallidurans* and *Acinetobacter radioresistens* are biofilm forming organisms that have been chosen as model organisms. The BIOFILMS experiment will study the biofilm formation potential of these organisms in microgravity on the International Space Station on inert surfaces (stainless steel AISI 304) as well as antimicrobial active copper (Cu) based metals that have undergone specific surface modification by Ultrashort Pulsed Direct Laser Interference Patterning (USP-DLIP). Data collected in 1 x g has shown that these surface modifications enhance the antimicrobial activity of Cu based metals. In the scope of this, the interaction between the surfaces and bacteria, which is highly determined by topography and surface chemistry, will be investigated. The data generated will be indispensable for the future selection of antimicrobial materials in support of human- and robotic-associated activities in space exploration.

Keywords: biofilms, direct laser interference patterning technique (DLIP), contamination (equipment), antimicobial, surfaces

INTRODUCTION

An enduring human presence in space is required to achieve the primary goals of space programs worldwide. As longer human missions, (e.g., to Moon and Mars) are being planned for the foreseeable future, the optimization of isolated self-sustaining habitats is of prime importance. One key aspect in this regard is extensive microbial control. The ubiquity of microorganisms in crewed spacecrafts such as the International Space Station (ISS) poses several critical risks to astronauts as well as to structural spacecraft materials. Decreasing unwanted microbial growth and biofilm formation within a space craft will also aid in inhibiting forward and backward contamination of extraterrestrial systems as for improved adherence to planetary protection protocols. Nevertheless, microorganisms have shown unparalleled potential for regenerative life support systems, such as MELiSSA, which has been designed to enable long-term manned missions in space (Lasseur et al., 2010).

Microbiological studies have shown the pervasive presence of microorganisms aboard the ISS associated with dust particles (Checinska et al., 2015; Mora et al., 2016), filter debris (Venkateswaran et al., 2014; Be et al., 2017), air vents (Lang et al., 2017), walls and panels (Singh and Wade, 2014), as well as touch surfaces such as laptop keyboards and handrails (Lang et al., 2017). The microbial population described in these studies is mostly composed of human-associated strains, but environmental organisms are also present. Several bacterial and fungal strains have been characterized in detail, often with specific attention towards antimicrobial resistance (AMR) and stress responses (Mijnendonckx et al., 2013; Romsdahl et al., 2018; Seuylemezian et al., 2018). The prevalence of AMR genes in the ISS microbiome was examined in a longitudinal study, indicating multiple multidrug-resistant organisms (Urbaniak et al., 2018). A similar study showed the persistence of several opportunistic pathogens, including *Klebsiella pneumoniae* and *Staphylococcus aureus* (Singh et al., 2018) that showed an increase in AMR genes and virulence observed over the duration of the study. These results are worrying in light of a decreased immune function of astronauts during spaceflight (Sonnenfeld and Shearer, 2002; Sonnenfeld et al., 2003; Aponte et al., 2006). In contrast, it has been proposed that these health concerns are unjustified, and that the risks accompanying unchecked microbial contamination are associated with degradation of equipment integrity rather than human health-related (Mora et al., 2019). This hypothesis is validated by the low number of observed health issues and infections of crew members (Crucian et al., 2016).

Monitoring and controlling microbial contamination on the ISS has been reviewed by Van Houdt and Leys (2020). While air and surface contamination levels were generally within acceptable levels, onboard potable water sources were found to be unsuited for human consumption in 60% of cases (Bruce et al., 2005), leading to increased costs and loss of crew time. Despite repeated decontamination attempts, (e.g., with silver), microbial counts rapidly increased above acceptable levels. These results could be caused by the possible prevalence of silver resistance mechanisms in contaminating cells (Mijnendonckx et al., 2013), as well as adaptation to the oligotrophic environment by entering a viable but non-culturable (VBNC) state (Davey, 2011; Schottroff et al., 2018) that could be more resistant to extant biocides. Lastly, the formation of biofilms on equipment surfaces could impair the functioning of biocidal applications.

Biofilms have been defined as aggregated cell communities enveloped in self-produced extracellular polymeric substances (EPS) often associated with surfaces (Flemming et al., 2016). Microorganisms in biofilms are often more resistant to antimicrobial agents because of a decreased permeation of these agents into the biofilm (Koo et al., 2017), and a high cellular heterogeneity including dormant cells with increased stress resistance (Singh et al., 2017). Biofilm formation on spacecraft materials has been observed in the ISS (Novikova et al., 2006; Perrin et al., 2018), as well as in the Mir space station (Klintworth et al., 1999; Ilyin, 2005). The presence of biofilms is known to cause damage to structural equipment via polymer deterioration, metal corrosion and biofouling. Microbial cells in space, in the planktonic phase as well as in biofilms, are not subjected to the same net gravitational field as on Earth due to a lack of convection, decreasing mixing in the system. Consequently, mass transfer between the cell and its immediate environment is limited to diffusion (Horneck et al., 2010). This leads to depletion of nutrients and accumulation of metabolites in the immediate extracellular environment that elicits a biological response in the cell. To study the effects of spaceflight on biofilm formation several experiments have been conducted (reviewed by Zea et al. (2018). For example, *Pseudomonas aeruginosa* is able to form biofilms in microgravity (McLean et al., 2001) and shows an increased propensity for biofilm formation dependent on nutrient availability and flagella-driven cell motility (Kim et al., 2013). This effect of motility on mixing rates in the fluid surrounding the cell has been hypothesized to partially negate the effects of microgravity and decreased convective phenomena (Horneck et al., 2010). In microgravity, *Escherichia coli* clustered together in liquid medium rather than being homogeneously distributed in the medium, indicating enhanced biofilm formation in space (Zea et al., 2017). Lastly, it must be noted that the function of quorum sensing mechanisms that depend on small signaling molecules can be impacted in microgravity. Cell-cell communication via quorum sensing plays a key role in biofilm formation and adaptation to a changing environment, but also bacterial virulence (Li and Tian, 2012). An increased concentration of N-acyl-homoserine lactones, that function as signaling compounds, was shown in *Rhodospirillum rubrum* in simulated microgravity while cell density was unaltered (Mastroleo et al., 2013).

The prevalence of multispecies biofilms and their possible effects on human health and equipment integrity, in combination with the frequent problems with bacterial contamination of drinking water, illustrates the need for advanced, integrated decontamination systems (Van Houdt et al., 2012). One promising alternative for existing antimicrobial strategies is the use of copper (Cu) surfaces. Metallic Cu is extremely efficient in killing microorganisms in atmospherically dry conditions, with near-complete inactivation in minutes to hours (Vincent et al., 2018). Among the modes of action of copper toxicity direct cell-to-metal contact is important in the inactivation kinetics and has led to the term "contact killing" (Mathews et al., 2013). Additional killing modes or parameters include ambient temperature and Cu concentration in any alloys used (Wilks et al., 2005; Noyce et al., 2006). Interestingly, in wet applications the antimicrobial effects of Cu surfaces are diminished, having inactivation times of several hours (Dwidjosiswojo et al., 2011; Maertens et al., 2020). The antimicrobial potential of Cu surfaces is currently being studied in drinking water production, air conditioning and in hospital settings (Vincent et al., 2016).

Copper, while an indispensable micronutrient, rapidly induces toxic effects in bacteria upon exposure to excess concentrations. A key aspect of Cu toxicity is the catalysis of intracellular reactive oxygen species (ROS) production via a Fenton-like reaction (Lemire et al., 2013). In addition, membrane and DNA damage, as well as inactivation of Fe-S clusters have been reported (Vincent et al., 2018). Amino acid and lipid metabolism in space-grown bacteria are often pre-adapted to increased oxidative stress, that has been linked to an elevated dose of ionizing radiation in space (Crabbe et al., 2011; Li J. et al., 2014). Interestingly, copper toxicity has been shown to induce the VBNC state in bacterial cells suspended in oligotrophic media, which is sometimes associated with subsequent recovery and virulence (Dwidjosiswojo et al., 2011; Li L. et al., 2014; Dopp et al., 2017; Maertens et al., 2021). In addition, bacteria have evolved a multitude of mechanisms to maintain Cu homeostasis. While import mechanisms have been relatively rarely studied (Lutkenhaus, 1977; Balasubramanian et al., 2011; Ekici et al., 2012), many Cu export systems are known (Arguello et al., 2013). These exporters are supplemented by cytoplasmic and periplasmic Cu chelators and chaperones, and the integration of such systems into complex regulatory networks can lead to high levels of Cu resistance (Monsieurs et al., 2011; Monsieurs et al., 2015).

The antibacterial efficiency of Cu surfaces has been proven to be directly linked to the quantitative release of Cu ions, independent of the composition of the surface (purely metallic or embedded in matrix material) or Cu particle size in the case of nanoparticles (Hans et al., 2013; Hans et al., 2014; Sun et al., 2018; Bastos et al., 2020). This mechanism is also responsible for the decreasing antibacterial properties with depleting Cu content, and is why additional surface functionalization focusing on increased antibacterial efficiency is key to further improvement of Cu-based antimicrobial surfaces. Surface functionalization involving surface chemistry (Tripathy et al., 2018; Maikranz et al., 2020) and topography (Helbig et al., 2016) can alter bacterial adhesion by repelling or additional killing mechanisms, similar to the mechanical destruction of the cell wall on *Cicada Wings* (Tripathy et al., 2017). However, inherent antimicrobial capacities might as well be decreased alongside surface functionalization due to degraded Cu ion release (Boinovich et al., 2019) emphasizing the need for a considered approach to surface modification. Ion release itself was shown to be mainly driven by corrosive interaction with the contacting medium, where Cu scavenging of bacteria alongside nutrient ingestion additionally increases ion release rates by preventing the formation of a passivating Cu-oxide layer (Luo et al., 2019). In this context, bacterial mortality on Cu surfaces has recently been shown to be at least as dependent on metabolic activity as on sufficiently high Cu ion release rates. Here, topographical and chemical surface functionalization by Ultrashort Pulsed Direct Laser Interference Patterning (USP-DLIP) at the scale of single bacterial cells (Pattern periodicity P = Bac) targeting increased bacterial adhesion induced an amplification of Cu sensitivity of *E. coli* (Müller et al., 2021).

Copper containing antimicrobial surfaces have been successfully applied before in clinical environments. The replacement of frequent-touch items from standard materials to copper alloys reduced the overall microbial burden significantly. It also led to a decline in contamination with antibiotic resistant microorganisms such as vancomycin resistant enterococci and methicillin resistant *S. aureus* (Karpanen et al., 2012). Regarding the astronauts' health and the integrity of the spacecraft, the application of copper containing antimicrobial surfaces and coatings can be beneficial also for spaceflight purposes (Hahn et al., 2017; Zea et al., 2020). However, antimicrobial copper surfaces especially those with surface functionalization have not been tested for their potential against biofilm formation under spaceflight conditions yet and it is not known to what extent the antimicrobial activity might change in microgravity.

Scientific Aims and Approach

The BIOFILMS (Biofilm Inhibition on Flight equipment and on board the ISS using microbiologically Lethal Metal Surfaces) experiment proposal was submitted and accepted by ESA within an open call for experiments in 2014 (ILSRA-2014-054). The goal of the experiment is to compare how biofilms are formed in microgravity in a liquid environment on inhibiting and non-inhibiting metal surfaces to investigate the antibacterial efficacy of several copper-based antimicrobial surface pattern designs under different space-relevant gravity conditions. Within a single experiment different microbial species will be tested and the different metal surfaces will be cross-compared from different gravity regimes. To accomplish this, three specifically selected bacterial species will be exposed to topographically functionalized metallic surfaces with and without inherent antimicrobial material properties under microgravity (µg) (ISS and space travel conditions), 0.4 x g (approximated gravity level on Mars) and 1 x g (terrestrial gravity control). Post-flight, the metal surfaces alongside the adhering biofilms will be subjected to in-depth microbiological and molecular biological analyses as well as high-resolution spectroscopic and metallographic characterization of the metal surfaces to determine altered surface properties.

The BIOFILMS project will evaluate the applicability of topographically functionalized antimicrobial contact surfaces for contamination control in extra-terrestrial environments, including a focussed investigation on the role of the actual bacteria/substrate contact. A recent study following a similar approach of functionalized Cu contact surfaces has shown enhanced antibacterial efficiency in close relation to altered bacteria/surface interaction on Earth in 1 x g (Müller et al., 2021). Expectedly, the data generated will be indispensable for the future selection of antimicrobial materials in support of astronaut-/robotic-associated activities in space exploration. An overview of the whole timeline of the BIOFILMS experiment can be found in the **Supplementary Material** (**Supplementary Figure S1**).

MATERIALS AND METHODS

Selection Criteria for Buffer, Growth Medium and Fixative

The bacterial cells of the three species included in BIOFILMS need to be stored in the flight hardware as pre-test inoculation cultures until the experiment is activated aboard the ISS. For this, we considered liquid buffers that fulfilled specific requirements. Namely, the storage buffer needs to limit bacterial activity during the storage phase, but keep the cells in an intact and viable condition allowing growth when the experiment is activated. Furthermore, in the selection process for the liquid growth medium that will be present during the incubation and biofilm formation phase of the experiment various factors were considered. Since different bacterial species need different amounts of nutrient for growth and biofilm formation, the growth medium will need to support growth and biofilm formation of all three selected strains. Furthermore, a growth medium that only includes low concentrations of available nutrients was sought to more closely resemble realistic environmental conditions. Another important point in the selection process was the comparability to other spaceflight experiments, that can be limited in case different types of growth media are used. After the cultivation phase the experiment will be fixed to prevent further bacterial activity during onboard storage, download from the station and transport and storage post flight. The selection criteria for a chemical fixative were the compatibility with the chosen bacterial strains, the metal sample plates and the experimental hardware. Additionally, the chemical hazard of the fixative had to be minimized.

Bacterial Species Selection Criteria

The bacterial species and strains for BIOFILMS were selected for 1) their ability to form biofilms, 2) their relevance for spaceflight and 3) their potential risk to the crew. Spaceflight relevance was defined here as either relevant for the astronaut’s health or the integrity of spaceflight equipment. Moreover, species and strains were considered that had been isolated from spacecrafts or the International Space Station itself. We only considered bacteria that are classified in the lowest risk group to eliminate possible health risks in the unlikely event of exposure. The selected strains were tested for their ability to grow in the chosen growth medium, their biofilm formation on inert surfaces and their compatibility with the experimental setup and chosen fixative. Furthermore, an appropriate protocol for preparing the pre-test inoculation cultures for flight was developed.

Antimicrobial Surface Functionalization

The concept of antimicrobial efficacy involves both topographical influence on bacterial adhesion (Helbig et al., 2016) as well as inherent bactericidal capacities of the materials. Since, the goal of the BIOFILMS experiment is to evaluate topographically functionalized antimicrobial surfaces under space conditions, the selection of the materials itself and the method for generating the different topographies was an integral part of the experiment. As inert non-antibacterial reference surface stainless steel (AISI 304) was selected for evaluating bacterial biofilm formation. Furthermore, copper (OF-Cu) and brass as a copper alloy (CuZn37) were selected as appropriate metal surfaces with antimicrobial properties. In this selection process for the antimicrobial surfaces it was important that the metal itself had been well studied for its antimicrobial properties and that it was suitable for topographic functionalization. In the experiment, each material will be tested with three topography modifications: smooth, patterned at or very near the bacterial scale ($P \approx$ Bac), patterned smaller than the bacterial scale ($P <$ Bac). With this we will include the effect of topography on bacteria-surface interactions. The proposed effective interplay of mechanisms is listed in **Table 1** for each of the surface modifications.

Sterilization of Metal Sample Plates

Because the setup for the BIOFILMS experiment will be based on a single species biofilm formation microbial contamination on the metal sample plates will be prevented in advance of the experiment. Copper containing surfaces may form additional oxides during passivation in contact with water, therefore a specific sterilization treatment with minimal contact with water was developed, because the standard sterilization methods such as autoclaving and treatment with 70% ethanol are not suitable. We tested different combinations of ultrasound, ethanol and UV-C treatment. To test the sterilization efficacy of each, smooth steel surfaces were intentionally contaminated with bacteria (*Staphylococcus capitis* subsp. *capitis* strain DSM 111179) by placing the surfaces into petri dishes with 10 ml of liquid growth medium (R2A) inoculated with 10^7 CFU/ml and incubated overnight at 37°C. Next, the plates were treated either with different concentrations of ethanol in tubes in the ultrasonic bath at 50% for 30 min *(Sonorex Digital 10P, Bandelin, Berlin, Germany)* followed by a UV-C treatment (total dose 840 J/m^2), autoclaved (positive control) or not treated (negative control). To verify effective sterilization the sample plates were placed in Erlenmeyer flasks containing 20 ml of liquid growth medium (R2A) and incubated overnight at 37°C in a shaking incubator at 100 rpm. The sterilization procedure was scored effective in the absence of visual growth.

Scientific Requirements of the Experimental Hardware

For the hardware design of the BIOFILMS experiment several scientific requirements were stated. The basic principle for the hardware design had to allow bacterial biofilm formation on different metal sample plates in a controlled oxygenated environment that will permit distinct activation and termination of the experiment with little crew time involved. The specific scientific requirements are listed below:

TABLE 1 | Material/Topography sample set-ups involving the targeted bacteria/surface interaction.

Topography Material	Smooth	P ≈ Bac	P < Bac
Stainless Steel	neutral contact inert	retaining inert	repelling Inert
Copper	neutral contact bactericidal	retaining bactericidal	repelling bactericidal
CuZn37	neutral contact moderate bactericidal	retaining moderate bactericidal	repelling moderate bactericidal

(1) The experiment hardware needs to be equipped with culture chambers, each one hosting five metal sample plates.
(2) Each chamber should offer sufficient room to accommodate all five metal sample plates without touching or damaging their surfaces during their placement into or removal from the chamber.
(3) The bacteria need to be uploaded as "ready-to-start" pre-test cultures. The volume of a pre-test culture should be 0.25 ml for each culture chamber. The experiment hardware needs to be capable of activating the pre-test cultures by the addition of liquid growth medium.
(4) The experiment hardware must be capable of transferring the activated culture into the culture chamber containing the metal sample plates. The transfer should occur directly after activation.
(5) The experiment hardware must be capable of filling the complete culture chamber, covering all five metal sample plates with growth medium and activated bacterial cultures. The chamber must remain free of liquid until the cultures are introduced to prevent premature chemical alterations of the metal sample plates.
(6) The growth medium must not be stirred after the chamber is filled.
(7) The introduction of air bubbles must be prevented, since these may obstruct the biofilm formation in an unpredictable and non-verifiable way.
(8) The experiment hardware must be capable of providing the bacterial cultures with oxygen throughout incubation.
(9) The experiment hardware must be capable of replacing the liquid growth medium with a fixing solution.
(10) The culture chambers must be sterilizable (preferably via autoclaving).

Moreover, a safety requirement is to maintain a level of containment that will prevent any leakage from the experiment hardware container once it is aboard the ISS. Furthermore, aboard the ISS, the experiment must be integrated into Kubik; a temperature-controlled cube shaped facility with a centrifuge in its center to simulate gravity. Therefore, the outer measures and electronic connections need to be compatible between the experiment hardware and Kubik.

The experiment hardware was designed and produced by Kayser Italia, SRL, Livorno LI, Italy. During the design process, two prototypes, the reduced model and the scientific model, were provided to the science team for initial tests before the actual flight models were produced. Pre-flight hardware tests included a biocompatibility test and a science verification test (SVT). Additionally, an experiment sequence test was performed to validate the overall set-up including the respective timeframes of the experiment.

Biocompatibility Test

To confirm that all materials used in the BIOFILMS hardware are biocompatible, thereby ensuring inhibition of bacterial growth would not occur, a biocompatibility test was performed. All materials (**Table 2**) were autoclaved in advance, put into test tubes with plastic lids, and covered with 5 ml of liquid growth medium (double concentrated R2A). An additional tube was inoculated without including any material (positive control) and a set of blank samples (materials without bacteria) was included. The optical density at 600 nm (OD_{600nm}) of an overnight culture in double concentrated R2A of the bacterial strains was measured with an absorbance reader (ELx808, BioTek). An appropriate amount of overnight culture was used to inoculate the medium in the test tubes so that final OD_{600nm} was at 0.1. For the positive control bacteria were cultivated in medium only. After 5 h and 15 days of incubation at room temperature (20–22°C), tubes were vortexed and OD_{600nm} was determined.

Science Verification Test

For the science verification test the science success criteria were defined to determine if the hardware design allows for the successful implementation of the experiment and at the same time ensures that the scientific questions are answered. For BIOFILMS the following science success criteria were defined:

(1) Successful integration of samples (5 metal plates per hardware unit) and fluids into the experiment units (0.25 ml of bacteria suspended in buffer in the bacterial reservoir, 2.1 ml growth medium in the medium reservoir and 2.1 ml chemical fixative in the fixative reservoir)
(2) Successful filling of the culture chambers with growth medium (activation of experiment)
(3) Successful termination of experiments with injection of the fixative into the respective culture chambers (termination of experiment)
(4) Successful growth and even distribution of biofilm in the chambers including steel sample plates
(5) Detection of traces of bacteria in the chambers containing the antimicrobial sample plates
(6) Successful completion of the experiment without contamination by other bacteria

TABLE 2 | List of materials from the BIOFILMS hardware that were tested for biocompatibility.

#	Material	Use and Location
1	American Iron and Steel Institute (AISI) 316 stainless steel	Cover of culturing chamber, Duckbill valve retainer, stop valve screw
2A	Silicone *a*	O-rings
2B	Silicone *b*	O-rings
2C	Silicone *a* with Vaseline	O-rings
2D	Silicone *b* with Vaseline	O-rings
3	Silicone for LSR injection molding	Gas permeable membrane
4A	Ethylene propylene diene monomer *a*	O-rings
4B	Ethylene propylene diene monomer *b*	O-rings
4C	Ethylene propylene diene monomer *a* with silicone grease	O-rings
4D	Ethylene propylene diene monomer *b* with silicone grease	O-rings
5	Silicone mL	Duckbill valve
6	Polyetheretherketone	Hardware body
7	AISI 304 stainless steel	Screws

The timeline for the test itself consisted of 2 days for assembly and filling the experiment hardware, 7 days of storage at 4°C followed by culturing for 14 days at 20°C. After this, the experiment hardware was shipped at 20°C to the science team for hardware disassembly o and sample retrieval from the experiment units. Samples were analyzed via microscopy.

Development of an Experimental Setup for Spaceflight

Gravity Conditions and Development of a Flight Plan

The BIOFILMS experiment will investigate biofilm formation of three different bacterial species on three types of metal sample plates with three different surface topographies in different gravitational conditions. As a control, blank samples will be included as well and the ground experiments will be performed in the same setup. In the experiment gravity parameters important for spaceflight were selected to study the corresponding biofilm morphology and antimicrobial activity. These gravity parameters are microgravity (µg), Mars gravity (0.38 x g) and Earth gravity (1 x g) as control. For the simulation of the gravity parameters on the ISS, two Kubik facilities aboard the ISS are going to be used. To accommodate all sample types and combinations throughout three flights with limited space available in the two Kubik facilities, a specific flight plan was developed that allows evaluation of the sample types such that a successful comparison among the sample types and references can be obtained throughout the different gravitational parameters.

Experiment Sequence of Individual Flights

The experiment sequence must be identical for all three BIOFILMS flights. Certain factors such as temperature and duration can vary within the experiment sequence itself due to their difficulty to control. Therefore, certain temperature ranges and time periods were established that define the minimum and maximum temperature fluctuations and duration of incubation and storage time. The experimental design for the ground-based experiments was developed that provides for a detailed comparison between space and ground conditions. For testing purposes, the whole experiment sequence was simulated during the experiment sequence test over a 2-month time period.

RESULTS AND DISCUSSION

Selected Buffer, Growth Medium and Fixative

For the onboard storage of the bacteria inside the BIOFILMS hardware phosphate buffered saline (PBS) was selected to ensure there is an osmotic balance between the bacterial cells and the ambient medium. Also, storage in PBS keeps the metabolic activity of the bacteria minimal compared to storage in a nutrient rich medium. The make-up of the PBS to be used for BIOFILMS contains 7.0 g/L Na_2HPO_4, 3.0 g/L KH_2PO_4, 4.0 g/L NaCl in ddH_2O with pH 7.5 and is sterilized by autoclaving. The selected liquid growth medium that provides nutrients for the bacteria during the incubation phase of experiment is double concentrated R2A medium (Teknova R0005: 0.5 g/L yeast extract, 0.5 g/L peptone, 0.5 g/L casamino acids, 0.5 g/L glucose, 0.5 g/L soluble starch, 0.3 g/L sodium pyruvate, 0.3 g/L KH_2HPO_4, 0.05 g/L $MgSO_4 \cdot 7H_2O$ in ddH_20; pH 7.2). This medium was selected because: (I) It supports growth of the selected bacterial species, (II) it is a growth medium that contains only small amounts of nutrients resembling a more realistic biofilm formation scenario, and (III) it was already used in previous spaceflight experiments such as BioRock (Loudon et al., 2018; Cockell et al., 2020) and therefore allows comparability with the published results.

The chosen fixative for BIOFILMS is a mixture of 1% paraformaldehyde (PFA; Merck 104005) and 2.5% glutaraldehyde (GA; Roth 3778.1) in 0.05 M Hepes buffer (pH 7.2–7.4). This fixative is a standard for ultrastructural research, especially for clinical specimens. It is a variant of the Karnovsky´s fixative (4% PFA, 5% GA) (Karnovsky, 1965) which uses higher concentrations and is suitable for a wide range of biological samples (Bozzola and Russell, 1999). The reason for using 1% of PFA instead of 4%, as used in Karnovsky´s fixative, is that at this concentration a substantial fraction of the PFA is persistently present as formaldehyde in the mixture providing a stable fixative over time.

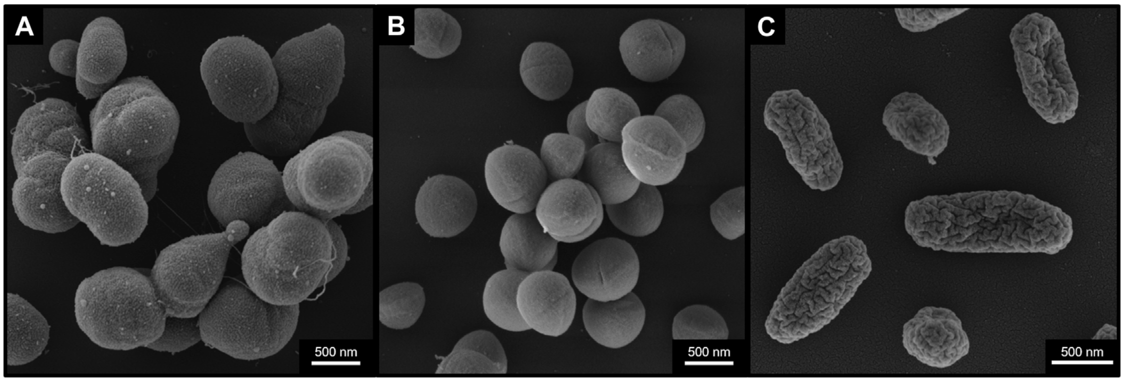

FIGURE 1 | Selected bacterial species for BIOFILMS. Scanning Electron Microscopy images of *Acinetobacter radioresistens* strain 50v1 **(A)**, *Staphylococcus capitis* subsp. *capitis* strain DSM 111179 **(B)** and *Cupriavidus metallidurans* strain CH34 **(C)** after 18 h incubation in R2A liquid growth medium at 37°C (*S. capitis* subsp. *capitis*) or 30°C (*A. radioresistens* and *C. metallidurans*) at constant agitation of 150 rpm. Cells were fixed with 1% PFA, 2.5% GA in 0.05 M Hepes buffer for 2 h at room temperature and stored at 4°C afterwards. Scale bars represent 500 nm.

Selected Bacterial Strains for BIOFILMS

Three bacterial species with different spaceflight implications were selected for the BIOFILMS experiment: *Acinetobacter radioresistens*, *Staphylococcus capitis* and *Cupriavidus metallidurans*. In the following sections, the rationale for specific bacterial strain selection is presented.

Acinetobacter radioresistens

Members of the genus *Acinetobacter* are non-motile, Gram-negative and strictly aerobic bacteria that can form biofilms (Martí et al., 2011; Towner et al., 2013). The cells are rod shaped, but become more coccoid as they approach and enter stationary phase (Henriksen, 1973). Most clinically relevant is *Acinetobacter baumannii*, a global pathogen that causes serious infections particularly in intensive care units and is known for its antibiotic resistance (Peleg et al., 2008). For the BIOFILMS experiment *A. radioresistens* strain 50v1 isolated from the surface of the Mars Odyssey spacecraft prior to flight (La Duc et al., 2003) (**Figure 1A**) was selected. Studies show that strain 50v1 is remarkably resistant to extreme conditions including UV-radiation, hydrogen peroxide and desiccation (La Duc et al., 2003; McCoy et al., 2012). Furthermore, 50v1 is not only highly resistant to cleaning reagents such as Kleenol 30, but can biodegrade them (Mogul et al., 2018).

Staphylococcus capitis subsp. *capitis*

S. capitis is a Gram-positive skin-associated bacterium isolated predominantly from the human head (Kloos and Schleifer, 1975; Byrd et al., 2018). *S. capitis* has the ability to form biofilms and is a causative agent of infections such as endocarditis, urinary tract infections and catheter induced bacteremia (Cui et al., 2013). In contrast to most other staphylococcal species, *S. capitis* is classified as a biosafety level 1 according to the U.S. Public Health Service Guidelines. In BIOFILMS we use the strain *S. capitis* subsp. *capitis* DSM 111179 (**Figure 1B**) isolated from an exposure experiment aboard the ISS, where different materials, including antimicrobial materials containing silver and ruthenium, were exposed to the ISS indoor environment (Sobisch et al., 2019). The materials were in the pathway of crew members and therefore were exposed to microorganisms originating from the astronauts' skin, hair and clothing. DSM 111179 was isolated after 19 months from V2A steel (Sobisch et al., 2019). The strain was selected for BIOFILMS because of its strong biofilm formation, its phylogenetic proximity to other clinically relevant staphylococcal species and its origin from the space station indoor environment.

Cupriavidus metallidurans

C. metallidurans is a non-pathogenic β-proteobacterial species. The cells are Gram-negative peritrichously flagellated rods that are resistant to high concentrations of metal ions (Vandamme and Coenye, 2004). The species has often been isolated from harsh, oligotrophic, artificial environments, including the ISS (Mijnendonckx et al., 2013). For BIOFILMS, *C. metallidurans* type strain CH34 will be used (**Figure 1C**), which was first isolated from a zinc decantation basin in a non-ferrous metallurgical plant near Engis, Belgium (Mergeay et al., 1978). Strain CH34 has since become a model organism for bacterial metal resistance, owing to its tolerance to a surprisingly wide range of metal ions. This tolerance is mediated by a large number of gene clusters associated with metal resistance as well as its adaptation potential during metal exposure (Janssen et al., 2010; Monsieurs et al., 2015; Ali et al., 2019; Mijnendonckx et al., 2019; Van Houdt et al., 2021). These properties have led to the selection of CH34 for several other space experiments (Leys et al., 2009; Loudon et al., 2018). For BIOFILMS, this strain was selected for its Cu tolerance, its ability to survive in harsh environments and its previous space experiments.

Criteria for Suitability of Bacterial Strains

During the selection process, the strains were tested for several parameters that are important for the space experimental setup. These parameters include, but are not limited to: growth in R2A liquid medium, biofilm formation on reference surfaces (smooth stainless steel), inactivation by the selected fixative. All the parameters were fulfilled by the selected strains (**Table 3**).

TABLE 3 | Selection process criteria for BIOFILMS bacterial strains.

Parameter	*A. radioresistens* 50v1	*S. capitis* subsp. *capitis* DSM 111179	*C. metallidurans* CH34
Growth in R2A liquid growth medium	✓	✓	✓
Biofilm formation on stainless steel	✓	✓	✓
Inactivation by Fixative	✓	✓	✓
Long-term storage in buffer	✓	✓	✓
Revival in growth medium after long-term storage in PBS	✓	✓	✓

Preparation of Pre-test Inoculation Cultures

The bacterial culture preparation for flight will occur prior to the assembly of the hardware to assure that any contamination can be detected before the cultures are loaded into the hardware. For backup, three individual cultures will be prepared and cultivated on double concentrated R2A agar plates for 48 h. DSM 111179 is cultivated at 37°C and the other two strains are cultivated at 30°C. After cultivation (colonies formed) the plates are stored at room temperature. For preparation of the flight bacterial samples, 50 ml of a double concentrated R2A liquid culture will be inoculated in 200 ml Erlenmeyer flasks containing the growth medium, and incubated as described above for 16–18 h in two shaking incubators at 200 rpm. Cultures will be transferred to 50 ml tubes and centrifuged for 10 min at 4000 x g. Cultures are washed three times with 30 ml phosphate buffered saline and the final cell pellet is resuspended in 10 ml phosphate buffered saline. One mL of each culture is aliquoted into individual 1.5 ml tubes and stored at 4°C until they are inoculated into the experimental hardware. The final concentration is approximately 10^9 colony forming units per ml (CFU/ml) for all three bacterial species. This high concentration is used to assure sufficient cell survival due to the possible 1-month time lag for storage and uploading before the initiation of the experiment. When the experiment is initiated the bacterial sample is diluted by the addition of growth medium (dilution factor: 8.4).

Metal Sample Plates: Antimicrobial and Reference Surfaces

The three different metals addressed in *Materials and Methods* will be evaluated for their ability to prevent or affect microbial growth and thus biofilm formation in the BIOFILMS hardware. To fit into the experimental hardware designed for the flight experiments, 1 mm sheets of of-Cu (Cu >99.95%), CuZn37 (Cu 63%, Zn 37%) (*Wieland, Ulm, Germany*) and AISI 304 Stainless Steel (*Brio, Lüdenscheid, Germany*) are cut into plates of 10 × 25 mm^2 dimension. The Cu-based metals are mirror-polished on an automated *TegraPol-21* system (*Struers, Willich, Germany*). The steel sample plates, however, are provided with polished surfaces. The polished plates of each material are used as reference samples of smooth surface topography and as starting material for topographic surface functionalization.

Topographic Surface Functionalization

Topographic surface functionalization is done via USP-DLIP, whereby both micro- and nanometer pattern scales are achieved in high pattern quality (Müller et al., 2020a) under low chemical surface modification (Müller et al., 2020b). This technique enables both matching the required size relation to single bacterial cells while retaining the inherent antibacterial capacity of the Cu-based substrates (Müller et al., 2021). The USP-DLIP setup consists of a Ti: Sapphire *Spitfire* laser system (*Spectra Physics, Irvine, US*) that emits ultrashort pulses of t_p = 100 fs pulse duration (Full Width at Half Maximum, FWHM) at a centered wavelength λ of 800 nm at 1 kHz pulse frequency. The optical setup induces two beam interference by dividing the seed beam in a diffractive optical element (DOE) and overlapping the individual beams on the sample surface using a lens system. By varying the incident angle θ the periodicity P of the one-dimensional interference pattern can be modified applying the correlation stated in **Eq. 1** (Müller et al., 2020a).

$$p = \frac{\lambda}{2\tan(\theta)} \tag{1}$$

To achieve topographies in the size range of single bacterial cells ($P \approx$ Bac) the periodicity is set to 3 μm. Surface patterning is conducted in scanning mode at a fluence of 3 J/cm^2 and 90% pulse overlap, that induces homogeneous surface properties on the three different metallic materials as described in Müller et al. (2020a). For pattern scales below a single bacterial cell size ($P <$ Bac) the periodicity is set to 800 nm, while patterning is conducted modifying the lasing parameters according to Müller et al. (2020a) to achieve comparable pattern morphology on each material. The laser processed samples are subsequently selected to undergo immersion etching in 3% citric acid in an ultrasonic bath to remove process-induced surface oxide and sub-structures (Müller et al., 2020b). SEM images of the USP-DLIP patterned surface topographies after post-processing are displayed in **Figure 2**.

Sterilization of Sample Plates

Figure 3 shows the efficacy of the different tested sterilization methods. Visual bacterial growth was only observed in the untreated control (**Figure 3A**). All other sterilization methods did not show visual growth, thus effectively inactivating and removing all contaminants (**Figures 3B–D**). The bactericidal activity of ethanol is normally achieved at a concentration of 70%. However, ≥99.9% ethanol in combination with ultrasound and UV-C treatment was shown to be equally effective. The latter approach prevents the metal sample plates from coming in

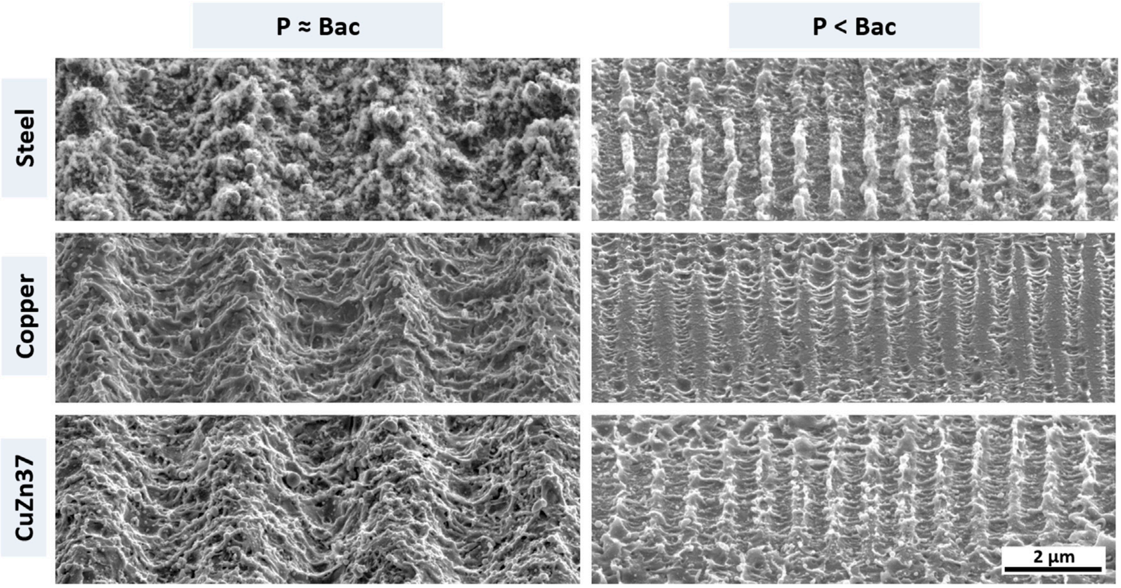

FIGURE 2 | SEM images of topographically functionalized surfaces of the three different metallic materials used in the experiments. The left column lists patterns targeting retaining bacterial adhesion due to increased contact area. The right column presents sub-µm scaled patterns aspiring a repelling effect on bacterial cells by decreased contact area. The single scale bar applies for all sub-images.

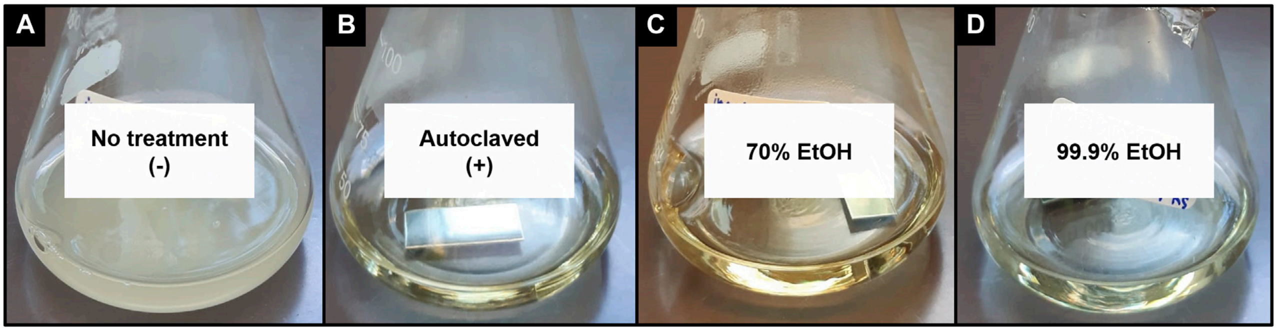

FIGURE 3 | Smooth steel sample plates after incubation in growth medium overnight at 37°C in a shaking incubator at 100 rpm after deliberate contamination and different sterilization methods: **(A)** no treatment as negative control, **(B)** autoclaved as positive control, **(C)** incubated in the ultrasonic bath with 70% ethanol + UV-C treatment, **(D)** incubated with 99.9% ethanol + UV-C treatment.

contact with water prior to the start of the experiment, which could induce chemical alterations of the surfaces. Therefore, this combination was selected for the BIOFILMS experiment with the exact protocol being:

Metal sample plates are spray rinsed with ethanol (≥99.9%). The plates are then placed into 5 ml tubes and submerged in 4 ml ethanol (≥99.9%). The tubes are placed in an ultrasonic bath and sonicated for 30 min. The ultrasonic treatment removes all unwanted particles on the surface such as dust and other particles. After that, the metal sample plates are placed into sterile petri dishes with sterile tweezers and air dried in a tilted state by leaning them against the wall of the petri dish. Once the samples are dried completely, the samples are UV-C irradiated with a dose of 420 J/m^2 on each side. Sample plates are stored in sterile petri dishes until they are integrated into the BIOFILMS hardware.

BIOFILMS Hardware

The BIOFILMS hardware was manufactured by Kayser Italia. Before the actual flight model was produced, two prototypes were built. The first prototype, the Reduced Model (RM), only fits one metal sample plate and served as a first testbed. Here, the bacteria in the growth medium were injected directly into the hardware, where they were incubated in direct contact with the metal sample plate. **Figure 4** shows the principle of experiment activation and gas exchange during the experiment. For oxygen exchange, a gas permeable membrane is placed on top of the sample plate to allow gas exchange with the air pocket that

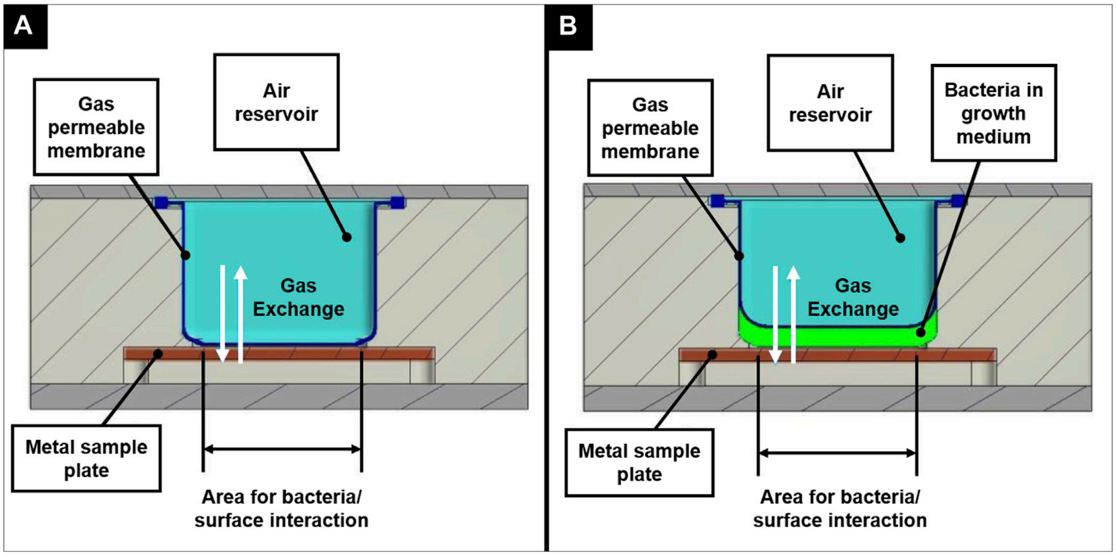

FIGURE 4 | Principle of experiment activation shown for the Reduced Model in an inactivated state **(A)** and after activation **(B)**, illustrating the concept of oxygen exchange during the incubation period.

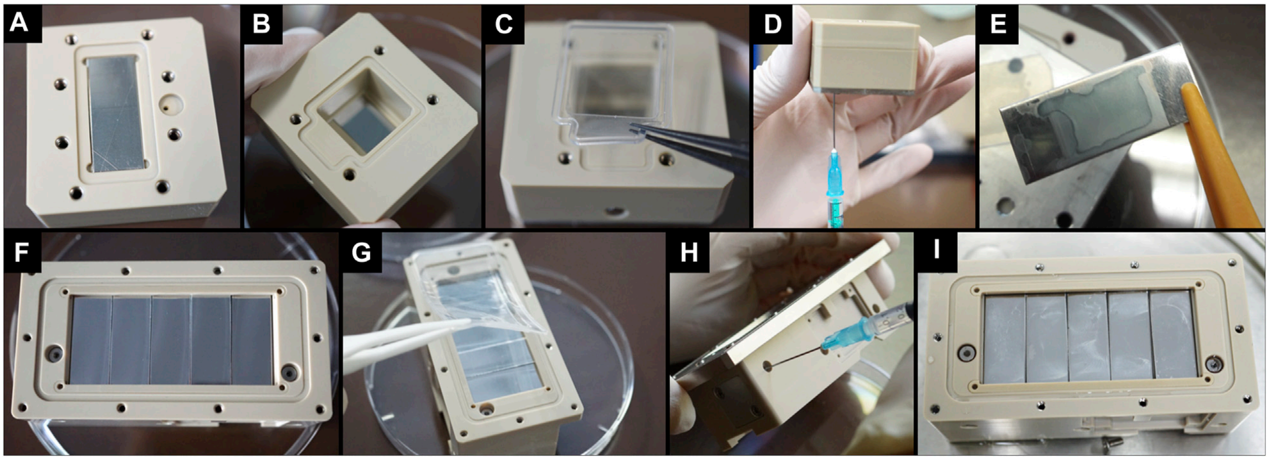

FIGURE 5 | Overview of the assembly process and filling process of the BIOFILMS experiment unit prototypes. **(A–D)** Assembly and filling of Reduced Model (RM) as prototype for first tests on basic experimental concept. **(E)** Image of a smooth stainless steel sample plate that was incubated inside the RM with *S. capitis* subsp. *capitis* DSM111179 for 24 h at 37°C. **(F–H)** Assembly and filling of Scientific Model (SM) as prototype for further testing of the actual setup of the flight models. **(I)** Top view of the SM after incubation of smooth stainless steel plates with *S. capitis* subsp. *capitis* DSM111179 for 10 days at RT.

is located above (**Figure 5G**). During assembly, the membrane first is in direct contact with the metal sample plate, without any space in between. When the medium with the bacteria is injected in between the metal plate and the sample plate, the gas permeable membrane bulges upwards.

After the successful first tests with the RM, the Scientific Model (SM) was developed, in the same way as the experiment units of the flight models would later be designed, and was used for testing whether this design fulfils the scientific requirements of the experiment. The assembly and filling process of the RM and SM are depicted in **Figure 5**. In addition, the figure shows how the metal plates (in this case smooth stainless steel) appear after incubation in the experiment units with bacteria in growth medium (**Figures 5E,I**). The tests with the SM showed that the hardware design is suitable for the BIOFILMS experiment since all requirements were met (*Scientific requirements of the experimental hardware*) and therefore the same design was incorporated into the experiment units of the flight models. Since the flight hardware requires a double level of containment to prevent leakage of contents in any case. The experiment unit is integrated into an outer container, the experiment container, that is inserted into Kubik during the experiment sequence. Inside each experiment container is one experiment unit that contains the sample plates, bacteria, growth medium, fixative and electronic equipment (**Figure 5**). The whole BIOFILMS experimental hardware system is the assembled experiment unit inside the experiment hardware. For BIOFILMS, the experiment units are specifically designed to allow biofilm formation in a controlled environment on the antimicrobial and inert sample plates. Five sample plates can be accommodated on the bottom of the culture chamber inside the experiment unit. The gas permeable membrane is placed on top of the sample plates to allow gas exchange with the air pocket located above (**Figure 5G**). The experiment unit has three reservoirs that are separated from each other and from the culture chamber by flat head valves. One reservoir has a capacity of 0.25 ml and serves as a means of storage for the bacterial inoculation suspensions. The other two reservoirs have a capacity of 2.1 ml and are filled with sterile syringes and needles during assembly with the growth medium and fixative, respectively (**Figure 5H**). The BIOFILMS experiment is activated by a release system with springs and pistons that are controlled by internal electronics. The initiation of the experiment is done by a ground controller providing Kubik power to the experiment containers. This enables the experiment to be conducted inside Kubik without extensive crew interaction. When the experiment is initiated, a spring is released that pushes a piston through the medium reservoir. By doing so, the medium is flushed through the bacterial reservoir into the culture chamber, delivering the bacterial cells. After activation, the experiment is incubated for 14 days at 20°C. During the incubation period, the bacteria are incubated in the culture chamber in spatial proximity to the sample plates. The contact area for bacteria/surface interaction is 2.1 cm^2 (10 mm × 21 mm) per sample plate, totaling to 10.5 cm^2. The experiment is terminated by activating the release system of the fixative reservoir forcing the fixative directly into the culture chamber. The fixative mixes with the liquid inside the chamber and chemically fixes the experiment to prevent further microbial activity.

Biocompatibility and Science Verification Test

The biocompatibility test with all materials that were incorporated in the BIOFILMS hardware revealed that none of the materials were inhibitory to microbial growth (**Figure 6**). For *A. radioresistens* and *C. metallidurans*, a strong increase in OD_{600nm} was observed between 5 h and 15 days of incubation in all test tubes, including the test tube without any material. The OD_{600nm} for *S. capitis* subsp. *capitis* remained the same (3, 4B, 4C, 4D, 5, 6, Blank) or increased only slightly between the two measuring points (1, 2A, 2B, 2C, 2D, 4A, 7). However, this seemed to be due to insufficient mixing of the vial before taking an aliquot for determining the OD_{600nm} rather than actual inhibition of growth induced by the material. Microbial growth was clearly visible as turbidity around the materials on the bottom in the test tubes as shown in **Figure 6** with a white arrow indicating strong cell agglomeration.

During the science verification test it was shown that the design of the BIOFILMS hardware is able to meet the defined science success criteria. The hardware was filled according to the protocol and after incubation, an evenly distributed biofilm formation was observed on the reference surfaces. Detailed results of the science verification test can be found in **Supplementary Table S1**. During the test, one of the experiment units became contaminated. Nevertheless, all other units including the blank units had no problems with contamination, which is why the test was considered as an overall success. However, the protocol for sterilization of the experiment units and the sample plates was revised accordingly.

Experimental Setup for Spaceflight

Gravity Conditions

Within the BIOFILMS experiment, biofilm formation will be investigated under three different gravitational levels aboard the ISS. Gravity levels tested will be microgravity (µg), an approximation of Martian gravity (0.4 x g) and Earth gravity (1 x g) as a control. Additionally, ground experiments on Earth will be performed. The two Kubiks that are currently located in the Columbus module aboard the station will be employed. An astronaut will integrate the experiment hardware into the two Kubiks, which are controlled by a ground controller. Once the Kubik power buses deliver power to the experiment containers, the programmed experiment timeline is executed automatically, meaning that the experiment is activated and terminated automatically once the experiment container has been integrated. This way the required crew time can be kept to a minimum. Kubik can be set to specific temperatures, for BIOFILMS this is 20°C. Furthermore, each Kubik has eight slots for experiment containers, where gravitational forces can be created via centrifugation (**Figure 7A**). Here, the gravitational vector is directed towards the sample plates within the BIOFILMS experiment. One Kubik will be set to a centrifugal setting resembling 1 x g and the other one to 0.4 x g. Moreover, in each Kubik, four slots in the corners outside of the centrifugal rotor are used to subject the experiment containers to µg.

Flight Plan

Because there are only two Kubiks available at the station and each has a limited number of slots, a specific flight plan had to be developed to accommodate all sample types that require testing during the BIOFILMS experiment. In total the BIOFILMS experiment requires 72 slots. Biofilm formation of *A. radioresistens* and *S. capitis* subsp. *capitis* will be tested on steel, copper and brass with the three metal topographies (Smooth, P ≈ Bac, P < Bac). Due to limited space for sample accommodation, *C. metallidurans* will be tested only on steel and copper surfaces with the three types of metal topographies. The innovative aspect of the BIOFILMS experiment is the use of different metal surface topographies for increasing the antimicrobial efficacy. Therefore, the direct comparison of the different topographies had the highest priority. Importantly, each flight set had to include at least one sample set with stainless steel, because it is the reference surface without antimicrobial efficacy and at least one blank sample, to exclude the occurrence of outside contamination. The flight plan is depicted in (**Figure 7B**). With this flight plan, the direct effect of the metal topographies on

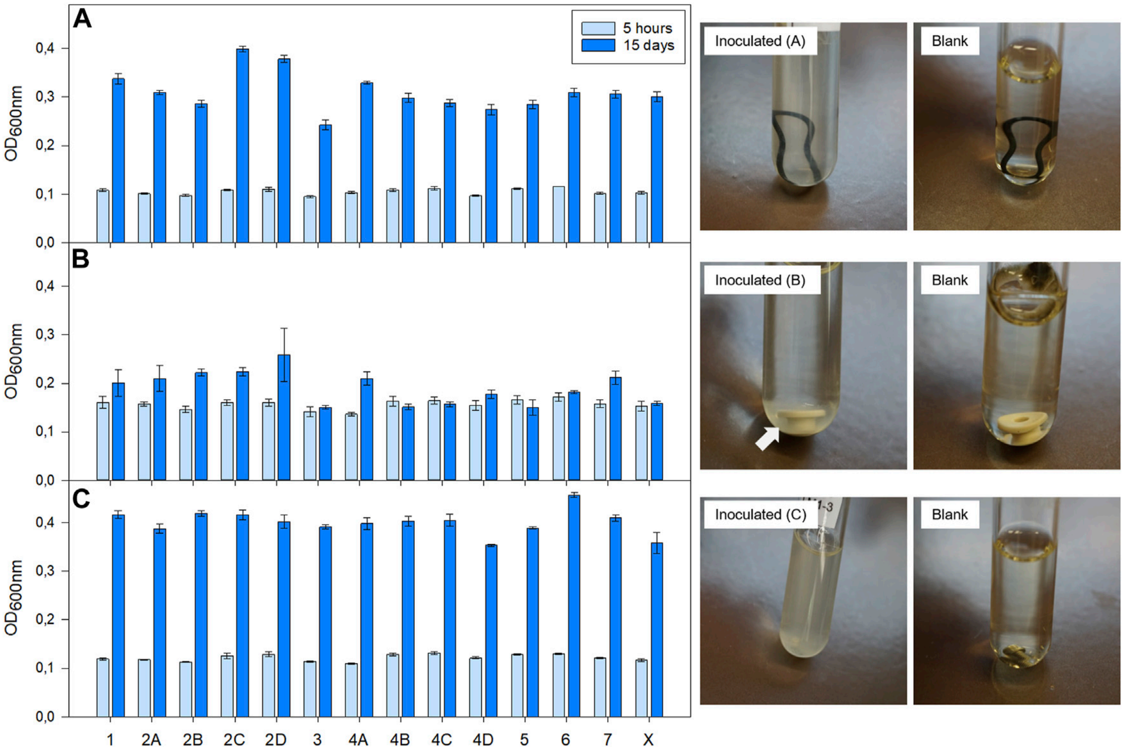

FIGURE 6 | Results of biocompatibility test with bacteria selected for BIOFILMS: **(A)** *A. radioresistens* 50v1, **(B)** *S. capitis* subsp. *capitis* DSM 111179, **(C)** *C. metallidurans* CH34. Bacteria were incubated at room temperature (20–22°C) in a test tube with double concentrated R2A growth medium in presence of different hardware related materials: (1) AISI 316 stainless steel, (2A) Silicone *a*, (2B) Silicone *b*, (2C) Silicone *a* with Vaseline, (2D) Silicone *b* with Vaseline, (3) Silicone for LSR injection molding, (4A) Ethylene propylene diene monomer *a*, (4B) Ethylene propylene diene monomer *b*, (4C) Ethylene propylene diene monomer *a* with silicone grease (4D) Ethylene propylene diene monomer *b* with silicone grease, (5) Silicone mL, (6) Polyetheretherketone, (7) AISI 304 stainless steel (X) positive control without material. Optical density was measured at in a 96-well-plate a wavelength of 600 nm (OD600 nm) after 5 h and 15 days post inoculation with an absorbance reader. Pictures on the right are exemplary for bacterial growth in the presence of material 4B **(A)**, material 6 **(B)** and material 7 **(C)**. The respective blank samples are shown as well.

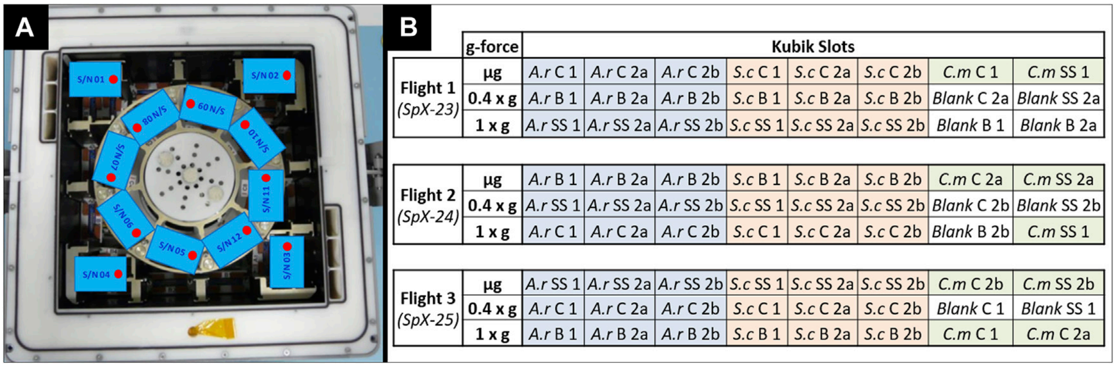

	g-force	Kubik Slots							
Flight 1 *(SpX-23)*	µg	*A.r* C 1	*A.r* C 2a	*A.r* C 2b	*S.c* C 1	*S.c* C 2a	*S.c* C 2b	*C.m* C 1	*C.m* SS 1
	0.4 x g	*A.r* B 1	*A.r* B 2a	*A.r* B 2b	*S.c* B 1	*S.c* B 2a	*S.c* B 2b	*Blank* C 2a	*Blank* SS 2a
	1 x g	*A.r* SS 1	*A.r* SS 2a	*A.r* SS 2b	*S.c* SS 1	*S.c* SS 2a	*S.c* SS 2b	*Blank* B 1	*Blank* B 2a
Flight 2 *(SpX-24)*	µg	*A.r* B 1	*A.r* B 2a	*A.r* B 2b	*S.c* B 1	*S.c* B 2a	*S.c* B 2b	*C.m* C 2a	*C.m* SS 2a
	0.4 x g	*A.r* SS 1	*A.r* SS 2a	*A.r* SS 2b	*S.c* SS 1	*S.c* SS 2a	*S.c* SS 2b	*Blank* C 2b	*Blank* SS 2b
	1 x g	*A.r* C 1	*A.r* C 2a	*A.r* C 2b	*S.c* C 1	*S.c* C 2a	*S.c* C 2b	*Blank* B 2b	*C.m* SS 1
Flight 3 *(SpX-25)*	µg	*A.r* SS 1	*A.r* SS 2a	*A.r* SS 2b	*S.c* SS 1	*S.c* SS 2a	*S.c* SS 2b	*C.m* C 2b	*C.m* SS 2b
	0.4 x g	*A.r* C 1	*A.r* C 2a	*A.r* C 2b	*S.c* C 1	*S.c* C 2a	*S.c* C 2b	*Blank* C 1	*Blank* SS 1
	1 x g	*A.r* B 1	*A.r* B 2a	*A.r* B 2b	*S.c* B 1	*S.c* B 2a	*S.c* B 2b	*C.m* C 1	*C.m* C 2a

FIGURE 7 | (A) Exemplary accommodation of BIOFILMS experiment containers inside one Kubik aboard the ISS. 8 slots are located inside the centrifugal rotor where gravitational forces (1 x g/0.4 x g) are resembled via centrifugation. 4 slots are located outside the rotor where µg is acting on the containers. **(B)** Flight plan for the three flights of the BIOFILMS experiment with *A.r.: A. radioresistens, S.c.: S. capitis* subsp. *capitis, C.m.: C.*metallidurans for the three selected bacterial species and C: Copper, B: Brass and SS: Stainless steel for the types of metals. The numbers account for the different types of metal topography with 1: smooth, 2a: USP-DLIP pattern at P ≈ Bac and 2b: USP-DLIP pattern at P < Bac.

the biofilm formation of one bacterial species can be compared on one type of metal in gravitational condition each. The comparison between the different flights and therefore, the comparison between the different types of metals and gravity conditions can still be made by evaluating all influencing factors such as temperature variances, differences in storage time pre and

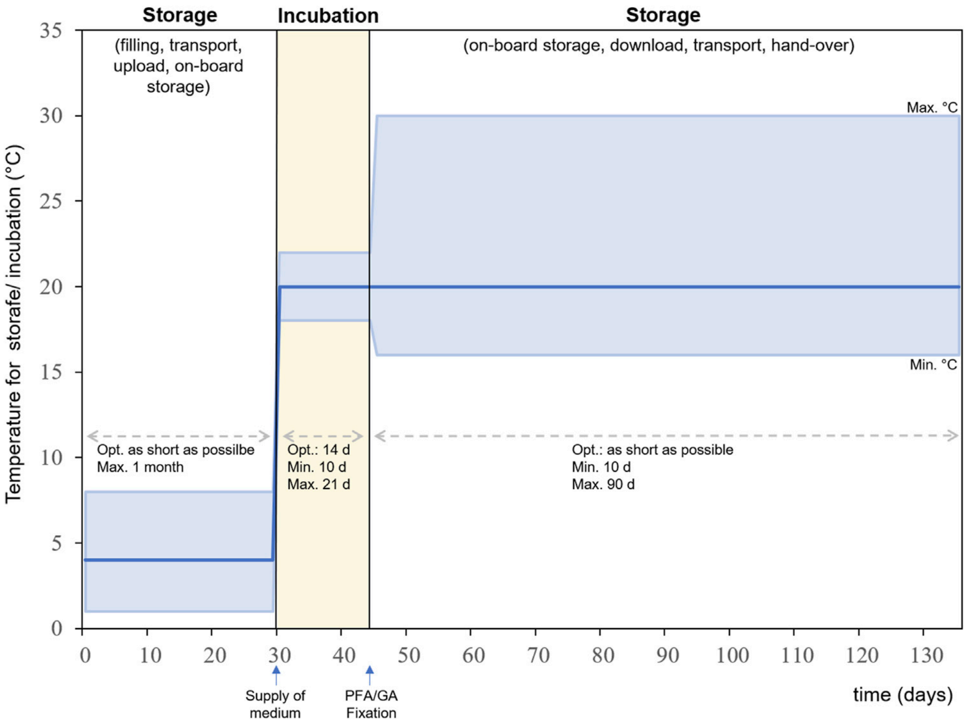

FIGURE 8 | Experiment sequence for BIOFILMS showing the timeline for storage and incubation and the according temperature ranges. Dark blue line: optimal temperature, upper light blue line: maximum temperature, lower light blue line: minimum temperature.

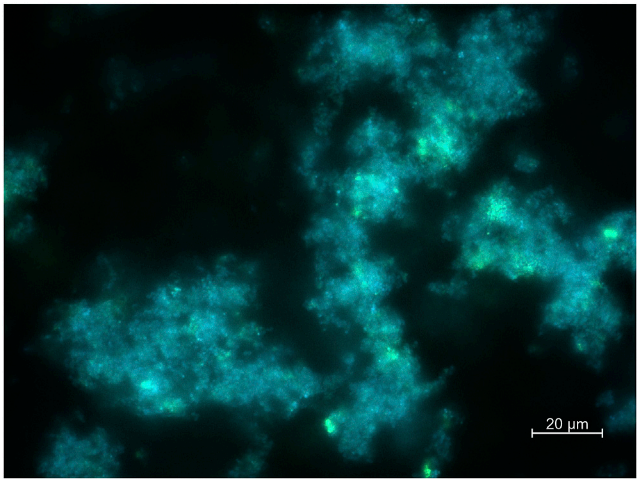

FIGURE 9 | Exemplary fluorescence microscopic image of *Staphylococcus capitis* subsp. *capitis* biofilm on the smooth stainless steel reference sample plate from the BIOFILMS science verification test. DSM 111179 was incubated for 14 days at 20°C within the BIOFILMS flight hardware with an initial cold storage time of 7 days at 4°C and a post-incubation storage time of 2 days at 20°C in a fixed state. Staining was performed with DAPI (5 µg/ml) and FITC conjugated WGA (10 µg/ml). Imaging was performed by using an Axio Imager M2 with AxioCamMR3. Scale bar represents 20 µm.

post incubation, incubation time and period as well as possible disturbances during upload and download to the station.

Experiment Sequence

For each flight of the BIOFILMS experiment, the experimental sequence will be identical. However, due to unpredictable events that can occur during launch or integration on board, shifts in time and temperature range can occur and the conditions might differ slightly between flights. Sample preparation and analysis is carried out with sufficient lead time ahead of the actual flight experiment. For each flight, two sets of ground experiments will be performed. One will be performed in parallel to the flight with the same bacterial cultures. The other ground experiment will be performed at a later stage when all data from the flight are retrieved and the exact condition from flight, such as storage duration and temperature, can be recreated on Earth. The experiment sequence for BIOFILMS is listed in following:

I. Pre-flight preparations in science lab
    (1) USP-DLIP sample production and pre-flight analysis
    (2) Preparation of growth medium and fixative
    (3) Preparation of pre-test inoculation cultures
    (4) Filling and assembly of the experiment hardware
II. Mission Operations
    (1) Transport of experiment hardware to the launch site

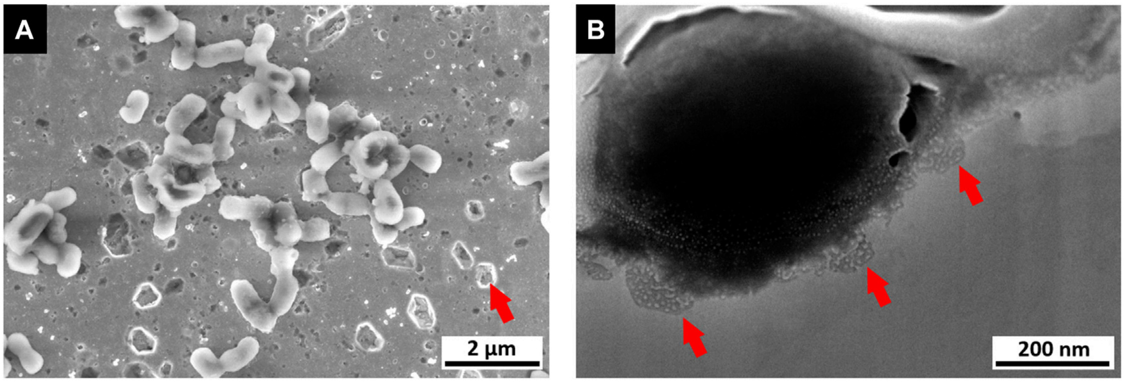

FIGURE 10 | Image of a microbial corrosion analysis (data obtained from contact killing experiment). **(A)** SEM image of a polished copper surface exhibiting sites of pitting corrosion, especially in close vicinity to bacteria (*E. coli* as tested reference organism). **(B)** FIB/SEM cross section of single bacteria cell on copper surface exhibiting smaller sites of pitting corrosion below.

(2) Upload in phase change material
(3) On-board cold storage at +4°C
(4) Integration into Kubik
(5) Automated supply of medium
(6) Incubation period: culturing at µg, 0.4 x g, 1 x g for 14 days at 20°C
(7) Automated supply of fixative
(8) On board storage
(9) Download, transport and hand-over to science team

III. Post-flight sample laboratory analysis
(1) Analysis of biofilms, metal surfaces and growth medium

For each step of the experimental sequence specific time frames and temperature ranges are required (**Figure 8**). All steps have an optimal temperature profile and time frame, but certain deviations from the optimum can be tolerated within the experimental setup. The first steps are the pre-flight preparation of the metal sample plates and the pre-test of bacterial cultures as well as the preparation of the growth medium and fixative. Followed by the assembly and filling of the experiment hardware. The experiment is packed and transported to the launch site for upload to the ISS in its stored state. The time between filling the hardware and activation of the experiment aboard the ISS should be as short as possible and must not exceed 1 month. The temperature for this time period should optimally be 4°C but can range between 1 and 8°C. The incubation period begins when the experiment is integrated into Kubik and the medium is supplied to the culture chamber. The optimal duration for incubation is 14 days but can be shortened to a minimum of 10 ays and lengthened to 20 days maximum. The optimal temperature during incubation is 20°C but can range between 18 and 22°C. The incubation period is terminated by the addition of fixative into the culture chamber. After fixation the experiment hardware will be stored until download at ambient temperature. Here the tolerable temperature is between 15 and 30°C. The preferred timeframe for storage, download, transport and handover to the science team should be as short as possible but can be extended up to 90 days maximum. Within the experiment sequence test it was shown that this anticipated experiment sequence is suitable for the successful implementation of the experiment.

PLANNED POST-FLIGHT ANALYSIS

Biofilm Topography and Cell Viability

Post flight microbiological analysis will include scanning electron microscopy (SEM) and fluorescence microscopy of the bacterial cultures and biofilms. The SEM analysis will allow detailed insights into biofilm morphology, matrix structure and overall integrity of the bacteria. Via Focused Ion Beam cross sectioning (FIB/SEM), biofilm thickness and structure in direct relation to the available surface topography can be assessed by high resolution imaging. For the fluorescence microscopic analysis, different fluorescent dyes will be used such as DAPI for straining nucleic acids and biofilm matrix straining dyes such as FITC-marked wheat germ agglutinin (WGA). A typical image of a *Staphylococcus capitis* (DSM 111179) biofilm on the smooth stainless-steel reference surface from the BIOFILMS science verification test is shown in **Figure 9**.

Material Characterization

By comparing the data from the pre-flight experiments, the topographical and chemical influence of the bacteria (e.g. through corrosive material removal) on the substrate is determined. This allows both the ability to determine the damaging influence of bacterial biofilms on the surface, and local damage providing an indication of the presence and activity of bacteria during the experiment (an example of localized corrosion sites is illustrated in **Figure 10**).

This provides data to determine any differences in bacterial behavior due to changes in gravity, as well as the weighting of short-scale interactions such as Van der Waals forces on colonization behavior through close comparison with the proteomic analyses. Localized surface disruption, oxide growth and chemical surface modification are investigated localized via FIB/SEM and energy dispersive X-ray spectroscopy (EDS), while phase analysis of the substrate and oxide films is conducted via grazing incidence X-ray diffraction (GI-XRD). Additionally, inductively coupled plasma mass spectrometry (ICP-MS) is used for the analysis of metal ions diffused into the medium. The method allows the determination of metal ions in a wide dynamic concentration range from parts-per-trillion (ppt) to parts-per-million (ppm).

CONCLUSION

The BIOFILMS experiment successfully passed all preflight tests including biocompatibility, science verification test (SVT) and experiment sequence test (EST), indicating that the hardware is biocompatible and meets the scientific requirements. The hardware itself, including the two prototypes, allows for the cultivation of bacteria in direct spatial proximity to the different metal sample plates. As such, biofilm formation on the inert reference (stainless steel) and antimicrobial surfaces can be compared, thereby exposing inhibitory effects. Although the extended results of the SVT and EST are out of the scope of this article, both proved that the hardware designed by Kayser Italia fulfilled the scientific requirements of the experiment, allowing biofilm formation on the inert reference surfaces including both smooth and P ≈ Bac patterned surfaces. P < Bac patterned surfaces were not tested within the scope of the pre-flight tests. However, the antimicrobial surfaces, both brass and copper showed an inhibiting effect on bacterial biofilm formation with a stronger effect caused by the P ≈ Bac patterned copper surfaces, which is in good correspondence to preliminary results (Müller et al., 2021). The data that will be generated within the BIOFILMS project will be valuable for the future selection of antimicrobial materials in support of human- and robotic-associated activities in space exploration.

DATA AVAILABILITY STATEMENT

The original contributions presented in the study are included in the article/**Supplementary Material**, further inquiries can be directed to the corresponding authors.

AUTHOR CONTRIBUTIONS

KS, DM, LM, and AA performed the pre-flight experiments, USP-DLIP sample preparation and characterization, analyzed the data, and wrote the manuscript. RM, RH, RLM, and FM were responsible for the conception and design of the experiment and manuscript preparation. DM, GH, and ML are responsible for the electron microscopic images of the bacterial strains while the latter two also contributed in the manuscript preparation. SB, KZ, and RK carried out the element trace analysis and evaluations of the metal release from the different surfaces. NC, JK, MV, AT, and CR contributed to the realization of the experiment, the hardware development, the pre-flight tests and the manuscript evaluation.

FUNDING

KS and RM were supported by the DLR grant FuE-Projekt “ISS LIFE” (Programm RF-FuW, Teilprogramm 475). DM and AA were supported by German Aerospace Center—Space Administration (DLR) within the project “Investigation of antimicrobial metal surfaces under space conditions—An effective strategy to prevent microbial biofilm formation” (project number 50WB1930). LM and RH were supported by the European Space Agency (ESA-PRODEX) and the Belgian Science Policy (Belspo) through the BIOFILMS project (C4000129318). RLM was supported by NASA Space Biology grant 80NSSC18K0751 (BIOFILMS) to the Bay Area Environmental Research Institute.

ACKNOWLEDGMENTS

We would like to thank the team of the Aerospace Microbiology Group at the German Aerospace Center (DLR) in Cologne (Köln) namely, Andrea Schröder, Stella Koch, Erika Muratov, Marta Cortesao, Yen Ly and Katharina Runzheimer for their help in the preparation and performance of the pre-flight tests such as SVT and EST. We express our gratitude to Elisabeth Grohmann for cordially providing the *Staphylococcus capitis* subsp. *capitis* strain. This research is part of the PhD theses of KS, DM, and LM.

SUPPLEMENTARY MATERIAL

The Supplementary Material for this article can be found online at: https://www.frontiersin.org/articles/10.3389/frspt.2021.773244/full#supplementary-material

REFERENCES

Ali, M. M., Provoost, A., Maertens, L., Leys, N., Monsieurs, P., Charlier, D., et al. (2019). Genomic and Transcriptomic Changes that Mediate Increased Platinum Resistance in *Cupriavidus metallidurans*. *Genes* 10 (1), 63. doi:10.3390/genes10010063

Aponte, V. M., Finch, D. S., and Klaus, D. M. (2006). Considerations for Non-invasive In-Flight Monitoring of Astronaut Immune Status with Potential Use of MEMS and NEMS Devices. *Life Sci.* 79 (14), 1317–1333. doi:10.1016/j.lfs.2006.04.007

Argüello, J. M., Raimunda, D., and Padilla-Benavides, T. (2013). Mechanisms of Copper Homeostasis in Bacteria. *Front. Cel. Infect. Microbiol.* 3, 73. doi:10.3389/fcimb.2013.00073

Balasubramanian, R., Kenney, G. E., and Rosenzweig, A. C. (2011). Dual Pathways for Copper Uptake by Methanotrophic Bacteria. *J. Biol. Chem.* 286 (43), 37313–37319. doi:10.1074/jbc.M111.284984

Bastos, C. A. P., Faria, N., Wills, J., Malmberg, P., Scheers, N., Rees, P., et al. (2020). Copper Nanoparticles Have Negligible Direct Antibacterial Impact. *NanoImpact* 17, 100192. doi:10.1016/j.impact.2019.100192

Be, N. A., Avila-Herrera, A., Allen, J. E., Singh, N., Checinska Sielaff, A., Jaing, C., et al. (2017). Whole Metagenome Profiles of Particulates Collected from the

International Space Station. *Microbiome* 5 (1), 81. doi:10.1186/s40168-017-0292-4

Boinovich, L. B., Kaminsky, V. V., Domantovsky, A. G., Emelyanenko, K. A., Aleshkin, A. V., Zulkarneev, E. R., et al. (2019). Bactericidal Activity of Superhydrophobic and Superhydrophilic Copper in Bacterial Dispersions. *Langmuir* 35 (7), 2832–2841. doi:10.1021/acs.langmuir.8b03817

Bozzola, J. J., and Russell, L. D. (1999). *Electron Microscopy: Principles and Techniques for Biologists*. Burlington: Jones & Bartlett Learning.

Bruce, R. J., Ott, C. M., Skuratov, V. M., and Pierson, D. L. (2005). Microbial Surveillance of Potable Water Sources of the International Space Station. *SAE Tech. Paper* 114, 283–292. doi:10.4271/2005-01-2886

Byrd, A. L., Belkaid, Y., and Segre, J. A. (2018). The Human Skin Microbiome. *Nat. Rev. Microbiol.* 16 (3), 143–155. doi:10.1038/nrmicro.2017.157

Checinska, A., Probst, A. J., Vaishampayan, P., White, J. R., Kumar, D., Stepanov, V. G., et al. (2015). Microbiomes of the Dust Particles Collected from the International Space Station and Spacecraft Assembly Facilities. *Microbiome* 3, 50. doi:10.1186/s40168-015-0116-3

Cockell, C. S., Santomartino, R., Finster, K., Waajen, A. C., Eades, L. J., Moeller, R., et al. (2020). Space Station Biomining experiment Demonstrates Rare Earth Element Extraction in Microgravity and Mars Gravity. *Nat. Commun.* 11 (1), 5523. doi:10.1038/s41467-020-19276-w

Crabbé, A., Schurr, M. J., Monsieurs, P., Morici, L., Schurr, J., Wilson, J. W., et al. (2011). Transcriptional and Proteomic Responses of *Pseudomonas aeruginosa* PAO1 to Spaceflight Conditions Involve Hfq Regulation and Reveal a Role for Oxygen. *Appl. Environ. Microbiol.* 77 (4), 1221–1230. doi:10.1128/AEM.01582-10

Crucian, B., Babiak-Vazquez, A., Johnston, S., Pierson, D., Ott, C. M., and Sams, C. (2016). Incidence of Clinical Symptoms during Long-Duration Orbital Spaceflight. *Int. J. Gen. Med.* 9, 383–391. doi:10.2147/ijgm.S114188

Cui, B., Smooker, P. M., Rouch, D. A., Daley, A. J., and Deighton, M. A. (2013). Differences between Two Clinical *Staphylococcus Capitis* Subspecies as Revealed by Biofilm, Antibiotic Resistance, and Pulsed-Field Gel Electrophoresis Profiling. *J. Clin. Microbiol.* 51 (1), 9–14. doi:10.1128/JCM.05124-11

Davey, H. M. (2011). Life, Death, and In-Between: Meanings and Methods in Microbiology. *Appl. Environ. Microbiol.* 77 (16), 5571–5576. doi:10.1128/AEM.00744-11

Dopp, E., Richard, J., Dwidjosiswojo, Z., Simon, A., and Wingender, J. (2017). Influence of the Copper-Induced Viable but Non-culturable State on the Toxicity of *Pseudomonas aeruginosa* towards Human Bronchial Epithelial Cells *In Vitro*. *Int. J. Hyg. Environ. Health* 220 (8), 1363–1369. doi:10.1016/j.ijheh.2017.09.007

Dwidjosiswojo, Z., Richard, J., Moritz, M. M., Dopp, E., Flemming, H.-C., and Wingender, J. (2011). Influence of Copper Ions on the Viability and Cytotoxicity of *Pseudomonas aeruginosa* under Conditions Relevant to Drinking Water Environments. *Int. J. Hyg. Environ. Health* 214, 485–492. doi:10.1016/j.ijheh.2011.06.004

Ekici, S., Yang, H., Koch, H.-G., and Daldal, F. (2012). Novel Transporter Required for Biogenesis of Cbb 3 -Type Cytochrome C Oxidase in Rhodobacter Capsulatus. *mBio* 3 (1), 1–11. doi:10.1128/mBio.00293-11

Flemming, H.-C., Wingender, J., Szewzyk, U., Steinberg, P., Rice, S. A., and Kjelleberg, S. (2016). Biofilms: an Emergent Form of Bacterial Life. *Nat. Rev. Microbiol.* 14 (9), 563–575. doi:10.1038/nrmicro.2016.94

Hahn, C., Hans, M., Hein, C., Mancinelli, R. L., Mücklich, F., Wirth, R., et al. (2017). Pure and Oxidized Copper Materials as Potential Antimicrobial Surfaces for Spaceflight Activities. *Astrobiology* 17 (12), 1183–1191. doi:10.1089/ast.2016.1620

Hans, M., Erbe, A., Mathews, S., Chen, Y., Solioz, M., and Mücklich, F. (2013). Role of Copper Oxides in Contact Killing of Bacteria. *Langmuir* 29 (52), 16160–16166. doi:10.1021/la404091z

Hans, M., Támara, J. C., Mathews, S., Bax, B., Hegetschweiler, A., Kautenburger, R., et al. (2014). Laser Cladding of Stainless Steel with a Copper-Silver alloy to Generate Surfaces of High Antimicrobial Activity. *Appl. Surf. Sci.* 320, 195–199. doi:10.1016/j.apsusc.2014.09.069

Helbig, R., Günther, D., Friedrichs, J., Rößler, F., Lasagni, A., and Werner, C. (2016). The Impact of Structure Dimensions on Initial Bacterial Adhesion. *Biomater. Sci.* 4 (7), 1074–1078. doi:10.1039/C6BM00078A

Henriksen, S. D. (1973). Moraxella, Acinetobacter, and the Mimeae. *Bacteriol. Rev.* 37 (4), 522–561. doi:10.1128/br.37.4.522-561.1973

Horneck, G., Klaus, D. M., and Mancinelli, R. L. (2010). Space Microbiology. *Microbiol. Mol. Biol. Rev.* 74 (1), 121–156. doi:10.1128/MMBR.00016-09

Ilyin, V. K. (2005). Microbiological Status of Cosmonauts during Orbital Spaceflights on Salyut and Mir Orbital Stations. *Acta Astronautica* 56 (9-12), 839–850. doi:10.1016/j.actaastro.2005.01.009

Janssen, P. J., Van Houdt, R., Moors, H., Monsieurs, P., Morin, N., Michaux, A., et al. (2010). The Complete Genome Sequence of *Cupriavidus metallidurans* Strain CH34, a Master Survivalist in Harsh and Anthropogenic Environments. *PLoS One* 5 (5), e10433. doi:10.1371/journal.pone.0010433

Karnovsky, M. J. (1965). A Formaldehyde Glutaraldehyde Fixative of High Osmolality for Use in Electron Microscopy. *J. Cel Biol* 27 (2), 1A–149A. Abstracts of Papers Presented at the Fifth Annual Meeting: The American Society for Cell Biology.

Karpanen, T. J., Casey, A. L., Lambert, P. A., Cookson, B. D., Nightingale, P., Miruszenko, L., et al. (2012). The Antimicrobial Efficacy of Copper Alloy Furnishing in the Clinical Environment: A Crossover Study. *Infect. Control. Hosp. Epidemiol.* 33 (1), 3–9. doi:10.1086/663644

Kim, W., Tengra, F. K., Young, Z., Shong, J., Marchand, N., Chan, H. K., et al. (2013). Spaceflight Promotes Biofilm Formation by *Pseudomonas aeruginosa*. *PLoS One* 8 (4), e62437. doi:10.1371/journal.pone.0062437

Klintworth, R., Reher, H. J., Viktorov, A. N., and Bohle, D. (1999). Biological Induced Corrosion of Materials II: New Test Methods and Experiences from MIR Station. *Acta Astronaut* 44 (7-12), 569–578. doi:10.1016/s0094-5765(99)00069-7

Kloos, W. E., and Schleifer, K. H. (1975). Isolation and Characterization of Staphylococci from Human Skin II. Descriptions of Four New Species: *Staphylococcus warneri, Staphylococcus capitis, Staphylococcus hominis, and Staphylococcus simulans*. *Int. J. Syst. Bacteriol.* 25(1), 62–79. doi:10.1099/00207713-25-1-62

Koo, H., Allan, R. N., Howlin, R. P., Stoodley, P., and Hall-Stoodley, L. (2017). Targeting Microbial Biofilms: Current and Prospective Therapeutic Strategies. *Nat. Rev. Microbiol.* 15 (12), 740–755. doi:10.1038/nrmicro.2017.99

La Duc, M. T., Nicholson, W., Kern, R., and Venkateswaran, K. (2003). Microbial Characterization of the Mars Odyssey Spacecraft and its Encapsulation Facility. *Environ. Microbiol.* 5 (10), 977–985. doi:10.1046/j.1462-2920.2003.00496.x

Lang, J. M., Coil, D. A., Neches, R. Y., Brown, W. E., Cavalier, D., Severance, M., et al. (2017). A Microbial Survey of the International Space Station (ISS). *PeerJ* 5, e4029. doi:10.7717/peerj.4029

Lasseur, C., Brunet, J., de Weever, H., Dixon, M., Dussap, G., Godia, F., et al. (2010). MELiSSA: The European Project of Closed Life Support System. *Grav Space Biol.* 23 (2), 3–12.

Lemire, J. A., Harrison, J. J., and Turner, R. J. (2013). Antimicrobial Activity of Metals: Mechanisms, Molecular Targets and Applications. *Nat. Rev. Microbiol.* 11 (6), 371–384. doi:10.1038/nrmicro3028

Leys, N., Baatout, S., Rosier, C., Dams, A., s'Heeren, C., Wattiez, R., et al. (2009). The Response of *Cupriavidus metallidurans* CH34 to Spaceflight in the International Space Station. *Antonie Van Leeuwenhoek* 96 (2), 227–245. doi:10.1007/s10482-009-9360-5

Li, J., Liu, F., Wang, Q., Ge, P., Woo, P. C. Y., Yan, J., et al. (2014a). Genomic and Transcriptomic Analysis of NDM-1 *Klebsiella pneumoniae* in Spaceflight Reveal Mechanisms Underlying Environmental Adaptability. *Sci. Rep.* 4, 6216. doi:10.1038/srep06216

Li, L., Mendis, N., Trigui, H., Oliver, J. D., and Faucher, S. P. (2014b). The Importance of the Viable but Non-culturable State in Human Bacterial Pathogens. *Front. Microbiol.* 5, 258. doi:10.3389/fmicb.2014.00258

Li, Y.-H., and Tian, X. (2012). Quorum sensing and Bacterial Social Interactions in Biofilms. *Sensors* 12 (3), 2519–2538. doi:10.3390/s120302519

Loudon, C.-M., Nicholson, N., Finster, K., Leys, N., Byloos, B., Van Houdt, R., et al. (2018). BioRock: New Experiments and Hardware to Investigate Microbe-mineral Interactions in Space. *Int. J. Astrobiology* 17 (4), 303–313. doi:10.1017/S1473550417000234

Luo, J., Hein, C., Ghanbaja, J., Pierson, J.-F., and Mücklich, F. (2019). Bacteria Accumulate Copper Ions and Inhibit Oxide Formation on Copper Surface during Antibacterial Efficiency Test. *Micron* 127, 102759. doi:10.1016/j.micron.2019.102759

Lutkenhaus, J. F. (1977). Role of a Major Outer Membrane Protein in *Escherichia coli*. *J. Bacteriol.* 131 (2), 631–637. doi:10.1128/jb.131.2.631-637.1977

Maertens, L., Coninx, I., Claesen, J., Leys, N., Matroule, J.-Y., and Van Houdt, R. (2020). Copper Resistance Mediates Long-Term Survival of Cupriavidus Metallidurans in Wet Contact with Metallic Copper. *Front. Microbiol.* 11, 1208. doi:10.3389/fmicb.2020.01208

Maertens, L., Matroule, J.-Y., and Van Houdt, R. (2021). Characteristics of the Copper-induced Viable-but-non-culturable State in Bacteria. *World J. Microbiol. Biotechnol.* 37 (3), 1–9. doi:10.1007/s11274-021-03006-5

Maikranz, E., Spengler, C., Thewes, N., Thewes, A., Nolle, F., Jung, P., et al. (2020). Different Binding Mechanisms of *Staphylococcus aureus* to Hydrophobic and Hydrophilic Surfaces. *Nanoscale* 12 (37), 19267–19275. doi:10.1039/d0nr03134h

Martí, S., Rodríguez-Baño, J., Catel-Ferreira, M., Jouenne, T., Vila, J., Seifert, H., et al. (2011). Biofilm Formation at the Solid-Liquid and Air-Liquid Interfaces by *Acinetobacter* Species. *BMC Res. Notes* 4 (1), 5. doi:10.1186/1756-0500-4-5

Mastroleo, F., Van Houdt, R., Atkinson, S., Mergeay, M., Hendrickx, L., Wattiez, R., et al. (2013). Modelled Microgravity Cultivation Modulates N-Acylhomoserine Lactone Production in *Rhodospirillum rubrum* S1H Independently of Cell Density. *Microbiology* 159 (Pt 12), 2456–2466. doi:10.1099/mic.0.066415-0

Mathews, S., Hans, M., Mücklich, F., and Solioz, M. (2013). Contact Killing of Bacteria on Copper Is Suppressed if Bacterial-Metal Contact Is Prevented and Is Induced on Iron by Copper Ions. *Appl. Environ. Microbiol.* 79 (8), 2605–2611. doi:10.1128/aem.03608-12

McCoy, K. B., Derecho, I., Wong, T., Tran, H. M., Huynh, T. D., La Duc, M. T., et al. (2012). Insights into the Extremotolerance of *Acinetobacter radioresistens 50v1*, a Gram-Negative Bacterium Isolated from the Mars Odyssey Spacecraft. *Astrobiology* 12 (9), 854–862. doi:10.1089/ast.2012.0835

McLean, R. J. C., Cassanto, J. M., Barnes, M. B., and Koo, J. H. (2001). Bacterial Biofilm Formation under Microgravity Conditions. *FEMS Microbiol. Lett.* 195 (2), 115–119. doi:10.1111/j.1574-6968.2001.tb10507.x

Mergeay, M., Houba, C., and Gerits, J. (1978). Extrachromosomal Inheritance Controlling Resistance to Cadmium, Cobalt, Copper and Zinc Ions: Evidence from Curing in a Pseudomonas [proceedings]. *Arch. Int. Physiol. Biochim.* 86 (2), 440–442. PMID: 81018.

Mijnendonckx, K., Ali, M. M., Provoost, A., Janssen, P., Mergeay, M., Leys, N., et al. (2019). Spontaneous Mutation in the AgrRS Two-Component Regulatory System of *Cupriavidus metallidurans* results in Enhanced Silver Resistance. *Metallomics* 11 (11), 1912–1924. doi:10.1039/c9mt00123a

Mijnendonckx, K., Provoost, A., Ott, C. M., Venkateswaran, K., Mahillon, J., Leys, N., et al. (2013). Characterization of the Survival Ability of *Cupriavidus metallidurans* and *Ralstonia rickettii* from Space-Related Environments. *Microb. Ecol.* 65 (2), 347–360. doi:10.1007/s00248-012-0139-2

Mogul, R., Barding, G. A., Jr., Lalla, S., Lee, S., Madrid, S., Baki, R., et al. (2018). Metabolism and Biodegradation of Spacecraft Cleaning Reagents by Strains of Spacecraft-Associated *Acinetobacter*. *Astrobiology* 18 (12), 1517–1527. doi:10.1089/ast.2017.1814

Monsieurs, P., Hobman, J., Vandenbussche, G., Mergeay, M., and Van Houdt, R. (2015). "Response of *Cupriavidus metallidurans* CH34 to Metals," in *Metal Response in Cupriavidus metallidurans*. Editors M. Mergeay, and R. Van Houdt (Switzerland: Springer International Publishing), 45–89. doi:10.1007/978-3-319-20594-6_3

Monsieurs, P., Moors, H., Van Houdt, R., Janssen, P. J., Janssen, A., Coninx, I., et al. (2011). Heavy Metal Resistance in *Cupriavidus metallidurans* CH34 Is Governed by an Intricate Transcriptional Network. *Biometals* 24 (6), 1133–1151. doi:10.1007/s10534-011-9473-y

Mora, M., Perras, A., Alekhova, T. A., Wink, L., Krause, R., Aleksandrova, A., et al. (2016). Resilient Microorganisms in Dust Samples of the International Space Station-Survival of the Adaptation Specialists. *Microbiome* 4 (65), 1–21. doi:10.1186/s40168-016-0217-7

Mora, M., Wink, L., Kögler, I., Mahnert, A., Rettberg, P., Schwendner, P., et al. (2019). Space Station Conditions Are Selective but Do Not Alter Microbial Characteristics Relevant to Human Health. *Nat. Commun.* 10 (1), 3990. doi:10.1038/s41467-019-11682-z

Müller, D. W., Fox, T., Grützmacher, P. G., Suarez, S., and Mücklich, F. (2020a). Applying Ultrashort Pulsed Direct Laser Interference Patterning for Functional Surfaces. *Sci. Rep.* 10 (1), 3647. doi:10.1038/s41598-020-60592-4

Müller, D. W., Holtsch, A., Lößlein, S., Pauly, C., Spengler, C., Grandthyll, S., et al. (2020b). In-Depth Investigation of Copper Surface Chemistry Modification by Ultrashort Pulsed Direct Laser Interference Patterning. *Langmuir* 36 (45), 13415–13425. doi:10.1021/acs.langmuir.0c01625

Müller, D. W., Lößlein, S., Terriac, E., Brix, K., Siems, K., Moeller, R., et al. (2021). Increasing Antibacterial Efficiency of Cu Surfaces by Targeted Surface Functionalization via Ultrashort Pulsed Direct Laser Interference Patterning. *Adv. Mater. Inter.* 8 (5), 2001656. doi:10.1002/admi.202001656

Novikova, N., De Boever, P., Poddubko, S., Deshevaya, E., Polikarpov, N., Rakova, N., et al. (2006). Survey of Environmental Biocontamination on Board the International Space Station. *Res. Microbiol.* 157 (1), 5–12. doi:10.1016/j.resmic.2005.07.010

Noyce, J. O., Michels, H., and Keevil, C. W. (2006). Use of Copper Cast Alloys to Control *Escherichia coli* O157 Cross-Contamination during Food Processing. *Appl. Environ. Microbiol.* 72 (6), 4239–4244. doi:10.1128/AEM.02532-05

Peleg, A. Y., Seifert, H., and Paterson, D. L. (2008). Acinetobacter Baumannii : Emergence of a Successful Pathogen. *Clin. Microbiol. Rev.* 21 (3), 538–582. doi:10.1128/cmr.00058-07

Perrin, E., Bacci, G., Garrelly, L., Canganella, F., Bianconi, G., Fani, R., et al. (2018). Furnishing Spaceship Environment: Evaluation of Bacterial Biofilms on Different Materials Used inside International Space Station. *Res. Microbiol.* 169 (6), 289–295. doi:10.1016/j.resmic.2018.04.001

Romsdahl, J., Blachowicz, A., Chiang, A. J., Singh, N., Stajich, J. E., Kalkum, M., et al. (2018). Characterization of *Aspergillus niger* Isolated from the International Space Station. *mSystems* 3 (5), e00112–18. doi:10.1128/mSystems.00112-18

Schottroff, F., Fröhling, A., Zunabovic-Pichler, M., Krottenthaler, A., Schlüter, O., and Jäger, H. (2018). Sublethal Injury and Viable but Non-culturable (VBNC) State in Microorganisms during Preservation of Food and Biological Materials by Non-thermal Processes. *Front. Microbiol.* 9, 2773. doi:10.3389/fmicb.2018.02773

Seuylemezian, A., Vaishampayan, P., Cooper, K., and Venkateswaran, K. (2018). Draft Genome Sequences of *Acinetobacter* and *Bacillus* Strains Isolated from Spacecraft-Associated Surfaces. *Genome Announc* 6 (6), e01554–17. doi:10.1128/genomeA.01554-17

Singh, N. K., Wood, J. M., Karouia, F., and Venkateswaran, K. (2018). Succession and Persistence of Microbial Communities and Antimicrobial Resistance Genes Associated with International Space Station Environmental Surfaces. *Microbiome* 6 (1), 204. doi:10.1186/s40168-018-0585-2

Singh, N., and Wade, J. T. (2014). Identification of Regulatory RNA in Bacterial Genomes by Genome-Scale Mapping of Transcription Start Sites. *Methods Mol. Biol.* 1103, 1–10. doi:10.1007/978-1-62703-730-3_1

Singh, S., Singh, S. K., Chowdhury, I., and Singh, R. (2017). Understanding the Mechanism of Bacterial Biofilms Resistance to Antimicrobial Agents. *Tomicroj* 11, 53–62. doi:10.2174/1874285801711010053

Sobisch, L.-Y., Rogowski, K. M., Fuchs, J., Schmieder, W., Vaishampayan, A., Oles, P., et al. (2019). Biofilm Forming Antibiotic Resistant Gram-Positive Pathogens Isolated from Surfaces on the International Space Station. *Front. Microbiol.* 10, 543. doi:10.3389/fmicb.2019.00543

Sonnenfeld, G., Butel, J. S., and Shearer, W. T. (2003). Effects of the Space Flight Environment on the Immune System. *Rev. Environ. Health* 18 (1), 1–18. doi:10.1515/reveh.2003.18.1.1

Sonnenfeld, G., and Shearer, W. T. (2002). Immune Function during Space Flight. *Nutrition* 18 (10), 899–903. doi:10.1016/s0899-9007(02)00903-6

Sun, C., Li, Y., Li, Z., Su, Q., Wang, Y., and Liu, X. (20182018). Durable and Washable Antibacterial Copper Nanoparticles Bridged by Surface Grafting Polymer Brushes on Cotton and Polymeric Materials. *J. Nanomater.* 2018, 1–7. doi:10.1155/2018/6546193

Towner, K. J., Bergogne-Bérézin, E., and Fewson, C. (2013). *The Biology of Acinetobacter: Taxonomy, Clinical Importance, Molecular Biology, Physiology, Industrial Relevance*. Luxemburg: Springer Science & Business Media.

Tripathy, A., Kumar, A., Sreedharan, S., Muralidharan, G., Pramanik, A., Nandi, D., et al. (2018). Fabrication of Low-Cost Flexible Superhydrophobic Antibacterial Surface with Dual-Scale Roughness. *ACS Biomater. Sci. Eng.* 4 (6), 2213–2223. doi:10.1021/acsbiomaterials.8b00209

Tripathy, A., Sen, P., Su, B., and Briscoe, W. H. (2017). Natural and Bioinspired Nanostructured Bactericidal Surfaces. *Adv. Colloid Interf. Sci.* 248, 85–104. doi:10.1016/j.cis.2017.07.030

Urbaniak, C., Sielaff, A. C., Frey, K. G., Allen, J. E., Singh, N., Jaing, C., et al. (2018). Detection of Antimicrobial Resistance Genes Associated with the International

Space Station Environmental Surfaces. *Sci. Rep.* 8 (1), 814. doi:10.1038/s41598-017-18506-4

Van Houdt, R., and Leys, N. (2020). “Monitoring the Microbial Burden in Manned Space Stations,” in *Stress Challenges and Immunity in Space*. Editor A. Chouker (Springer), 463–475. doi:10.1007/978-3-030-16996-1_25

Van Houdt, R., Mijnendonckx, K., and Leys, N. (2012). Microbial Contamination Monitoring and Control during Human Space Missions. *Planet. Space Sci.* 60 (1), 115–120. doi:10.1016/j.pss.2011.09.001

Van Houdt, R., Vandecraen, J., Leys, N., Monsieurs, P., and Aertsen, A. (2021). Adaptation of *Cupriavidus metallidurans* CH34 to Toxic Zinc Concentrations Involves an Uncharacterized ABC-type Transporter. *Microorganisms* 9 (2), 309. doi:10.3390/microorganisms9020309

Vandamme, P., and Coenye, T. (2004). Taxonomy of the Genus Cupriavidus: a Tale of Lost and Found. *Int. J. Syst. Evol. Microbiol.* 54 (6), 2285–2289. doi:10.1099/ijs.0.63247-0

Venkateswaran, K., Vaishampayan, P., Cisneros, J., Pierson, D. L., Rogers, S. O., and Perry, J. (2014). International Space Station Environmental Microbiome - Microbial Inventories of ISS Filter Debris. *Appl. Microbiol. Biotechnol.* 98 (14), 6453–6466. doi:10.1007/s00253-014-5650-6

Vincent, M., Duval, R. E., Hartemann, P., and Engels-Deutsch, M. (2018). Contact Killing and Antimicrobial Properties of Copper. *J. Appl. Microbiol.* 124 (5), 1032–1046. doi:10.1111/jam.13681

Vincent, M., Hartemann, P., and Engels-Deutsch, M. (2016). Antimicrobial Applications of Copper. *Int. J. Hyg. Environ. Health* 219 (7 Pt A), 585–591. doi:10.1016/j.ijheh.2016.06.003

Wilks, S. A., Michels, H., and Keevil, C. W. (2005). The Survival of *Escherichia coli* O157 on a Range of Metal Surfaces. *Int. J. Food Microbiol.* 105 (3), 445–454. doi:10.1016/j.ijfoodmicro.2005.04.021

Zea, L., Larsen, M., Estante, F., Qvortrup, K., Moeller, R., Dias de Oliveira, S., et al. (2017). Phenotypic Changes Exhibited by *E. coli* Cultured in Space. *Front. Microbiol.* 8, 1598. doi:10.3389/fmicb.2017.01598

Zea, L., McLean, R. J. C., Rook, T. A., Angle, G., Carter, D. L., Delegard, A., et al. (2020). Potential Biofilm Control Strategies for Extended Spaceflight Missions. *Biofilm* 2, 100026. doi:10.1016/j.bioflm.2020.100026

Zea, L., Nisar, Z., Rubin, P., Cortesão, M., Luo, J., McBride, S. A., et al. (2018). Design of a Spaceflight Biofilm experiment. *Acta Astronautica* 148, 294–300. doi:10.1016/j.actaastro.2018.04.039

Conflict of Interest: The authors declare that the research was conducted in the absence of any commercial or financial relationships that could be construed as a potential conflict of interest.

Supplementary Material

Testing Laser-Structured Antimicrobial Surfaces Under Space Conditions: The Design of the ISS Experiment BIOFILMS

Supplementary Table 1: Overview of BIOFILMS SVT results. Following science success criteria were validate: A) Successful integration of samples (5 metal plates per hardware) and fluids into experiment units (0.25 mL bacteria suspended in buffer in bacteria reservoir, 2.1 mL growth medium in medium reservoir and 2.1 mL chemical fixative in fixative reservoir). B) Successful filling of the cultural chambers with growth media (activation of experiment). C) Successful termination of experiments with injection of fixative into the respective culture chamber (termination of experiment). D) Successful growth and evenly distributed biofilm formation in chambers including steel sample plates (Biofilm formation was rated after viewing fluorescence microscopic images as: +++ very strong; ++ strong; + moderate; ~ weak; 0 no biofilm). E) Traces of bacteria in the chambers containing copper and brass samples. F) Successful completion of experiment without contamination by other bacteria.

				Science success criteria						
#	**Surface**	**Treatment**	**Bacteria**	**A**	**B**	**B**	**D**	**E**	**F**	**Damage to membrane**
1	Stainless Steel	polished	*S. capitis*	yes	yes	yes	+++	/	yes	no
2	Stainless Steel	polished	*C. metallidurans*	yes	yes	yes	+/~	/	yes	no
3	Stainless Steel	polished	*A. radioresistens*	yes	yes	yes	+++	/	yes	no
4	Stainless Steel	polished	Blank	yes	yes	yes	0	/	yes	no
5	Stainless Steel	patterned	*S. capitis*	yes	yes	yes	+	/	no	no
6	Stainless Steel	polished	*C. metallidurans*	yes	yes	yes	~	/	yes	no
7	Stainless Steel	patterned	*A. radioresistens*	yes	yes	yes	++	/	yes	no
8	Stainless Steel	patterned	Blank	yes	yes	yes	0	/	yes	no
9	Copper	polished	*S. capitis*	yes	yes	yes	contamination	yes	no	no
10	Copper	polished	*C. metallidurans*	yes	yes	yes	+++	yes	yes	no
11	Copper	polished	*A. radioresistens*	yes	yes	yes	+/++	yes	yes	no
12	Copper	polished	Blank	yes	yes	yes	0	/	yes	no
13	Copper	patterned	*S. capitis*	yes	yes	yes	0	yes	yes	no
14	Copper	patterned	*C. metallidurans*	yes	yes	yes	++	yes	yes	no
15	Copper	patterned	*A. radioresistens*	yes	yes	yes	+	yes	yes	no
16	Copper	patterned	Blank	yes	yes	yes	0	/	yes	no
17	Brass	polished	*S. capitis*	yes	yes	yes	~	yes	yes	no
18	Brass	polished	*C. metallidurans*	yes	yes	yes	~	yes	yes	no
19	Brass	polished	*A. radioresistens*	yes	yes	yes	0	yes	yes	no
20	Brass	polished	Blank	yes	yes	yes (2h later)	0	/	yes	no
21	Brass	patterned	*S. capitis*	yes	yes	yes	0	yes	yes	no
22	Brass	patterned	*C. metallidurans*	yes	yes	yes	0	yes	yes	no
23	Brass	patterned	*A. radioresistens*	yes	yes	yes (2h later)	0	yes	yes	no
24	Brass	patterned	Blank	yes	yes	yes (2h later)	0	/	yes	no
25	Stainless Steel	patterned	*C. metallidurans*	yes	yes	yes	~	yes	yes	no

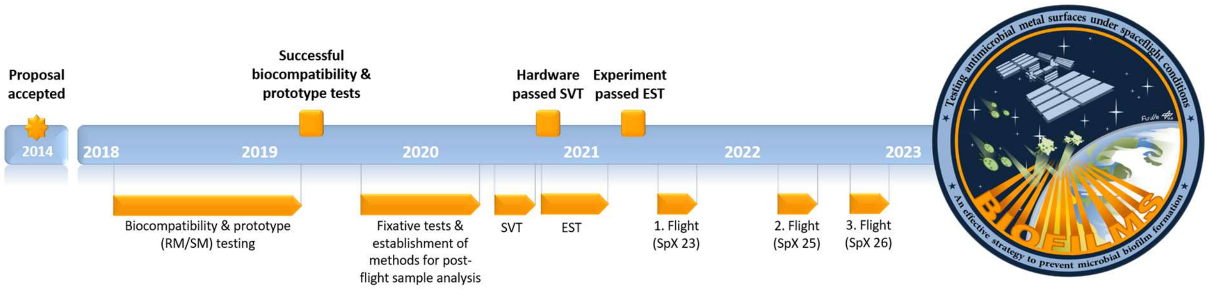

Supplementary Figure 1: project timeline and flight plan for BIOFILMS (state of late 2021)

VI | Conclusions and Outlook

The central scope of this dissertation is the investigation on how functional surface modification by ultrashort pulsed laser interference can be utilized to improve the antibacterial efficacy of actively bactericidal Cu surfaces. This involves the development of an ultrashort pulsed laser interference based processing methodology (USP-DLIP) for the design and production of deterministic surface patterns in the low µm and sub-µm scale to effectively modify bacterial contact conditions on technical surfaces in Objective (A). Since bacterial surface interaction was shown to be similarly influenced by physicochemical surface properties a central aspect of the investigation focuses the chemical and microstructural modification of the superficial Cu substrate as well as its functional surface properties in Objective (B). Based on a fundamental understanding of laser-induced surface modification, the integrated impact of USP-DLIP on the antimicrobial efficacy of actively bactericidal Cu is examined in Objective (C). The key findings of this work are summarized below in allocation to the respective objectives.

Objective (A): Process Development

In the initial phase of this research, an optical setup that enables the generation of laser interference at ultrashort pulse durations down to 100 fs for the processing of technical substrates was successfully developed. The high power density of the ultrashort pulses in the NIR wavelength spectrum was shown to allow for processing of a broad range of different material classes, including metals, dielectrics, ceramics, and glass (the latter by means of multi-photon absorption due to the high bandgaps). With a spectrum of line-like pattern periodicities between < 0.7 µm and > 10 µm, the technical requirements for further investigation according to the scope of this work, were successfully met.

Pattern formation on metals by USP-DLIP

In addition to establishing the proof of concept for the machinability of different material classes, a particular emphasis was placed on investigating the laser/material interaction involved in pattern shaping by USP-DLIP. The design of the primary DLIP pattern geometry was found to be adjustable by the laser fluence applied in USP-DLIP, where ablation area width follows the material specific ablation threshold with respect to spatial intensity modulation by interference. In addition, material specific thermal interaction in response to USP-irradiation is shown to exert an individual impact on pattern geometries, which is especially the case for metals. To this end, a 2D finite element method (FEM) simulation model was introduced and further developed to reproduce the thermal interaction of metallic substrates in response to ultrashort pulse durations in conjunction with an interference-modulated energy input and localized deviation of laser absorption. The TTM-based numerical model supported the assessment of the influence of pulse-wise laser/material interaction on the formation of the pattern geometry and surface morphology on metals, as well as (USP-)DLIP-specific incubation effects on Cu.

In terms of USP-DLIP-specific pattern formation on Cu, the two USP ablation mechanisms of thermomechanical spallation and photothermal phase explosion observed for Cu could be shown to exert a considerable influence on the pattern geometry through the formation of distinctive ablation-related sub-patterns. The sub-pattern superimposes the primary DLIP pattern where both might eventually merge with an increasing number of overlapping pulses. This exerts and either constructive or destructive impact on the primary DLIP pattern at pattern periodicities in the low and sub-µm range. Targeted parametrization including low- to mid-regime fluences as well as beam polarization could be shown to allow for an exploitation of the topography shaping effects of sub-pattern and primary pattern interaction alongside multi-pulsed USP-DLIP, supplemented by in-depth analyzation further addressed in Objective (B). Based on this, pattern scale specific processing strategies for Cu surfaces were developed including the superimposed sub-pattern morphology in the targeted surface design to influence quantitative bacteria/surface contact.

Objective (B): Targeted Substrate Modification

Referring to the state of research on bacteria/surface interaction, a potential multi-level impact of physicochemical surface modification by USP-DLIP was comprehensively considered on bacterial interaction. This includes chemical and microstructural modification of the Cu substrate and its respective impact on laser/material interaction and functional surface properties. A thermal induction of enhanced surface oxidation could not be observed, where process-related modification of the surface chemistry is found to predominantly occur through the ballistic redeposition of ablated matter, instead. Redeposition leads to the accumulation of a nm-scaled oxidic surface layer that is preferentially allocated at the exposed structural peaks, resulting in heterogeneous surface properties between topographic peaks and valleys. Surface oxides exhibit a predominant phase composition of Cu_2O and were shown to be easily detachable by mild etching enabling the generation of a native oxidation state on USP-DLIP processed Cu surfaces. Irrespective of the post-treatment, the USP-DLIP surfaces accumulate functional C-groups on the surface over a passivation period of several weeks. This induced a transformation from hydrophilic to metastable (super-)hydrophobic wetting behavior. In addition to the reattachment of oxidic agglomerates, the eruptive removal of material alongside USP-DLIP process was found to impact the near-surface microstructure by thermomechanical defect implantation. The resulting superficial microstructure deformation is confined to a depth of a few µm and results in an increased density of GND and the formation of nanoscale grains.

The impact of the evidenced USP-DLIP associated modification of surface chemistry and microstructure on both laser/material interaction alongside laser processing as well as the functional surface wettability and corrosion behavior of Cu surfaces was further investigated.

Laser/material interaction in multi-pulsed USP-DLIP

The mutual impact of the determined chemical, topographic and microstructural substrate modification during USP-DLIP processing of Cu was revealed to induce a (USP-)DLIP specific incubation behavior. This involves a delicate impact of locally modulated absorption on surface morphology formation, which was integrated in a numerical model of localized absorption profiles. This novel approach revealed a notable divergence of DLIP-specific incubation to the Gaussian intensity profile based models that have previously been proposed. The observed mechanisms of incubation are considered subdivided between the individual modes of surface modification:

Chemical incubation: In case of NIR irradiation of Cu, oxide redeposition was shown to play a dominant role in the pulse-wise increase of laser absorption during continuous surface treatment. This can be attributed to the low band gaps of the Cu oxide phases Cu_2O (2.02 to 2.62 eV) and CuO (1.2 to 1.9 eV) ranging close to the electromagnetic energy level of NIR wavelengths, as well as a high surface/volume ratio of the redeposited oxide particle. The ablation mechanism applied in Cu processing was found to be highly involved in chemical incubation, where phase explosion induces higher levels of oxidic agglomerations compared to spallation under similar accumulated fluence. Hence, the impact of ablation kinetics on both primary and sub-pattern pattern formation is accompanied by a parallel enhancement of incubation mediated absorption further affecting the primary DLIP pattern stability with decreasing pattern size, which was considered in process design.

Topographic incubation: In addition to the general increase in absorption resulting from the modified surface chemistry, the progressive topography modification induces a polarization-dependent incubation effect. In both the primary DLIP and the secondary sub-pattern, the ablation area exhibits a pulse-wise broadening in the direction of the beam polarization vector. This behavior has a direct impact on the pattern geometry and sub-pattern formation and can be attributed to the preferential absorption of p-polarized radiation at topographic inclinations. Polarization dependent preferential absorptance was also found to be involved in USP-DLIP processing at increased incidence angles θ, where p-oriented beam polarization contributes to ablation and pattern formation in the sub-µm scale despite a low interference modulation contrast.

Microstructural incubation: In the low and mid-fluence regime relevant for USP-DLIP processing, a microstructure-related incubation effect relevant for processing cannot be determined. The initial NIR absorptance of Cu surfaces is found to be increased in case of a mechanically polished over a deformation free microstructure state. This effect was however found to parallelly involve a chemical impact on absorptance by an increased thickness of native oxide due to a higher superficial microstructure defect density. In the case of an almost deformation-free initial Cu surface, grain orientation-dependent incubation by defect accumulation was found to scale in the ratio of {111} > {110} >> {100} for low-index grain orientations. An increase of laser absorption by microstructure related incubation did not occur on mechanically pre-deformed as-polished surfaces.

The impact of USP-DLIP on the functional properties of Cu surfaces

Microstructure: Contrary to the low incubation effect during laser processing, the microstructure modification by USP-DLIP has a significant influence on functional surface properties. It could be shown that the laser-induced superficial microstructure deformation is directly related to the degree of hydrophobic wetting behavior of USP-DLIP surfaces after several weeks of passivation. The hydrophobicity on similar pattern geometries levels with the amount of accumulated microstructure deformation, including a shift between Cassie-Baxter and Wenzel wetting. The process-related microstructure modification was furthermore shown to induce a change in Cu corrosion from heterogeneous pitting involving the formation of galvanic microcells to a homogeneous surface attack in saline environment. The change in corrosion behavior is accompanied by enhanced surface passivation, which indicates an increase in corrosion resistance of Cu surfaces by USP-DLIP associated superficial microstructure modification.

Chemistry: The process-induced oxidic particle redeposition adds to corrosive passivating in saline environment by the formation of a thickened initial oxide layer that supports further oxide nucleation. The oxidic surface agglomerations were furthermore found to reinforce the hydrophobic character of passivated USP-DLIP Cu surfaces both by morphology and a higher proportion of C-C and C-H bonds within the accumulated functional C-groups.

Topography: USP-DLIP pattern geometry impacts surface wettability aside of the physicochemical impact of USP-DLIP processing in accordance to the Wenzel wetting theory. Hydrophobic wetting was found to scale with increasing pattern size between line-like surface patterns ranging in periodicity from 0.7 µm to 3 µm due to a parallel increase in overall surface area between the different patterns.

Objective (C): Antimicrobial Properties

Building on the examination of the topographic, chemical and microstructural Cu surface modification by USP-DLIP in Objective (A) and (B), the respective contribution of these individual impacts to the antibacterial efficacy of Cu substrates has been investigated in Objective (C). In fact, the bactericidal surface properties of Cu surfaces processed by USP-DLIP were shown to form a delicate relation to process-related impacts on the functional properties of the Cu substrate.

Surface wettability: In addition to an improved topographic bacteria/surface contact condition, surface wettability was identified as a primary factor contributing an enhancement in bactericidal activity by USP-DLIP processing. Line-like surface patterns of P = 3 µm exhibiting either hydrophilic or hydrophobic wettability were both found to increase antimicrobial efficacy against *E. coli*. However, the enhancement of the bactericidal effect on hydrophilic surfaces was limited to the extent of the topographically induced surface enlargement, whereas bacterial killing on the hydrophobic surfaces exceeded this extent. The effect of enhanced antimicrobial efficacy by hydrophobic surface wettability was found to occur independent of the quantitative proportion of Cu ions released.

Chemical bacteria/surface interaction: Bacterial exposure was shown to affect the Cu surfaces by chemical surface modification. This includes an increase of surface wettability of USP-DLIP surfaces by bacterial surface conditioning, as well as a catalyzation of Cu corrosion in saline environment. The latter induces a significant increase in Cu-ion release rate in the case of *E. coli* corresponding to the Cu-scavenging mechanism previously described. In *S. aureus* a catalytic effect on corrosion in saline environment is less pronounced, which appears to be linked to higher cell wall stability. Consequently, the release of Cu ions from USP-DLIP surfaces is reduced in comparison to mirror-polished reference surfaces in the case of *S. aureus* exposure, despite a larger surface area. This can be attributed to the passivating effect of the USP-DLIP surface treatment. The bacterial catalyzation of Cu corrosion was found to destabilize the process-induced agglomeration layer of oxide particles resulting in a considerable increase of Cu ion release compared to native oxidized USP-DLIP surfaces.

Microstructure: Under bacterial exposure, the superficial microstructure deformation induced by USP-DLIP remains a certain corrosion-inhibiting effect despite catalyzation of Cu corrosion. In contrast, Cu ion release is significantly increased on deformation-free USP-DLIP over reference surfaces exhibiting a grain orientation sensitive pitting mechanism in GI-XRD. In parallel, an elevated hydrophobicity on USP-DLIP Cu surfaces was found to level with an enhanced process induced deformation state of the superficial microstructure. Despite a significant deviation in quantitative Cu ion release, the antimicrobial efficacy in relation to the microstructure state of USP-DLIP Cu surfaces is again shown to correlate more dominantly with the level of hydrophobic wettability. The impact of microstructure modification by USP-DLIP on the bactericidal activity of Cu surfaces thus appears to be more related to its influence on physicochemical surface properties rather than corrosive modulation of quantitative Cu ion emission.

Topography: The topographical effect of varying geometric contact conditions on the antimicrobial efficacy against *E. coli* and *S. aureus* was determined by applying line-like USP-DLIP patterns slightly larger (P = 3 µm), equal (P = 1 µm) and smaller (P = 0.75 µm) than a single bacterial cell. Enhanced bacterial killing on USP-DLIP Cu surfaces is found to be directly attributable to the capacity of individual bacterial cells to establish a quantitative surface contact. Pattern geometries associated with an increased bactericidal efficacy are found to differ between the two bacterial strains, which was found to be connected to strain specific inter-cell interaction. *E. coli* was observed to be most efficiently deactivated on P = 1 µm patterns that enable a high single-cell contact. In contrast, the highest bactericidal activity against *S. aureus* was determined on P = 3 µm patterns. This appears to be related to the high affinity of *S. aureus* to form multi-cell clusters, which limits the capability of individual bacteria to establish a quantitative surface contact on P = 1 µm and P = 0.75 µm patterns.

P = 3 µm patterns in turn enable the intrusion of multi-cell clusters and thus to a higher overall bacteria/surface contact area. A topographic prevention of quantitative single cell contact was found to be accompanied by decreased antimicrobial efficacy, which in some cases even falls below the values measured on the flat reference surfaces.

In summary, this work demonstrates the potential of USP-DLIP to enhance the antimicrobial efficacy and corrosion resistance of Cu surfaces through the simultaneous modification of topographic, surface chemistry and superficial microstructure. Increased bactericidal activity on USP-DLIP Cu surfaces was found to be related to both topographic and physicochemical surface properties that exhibit a high conformity to the surface properties referred to preferential bacterial adhesion in the literature (illustrated in **Figure 5)**, independent of the bacterial strain. According to the current state of literature, topographies that enable an increased bacteria/surface contact in conjunction with beneficial physicochemical surface properties tend to induce enhanced adhesion forces, which potentially influence mechanosensory stimulation, metabolism and surface interaction of the bacterial cells. The modest dependency of increased antibacterial capacity on quantitative Cu ion release in the case of USP-DLIP Cu surfaces speaks in favor of a potential mechanosensory impact on bacterial Cu-sensitivity. This is indicated by the increased killing rates of both *E. coli* and *S. aureus* by several orders of magnitude on P = 3 µm (and P = 1 µm for *E. coli*) USP-DLIP surfaces despite an attenuated release of Cu ions due to the modified Cu corrosivity. A potential impact of bacterial activity on the bactericidal effect of Cu was furthermore implied by the implementation of both ambient temperature modulation and decreased bacterial fitness by increasing bacterial colony age in antibacterial testing.

However, at this state of research the actual intricate microbial mechanisms that are involved in the enhancement of Cu sensitivity and antibacterial efficacy observed on USP-DLIP processed Cu surfaces from the bacterial side remain far from being fully understood. Before this background, this work aims to provide a modest contribution to a better understanding of how to modify substrate surfaces with a potential impact on microbial interaction. A deeper understanding towards the development of more sophisticated surface concepts to control microbial contamination and mitigate the risk of contact-mediated transmission of infectious diseases might built upon these results, but requires scientific inquiry that far exceeds the scope of this work.

Outlook

Bacterial interaction on artificial surfaces is a matter of high complexity that offers great potential to improve microbial control in critical human environments or sensitive technical systems and facilities. Especially during the period of this dissertation this topic found increasing attention in research, where the multitude of different influences and aspects of bacterial behavior in response to external stimuli are starting to be investigated in higher depth and detail. This field of research is in its early stages of understanding the basics of bacteria/surface interaction, as well as its potential benefits in targeted application, which is highlighted by the novelty of the most groundbreaking publications that are mostly dating within the last five years.

In the scope of this dissertation, novel insights could be contributed to this topic, which includes both the development of a laser interference-based methodology to impacting bacterial/surface interaction on artificial surfaces as well as on its application to effectively amplify bacterial decontamination on Cu surfaces. Based on the results of this work, further expansion of future research activities in this field might offer promising prospects including an improved scientific understanding on how to purposefully influence bacteria/surface interaction to either design optimized decontamination concepts or increase the production efficacy of bioreactors, e.g.

The following section lists promising aspects for extending the research activities presented, some of which are already being addressed in parallel with this work.

Targeted modification of Cu surface wetting: The transition of wettability from hydrophilic to (super-) hydrophobic of USP-DLIP processed Cu surfaces in the course of extended atmospheric exposure was shown to be linked to a delicate mechanism of surface passivation. Further research is conducted to build a fundamental understanding of the correlation between the underlying C-group accumulation and the Cu surface conditioning potentially impacted by laser processing.

Extension of USP-DLIP surface optimization to Cu-alloys: Although the application of USP-DLIP on pure Cu presents a promising approach to increase the material inherent active antimicrobial surface properties, a wider application of this concept needs to enable a transfer to technically more relevant substrates exhibiting a higher mechanical robustness. This might involve Cu-based alloys like bronzes and brasses, where however additional impacts by USP-DLIP processing on functional surface properties involving the formation of intermetallic phases needs to be considered with respect to individual alloying systems.

Impact of USP-DLIP on bacterial interaction on inert surfaces: Aside of modified antimicrobial activity on Cu surfaces, USP-DLIP patterning on technical substrates might similarly affect bacterial interaction in terms of adhesion and biofilm formation. This includes a focused impact of separated bacterial strains, as well as a potential impact on biofilm dynamics in more application relevant multi-species environment. This is currently approached in terrestrial as well as space-related investigations within the ISS projects Touching Surface and BIOFILMS. First insights in µG biofilm formation of *P. aeruginosa* on USP-DLIP silicon surfaces were already elaborated in the frame of the ISS experiment “Space Biofilms”.

Applicability of USP-DLIP Cu surfaces in broadband decontamination: Further emphasis on the investigation of a similarly antimicrobial effect of USP-DLIP Cu surfaces against fungi and viruses appears worthwhile in view of the very recent COVID-19 pandemic. In the case of viruses, the current knowledge of antiviral Cu modes of action suggests a potential deactivation impact of Cu exposure, whereas in fungi a high resilience towards increased levels on environmental Cu has been reported. Here, a modified surface interaction by USP-DLIP functionalization might improve the antifungal effect of Cu, which is currently investigated in cooperation with the DLR in Cologne.

Biomedical surface functionalization: Topographic and physicochemical surface functionalization by USP-DLIP might benefit biomedical applications, e.g. by optimization of the body tissue/surface interaction on implant materials. This might follow an integrated pace aiming for both decreased bacterial surface contamination by passive or active antimicrobial mechanisms as well as an improved cell-interaction supporting tissue integration, e.g. by selective endothelization of stents and osseointegration in the case of dental implants. This is effectively aspired by both topographic as well as chemical surface design in view of the combined impact of topography and physicochemical surface properties on microbial surface interaction without material restriction.

USP-DLIP for technical surface functionalization: Aside of the previous focus on microbiological topics, the USP-DLIP methodology introduced in this work holds promising aspects in an implementation for surface functionalization in technical application involving advanced materials like metallic glasses, wear resistant MMCs, semiconductors and glass.

Further development of the USP-DLIP methodology: In parallel, further development of the USP-DLIP methodology paves the way for a promising expansion of the existing capabilities in surface functionalization. The currently applied imaging optical system e.g. facilitates the application of multiple partials beams in USP laser-interference allowing for a broader range of pattern geometries. Similarly, the minimal pattern scales generated by USP-DLIP might be further decreased down to < 300 nm by second and third harmonic generation based on the NIR seed wavelength. These conceptual considerations were implemented in the most recent modernization of the USP-DLIP laser system (DFG, INST 256/562-1 FUGG).

VII | Not included Papers

Further research was conducted in collaboration with various scientific partners in parallel to the doctoral research. An overview of related scientific publications that were not included in this work is provided below.

On the wetting of Cu surfaces

(1) S.M. Lößlein, M. Kasper, R. Merz, C. Pauly, **D.W. Müller**, M. Kopnarski, F. Mücklich, Patience Alone is not Enough - A Guide for the Preparation of Low-Defect Sections from Pure Copper Geduld allein reicht nicht! - Ein Leitfaden zur Herstellung defektarmer Schliffe von Reinkupfer, Prakt. Metallogr. Metallogr. 58 (2021) 388–407. https://doi.org/10.1515/pm-2021-0031

(2) S.M. Lößlein, R. Merz, **D.W. Müller**, M. Kopnarski, F. Mücklich, An in-depth evaluation of sample and measurement induced influences on static contact angle measurements, Sci. Rep. 12 (2022) 1–16. https://doi.org/10.1038/s41598-022-23341-3

(3) S.M. Lößlein, R. Merz, **D.W. Müller**, M. Kopnarski, F. Mücklich, The Influence of Adventitious Carbon Groups on the Wetting of Copper: A Study on the Effect of Microstructure on the Static Contact Angle, Langmuir. 39 (2023) 12020–12031. https://doi.org/10.1021/acs.langmuir.3c01060

The effect of USP-DLIP on the antibacterial properties of Cu-alloys

(4) A.S. Ahmed, **D.W. Müller**, S. Bruyere, A. Holtsch, F. Müller, J. Barrirero, K. Brix, S. Migot, R. Kautenburger, K. Jacobs, J. Pierson, F. Mücklich, Surface Modification of Brass via Ultrashort Pulsed Direct Laser Interference Patterning and Its Effect on Bacteria-Substrate Interaction, ACS Appl. Mater. Interfaces. (2023). https://doi.org/10.1021/acsami.3c04801

(5) A.S. Ahmed, **D.W. Müller**, S. Bruyère, A. Holtsch, F. Müller, K. Brix, S. Migot, R. Kautenburger, K. Jacobs, J.F. Pierson, F. Mücklich, Antibacterial property alterations induced by low zinc content in laser-structured brass, Appl. Surf. Sci. 665 (2024). https://doi.org/10.1016/j.apsusc.2024.160338

The Space Biofilms ISS experiment

(6) L. Zea, Z. Nisar, P. Rubin, M. Cortesão, J. Luo, S.A. Mcbride, R. Moeller, D. Klaus, **D. Müller**, K.K. Varanasi, F. Muecklich, L. Stodieck, Design of a space flight biofilm experiment, Acta Astronaut. 148 (2018) 294–300. https://doi.org/10.1016/j.actaastro.2018.04.039

(7) P. Flores, R. Schauer, S.A. McBride, J. Luo, C. Hoehn, S. Doraisingam, D. Widhalm, J. Chadha, L. Selman, **D.W. Mueller**, S. Floyd, M. Rupert, S. Gorti, S. Reagan, K.K. Varanasi, C. Koch, J.U. Meir, F. Muecklich, R. Moeller, L. Stodieck, S. Countryman, L. Zea, Preparation for and Performance of a Pseudomonas aeruginosa Biofilm Experiment On Board the International Space Station, Acta Astronaut. (2021). https://doi.org/10.1016/j.actaastro.2022.07.015

(8) P. Flores, J. Luo, **D.W. Mueller**, F. Muecklich, L. Zea, Space biofilms – An overview of the morphology of Pseudomonas aeruginosa biofilms grown on silicone and cellulose membranes on board the international space station, Biofilm. 7 (2024) 100182. https://doi.org/10.1016/j.bioflm.2024.100182

Applications towards fungi

(9) S.M. Koch, Y.T. Ly, F.S. Arndt, **D.W. Müller**, D. Schmeling, R. Moeller, Evaluating decontamination and prevention techniques by establishing standardized broad-range microbial testing platforms, in: 17th Int. Conf. Indoor Air Qual. Clim. INDOOR AIR 2022, (2022) https://elib.dlr.de/192979/

(10) S.M.Timofeev, K. Siems, **D.W. Müller**, A.S. Ahmed, A. Schiele, K. Brix, C.L. Krämer, F. Arndt, R. Kautenburger, F. Mücklich, S. Leuko, Stress response of *Aspergillus niger* spores to copper surfaces and the implications for antifungal surface functionalization, submitted in Advanced Materials Interfaces (2024)

(11) J. Figueira, S. Koch, **D.W. Müller**, S. Slawik, A. Cowley, R. Moeller, Biomining of Lunar regolith simulant EAC-1A with the fungus *Penicillium simplicissimum*, submitted in Frontiers in Materials (2023) https://doi.org/10.21203/rs.3.rs-2909117/v1

Applying USP-DLIP on implant materials and related applications

(12) J. Minguela, **D.W. Müller**, F. Mücklich, L. Llanes, M.P. Ginebra, J.J. Roa, C. Mas-Moruno, Peptidic biofunctionalization of laser patterned dental zirconia: A biochemical-topographical approach, Mater. Sci. Eng. C. 125 (2021) 112096. https://doi.org/10.1016/j.msec.2021.112096

(13) T. Fox, S.M. Lößlein, **D.W. Müller** and F. Mücklich, "Metallography and Biomimetics – Or New Surfaces Without Chemistry?" *Practical Metallography*, vol. 58, no. 7, 2021, pp. 446-459. https://doi.org/10.1515/pm-2021-0034

(14) T. Fox, P. Maria Delfino, F. Cortés, C. Pauly, **D.W. Müller**, M. Briesenick, G. Kickelbick, F. Mücklich, Single-step Production of Photocatalytic Surfaces via Direct Laser Interference Patterning of Titanium, ChemNanoMat. (2023) e202300314. https://doi.org/10.1002/cnma.202300314

USP(-DLIP) processing of advanced materials

(15) S. Fang, **D.W. Müller**, C. Rauch, Y. Cao, F. Mücklich, L. Llanes, D. Bähre, Fabrication of Interference Textures on Cemented Carbides Using Nanosecond and Femtosecond Laser Pulses, in: Procedia CIRP, Elsevier B.V., 2020: pp. 216–221. https://doi.org/10.1016/j.procir.2020.02.063

(16) M.A. Martins, **D.W. Müller**, J. Schmauch, M. Glaser, J.P. Bergmann, F. Mücklich, C. Pauly, Effects of Ultrashort Pulsed Direct Laser Writing on Ni / Al Reactive Multilayer Foils, Appl. Sci. 13, 4313 (2023) https://doi.org/10.3390/app13074313

References

[1] R. Koch, Die Aetiologie der Milzbrand-Krankheit, begründet auf die Entwicklungsgeschichte des Bacillus Anthracis, (1876). https://doi.org/10.1055/s-0029-1196567.

[2] C. Huttenhower, et al., Structure, function and diversity of the healthy human microbiome, Nature. 486 (2012) 207–214. https://doi.org/10.1038/nature11234.

[3] C.A. Lozupone, J.I. Stombaugh, J.I. Gordon, J.K. Jansson, R. Knight, Diversity, stability and resilience of the human gut microbiota, Nature. 489 (2012) 220–230. https://doi.org/10.1038/nature11550.

[4] M. Naghavi, Global mortality associated with 33 bacterial pathogens in 2019: a systematic analysis for the Global Burden of Disease Study 2019, Lancet. 6736 (2022) 02185. https://doi.org/10.1016/S0140-6736(22)02185-7.

[5] M. Cámara, W. Green, C.E. MacPhee, P.D. Rakowska, R. Raval, M.C. Richardson, J. Slater-Jefferies, K. Steventon, J.S. Webb, Economic significance of biofilms: a multidisciplinary and cross-sectoral challenge, Npj Biofilms Microbiomes. 8 (2022) 1–8. https://doi.org/10.1038/s41522-022-00306-y.

[6] N.D. Novikova, Review of the knowledge of microbial contamination of the Russian manned spacecraft, in: Microb. Ecol., 2004. https://doi.org/10.1007/s00248-003-1055-2.

[7] L. Zea, Z. Nisar, P. Rubin, M. Cortesão, J. Luo, S.A. Mcbride, R. Moeller, D. Klaus, D. Müller, K.K. Varanasi, F. Muecklich, L. Stodieck, Design of a space flight biofilm experiment, Acta Astronaut. 148 (2018) 294–300. https://doi.org/10.1016/j.actaastro.2018.04.039.

[8] C. Urbaniak, M.D. Morrison, J.B. Thissen, F. Karouia, D.J. Smith, S. Mehta, C. Jaing, K. Venkateswaran, Microbial Tracking-2, a metagenomics analysis of bacteria and fungi onboard the International Space Station, Microbiome. 10 (2022) 1–19. https://doi.org/10.1186/s40168-022-01293-0.

[9] D. Campoccia, L. Montanaro, C.R. Arciola, The significance of infection related to orthopedic devices and issues of antibiotic resistance, Biomaterials. 27 (2006) 2331–2339. https://doi.org/10.1016/j.biomaterials.2005.11.044.

[10] J.R. Brooks, D.J. Chonko, M. Pigott, A.C. Sullivan, K. Moore, P. Stoodley, Mapping bacterial biofilm on explanted orthopedic hardware: An analysis of 14 consecutive cases, APMIS. 131 (2023) 170–179. https://doi.org/10.1111/apm.13295.

[11] H.T. Michels, W. Moran, J. Michel, Antimicrobial Properties of Copper Alloy Surfaces , with a Focus on Hospital-Acquired Infections, Adv. Mater. Process. (2008). https://doi.org/10.1361/amp1108copper.

[12] N. Yamaguchi, M. Roberts, S. Castro, C. Oubre, K. Makimura, N. Leys, E. Grohmann, T. Sugita, T. Ichijo, M. Nasu, Microbial Monitoring of Crewed Habitats in Space—Current Status and Future Perspectives, Microbes Environ. 29 (2014) 250–260. https://doi.org/10.1264/jsme2.ME14031.

[13] G. Horneck, D.M. Klaus, R.L. Mancinelli, Space Microbiology, Microbiol. Mol. Biol. Rev. 74 (2010). https://doi.org/10.1128/mmbr.00016-09.

[14] T.F.C. Mah, G.A. O'Toole, Mechanisms of biofilm resistance to antimicrobial agents, Trends Microbiol. 9 (2001) 34–39. https://doi.org/10.1016/S0966-842X(00)01913-2.

[15] L. Zea, R.J.C. Mclean, T.A. Rook, G. Angle, D.L. Carter, A. Delegard, A. Denvir, R. Gerlach, S. Gorti, D. Mcilwaine, M. Nur, B.M. Peyton, P.S. Stewart, P. Sturman, Y. Ann, V. Justiniano, Potential biofilm control strategies for extended space flight missions, Biofilm. 2 (2020) 100026. https://doi.org/10.1016/j.bioflm.2020.100026.

[16] G. Grass, C. Rensing, M. Solioz, Metallic copper as an antimicrobial surface, Appl. Environ. Microbiol. 77 (2011) 1541–1547. https://doi.org/10.1128/AEM.02766-10.

[17] A. Tripathy, P. Sen, B. Su, W.H. Briscoe, Natural and bioinspired nanostructured bactericidal surfaces, Adv. Colloid Interface Sci. 248 (2017) 85–104. https://doi.org/10.1016/j.cis.2017.07.030.

[18] W. Barthlott, C. Neinhuis, H. Verlot, C.L. Schott, Purity of the sacred lotus , or escape from contamination in biological surfaces, Planta. 202 (1997) 1–8.

[19] A. Elbourne, R.J. Crawford, E.P. Ivanova, Nano-structured antimicrobial surfaces: From nature to synthetic analogues, J. Colloid Interface Sci. 508 (2017) 603–616. https://doi.org/10.1016/j.jcis.2017.07.021.

[20] J. Hasan, H.K. Webb, V.K. Truong, S. Pogodin, V.A. Baulin, G.S. Watson, J.A. Watson, R.J. Crawford, E.P. Ivanova, Selective bactericidal activity of nanopatterned superhydrophobic cicada Psaltoda claripennis wing surfaces, Appl. Microbiol. Biotechnol. 97 (2013) 9257–9262. https://doi.org/10.1007/s00253-012-4628-5.

[21] C. Sengstock, M. Lopian, Y. Motemani, A. Borgmann, C. Khare, P.J.S. Buenconsejo, T.A. Schildhauer, A. Ludwig, M. Köller, Structure-related antibacterial activity of a titanium nanostructured surface fabricated by glancing angle sputter deposition, Nanotechnology. 25 (2014). https://doi.org/10.1088/0957-4484/25/19/195101.

[22] K.A. Whitehead, J. Verran, The Effect of Surface Topography on the Retention of Microorganisms, Food Bioprod. Process. 84 (2006) 253–259. https://doi.org/10.1205/fbp06035.

[23] M. Graham, N. Cady, Nano and Microscale Topographies for the Prevention of Bacterial Surface Fouling, Coatings. 4 (2014) 37–59. https://doi.org/10.3390/coatings4010037.

[24] A. Cunha, A.-M. Elie, L. Plawinski, A.P. Serro, A.M. Botelho do Rego, A. Almeida, M.C. Urdaci, M.-C. Durrieu, R. Vilar, Femtosecond laser surface texturing of titanium as a method to reduce the adhesion of Staphylococcus aureus and biofilm formation, Appl. Surf. Sci. 360 (2016) 485–493. https://doi.org/10.1016/j.apsusc.2015.10.102.

[25] R. Helbig, D. Günther, J. Friedrichs, F. Rößler, A. Lasagni, C. Werner, The impact of structure dimensions on initial bacterial adhesion, Biomater. Sci. 4 (2016) 1074–1078. https://doi.org/10.1039/C6BM00078A.

[26] J. Valle, S. Burgui, D. Langheinrich, C. Gil, C. Solano, A. Toledo-Arana, R. Helbig, A. Lasagni, I. Lasa, Evaluation of Surface Microtopography Engineered by Direct Laser Interference for Bacterial Anti-Biofouling, Macromol. Biosci. 15 (2015) 1060–1069. https://doi.org/10.1002/mabi.201500107.

[27] C. Satriano, G.M.L. Messina, S. Carnazza, S. Guglielmino, G. Marletta, Bacterial adhesion onto nanopatterned polymer surfaces, Mater. Sci. Eng. C. 26 (2006) 942–946. https://doi.org/10.1016/j.msec.2005.09.096.

[28] K. Lienkamp, A.E. Madkour, A. Musante, C.F. Nelson, K. Nüsslein, G.N. Tew, Antimicrobial polymers prepared by ROMP with unprecedented selectivity: A molecular construction kit approach, J. Am. Chem. Soc. 130 (2008) 9836–9843. https://doi.org/10.1021/ja801662y.

[29] C. Chen, A. Enrico, T. Pettersson, M. Ek, A. Herland, F. Niklaus, G. Stemme, L. Wågberg, Bactericidal surfaces prepared by femtosecond laser patterning and layer-by-layer polyelectrolyte coating, J. Colloid Interface Sci. 575 (2020) 286–297. https://doi.org/10.1016/j.jcis.2020.04.107.

[30] L.-Y. Sobisch, K.M. Rogowski, J. Fuchs, W. Schmieder, A. Vaishampayan, P. Oles, N. Novikova, E. Grohmann, Biofilm Forming Antibiotic Resistant Gram-Positive Pathogens Isolated From Surfaces on the International Space Station, Front. Microbiol. 10 (2019) 1–16. https://doi.org/10.3389/fmicb.2019.00543.

[31] T. Fox, P. Maria Delfino, F. Cortés, C. Pauly, D. Wyn Müller, M. Briesenick, G. Kickelbick, F. Mücklich, Single-step Production of Photocatalytic Surfaces via Direct Laser Interference Patterning of Titanium, ChemNanoMat. (2023) e202300314. https://doi.org/10.1002/cnma.202300314.

[32] S.A. Wilks, H. Michels, C.W. Keevil, The survival of Escherichia coli O157 on a range of metal surfaces, Int. J. Food Microbiol. 105 (2005) 445–454. https://doi.org/10.1016/j.ijfoodmicro.2005.04.021.

[33] M.G. Schmidt, B. Von Dessauer, C. Benavente, D. Benadof, P. Cifuentes, A. Elgueta, C. Duran, M.S. Navarrete, Copper surfaces are associated with significantly lower concentrations of bacteria on selected surfaces within a pediatric intensive care unit, Am. J. Infect. Control. 44 (2016) 203–209. https://doi.org/10.1016/j.ajic.2015.09.008.

[34] L. Weaver, H.T. Michels, C.W. Keevil, Potential for preventing spread of fungi in air-conditioning systems constructed using copper instead of aluminium, Lett. Appl. Microbiol. 50 (2010) 18–23. https://doi.org/10.1111/j.1472-765X.2009.02753.x.

[35] L.T. Liu, A.W.H. Chin, P. Yu, L.L.M. Poon, M.X. Huang, Anti-pathogen stainless steel combating COVID-19, Chem. Eng. J. 433 (2022) 133783. https://doi.org/10.1016/j.cej.2021.133783.

[36] K.S. Chaturvedi, J.P. Henderson, Pathogenic adaptations to host-derived antibacterial copper, Front. Cell. Infect. Microbiol. 4 (2014) 1–12. https://doi.org/10.3389/fcimb.2014.00003.

[37] G. Borkow, J. Gabbay, Copper, An Ancient Remedy Returning to Fight Microbial, Fungal and Viral Infections, Curr. Chem. Biol. 3 (2009) 272–278. https://doi.org/10.1557/mrs2005.10.

[38] S. Krupanidhi, A. Sreekumar, C.B. Sanjeevi, Copper & biological health, 2008. https://doi.org/10.1080/10937400600755911.

[39] M. Arredondo, M.T. Nunez, Iron and copper metabolism, Mol. Aspects Med. 26 (2005) 313–327. https://doi.org/10.1016/j.mam.2005.07.010.

[40] M. Haeili, C. Moore, C.J.C. Davis, J.B. Cochran, S. Shah, T.B. Shrestha, Y. Zhang, S.H. Bossmann, W.H. Benjamin, O. Kutsch, F. Wolschendorf, Copper complexation screen reveals compounds with potent antibiotic properties against methicillin-resistant Staphylococcus aureus, Antimicrob. Agents Chemother. 58 (2014) 3727–3736. https://doi.org/10.1128/AAC.02316-13.

[41] M. Vincent, P. Hartemann, M. Engels-Deutsch, Antimicrobial applications of copper, Int. J. Hyg. Environ. Health. 219 (2016) 585–591. https://doi.org/10.1016/j.ijheh.2016.06.003.

[42] M. Hans, Materialeinflüsse bei der Abtötung von Bakterien durch metallisches Kupfer, Diss. 2015.

[43] M. Hans, S. Mathews, F. Mücklich, M. Solioz, Physicochemical properties of copper important for its antibacterial activity and development of a unified model, Biointerphases. 11 (2016) 018902. https://doi.org/10.1116/1.4935853.

[44] J.O. Noyce, H. Michels, C.W. Keevil, Use of Copper Cast Alloys To Control Escherichia coli O157 Cross-Contamination during Food Processing, Appl. Environ. Microbiol. 72 (2006) 4239–4244. https://doi.org/10.1128/AEM.02532-05.

[45] R.E. Morsi, A.M. Alsabagh, S.A. Nasr, M.M. Zaki, Multifunctional nanocomposites of chitosan, silver nanoparticles, copper nanoparticles and carbon nanotubes for water treatment: Antimicrobial characteristics, Int. J. Biol. Macromol. 97 (2017) 264–269. https://doi.org/10.1016/j.ijbiomac.2017.01.032.

[46] C.D. Sifri, G.H. Burke, K.B. Enfield, Reduced health care-associated infections in an acute care community hospital using a combination of self-disinfecting copper-impregnated composite hard surfaces and linens, Am. J. Infect. Control. 44 (2016) 1565–1571. https://doi.org/10.1016/j.ajic.2016.07.007.

[47] J. Inkinen, R. Mäkinen, M.M. Keinänen-Toivola, K. Nordström, M. Ahonen, Copper as an antibacterial material in different facilities, Lett. Appl. Microbiol. 64 (2017) 19–26. https://doi.org/10.1111/lam.12680.

[48] A. Mikolay, S. Huggett, L. Tikana, G. Grass, J. Braun, D.H. Nies, Survival of bacteria on metallic copper surfaces in a hospital trial, Appl. Microbiol. Biotechnol. 87 (2010) 1875–1879. https://doi.org/10.1007/s00253-010-2640-1.

[49] C. Garcidueñas-Piña, I.E. Medina-Ramírez, P. Guzmán, R. Rico-Martínez, J.F. Morales-Domínguez, I. Rubio-Franchini, Evaluation of the Antimicrobial Activity of Nanostructured Materials of Titanium Dioxide Doped with Silver and/or Copper and Their Effects on Arabidopsis thaliana, Int. J. Photoenergy. (2016). https://doi.org/10.1155/2016/8060847.

[50] L. Zhu, J. Elguindi, C. Rensing, S. Ravishankar, Antimicrobial activity of different copper alloy surfaces against copper resistant and sensitive Salmonella enterica, Food Microbiol. 30 (2012) 303–310. https://doi.org/10.1016/j.fm.2011.12.001.

[51] M. Hans, A. Erbe, S. Mathews, Y. Chen, M. Solioz, F. Mücklich, Role of copper oxides in contact killing of bacteria, Langmuir. 29 (2013) 16160–16166. https://doi.org/10.1021/la404091z.

[52] M. Hans, J.C. Támara, S. Mathews, B. Bax, A. Hegetschweiler, R. Kautenburger, M. Solioz, F. Mücklich, Laser cladding of stainless steel with a copper-silver alloy to generate surfaces of high antimicrobial activity, Appl. Surf. Sci. 320 (2014) 195–199. https://doi.org/10.1016/j.apsusc.2014.09.069.

[53] S. Mathews, M. Hans, F. Mücklich, M. Solioz, Contact killing of bacteria on copper is suppressed if bacterial-metal contact is prevented and is induced on iron by copper ions, Appl. Environ. Microbiol. 79 (2013) 2605–2611. https://doi.org/10.1128/AEM.03608-12.

[54] J. Luo, C. Hein, J. Ghanbaja, J. Pierson, F. Mücklich, Bacteria accumulate copper ions and inhibit oxide formation on copper surface during antibacterial efficiency test, Micron. 127 (2019) 102759.

[55] M.L. Beeton, J.R. Aldrich-Wright, A. Bolhuis, The antimicrobial and antibiofilm activities of copper(II) complexes, J. Inorg. Biochem. 140 (2014) 167–172. https://doi.org/10.1016/j.jinorgbio.2014.07.012.

[56] P. Bleichert, L. Bütof, C. Rückert, M. Herzberg, R. Francisco, P. V. Morais, G. Grass, J. Kalinowski, D.H. Nies, Mutant Strains of Escherichia coli and Methicillin-Resistant Staphylococcus aureus Obtained

by Laboratory Selection To Survive on Metallic Copper Surfaces, Appl. Environ. Microbiol. 87 (2020) 1–21. https://doi.org/10.1128/AEM.01788-20.

[57] J. Baker, S. Sitthisak, M. Sengupta, M. Johnson, R.K. Jayaswal, J.A. Morrissey, Copper stress induces a global stress response in staphylococcus aureus and represses sae and agr expression and biofilm formations, Appl. Environ. Microbiol. 76 (2010) 150–160. https://doi.org/10.1128/AEM.02268-09.

[58] H.T. Michels, J.O. Noyce, C.W. Keevil, Effects of temperature and humidity on the efficacy of methicillin-resistant *Staphylococcus aureus* challenged antimicrobial materials containing silver and copper, Lett. Appl. Microbiol. 49 (2009) 191–195. https://doi.org/10.1111/j.1472-765X.2009.02637.x.

[59] A. Ananth, S. Dharaneedharan, M.S. Heo, Y.S. Mok, Copper oxide nanomaterials: Synthesis, characterization and structure-specific antibacterial performance, Chem. Eng. J. 262 (2015) 179–188. https://doi.org/10.1016/j.cej.2014.09.083.

[60] A. Singh, A. Ahmed, K.N. Prasad, S. Khanduja, S.K. Singh, J.K. Srivastava, N.S. Gajbhiye, Antibiofilm and membrane-damaging potential of cuprous oxide Nanoparticles against Staphylococcus aureus with reduced susceptibility to vancomycin, Antimicrob. Agents Chemother. 59 (2015) 6882–6890. https://doi.org/10.1128/AAC.01440-15.

[61] C.A.P. Bastos, N. Faria, J. Wills, P. Malmberg, N. Scheers, P. Rees, J.J. Powell, Copper nanoparticles have negligible direct antibacterial impact, NanoImpact. 17 (2020) 100192. https://doi.org/10.1016/j.impact.2019.100192.

[62] J.L. Smith, N. Tran, T. Song, D. Liang, M. Qian, Robust bulk micro-nano hierarchical copper structures possessing exceptional bactericidal efficacy, Biomaterials. 280 (2022) 121271. https://doi.org/10.1016/j.biomaterials.2021.121271.

[63] A. Tripathy, S. Sreedharan, C. Bhaskarla, S. Majumdar, S.K. Peneti, D. Nandi, P. Sen, Enhancing the Bactericidal Efficacy of Nanostructured Multifunctional Surface Using an Ultrathin Metal Coating, Langmuir. 33 (2017) 12569–12579. https://doi.org/10.1021/acs.langmuir.7b02291.

[64] G. Yi, S.N. Riduan, A. Armugam, J.T. Ong, P.Y. Hon, M.Y. Abdad, S. Vasoo, B.S.P. Ang, Y. Zhang, Nanostructured Copper Surface Kills ESKAPE Pathogens and Viruses in Minutes, ChemMedChem. 16 (2021) 3553–3558. https://doi.org/10.1002/cmdc.202100504.

[65] V. Selvamani, A. Zareei, A. Elkashif, M.K. Maruthamuthu, S. Chittiboyina, D. Delisi, Z. Li, L. Cai, V.G. Pol, M.N. Seleem, R. Rahimi, Hierarchical Micro/Mesoporous Copper Structure with Enhanced Antimicrobial Property via Laser Surface Texturing, Adv. Mater. Interfaces. 1901890 (2020) 1–11. https://doi.org/10.1002/admi.201901890.

[66] L.B. Boinovich, E.B. Modin, A. V. Aleshkin, K.A. Emelyanenko, E.R. Zulkarneev, I.A. Kiseleva, A.L. Vasiliev, A.M. Emelyanenko, Effective Antibacterial Nanotextured Surfaces Based on Extreme Wettability and Bacteriophage Seeding, ACS Appl. Nano Mater. 1 (2018) 1348–1359. https://doi.org/10.1021/acsanm.8b00090.

[67] K.A. Emelyanenko, N.A. Sanzharovsky, E. V. Chulkova, A.A. Ganne, A.M. Emelyanenko, L.B. Boinovich, Superhydrophobic corrosion resistant coatings for copper via IR nanosecond laser processing, Mater. Res. Express. 5 (2018) 115001. https://doi.org/10.1088/2053-1591/aadc16.

[68] A.M. Emelyanenko, I.S. Pytskii, V. V. Kaminsky, E. V. Chulkova, A.G. Domantovsky, K.A. Emelyanenko, V.D. Sobolev, A. V. Aleshkin, L.B. Boinovich, Superhydrophobic copper in biological liquids: Antibacterial activity and microbiologically induced or inhibited corrosion, Colloids Surfaces B Biointerfaces. 185 (2020) 110622. https://doi.org/10.1016/j.colsurfb.2019.110622.

[69] L.B. Boinovich, K.A. Emelyanenko, A.G. Domantovsky, E. V. Chulkova, A.A. Shiryaev, A.M. Emelyanenko, Pulsed Laser Induced Triple Layer Copper Oxide Structure for Durable Polyfunctionality of Superhydrophobic Coatings, Adv. Mater. Interfaces. 5 (2018) 1–10. https://doi.org/10.1002/admi.201801099.

[70] D. Guenther, J. Valle, S. Burgui, C. Gil, C. Solano, D. Guenther, J. Valle, S. Burgui, C. Gil, C. Solano, A. Toledo-arana, R. Helbig, C. Werner, I. Lasa, F. Andrés, Direct laser interference patterning for decreased bacterial attachment, in: SPIE 9736, Laser-Based Micro- Nanoprocessing X, 2016. https://doi.org/10.1117/12.2216065.

[71] A.H.A. Lutey, L. Gemini, L. Romoli, G. Lazzini, F. Fuso, M. Faucon, R. Kling, Towards laser-textured antibacterial surfaces, Sci. Rep. 8 (2018) 1–10. https://doi.org/10.1038/s41598-018-28454-2.

[72] A. Peter, A.H.A. Lutey, S. Faas, L. Romoli, V. Onuseit, T. Graf, Direct laser interference patterning of

stainless steel by ultrashort pulses for antibacterial surfaces, Opt. Laser Technol. 123 (2020) 105954. https://doi.org/10.1016/j.optlastec.2019.105954.

[73] A. Rosenkranz, M. Hans, C. Gachot, A. Thome, S. Bonk, Direct Laser Interference Patterning : Tailoring of Contact Area for Frictional and Antibacterial Properties, Lubricants. 4 (2016). https://doi.org/10.3390/lubricants4010002.

[74] A.F. Lasagni, C. Gachot, K.E. Trinh, M. Hans, A. Rosenkranz, T. Roch, S. Eckhardt, T. Kunze, M. Bieda, D. Günther, V. Lang, F. Mücklich, Direct laser interference patterning, 20 years of development: from the basics to industrial applications, in: Proc. SPIE 10092, Laser-Based Micro- Nanoprocessing XI, 2017: p. 1009211. https://doi.org/10.1117/12.2252595.

[75] C. Díaz, M.C. Cortizo, P.L. Schilardi, S.G.G. de Saravia, M.A.F.L. de Mele, Influence of the nano-micro structure of the surface on bacterial adhesion, Mater. Res. 10 (2007) 11–14. https://doi.org/10.1590/S1516-14392007000100004.

[76] C. Díaz, P. Schilardi, M.F.L. De Mele, Influence of surface sub-micropattern on the adhesion of pioneer bacteria on metals, Artif. Organs. 32 (2008) 292–298. https://doi.org/10.1111/j.1525-1594.2008.00545.x.

[77] M. Hans, F. Müller, S. Grandthyll, S. Hüfner, F. Mücklich, Anisotropic wetting of copper alloys induced by one-step laser micro-patterning, Appl. Surf. Sci. 263 (2012) 416–422. https://doi.org/10.1016/j.apsusc.2012.09.071.

[78] M. Bieda, M. Siebold, A. Fabián, Fabrication of sub-micron surface structures on copper , stainless steel and titanium using picosecond laser interference patterning, Appl. Surf. Sci. 387 (2016) 175–182. https://doi.org/10.1016/j.apsusc.2016.06.100.

[79] A. Lasagni, M. Nejati, R. Clasen, F. Mücklich, Periodical Surface Structuring of Metals by Laser Interference MethodofTexturedSolarSelective Absorbers, Adv. Eng. Mater. 8 (2006) 580–584. https://doi.org/10.1002/adem.200500261.

[80] L.B. Boinovich, V. V. Kaminsky, A.G. Domantovsky, K.A. Emelyanenko, A. V. Aleshkin, E.R. Zulkarneev, I.A. Kiseleva, A.M. Emelyanenko, Bactericidal Activity of Superhydrophobic and Superhydrophilic Copper in Bacterial Dispersions, Langmuir. 35 (2019) 2832–2841. https://doi.org/10.1021/acs.langmuir.8b03817.

[81] C. Berne, C.K. Ellison, A. Ducret, Y. V. Brun, Bacterial adhesion at the single-cell level, Nat. Rev. Microbiol. 16 (2018) 616–627. https://doi.org/10.1038/s41579-018-0057-5.

[82] T. Kimkes, M. Heinemann, How Bacteria Recognise and Respond to Surface Contact, FEMS Microbiol. Rev. 44 (2020) 106–122.

[83] E. Maikranz, C. Spengler, N. Thewes, A. Thewes, F. Nolle, P. Jung, M. Bischoff, L. Santen, K. Jacobs, Different binding mechanisms of Staphylococcus aureus to hydrophobic and hydrophilic surfaces, Nanoscale. 12 (2020) 19267–19275. https://doi.org/10.1039/d0nr03134h.

[84] J. Palmer, S. Flint, J. Brooks, Bacterial cell attachment, the beginning of a biofilm, J. Ind. Microbiol. Biotechnol. 34 (2007) 577–588. https://doi.org/10.1007/s10295-007-0234-4.

[85] C. Lüdecke, K.D. Jandt, D. Siegismund, M.J. Kujau, E. Zang, M. Rettenmayr, J. Bossert, M. Roth, Reproducible biofilm cultivation of chemostat-grown escherichia coli and investigation of bacterial adhesion on biomaterials using a non-constant-depth film fermenter, PLoS One. 9 (2014). https://doi.org/10.1371/journal.pone.0084837.

[86] B. Yousuf, J.J. Ahire, L.M.T. Dicks, Understanding the antimicrobial activity behind thin- and thick-rolled copper plates, Appl. Microbiol. Biotechnol. 100 (2016) 5569–5580. https://doi.org/10.1007/s00253-016-7361-7.

[87] N. Thewes, P. Loskill, P. Jung, H. Peisker, M. Bischoff, M. Herrmann, K. Jacobs, Hydrophobic interaction governs unspecific adhesion of staphylococci: A single cell force spectroscopy study, Beilstein J. Nanotechnol. 5 (2014) 1501–1512. https://doi.org/10.3762/bjnano.5.163.

[88] N. Thewes, A. Thewes, P. Loskill, H. Peisker, M. Bischoff, M. Herrmann, L. Santen, K. Jacobs, Stochastic binding of Staphylococcus aureus to hydrophobic surfaces, Soft Matter. 11 (2015) 8913–8919. https://doi.org/10.1039/C5SM00963D.

[89] O.E. Petrova, K. Sauer, Sticky situations: Key components that control bacterial surface attachment, J. Bacteriol. 194 (2012) 2413–2425. https://doi.org/10.1128/JB.00003-12.

[90] N.P. Boks, W. Norde, H.C. van der Mei, H.J. Busscher, Forces involved in bacterial adhesion to

hydrophilic and hydrophobic surfaces, Microbiology. 154 (2008) 3122–3133. https://doi.org/10.1099/mic.0.2008/018622-0.

[91] Y. Ren, C. Wang, Z. Chen, E. Allan, H.C. van der Mei, H.J. Busscher, Emergent heterogeneous microenvironments in biofilms: Substratum surface heterogeneity and bacterial adhesion force-sensing, FEMS Microbiol. Rev. 42 (2018) 259–272. https://doi.org/10.1093/femsre/fuy001.

[92] C. Berne, A. Ducret, G.G. Hardy, Y. V. Brun, Adhesins involved in attachment to abiotic surfaces by gram-negative bacteria, Microbiol. Spectr. 3 (2015) 163–199. https://doi.org/10.1128/9781555817466.ch09.

[93] S. Subramanian, D.B. Kearns, Functional regulators of bacterial flagella, Annu. Rev. Microbiol. 73 (2019) 225–246. https://doi.org/10.1146/annurev-micro-020518-115725.

[94] L.A. Pratt, R. Kolter, Genetic analysis of Escherichia coli biofilm formation: Roles of flagella, motility, chemotaxis and type I pili, Mol. Microbiol. 30 (1998) 285–293. https://doi.org/10.1046/j.1365-2958.1998.01061.x.

[95] K. Otto, T.J. Silhavy, Surface sensing and adhesion of Escherichia coli controlled by the Cpx-signaling pathway, Proc. Natl. Acad. Sci. U. S. A. 99 (2002) 2287–2292. https://doi.org/10.1073/pnas.042521699.

[96] R. Van Houdt, C.W. Michiels, Role of bacterial cell surface structures in Escherichia coli biofilm formation, Res. Microbiol. 156 (2005) 626–633. https://doi.org/10.1016/j.resmic.2005.02.005.

[97] H.J. Busscher, H.C. van der Mei, How do bacteria know they are on a surface and regulate their response to an adhering state?, PLoS Pathog. 8 (2012) 1–3. https://doi.org/10.1371/journal.ppat.1002440.

[98] Y.F. Dufrêne, A. Persat, Mechanomicrobiology: how bacteria sense and respond to forces, Nat. Rev. Microbiol. 18 (2020) 227–240. https://doi.org/10.1038/s41579-019-0314-2.

[99] D.J. Müller, J. Helenius, D. Alsteens, Y.F. Dufrne, Force probing surfaces of living cells to molecular resolution, Nat. Chem. Biol. 5 (2009) 383–390. https://doi.org/10.1038/nchembio.181.

[100] C. Formosa-Dague, P. Speziale, T.J. Foster, J.A. Geoghegan, Y.F. Dufrêne, Zinc-dependent mechanical properties of Staphylococcus aureus biofilm-forming surface protein SasG, Proc. Natl. Acad. Sci. U. S. A. 113 (2016) 410–415. https://doi.org/10.1073/pnas.1519265113.

[101] R. Denise, S.S. Abby, E.P.C. Rocha, Diversification of the type IV filament superfamily into machines for adhesion, protein secretion, DNA uptake, and motility, 2019. https://doi.org/10.1371/journal.pbio.3000390.

[102] A. Persat, Y.F. Inclan, J.N. Engel, H.A. Stone, Z. Gitai, Type IV pili mechanochemically regulate virulence factors in Pseudomonas aeruginosa, Proc. Natl. Acad. Sci. U. S. A. 112 (2015) 7563–7568. https://doi.org/10.1073/pnas.1502025112.

[103] T. Tolker-Nielsen, Biofilm Development, Microbiol. Spectr. 3 (2015) 100043. https://doi.org/doi:10.1128/microbiolspec.MB-0001-2014.

[104] Y. Luo, K. Zhao, A.E. Baker, S.L. Kuchma, K.A. Coggan, M.C. Wolfgang, G.C.L. Wong, G.A. O'Toole, A hierarchical cascade of second messengers regulates Pseudomonas aeruginosa Surface Behaviors, MBio. 6 (2015). https://doi.org/10.1128/mBio.02456-14.

[105] G.N. Bruni, R.A. Weekley, B.J.T. Dodd, J.M. Kralj, Voltage-gated calcium flux mediates Escherichia coli mechanosensation, Proc. Natl. Acad. Sci. U. S. A. 114 (2017) 9445–9450. https://doi.org/10.1073/pnas.1703084114.

[106] R. Zöllner, E.R. Oldewurtel, N. Kouzel, B. Maier, Phase and antigenic variation govern competition dynamics through positioning in bacterial colonies, Sci. Rep. 7 (2017) 1–12. https://doi.org/10.1038/s41598-017-12472-7.

[107] W. Kim, F.K. Tengra, Z. Young, J. Shong, N. Marchand, H.K. Chan, R.C. Pangule, M. Parra, J.S. Dordick, J.L. Plawsky, C.H. Collins, Spaceflight Promotes Biofilm Formation by Pseudomonas aeruginosa, PLoS One. 8 (2013) 1–8. https://doi.org/10.1371/journal.pone.0062437.

[108] D.G. Davies, M.R. Parsek, J.P. Pearson, B.H. Iglewski, J.W. Costerton, E.P. Greenberg, The involvement of cell-to-cell signals in the development of a bacterial biofilm, Science (80-.). 280 (1998) 295–298. https://doi.org/10.1126/science.280.5361.295.

[109] M. Allesen-Holm, K.B. Barken, L. Yang, M. Klausen, J.S. Webb, S. Kjelleberg, S. Molin, M. Givskov, T. Tolker-Nielsen, A characterization of DNA release in Pseudomonas aeruginosa cultures and biofilms, Mol. Microbiol. 59 (2006) 1114–1128. https://doi.org/10.1111/j.1365-2958.2005.05008.x.

[110] B. Maier, How Physical Interactions Shape Bacterial Biofilms, Annu. Rev. Biophys. 50 (2021) 401–417. https://doi.org/10.1146/annurev-biophys-062920-063646.

[111] L. Craig, K.T. Forest, B. Maier, Type IV pili: dynamics, biophysics and functional consequences, Nat. Rev. Microbiol. 17 (2019) 429–440. https://doi.org/10.1038/s41579-019-0195-4.

[112] Z. You, D.J.G. Pearce, A. Sengupta, L. Giomi, Geometry and Mechanics of Microdomains in Growing Bacterial Colonies, Phys. Rev. X. 8 (2018) 31065. https://doi.org/10.1103/PhysRevX.8.031065.

[113] M.C. Duvernoy, T. Mora, M. Ardré, V. Croquette, D. Bensimon, C. Quilliet, J.M. Ghigo, M. Balland, C. Beloin, S. Lecuyer, N. Desprat, Asymmetric adhesion of rod-shaped bacteria controls microcolony morphogenesis, Nat. Commun. 9 (2018) 25–28. https://doi.org/10.1038/s41467-018-03446-y.

[114] J. Yan, C.D. Nadell, H.A. Stone, N.S. Wingreen, B.L. Bassler, Extracellular-matrix-mediated osmotic pressure drives Vibrio cholerae biofilm expansion and cheater exclusion, Nat. Commun. 8 (2017). https://doi.org/10.1038/s41467-017-00401-1.

[115] X. Wang, T.K. Wood, IS5 inserts upstream of the master motility operon flhDC in a quasi-Lamarckian way, ISME J. 5 (2011) 1517–1525. https://doi.org/10.1038/ismej.2011.27.

[116] C.N. Spaulding, H.L. Schreiber, W. Zheng, K.W. Dodson, J.E. Hazen, M.S. Conover, F. Wang, P. Svenmarker, A. Luna-Rico, O. Francetic, M. Andersson, S. Hultgren, E.H. Egelman, Functional role of the type 1 pilus rod structure in mediating host-pathogen interactions, Elife. 7 (2018) 1–25. https://doi.org/10.7554/eLife.31662.

[117] X.S. Zhang, R. García-Contreras, T.K. Wood, YcfR (BhsA) influences Escherichia coli biofilm formation through stress response and surface hydrophobicity, J. Bacteriol. 189 (2007) 3051–3062. https://doi.org/10.1128/JB.01832-06.

[118] M.H. Nguyen, Y. Ojima, T. Kawata, M. Taya, Alternation in colonization behaviors of Escherichia coli cells with rpoS or yggE deficiency on solid surfaces, Biotechnol. Bioeng. 110 (2013) 1050–1056. https://doi.org/10.1002/bit.24770.

[119] Y. Chao, T. Zhang, Probing roles of lipopolysaccharide, type 1 fimbria, and colanic acid in the attachment of Escherichia coli strains on inert surfaces, Langmuir. 27 (2011) 11545–11553. https://doi.org/10.1021/la202534p.

[120] G. Huang, D. Xia, T. An, T.W. Ng, H.Y. Yip, G. Li, H. Zhao, P.K. Wong, Dual roles of capsular extracellular polymeric substances in photocatalytic inactivation of Escherichia coli: Comparison of E. coli BW25113 and isogenic mutants, Appl. Environ. Microbiol. 81 (2015) 5174–5183. https://doi.org/10.1128/AEM.00775-15.

[121] F. Li, X.S. Xiong, Y.Y. Yang, J.J. Wang, M.M. Wang, J.W. Tang, Q.H. Liu, L. Wang, B. Gu, Effects of NaCl Concentrations on Growth Patterns, Phenotypes Associated With Virulence, and Energy Metabolism in Escherichia coli BW25113, Front. Microbiol. 12 (2021) 705326. https://doi.org/10.3389/fmicb.2021.705326.

[122] N.E. Paweli, P. Suryadarma, I. Mardhiati, D. Mangunwidjaja, The role of oxygenation on the attachment of Escherichia coli rpoS mutant under aerobic conditions, AIP Conf. Proc. 2049 (2018) 020015. https://doi.org/10.1063/1.5082420.

[123] N.F. Putri, P. Suryadarma, S. Zakiyyah, D. Mangunwidjaja, Phosphate addition play important role on Escherichia coli cell attachment under aerobic condition, AIP Conf. Proc. 2049 (2018) 020014. https://doi.org/10.1063/1.5082419.

[124] E.J.G. Pollitt, S.A. Crusz, S.P. Diggle, Staphylococcus aureus forms spreading dendrites that have characteristics of active motility, Sci. Rep. 5 (2015) 17698. https://doi.org/10.1038/srep17698.

[125] C. Formosa-Dague, C. Feuillie, A. Beaussart, S. Derclaye, S. Kucharíková, I. Lasa, P. Van Dijck, Y.F. Dufreîne, Sticky Matrix: Adhesion Mechanism of the Staphylococcal Polysaccharide Intercellular Adhesin, ACS Nano. 10 (2016) 3443–3452. https://doi.org/10.1021/acsnano.5b07515.

[126] M.H. Lin, J.C. Shu, H.Y. Huang, Y.C. Cheng, Involvement of iron in biofilm formation by staphylococcus aureus, PLoS One. 7 (2012) e34388. https://doi.org/10.1371/journal.pone.0034388.

[127] I. Fedtke, D. Mader, T. Kohler, H. Moll, G. Nicholson, R. Biswas, K. Henseler, F. Götz, U. Zähringer, A. Peschel, A Staphylococcus aureus ypfP mutant with strongly reduced lipoteichoic acid (LTA) content: LTA governs bacterial surface properties and autolysin activity, Mol. Microbiol. 65 (2007) 1078–1091. https://doi.org/10.1111/j.1365-2958.2007.05854.x.

[128] C. Weidenmaier, R.M. McLoughlin, J.C. Lee, The Zwitterionic cell wall teichoic acid of Staphylococcus aureus provokes skin abscesses in mice by a novel CD4+ T-cell-dependent mechanism, PLoS One. 5 (2010) e13227. https://doi.org/10.1371/journal.pone.0013227.

[129] M. Gross, S.E. Cramton, F. Götz, A. Peschel, Key role of teichoic acid net charge in Staphylococcus aureus colonization of artificial surfaces, Infect. Immun. 69 (2001) 3423–3426. https://doi.org/10.1128/IAI.69.5.3423-3426.2001.

[130] A. Komaromy, R.I. Boysen, H. Zhang, M.T.W. Hearn, D. V. Nicolau, Effect of various artificial surfaces on the colonization and viability of E. coli and S. aureus, Proc. SPIE. 6799 (2007) 67990J. https://doi.org/10.1117/12.762416.

[131] H.J. Busscher, W. Norde, P.K. Sharma, H.C. van der Mei, Interfacial re-arrangement in initial microbial adhesion to surfaces, Curr. Opin. Colloid Interface Sci. 15 (2010) 510–517. https://doi.org/10.1016/j.cocis.2010.05.014.

[132] Y. Cheng, G. Feng, C.I. Moraru, Micro-and nanotopography sensitive bacterial attachment mechanisms: A review, Front. Microbiol. 10 (2019) 1–17. https://doi.org/10.3389/fmicb.2019.00191.

[133] N. Mitik-Dineva, J. Wang, V.K. Truong, P.R. Stoddart, F. Malherbe, R.J. Crawford, E.P. Ivanova, Differences in colonisation of five marine bacteria on two types of glass surfaces, Biofouling. 25 (2009) 621–631. https://doi.org/10.1080/08927010903012773.

[134] S. Wu, S. Altenried, A. Zogg, F. Zuber, K. Maniura-Weber, Q. Ren, Role of the Surface Nanoscale Roughness of Stainless Steel on Bacterial Adhesion and Microcolony Formation, ACS Omega. 3 (2018) 6456–6464. https://doi.org/10.1021/acsomega.8b00769.

[135] P. Liu, Y. Hao, Y. Zhao, Z. Yuan, Y. Ding, K. Cai, Surface modification of titanium substrates for enhanced osteogenetic and antibacterial properties, Colloids Surfaces B Biointerfaces. 160 (2017) 110–116. https://doi.org/10.1016/j.colsurfb.2017.08.044.

[136] C. Spengler, E. Maikranz, B. Glatz, M.A. Klatt, H. Heintz, M. Bischoff, L. Santen, A. Fery, K. Jacobs, The adhesion capability of Staphylococcus aureus cells is heterogeneously distributed over the cell envelope, Soft Matter. 20 (2024). https://doi.org/https://doi.org/10.1039/D3SM01045G.

[137] T. Vissers, A.T. Brown, N. Koumakis, A. Dawson, M. Hermes, J. Schwarz-Linek, A.B. Schofield, J.M. French, V. Koutsos, J. Arlt, V.A. Martinez, W.C.K. Poon, Bacteria as living patchy colloids: Phenotypic heterogeneity in surface adhesion, Sci. Adv. 4 (2018) 1–9. https://doi.org/10.1126/sciadv.aao1170.

[138] P. Loskill, H. Hähl, N. Thewes, C.T. Kreis, M. Bischoff, M. Herrmann, K. Jacobs, Influence of the subsurface composition of a material on the adhesion of staphylococci, Langmuir. 28 (2012) 7242–7248. https://doi.org/10.1021/la3004323.

[139] M.R. Park, M.K. Banks, B. Applegate, T.J. Webster, Influence of nanophase titania topography on bacterial attachment and metabolism, Int. J. Nanomedicine. 3 (2008) 497–504. https://doi.org/10.2147/IJN.S4399.

[140] K.A. Whitehead, J. Colligon, J. Verran, Retention of microbial cells in substratum surface features of micrometer and sub-micrometer dimensions, Colloids Surfaces B Biointerfaces. 41 (2005) 129–138. https://doi.org/10.1016/j.colsurfb.2004.11.010.

[141] J. Verran, A. Packer, P. Kelly, K.A. Whitehead, The retention of bacteria on hygienic surfaces presenting scratches of microbial dimensions, Lett. Appl. Microbiol. 50 (2010) 258–263. https://doi.org/10.1111/j.1472-765X.2009.02784.x.

[142] L.C. Hsu, J. Fang, D.A. Borca-Tasciuc, R.W. Worobo, C.I. Moraru, Effect of micro- and nanoscale topography on the adhesion of bacterial cells to solid surfaces, Appl. Environ. Microbiol. 79 (2013) 2703–2712. https://doi.org/10.1128/AEM.03436-12.

[143] A.I. Hochbaum, J. Aizenberg, Bacteria pattern spontaneously on periodic nanostructure arrays, Nano Lett. 10 (2010) 3717–3721. https://doi.org/10.1021/nl102290k.

[144] R.S. Friedlander, H. Vlamakis, P. Kim, M. Khan, R. Kolter, J. Aizenberg, Bacterial flagella explore microscale hummocks and hollows to increase adhesion, PNAS. 110 (2013) 1–6. https://doi.org/10.1073/pnas.1219662110.

[145] C. Lüdecke, M. Roth, W. Yu, U. Horn, J. Bossert, K.D. Jandt, Nanorough titanium surfaces reduce adhesion of Escherichia coli and Staphylococcus aureus via nano adhesion points, Colloids Surfaces B Biointerfaces. 145 (2016) 617–625. https://doi.org/10.1016/j.colsurfb.2016.05.049.

[146] N. Epperlein, F. Menzel, K. Schwibbert, R. Koter, J. Bonse, J. Sameith, J. Krüger, J. Toepel, Influence of femtosecond laser produced nanostructures on biofilm growth on steel, Appl. Surf. Sci. 418 (2017) 420–424. https://doi.org/10.1016/j.apsusc.2017.02.174.

[147] D. Siegismund, A. Undisz, S. Germerodt, S. Schuster, M. Rettenmayr, Quantification of the interaction between biomaterial surfaces and bacteria by 3-D modeling, Acta Biomater. 10 (2014) 267–275. https://doi.org/10.1016/j.actbio.2013.09.016.

[148] C. Spengler, F. Nolle, J. Mischo, T. Faidt, S. Grandthyll, N. Thewes, M. Koch, F. Müller, M. Bischo, A. Klatt, K. Jacobs, Strength of bacterial adhesion on nanostructured surfaces quantified by substrate morphometry, Nanoscale. 11 (2019) 19713–19722. https://doi.org/10.1039/c9nr04375f.

[149] L. Pellegrino, L.S. Kriem, E.S.J. Robles, J.T. Cabral, Microbial Response to Micrometer-Scale Multiaxial Wrinkled Surfaces, ACS Appl. Mater. Interfaces. 14 (2022) 31463–31473. https://doi.org/10.1021/acsami.2c08768.

[150] A.K. Epstein, A.I. Hochbaum, P. Kim, J. Aizenberg, Control of bacterial biofilm growth on surfaces by nanostructural mechanics and geometry, Nanotechnology. 22 (2011) 494007–15. https://doi.org/10.1088/0957-4484/22/49/494007.

[151] R.N. Wenzel, Surface roughness and contact angle, J. Phys. Colloid Chem. 53 (1949) 1466–1467. https://doi.org/10.1021/j150474a015.

[152] E.A. Cuello, L.E. Mulko, C.A. Barbero, D.F. Acevedo, E.I. Yslas, Development of micropatterning polyimide films for enhanced antifouling and antibacterial properties, Colloids Surfaces B Biointerfaces. 188 (2020) 110801. https://doi.org/10.1016/j.colsurfb.2020.110801.

[153] S. Abban, M. Jakobsen, L. Jespersen, Attachment behaviour of Escherichia coli K12 and Salmonella Typhimurium P6 on food contact surfaces for food transportation, Food Microbiol. 31 (2012) 139–147. https://doi.org/10.1016/j.fm.2012.04.003.

[154] J.F. Schumacher, M.L. Carman, T.G. Estes, A.W. Feinberg, L.H. Wilson, M.E. Callow, J.A. Callow, J.A. Finlay, A.B. Brennan, Engineered antifouling microtopographies - Effect of feature size, geometry, and roughness on settlement of zoospores of the green alga Ulva, Biofouling. 23 (2007) 55–62. https://doi.org/10.1080/08927010601136957.

[155] R.N. Wenzel, Resistance of solid surfaces to wetting by water., J. Ind. Eng. Chem. (Washington, D. C.). 28 (1936) 988–994. https://doi.org/10.1021/ie50320a024.

[156] B.D. Cassie, A.B.D. Cassie, S. Baxter, Of porous surfaces, Trans. Faraday Soc. 40 (1944) 546–551. https://doi.org/10.1039/tf9444000546.

[157] A.K. Epstein, D. Hong, P. Kim, J. Aizenberg, Biofilm attachment reduction on bioinspired, dynamic, micro-wrinkling surfaces, New J. Phys. 15 (2013) 095018. https://doi.org/10.1088/1367-2630/15/9/095018.

[158] E. Fadeeva, B. Chichkov, Biomimetic Liquid-Repellent Surfaces by Ultrafast Laser Processing, Appl. Sci. 8 (2018). https://doi.org/10.3390/app8091424.

[159] E.P. Ivanova, V.K. Truong, J.Y. Wang, C.C. Bemdt, R.T. Jones, I.I. Yusuf, I. Peake, H.W. Schmidt, C. Fluke, D. Barnes, R.J. Crawford, Impact of nanoscale roughness of titanium thin film surfaces on bacterial Retention, Langmuir. 26 (2010) 1973–1982. https://doi.org/10.1021/la902623c.

[160] C. Dewald, C. Lüdecke, I. Firkowska-Boden, M. Roth, J. Bossert, K.D. Jandt, Gold nanoparticle contact point density controls microbial adhesion on gold surfaces, Colloids Surfaces B Biointerfaces. 163 (2018) 201–208. https://doi.org/10.1016/j.colsurfb.2017.12.037.

[161] E. Fadeeva, V.K. Truong, M. Stiesch, B.N. Chichkov, R.J. Crawford, J. Wang, E.P. Ivanova, Bacterial retention on superhydrophobic titanium surfaces fabricated by femtosecond laser ablation, Langmuir. 27 (2011) 3012–3019. https://doi.org/10.1021/la104607g.

[162] K. Schwibbert, F. Menzel, N. Epperlein, J. Bonse, J. Krüger, Bacterial Adhesion on Femtosecond Laser-Modified Polyethylene, Materials (Basel). 12 (2019) 16–25.

[163] E. Vassallo, M. Pedroni, T. Silvetti, S. Morandi, S. Toffolatti, G. Angella, M. Brasca, Bactericidal performance of nanostructured surfaces by fluorocarbon plasma, Mater. Sci. Eng. C. 80 (2017) 117–121. https://doi.org/10.1016/j.msec.2017.05.111.

[164] E.P. Ivanova, J. Hasan, H.K. Webb, G. Gervinskas, S. Juodkazis, V.K. Truong, A.H.F. Wu, R.N. Lamb, V.A. Baulin, G.S. Watson, J.A. Watson, D.E. Mainwaring, R.J. Crawford, Bactericidal activity of black

silicon, Nat. Commun. 4 (2013) 1–7. https://doi.org/10.1038/ncomms3838.

[165] T. Sjöström, A.H. Nobbs, B. Su, Bactericidal nanospike surfaces via thermal oxidation of Ti alloy substrates, Mater. Lett. 167 (2016) 22–26. https://doi.org/10.1016/j.matlet.2015.12.140.

[166] X. Li, Bactericidal mechanism of nanopatterned surfaces, Phys. Chem. Chem. Phys. 18 (2016) 1311–1316. https://doi.org/10.1039/C5CP05646B.

[167] S. Ghosh, S. Niu, M. Yankova, M. Mecklenburg, S.M. King, J. Ravichandran, R.K. Kalia, A. Nakano, P. Vashishta, P. Setlow, Analysis of killing of growing cells and dormant and germinated spores of Bacillus species by black silicon nanopillars, Sci. Rep. 7 (2017) 1–13. https://doi.org/10.1038/s41598-017-18125-z.

[168] C.J. Murray, et al., Global burden of bacterial antimicrobial resistance in 2019: a systematic analysis, Lancet. 399 (2022) 629–655. https://doi.org/10.1016/S0140-6736(21)02724-0.

[169] L.P. Arendsen, R. Thakar, A.H. Sultan, The use of copper as an antimicrobial agent in health care, including obstetrics and gynecology, Clin. Microbiol. Rev. 32 (2019) 1–28. https://doi.org/10.1128/CMR.00125-18.

[170] M. Colin, E. Charpentier, F. Klingelschmitt, C. Bontemps, C. De Champs, F. Reffuveille, S.C. Gangloff, Specific antibacterial activity of copper alloy touch surfaces in five long-term care facilities for older adults, J. Hosp. Infect. 104 (2020) 283–292. https://doi.org/10.1016/j.jhin.2019.11.021.

[171] K. Siems, D.W. Müller, L. Maertens, A. Ahmed, R. Van Houdt, R.L. Mancinelli, S. Baur, K. Brix, R. Kautenburger, N. Caplin, J. Krause, R. Demets, M. Vukich, A. Tortora, C. Roesch, G. Holland, M. Laue, F. Mücklich, R. Moeller, Testing Laser-Structured Antimicrobial Surfaces Under Space Conditions: The Design of the ISS Experiment BIOFILMS, Front. Sp. Technol. 2 (2022) 1–18. https://doi.org/10.3389/frspt.2021.773244.

[172] K. Alasvand Zarasvand, V.R. Rai, Microorganisms: Induction and inhibition of corrosion in metals, Int. Biodeterior. Biodegrad. 87 (2014) 66–74. https://doi.org/10.1016/j.ibiod.2013.10.023.

[173] L. Weaver, J.O. Noyce, H.T. Michels, C.W. Keevil, Potential action of copper surfaces on meticillin-resistant Staphylococcus aureus, J. Appl. Microbiol. 109 (2010) 2200–2205. https://doi.org/10.1111/j.1365-2672.2010.04852.x.

[174] C. Espírito Santo, P.V. Morais, G. Grass, Isolation and Characterization of Bacteria Resistant to Metallic Copper Surfaces, Appl. Environ. Microbiol. 76 (2010) 1341–1348. https://doi.org/10.1128/AEM.01952-09.

[175] H.L. Karlsson, P. Cronholm, Y. Hedberg, M. Tornberg, L. De Battice, S. Svedhem, I.O. Wallinder, Cell membrane damage and protein interaction induced by copper containing nanoparticles-Importance of the metal release process, Toxicology. 313 (2013) 59–69. https://doi.org/10.1016/j.tox.2013.07.012.

[176] P. Bleichert, C. Espírito Santo, M. Hanczaruk, H. Meyer, G. Grass, Inactivation of bacterial and viral biothreat agents on metallic copper surfaces, BioMetals. 27 (2014) 1179–1189. https://doi.org/10.1007/s10534-014-9781-0.

[177] C.E. Santo, D. Quaranta, G. Grass, Antimicrobial metallic copper surfaces kill Staphylococcus haemolyticus via membrane damage, Microbiologyopen. 1 (2012) 46–52. https://doi.org/10.1002/mbo3.2.

[178] C. Wang, C.J. Ehrhardt, V.K. Yadavalli, Nanoscale imaging and hydrophobicity mapping of the antimicrobial effect of copper on bacterial surfaces, Micron. 88 (2016) 16–23. https://doi.org/10.1016/j.micron.2016.05.005.

[179] P. Wang, T.B. Kinraide, E. Smolders, D.M. Zhou, N.W. Menzies, S. Thakali, W.W. Xia, X.Z. Hao, W.J.G.M. Peijnenburg, P.M. Kopittke, An electrostatic model predicting Cu and Ni toxicity to microbial processes in soils, Soil Biol. Biochem. 57 (2013) 720–730. https://doi.org/10.1016/j.soilbio.2012.09.002.

[180] M. Solioz, H.K. Abicht, M. Mermod, S. Mancini, Response of Gram-positive bacteria to copper stress, J. Biol. Inorg. Chem. 15 (2010) 3–14. https://doi.org/10.1007/s00775-009-0588-3.

[181] L. Macomber, J.A. Imlay, The iron-sulfur clusters of dehydratases are primary intracellular targets of copper toxicity, Proc. Natl. Acad. Sci. 106 (2009) 8344–8349. https://doi.org/10.1073/pnas.0812808106.

[182] A.R. Karlstrom, R.L. Levine, Copper inhibits the protease from human immunodeficiency virus 1 by both cysteine-dependent and cysteine-independent mechanisms, Proc. Natl. Acad. Sci. U. S. A. 88 (1991) 5552–5556. https://doi.org/10.1073/pnas.88.13.5552.

[183] J.O. Noyce, H. Michels, C.W. Keevil, Inactivation of influenza A virus on copper versus stainless steel

surfaces, Appl. Environ. Microbiol. 73 (2007) 2748–2750. https://doi.org/10.1128/AEM.01139-06.

[184] S.L. Warnes, E.N. Summersgill, C.W. Keevil, Inactivation of Murine Norovirus on a Range of Copper Alloy Surfaces Is Accompanied by Loss of Capsid Integrity, Appl. Environ. Microbiol. 81 (2015) 1085–1091. https://doi.org/10.1128/AEM.03280-14.

[185] S.L. Warnes, Z.R. Little, C.W. Keevil, Human coronavirus 229E remains infectious on common touch surface materials, MBio. 6 (2015) 1–10. https://doi.org/10.1128/mBio.01697-15.

[186] T.L. Meister, J. Fortmann, M. Breisch, C. Sengstock, E. Steinmann, M. Köller, S. Pfaender, A. Ludwig, Nanoscale copper and silver thin film systems display differences in antiviral and antibacterial properties, Sci. Rep. 12 (2022) 1–10. https://doi.org/10.1038/s41598-022-11212-w.

[187] F.X. Abad, R.M. Pinto, J.M. Diez, A. Bosch, Disinfection of human enteric viruses in water by copper and silver in combination with low levels of chlorine, Appl. Environ. Microbiol. 60 (1994) 2377–2383. https://doi.org/10.1128/aem.60.7.2377-2383.1994.

[188] J. Li, J.J. Dennehy, Differential bacteriophage mortality on exposure to copper, Appl. Environ. Microbiol. 77 (2011) 6878–6883. https://doi.org/10.1128/AEM.05661-11.

[189] Z. Weissman, R. Shemer, D. Kornitzer, Deletion of the copper transporter CaCCC2 reveals two distinct pathways for iron acquisition in Candida albicans, Mol. Microbiol. 44 (2002) 1551–1560. https://doi.org/10.1046/j.1365-2958.2002.02976.x.

[190] A. Kapoor, T. Viraraghavan, D.R. Cullimore, Removal of heavy metals using the fungus Aspergillus niger, Bioresour. Technol. 70 (1999) 95–104.

[191] N.L. Iskandar, N.A.I.M. Zainudin, S.G. Tan, Tolerance and biosorption of copper (Cu) and lead (Pb) by filamentous fungi isolated from a freshwater ecosystem, J. Environ. Sci. 23 (2011) 824–830. https://doi.org/10.1016/S1001-0742(10)60475-5.

[192] B. Dudová, D. Hudecová, R. Pokorný, M. Mikulášová, M. Palicová, P. Segl'a, M. Melník, Copper complexes with bioactive ligands part I - Antimicrobial activity, Folia Microbiol. (Praha). 46 (2001) 379–384. https://doi.org/10.1007/BF02814425.

[193] E. Ghasemian, A. Naghoni, B. Tabaraie, T. Tabaraie, In vitro susceptibility of filamentous fungi to copper nanoparticles assessed by rapid XTT colorimetry and agar dilution method, J. Mycol. Med. 22 (2012) 322–328. https://doi.org/10.1016/j.mycmed.2012.09.006.

[194] M.G. Palmgren, P. Nissen, P-Type ATPases, Annu. Rev. Biophys. 40 (2011) 243–266. https://doi.org/10.1146/annurev.biophys.093008.131331.

[195] E. Ladomersky, M.J. Petris, Copper tolerance and virulence in bacteria, Metallomics. 7 (2015) 957–964. https://doi.org/10.1039/c4mt00327f.

[196] D.H. Nies, Efflux-mediated heavy metal resistance in prokaryotes, FEMS Microbiol. Rev. 27 (2003) 313–339. https://doi.org/10.1016/S0168-6445(03)00048-2.

[197] M. Solioz, Copper and Bacteria Evolution, Homeostasis and Toxicity, 2018.

[198] J. Bai, Y. Chao, Y. Chen, S. Wang, R. Qiu, Immobilization of Cu by Bacillus subtilis DBM and the Role of Extracellular Polymeric Substances, Water, Air, Soil Pollut. 228 (2017) 86. https://doi.org/10.1007/s11270-017-3269-9.

[199] K. San, J. Long, C.A. Michels, N. Gadura, Antimicrobial copper alloy surfaces are effective against vegetative but not sporulated cells of gram-positive Bacillus subtilis, Microbiologyopen. 4 (2015) 753–763. https://doi.org/10.1002/mbo3.276.

[200] R. Rajaram, J.S. Banu, K. Mathivanan, Biosorption of Cu (II) ions by indigenous copper-resistant bacteria isolated from polluted coastal environment, Toxicol. Environ. Chem. 95 (2013) 590–604. https://doi.org/10.1080/02772248.2013.801979.

[201] A.G. González, L.S. Shirokova, O.S. Pokrovsky, E.E. Emnova, R.E. Martínez, J.M. Santana-Casiano, M. González-Dávila, G.S. Pokrovski, Adsorption of copper on Pseudomonas aureofaciens: Protective role of surface exopolysaccharides, J. Colloid Interface Sci. 350 (2010) 305–314. https://doi.org/10.1016/j.jcis.2010.06.020.

[202] S. Liu, X.X. Zhang, Small colony variants are more susceptible to copper-mediated contact killing for Pseudomonas aeruginosa and Staphylococcus aureus, J. Med. Microbiol. 65 (2016) 1143–1151. https://doi.org/10.1099/jmm.0.000348.

[203] J.R. Williams, A.G. Morgan, D.A. Rouch, N.L. Brown, Copper-Resistant Enteric Bacteria from United Kingdom and Australian Piggeries, Appl. Environ. Microbiol. 59 (1993) 2531–2537.

[204] S. Shafeeq, H. Yesilkaya, T.G. Kloosterman, G. Narayanan, M. Wandel, P.W. Andrew, O.P. Kuipers, J.A. Morrissey, The cop operon is required for copper homeostasis and contributes to virulence in Streptococcus pneumoniae, Mol. Microbiol. 81 (2011) 1255–1270. https://doi.org/10.1111/j.1365-2958.2011.07758.x.

[205] F. Wolschendorf, D. Ackart, T.B. Shrestha, L. Hascall-Dove, S. Nolan, G. Lamichhane, Y. Wang, S.H. Bossmann, R.J. Basaraba, M. Niederweis, Copper resistance is essential for virulence of Mycobacterium tuberculosis, Proc. Natl. Acad. Sci. 108 (2011) 1621–1626. https://doi.org/10.1073/pnas.1009261108.

[206] C. Pal, J. Bengtsson-Palme, E. Kristiansson, D.G.J. Larsson, Co-occurrence of resistance genes to antibiotics, biocides and metals reveals novel insights into their co-selection potential, BMC Genomics. 16 (2015) 964. https://doi.org/10.1186/s12864-015-2153-5.

[207] J. Baker, M. Sengupta, R.K. Jayaswal, J.A. Morrissey, The Staphylococcus aureus CsoR regulates both chromosomal and plasmid-encoded copper resistance mechanisms, Environ. Microbiol. 13 (2011) 2495–2507. https://doi.org/10.1111/j.1462-2920.2011.02522.x.

[208] S.L. Warnes, Laboratory studies to investigate the efficacy and mechanism of action of copper alloys to kill a range of bacterial pathogens and inactivate norovirus, 2014.

[209] C.E. Santo, E.W. Lam, C.G. Elowsky, D. Quaranta, D.W. Domaille, C.J. Chang, G. Grass, Bacterial Killing by Dry Metallic Copper Surfaces ന, 77 (2011) 794–802. https://doi.org/10.1128/AEM.01599-10.

[210] J. Abraham, K. Dowling, S. Florentine, Can copper products and surfaces reduce the spread of infectious microorganisms and hospital-acquired infections?, Materials (Basel). 14 (2021) 1–27. https://doi.org/10.3390/ma14133444.

[211] E.A. Bryce, B. Velapatino, H. Akbari Khorami, T. Donnelly-Pierce, T. Wong, R. Dixon, E. Asselin, In vitro evaluation of antimicrobial efficacy and durability of three copper surfaces used in healthcare , Biointerphases. 15 (2020) 011005. https://doi.org/10.1116/1.5134676.

[212] A.L. Casey, D. Adams, T.J. Karpanen, P.A. Lambert, B.D. Cookson, P. Nightingale, L. Miruszenko, R. Shillam, P. Christian, T.S.J. Elliott, Role of copper in reducing hospital environment contamination, J. Hosp. Infect. 74 (2010) 72–77. https://doi.org/10.1016/j.jhin.2009.08.018.

[213] T.J. Karpanen, A.L. Casey, P.A. Lambert, B.D. Cookson, P. Nightingale, L. Miruszenko, T.S.J. Elliott, The Antimicrobial Efficacy of Copper Alloy Furnishing in the Clinical Environment: A Crossover Study, Infect. Control Hosp. Epidemiol. 33 (2012) 3–9. https://doi.org/10.1086/663644.

[214] J. Luo, C. Hein, J. Pierson, F. Mücklich, Early-stage corrosion , ion release , and the antibacterial effect of copper and cuprous oxide in physiological buffers : Phosphate-buffered saline vs Na-4- (2-hydroxyethyl) -1-piperazineethanesulfonic acid, Biointerphases. 14 (2019). https://doi.org/10.1063/1.5123039.

[215] J. Luo, C. Hein, J.F. Pierson, F. Mücklich, Sodium chloride assists copper release, enhances antibacterial efficiency, and introduces atmospheric corrosion on copper surface, Surfaces and Interfaces. 20 (2020) 100630. https://doi.org/10.1016/j.surfin.2020.100630.

[216] P. Flores, R. Schauer, S.A. McBride, J. Luo, M. Cortesão, C. Hoehn, S. Doraisingam, D. Widhalm, J. Chadha, H. Meyerson, E. Mitzak, V. Hurd, L. Selman, M. Vellone, S. Floyd, S. Tozer, M. Rupert, S. Gorti, S. Reagan, K.K. Varanasi, F. Muecklich, R. Moeller, L. Stodieck, S. Countryman, L. Zea, Preparation for and Performance of a Pseudomonas aeruginosa Biofilm Experiment On Board the International Space Station, Acta Astronaut. (2021). https://doi.org/10.1016/j.actaastro.2022.07.015.

[217] J. Luo, C. Hein, J. Pierson, F. Mücklich, Localised corrosion attacks and oxide growth on copper in phosphate-buffered saline, Mater. Charact. 158 (2019) 109985. https://doi.org/10.1016/j.matchar.2019.109985.

[218] M.T. González-Muñoz, C. Rodriguez-Navarro, F. Martínez-Ruiz, J.M. Arias, M.L. Merroun, M. Rodriguez-Gallego, Bacterial biomineralization: New insights from Myxococcus-induced mineral precipitation, Geol. Soc. London, Spec. Publ. 336 (2010) 31–50. https://doi.org/10.1144/SP336.3.

[219] N. Ben Omar, M.M. Nez-canamero, J.M. Arias, F. Huertas, Myxococcus xanthus' killed cells as inducers of struvite crystallization, Its possible role in the biomineralization processes., Chemosphere. 30 (1995) 2387–2396.

[220] M.A. Rivadeneyra, I. Pérez-García, A. Ramos-Cormenzana, Influence of ammonium ion on bacterial

struvite production, Geomicrobiol. J. 10 (1992) 125–137. https://doi.org/10.1080/01490459209377912.

[221] G. He, W. Hu, C.M. Li, Spontaneous interfacial reaction between metallic copper and PBS to form cupric phosphate nanoflower and its enzyme hybrid with enhanced activity, Colloids Surfaces B Biointerfaces. 135 (2015) 613–618. https://doi.org/10.1016/j.colsurfb.2015.08.030.

[222] M.L. Merroun, N. Ben Omar, E. Alonso, J.M. Arias, M.T. González-Muñoz, Silver sorption to myxococcus xanthus biomass, Geomicrobiol. J. 18 (2001) 183–192. https://doi.org/10.1080/01490450117323.

[223] J. Porcayo-Calderon, R.A. Rodríguez-Díaz, E. Porcayo-Palafox, L. Martinez-Gomez, Corrosion Performance of Cu-Based Coins in Artificial Sweat, J. Chem. 2016 (2016). https://doi.org/10.1155/2016/9542942.

[224] I. Platzman, R. Brener, H. Haick, R. Tannenbaum, Oxidation of Polycrystalline Copper Thin Films at Ambient Conditions, J. Phys. Chem. C. (2008) 1101–1108.

[225] L. Lapeire, E. Martinez Lombardia, K. Verbeken, I. De Graeve, L.A.I. Kestens, H. Terryn, Effect of neighboring grains on the microscopic corrosion behavior of a grain in polycrystalline copper, Corros. Sci. 67 (2013) 179–183. https://doi.org/10.1016/j.corsci.2012.10.017.

[226] K.R. Lawless, A.T. Gwathmey, The Structure of oxide Films on Different Faces of a single Crystal of Copper, Acta Metall. 4 (1956) 153–163.

[227] W. Li, D.Y. Li, Variations of work function and corrosion behaviors of deformed copper surfaces, Appl. Surf. Sci. 240 (2005) 388–395. https://doi.org/10.1016/j.apsusc.2004.07.017.

[228] S. Yin, D.Y. Li, Effects of prior cold work on corrosion and corrosive wear of copper in HNO3 and NaCl solutions, Mater. Sci. Eng. A. 394 (2005) 266–276. https://doi.org/10.1016/j.msea.2004.11.054.

[229] V. Parmar, K. Changela, B. Srinivas, M.M. Sankar, S. Mohanty, S.K. Panigrahi, K. Hariharan, D. Kalyanasundaram, Relationship between dislocation density and antibacterial activity of cryo-rolled and cold-rolled copper, Materials (Basel). 12 (2019) 1–11. https://doi.org/10.3390/ma12020200.

[230] M. Razavipour, M. Gonzalez, N. Singh, C.E. Cimenci, N. Chu, E.I. Alarcon, J. Villafuerte, B. Jodoin, Biofilm Inhibition and Antiviral Response of Cold Sprayed and Shot Peened Copper Surfaces: Effect of Surface Morphology and Microstructure, J. Therm. Spray Technol. 31 (2022) 130–144. https://doi.org/10.1007/s11666-021-01315-7.

[231] O. Sharifahmadian, H.R. Salimijazi, M.H. Fathi, J. Mostaghimi, L. Pershin, Relationship between surface properties and antibacterial behavior of wire arc spray copper coatings, Surf. Coatings Technol. 233 (2013) 74–79. https://doi.org/10.1016/j.surfcoat.2013.01.060.

[232] M. Zeiger, M. Solioz, H. Edongué, E. Arzt, A.S. Schneider, Surface structure influences contact killing of bacteria by copper, Microbiologyopen. 3 (2014) 327–332. https://doi.org/10.1002/mbo3.170.

[233] A. Vinogradov, T. Mimaki, S. Hashimoto, R. Valiev, On the corrosion behaviour of ultra-fine grain copper, Scr. Mater. 41 (1999) 319–326. https://doi.org/10.1016/S1359-6462(99)00170-0.

[234] H. Miyamoto, K. Harada, T. Mimaki, A. Vinogradov, S. Hashimoto, Corrosion of ultra-fine grained copper fabricated by equal-channel angular pressing, Corros. Sci. 50 (2008) 1215–1220. https://doi.org/10.1016/j.corsci.2008.01.024.

[235] A. Nikfahm, I. Danaee, A. Ashrafi, M.R. Toroghinejad, Effect of grain size changes on corrosion behavior of copper produced by accumulative roll bonding process, Mater. Res. 16 (2013) 1379–1386. https://doi.org/10.1590/S1516-14392013005000135.

[236] O. Imantalab, M.K. Keshavarz, Y. Mazaheri, Electrochemical Behavior of Pure Copper in Phosphate Buffer Solutions : A Comparison Between Micro- and Nano-Grained Copper, J. Mater. Eng. Perform. 25 (2016) 697–703. https://doi.org/10.1007/s11665-015-1836-z.

[237] H. Miyamoto, Corrosion of ultrafine grained materials by severe plastic deformation, an overview, Mater. Trans. 57 (2016) 559–572. https://doi.org/10.2320/matertrans.M2015452.

[238] Z. Zhang, S. Yang, P. Lv, Y. Li, X. Wang, X. Hou, Q. Guan, Applied Surface Science The microstructures and corrosion properties of polycrystalline copper induced by high-current pulsed electron beam, Appl. Surf. Sci. 294 (2014) 9–14.

[239] V. Gopinath, S. Priyadarshini, A.R. Al-Maleki, M. Alagiri, R. Yahya, S. Saravanan, J. Vadivelu, In vitro toxicity, apoptosis and antimicrobial effects of phyto-mediated copper oxide nanoparticles, RSC Adv. 6 (2016) 110986–110995. https://doi.org/10.1039/C6RA13871C.

[240] A.L. Ulloa-Ogaz, H.A. Piñón-Castillo, L.N. Muñoz-Castellanos, M.S. Athie-García, M.D.L. Ballinas-Casarrubias, J.G. Murillo-Ramirez, L.Á. Flores-Ongay, R. Duran, E. Orrantia-Borunda, Oxidative damage to Pseudomonas aeruginosa ATCC 27833 and Staphylococcus aureus ATCC 24213 induced by CuO-NPs, Environ. Sci. Pollut. Res. 24 (2017) 22048–22060. https://doi.org/10.1007/s11356-017-9718-6.

[241] M. Ben-Sasson, K.R. Zodrow, Q. Genggeng, Y. Kang, E.P. Giannelis, M. Elimelech, Surface functionalization of thin-film composite membranes with copper nanoparticles for antimicrobial surface properties, Environ. Sci. Technol. 48 (2014) 384–393. https://doi.org/10.1021/es404232s.

[242] D. Franco, G. Calabrese, S.P.P. Guglielmino, S. Conoci, Metal-Based Nanoparticles: Antibacterial Mechanisms and Biomedical Application, Microorganisms. 10 (2022). https://doi.org/10.3390/microorganisms10091778.

[243] C. Gargioni, M. Borzenkov, L. D'alfonso, P. Sperandeo, A. Polissi, L. Cucca, G. Dacarro, P. Grisoli, P. Pallavicini, A. D'agostino, A. Taglietti, Self-assembled monolayers of copper sulfide nanoparticles on glass as antibacterial coatings, Nanomaterials. 10 (2020). https://doi.org/10.3390/nano10020352.

[244] A. Tripathy, A. Kumar, S. Sreedharan, G. Muralidharan, A. Pramanik, D. Nandi, P. Sen, Fabrication of Low-Cost Flexible Superhydrophobic Antibacterial Surface with Dual-Scale Roughness, ACS Biomater. Sci. Eng. 4 (2018) 2213–2223. https://doi.org/10.1021/acsbiomaterials.8b00209.

[245] N. Ghasemi, F. Jamali-Sheini, R. Zekavati, CuO and Ag/CuO nanoparticles: Biosynthesis and antibacterial properties, Mater. Lett. 196 (2017) 78–82. https://doi.org/10.1016/j.matlet.2017.02.111.

[246] A.M. Emelyanenko, V. V. Kaminskii, I.S. Pytskii, A.G. Domantovsky, K.A. Emelyanenko, A. V. Aleshkin, L.B. Boinovich, Antibacterial Properties of Superhydrophilic Textured Copper in Contact with Bacterial Suspensions, Bull. Exp. Biol. Med. 168 (2020) 488–491. https://doi.org/10.1007/s10517-020-04737-5.

[247] A.-M. Kietzig, S.G. Hatzikiriakos, P. Englezos, Patterned superhydrophobic metallic surfaces, Langmuir. 25 (2009) 4821–4827. https://doi.org/10.1021/la8037582.

[248] J.C. Kieffer, P. Audebert, M. Chaker, J.P. Matte, H. Pepin, T.W. Johnston, P. Maine, D. Meyerhofer, J. Delettrez, D. Strickland, P. Bado, G. Mourou, Short-Pulse Laser Absorption in Very Steep Plasma Density Gradients, Phys. Rev. Lett. 62 (1989) 760–763.

[249] S. Nolte, Ultrashort Pulse Laser Technology, 2016. https://doi.org/10.1007/978-3-319-17659-8.

[250] K. Sugioka, M. Meunier, A. Pique, Laser Precision Microfabrication, Springer, 2010.

[251] S. Amoruso, X. Wang, C. Altucci, C. De Lisio, M. Armenante, R. Bruzzese, R. Velotta, Thermal and nonthermal ion emission during high-fluence femtosecond laser ablation of metallic targets, Appl. Phys. Lett. 77 (2000) 3728–3730. https://doi.org/10.1063/1.1329869.

[252] S. Amoruso, X. Wang, C. Altucci, C. De Lisio, M. Armenante, Double-peak distribution of electron and ion emission pro ® le during femtosecond laser ablation of metals, Appl. Surf. Sci. 186 (2002) 358–363.

[253] A.A. Ionin, S.I. Kudryashov, L. V. Seleznev, D. V. Sinitsyn, V.N. Lednev, S.M. Pershin, Preablation electron and lattice dynamics on the silicon surface excited by a femtosecond laser pulse, J. Exp. Theor. Phys. 121 (2015) 737–746. https://doi.org/10.1134/S106377611511014X.

[254] J. Winter, S. Rapp, M. Schmidt, H.P. Huber, Ultrafast laser processing of copper : A comparative study of experimental and simulated transient optical properties, Appl. Surf. Sci. 417 (2017) 2–15. https://doi.org/10.1016/j.apsusc.2017.02.070.

[255] S. Nolte, C. Momma, H. Jacobs, A. Tünnermann, B.N. Chichkov, B. Wellegehausen, H. Welling, Ablation of metals by ultrashort laser pulses., J. Opt. Soc. Am. B. 14 (1997) 2716–2722. https://doi.org/10.1364/JOSAB.14.002716.

[256] S. Nolte, B.N. Chichkov, H. Welling, Y. Shani, K. Lieberman, H. Terkel, Nanostructuring with spatially localized femtosecond laser pulses, Opt. Lett. 24 (1999) 914. https://doi.org/10.1364/OL.24.000914.

[257] P. Simon, J. Ihlemann, Ablation of submicron structures on metals and semiconductors by femtosecond UV-laser pulses, Appl. Surf. Sci. 109–110 (1997) 25–29. https://doi.org/10.1016/S0169-4332(96)00615-0.

[258] J. Hohlfeld, S.-S. Wellershoff, J. Güdde, U. Conrad, V. Jähnke, E. Matthias, Electron and lattice dynamics following optical excitation of metals, Chem. Phys. 251 (2000) 237–258. https://doi.org/10.1016/S0301-0104(99)00330-4.

[259] A.A. Ionin, I.S. Kudryashov, V.L. Seleznev, V.D. Sinitsyn, F.A. Bunkin, N. V Lednev, M.S. Pershin, Thermal melting and ablation of silicon by femtosecond laser radiation, J. Exp. Theor. Phys. 116 (2013) 347–362. https://doi.org/10.1134/S106377611302012X.

[260] M. Huang, F. Zhao, Y. Cheng, N. Xu, Z. Xu, Mechanisms of ultrafast laser-induced deep-subwavelength gratings on graphite and diamond, Phys. Rev. B - Condens. Matter Mater. Phys. 79 (2009) 1–9. https://doi.org/10.1103/PhysRevB.79.125436.

[261] A.A. Ionin, S.I. Kudryashov, A.A. Samokhin, Material surface ablation produced by ultrashort laser pulses, Uspekhi Fiz. Nauk. 187 (2017) 159–172. https://doi.org/10.3367/UFNr.2016.09.037974.

[262] V. Recoules, J. Clérouin, G. Zérah, P.M. Angalde, S. Mazevet, Effect of Intense Laser Irradiation on the Lattice Stability of Semiconductors and Metals, Phys. Rev. Lett. 96 (2006) 1–4. https://doi.org/10.1103/PhysRevLett.96.055503.

[263] N. Jourdain, L. Lecherbourg, V. Recoules, P. Renaudin, F. Dorchies, Ultrafast Thermal Melting in Nonequilibrium Warm Dense Copper, Phys. Rev. Lett. 126 (2021) 65001. https://doi.org/10.1103/PhysRevLett.126.065001.

[264] A.A. Ionin, S.I. Kudryashov, S. V. Makarov, P.N. Saltuganov, L. V. Seleznev, D. V. Sinitsyn, V.A. Lednev, S.M. Pershin, Electron emission and ultrafast low-fluence plasma formation during single-shot femtosecond laser surface ablation of various materials, JETP Lett. 101 (2015) 308–312. https://doi.org/10.1134/S0021364015050112.

[265] J. Winter, M. Spellauge, J. Hermann, C. Eulenkamp, H.P. Huber, M. Schmidt, Ultrashort single-pulse laser ablation of stainless steel, aluminium, copper and its dependence on the pulse duration, Opt. Express. 29 (2021) 14561. https://doi.org/10.1364/oe.421097.

[266] S.Y. Wang, Y. Ren, C.W. Cheng, J.K. Chen, D.Y. Tzou, Micromachining of copper by femtosecond laser pulses, Appl. Surf. Sci. 265 (2013) 302–308. https://doi.org/10.1016/j.apsusc.2012.10.200.

[267] I.A. Artyukov, D.A. Zayarniy, A.A. Ionin, S.I. Kudryashov, S. V Makarov, P.N. Saltuganov, Relaxation Phenomena in Electronic and Lattice Subsystems on Iron Surface during Its Ablation by Ultrashort Laser Pulses, JETP Lett. 99 (2014) 54–58. https://doi.org/10.1134/S0021364014010020.

[268] J. Schille, L. Schneider, U. Loeschner, Process optimization in high-average-power ultrashort pulse laser microfabrication: how laser process parameters influence efficiency, throughput and quality, Appl. Phys. A Mater. Sci. Process. 120 (2015) 847–855. https://doi.org/10.1007/s00339-015-9352-4.

[269] S.I. Anisimov, B.L. Kapeliovich, T.L. Perel′man, Electron emission from metal surfaces exposed to ultrashort laser pulses, Sov. Phys.-JETP. 39 (1974) 375–377.

[270] N.L. Interaction, M.N. Libenson, S.I. Anisimov, B. Rethfeld, ON THE THEORY OF ULTRASHORT LASER PULSE INTERACTION WITH A METAL, 192 (1997) 192–203.

[271] J. Cheng, C. Liu, S. Shang, D. Liu, W. Perrie, G. Dearden, K. Watkins, Optics & Laser Technology A review of ultrafast laser materials micromachining, Opt. Laser Technol. 46 (2013) 88–102. https://doi.org/10.1016/j.optlastec.2012.06.037.

[272] B. Rethfeld, D.S. Ivanov, M.E. Garcia, S.I. Anisimov, Modelling ultrafast laser ablation, J. Phys. D. Appl. Phys. 50 (2017) 01–39. https://doi.org/10.1088/1361-6463/50/19/193001.

[273] P.E. Hopkins, P.M. Norris, Substrate influence in electron – phonon coupling measurements in thin Au films, 253 (2007) 6289–6294. https://doi.org/10.1016/j.apsusc.2007.01.065.

[274] Y. Ren, J.K. Chen, Y. Zhang, Optical properties and thermal response of copper films induced by ultrashort-pulsed lasers, J. Appl. Phys. 110 (2011) 1–7. https://doi.org/10.1063/1.3662897.

[275] C.W. Cheng, S.Y. Wang, K.P. Chang, J.K. Chen, Femtosecond laser ablation of copper at high laser fluence: Modeling and experimental comparison, Appl. Surf. Sci. 361 (2016) 41–48. https://doi.org/10.1016/j.apsusc.2015.11.055.

[276] L. V. Zhigilei, Z. Lin, D.S. Ivanov, Atomistic modeling of short pulse laser ablation of metals: Connections between melting, spallation, and phase explosion, J. Phys. Chem. C. 113 (2009) 11892–11906. https://doi.org/10.1021/jp902294m.

[277] B. Rethfeld, A. Kaiser, M. Vicanek, G. Simon, Ultrafast dynamics of nonequilibrium electrons in metals under femtosecond laser irradiation, Phys. Rev. B. 65 (2002) 1–11. https://doi.org/10.1103/PhysRevB.65.214303.

[278] B. Rethfeld, K. Sokolowski-Tinten, D. von der Linde, S.I. Anisimov, Ultrafast thermal melting of laser-

excited solids by homogeneous nucleation, Phys. Rev. B. 65 (2002) 1–4. https://doi.org/10.1103/PhysRevB.65.092103.

[279] N.A. Smirnov, Copper, gold, and platinum under femtosecond irradiation: Results of first-principles calculations, Phys. Rev. B. 101 (2020) 1–11. https://doi.org/10.1103/PhysRevB.101.094103.

[280] A. Grolleau, F. Dorchies, N. Jourdain, K. Ta Phuoc, J. Gautier, B. Mahieu, P. Renaudin, V. Recoules, P. Martinez, L. Lecherbourg, Femtosecond Resolution of the Nonballistic Electron Energy Transport in Warm Dense Copper, Phys. Rev. Lett. 127 (2021) 275901. https://doi.org/10.1103/PhysRevLett.127.275901.

[281] S.E. Kirkwood, Y.Y. Tsui, R. Fedosejevs, A. V. Brantov, V.Y. Bychenkov, Experimental and theoretical study of absorption of femtosecond laser pulses in interaction with solid copper targets, Phys. Rev. B - Condens. Matter Mater. Phys. 79 (2009) 1–7. https://doi.org/10.1103/PhysRevB.79.144120.

[282] P.A. Loboda, N.A. Smirnov, A.A. Shadrin, N.G. Karlykhanov, Simulation of absorption of femtosecond laser pulses in solid-density copper, High Energy Density Phys. 7 (2011) 361–370. https://doi.org/10.1016/j.hedp.2011.06.007.

[283] Z. Lin, L. V. Zhigilei, V. Celli, Electron-phonon coupling and electron heat capacity of metals under conditions of strong electron-phonon nonequilibrium, Phys. Rev. B - Condens. Matter Mater. Phys. 77 (2008) 1–17. https://doi.org/10.1103/PhysRevB.77.075133.

[284] Z. Lin, E. Leveugle, E.M. Bringa, L. V Zhigilei, Molecular Dynamics Simulation of Laser Melting of Nanocrystalline Au †, (2010) 5686–5699.

[285] M.R. Karim, M. Kattoura, S.R. Mannava, V.K. Vasudevan, A.S. Malik, D. Qian, A computational study on the microstructural evolution in near-surface copper grain boundary structures due to femtosecond laser processing, Comput. Mech. 61 (2018) 105–117. https://doi.org/10.1007/s00466-017-1449-5.

[286] Y. Levy, T.J.Y. Derrien, N.M. Bulgakova, E.L. Gurevich, T. Mocek, Relaxation dynamics of femtosecond-laser-induced temperature modulation on the surfaces of metals and semiconductors, Appl. Surf. Sci. 374 (2016) 157–164. https://doi.org/10.1016/j.apsusc.2015.10.159.

[287] C. Gaudiuso, G. Giannuzzi, A. Volpe, P.M. Lugarà, I. Choquet, A. Ancona, Incubation during laser ablation with bursts of femtosecond pulses with picosecond delays, 26 (2018) 8958–8968. https://doi.org/10.1364/OE.26.003801.

[288] J.H. Klein-Wiele, A. Blumenstein, P. Simon, J. Ihlemann, Laser interference ablation by ultrashort UV laser pulses via diffractive beam management, Adv. Opt. Technol. (2020). https://doi.org/10.1515/aot-2019-0068.

[289] A. Blumenstein, M.E. Garcia, B. Rethfeld, P. Simon, J. Ihlemann, D.S. Ivanov, Formation of periodic nanoridge patterns by ultrashort single pulse UV laser irradiation of gold, Nanomaterials. 10 (2020) 1998. https://doi.org/10.3390/nano10101998.

[290] M. Obergfell, J. Demsar, Tracking the Time Evolution of the Electron Distribution Function in Copper by Femtosecond Broadband Optical Spectroscopy, Phys. Rev. Lett. 124 (2020) 37401. https://doi.org/10.1103/PhysRevLett.124.037401.

[291] Q. Xiong, Z. Li, T. Kitamura, Effect of Crystal Orientation on Femtosecond Laser-Induced Thermomechanical Responses and Spallation Behaviors of Copper Films, Sci. Rep. (2017) 1–14. https://doi.org/10.1038/s41598-017-09559-6.

[292] Y. Jee, M.F. Becker, R.M. Walser, Laser-induced damage on single-crystal metal surfaces, J. Opt. Soc. Am. B. 5 (1988) 648–659. https://doi.org/10.1364/josab.5.000648.

[293] J. Bonse, J. Krüger, S. Höhm, a. Rosenfeld, Femtosecond laser-induced periodic surface structures, J. Laser Appl. 24 (2012) 042006. https://doi.org/10.2351/1.4712658.

[294] Z. Sun, M. Lenzner, W. Rudolph, Generic incubation law for laser damage and ablation thresholds, J. Appl. Phys. 117 (2015). https://doi.org/10.1063/1.4913282.

[295] P.T. Mannion, J. Magee, E. Coyne, G.M. O'Connor, T.J. Glynn, The effect of damage accumulation behaviour on ablation thresholds and damage morphology in ultrafast laser micro-machining of common metals in air, Appl. Surf. Sci. 233 (2004) 275–287. https://doi.org/10.1016/j.apsusc.2004.03.229.

[296] S.E. Kirkwood, A.C. Van Popta, Y.Y. Tsui, R. Fedosejevs, Single and multiple shot near-infrared femtosecond laser pulse ablation thresholds of copper, Appl. Phys. A Mater. Sci. Process. 81 (2005) 729–735. https://doi.org/10.1007/s00339-004-3135-7.

[297] G. Račiukaitis, M. Brikas, P. Gečys, B. Voisiat, M. Gedvilas, Use of high repetition rate and high power lasers in microfabrication: How to keep the efficiency high?, J. Laser Micro Nanoeng. 4 (2009) 186–191. https://doi.org/10.2961/jlmn.2009.03.0008.

[298] A.Y. Vorobyev, C. Guo, Reflection of femtosecond laser light in multipulse ablation of metals, J. Appl. Phys. 110 (2011) 043102. https://doi.org/10.1063/1.3620898.

[299] K.K. Anoop, R. Fittipaldi, A. Rubano, X. Wang, D. Paparo, A. Vecchione, L. Marrucci, R. Bruzzese, S. Amoruso, Direct femtosecond laser ablation of copper with an optical vortex beam, J. Appl. Phys. 116 (2014) 113102. https://doi.org/10.1063/1.4896068.

[300] A. Rudenko, C. Mauclair, F. Garrelie, R. Stoian, J.P. Colombier, Self-organization of surfaces on the nanoscale by topography-mediated selection of quasi-cylindrical and plasmonic waves, Nanophotonics. 8 (2019) 459–465. https://doi.org/10.1515/nanoph-2018-0206.

[301] A.Y. Vorobyev, C. Guo, Enhanced absorptance of gold following multipulse femtosecond laser ablation, Phys. Rev. B. 72 (2005) 1–5. https://doi.org/10.1103/PhysRevB.72.195422.

[302] A. Rudenko, A. Abou-Saleh, F. Pigeon, C. Mauclair, F. Garrelie, R. Stoian, J.P. Colombier, High-frequency periodic patterns driven by non-radiative fields coupled with Marangoni convection instabilities on laser-excited metal surfaces, Acta Mater. 194 (2020) 93–105. https://doi.org/10.1016/j.actamat.2020.04.058.

[303] Y. Fuentes-Edfuf, J.A. Sánchez-Gil, C. Florian, V. Giannini, J. Solis, J. Siegel, Surface Plasmon Polaritons on Rough Metal Surfaces: Role in the Formation of Laser-Induced Periodic Surface Structures, ACS Omega. 4 (2019) 6939–6946. https://doi.org/10.1021/acsomega.9b00546.

[304] J. Bonse, S. Gräf, Maxwell Meets Marangoni—A Review of Theories on Laser-Induced Periodic Surface Structures, Laser Photonics Rev. 14 (2020) 1–25. https://doi.org/10.1002/lpor.202000215.

[305] J. Bonse, J. Krüger, S. Höhm, A. Rosenfeld, Femtosecond laser-induced periodic surface structures, J. Laser Appl. 24 (2012) 042006. https://doi.org/10.2351/1.4712658.

[306] T.T.D. Huynh, A. Petit, N. Semmar, Picosecond laser induced periodic surface structure on copper thin films, Appl. Surf. Sci. 302 (2014) 109–113. https://doi.org/10.1016/j.apsusc.2013.10.172.

[307] C.L. Chang, C.W. Cheng, J.K. Chen, Femtosecond laser-induced periodic surface structures of copper: Experimental and modeling comparison, Appl. Surf. Sci. 469 (2019) 904–910. https://doi.org/10.1016/j.apsusc.2018.11.059.

[308] J. JJ. Nivas, M. Hu, M. Valadan, M. Salvatore, R. Fittipaldi, M. Himmerlich, E. Bez, M. Rimoldi, A. Passarelli, S.L. Oscurato, A. Vecchione, C. Altucci, S. Amoruso, A. Andreone, S. Calatroni, M. Rosaria Masullo, Laser-induced periodic surface structuring for secondary electron yield reduction of copper: dependence on ambient gas and wavelength, Appl. Surf. Sci. 622 (2023) 156908. https://doi.org/10.1016/j.apsusc.2023.156908.

[309] C. Florian, J.L. Déziel, S. V. Kirner, J. Siegel, J. Bonse, The role of the laser-induced oxide layer in the formation of laser-induced periodic surface structures, Nanomaterials. 10 (2020). https://doi.org/10.3390/nano10010147.

[310] M.I. Arzuov, A.I. Barchukov, F. V Bunkin, N.A. Kirichenko, V.I. Konov, B.S. Luk'yanchuk, Influence of interference effects in oxide films on the kinetics of laser heating of metals, Sov. J. Quantum Electron. 9 (1979) 281–284. https://doi.org/10.1070/qe1979v009n03abeh008765.

[311] K.F. Kusano, M. Uchikoshi, K. Mimura, M. Isshiki, Low-Temperature Oxidation of Cu(100), Cu(110) and Cu(111), Oxid. Met. 82 (2014) 181–193. https://doi.org/10.1007/s11085-014-9486-3.

[312] K. Fujita, D. Ando, M. Uchikoshi, K. Mimura, M. Isshiki, New model for low-temperature oxidation of copper single crystal, Appl. Surf. Sci. 276 (2013) 347–358. https://doi.org/10.1016/j.apsusc.2013.03.096.

[313] C.H. Tseng, K.N. Tu, C. Chen, Comparison of oxidation in uni-directionally and randomly oriented Cu films for low temperature Cu-to-Cu direct bonding, Sci. Rep. 8 (2018) 10671. https://doi.org/10.1038/s41598-018-28812-0.

[314] J.O. Porteus, D.L. Decker, J.L. Jernigan, W.N. Faith, M. Bass, 17.7 Evaluation of Metal Mirrors for High-Power Applications by Multi-Threshold Damage Analysis, IEEE J. Quantum Electron. 14 (1977) 896–897. https://doi.org/10.1109/JQE.1977.1069587.

[315] C. Gattinoni, A. Michaelides, Atomistic details of oxide surfaces and surface oxidation: the example of copper and its oxides, Surf. Sci. Rep. 70 (2015) 424–447. https://doi.org/10.1016/j.surfrep.2015.07.001.

[316] K. Nassau, The fifteen causes of colour: The physics and chemistry of colour, 1987. https://doi.org/10.1002/col.5080120105.

[317] L.I. Berger, M. Frenkel, C.A. Koh, P.E. Bradley, J.R. Fuhr, W.H. Koppenol, T.J. Bruno, CRC Handbook of Chemistry and Physics, 2014.

[318] M. Anderson, A. Ediger, A. Tsubaki, C. Zuhlke, D. Alexander, G. Gogos, J.E. Shield, Surface and microstructure investigation of picosecond versus femtosecond laser pulse processed copper, Surf. Coatings Technol. 409 (2021) 126872. https://doi.org/10.1016/j.surfcoat.2021.126872.

[319] N. Tsakiris, K.K. Anoop, G. Ausanio, M. Gill-Comeau, R. Bruzzese, S. Amoruso, L.J. Lewis, Ultrashort laser ablation of bulk copper targets: Dynamics and size distribution of the generated nanoparticles, J. Appl. Phys. 115 (2014) 243301. https://doi.org/10.1063/1.4885196.

[320] P. Buffat, J.P. Borel, Size effect on the melting temperature of gold particles, Phys. Rev. A. 13 (1976) 2287–2298. https://doi.org/10.1103/PhysRevA.13.2287.

[321] S. Slawik, S. Bernarding, F. Lasagni, C. Navarro, A. Periñán, F. Boby, S. Migot-Choux, J. Domínguez, F. Mücklich, Microstructural analysis of selective laser melted Ti6Al4V modified by laser peening and shot peening for enhanced fatigue characteristics, Mater. Charact. 173 (2021) 110935. https://doi.org/10.1016/j.matchar.2021.110935.

[322] J. Vincenc Oboňa, V. Ocelík, J.C. Rao, J.Z.P. Skolski, G.R.B.E. Römer, A.J. Huis In ’T Veld, J.T.M.D. Hosson, Modification of Cu surface with picosecond laser pulses, Appl. Surf. Sci. 303 (2014) 118–124. https://doi.org/10.1016/j.apsusc.2014.02.104.

[323] M.P. Echlin, M.S. Titus, M. Straw, P. Gumbsch, T.M. Pollock, Materials response to glancing incidence femtosecond laser ablation, Acta Mater. 124 (2017) 37–46. https://doi.org/10.1016/j.actamat.2016.10.055.

[324] P.P. Rajeev, S. Sengupta, A. Das, P. Taneja, P. Ayyub, P.K. Kaw, G.R. Kumar, Laser absorption in short-lived metal and nanoplasmas, Appl. Phys. B Lasers Opt. 80 (2005) 1015–1019. https://doi.org/10.1007/s00340-005-1827-0.

[325] X. Sedao, M. V. Shugaev, C. Wu, T. Douillard, C. Esnouf, C. Maurice, S. Reynaud, F. Pigeon, F. Garrelie, L. V. Zhigilei, J.P. Colombier, Growth Twinning and Generation of High-Frequency Surface Nanostructures in Ultrafast Laser-Induced Transient Melting and Resolidification, ACS Nano. 10 (2016) 6995–7007. https://doi.org/10.1021/acsnano.6b02970.

[326] Spectra-physics, Mai Tai Series, (2011) 1–2.

[327] Spectra-Physics, Spitfire Ti:Sapphire Regenerative Amplifier, (2006) 116.

[328] F. Korte, S. Nolte, B.N. Chichkov, T. Bauer, G. Kamlage, T. Wagner, C. Fallnich, H. Welling, Far-field and near-field material processing with femtosecond laser pulses, Appl. Phys. A Mater. Sci. Process. 69 (1999) 7–11. https://doi.org/10.1007/s003390051346.

[329] F. Korte, J. Serbin, J. Koch, A. Egbert, C. Fallnich, A. Ostendorf, B.N. Chichkov, Towards nanostructuring with femtosecond, Appl. Phys. A. 77 (2003) 229–235. https://doi.org/10.1007/s00339-003-2110-z.

[330] Z. Liu, X.K. Meng, T. Recktenwald, F. Mücklich, Patterned intermetallic reaction of Ni 3 Al by laser interference structuring, Mater. Sci. Eng. A342. (2003) 2002–2004.

[331] C. Daniel, A. Lasagni, F. Mücklich, Stress and texture evolution of Ni y Al multi-film by laser interference irradiation, Surf. Coatings Technol. 181 (2004) 478–482. https://doi.org/10.1016/j.surfcoat.2003.10.091.

[332] A. Lasagni, F. Mücklich, Study of the multilayer metallic films topography modified by laser interference irradiation, Appl. Surf. Sci. 240 (2005) 214–221. https://doi.org/10.1016/j.apsusc.2004.06.143.

[333] P. Li, U. Bakowsky, F. Yu, C. Loehbach, F. Mücklich, C. Lehr, Laser Ablation Patterning by Interference Induces Directional Cell Growth, IEEE Trans. Nanobioscience. 2 (2003) 138–145.

[334] E. Favret, O. Fuentes, F. Yu, RIMAPS and variogram analysis of the surface topography induced by laser interference micropatterning, Appl. Surf. Sci. 230 (2004) 60–72. https://doi.org/10.1016/j.apsusc.2003.12.036.

[335] A. Lasagni, C. Daniel, F. Mücklich, Laser interference metallurgy — periodic surface patterning and formation of intermetallics, Intermetallics. 13 (2005) 437–442. https://doi.org/10.1016/j.intermet.2004.07.005.

[336] A.F. Lasagni, Advanced design of periodical structures by laser interference metallurgy in the micro / nano scale on macroscopic areas, 2006.

[337] F. Mücklich, A. Lasagni, D. Claus, Laser Interference Metallurgy – using interference as a tool for micro / nano structuring, Int. J. Mater. Res. 97 (2006) 1337–1344.

[338] B.A.F. Lasagni, D.F. Acevedo, C.A. Barbero, F. Mücklich, One-Step Production of Organized Surface Architectures on Polymeric Materials by Direct Laser Interference Patterning **, Adv. Eng. Mater. 9 (2007) 99–103. https://doi.org/10.1002/adem.200600171.

[339] A.F. Lasagni, H.K. Schmidt, F. Mücklich, Direct laser interference patterning of multi-walled carbon nanotube-based transparent conductive coatings, Appl. Surf. Sci. 254 (2008) 5874–5878. https://doi.org/10.1016/j.apsusc.2008.03.140.

[340] T. Kondo, S. Matsuo, S. Juodkazis, H. Misawa, Femtosecond laser interference technique with diffractive beam splitter for fabrication of three-dimensional photonic crystals, Appl. Phys. Lett. 79 (2001) 725–727. https://doi.org/10.1063/1.1391232.

[341] T. Kondo, S. Matsuo, S. Juodkazis, V. Mizeikis, H. Misawa, Multiphoton fabrication of periodic structures by multibeam interference of femtosecond pulses, Appl. Phys. Lett. 82 (2003) 2758–2760. https://doi.org/10.1063/1.1569987.

[342] T. Jia, M. Baba, M. Suzuki, R. a Ganeev, H. Kuroda, J. Qiu, X. Wang, R. Li, Z. Xu, Fabrication of two-dimensional periodic nanostructures by two-beam interference of femtosecond pulses., Opt. Express. 16 (2008) 1874–8. https://doi.org/10.1364/OE.16.001874.

[343] A.F. Lasagni, P. Shao, J.L. Hendricks, C.M. Shaw, D.C. Martin, S. Das, Direct fabrication of periodic patterns with hierarchical sub-wavelength structures on poly(3,4-ethylene dioxythiophene)-poly(styrene sulfonate) thin films using femtosecond laser interference patterning, Appl. Surf. Sci. 256 (2010) 1708–1713. https://doi.org/10.1016/j.apsusc.2009.09.099.

[344] L. Reinert, F. Lasserre, C. Gachot, P. Grützmacher, T. Maclucas, N. Souza, F. Mücklich, S. Suarez, Long-lasting solid lubrication by CNT-coated patterned surfaces, Sci. Rep. 7 (2017) 1–13. https://doi.org/10.1038/srep42873.

[345] C. Gachot, A. Rosenkranz, R. Leander, E. Ramos-Moore, N. Souza, M.H. Müser, F. Mücklich, Dry Friction Between Laser-Patterned Surfaces : Role of Alignment , Structural Wavelength and Surface Chemistry, (2013) 193–202. https://doi.org/10.1007/s11249-012-0057-y.

[346] P.G. Grützmacher, A. Rosenkranz, A. Szurdak, M. Grüber, C. Gachot, G. Hirt, F. Mücklich, Multi-scale surface patterning – an approach to control friction and lubricant migration in lubricated systems, Ind. Lubr. Tribol. 71 (2019) 1007–1016. https://doi.org/10.1108/ILT-07-2018-0273.

[347] B.M. Soldera, K. Taretto, J. Berger, Potential of Photocurrent Improvement in m c-Si : H Solar Cells with TCO Substrates Structured by Direct Laser Interference Patterning, Adv. Eng. Mater. 18 (2016) 1674–82. https://doi.org/10.1002/adem.201600225.

[348] P.G. Grützmacher, A. Rosenkranz, C. Gachot, How to guide lubricants – Tailored laser surface patterns on stainless steel, Appl. Surf. Sci. 370 (2016) 59–66. https://doi.org/10.1016/j.apsusc.2016.02.115.

[349] S. Milles, J. Dahms, M. Soldera, A.F. Lasagni, Stable superhydrophobic aluminum surfaces based on laser-fabricated hierarchical textures, Materials (Basel). 14 (2021) 1–17. https://doi.org/10.3390/ma14010184.

[350] C. Zwahr, D. Günther, T. Brinkmann, N. Gulow, S. Oswald, Laser Surface Pattering of Titanium for Improving the Biological Performance of Dental Implants, Adv. Healthc. Mater. 6 (2017) 1–9. https://doi.org/10.1002/adhm.201600858.

[351] R. Schieber, F. Lasserre, M. Hans, M. Fernández-yagüe, M. Díaz-ricart, G. Escolar, M. Ginebra, F. Mücklich, M. Pegueroles, Direct Laser Interference Patterning of CoCr Alloy Surfaces to Control Endothelial Cell and Platelet Response for Cardiovascular Applications, Adv. Healthc. Mater. 6 (2017) 1–14. https://doi.org/10.1002/adhm.201700327.

[352] C. Strehmel, H. Perez-hernandez, Z. Zhang, A. Lo, F. Lasagni, M.C. Lensen, Geometric Control of Cell Alignment and Spreading within the Confinement of Antiadhesive Poly(Ethylene Glycol) Microstructures on Laser-Patterned Surfaces, (2015). https://doi.org/10.1021/ab5001657.

[353] B. Voisiat, W. Wang, M. Holzhey, A.F. Lasagni, Improving the homogeneity of diffraction based colours by fabricating periodic patterns with gradient spatial period using Direct Laser Interference Patterning, Sci. Rep. 9 (2019) 7801. https://doi.org/10.1038/s41598-019-44212-4.

[354] M.D. Alessandria, F. Mücklich, Tailoring the chemical behavior of aluminum for selective etching by laser interference metallurgy, Appl. Phys. A. 98 (2010) 311–320. https://doi.org/10.1007/s00339-009-5398-5.

[355] A.A. Maznev, T.F. Crimmins, K.A. Nelson, How to make femtosecond pulses overlap, Opt. Lett. 23 (1998) 1378. https://doi.org/10.1364/OL.23.001378.

[356] S. Indrisiunas, B. Voisiat, G. Raciukaitis, Direct Laser Beam Interference Patterning Technique for Fast High Aspect Ratio Surface Structuring, Proc. SPIE. 9350 (2015). https://doi.org/10.1117/12.2079826.

[357] M. Gedvilas, S. Indrišiunas, B. Voisiat, E. Stankevičius, A. Selskis, G. Račiukaitis, Nanoscale thermal diffusion during the laser interference ablation using femto-, pico-, and nanosecond pulses in silicon, Phys. Chem. Chem. Phys. 20 (2018) 12166–12174. https://doi.org/10.1039/c7cp08458g.

[358] F. Fraggelakis, G.D. Tsibidis, E. Stratakis, Tailored Sub-micrometer Periodic Surface Structures via Ultrashort Pulsed Direct Laser Interference Patterning, Phys. Rev. B. 103 (2021) 054105. https://doi.org/10.1103/physrevb.103.054105.

[359] A. Lasagni, M. D'Alessandria, R. Giovanelli, F. Mücklich, Advanced design of periodical architectures in bulk metals by means of Laser Interference Metallurgy, Appl. Surf. Sci. 254 (2007) 930–936. https://doi.org/10.1016/j.apsusc.2007.08.010.

[360] F. Fraggelakis, G.D. Tsibidis, E. Stratakis, Ultrashort pulsed laser induced complex surface structures generated by tailoring the melt hydrodynamics, Opto-Electronic Adv. 5 (2022) 210052. https://doi.org/10.29026/oea.2022.210052.

[361] B.V. Lang, A. Rank, Large Area One-Step Fabrication of Three-Level Multiple-Scaled Micro and Nanostructured Nickel Sleeves for Roll-to-Roll Hot Embossing **, (2017) 1–9. https://doi.org/10.1002/adem.201700126.

[362] C. Zwahr, R. Helbig, C. Werner, A.F. Lasagni, Fabrication of multifunctional titanium surfaces by producing hierarchical surface patterns using laser based ablation methods, Sci. Rep. 9 (2019) 1–13. https://doi.org/10.1038/s41598-019-43055-3.

[363] A. Sikora, M. Faucon, L. Gemini, R. Kling, G. Mincuzzi, LIPSS and DLIP: From hierarchical to mutually interacting, homogeneous, structuring, Appl. Surf. Sci. 591 (2022) 153230. https://doi.org/10.1016/j.apsusc.2022.153230.

[364] A. Nakajima, M. Omiya, J. Yan, Generation of micro/nano hybrid surface structures on copper by femtosecond pulsed laser irradiation, Nanomanufacturing Metrol. (2022). https://doi.org/10.1007/s41871-022-00135-9.

[365] M. Ellman, A. Rodríguez, N. Pérez, M. Echeverria, Y.K. Verevkin, C.S. Peng, T. Berthou, Z. Wang, S.M. Olaizola, I. Ayerdi, High-power laser interference lithography process on photoresist: Effect of laser fluence and polarisation, Appl. Surf. Sci. 255 (2009) 5537–5541. https://doi.org/10.1016/j.apsusc.2008.07.201.

[366] S. Indrišiūnas, B. Voisiat, M. Gedvilas, G. Račiukaitis, Polarisation Control in Direct Laser Interference Ablation Setup for Flexible Generation of Periodic Patterns, Proc. LPM2017. (2017) 1–5. http://www.jlps.gr.jp/lpm/lpm2017/.

[367] B. Voisiat, C. Zwahr, A.F. Lasagni, Growth of regular micro-pillar arrays on steel by polarization-controlled laser interference patterning, Appl. Surf. Sci. 471 (2019) 1065–1071. https://doi.org/10.1016/j.apsusc.2018.12.083.

[368] C. Zwahr, B. Voisiat, A. Welle, D. Günther, One-Step Fabrication of Pillar and Crater-Like Structures on Titanium Using Direct Laser Interference Patterning, 1800160 (2018) 1–9. https://doi.org/10.1002/adem.201800160.

[369] S. Indrišiūnas, B. Voisiat, M. Gedvilas, G. Račiukaitis, New opportunities for custom-shape patterning using polarization control in confocal laser beam interference setup, J. Laser Appl. 29 (2017) 011501. https://doi.org/10.2351/1.4976679.

[370] L. Caro-Lara, I.T. Vargas, E. Ramos-Moore, C. Galarce, D. Diaz-Droguett, G.E. Pizarro, Enhancing the contact-killing effect of copper by surface laser texturing, J. Environ. Chem. Eng. 10 (2022) 108497. https://doi.org/10.1016/j.jece.2022.108497.

[371] J. Long, P. Fan, D. Gong, D. Jiang, H. Zhang, L. Li, M. Zhong, Superhydrophobic surfaces fabricated by femtosecond laser with tunable water adhesion: From lotus leaf to rose petal, ACS Appl. Mater. Interfaces. 7 (2015) 9858–9865. https://doi.org/10.1021/acsami.5b01870.

[372] Holleman A. F., N. Wiberg, Lehrbuch der Anorganischen Chemie, 2007.

Figures